# The stratigraphy and emplacement of welded and lava-like ignimbrites of the Las Cañadas Caldera, Tenerife

Pamela Louise Campbell

BSc (Hons), University of Glasgow


Submitted in fulfilment of the requirements for the degree of Doctor of Philosophy

School of Geographical and Earth Sciences

College of Science and Engineering

University of Glasgow

September 2020

Chaos is where things are so complex you can’t handle it, and order is where things are so rigid that it’s too restrictive. In between there’s a place, a place that’s meaningful.

- Jordan B. Peterson

# Abstract

Lava-like and welded pyroclastic deposits are commonly associated with vent-proximal, high-temperature explosive eruptions, and due to the nature of welding of these deposits, evidence of the depositional and sedimentological aspect of the deposit is often absent. As a result, the dynamics and mechanisms of deposition and welding processes in high-temperature eruptions are poorly understood and this has often led to the misinterpretation of such welded deposits. This limited understanding can lead to misleading interpretations and underestimations of the potential hazards associated with active volcanic environments. This project is an investigation into the behaviour and emplacement of the welded and lava-like deposits belonging to the Ucanca and Guajara Formations of the southern flank of the Las Cañadas Caldera, Tenerife.

Six individual eruptive packages are described and documented, representing explosive, destructive and constructive stages of the Ucanca and Guajara caldera-forming episodes. A systematic field campaign involving mapping and detailed stratigraphic logging of the deposits, combined with methodological sampling for petrographic, geochemical and thermal analysis, together with determination of the rocks' physical properties, has established the emplacement dynamics of the units, as well as geochemical and welding variations throughout individual units and across the proposed members. The description and analysis of welding textures at different scales allowed for sensitive mapping of welding intensity, providing insights into the controls and depositional factors contributing to the deformation of pyroclasts, both syn- and post-emplacement.

Together these data provide the first detailed robust interpretation of the Ucanca and Guajara deposits, a key stage in the volcanic evolution of Tenerife. Extensive evidence is presented in support of their interpretation as deposits from a series of extremely high-grade pyroclastic density currents (PDCs). A variety of novel and exciting welding textures are documented, providing insight into the emplacement dynamics, thermal histories, and constraints on welding such as current interaction with variable lithic input. This work proposes a new classification system for high-grade ignimbrites, which are overly simplified and omitted in existing schemes, and may be applied to deposits in other volcanic settings.

# Table of Contents

# List of Figures

# List of Tables

# List of Accompanying Material

# Acknowledgements

To my friend and supervisor Davie Brown, who has taught me so much, thank you for the endless support and encouragement over the years, and for the opportunity to travel the world, from Ardnamurchan to Engare Sero, to study ignimbrites. I am sure it has not always been an easy job but thank you for always believing in me.

With thanks to the School of Geographical and Earth Sciences and the College of Science of Engineering (UofG) for supporting my research with mobility funding, conference support, and the Michael Golden and Sir Alwyn Williams Postgraduate Scholarships. I would also like to thank the Richard Stapley Educational Trust, the Geological Society, Volcanic and Magmatic Studies Group, Terra Tek Ltd, and MATtest Ltd for their support and generosity in funding my fieldwork and analysis.

To the brilliant support and technical staff – John Gilleece, Kenny Roberts, and Robert McDonald, for all your time and teaching me the art of preparing thin sections and flying drones, to Anne Dunlop and Aileen Quinn for all your encouragement and support in my multiple GTA roles in the School, and to Nic Odling at Edinburgh for your time and facilitating my analysis.

To Kai Hess at LMU for your support and guidance with my thermal analysis, and for the valuable skype discussions, thank you.

To my field assistants - Bob, Sapphire and my guapa chica Claire. Thanks for all the fieldwork laughs, leche leches, and for suffering the crazy roads, broken coccyx adventures, and barrancos of death.

To my 206 compadres - Eamon and Allan, thanks for making the office a place I wanted to be - misery sure loves company! Thanks for all the laughs (mostly at the expense of Allan…).

To those in Vo@G, past and present - Brian, Iain Jonny, Sapphire, Charlotte, Heather, and Katie, thanks for the friendship, advice and encouragement. Special thanks to Iain for Zoom discussions and reading over my drafts.

To my mentors in the department, and those who have taken me under their wing – Hannah Mathers, Mike Keen and Cristina Persano, you have done more for me than you will know. Thank you for always cheering me on.

Lastly, to my husband Ruairidh, forever my constant in all the chaos, for everything.

In memory of Andrew Brown

# Author's Declaration

I declare that this thesis, except where acknowledged to others, represents my own work carried out in the School of Geographical and Earth Sciences, University of Glasgow. The research submitted here has not been submitted for any other degree at the University of Glasgow, nor at any other institution. Any published or unpublished work by authors has been given full acknowledgement in the text.

Pamela Campbell

# Chapter 1

## 1. Introduction

The volcanic deposits of the Ucanca and Guajara Formations of the Las Cañadas Caldera of Tenerife represent significant periods of explosivity, construction, and destruction of the volcano. Despite the controversy surrounding the formation of Las Cañadas Caldera, there is limited documentation and understanding of the Ucanca and Guajara deposits, their eruptive stratigraphy, and their mode of emplacement. This thesis reports an investigation into the emplacement mechanisms of these caldera-forming eruptions, the deposits of which are primarily interpreted as ignimbrites. A multi-faceted approach combining field analysis and a variety of analytical techniques is used to determine the nature of the welding and deformation experienced by the deposits, both syn- and post-emplacement.

The southern wall of the Las Cañadas Caldera provides excellent exposure and access of stacked, variably welded and lava-like deposits, providing an ideal location to investigate the nature and control of vent-proximal welding processes and the emplacement mechanisms of welded and rheomorphic lava-like ignimbrites.

### 1.1. Research aims

There are two main areas of focus of this project:

i. To build upon the volcanic stratigraphy of the Ucanca Formation and lower Guajara Formation, and establish their relationships and place in the formation of the Las Cañadas Caldera;

ii. To investigate the emplacement and deformation of the welded and lava-like deposits, using both a field-based and analytical approach, with the aim of constructing a stronger framework for classifying welding intensity and understanding the processes associated with high-grade pyroclastic eruptions.

## 1.2. Methods of study

This research combines data from three months of fieldwork on the southern Las Cañadas caldera wall, Tenerife, Canary Islands, and from a variety of analytical and experimental methods. Field mapping and detailed stratigraphic logging using a lithofacies approach tracked the lateral and vertical variation across the deposits, particularly concerning the intensity of welding. A suite of samples collected from the base, middle, and uppermost horizons of each unit were processed for a combination of: i) geochemical analysis using X-ray fluorescence spectrometry (XRF) and electron microprobe analysis (EMPA); ii) analysis of the physical properties, including porosity, density and rock strength; iii) petrographic analysis, including optical microscopy and scanning electron microscopy (SEM); and iv) thermogravimetric (TGA) analysis using differential scanning calorimetry (DSC). Together, these data were used to investigate the nature of compositional variation, welding intensity, textural variation through the stratigraphy, and the controls on welding intensity respectively. Details of these techniques and methodologies are discussed in the relevant chapters. Four accompanying appendices of raw data and supplementary material are also included in the thesis.

## 1.3. Project outline and objectives

An overview of Chapters 2-8 is presented below. The chapters are structured with the intention of presenting a comprehensive, multi-faceted analysis of the deposits, building up to, and in support of, the interpretive emplacement model presented in Chapter 7.

**Chapter 2** presents a review of pyroclastic density current transport and ignimbrite deposition, focussing on the factors controlling welding and rheomorphism during these stages of emplacement, and outlines the underpinning approaches used in the descriptions of units, and the terminology used throughout this study.

**Chapter 3** covers the regional geological context of Tenerife and the structure and formation of the Las Cañadas Caldera. Previous work and interpretations on

the deposits of the Ucanca and Guajara Formations are reviewed, documenting the controversial and fleeting views on many of these units.

**Chapter 4** presents the field-based study of the deposits of the Ucanca and Guajara Formations with the main objectives of: i) documenting and establishing the stratigraphy and field relationships of the deposits associated with each Formation; ii) mapping the distribution, thickness and lateral extent of units; iii) documenting the range of lithofacies and welding intensities exhibited by the deposits; iv) developing interpretations for the deposit, based largely on the lithofacies approach of Branney & Kokelaar (2002); v) using the field analysis to interpret the rheomorphic fabrics and structures exhibited by many of the deposits.

**Chapter 5** demonstrates the approach used in describing welding intensities of high-grade ignimbrites, and develops a semi-quantitative welding classification framework accommodating higher intensities of welding and rheomorphism, based on both textural criteria and measurements of the physical properties (e.g. porosity, density, oblateness, and rock strength), building upon the ranking scheme of Quane & Russell (2002).

The geochemistry and petrology of the mapped units is outlined in **Chapter 6,** based on XRF analysis and EMPA, with the main objectives of: i) characterising the composition and petrography of the deposits; ii) establishing the nature of chemical stratigraphy; and iii) elucidating the textural description of the welded facies from Chapter 5.

**Chapter 7** discusses further insights into the controls on welding and emplacement processes, presenting results from investigation into the thermal history from TGA of glasses and modelling of the viscosity and water content, and presents a summary of the structural and textural evidence, leading to illustrative emplacement models for each of the members.

The main findings and implications of this research project is summarised in **Chapter 8,** and discusses the areas planned for future studies.

# Chapter 2

# 2. Ignimbrites: their emplacement and welding

The general term 'ignimbrite' refers to the deposits, formed by rapid sedimentation, of pyroclastic density currents during explosive volcanism (often previously referred to as ash-flow tuffs in the literature) (Marshall, 1935; Branney & Kokelaar, 2002). Pyroclastic density currents (PDCs) are density-driven, ground-hugging, inhomogeneous multi-phase mixtures of fluidised volcanic particles and gas (volatiles and atmospheric gas) expelled during explosive volcanism (Freundt & Bursik, 1998). Deposits of PDCs are highly variable in terms of scale and volume, ranging from a few hundred $km^2$ to tens of thousands $km^2$ (Cas et al., 2011; Brown & Andrews, 2015). With the capacity to cover distances of up to >100 km, transporting thousands of cubic kilometres of material in extremely short timescales (seconds to hours), they are considered to be one of the greatest hazards associated with volcanism due to their volatile and intractable nature (Auker et al., 2013). This chapter outlines the transportation and deposition of ignimbrites, focussing on the welding processes during these stages of emplacement.

## 2.1. Ignimbrite emplacement

Without any quantifiable means of documenting their transport and emplacement, our understanding of PDCs is restricted to careful and rigorous analysis of field deposits (e.g. Wilson 1985; Wilson & Walker, 1982; Brown & Branney 2004i), and experimental laboratory-based modelling (e.g. Bursik & Woods, 2000, Dade & Huppert, 1996), albeit remote sensing now offers further opportunities in this area (e.g. Pallister et al., 2019; Scharff et al., 2019). Modelling the development and emplacement mechanisms of ignimbrites using detailed lithofacies classification (e.g. Branney & Kokelaar, 2002; Brown & Branney, 2004ii) and interpretation is fundamental in understanding these deposits, as well as the hazards of PDCs and mitigating the associated risks. Due to the high frequency of PDCs in volcanic environments world-wide, and their devasting impacts, efforts towards better understanding of PDC behaviour and generation is a high priority in the field of volcanology.

### 2.1.1. PDC behaviour

The theory and understanding of the transport and behaviour of pyroclastic density currents and the emplacement mechanisms of ignimbrites is an evolving science, based largely on interpretive field studies which gained momentum after the late 1960's, with a strong focus on large scale caldera volcanoes of the western USA, the Mediterranean region, South East Asia, South America, New Zealand and the Canary Islands (Branney & Kokelaar, 2002). Much of the pioneering work is based on localised, small scale recent deposits, due to their historic significance and good preservation potential (e.g. Mt St. Helens: Rowley et al., 1985; Soufriere Hills: Loughlin et al., 2000; Pinatubo: Scott et al., 1996). Due to the complex interaction between the various processes and conditions that control the characteristics of ignimbrites, understanding of their depositional mechanics remains incomplete.

PDCs are typically formed during the disintegration and fluidisation of magma and rock fragments during an eruption, which can result in a fountain-like collapse of an eruption column, from lateral blasts of material, or high temperature avalanches associated with collapsing lava domes (Branney & Kokelaar, 2002). The resulting density driven currents can extend to over 100 km and are capable of bypassing and surmounting topographic obstacles and depressions, due to thermal expansion and the mobility of exsolved gasses from entrapped particles within the current (Sparks, 1976). Deposits typically consist of a combination of pumice and lithic lapilli within a matrix of ash, vitric shards (i.e. cuspate and bubble wall shards) and crystal fragments, and it is estimated that particles under 4 mm in diameter make up over 50% of a typical tuff deposit (Ross & Smith, 1961; Fisher & Schmincke, 1984).

Deposits were sorted into two over-simplified, end-member categories; pyroclastic 'flow' and pyroclastic 'surge' deposits (Fisher & Schmincke 1984) as well as block-and ash-flow deposits (Branney & Kokelaar, 2002), according to their field characteristics, composition and internal structure. Pyroclastic flow deposits was the name given to widespread, massive, very poorly sorted lapilli tuffs, interpreted as deposits of 'en masse' deposition (Figure 2–1). These were thought to represent a reduced fraction of a partially-fluidised, laminar plug flow, that

deflates during motion and halts ‘en masse’ to produce a massive unit with an inversely graded base (Sparks, 1976; Sparks et al., 1973; Wright & Walker, 1981; Wright, 1981).

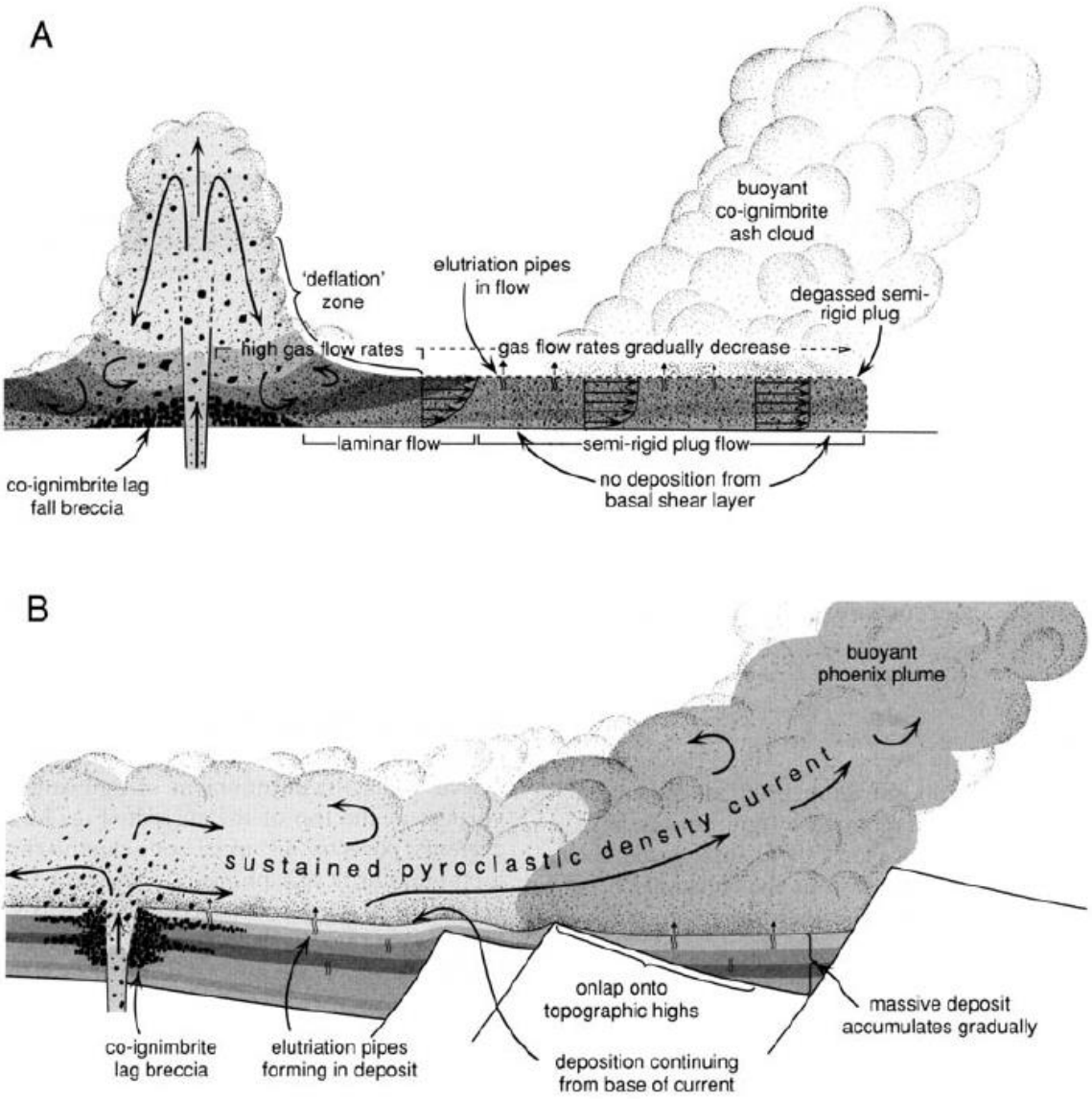


**Figure 2–1.** Ignimbrite emplacement models (Branney & Kokelaar, 2002, after Branney and Kokelaar, 1997) A: En-masse deposition model based on ideas from Wright & Walker, 1891; Druitt & Sparks, 1982; and Walker (1985). This model involves laminar, semi-fluidised flow, originating from a proximal ‘deflation zone’, which decelerates into semi-rigid plug-flow, before the deposit comes to a halt en masse. The upper, buoyant co-ignimbrite ash cloud is generated by elutriation (gas escape) from the laminar to semi-rigid plug-like fluidised pyroclastic flow. B: A sustained pyroclastic density current is generated, and expands, developing density stratification, with clast concentrations increasing towards the base along the runout due to sedimentation, density segregation and flow-boundary effects. Elutriation pipes are generated within the deposit, and not in the current. Less dense parts of the current are air lofted to form a buoyant phoenix plume (or co-ignimbrite plume).

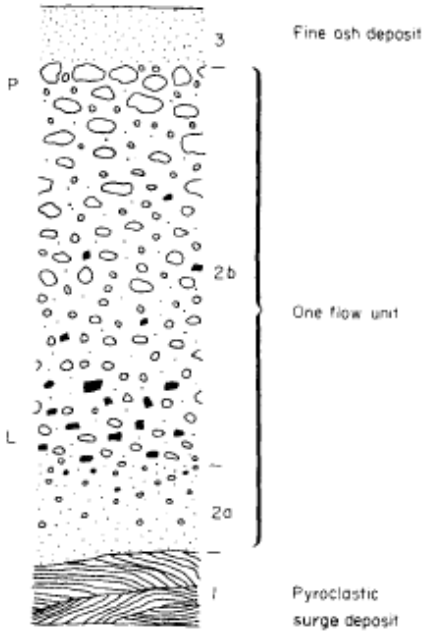


**Figure 2–2.** 'Standard ignimbrite flow unit' proposed by Sparks et al. (1973). A schematic section through the deposits of a (flow unit) pyroclastic eruption is represented, with a pyroclastic 'surge' deposit underlying layers 2 a and b which display reverse grading of pumice clasts, and normal grading of lithics; overlain by layer 3, a fine ash deposit.

The 'standard ignimbrite flow unit' (Figure 2–2) proposed by Sparks et al. (1973) accounted for the most common and widely observed grain size distributions found across ignimbrites, which envisaged en masse deposition from partially fluidised, highly concentrated, granular based currents. The en-masse emplacement model was highly influential among workers at the time (e.g. Sparks et al., 1973, Sparks, 1976, Sheridan, 1979; Walker et al., 1980; Wright & Walker, 1981; Freundt & Schmincke, 1986).

Pyroclastic surge deposits described ignimbrites that were significantly better sorted and with distinct bedding. In terms of fluid dynamics, it was initially suggested that the emplacement of pyroclastic flows were fundamentally different from those of pyroclastic surges. Fisher (1996) proposed that surge deposits were the result of progressive sedimentation from turbulent currents. This was later challenged, and it was suggested that surge deposits form stratigraphically from the base upwards in relation to the tail of pyroclastic flows, which form by progressive sedimentation (Walker et al., 1981; Wilson, 1985; Fisher, 1990) and can also be turbulent (Fisher et al., 1993; Baer et al., 1997).

However, it is now accepted that deposits are not restricted to the boundaries of these classifications and can grade into one another (Fisher 1990), such as seen in the lateral grading of a massive lapilli-tuff into the stratified facies at Mount St. Helens (Druitt 1992). It was realised that both particle-dominated ('pyroclastic flows') and dilute ('pyroclastic surges') currents can both develop density stratification, the deposits of each displaying various stratification, which made Fisher's (1966) 'en masse' model largely redundant, and it is likely that both end-members are formed through a similar, and interchangeable process (Branney and Kokelaar, 1992, 2002; Druitt, 1998).

The two-end member types proposed by Branney & Kokelaar (2002) are now widely accepted, and account for the density stratification observed across all deposits: (i) fully dilute PDCs, which are typically parallel and cross stratified due to the effects of a turbulent fluid phase, involving traction and saltation and lack of interaction between grains; and (ii) granular fluid-based PDCs, which are typically massive, diffuse bedded and exhibit various grading due to a particle content high enough to support collisional momentum between particles and/or fluid escape.

### 2.1.2. PDC eruptive styles

PDCs occur in a variety of forms from a variety of eruptive processes, originating from rapid disintegration and fluidisation of magma and rock fragments in short-lived, unsteady or long-lived sustained, unsteady to quasi-steady, eruptive pulses (Branney & Kokelaar, 2002). PDCs are typically generated during: i) fountain-style collapse of an eruption column (pyroclastic fountaining); ii) from laterally migrating blasts of material, or from: iii) collapsing lava domes resulting in pyroclastic avalanches (Branney and Kokelaar, 2002), the common models of which are outlined in Figure 2–3.

In PDCs that are generated explosively, the concentration and dispersion of clasts throughout a deposit is thought to reflect the eruption style (e.g. high or low pyroclastic fountaining) and is related to: the rheology of the magma and mass flux; the concentration of volatiles, species and exsolution rates; the nature and development of vesicles and cracks during fragmentation; and the size and concentration of accidental lithics (Branney and Kokelaar, 2002).

Early work focussing on 'ash-flow tuffs' and 'nueé ardentes' (early nomenclature for ignimbrites) in the early 1900's attributed welding (discussed further in Section 2.2) observed in these deposits to Peléan eruptions, following observations of deposits from the devastating 1902 eruptions of Mount Pelée, Martinique and Soufriére, St. Vincent (e.g. Anderson & Flett, 1903; Lacroix, 1903; 1904). These eruptions brought much attention to a previously undocumented type of volcanism. 'Nueé ardente' was coined by Lacroix (1903; 1904) to describe the nature of the 1902 Mount Pelée (Peléan) eruption and used frequently in the literature as a term for pyroclastic eruptions.

#### 2.1.2.1. Pyroclastic Fountaining

As PDCs behave as Newtonian, compressible fluids, they can be ejected from vents as sonic to supersonic over-pressured debris jets (Lagmay et al., 1999) during explosive eruptions. A PDCs behaviour is controlled by the mechanisms of pyroclastic fountaining (expansion of an over-pressurised jet), and many form as a result of gravitational collapse of these gas-thrust, over-pressured jets due to loss of momentum (failure to entrain enough air to remain buoyant) (Sparks et al., 1997; Branney & Kokelaar, 2002). These processes may be short-lived (highly-unsteady), or long-lived (Figure 2–3 a, d & e) sustained, unsteady to quasi-steady currents (Figure 2–3 b & c) (Branney & Kokelaar, 2002).

This process may be accompanied by a Plinian eruption column (Figure 2–1 b) above the pyroclastic fountain, resulting in a subsequent pumice fall (Sparks et al., 1985; Branney & Kokelaar, 2002). Low pyroclastic fountaining or 'boil-over' eruptions (Figure 2–3 c) (Cas and Wright, 1987; Fisher & Schmincke, 1984; Branney and Kokelaar, 2002) are typically prolonged, sustained eruptions, lacking the kinetic energy of that of a high-fountaining eruption, and may or may not be associated with a Plinian eruption column. Post-1980 eruptions of Mount St. Helens (Hoblitt, 1986) and Soufriere Hills Volcano collapse during the 1990's (Cole et al., 2002) are some historic instances of low-column eruptions.

#### 2.1.2.2. Dome Collapse

Historic examples of dome collapse are well documented at Merapi, Indonesia (Bardintzeff, 1984; Abdurachman et al., 2000; Newhall et al; 2000; Voight et al.,

2000); Unzen, Japan (Yamamoto et al., 1993; Ui et al., 1999); and Soufriere Hills, Montserrat (Cole et al., 2002; Wadge et al., 2014). The products of dome collapse-generated PDCs are typically small volume block-and-ash flow deposits (Boudon et al., 1993; Cole et al., 2002; Branney & Kokelaar, 2002). The collapse of lava domes, typically intermediate to silicic accumulations of viscous lavas associated with or within a conduit or vent (i.e., crypto-dome: Calder et al., 2015), or the collapse of a lava-flow front, can occur as a result of: gravitational collapse; gas over-pressurisation; instability and over-steepening of slope, or thermal fracture propagation due to a dome advancing over steep slopes (Calder et al., 2015; Fink, 1990) Figure 2–3 e).

#### 2.1.2.3. Lateral Blasts

PDCs can be generated as a result of rapid decompression of a dome, and explode laterally as decompression jets (Figure 2–3 d). The 1980 lateral blast of Mount St. Helens is the most famous example of a lateral blast, which occurred due to partial collapse of the volcano triggering decompression of a cryptodome (Hoblitt 1986). Known examples (e.g. the 1956 Bezymianny eruption: Bogoyavlenskaya et al., 1985; Belousov, 1996; and Soufriere Hills: Belousov et al., 2007) are typically short-duration and are associated with small-scale volume deposits.

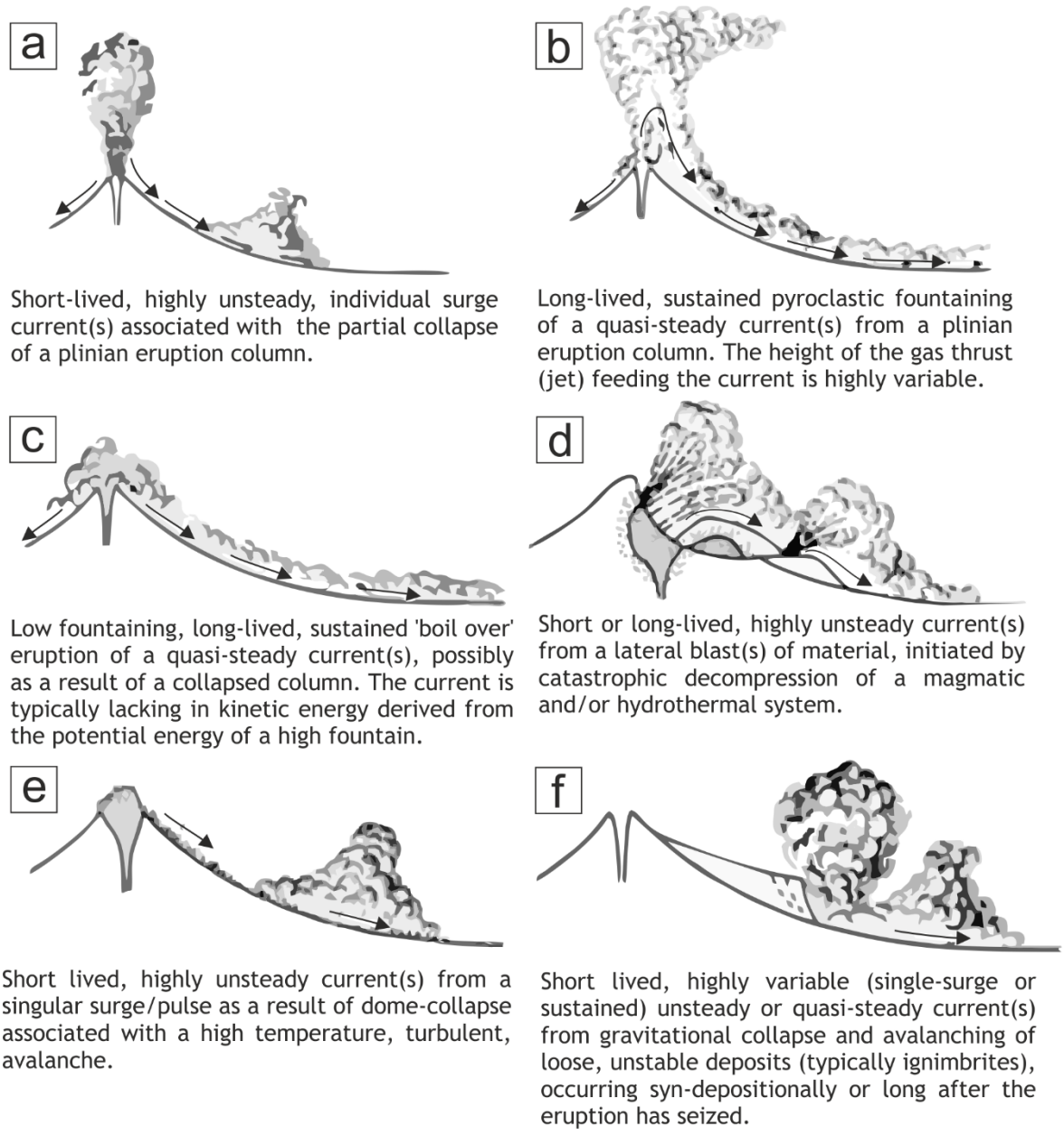


**Figure 2–3.** Summary of the generation and eruption styles of PDCs. Adapted after Branney & Kokelaar (2002) & Sparks (1985).

### 2.1.3. Emplacement and deposition

The concept of progressive aggradation describes the accumulating nature of a deposit by continuous sedimentation from the base upwards of a PDC (Fisher, 1966; Branney & Kokelaar, 1992, 2002). In a progressively aggrading current, laminar flow occurs at the base, underlying a turbulent upper flow. It is recognised that ignimbrites have similar characteristics to high concentration sedimentary flows, such as mud-flows and turbidity currents, the depositional processes of which, record progressive aggradation. Bouma sequences in turbidite

beds, are a series of vertical strata displaying vertical variations in internal structure, grain size and sorting that represent a single flow-unit (Bouma, 1962), and document the changes in the turbidity current mechanics and reflect the depositional boundary conditions. Similarly to Bouma sequences, PDCs can exhibit vertical gradational features, such as chemical zonation, diffuse and cross stratification, and lateral gradation and migrating flow structures and fabrics that record alternating flow directions, indicative of incremental deposition from a sustained current (Hughes & Druitt 1998; Branney & Kokelaar, 1992, 1997, 1998; Branney et al., 2004i).

Sparks et al. (1973) noted the difficulties in distinguishing between non-welded ignimbrites with reworked volcaniclastic, pumiceous mud-flow deposits, due to their textural and structural similarities, such as the debris flow deposits of northern Tenerife, which consist almost exclusively of pumice and ash. Mud-flows are similarly able to travel across wide areas over relatively low angle slopes and their deposits are poorly sorted, display reverse grading and occasionally display a reversely graded fine basal layer. Mud-flows travel by laminar flow and are able to suspend and transport large blocks due to their high particle concentration, which increases the apparent viscosity of flow several orders of magnitude greater than the supporting fluid (i.e. water) (Sparks et al., 1973). A similar process is suggested to account for a PDCs ability to carry large lithic blocks, resulting in subsequently poorly sorted deposits, as a current with a high particle concentration increases the yield strength of the supporting gas (Sparks et al. 1973), rather than by means of a turbulent flow, as suggested by Fisher (1966).

The deposit of a single PDC is termed a ‘flow unit’ (Smith, 1660; Sparks et al., 1973) and is bound by distinct temporal horizons. An individual ‘flow unit’ can be highly variable, and typically have non-welded bases and tops with gradual thinning at the edges of the unit (Henry & Wolff, 1992; Smith, 1960). Units with no distinct boundaries or internal marker horizons are understood to be the products of a sustained current, whereby continuous sedimentation, by means of progressive aggradation, leaves no evidence of punctuations between individual flow units (Fisher, 1966; Wilson & Hildreth, 2003; Branney & Kokelaar, 1992). Erosion and bypassing of subsequent PDCs can also obscure and obliterate evidence of individual flow units (e.g., Brown & Branney, 2004). Autobrecciated

basal layers, similarly to those of lava flows, can occur in the emplacement of PDCs, and where visible, can indicate flow unit boundaries. Post emplacement deformation (welding/ rheomorphism), overprinting by devitrification (vapour phase alteration), recrystallization (vapour phase crystallisation) and alteration can also obscure individual unit boundaries (Wilson and Walker, 1982; Wilson & Hildreth, 2003), discussed further in Section 2.2.6. During vapour phase alteration, the juvenile fragments, such as glass shards and pumice clasts are broken down or can be completely destroyed depending on the extent of alteration, forming axiolitic (elongate fibres) intergrowths of cristobalite, tridymite, and sodium-rich and potassium-rich alkali feldspars within the groundmass (Ross & Smith, 1961; McArthur et al., 1998). Mineralisation of cristobalite, tridymite, alkali feldspar and quartz can occur from precipitation of exsolved gasses and percolating heated groundwater during cooling, resulting in spherulites, which can occur independently of welding and compaction (Ross & Smith, 1961).

Post depositional structures are dependent on the process of cooling. 'Cooling unit' was introduced by Smith (1960) to describe the cooling history of a body of the material, which may be a single, or multiple individual flow units, that have the same cooling history, thus the basal unit was still hot when the latest material was emplaced (Wilson & Hildreth, 2003). A 'simple cooling unit' describes a body that has accumulated so rapidly that it has cooled as a singular unit, with the maximum welding occurring within the lower half of the deposit, and typically poorly welded at the base and top. A vitrophyre, the textural term for a porphyritic rock with a glassy groundmass (Vogelsang, 1872), marking the base of a cooling unit indicates a rapidly cooled deposit emplaced over a completely cooled ignimbrite and illustrates a hiatus in deposition, as does autobrecciation in the basal layer. The name given to a cooling history that strays from the simple cooling unit profile is a 'compound cooling unit' (Smith, 1960; Riehle, 1973). A deposit punctuated by significant hiatuses, such as erosional surfaces, sedimentary layers and lavas, with evidence that they have cooled prior to later emplacement are termed 'composite sheets' (Smith, 1960) and can contain both single and compound cooling units within them.

### 2.1.4. Flow boundary zone approach

The flow boundary zone (FBZ) approach, largely developed by Branney and Kokelaar (2002), is widely used and suggests that the conditions of the FBZ controls the physical characteristics of a deposit (e.g. Fisher, 1990). The FBZ (Figure 2–4) is the particle-dominated to non-particulate transition zone (PNP), consisting of the uppermost part of the aggrading deposit (non-particulate (NP)) and the basal part of the current (particle-dominated (P)) in which sorting and bedform characteristics are controlled by different conditions of the zone, such as particle concentration and shear distributions (Branney & Kokelaar, 2002). In simple terms, it is the interface between a PDC and the underlying substrate. The FBZ controls both the stratification and sorting of a progressively aggrading deposit, which is considered to reflect the properties and conditions of the depositional zone (Figure 2–4 & Figure 2–5).

Branney and Kokelaar (2002) propose four end-member types of FBZ (Figure 2–5), which have been widely implemented in the interpretation of a range of PDC deposits (e.g. Brown & Branney, 2004; Andrews & Branney, 2011):

i) direct-fall-out-dominated flow boundaries whereby individual particles settle out unhindered, involving very little particle interaction or lateral shear (Figure 2-5A);

ii) traction-dominated flow boundaries involve a fully-dilute current, where particles are supported by means of fluid turbulence and migrate along beds by traction and saltation, creating a sharp transition between the deposit and the overriding current (Figure 2-5B);

iii) granular-flow-dominated boundary zones, occur in granular-fluid based currents with high particle concentrations, which allows for collisional momentum between grains, and finally (Figure 2-5C);

iv) fluid-escape-dominated flow boundaries are granular fluid-based currents by which the upwards propulsion of fluid (escaping) is the dominant particle support system (Figure 2-5D, E, F, & G).

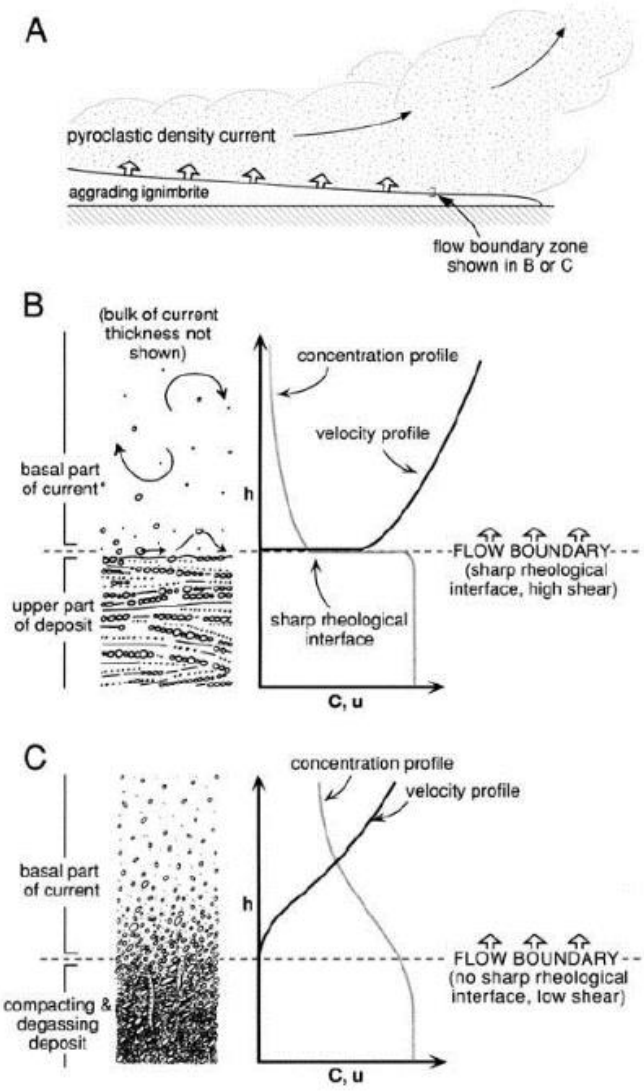


**Figure 2–4**. Progressive aggradation of a deposit from a sustained PDC, (shown by A) displaying the instantaneous positioning of a rising flow boundary zone (FBZ), including the lowermost part of the current, the flow boundary, and the upper-part of the forming deposit. B and C illustrate the two end-member models of FBZ (not including profiles above the FBZ). B: FBZ at the base of a low-concentration current, with a sudden increase in clast concentration, and an abrupt decrease in velocity down towards, and into the top of the aggrading deposit. Traction occurs due to impinging turbulence close to the flow boundary. C: FBZ at the base of a high-concentration current, with a gradual increase in clast concentration, and gradational decrease in velocity with depth through the flow boundary zone. Traction is inhibited at the flow boundary, due to concentrations approaching those of the underlying forming deposit, with low velocities so that a massive deposit aggrades when the current is quasi-steady (Branney and Kokelaar, 2002).

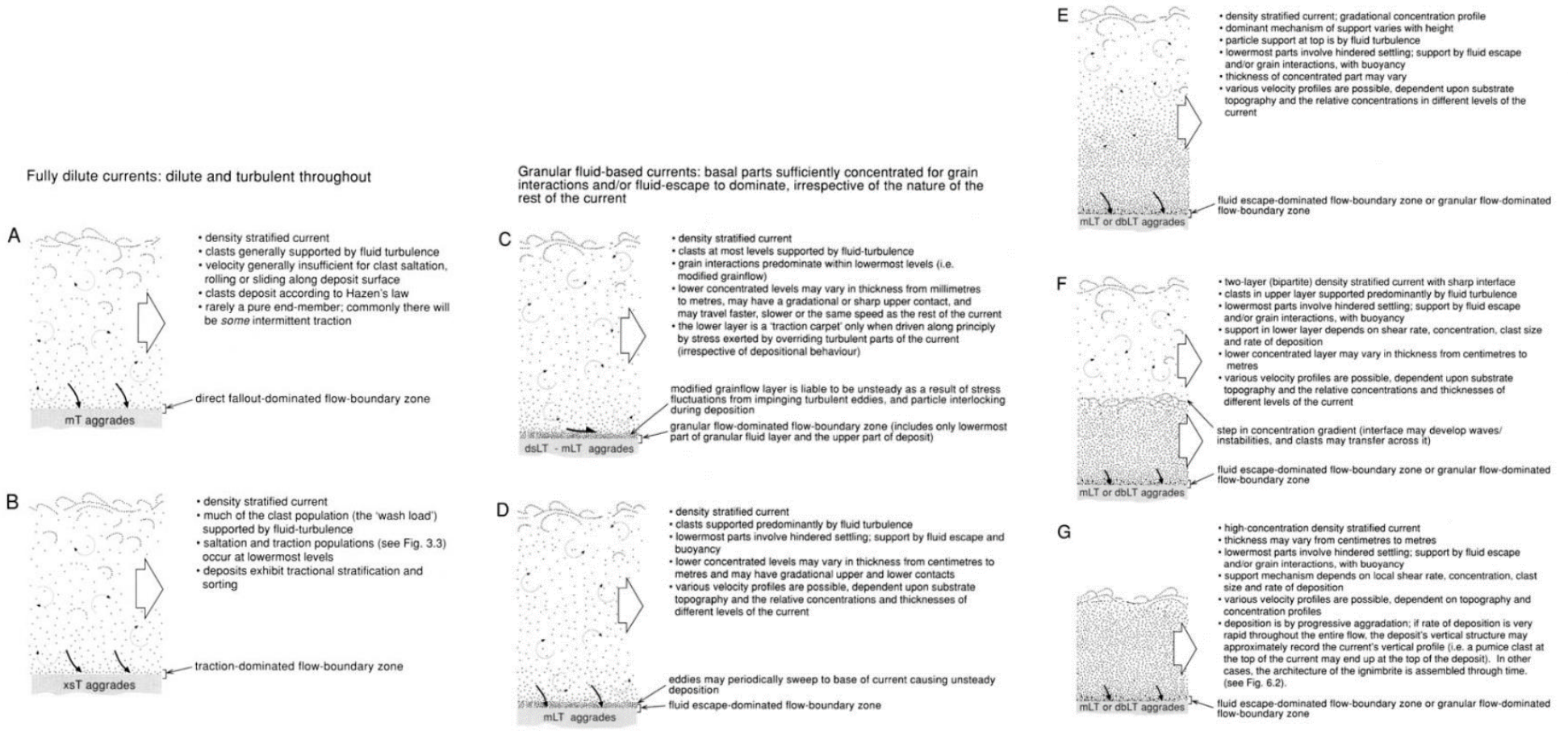


**Figure 2–5.** Spectrum of intergradational PDCs, divided into: fully dilute currents (A & B) and granular fluid-based currents (C – G). (D – G all have similar depositional FBZ and could be capable of producing similar lithofacies, with the nature of the overriding parts of the current highly variable between the types. (Branney and Kokelaar, 2002)

There are many factors which control the FBZ, and as currents are intrinsically heterogeneous, an individual current is not restricted to within the boundaries of a particular type, and variation can occur both temporally and spatially within a current. Current unsteadiness is recorded in the vertical lithofacies of a deposit, and the variability relates to temporal changes of the current itself, such as in mass flux and particle supply, i.e. waxing (increasing supply); waning (decreasing supply); or quasi-steady (constant supply). Current non-uniformity, involving external and environmental factors also have variable controls over the FBZ, such as topographical variation, slope changes, clast and substrate interaction, elutriation, and air ingestion. Lateral (spatial) gradational variations in a deposit can indicate a downwards increase or decrease of a particular parameter (i.e. velocity, competence, acceleration etc.) with an accumulative current representing an increase and a depletive current, representing a decrease (Branney & Kokelaar, 2002). This would suggest that the rate of the depositing current has control on the distance of current transport, and thus the deposit thickness does not represent the thickness of the depositing current but is a result of the rate and extent of the sedimentation.

### 2.1.5. Field classification and interpretation

Much of the pioneering work concerning the description and classification of ignimbrites began in the 1960's (e.g. Smith, 1960; Fisher, 1966) which laid the foundation for the wide range of classification schemes, depositional models and subsequent experimental modelling and lab techniques. In the simplest of terms, ignimbrites are classified in the field according to their average grain size, into tuffs; lapilli tuffs; and breccias, which have a crude relation to the energy of the current (Table 2–1).

| **Categorising ignimbrite deposits:** | | | |
|---|---|---|---|
| **Average particle size (mm)** | **Unconsolidated component** | **Rock name classification** | **Clastic sediment equivalent** |
| **<0.124** | Fine ash | Tuff (T) | Fine sand |
| **0.125-1** | Coarse ash | | Coarse sand |
| **2-64** | Lapilli | Lapilli Tuff (LT) | Gravel |
| **>64** | Block | Breccia (Br) | Boulders/Cobbles |

**Table 2–1.** Categorising ignimbrite deposits according to average grain size determinations, paired with clastic sediment equivalents.

A widely used lithofacies classification scheme subdivides lithological units (Table 2–2) according to the character and qualities of each subunit, from field observation and description. The nature of stratification, average grain size and shape, sorting, grain fabrics and composition are taken into consideration (Table 2–2). For example, mLTe would describe a massive lapilli tuff displaying a eutaxitic texture (Branney and Kokelaar, 2002). The lithofacies approach is largely a means of description and indirectly corresponds to the changing conditions of the eruption and the evolving flow boundary-zone processes over time. These changes provide a standardised framework for interpretation of the preserved flow conditions.

Vertical and horizontal lithofacies variation through a section records temporal changes in the flow boundary-zone of a current, with sharp horizons representing abrupt, immediate changes, and gradational horizons representing gradual, fluctuating conditions. These changes can come from the varying eruption source temperature or composition; interaction of the current with the topography and environment (substrate, presence of water, burial etc.); or within the flow boundary-zone itself, which can result in current instability and/or collapse (Branney & Kokelaar, 2002).

The most common ignimbrite lithofacies in the literature is a massive lapilli tuff (mLT) (e.g. Ross & Smith 1961; Sparks 1976; Branney & Kokelaar 1997), representing a poorly sorted typical lapilli tuff comprising of lithic lapilli and pumice within a matrix of vitric ash and possible crystal fragments and lacking in internal structure (Branney and Kokelaar, 2002). Developed fabrics can be displayed in massive deposits if the lapilli, crystals and/or matrix constituents have a linear arrangement preference (i.e. clast imbrication) (Elston & Smith, 1970; Kamata & Mimura, 1983). mLT deposits have been interpreted as the products of progressive aggradation of a PDC with a fluid escape-dominated flow boundary-zone in which suspended grains do not undergo tractional shear due to a high particle concentration (Branney & Kokelaar, 1992; 1997; 2002).

| Ignimbrite lithofacies classification | | |
|---|---|---|
| | **Symbol/ Abbreviation** | **Lithofacies Characteristic** |
| Lithology | T | tuff (ash) |
| | LT | lapilli-tuff |
| | L | lapilli |
| | Br | breccia |
| Components | Co | cobbles (i.e. rounded clasts) |
| | p | pumice-rich (e.g. pL = pumice lapilli) |
| | l | lithic-rich |
| | sc | scoria-rich |
| | fpoor | fines-poor |
| | frich | fines-rich |
| | acc | accretionary lapilli-bearing |
| | pods | pods (e.g. lBrpods = pods of lithic breccia) |
| | lens | lens(es) (e.g. lenspL = lens of pumice lapilli) |
| Structure (sorting, stratification, fabric, texture) | m | massive |
| | (n) | normally-graded |
| | (nl) | normally-graded lithics |
| | (i) | inversely-graded |
| | (ip) | Inversely-graded pumices |
| | s | stratified (e.g. tractional) |
| | xs | cross-stratified (e.g. tractional) |
| | //s | parallel-stratified (laminated) |
| | //b | parallel-bedded (thin bedded) |
| | f | directional grain fabric |
| | i | isotropic (no directional grain fabric) |
| | ves | vesicular |
| | vap | vapour-phase altered (e.g. sillar) |
| | e | eutaxitic |
| | pip | fines-poor pipe (e.g. elutriation) |
| | j | sheet-jointed |
| Welding | lava-like | lava-like |
| | rheo | rheomorphic |
| | v | vitrophyre (welded and glassy) |

**Table 2–2**. Lithofacies classification scheme: Non-genetic lithofacies terms, descriptors and abbreviations used in field observations (adapted from Branney and Kokelaar, 2002).

## 2.2. Lava-like and welded ignimbrites

Lava-like ignimbrites are extremely high grade and intensely welded, which can extend to the upper surfaces of the deposit, creating a 'lava-like' lithofacies with a texture indistinguishable from that of a lava (Ekren et al., 1985; Branney et al., 1992). They are typically associated with high-intensity explosive volcanic activity (VEI >4), and due to their ability to maintain higher temperatures, deposit characteristics can differ greatly from their non-welded counterparts in regards to interaction with topography, depositional process (sedimentation) and deformation. Welding in ignimbrites is observed across a wide range of volcano-tectonic environments, from continental arc volcanism (i.e., Wineglass Tuff: Kamata et al., 1993 and Bad Step Tuff: Branney & Kokelaar, 1992), intra-continental volcanism (i.e., Pagosa Peak Dacite: Bachmann et al., 2000 and Snake River Plain: Bonnichsen & Citron; 1982, Andrews & Branney, 2011), to intra-oceanic settings (i.e., Ignimbrite 'TL': Sumner & Wolff 2001; 2003).

Due to their lithological and textural similarities with lava flows, there has been much controversy concerning the interpretation and origins of such deposits, discussed further in Section 2.8. 'Lava-like' lithofacies refers to the similarity in characteristics observed between extremely high grade ignimbrites (products of PDCs that have coalesced and rheomorphically deformed) with those diagnostic of silicic lavas (i.e. those that are effused from a volcanic vent). A lava-like lithofacies is typically devoid of vitroclastic and eutaxitic (fiamme) textures symptomatic of ignimbrites due to both syn- and post-depositional processes (i.e., vapor-phase alteration, devitrification and recrystallization) (Branney et al., 1992; Sumner & Branney, 2002). Advances in understanding the processes associated with welding in relation to the emplacement of ignimbrites (e.g., Branney & Kokelaar, 1992, 2002; Ekren et al. 1984; Mahood, 1984) has allowed for a reappraisal of lava-like ignimbrite lithofacies (e.g., the Bad Step Tuff, Lake District: Branney et al. 1992; Ignimbrite 'TL', Gran Canaria: Sumner & Branney, 2002) in deposits, however the temporal and physical controls on the emplacement of these deposits remain poorly understood.

### 2.2.1. Welding

Welding is the adhesion, through coalescence, 'flattening' and compaction, of hot pyroclasts (e.g. juvenile fragments, pumice shards) (Smith, 1960i; Sparks et al., 1999, Branny & Kokelaar, 1992) within an ignimbrite. This can range from the weak sintering of clast edges, up to total elimination of pore space, whereby juvenile fragments are coalesced through rheomorphism (hot-state ductile flow), at temperatures above the glass transition phase, (Marshall, 1935; Gilbert, 1938; Smith, 1960; Ross & Smith, 1961) leading to significant densification of the deposit (Grunder & Russell, 2005). Densification is a result of the annealing of hot particles (ash and pumice lapilli) to varying degrees, by ductile deformation. This reduces the pore spaces, increasing the mechanical strength and competence of deposits in comparison to their non-welded counterparts. Welding is commonly referred to, and associated with, the presence of fiamme and exhibiting a eutaxitic texture (Figure 2–6), however, a range of complex and dynamic welding processes, textures and degrees exist out with these associations.

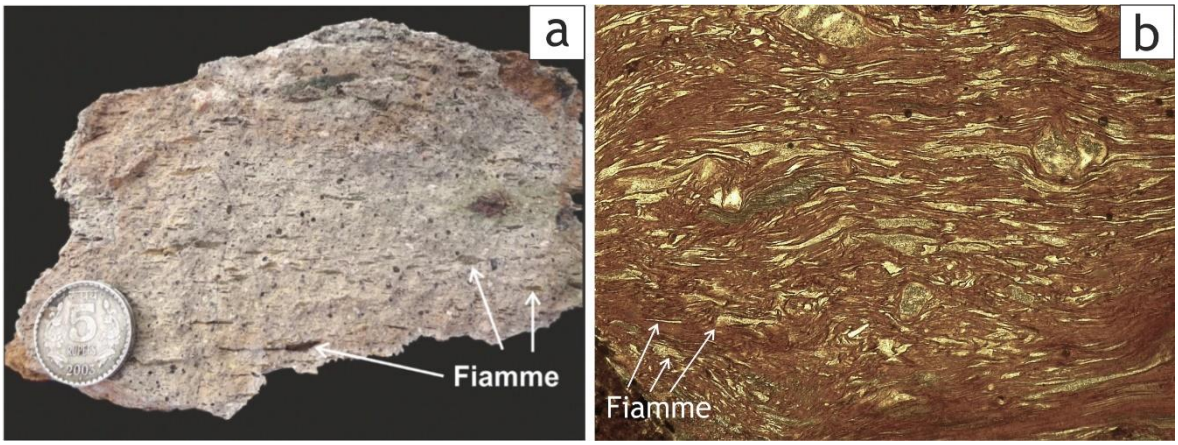


**Figure 2–6.** Eutaxitic texture in ignimbrites. a) hand specimen of a eutaxitic ignimbrite from Bhaguda, India, displaying aligned pumice fiamme, as indicated. The coin is 2.3 cm diameter. (Sheikh et al., 2020). b) Photomicrograph: welded ignimbrite from Slieve Gullion, Northern Ireland. Scale: 5 mm.

Agglutination is a non-genetic term given to the immediate sintering of particles on contact, whereby particle outlines remain, and depends on factors such as the viscosity of the pyroclasts, applied force and duration of contact. (Branney & Kokelaar, 2002). Coalescence, on the other hand, is the absolute obliteration of particle outlines, whereby particles are transformed into a homogenous liquid (non-particulate-flow) if particles are still in the fluid state during deposition. The degree of welding is controlled by deposition rate, high emplacement

temperatures (Freundt, 1998), the rheology of pyroclasts (Dingwell & Hess, 1998; Giordano et al., 2005), composition of the melt, and the style of eruption (Smith, 1960; Andrews & Branney, 2011).

The welding process can occur at any stage throughout the deposition of a deposit: by pre-agglutination during low-fountaining activity (i.e. in clastogenic spatter-fed lava flows and in spatter-cone construction) (Chapin & Lowell, 1979); during the cooling of a deposit, associated with gas expulsion and compaction (gravitational loading) (Branney & Kokelaar, 1992); or during post-depositional rheomorphism of an entire deposit (slumping and settling) (Sparks, 1976, Druitt, 1998). As a result of this, the grade of welding is often transitional throughout a deposit, ranging from non-welded to lava-like in a singular deposit (Chapin & Elston, 1979; Branny & Kokelaar, 2002), and is dependent on a range of factors discussed in Section 2.2.2.

Much of the terminology used to categorise welding is based on general descriptive terms used by Ross & Smith (1961) and Smith (1960i; 1960ii) where the distinctions between non-welded, partially-welded and welded facies were introduced, and they suggested that crystallisation phases (granophyric, devitrification and vapour phase) correspond to the degree of welding. Walker (1983) proposed a method of grading ignimbrites based on the rheology of pyroclasts from fluidal (low viscosity) to brittle solids (high viscosity) across a continuum (Figure 2–7). This scheme was adapted and modified by Branney & Kokelaar, 1992), classifying intensity relative to the degree of welding and compaction), from ‘low grade’ exhibiting negligible welding-compaction (e.g. the Citlaltépetl Ignimbrite, Eastern México: Gómez-Tuena and Carrasco-Núnez, 1999; the Campanian ignimbrite: Barberi et al., 1978), up to a predominantly welded ‘high grade’ with zones of intense welding and rheomorphism (e.g. the Bishop Tuff, California: Ragan & Sheridan, 1972 and Wilson & Hildreth, 2003).

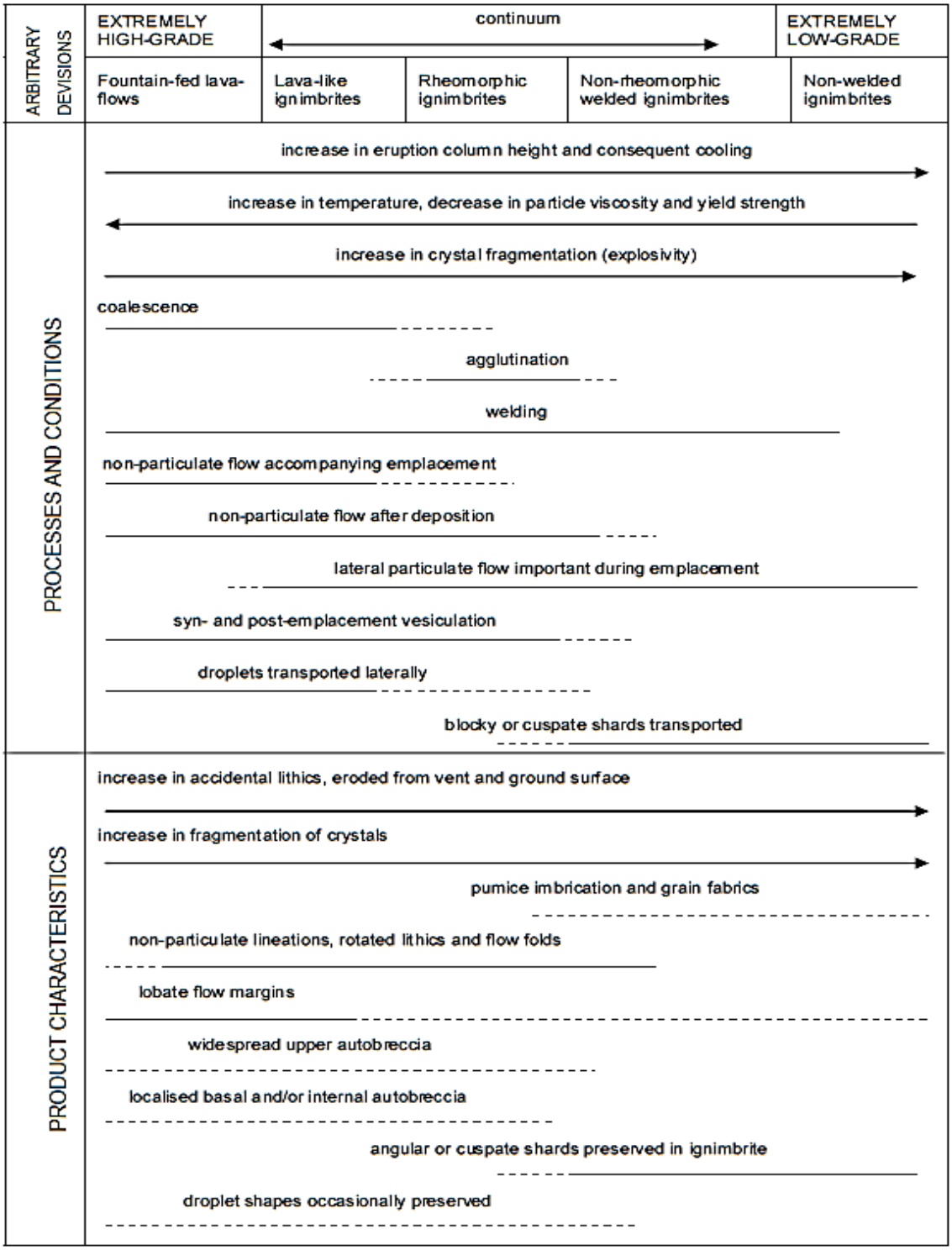


**Figure 2–7**. The ignimbrite welding grade continuum (Branney and Kokelaar, 1992).

The degree to which a deposit is welded is thought to correlate with the type of welding (aggregation vs. load). With reference to Branney & Kokelaar's (1992) continuum (Figure 2–7), the pyroclasts in extremely high-grade eruptions will be liquid, and coalesce rapidly during deposition, similar to fire-fountaining Hawaiian-style eruptions (Capaccioni & Cuccoli, 2005). Extremely welded, rheomorphic or lava-like deposits are so intensely coalesced that the deposits closely mimic a silicic lava (e.g. Sgurr of Eigg: Brown & Bell, 2013; 'TL' ignimbrite, Gran Canaria: Sumner & Branney 2002; the Greys Landing ignimbrite, Idaho: Andrews et al., 2008), and are understood to be a result of predominantly aggregation-welding (syn-emplacement) and may be associated with enclaves or globules (Hay et al., 1979). High-grade deposits are typically welded throughout but with variable welding profiles (intensely welded with rheomorphic zones to moderately welded with eutaxitic fabrics: the Green Tuff, Mahood & Hildreth, 1986), and are thought to be a result of a combination of load-welding and aggregation welding with the latter being dominant. Load-welding is thought to be the dominant style for intermediate-grade tuffs (i.e. the Bishop Tuff, Wilson and Hildreth, 1997), which are typically associated with non-welded basal and upper zones, and a central welded zone with variations throughout. Thermal and mechanical modelling of load welding have been based on observations from intermediate-grade tuffs (e.g. Smith and Bailey, 1996; Sheridan and Ragan, 1976; Peterson, 1979; Streck and Grunder, 1995; Wilson & Hildreth, 2003; Grunder et al., 2005; Quane & Russell, 2005i). Post-emplacement vapour-phase crystallization may deform (by cementation, or sintering) non-welded, low-grade deposits.

Streck & Grunder (1995) described the Rattlesnake Tuff in eastern Oregon using five welding degrees: i) non-welded; ii) incipiently welded; iii) partially welded with pumice; iv) partially welded with fiamme and; v) densely welded (Table 2–3) on the basis of density, clast adhesion and deformation (pumice vs. fiamme), colour and lustre.

Quane and Russel (2005) proposed a ranking scheme of six divisions (I-VI) based on a deposit's physical properties (density, porosity, oblateness of pumice lapilli and micro-fabric orientation, point-load strength, and uniaxial compressive strength) (Table 2–4).

| Welding facies | Density g/cm$^3$ | Deformation of clasts | | Adhesion of clasts | Typical color and luster |
|---|---|---|---|---|---|
| | | Pumices | Shards | | |
| Nonwelded | **<1.5** [1.43] | None | None | None to little | White to gray, dull |
| Incipiently welded | **1.50–1.65** [1.48, 1.57, 1.64] | None | None | Slight | Gray to pink, dull |
| Partially welded with pumice | **1.65–2.05** [1.63, 1.67, 1.74, 1.80, 1.83] | Slight | Slight | Moderate | Gray to dark gray, vitreous |
| Partially welded with fiamme | **2.05–2.30** [2.15, 2.20, 2.29] [2.07, 2.11, 2.12, 2.13] | Moderate | Slight | Strong | Dark gray to black, vitreous |
| Densely welded | **2.30–2.34** [2.34] | Moderate to strong | Strong | Complete | Black, vitreous |

Bold values for density are the range for a particular facies. Values in brackets are measured values. Under partially welded with fiamme, the second set of values is for samples with pumice and fiamme. Luster refers to hand samples from the vitric zone

**Table 2–3.** Summary of the five welding facies of Streck and Grunder (1995).

| Rank | *Ash matrix* | *Pumice lapilli* |
|---|---|---|
| I | Unconsolidated[1], noncoherent[4], loosely packed[2], little to no adhesion between shards[3] | Lack deformation[3], randomly oriented[2] |
| II | Coherent[4], some adhesion between shards[3], no coalescence of glassy material[3] | Randomly oriented[2], no deformation[3], no eutaxitic texture[4], fracture takes place around rather than through pumice[1] |
| III | Highly porous and soft[4], dull luster and hackly fracture[1], originally spherical bubble shards slightly ellipsoidal[3], some coalescence of glassy material[3] | Incipiently[1] or slightly[3] flattened[4]; fracture takes place through rather than around pumice[1] |
| IV | Relatively soft[4], moderately foliated[5] but individual shards only slightly deformed[3], contact area between shards increased[5] and clasts are moderatly adhered to one another[3] | Foliated into clear eutaxitic texture[4] with both moderately deformed pumice and fully collapsed fiamme present[3,5] |
| V | Shards strongly foliated[5], strongly adhered to one another[3] and moderately deformed[3] | Foliated into strong eutaxitic texture[4], collapsed to fiamme[3] that are obsidian-like although traces of former vesicles can be seen[1] |
| VI | Obsidian-like vitrophyre[1,3], shards are thoroughly collapsed[1,3], and completely adhered to one another[3] | Eutaxitic texture and obsidian-like fiamme are faintly visible[1] or difficult to detect[3] |

[1]Smith 1960b; [2] Sheridan and Ragan 1972; [3]Streck and Grunder 1995; [4]Wilson and Hildreth 2003; [5] This study

**Table 2–4.** Petrographic characteristics used by Quane and Russel (2005) to define ranks of welding.

In an attempt to elucidate the various proposed welding grading systems, a 'simplified scheme' of classification was proposed by Mundula et al. (2009), which subdivided welding into three basic classifications (unwelded, partially welded and densely welded). These classifications are based solely on observational features: aspect ratio of fiamme (flattening of juvenile fragments); shape and orientation of glass shards and styles of matrix crystallisation (eight styles: glassy, granophyric, open spherulitic, closed spherulitic, equigranular cripto-microcrystalline, pectinated (axiolitic), transitional glassy to cryptocrystalline and vitroclastic not recrystallised) Spherulites and associated textures are discussed further in Section 2.2.6.

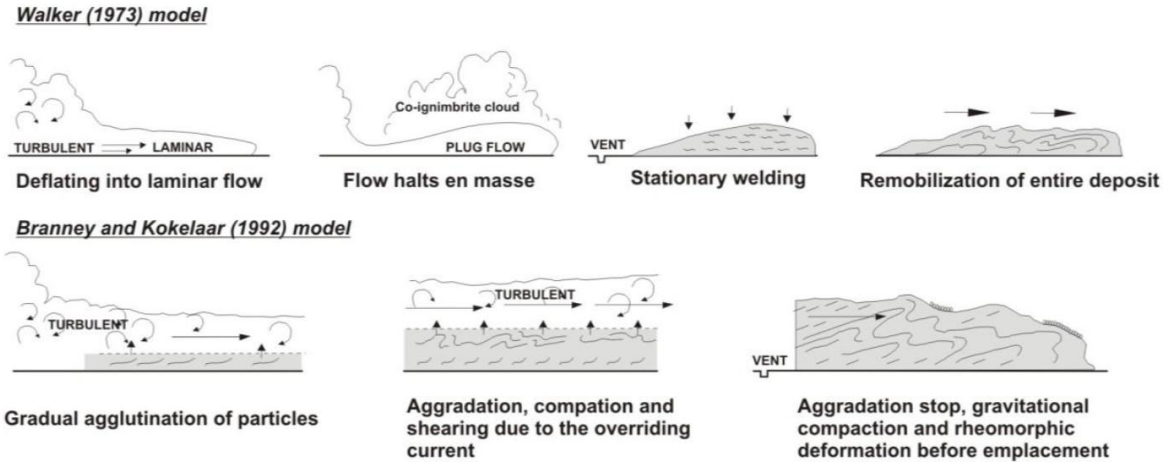


**Figure 2–8.** End-member emplacement models for high temperature ignimbrites based on the models of Walker (1973) and Branney and Kokelaar (1992).

There are two end-member models of welding in high-temperature ignimbrite emplacement; the earlier (i) load welding model (Walker, 1973; Sparks, 1976;) and (ii) the aggregation welding conceptual model (Riehle et al., 1995, Freundt, 1999). Early works, such as those concerning moderately rheomorphic ignimbrites of western USA (e.g. Smith 1660, Ross & Smith, 1961, Riehle, 1973; Ragan and Sheridan, 1972; Peterson, 1979), favoured the idea of load welding, inferring that welding occurred post-depositionally, in-situ, as a result of loading from the uppermost part of the cooling deposit, with the most intense area of welding occurring a third of the way up from the deposit's base, the degree of which was controlled by the deposit thickness and cooling rates (Figure 2–8) (Smith 1960; Friedman et al., 1963; Peterson, 1979; Sparks & Wright, 1979). In this model, the entire deposit undergoes laminar or plug flow en-masse (Sparks, 1976) and poor sorting was attributed to high-particle concentration of a poorly expanded flow (Figure 2–9).

The load stress model is problematic in welded deposits with thicknesses of 10 m and below (e.g. as seen in ignimbrite P1 – Freundt and Schmincke, 1995; and Brown's View Member – Andrews et al., 2008) as well as in intensely welded and rheomorphic ignimbrites which are welded to their uppermost horizons, with no means of burial or loading, and exhibit complex small-scale folds, fabrics and imbricate fiamme, indicative of syn-emplacement rheomorphism (Sumner & Branney, 2002; Andrews & Branney, 2011; Schmincke & Swanson, 1967).

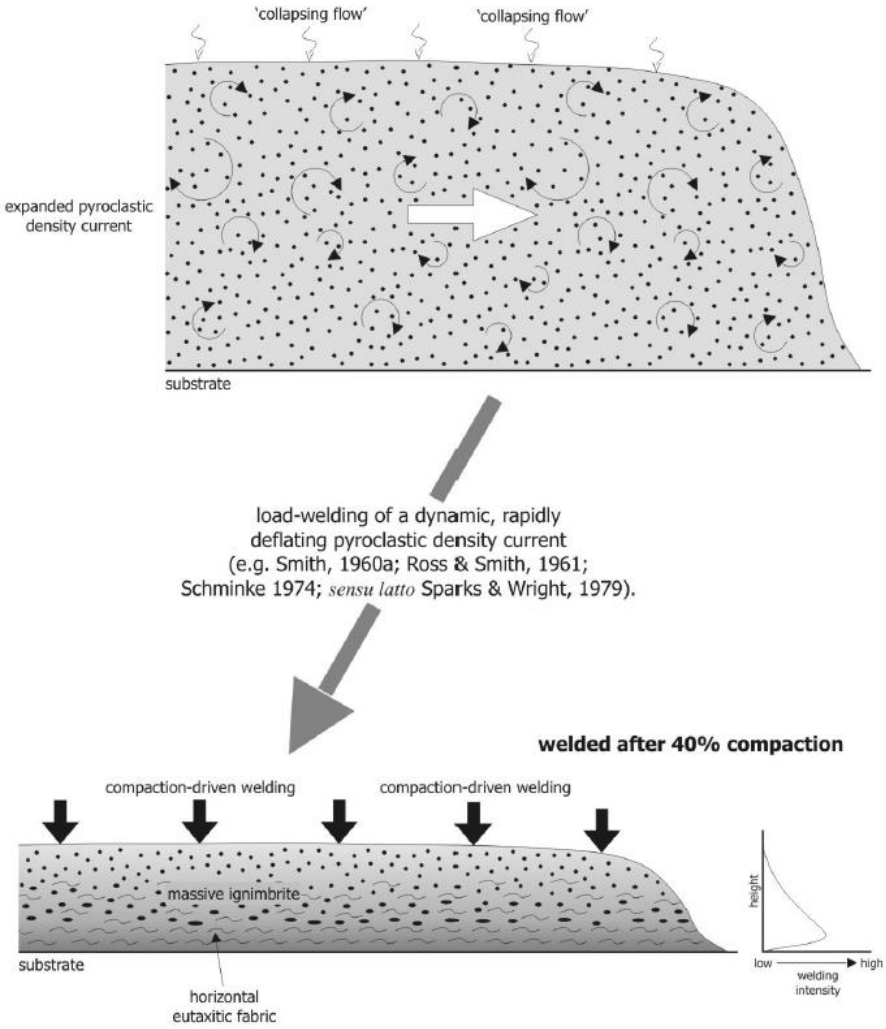


**Figure 2–9.** Schematic representative welding profile of a deflated deposit from a dynamic, turbulent PDC, following the load-welding (compaction) model, with the greatest strain (as indicated by welding intensities derived from fiamme / pumice flattening) being constrained to the lower-central part of the deposit (Andrews, 2006).

For deposits such as these, the gradual aggradation model (Figure 2–10), whereby hot pyroclasts agglutinate rapidly and coalesce during continuous sedimentation applies (Freundt, 1998; 1999) and due to the low viscosities of hot pyroclastic particles, welding can occur instantaneously without an applied load strain (Freundt, 1998; Branney & Kokelaar, 1992; Andrews, 2006; Capaccioni & Cuccoli, 2005). Welding in this model is attributed to compaction and shear during the passage of an overriding, high-temperature, highly expanded PDC, as shear fabrics are found throughout entire ignimbrite sheets. High emplacement temperatures and prolonged cooling are understood to be significant in the process of intense welding, vesiculation and rheomorphism (Schmincke 1974; Mahood, 1974; Branney et al., 1992) as suggested by the occurrence of enclaves and 'globules',

interpreted to be droplets of magma within deposits (Hay et al., 1979; Milner et al., 1992; Elburg, 1996). This model is further supported by lateral changes in lithofacies, gradual changes in flow direction due to topographic controls, as well as vertical compositional zoning (e.g. the Crater Lake ignimbrite: Bacon, 1987).

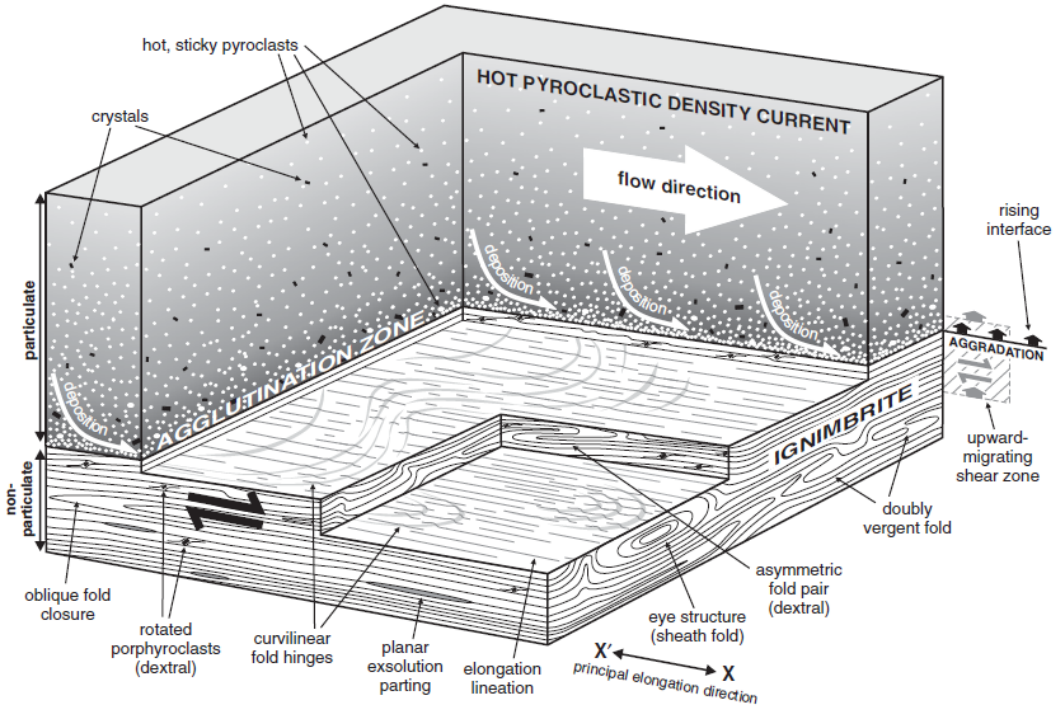


**Figure 2–10.** A schematic diagram illustrating the deposition and emplacement of a high grade, highly welded, rheomorphic ignimbrite, by the process of progressive aggradation from a granular-based PDC, whereby the overriding current can 'detach' from the flow boundary zone, resulting in shear induced rheomorphism (Andrews and Branney, 2011; adapted from Branney and Kokelaar, 1992; Pioli and Rossi, 2005). Hot, ductile pyroclasts and rigid crystals are deposited from a high-concentration, upward migrating shear zone, where they agglutinate and undergo ductile deformation, in the uppermost parts of the hot deposit, which gives rise to flow banding planar exsolution partings, stretched and elongated crystals, recumbent and sheath folding, and fabrics rotated around crystals. This diagram does not depict later (post-emplacement) deformation and rheomorphism (Andrews and Branney, 2011).

### 2.2.2. Factors influencing welding and rheomorphism

It is recognised that deposits with high water content or those with a peralkaline composition are more susceptible to both welding and rheomorphism (Giordano, 2005; Barclay et al., 1996; Lowenstern & Mahood, 1991). Rheomorphic ignimbrites are common-place in a variety of volcano-tectonic settings with peralkaline (oversaturated in alkalis; Na + K, and thus undersaturated in Al) magmatic compositions (Na + K / AL > 1.1) (Mahood, 1984): in continental rift zones and

extensional regimes (e.g. Pantelleria: Mahood, 1984; Wright, 1980; Williams et al., 2014; the Fantale Tuff, African Rift, Gibson, 1974; 1970; the McDermitt caldera complex, Oregon; Hargrove et al., 1984; Wallace et al., 1980; the Gomez Tuff, Parker and White, 2008); and in oceanic island settings (e.g. Mogán and Fataga Formations, Gran Canaria, Freundt & Schmincke, 1992; Leat & Schmincke 1993; Sumner & Branney 2002).

The degree of welding in a deposit, occurring both during (syn-) emplacement (Mahood, 1984; Chapin and Lowell, 1979; Freundt 1998; Branney and Kokelaar 1992; Branney et al., 2002) and post-emplacement (Ross and Smith, 1961; Russel and Quane, 2005; Sheridan and Ragan, 1976) is controlled by many factors:

i) the eruption temperature (discussed further in Section 2.2.4 and Chapter 7), i.e. higher temperatures result in increased coalescence, thus low-grade ignimbrites may form at ambient temperatures;

ii) the composition of magma, as this ultimately controls the particle density (Branney & Kokelaar, 1991), discussed further in Chapter 6;

iii) viscosity, which can control a particle's ability to agglutinate (Mahood, 1984; Freundt 1998), discussed further in Chapter 7;

iv) load stress (as discussed in Section 2.2.1) (Smith, 1960; Ross & Smith, 1961; Riehle 1973);

v) the volatile content, as with an increasing proportion of volatiles, overall viscosity is reduced (Schmincke, 1974; Branney & Kokelaar, 1991), and;

vi) air ingestion, degassing and elutriation, discussed further in Chapter 7.

These factors (i-vi) in turn, affect the rheological and mechanical behaviour of pyroclasts during and after deposition, and control the welding profiles of cooling, successively emplaced deposits (Branney & Kokelaar, 2002).

Rheology is the response of a material to deformation, and the changes in the physical properties of both: i) 'pre-eruption' effects of the melt and ii) 'post-

eruption' effects of pyroclasts during eruption, transport, deposition, cooling and degassing; these control and progressively alter the rheology of pyroclasts during welding (Andrews, 2006). As this is a measure of applied strain, and strain rate, the rheology of a material is not accurately measured. However, the viscosity of a material can be measured to obtain the material's ability to withstand ductile deformation, and a magma's viscosity is understood to be related to the degree of silicate polymer development in the melt (Webb & Dingwell, 1990) (i.e. the higher the degree of polymer development, the higher the viscosity). The degree of polymerisation in a magma is controlled by (Dingwell, 1998i):

i. the melt temperature, which has the dominant control over a silicate magma's viscosity, and is inversely proportional to a melt's viscosity, due to progressive polymer break-down with increasing temperatures (McBirney & Murase, 1984; Dingwell, 1998i, Andrews, 2006). Above the melt's liquidus temperature, polymer chains break-down resulting in low viscosity (Bottinga, 1994);

ii. the melt composition, with it being known that silicic magmas (i.e. metaluminous rhyolite) have higher viscosities than mafic and peralkaline (i.e. phonolites) magmas (McBirney & Murase, 1984; Giordano et al., 2005);

iii. dissolved volatile content and composition, as dissolved volatiles significantly lower a melt's viscosity. Evolved silicic magmas are relatively rich in volatiles compared to mafic compositions, with $H_2O$, F and Cl having the greatest effects on viscosity in rhyolite melts (Lange, 1994; Stevenson et al., 1998);

iv. crystal content, as an increase in effective viscosity is observed with progressive crystal content in a melt, due to interactions between inter-crystals, and behaves like a solid when crystal content is ~ 70% (Stevenson et al., 1996) and;

v. vesicularity, with the effective bulk viscosity of a melt correlating with bubble fractions (i.e. increasing with progressive vesicularity, similar to

crystal content) (McBirney & Murase, 1984; Bagdassarov & Dingwell, 1992; 1993).

### 2.2.3. Rheomorphism

Features common in highly welded ignimbrites such as: both open and tight, isoclinal, curvilinear and sheath- fold structures (Andrews & Branney, 2011), flow banding, stretching lineations, foliated fabrics, elongated (stretched) pumice clasts and vesicles, fiamme and boudins, are a result of rheomorphism (Branney & Kokelaar, 1992, 2002; Schmincke & Swanson, 1967; Sumner & Branney, 2002), produced during ductile deformation of high temperature, welded material, above the $T_g$ (Giordano et al., 2005), and first described by Schmincke and Swanson (1967). This may occur both during (syn-emplacement) or after deposition (post-emplacement), and determinations between the two in terms of timings and processes can be difficult to distinguish.

In extremely high-grade ignimbrites, syn-emplacement rheomorphism occurs through the rapid agglutination and coalescence of hot pyroclasts in an aggrading current, previously described as 'primary' rheomorphism (Wolff & Wright, 1981; Branney & Kokelaar, 1992; Freundt, 1998), and develops shear zones in the upper flow boundary zone, due to gravity, interaction with the overriding current and lateral momentum, which can give rise to rheomorphic fold structures, flow banding and lineations (Figure 2–10) (Branney & Kokelaar, 1992; Andrews & Branney, 2011). Rheomorphism produces a variety of kinematic indicators including: pronounced elongation lineations (flow-banding); stretched vesicles; boudins; and a range of flow folds in the fabric (Schmincke & Swanson, 1967; Chapin & Lowell, 1979; Wolff & Wright, 1981; Branney & Kokelaar, 1992, 2002; Leat & Schmincke, 1993; Sumner & Branney, 2002; Pioli and Rosi, 2005), which can be used in field determinations of flow direction and processes. Pervasive sheath folding in the fabric has been interpreted to represent narrow shear zones (Branney et al., 2004ii), and changes observed in sheath fold axes and linear fabrics are thought to record variation in flow direction during deposition (Branney et al., 2004ii).

This can be followed by post-depositional (post-emplacement) rheomorphism, previously referred to as 'secondary' rheomorphism (Wolf & Wright, 1981), whereby fold structures and deformation occurs as a result of gravity induced remobilisation (spreading and slumping) of a plastic body. This type of deformation produces large-scale folding affecting the entire deposit thickness, and ramp structures (e.g., Leat & Schmincke, 1993) as a result of fold thrusts. Post-depositional welding and deformation can also be the result of hot deformation induced by autobrecciation at the base of currents, by cold burial-compaction during diagenesis or deformation linked to tectonic processes (Branney & Sparks, 1990), but typically, this post-emplacement rheomorphism is associated with large scale structures (distorted folding, buckling and ramping) with associated deformation observed throughout the entire deposit and may overprint pre-existing evidence of rheomorphism acquired during syn-emplacement deformation.

Both processes of rheomorphism (syn- and post-emplacement) can overlap and occur in conjunction with one and other, and the resulting features and structures of each stage can be difficult to distinguish between, and the term 'rheomorphism' can be used to refer to both processes (Branney et al., 1992). Intensely welded, rheomorphic ignimbrites exhibiting two-stage rheomorphism tend to be the result of higher temperature eruptions (as discussed in 2.6) that are capable of maintaining their high temperatures for longer durations (Andrews & Branney, 2010; Freundt, 1998). Field evidence and textural analysis, such as inclined lineations, erosional truncation of welding fabrics, indicate that welding can start virtually immediately, during sedimentation, by the process of 'agglutination', where the hot, fluidised particles fuse on contact with one another (Branney & Kokelaar, 1992; 2002). Pyroclasts develop a superficial flow of hot glass, known as a 'sinter neck' (Seville et al., 1998; Freundt, 1998) on contact, and the process is controlled by their viscosity and the force and duration of the interaction. The process of aggradation supports the theory that currents are essentially low-concentration, turbulent suspensions with very little grain interactions (Fisher, 1989; Freundt, 1998). In contrast, pyroclasts in high concentration, granular based currents have less capacity to agglomerate, due to

the abrupt, high intensity interactions, which are conditions not favoured by sintering (Seville et al., 1998).

The applied strain during rheomorphism controls the deformational structures (i.e. compaction, folding of fabrics, pervasive sheet jointing, prolate vesicles and fiamme, localised boudinage, thrusts and localised autobrecciation) (Chapin & Lowell, 1979; Pioli & Rosi, 2005; Andrews & Branney, 2010), and the deformation history of a body can be deduced from these structures. Strain measurements and observations are used to calculate the extent of welding in deposits, focussing on the bulk unit porosity, density and fiamme axial ratio. Highly welded ignimbrites typically have high bulk densities, low porosity and a high fiamme axial ratio, often displaying a eutaxitic texture, whereas non-welded ignimbrites are associated with low bulk densities and high porosities.

Where a body has passed through various phases of deformation (i.e., undergoing both syn- and post-emplacement rheomorphism), the final strain state (finite strain) is typically what can be observed and measured, although it can be possible to observe structures that exhibit different strain histories (incremental or infinitesimal strain) known as progressive deformation (Ramsay, 1967; Andrews, 2006). An object's strain is the measured physical response (deformation) experienced during rheomorphism, and in welded ignimbrites, this can be measured from volume strain (compressional), both simple- and pure-shear strain, and combinations of both (Ramsay, 1976; Ramsay & Huber, 1983). Pure shear flow, or 'coaxial flow' is deformation whereby material lines remain fixed at a position relative to one another, parallel to the stretching axis, and with the direction of principle strain remaining constant during progressive deformation (Twiss & Moores, 1992).

During simple shear flow, the principal strain axes do not remain constant, involving no change in area but compression and extension (Means, 1976). Rotational deformation occurs as a result of simultaneous simple and pure shear, whereby an object undergoes rotation, compression and extension, known as 'general strain'.

The structural elements and fabrics found within welded deposits as a result of rheomorphism have been divided into four broad and non-generic groups by Andrews (2006):

i. Planar fabrics (e.g., axial planar cleavages, crenulation cleavages) (Figure 2–11 a & b), the penetrative planar features within a deposit, may respond passively to strain (mechanically isotropic) or may control the structural fabric element of a rock in terms of distribution and scale (anisotropic). These may be original or 'primary' features (Passchier & Trouw, 2005) such as lamination, or planar fabrics associated with oblate strain in deformed rocks, termed 'secondary' structures (Passchier & Trouw, 2005), such as eutaxitic textures (e.g., Figure 2–6) (Wolff & Wright, 1981; Sumner & Branney, 2002).

ii. Linear fabrics (e.g., stretched clasts, prolate vesicles, lineations; magnetic fabrics of Knight & Walker, 1988) (Figure 2–11 c & d) are typical of prolate and plane strain deformation and are understood to be parallel to the maximum applied principal strain axis (Cloos, 1957; Andrews, 2006).

iii. Kinematic indicators (e.g., fabric rotated around clasts and folds) may record non-coaxial shear sense, associated with the actual transport direction (i.e., fold hinges aligned with post-emplacement rheomorphic slumping), and two types exist: rotational and non-rotational (e.g. shear bands in metamorphic rocks – Passchier & Trouw, 2005) and these are typically rotational (i.e. fabric rotated around crystals or lithics (e.g. Schmincke & Swanson, 1967)) in welded ignimbrites (Figure 2–11 e & f).

iv. Folds (i.e., sheath folding of fabrics) are common in most deformational regimes and occur at all scales (microscopic to several hundreds of kilometres) as a result of ductile shortening of planar fabrics. The type and style of fold reflects the physical (e.g., applied stresses, temperature and pressure) and mechanical (thickness, competence) properties of the rock during folding. Understanding the relationship of fold geometries with foliations, lineations and kinematic indicators are

key in understanding the conditions under which deformation occurs (Andrews, 2006). Syn-depositional rheomorphism in ignimbrites gives rise to sheath and oblique closure folds (Figure 2–11 g & h), with limbs parallel to the principal elongation direction in the basal shear zone of a current, as illustrated in Figure 2–10. Fold geometries related to post-depositional rheomorphism are typically open, loose and buckle folds, and associated with re-folding of primary (syn-depositional) sheath and curvilinear folds (Figure 2–11 i & j).

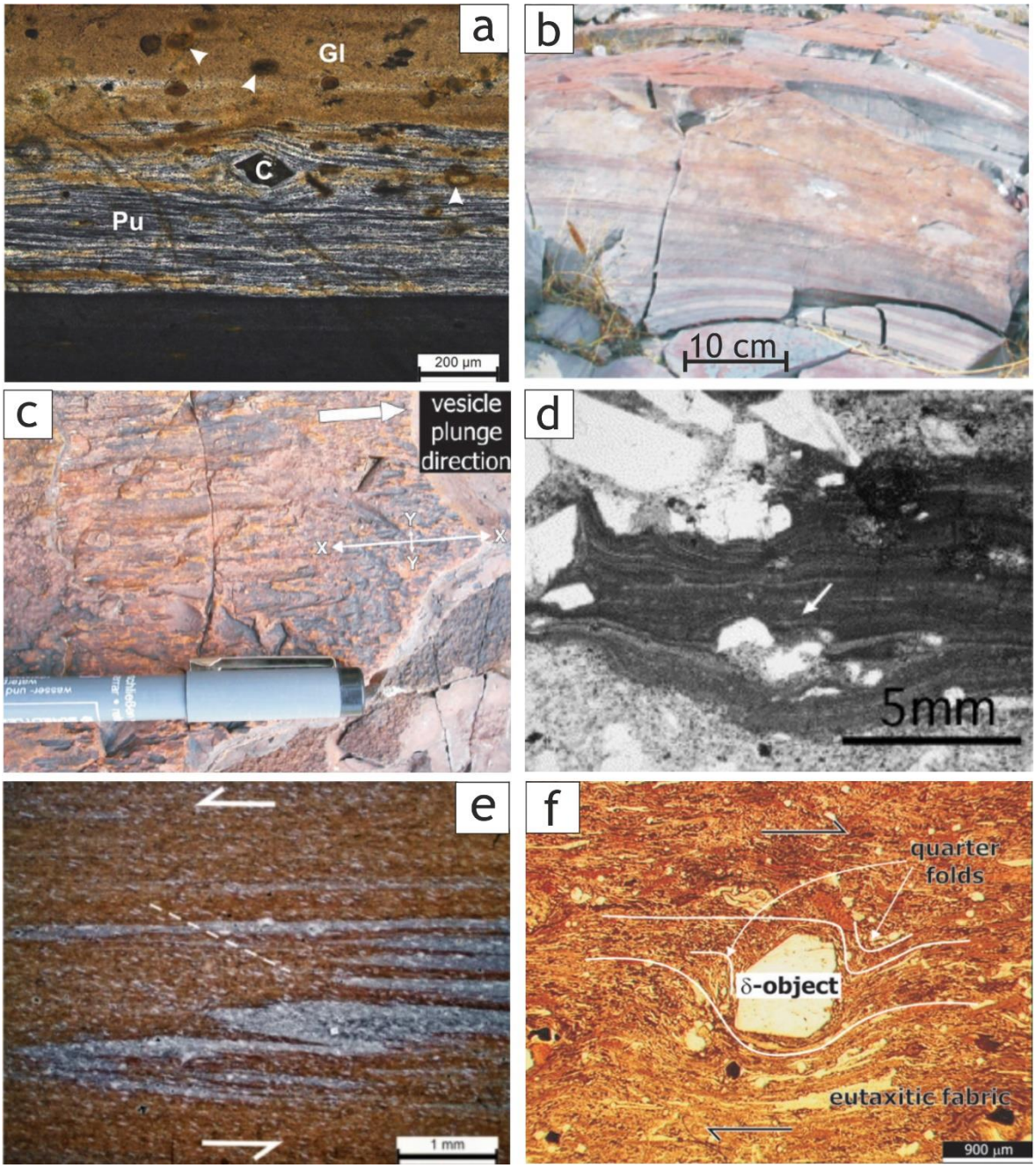


Continues overleaf

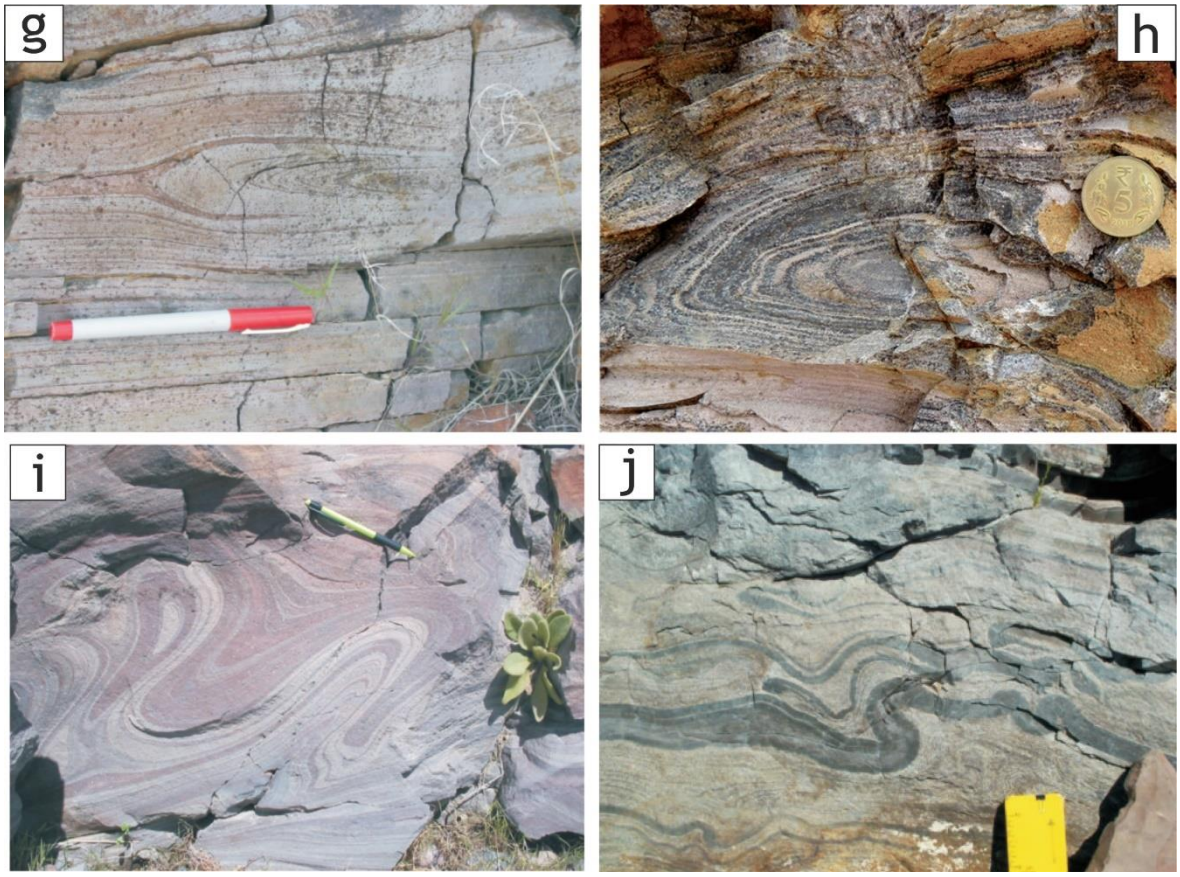


**Figure 2–11.** Structural elements and fabrics of rheomorphic ignimbrites. a) Photomicrograph of planar fabrics in the Osham Hill Vitrophyre, India, displaying a brown glassy upper band, a central band rich in fiamme and a lower dark grey compacted pumice band. (Sheikh, 2020) b) Planar fabrics and penetrative colour banding in the Grey's Landing ignimbrite at Cedar Creek Reservoir, Idaho (Andrews, 2006). c) Stretched and elongated vesicles in lithoidal rhyolite (Grey's Landing ignimbrite) at Norton Canyon, Idaho (Andrews, 2006). d) Stretched and deformed fabrics of the welded facies of the Nuraxi tuff, Italy (Pioli & Rosi, 2005). Note the fractures and dislocated crystal (marked by the arrow). e) Photomicrograph of asymmetric folding within a banded vitrophyre, suggesting sinstral (top to left) sense of shear in the Osham Hill Vitrophyre, India (Sheikh, 2020). f) Rotated porphyroclast as a kinematic indicator: a euhedral δ-object in the eutaxitic vitrophyre (Grey's Landing ignimbrite) at Cedar Creek Reservoir, Idaho. g) Syn-depositional 'floating' isoclinal hinge of a sheath-like fold, parallel to elongation direction and planar fabrics (Grey's Landing ignimbrite) at West Bay, Idaho. h) Sheath folding in the Osham Hill ignimbrite, India (Sheikh, 2020). i) Complex post-depositional folding as a result of refolding of intrafolial sheath folds by inclined and curvilinear, extrafolial folds in the Grey's Landing ignimbrite, at Too Cool, Idaho (Andrews, 2006). j) Upright and inclined, post-depositional buckle-style folding in a colour-banded ignimbrite, indicating significant competency contrasts across bands (Grey's Landing ignimbrite) at Salmon Dam, Idaho (Andrews, 2006).

### 2.2.4. Emplacement conditions

The emplacement processes by which intensely welded and lava-like ignimbrites form are inherently different to that of lower grade ignimbrites. In terms of flow boundary zone conditions, as discussed in Section 2.1.4, a shear stress is applied by the overriding, progressively aggrading current, creating a shearing depositional surface (Figure 2–10). 'Agglutination' (rapid welding of pyroclasts) and 'coalescence' (merging of fluidal pyroclasts into a homogenous mass) of hot particles and pyroclasts within this zone is a result of both the shear-induced deformation and the high temperatures (above the glass transition temperature - Giordano et al., 2005) maintained by the current (Branney & Kokelaar, 1992, 2002; Freundt & Schmincke, 1995). Intense coalescence of fluidal pyroclasts results in hot-state ductile flow behaviour, obliterating all/any vitroclastic textures (e.g. eutaxitic) and pyroclast boundaries/outlines, producing a lava-like lithofacies (Sumner & Branney, 2002; Freundt & Schmincke, 1995). Ductile flow also accounts for immediate post-emplacement rheomorphism, which gives rise to spectrum of welding intensities observed throughout singular deposits, ranging from a predominantly non-welded lithofacies, with very little to no observable deformation; through to 'intensely'/extremely welded, with a distinct eutaxitic texture (i.e. emLT); to 'coalescence', the highest grade, with evidence of vitroclastic textures and pyroclasts boundaries (outlines) obliterated, resulting in a lava-like lithofacies (mT (lava-like)) (Branney et al., 1992; Freundt & Schmincke, 1995; Branney & Kokelaar, 2002), as discussed in Section 2.2.1. The process by which these deposits are emplaced has been broken down into six stages (Andrews, 2006): i) pre-eruption conditions within the magma chamber; ii) eruption; iii) transport; iv) deposition; v) welding; and iv) rheomorphism; followed by post-emplacement residual static cooling.

In order to maintain the high temperatures necessary for rheomorphism to take place, lava-like ignimbrites have been associated with, but are not restricted to, low-fountaining, 'boil-over' eruptions (discussed in Section 2.1.2.1), with rapid sedimentation by quasi-steady PDCs, which are far less violent than their lower grade counterparts. A less-violent eruptive process is indicated by a much lower number of accidental lithics (those picked up locally by the current), as well as a reduction in crystal breakage, due to ductile, rheomorphic flowage around

crystals, rather than explosive fragmentation in more violent eruptions (Branney et al., 1992). The occurrence of accidental clasts, lithics and crystals are similar to those of fountain-fed basalt lavas (Branney & Kokelaar, 1992).

### 2.2.5. Emplacement temperatures

The grade, and thus the degree of welding, is regarded as the most significant quantifiable parameter in determining the emplacement temperature (Ragan & Sheridan, 1972; Riehle, 1973) and cooling history. The emplacement temperatures of a rhyolitic magma, which vary within the range of 660° (Bindeman & Valley, 2003) to 1150°C (Kirstein et al., 2001), are typically considered to be lower than the magmatic temperature, and are dependent on the rate of cooling (Thomas & Sparks, 1992), with an estimated temperature loss of between 100 °C and 150°C during transport (Riehle et al., 1995; Sheridan & Wang, 2005) due to a pyroclastic density current's interaction with cold air (Freundt, 1998; 1999). However, in ignimbrite emplacement, factors such as the eruption temperature, volatile content, mass flux, flow dynamics, volume of air engulfed in the flow during transport, and lithic content control the emplacement temperature (Pioli, 2002).

Emplacement temperatures for high grade ignimbrites are considered to be greater than the temperature of the glass transition phase ($T_g$), a kinetic boundary between the liquid-state (viscous) and solid-state (elastic) mechanical response to applied stress, estimated to be around 650°C for rhyolitic deposits (Giordano et al., 2005). Above this boundary, glassy particles deform viscously, allowing welding to take place, whereas, at temperatures below this boundary, glass behaves elastically, inhibiting welding, and welding is seized immediately following passage through the $T_g$ via quenching and rapid cooling (Giordano et al., 2005). The parameters of the $T_g$ during emplacement of a PDC is dependent on: i) the melt composition, as lower viscosities are associated with Tg in peralkaline melts; ii) volatile composition, and; iii) cooling rate, and represented by a time-temperature curve, rather than a defined temperature range (Dingwell & Webb, 1990; Giordano et al., 2005). Experimental estimations of the minimum $T_g$ temperature limits for the for the rapid and intense welding during ignimbrite emplacement have arrived at ≥ 400ºC, occurring over timescales of seconds (10 s

of) to minutes (10 s of) (Giordano et al., 2000; 2005). These concepts are discussed in detail in Chapter 7.

### 2.2.6. Vapour-phase alteration

Vapour-phase alteration and crystallisation both occur post deposition, during the cooling stage of a deposit or lava as a result of element-rich, high-temperature vapours during magmatic gas-exsolution (degassing) and from heated groundwater (typically enriched in $H_2O$, $CO_2$, and $SO_2$) reactions, and radically alter the textures of ignimbrites (i.e., the Matahina ignimbrite, New Zealand - Carr, 1981). Crystallisation occurs in the pore spaces and open cavities as vapours rise upwards both through the current and cooling deposit.

Significant recrystallization and alteration during the vapor-phase can produce sillars, which can consist of entire units, or localised areas around elutriation pipe structures (Fenner, 1948; Branney & Kokelaar, 2002). As a result of advanced cementation and recrystallization (of alkali feldspar, cristobalite and tridymite), sillars are typically devoid of pore space, coherent and light coloured. Spherulites are common in both felsic lavas (e.g., rhyolites) and welded, rheomorphic ignimbrites. They range from microscopic (mm) scale up to 10 cm in diameter (rarely metre-scale) and consist of radially arranged fibrous, acicular and lath-shaped crystal aggregates, commonly composed of alkali feldspar, cristobalite and tridymite, and commonly associated with the vitrified base of a deposit (the glassy carapace). Entire horizons can be spherulitic in a deposit, and spherulitic growths can be associated with lithophysae (Figure 2–12), forming radiating aggregates of fibrous crystals which form around expanding vesicles in a deposit, associated with deposition or formed in a body which is still capable of flowage. Lithophysae form from gas expansion during volatile exsolution in high-silica melts (glassy lavas and welded ignimbrites) during cooling, resulting in the formation of cavities (Breitkreuz, 2013).

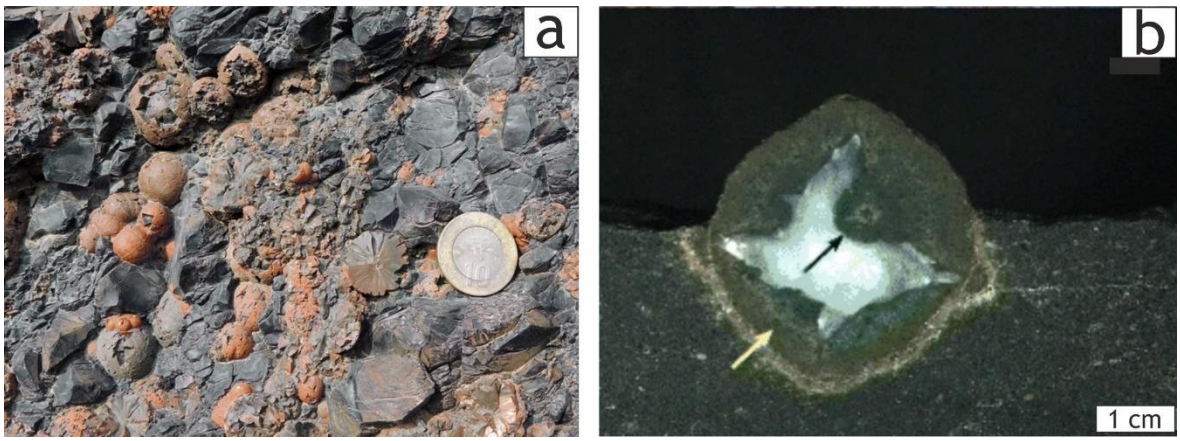


**Figure 2–12.** Examples of spherulites and lithophysae. a) Spherulites in a vitrophyre at Osham Hill, India. Note internal radial growth structure of the spherulites. Diameter of the coin is 2.6 cm (Sheikh, 2020). b) Cut rock slab of a lithophysa (yellow arrow) consisting on an infilled star-shaped cavity, with an initial spherulite, marked by the black arrow, within a vitrophyre ash-rich ignimbrite, Early Permian, Planitz Formation, Zwickau, Germany (Breitkreuz, 2013).

Since the growth of lithophysae is considered syn-depositional, crusted, deformed and broken lithophysae can be indicators of secondary flowage (post-depositional). Streck & Grunder (1995) identified four crystallisation facies in the Rattlesnake Tuff, eastern Oregon, which form the basis of the terminology and descriptions used in this thesis: i) a vapour-phase zone; ii) a pervasively devitrified zone; iii) a spherulite zone, and; iv) a lithophysae zone, with gradational transitions between crystallisation zones, all overprinting welding textures.

### 2.2.7. Misinterpreting lava-like lithofacies in ignimbrites

The problems distinguishing between lavas and intensely welded to lava-like lithofacies in ignimbrites was first highlighted by Dell'Erba (1892), with his controversial early work on the Campi Flegrei "lavas" (piperno) in Italy, interpreting them instead as tuffs that had maintained a high temperature during deposition. This idea was supported in the later work of Zambonini (1919) which attributed the obsidian fiamme ('lenticular glass fragments') in the piperno to collapsed and flattened (welded) pumice fragments, suggesting the hot pyroclasts provided the heat for welding and compaction.

After a century of advances in the understanding of high-grade ignimbrites, their emplacement and attempts at determining criteria in field observations, distinguishing between intensely welded and lava-like ignimbrites from silicic

lavas is still problematic (Henry & Wolff, 1992). The obliteration of vitroclastic textures (e.g. fiamme and welded shards) during welding and devitrification (Ross & Smith, 1961) in intensely welded and lava-like lithofacies make hand specimen or petrographic determinations alone unattainable. Distinctions between lava-like and rheomorphic ignimbrites with lavas or other rheomorphic and welded fall deposits (e.g. Sparks and Wright, 1979; Calderone, 1988) are ultimately reliant on detailed morphological, textural and structural characteristics.

Shared features with lavas, such as low lithic concentrations and columnar jointing (polygonal and orthogonal cooling joints) are common features exhibited by intensely welded and lava-like ignimbrites. Few lava-like ignimbrites have been associated with localised autobrecciation (e.g. Henry et al., 1989; Branney et al., 1992; Sumner & Branney, 2002), but extensive autobreccias are typically absent at the base of rheomorphic ignimbrites (e.g. Branney et al., 1992; Beddoe-Stephens & Millward, 2000; Branney et al., 2008, Andrews & Branney, 2011; Sommer et al., 2013; Brown & Bell, 2013), in contrast to lavas which have thick, widespread basal and upper autobreccias, as well as terminal talus aprons (e.g. Branney et al., 2008; Bonnichsen & Kauffman, 1987; Henry & Wolff, 1992). Columnar jointing in high-grade ignimbrites forms during latestage cooling (Kobberger & Schmincke, 1999), and is not common in non-crystalline and non-welded facies (Ross & Smith, 1961). It can be variable across the unit, as seen in the Bandelier Tuff, New Mexico, with polygonal jointing across the lower and upper deposit with a section of orthogonal jointing in between (Ross & Smith, 1961). It is recognised that there is a correlation between the degree of welding and the spacing of joints, with the most intensely welded ignimbrites exhibiting the closest spacing (i.e., Valles mountain ignimbrites: Ross & Smith, 1961). Many of these characteristics made distinctions between the Snake-River-type (SR-type) rhyolite lavas and ignimbrites (Branney et al., 2008), with typically thinner, low-aspect ratio topographically-controlled lava-like ignimbrites, as opposed to thicker, lobe-fronted rhyolites, with extensive basal and upper autobreccias (Figure 2–13).

Geochemical variation and compositional zoning have also been considered as distinguishing criteria between rheomorphic and lava-like ignimbrites and lavas (Henry & Wolff, 1992), with the broad assumption that lavas are commonly

homogenous (e.g. Henry et al. 1988; 1990; Bonnichsen & Kauffman, 1987), and compositional zoning is widely described in welded and lava-like ignimbrites (e.g. Mahood & Hildreth, 1986; Crisp & Spera, 1987; Briggs et al., 1993; Sumner & Branney, 2002; Hildreth & Wilson, 2007; Brown & Bell, 2013; Williams et al., 2014; Forni et al., 2016). As there are numerous exceptions in both associations, with striking homogeneity seen in welded and lava-like ignimbrites (e.g., Ekren, 1984; Milner, 1992; Beddoe-Stephens & Millward, 2000) and zoning associated with lavas (e.g., Allen & McPhie, 2002), this generalisation is problematic as a diagnostic tool. Trace element enrichment patterns can be indicative of emplacement style, as magmas with higher concentrations of halogens are typically associated with lower viscosities, and thus a more effusive eruptive style (Kirstein et al., 2001).

To confuse matters further, vitroclastic, eutaxitic textures and fiamme can be present in silicic lavas (e.g., Allen, 1988; Dadd, 1992i; Sparks et al., 1993), attributed to the alteration and viscous shear of an underlying pumiceous breccia of hot pumiceous autobreccia (i.e., fiamme (flattened pumiceous material) in the Comerong rhyolite lava: Dadd, 1992ii; fiamme and flow banding in andesite lavas of Lascar Volcano, Chile: Sparks et al., 1993). Flow banding lineations and a variety of fold structures are also common in lavas (e.g., Flinn, 1962; Smith & Marshall, 1992; Smith & Houston, 1993; Crisci et al., 1991), highlighting the importance of methodological and detailed field analysis when dealing with lava-like lithofacies.

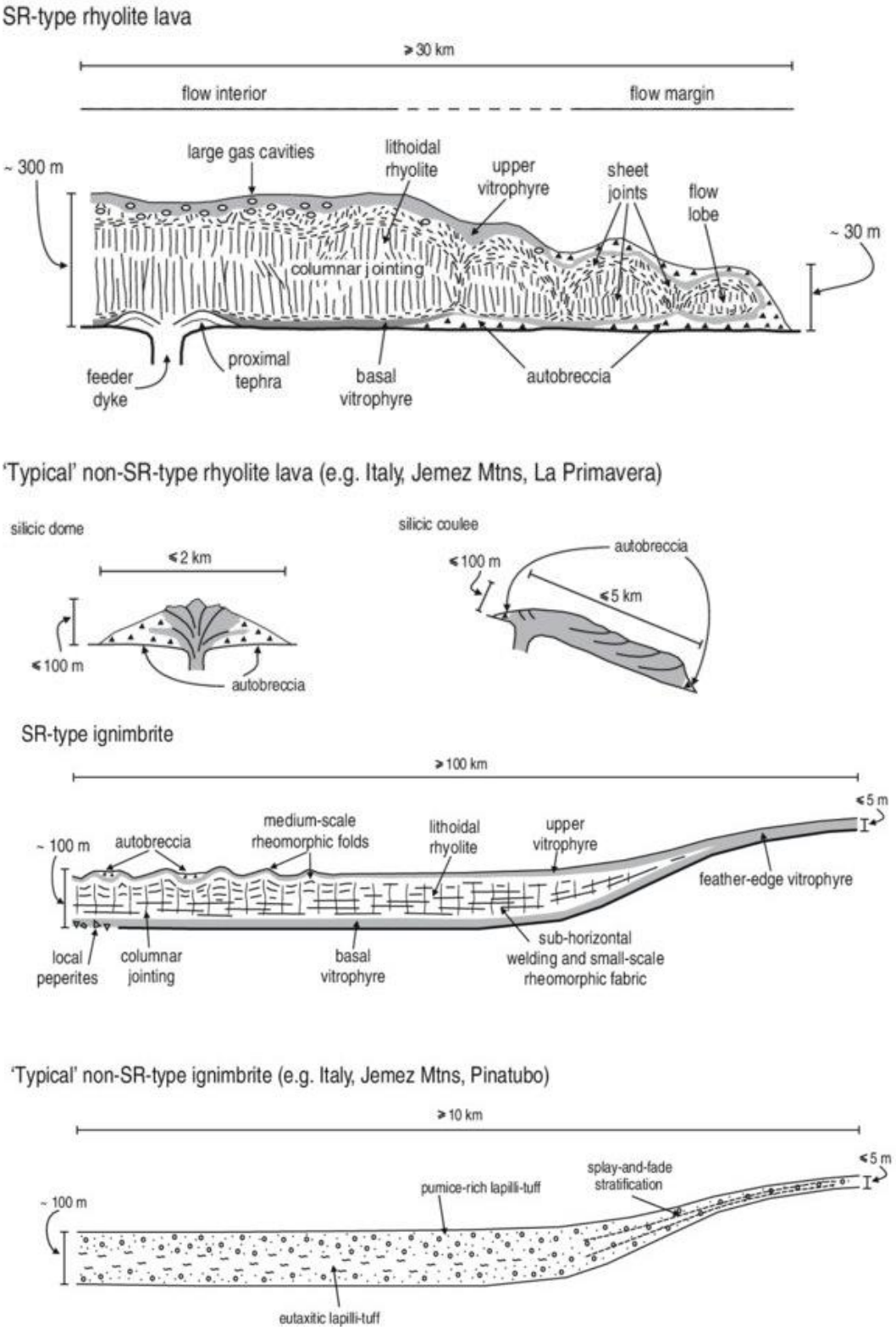


**Figure 2–13.** Contrast and comparison of the characteristic features of Snake-River type rhyolite lavas and ignimbrites, with other non-Snake-Rive type examples. Snake-River-type lavas are more extensive with lower aspect ratios than other (non-Snake-Rive-type) examples. SR-type ignimbrites are extremely high-grade, typically lacking in pumice lapilli or fiamme, exhibiting intensely welded and lava-like facies with evidence of rheomorphism. They are distinguished from the SR-type lavas by their tapering margins, zones of vitroclastic textures, and the absence of a basal autobreccia, with blunt, lobate terminal margins. (Branney et al., 2007)

# Chapter 3

## 3. Regional geology and previous work

### 3.1. Geological overview of Tenerife

Tenerife is the largest (2058 km$^2$) of seven intra-plate plume-related islands, as well as islets and submarine mounts, that belong to the Canary Islands Seamount Province (CISP). The seamounts of the CISP are located on the Jurassic oceanic crust of the African Plate, and extend 490 km across the Atlantic Ocean, 300 km west of Morocco, North Africa (Figure 3-1a). The origin of the archipelago is largely attributed to some form of plume-related, hot-spot volcanism (e.g. Martí et al., 1994; 1997; Carracedo, 1975; Fúster et al., 1968; Ancochea et al., 1990), although there are a host of alternative interpretations to account for the complex volcanic evolution of the CISP and its close proximity to the SW extension of the South Atlas Fault Zone (e.g. the 'blob' model: Hoernle & Schmincke, 1993; NNW-SSE extension of oceanic lithosphere: Anguita & Hernan, 1975; 2000; reactivation of a pre-existing fracture zone: Favela & Anderson, 2000).

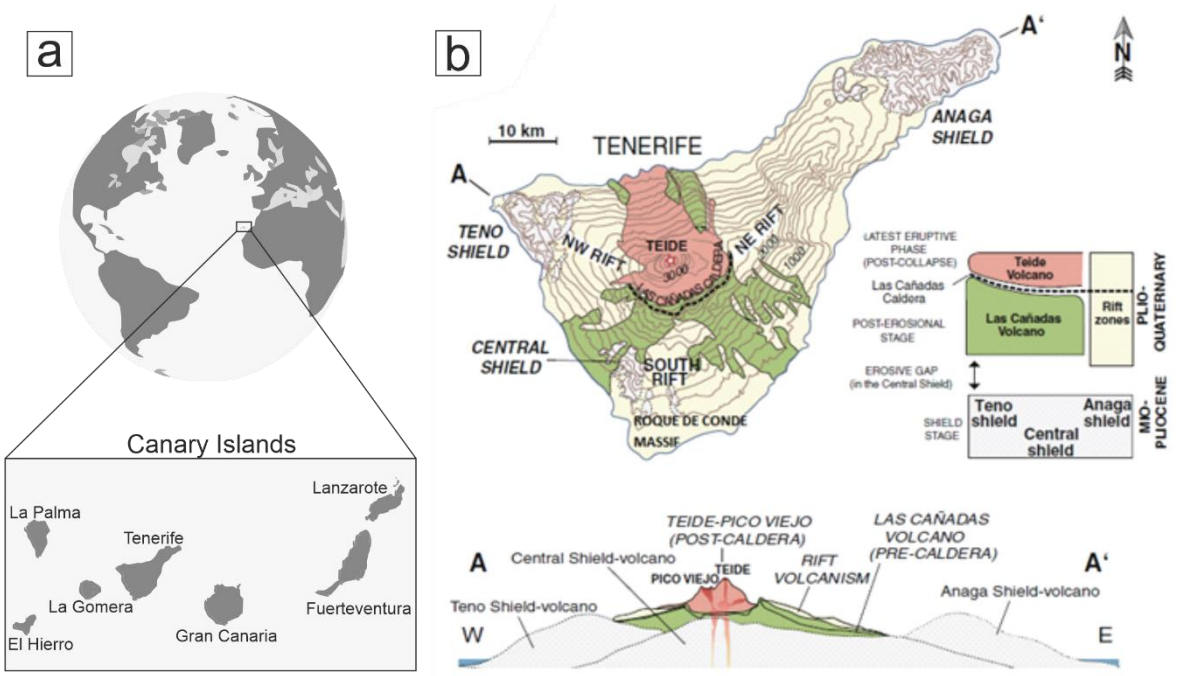


**Figure 3–1. a)** Cartoon map illustrating the geographical location of the Canary Islands archipelago on the west coast of North Africa. **b)** Summarised geological map and cross section through the island of Tenerife, showing the location of the Las Cañadas caldera depression in the centre (adapted from Carracedo et al., 2013, after Ancochea et al., 1990).

The Canarian archipelago is a result of 20 My of intraplate volcanism, beginning with submarine eruptions of poorly differentiated alkali basalts from NE-SW and NW-SE oriented fissures, parallel to the main regional tectonic trends across the Canaries (Martí et al., 1994). Tenerife exhibits a complex volcanic and geological history, with continuous subaerial volcanism over the last 12 My. Initial submarine stage volcanism (>20 Ma) resulted in extensive pillow lavas, breccias and hyaloclastites. Subaerial volcanism began with the shield-building phase, known as the 'Old Basaltic Series' (11.6 Ma to 3.5 Ma) (Ancochea et al., 1990), with the generation of fissure-fed, basaltic and alkali-basaltic, early shield volcanoes on the proposed oceanic islands of early Tenerife; Teno and Anaga, as well as the Roque del Conde massif (Fúster et al., 1968; Ancochea et al., 1990; Martí et al., 1994) (Figure 3-1b). However, it is argued that an early central shield system existed during this time, which has been lost to early lateral collapse event(s) (Gottsmann et al., 2008).

A prolonged period of erosion and mass wasting followed the shield building phase from 4.2 to 3.5 Ma, producing a highly irregular erosional unconformity, well exposed in various localities around the island (e.g. Santiago del Teide) (Gill & Thirwall, 2003). The mafic pile of the Boca Tauce edifice, uncovered by magnetic and gravity surveys (Ablay & Hürlimann, 2000; Ablay & Kearey, 2000) represents the oldest post-shield activity (3.8 – 3.5 Ma), which underlies the Las Cañadas deposits on the southwestern caldera rim.

Following the erosive hiatus, (3 – 1 Ma), a large, central complex, often referred to as the Cañadas 'volcano' or 'edifice', was built up as a result of continuous basaltic and differentiated (trachytes and phonolites) volcanism. 'The Rejuvenation Stage', from 2 Ma, comprised eruptions of large volumes of basalts and evolved trachytes and peralkaline phonolitic material (lavas, ignimbrites, and fall deposits) in the 'constructional phase' of the central complex, belonging to the 'Las Cañadas Stage' volcanism. This period is commonly described as the growth of a large, composite shield volcano, estimated to have reached 2500 m in height and 40 km in diameter (Carracedo et al., 2013). However, this concept often fails to acknowledge the likely cyclic and periodical growth and destruction of a series of individual stratovolcanoes (e.g. the Fasnia and Granadilla volcanoes) within the Cañadas Stage episode (Smith, 2012). Towards the end of the Cañadas

Stage, basaltic eruptions led to the construction of the Cordillera Dorsal, belonging to the 'Dorsal series' (0.9 to 0.0.43 Ma) (Fúster et al., 1968; Ancochea et al., 1990). This extensive outpouring of basalts along the spine of the SW-NE trending dorsal ridge (Cumbre de Pedro Gil) connected the partial seamount of Anaga massif with the central shield edifice (Figure 3–1b).

Subsequent collapse and multiphase subsidence of the Cañadas Stage deposits led to the 'caldera-building phase' (1.5 to 0.17 Ma), largely attributed to structural collapse of a depleting, high level, differentiated magma chamber below the central complex, producing the central, oblong depression known as the Cañadas Caldera, discussed further in Section 3.2.

Late stage volcanism over the last 1 Ma has produced the active stratovolcanoes of Teide (3718 m) and Pico Viejo (3135 m), which partially fill the Cañadas depression (Martí et al., 1994) with basalts, trachytes and phonolites, followed by cyclical periods of dormancy, volcanism, mass wasting, and erosion. The 1798 eruption of Chacharro on the southwestern flank of Teide-Pico Viejo marked the latest activity associated with the Teide-Pico Viejo complex, with the most recent volcanism on Tenerife belonging to the 'Recent Basaltic Series' (Fúster et al., 1968) with the 1909 eruption of Chinyero scoria scone and coeval basaltic lavas.

## 3.2. Las Cañadas Stage volcanism

Deposits of the Las Cañadas stage volcanism (3.5 Ma onwards, both pre- and post-collapse), account for much of the central and southern topography of the island. They formed from the result of multiple collapse events and cyclic episodes of explosive eruptions of predominantly felsic alkaline magma during both the construction of the Cañadas volcanic edifice(s) and subsequent collapse(s). Many of these deposits are exposed on the southern Cañadas caldera wall and the southern slopes of the island, forming extensive, proximal ignimbrite sheets along the 2 km high caldera walls, with basaltic and phonolitic lavas and more widely distributed ignimbrites and fall deposits of the Bandas del Sur Group.

The general stratigraphy of Cañadas Stage volcanism remains an area of controversy with conflicting stratigraphic timelines, based on field studies and limited dating of the deposits (e.g. Martí et al., 1994; Bryan et al., 1998; Ancochea

et al., 1995; 1999). The dominant mafic early eruptions (>2 Ma) were predominantly basaltic and basanitic effusive eruptions, associated with periods of quiescence, classified as the Cañadas edifice phase I (CE I) (Ancochea et al., 1999) (Figure 3–2). Contrastingly, this stage is classified as the Cañadas Lower Group (3.5-2.1 Ma) in the Cañadas stratigraphy as proposed by Martí et al., (1994) and supported by Bryan et al., (1998) (Figure 3–3). The base of both stratigraphic models of the early Cañadas deposits occur approx. 3.5 Ma, creating an erosional unconformity with the Old Basaltic Series of Tenerife.

In the stratigraphic timeline proposed by Martí et al. (1994), which is generally the most accepted (e.g. Bryan et al., 1998; Ancochea et al., 1995; 1999), the Lower Group is followed by an erosive hiatus between 2.0 Ma and 1.56 Ma, and deposits thereafter, between 1.56 Ma and 0.17 Ma are classified as the Upper Group, and subdivided into three eruptive cycles: the Ucanca Fm (1.56 – 1.07 Ma); the Guajara Fm (0.85 – 0.65 Ma) and the Diego Hernandez Fm (0.37 – 0.17) (Figure 3–3). This chronology differs from that proposed by Ancochea et al. (1995; 1999) in that there is no significant erosive hiatus between 2.0 Ma and 1.56 Ma, instead the Cañadas stratigraphy is separated into three phases, CE I, CE II and CE III (Figure 3–2). These later deposits of the 'Upper Group' (Martí et al., 1994; Bryan et al., 1998) and 'CE III' are predominantly deposits from more-evolved felsic, trachytic and phonolitic explosive pyroclastic eruptions which increase in magnitude and frequency between 1.59 Ma and 0.178 Ma (Ancochea et al., 1999; Huertas et al., 2002; Ancochea et al., 1995; 1999; Martí et al., 1994).

The localised stratigraphy, structure and nature of many of the Las Cañadas deposits are documented (e.g. 1987; Martí et al., 1990; 1994; Bryan et al., 1998; Ancochea et al., 1999; Edgar et al., 2002; Brown et al., 2003; Brown & Branney, 2004; Pittari et al., 2005; 2006), illustrating a highly complex and evolving volcanic history. However, much of the Las Cañadas Stage stratigraphy remains speculative, incomplete and controversial. Field determinations and correlations are made difficult as a result of multiple vertical flank collapse events and the destructive, erosive nature of cyclic explosive volcanism.

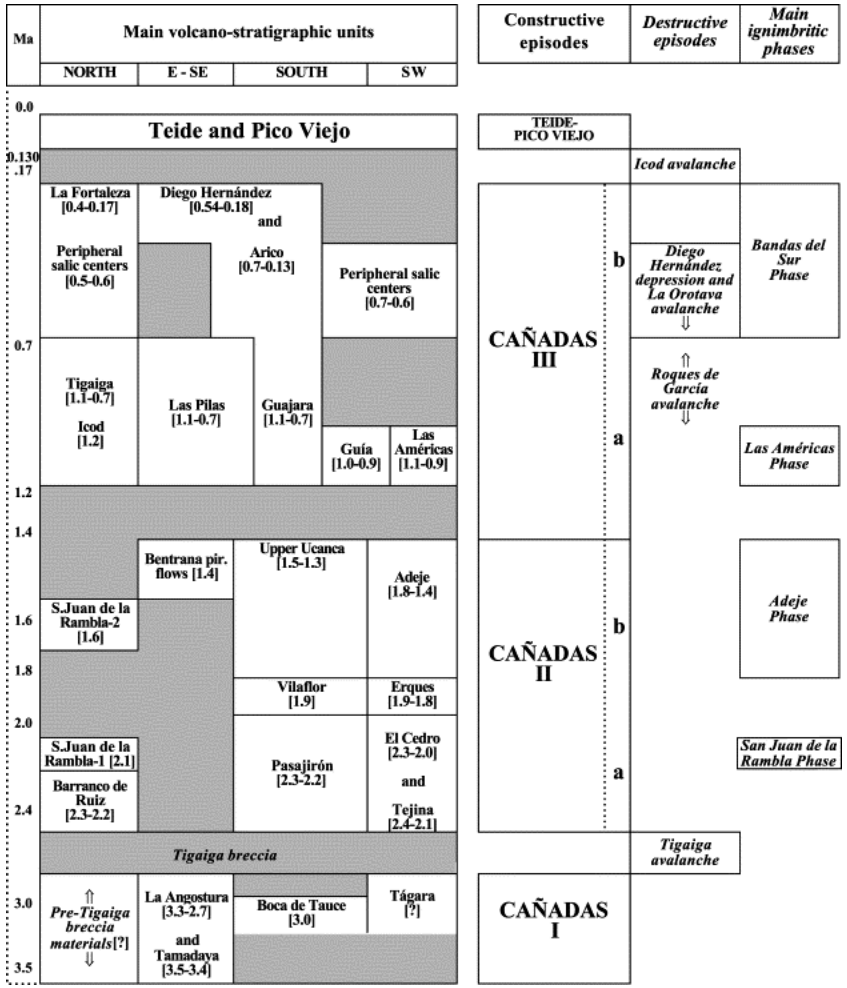


**Figure 3–2.** Generalised chronology of the main volcano-stratigraphic units of the Cañadas edifice. Shaded zones represent a lack of exposure, sampling, or measurement and not necessarily due to absence of volcanic activity. Huertas et al., (2002), adapted from Ancochea et al., (1999)

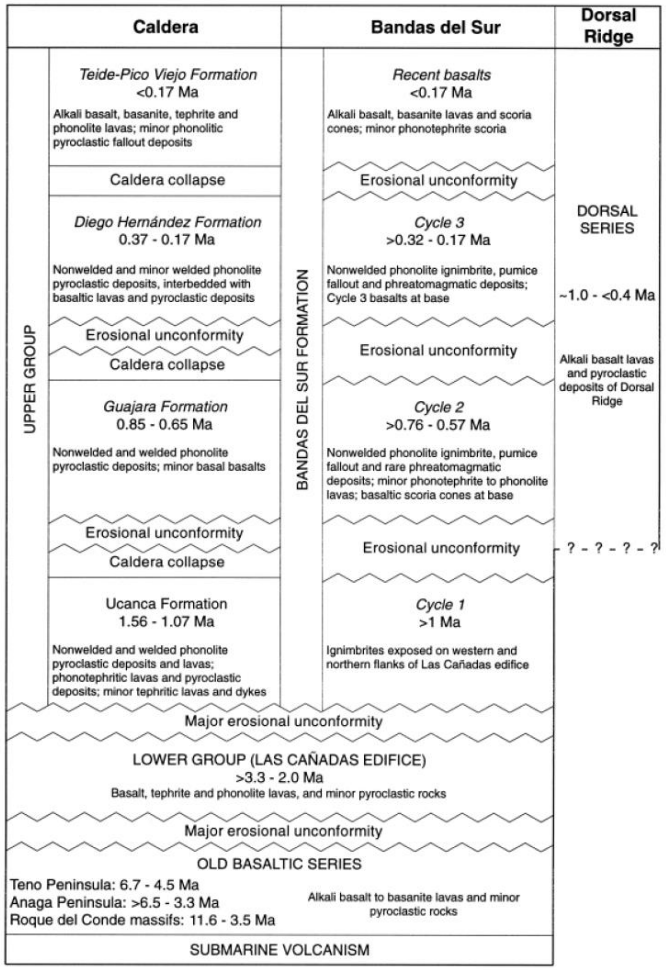


**Figure 3–3.** Generalised chronology of the stratigraphic section of the 'Upper Group' proposed by Martí et al., (1994). Three correlative eruptive cycles are proposed by Bryan et al., (1998).

Due to the lack of exposure, correlations between many proximal deposits from caldera-forming eruptive episodes, and the more distal, well-exposed deposits, particularly those blanketing the southern coast, are not straightforward (Huertas et al., 2002; Bryan, 1998).

Caldera collapse and subsidence is commonly associated with explosive eruptions, leading to the generation of many cubic kilometres of material (Lipman, 1997). It is suggested that the pyroclastic deposits documented across Tenerife only account for a small percentage of material erupted during episodes of explosive volcanism, with much pyroclastic material being lost from the stratigraphic record as eruptions entered the sea (Rodehorst et al., 1998; Schmincke & Sumita, 1998; Brown et al., 2003). Ignimbrite material volume estimates for the Gran Canaria apron were increased two-fold following the discovery of volcaniclastic material on the seafloor (Schmincke & Sumita, 1998). Furthermore, the subsequent and extensive growth of the Teide-Pico Viejo complex and associated products conceals possible intra-caldera ignimbrites which may be crucial to determining the lower stratigraphy and understanding of the caldera collapse process (Brown et al., 2003).

### 3.2.1. Las Cañadas Caldera stratigraphy

Partial exposures of pre- and post-collapse (Lower and Upper Cañadas groups) can be observed across the present configuration of the Las Cañadas Caldera, which forms a scalloped, oblong, elliptical depression extending 16 x 9 km (Figure 3-4). The southern, truncated Las Cañadas caldera wall provides excellent, almost continuous vertical exposure in the uppermost 100 m, recording up to 2 Ma of several destructive volcanic episodes. Intrusions, degradation, weathering, and scree cover obscure much of the lower wall stratigraphy and structure. The nature of the terraced, sloped landscape to the south of the caldera wall and deeply incised barrancos and gullies allow for good access and observation of the deposits (Figure 3–4).

The structure and stratigraphy of deposits along the caldera wall has been a focus of many studies (e.g. Araña, 1971; Araña & Brandle, 1969; Ridley, 1970; 1971; Martí et al., 1994; Soriano et al., 2002; 2006; Smith & Kokelaar, 2013) in an attempt to decipher the nature of deposits and their role in caldera formation and

eruptive stratigraphy of the island. Much speculation surrounds the origin and emplacement mechanisms behind much of the welded deposits, with a lack of documentation and definitive interpretation of the deposits. Poorly constrained units and the lack of a detailed stratigraphy affects the overall evolutionary model of the Las Cañadas Caldera, leading to an incomplete and poorly documented eruptive history of this stage of volcanism.

### 3.2.2. Caldera formation

The formation and structural evolution of Las Cañadas caldera is crucial in understanding the nature and behaviour of the proximal, caldera-forming ignimbrites. There are two main schools of thought concerning the formation of the current-day architecture of the Las Cañadas caldera, relating to the subsidence and collapse of the Las Cañadas edifice (1.5 to 0.17 Ma):

i) the most favoured model relates to multicyclic vertical collapse controlled by repeated movement of a ring fault system (e.g. Ridley, 1972; Booth, 1973; Martí et al., 1994; 1995; 1997; Bryan et al. 1998; Brown et al., 2003; Booth, 1973; Martí & Gudmundsson, 2000; Edgar et al., 2002; 2007; 2017; Martí et al., 2010; Prudencio et al., 2015; Piña-Varas et al., 2015), with each stage associated with major ignimbrite-forming pyroclastic eruptions, producing the Upper Group: Ucanca Fm, Guajara Fm and the Diego Hernandez Fm (Martí et al. 1994; Brown et al., 2003); and;

ii) multistage landslide events associated with successive periods of flank sector collapse (e.g. Ancochea et al., 1990; 1998; 1999; Cantagrel et al., 1999; Carracedo, 1994; Arnaud et al., 2001; Masson et al., 2002; Carracedo et al., 2007; Boulesteix et al., 2012), resulting in the landslides of Guimar (0.85 – 0.56 Ma), La Orotava (0.56 Ma) and Icod (0.18 Ma). Geomorphological studies and sea-floor investigations around the valley scarps of these landslides, and the presence of chaotic breccias in theses valleys lead to the interpretation that they represent large-scale sector collapse events, with displacement of >100 $km^3$ of material (Navarro & Coello, 1989; Ancochea et al., 1990; Cantagrel et al., 1999; Watts & Masson, 1995)

Although these large-scale landslides associated with flank collapse have had a significant impact on the landscape and configuration of Tenerife (Figure 3–4), there is evidence supporting the assertion that these collapse events are not solely responsible for the formation of the Las Cañadas caldera depression. The current configuration and shape of the Cañadas caldera is likely the result of a series of vertical, nested collapses (Brown et al., 2003; Martí et al., 1994) coupled with multiple caldera-forming, explosive eruptions, forming the eastward younging calderas, as well as the destruction of the northern flank during the Icod landslide and collapse (Brown et al. 2003; Edgar et al., 2007; Martí et al., 1994). Deposits interpreted to represent cyclical explosive and wasting events are widely recognised in the stratigraphy (e.g. Bryan et al., 1998i; Brown et al., 2003; Edgar et al., 2007), indicating significantly more frequent instability and collapse events than the simple three discrete collapses model. The presence of lithic breccia lithofacies in ignimbrite deposits have been interpreted to record collapse events, particularly if the material is vent-derived (e.g. containing syenite material - Bryan et al., 1998i; or lithics exhibiting thermal 'spalling' - Branney & Kokelaar, 2002). However, whether many of these lithic breccias represent individual caldera-forming eruptions (e.g. Brown et al., 2003; Edgar et al., 2007), have originated from material picked up by current(s), or are late-stage flux(es) of lithic material sourced from the vent (e.g. Bryan et al., 1998ii) remains a significant topic of debate.

The Roques de Garcia, an outcrop of intrusive phonolitic sheets and dykes, breccias, sedimentary and pyroclastic units, belonging to the Lower Group, is proposed to mark the boundary between the nested calderas of the Ucanca and Guajara Formation, but much of the Ucanca caldera structure to the west and north is presumed lost by the Icod collapse and subsequent Teide-Pico Viejo cover. Due to similarities between the Roques de Garcia Formation and Lower Group deposits and phonolitic intrusions exposed in the lower caldera, it is suggested that this outcrop is internally consistent within the Ucanca caldera, with the largest of the intrusions representing conduits for the deposits of the Upper Group, some of which are described in Chapter 4. This implies that the margins of the early caldera configuration did not form the headwall of flank collapse.

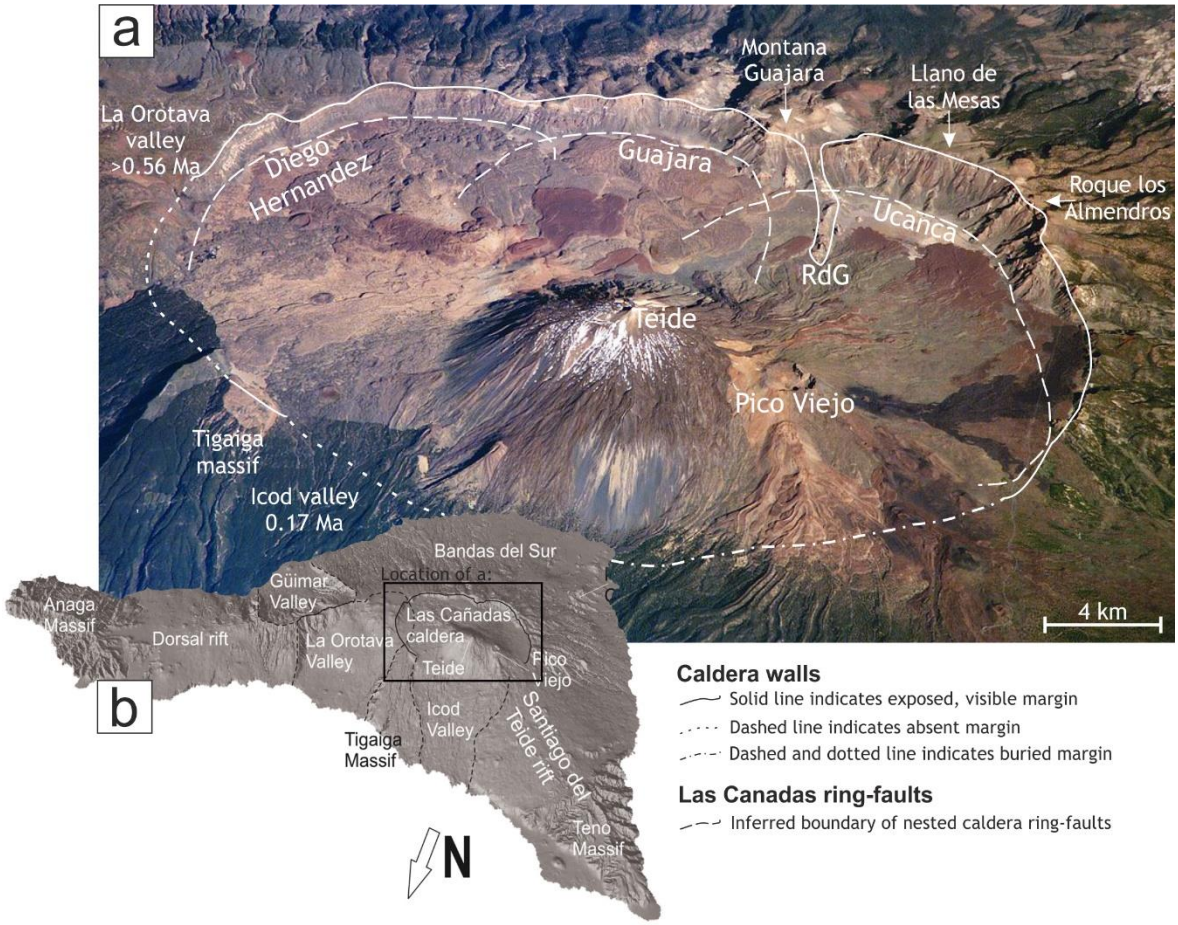


**Figure 3–4.** Las Cañadas Caldera: a**)** Aerial photograph of the Las Cañadas Caldera from the International Space Station, highlighting the inferred boundaries of the nested calderas after Martí et al. (1997) and the margins of the caldera wall; b) location of the aerial photograph, highlighting the main morphological features of Tenerife and the three landslide scarps, adapted from Martí (2019).

## 3.3. Previous work

The deposits of the Ucanca Formation remain the least documented of the three nested calderas forming the Las Cañadas depression. Despite their significance in terms of caldera-forming eruptions, and their abundance in the caldera wall stratigraphy, there is a lack of detailed analysis concerning both the stratigraphy and characteristics of these deposits, as well as the processes governing their emplacement and welding. Both the Ucanca and Guajara Formation predominantly consist of a stacked sequence of thick, welded pyroclastic rocks, representing important explosive phonolitic eruptive cycles, and this section provides an overview of the previous interpretations and work on these deposits.

Many of the welded and lava-like units have been subject to fleeting and conflicting interpretations, being variously described as: i) phonolite lavas (Fúster et al., 1968; Ridley, 1972; Troll & Carracedo, 2016; Ancochea et al., 1990); ii) welded Plinian fall deposits (Martí et al., 1994; Martí & Ablay, 1994; Soriano et al., 2002; 2006; Bryan, 1998); and iii) as welded ignimbrites (Martí et al., 1994; Martí & Ablay, 1994). Early work refers to the deposits as Eutaxites (Araña, 1971; Ridley, 1972), briefly interpreting them as thick phonolitic lavas, due to the presence of flow banding, fluidal textures, columnar jointing and the massive, lava-like facies (Fúster et al., 1968; Araña, 1971; Ridley, 1972; Ancochea et al., 1990). Soriano et al. (2002; 2006) provides the most recent descriptions for select units of the Ucanca and Guajara Formations, attributing the welded and lava-like units to vent-proximal Plinian fallout, undergoing post-emplacement rheomorphic flow down-slope.

Much of the distinction made between densely welded fall and ignimbrite is based on textural analysis, assuming a fallout mechanism for facies that exhibit: i) a lack in interstitial ash or a fine-grained matrix component; ii) clast-supported textures; iii) well-developed eutaxitic fabrics (typically with 1-20 cm long glassy and devitrified fiamme); iv) horizons of coarse (<30 cm) lithics; and v) possible lateral or vertical gradation(s) into lesser welded well-sorted pumice-rich facies, clastogenic lavas or a lava-like facies (Martí et al., 1994; 1995i; Bryan, 1998). The interpretation of ignimbrite has been given to associated relatively much thinner deposits, exhibiting fine-grained ash matrix with typically shorter fiamme (0.1 – 5 cm in length) (Martí et al., 1994; 1995i; Martí & Ablay, 1994; Bryan, 1998). The extent of welding exhibited by these deposits is considered to be related to vent proximity, displaying similarities with other calc-alkaline and peralkaline systems (e.g. Sparks & Wright, 1978; Mahood, 1984). The absence of extensive welding in deposits of the Diego Hernandez Formation, products of the youngest caldera-forming eruption, is attributed to a more distal vent source.

### 3.3.1. The Ucanca Formation

The Ucanca Formation (1.56-1.07 Ma) dominates much of the central caldera wall, having a recorded thickness of up to 300 m in the most western sector of the wall, and up to 70 m thick towards the eastern sector. The base of the Ucanca Fm (1.56 Ma) unconformably overlies the plagioclase-phyric basalt lavas of the Boca Tauce

sequence and associated deposits to the north west of the caldera margins (Martí et al., 1994), and presumably deposits belonging to the Lower Group for much of its lateral extent. Dating by Ancochea et al. (1990) estimated that the base of the Lower Group is 3.2 Ma, however it is debated by other workers (e.g., Martí et al. 1994) that due to the stratigraphic relationships with earlier deposits of the Lower Group, caldera activity may have occurred much earlier. Extra-caldera Lower Group deposits are poorly constrained in the literature, due to poor and sporadic exposure and record considerably complex stratigraphies.

The units belonging to the Ucanca Fm are largely classified as undifferentiated vent-proximal welded fall deposits, typically lacking in interruption (i.e., palaeosols, partings, disconformities), and described as exhibiting simple vertical welding profiles, with a non-welded base, grading into a densely welded, lava-like facies (Soriano et al., 2002; 2006), interbedded with ignimbrites and lavas. Individual members representing eruptive packages for a portion of the western sector of the caldera wall was presented by Soriano et al. (2002), with seven proposed members overlying the lower Ucanca Formation from El Sombrerito in the west, to beyond the Chasna Ridge (Figure 4-1). These units are interpreted as welded and non-welded spatter and fall deposits, with the exception of the 'Boca de Tauce Member' (not to be confused with the older Boca de Tauce sequence), exposed in the caldera wall, which is interpreted as welded ignimbrites, co-ignimbrite, breccias, and surge deposits (Figure 3–5).

Thickening of the welded fall sheets around their conduit is attributed to rheomorphic flowage of material and detachment of the upper-most welded component (e.g., Soriano et al., 2006; 2009; Reedman et al., 1987). This is discussed further in detail in Chapter 7. However, in general, the Ucanca deposits are stacked sub-horizontally along the extent of the caldera rim. A local thickening of many of the sheets towards the caldera rim (e.g., in the Pasajiron Mb, El Sombrero Mb, Los Retamares Mb and La Grieta Mb – Soriano et al., 2002; 2006) is observed (see Figure 3-5), with steep dips of up to 60°.

A network of phonolitic dykes and inclined sheets border the caldera wall margin, obscuring much of the lower stratigraphy, and many of which have been identified as feeder vents and conduit structures by Soriano et al. (2006) to the proximal

deposits between, and including El Cedro to the west and Sombrero de Chasna. Soriano et al. (2006) attributes the welding profile of each member directly to the proximity to, and relationship with, these conduit-vent structures. It is suggested that the upper, flared geometry of the vent systems are filled with welded fall material that has undergone rheomorphic flow. The lowermost part of the vent system has been filled with lava plugs, which are hypothesised to agglutinate to a fluidal mass, infilling the conduit walls (Figure 3–6). The widespread, non-welded, pumice-rich basal components of many of the members are attributed to more distal fallout material produced early in the early, explosive stages of eruption, with welding of material leading to a transition from turbulent flow to a non-explosive, annular flow, correlating to the hypothesised thickening of rheomorphic fallout and laminar flow of magma infilling the vents, representing the end of activity (Soriano et al., 2006), discussed further in Chapter 7 (e.g. Figure 7–9).

Outside of these works, the majority of the units exposed along the caldera wall, between the Roque los Almendros towards Montaña Guajara, remain largely undifferentiated, with only brief reference to prominent and interesting features in guidebooks and excursion guides. Troll and Carracedo (2016) make reference to an interpretation of ‘Sombrero de Chasna’, an elliptical, flat-topped mound atop a series of stacked largely undifferentiated deposits, as a lava, erupted from a lava-dome (‘mini-chasna’) and pools to form a lava coulée, with very little explanation nor field evidence in support of this interpretation (Figure 3–7).

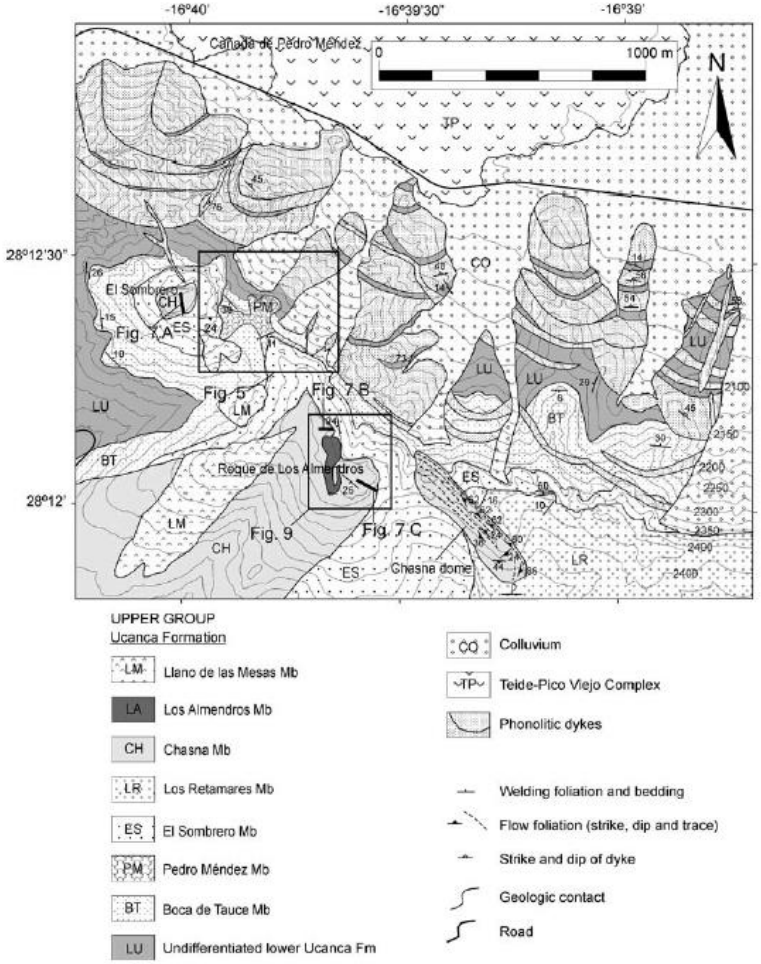


**Figure 3–5.** Geological map of the western sector of the Las Cañadas caldera wall presented by Soriano et al. (2002). Seven members are presented, representing individual eruptive packages.

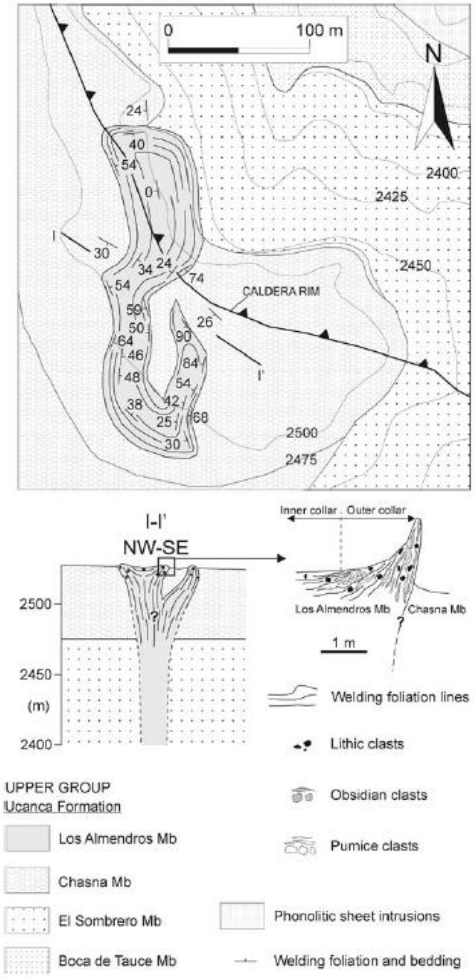


**Figure 3–6.** Geological map and cross section of the proposed conduit-vent structure of the Los Almendros Member at Roque Los Almendros (Soriano et al., 2006).

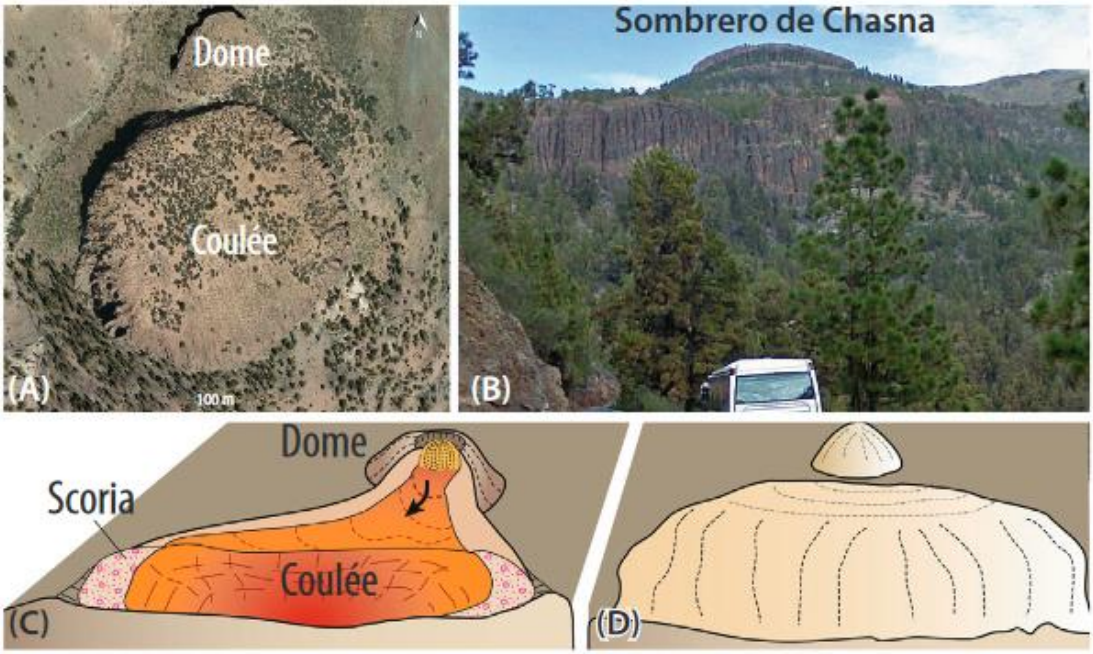


**Figure 3–7.** The Sombrero de Chasna interpreted as a lava 'coulee'. Taken from Troll & Carracedo (2016). a) Aerial photograph of the proposed coulee and dome; b) View looking northwards to the Sombrero de Chasna above the Riscos Atravesados; c) Sketch of the proposed features of the Sombrero de Chasna lava, with scoria at the flanks of the deposit; d) Geomorphological features of the Sombrero de Chasna and dome.

### 3.3.2. The Guajara Formation

The Guajara Formation (0.85-0.65 Ma) extends from the central caldera wall, overlying the Ucanca Fm at Llano de las Mesas and spanning 2 km eastwards, where it is overlain by the youngest Las Cañadas caldera-forming eruption(s) of the Diego Hernandez Formation. The deposits form a terraced stack of thick (up to 280 m thick) predominantly welded and lava-like deposits, with non-welded ignimbrite and fall deposits which compose Montaña Guajara, a prominent feature in the southern caldera wall (Figure 3-4).

The relationship between the Ucanca Formation and the overlying Guajara Formation is interpreted as conformable, with the Guajara Formation comprising phonolitic welded 'surge' and 'fallout' deposits and lavas, crosscut by N-S trending basaltic and phonolitic dykes and inclined sheets (Soriano et al., 2002; 2006) similar to that of the Ucanca Formation. A section of the caldera east of Montaña Guajara has been mapped and described by Soriano et al. (2002; 2006; 2009), identifying five individual members (La Camelita Mb, Pasajiron Mb, La Grieta Mb

and Valle Blanco Mb), with a similar mechanism of emplacement as the welded units of the Ucanca Fm attributed to the thick accumulation of the welded deposits of Guajara. Much of the underlying and overlying stratigraphy remains undifferentiated, and the relationship to the deposits of Montaña Guajara has not yet been established.

Early work by Martí & Ablay (1994) attributed the intensity of welding to progressive tapping of hotter, volatile-poor phonolite magma, resulting in an eruptive style from initially Plinian (cooler eruption, giving rise to the basal non-welded pumice fall), to a fire-fountaining style of eruption, with spatter producing a lava-like facies and generation of clastogenic lavas. Bryan (1998) discredited this model of emplacement in his study on the Guajara Welded Unit (GWU) (Figure 3-8), as the spatter-rich welded facies extends to the base of this unit, with rapid (<50 cm) vertical transitions in welding intensity from nonwelded to welded, with a lack of any geochemical variation through the sequence. These relationships cannot be attributed to the progressive tapping depletion of more volatile-rich magma, and the gradational lowering of an eruption column from high Plinian to Strombolian.

A model whereby vent-proximal fall is deposited from a low fountaining (strombolian-type) column, facilitating rapid agglutination on deposition is proposed by Bryan (1998), with periodic phreatomagmatic activity giving rise to localised pyroclastic fountaining as a result of groundwater interaction. The upwards increase in welding intensity is attributed to the eruption becoming progressively less explosive (e.g. Mahood, 1984), with the lava-like facies as a result of fewer ejecta and lithics incorporated, aiding the ability of the fall to retain heat and remain thermally insulated, allowing high-temperature devitrification, (Bryan, 1998) resulting in the glassy, lava-like texture (e.g. Stephenson et al., 1993). As discussed, this mechanism of emplacement is supported by Soriano et al. (2002; 2006; 2009) for the deposits of the Guajara Fm east of the GWU and those described as belonging to the Ucanca Fm.

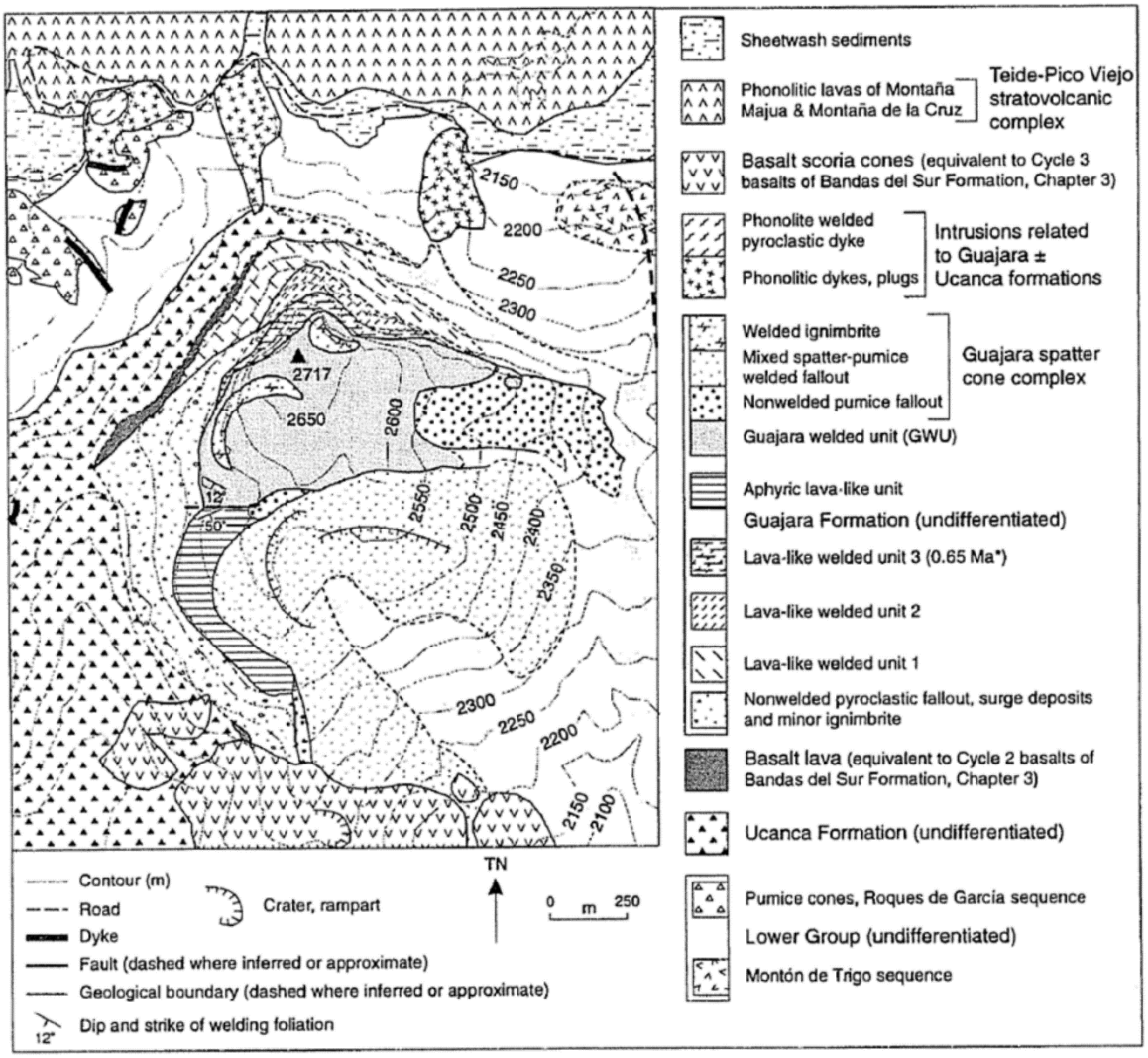


**Figure 3–8.** Bryan's (1998) generalised geological map and stratigraphy of Montaña Guajara. *Age date from Martí et al. (1994).

## 3.4. Summary

The multi-stage formation of the Cañadas caldera is highly complex and protracted. Although there are strong correlations between episodes of sector collapse and the caldera wall ignimbrites of the Upper Group (or CE III) (e.g. Martí et al., 1994, 1997; Brown et al., 2003) the exact timing of this relationship (i.e. during caldera collapse, or as a result of) remains largely undetermined. Although the age, timing and emplacement of these units is argued, it is widely accepted that the southern scalloped caldera rim is partitioned into three eastwardly migrating formations, formed from a hybrid of cyclical catastrophic collapse events, explosive caldera-forming eruptions and intermittent erosional modification of complex topography.

Despite the deposits providing exceptional preservation and exposure of proximal caldera-forming eruptions, much of the stratigraphy of the Ucanca and Guajara Formations along the caldera wall remains segmented and largely incomplete with conflicting and contrasting emplacement mechanisms. This chapter highlights the need for a consistent stratigraphic framework in order to better understand the early formation and eruptive episodes of the Las Cañadas caldera. This project aims to rectify this gap in our knowledge of the eruptive history of the Las Cañadas stage volcanism, through both an investigative field-based and analytical approach. In addressing these uncertainties, deeper insights into the caldera formation can be gained, as well as contributing to our understanding of the emplacement mechanisms of high-grade pyroclastic eruptive events.

# Chapter 4

## 4. Stratigraphy and Physical Volcanology

This chapter provides an overview of the mapped stratigraphy of the southern slopes of the central Las Cañadas caldera wall (Figure 4-0), documenting and describing the units belonging to each member, and their place in the stratigraphy.

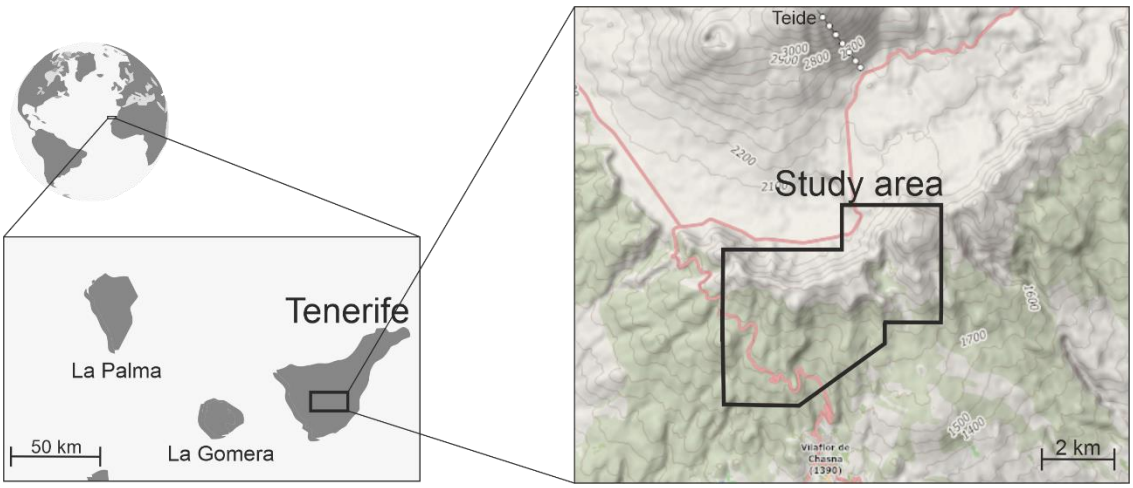


**Figure 4–0.** Map highlighting the spatial extent of the study area in the Las Cañadas caldera wall. Base Map from 4Umaps.com.

### 4.1. Las Cañadas Caldera stratigraphy

The stratigraphy of the central southern Las Cañadas caldera wall comprises stacked sequences of pyroclastic deposits, punctuated by erosional unconformities and minor volcaniclastic sedimentary horizons, belonging to the Ucanca and overlying Guajara Formations, as outlined in Chapter 3. The extra-caldera deposits of the Ucanca Fm remain the most neglected and poorly documented of the three Las Cañadas caldera-forming eruptions, with conflicting and contrasting interpretations loosely assigned to many of its units.

A revised stratigraphy of the central sector of Las Cañadas Caldera is presented, (Figure 4–1 & 4–5), detailing the units, descriptions, and architecture for each of the proposed members. The deposits of Ucanca Formation are documented in detail, but only a limited section of the Guajara Formation is described, providing more of a preliminary investigation. Interpretations are briefly outlined in this

chapter but are covered in more depth in Chapters 5 and 7. The mapped deposits are assigned individual units and are grouped into six members with shared physical and structural characteristics (colour, lithic composition, lithofacies profiles, textural components, etc). Individual eruptive units within the members have been identified on the basis of, but not limited to palaeosols, disconformable cooling joints, interruptive fall deposits, and reworked sedimentary horizons. However, due to the nature of welding observed in the deposits (outlined in detail in Chapters 3 & 5), and the potential for removal by scour, erosion and bypassing of PDC(s), the number of units could be underestimated, with the evidence of these events being obliterated during the welding processes. Extensive exposure, which can be traced both laterally and vertically through the caldera wall, road cuts and barrancos allowed for approximate estimations of unit thickness and lateral extent.

Post caldera-formation events and deposits such as scoria cone activity and associated lavas, although mapped, are not described nor included within the scope of this study.

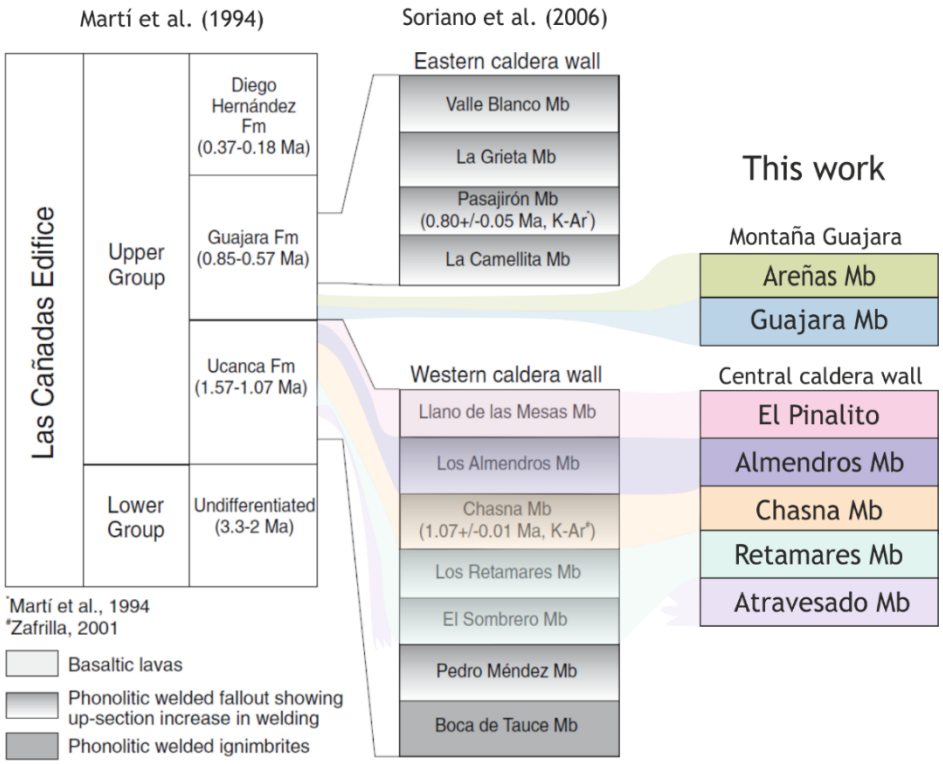


**Figure 4–1.** Context of the revised stratigraphy against previous work by Soriano et al. (2006). Units in the central southern caldera wall described in this Chapter overlap with those described by Soriano et al. (2006) in the western caldera wall, however many of the subunits and geological boundaries are not agreed.

### 4.1.1. Symbols and lithofacies abbreviations

Figure 4–2 outlines the graphic symbols and lithofacies abbreviations used in the stratigraphic logs, figures, and deposit descriptions throughout this chapter.

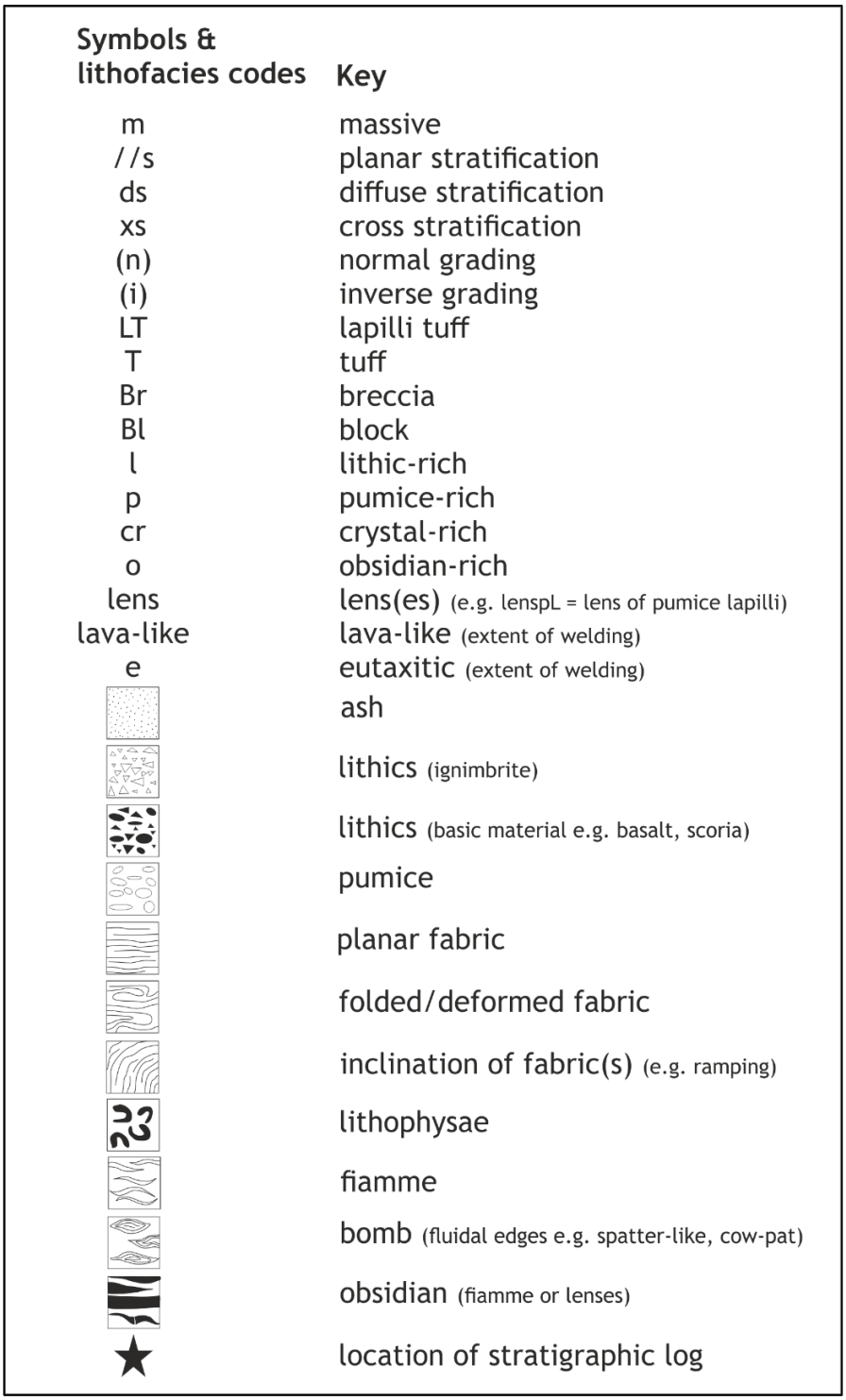


**Figure 4–2.** Summary key of the symbols and lithofacies abbreviations used throughout the logs, figures and descriptions. Lithofacies codes after Branney & Kokelaar (2002).

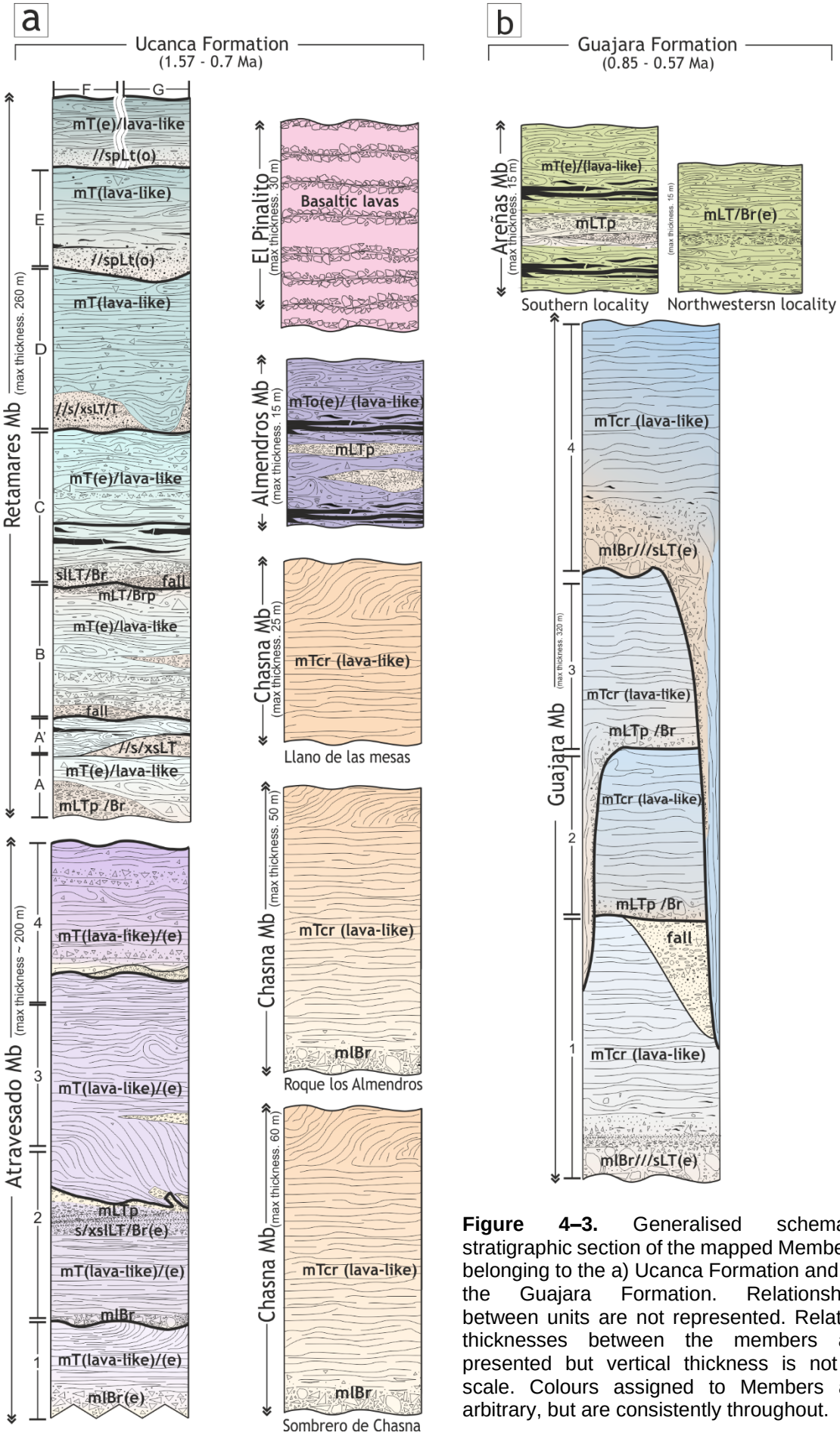


**Figure 4–3.** Generalised schematic stratigraphic section of the mapped Members, belonging to the a) Ucanca Formation and, b) the Guajara Formation. Relationships between units are not represented. Relative thicknesses between the members are presented but vertical thickness is not to scale. Colours assigned to Members are arbitrary, but are consistently throughout.

A summary of each of the mapped units of the Ucanca and Guajara Formations described in this chapter are presented in Table 4–1. Members and units are described from oldest to youngest. Further interpretation of the welding intensities is presented in Chapter 5, and investigation into the emplacement conditions and eruptive models are presented in Chapter 7.

| Fm | Member | Locations | Description | Interpretation |
|---|---|---|---|---|
| **Guajara Formation** | Guajara Member | Barranco de Erjis, forming Montaña Guajara, and continues westwards with undetermined limits. | Four thick, downslope thinning, columnar jointed, predominantly lava-like units, interbedded with minor pumice fall deposits. | A series of sustained, low-column 'boil-over' PDCs, initiated by explosive activity. Extensive welding attributed to both syn-depositional coalescence of rapidly aggrading pyroclasts, and post-depositional rheomorphism. |
| | Areñas Member | Two localities: i) northeast; and ii) southwards, of the summit of Montaña Guajara. | Thin, flow banded and rheomorphic, obsidian-rich and variably welded tuffs. | Result of topographically controlled, highly unstable PDCs, with oscillating phases of syn-depositional welding and rheomorphism. |
| **Ucanca Formation** | El Pinalito Lavas | Caldera wall at Llano de las Mesas to the town of Vilaflor to the south. | At least eight individual porphyritic basalt lava flows. | Dyke-fed series of lava flows from a basaltic vent(s) exposed in the caldera wall, post-dating the Chasna Member. |
| | Almendros Member | Summit of Roque los Almendros. | A thin, flow banded, obsidian-rich, variably welded lapilli tuff. | A result of a topographically controlled, fluid-escape dominated pyroclastic density current(s) deposited in a paleo-valley. |
| | Chasna Member | Three localities: i) Roque los Almendros; ii) Sombrero de Chasna; and iii) Llano de las Mesas. | Three rusty orange, columnar jointed, isolated tear-dropped shaped units. Crystal rich, lithic poor and displaying polyphase rheomorphic structures. | High-mass flux, rapid deposition of ash-rich material from sustained, low-column PDCs undergoing intense welding as a result of both syn-depositional coalescence of fines and hot-state deformation following emplacement. |
| | Retamares Member | Caldera wall margins, from Roque los Almendros to Montaña Guajara, extending southwards over Los Retamares, across the Sombrero de Chasna and Roque de Encaje. | Seven (units A - G) predominantly welded deposits, exhibiting highly variable welding intensities and textures. Lithic-rich, crystal poor low-aspect ratio deposits, interbedded with pumice-rich non-welded fall deposits. | Deposits represent pulses of highly unstable, dynamic and fluctuating PDC(s), from explosive, short-lived eruptions. Each eruption is initiated by a period of explosivity, associated with some evidence of Plinian activity, with deposits undergoing both syn- and post-depositional rheomorphism. |
| | Atravesado Member | North of Vilaflor to the caldera wall margin, forming much of the topography from Los Retamares and Las Lajas in the west to Roque de Encaje to the east. | Four (units 1 - 4) thick, predominantly lava-like, rheomorphic units, displaying both lateral and vertical variations in welding intensity. | A series of sustained PDCs, with evidence of initial current instability and explosivity, with transitions to a sustained, high mass-flux PDC associated with low column, 'boil-over' style of eruption(s), undergoing both syn- and post-depositional rheomorphism. |

**Table 4–1**. Summary of the location, description, and interpretation of the mapped members (Figure 4–4) that are described in this chapter.

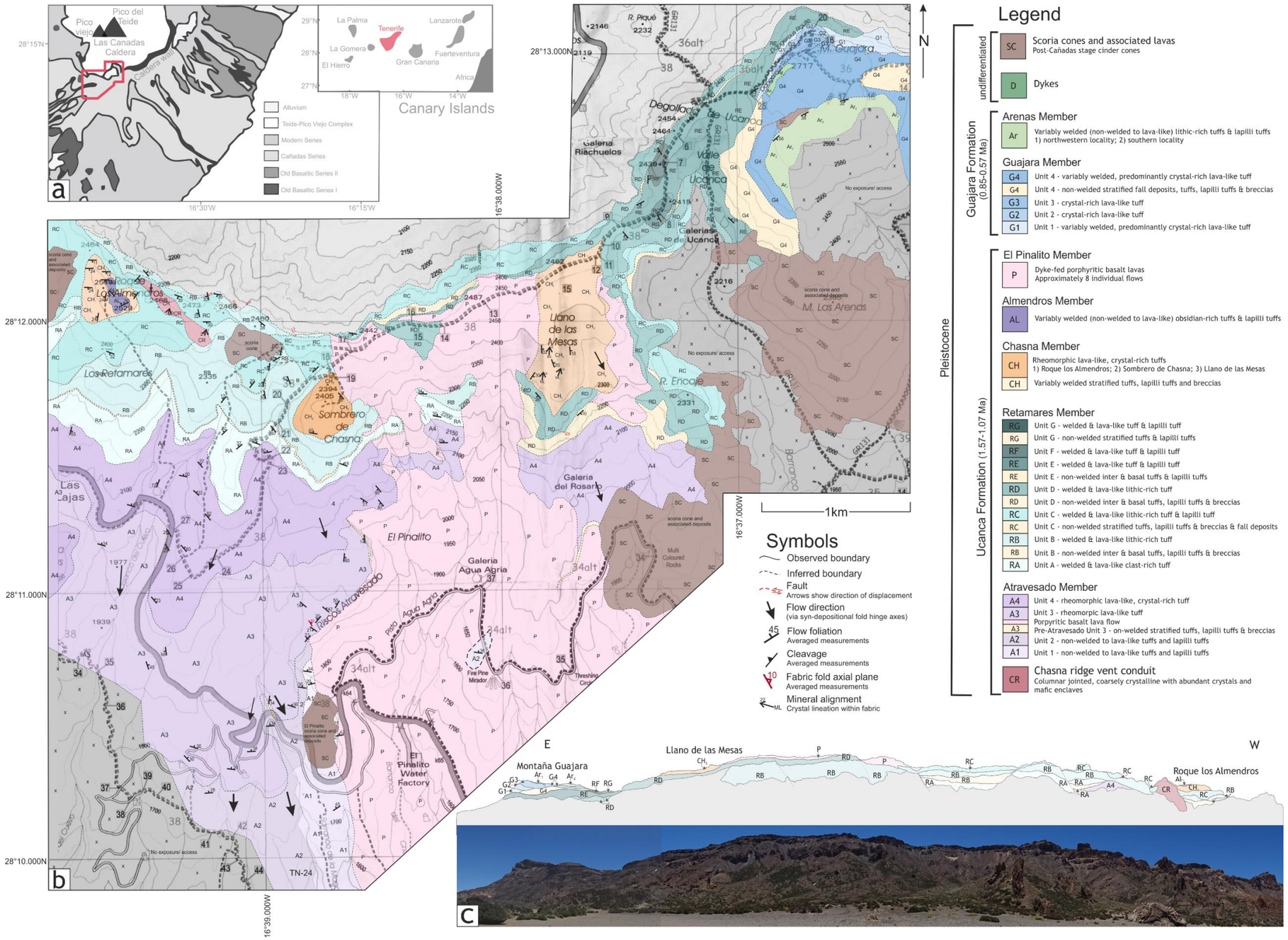


## Legend

**Pleistocene**

**Guajara Formation (0.85-0.57 Ma)**

undifferentiated

- SC — Scoria cones and associated lavas (Post-Cañadas stage cinder cones)
- D — Dykes

Arenas Member

- Ar — Variably welded (non-welded to lava-like) lithic-rich tuffs & lapilli tuffs; 1) northwestern locality; 2) southern locality

Guajara Member

- G4 — Unit 4 - variably welded, predominantly crystal-rich lava-like tuff
- G4 — Unit 4 - non-welded stratified fall deposits, tuffs, lapilli tuffs & breccias
- G3 — Unit 3 - crystal-rich lava-like tuff
- G2 — Unit 2 - crystal-rich lava-like tuff
- G1 — Unit 1 - variably welded, predominantly crystal-rich lava-like tuff

**Ucanca Formation (1.57-1.07 Ma)**

El Pinalito Member

- P — Dyke-fed porphyritic basalt lavas; Approximately 8 individual flows

Almendros Member

- AL — Variably welded (non-welded to lava-like) obsidian-rich tuffs & lapilli tuffs

Chasna Member

- CH — Rheomorphic lava-like, crystal-rich tuffs; 1) Roque los Almendros; 2) Sombrero de Chasna; 3) Llano de las Mesas
- CH — Variably welded stratified tuffs, lapilli tuffs and breccias

Retamares Member

- RG — Unit G - welded & lava-like tuff & lapilli tuff
- RG — Unit G - non-welded stratified tuffs & lapilli tuffs
- RF — Unit F - welded & lava-like tuff & lapilli tuff
- RE — Unit E - welded & lava-like tuff & lapilli tuff
- RE — Unit E - non-welded inter & basal tuffs & lapilli tuffs
- RD — Unit D - welded & lava-like lithic-rich tuff
- RD — Unit D - non-welded inter & basal tuffs, lapilli tuffs & breccias
- RC — Unit C - welded & lava-like lithic-rich tuff & lapilli tuff
- RC — Unit C - non-welded stratified tuffs, lapilli tuffs & breccias & fall deposits
- RB — Unit B - welded & lava-like lithic-rich tuff
- RB — Unit B - non-welded inter & basal tuffs, lapilli tuffs & breccias
- RA — Unit A - welded & lava-like clast-rich tuff

Atravesado Member

- A4 — Unit 4 - rheomorphic lava-like, crystal-rich tuff
- A3 — Unit 3 - rheomorpic lava-like tuff
- Porpyritic basalt lava flow
- A3 — Pre-Atravesado Unit 3 - on-welded stratified tuffs, lapilli tuffs & breccias
- A2 — Unit 2 - non-welded to lava-like tuffs and lapilli tuffs
- A1 — Unit 1 - non-welded to lava-like tuffs and lapilli tuffs

- CR — Chasna ridge vent conduit; Columnar jointed, coarsely crystalline with abundant crystals and mafic enclaves

**Figure 4–4.** Geological map and view of the caldera wall. a) Simplified geological map of Tenerife, with red outline highlighting mapped area. b) Simple geological map of the proposed members and units of the Ucanca and Guajara Formations in the central southern sector of the Las Cañadas caldera wall. The grid shows 1 km eastings and northings of the EUR50 grid system. c) Annotated field sketch and panorama photograph of the central southern sector of the Las Cañadas caldera wall, looking southwards from Llano de Ucanca within the caldera.

# Ucanca Formation

## 4.2. Atravesado Member

The Atravesado Member consists of four predominantly lava-like tuff units (Figure 4–5), which extend from 50 m north of Las Lajas (at N28°11'35.1" W016°39'54.4", ~ 2150 m elevation) to the town of Vilaflor (at N28°9'40" W016°38'46", ~ 1580 m elevation), with the lower limits of the lower units remaining undefined. These units young in a northern direction and exhibit a range of welding textures from non-welded, typically at the base of the deposits, grading up into intensely welded and lava-like lithofacies.


**Figure 4–5.** Field relationships of the lowest Atravesado Units (1, 2 and 3) bound by El Pinalito lavas to the east and obscured by scoria cone activity to the south (N28°10'29.8 W16°38'40.4).

### 4.2.1. Atravesado Unit 1

The western and southernmost limits of Unit 1 remain poorly constrained, but the unit is well exposed from N28°10'29.8" W16°38'40.4" (roadside exposure approximately 50 m south of Riscos Atravesado, ~ 1850 m elevation) to N28°9'40" W016°38'46" within the town of Vilaflor (~ 1650 m elevation) (Figure 4–5). The eastern extent of the exposure is bound by, and overlain by, the El Pinalito lavas (N28°10'29.8 W16°38'40.4) (Figure 4–9), and it is overlain to the west and the south by the younger Atravesado units.

The base of Unit 1, exposed in farmland north of the town of Vilaflor (Figure 4–6, 4–7, & 4–8) (N28°9'40" W016°38'46", 1580 m elevation) is predominantly southward dipping (lobed downhill), and comprises a non-welded, pumice-rich, stratified

base, with a pumice-rich horizon laterally and vertically grading into a massive lava-like tuff. The non-welded basal stratigraphy appears to be discontinuous, forming a 4.25 m wedge, which immediately (0.25 m) laterally grades into lava-like lithofacies, and tapers out to the east of the exposure.

The lava-like lithofacies accounts for the majority of the unit's thickness, with localised areas of eutaxitic texture and a persistent, planar base-parallel fabric throughout. In common with the other units of the Atravesado Mb, the unit is distinctly columnar jointed (12°-15°dip). The lava-like tuff is crystal-poor with occasional lithics and lithic-rich horizons (discontinuous lenses) (Figure 4–9). Lithics are predominantly pumiceous and ignimbrite (displaying varying degrees of welding from non-welded to lava-like) material. The unit thickens (up to 20.75 m thick), or 'pools' downslope, then thins out again at the most southerly extent of the exposure.

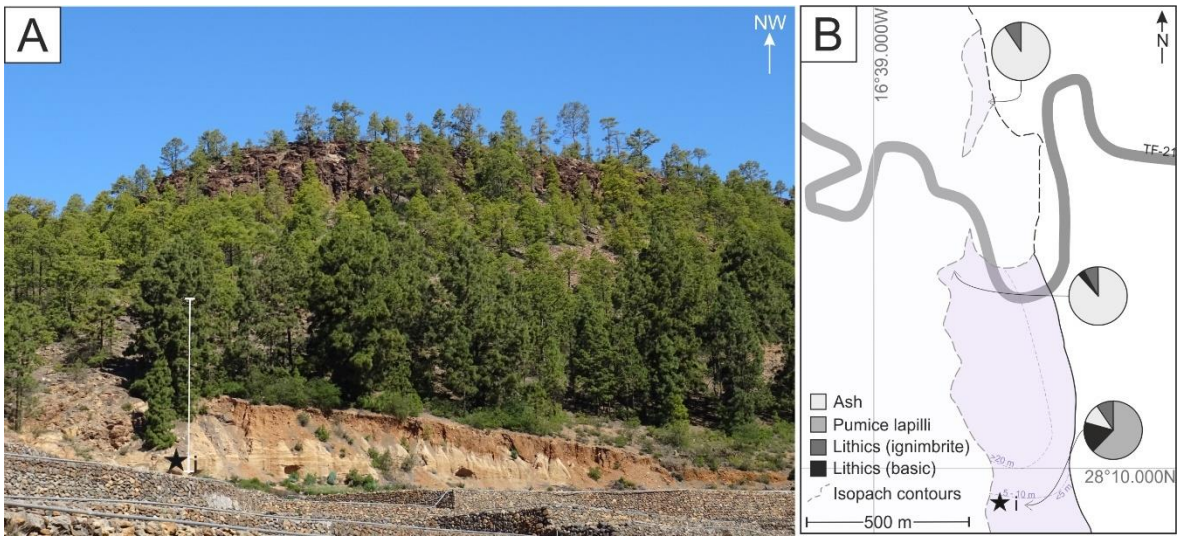


**Figure 4–6.** Atravesado Mb Unit 1: A) Southern extent of Unit 1 exposed in farmland north of the town of Vilafor, N28°9'40" W016°38'46, with the log location 1i highlighted. B) Mapped (dark shade) and predicted exposure (light shade), and isopach map, displaying distribution of grain size and lithic components.

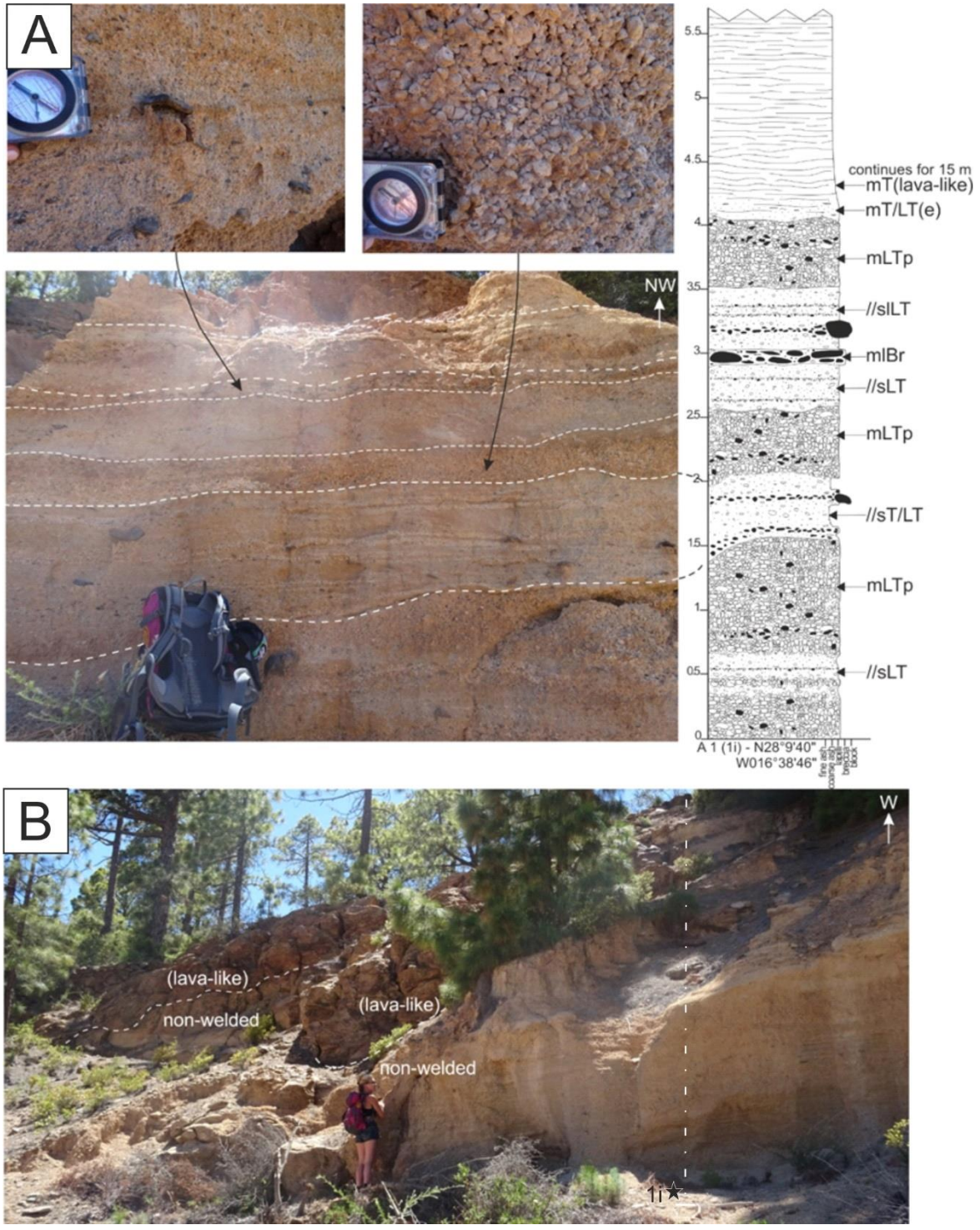


**Figure 4–7.** Atravesado Mb Unit 1 basal stratigraphy, exposed in farmland, north of the town of Vilaflor at N28°9'40" W016°38'46. A) Photographs and graphic log of the section through the basal, predominantly non-welded stratigraphy of Unit 1. Vertical scale in metres. B) Field photograph showing location of log 1i.

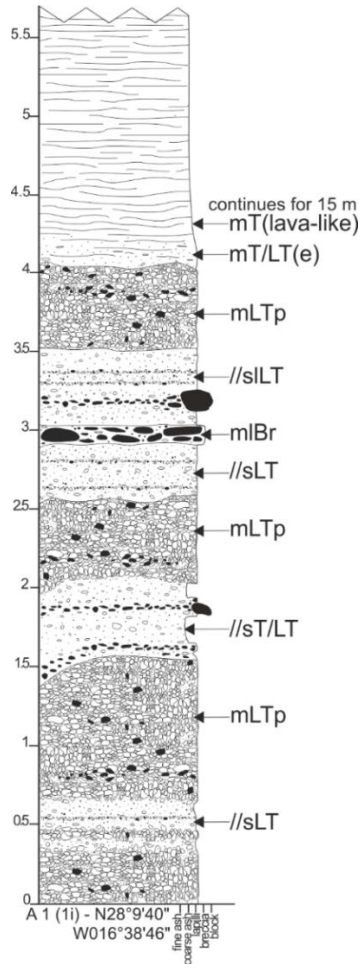


**Lithofacies description**

Crystal-poor, clast-poor, massive, lava-like tuff with a planar, persistent base-parallel fabric, exhibiting columnar jointing. Facies continues to approximately 20.75 m. Welding increasing upwards, stretched, and elongated pumice, fiamme.

Non-welded, pumice-rich, fines poor with occasional clasts of basic (basalt) and lava-like material. Clast supported, locally ash supported.

Imbricated clasts of predominantly well-rounded basic material. Ash matrix supported.

Non-welded, pumice-rich, fines poor with occasional clasts of basic and lava-like material. Pumice clast supported. Irregular, erosional contact with the underlying planar stratified tuffs – lapilli tuffs.

Non-welded, pumice-rich, fines poor with occasional lithics (rounded clasts of basic and angular lava-like material). Predominantly clast-supported with localised areas of ash-supported.
Non-welded, pumice-rich, fines poor with occasional clasts of basic and lava-like material with stratified areas.

**Figure 4–8.** Lithofacies description of stratigraphic log at base of Atravesado Mb Unit 1 (log 1i) (Vertical scale in metres).

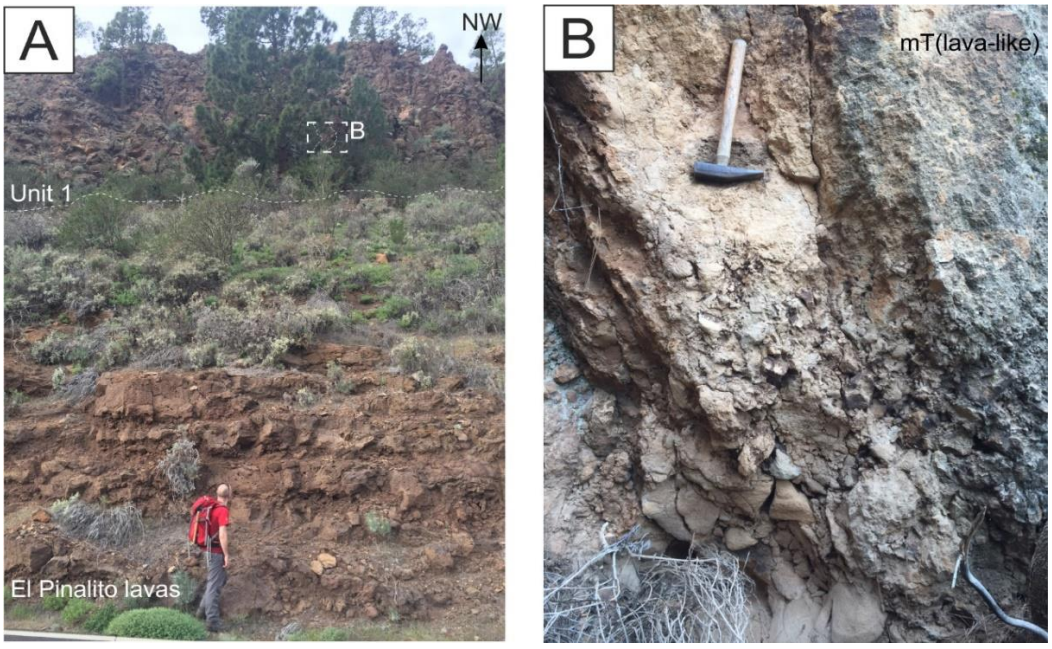


**Figure 4–9.** Atravesado Mb Unit 1 at N28°10'29.8 W16°38'40: A) bound by the El Pinalito lavas (at least 6 individual flows at this locality) to the east. A strong base-parallel fabric is seen throughout, with columnar jointing dipping 6 – 10 ° to the NW. Localised areas (pockets or lenses) of welded breccia, marked by the white box. B) Lithic-rich pocket of angular material within the mT(lava-like). Angular, poorly sorted breccia, with clasts of altered lava-like ignimbrite material.

### 4.2.2. Atravesado Unit 2

Atravesado Unit 2 overlies much of Unit 1 and extends from 10 m south of Riscos Atravesado (N28°10'29.8 W16°38'40.4") but is laterally poorly constrained to the northwest where it is overlain by Atravesado Units 3 and 4, and the southernmost limits remain undefined. Much of this unit consists of intensely welded lava-like tuff, with areas of both welded and non-welded lithic breccias, tuffs, and lapilli tuffs, rich in pumiceous material and lithic blocks.

The roadside exposure at N28°10'29.8" W16°38'40.4" consists of an orange, weakly columnar jointed (dipping 12°-15°NW) lava-like tuff with occasional clast-rich horizons. A 2.5 m lithic breccia (Figure 4–10 & 4–11) defines the basal stratigraphy, which progressively grades up into the lava-like lithofacies that extends up to the top surface at this locality. Brecciated (containing clasts of lava-like material, pumiceous material and autoclasts), spherulitic, welded and non-welded horizons are observed throughout the unit (Figure 4–12), with a greenish blue alteration of clasts (chlorite vapour phase alteration), as seen in the welded lithic breccias at the roadside exposure N28°10'28.5 W16°38'54.9.

The uppermost stratigraphy of Unit 2 (observed at N28°10'31.5 W16°38'57.3") consists of predominantly non-welded, diffusely and planar stratified tuffs, lapilli tuffs and breccias (Figure 4–13 & 4–14) dipping 34-55° NW. Clasts are angular pumiceous and lava-like material. Unit 2 is unconformably overlain by Unit 3, with an irregular, highly erosive contact, and blocks (rip-up clasts) of the uppermost deposits of Unit 2 are found within the autobrecciated base of the overlying Unit 3. This upper sequence is not seen at any other locality, where Unit 2 displays a lava-like lithofacies to the uppermost surface of the deposit, suggesting either erosion during the emplacement of Unit 3, or highly variable deposition (Figure 4–15).

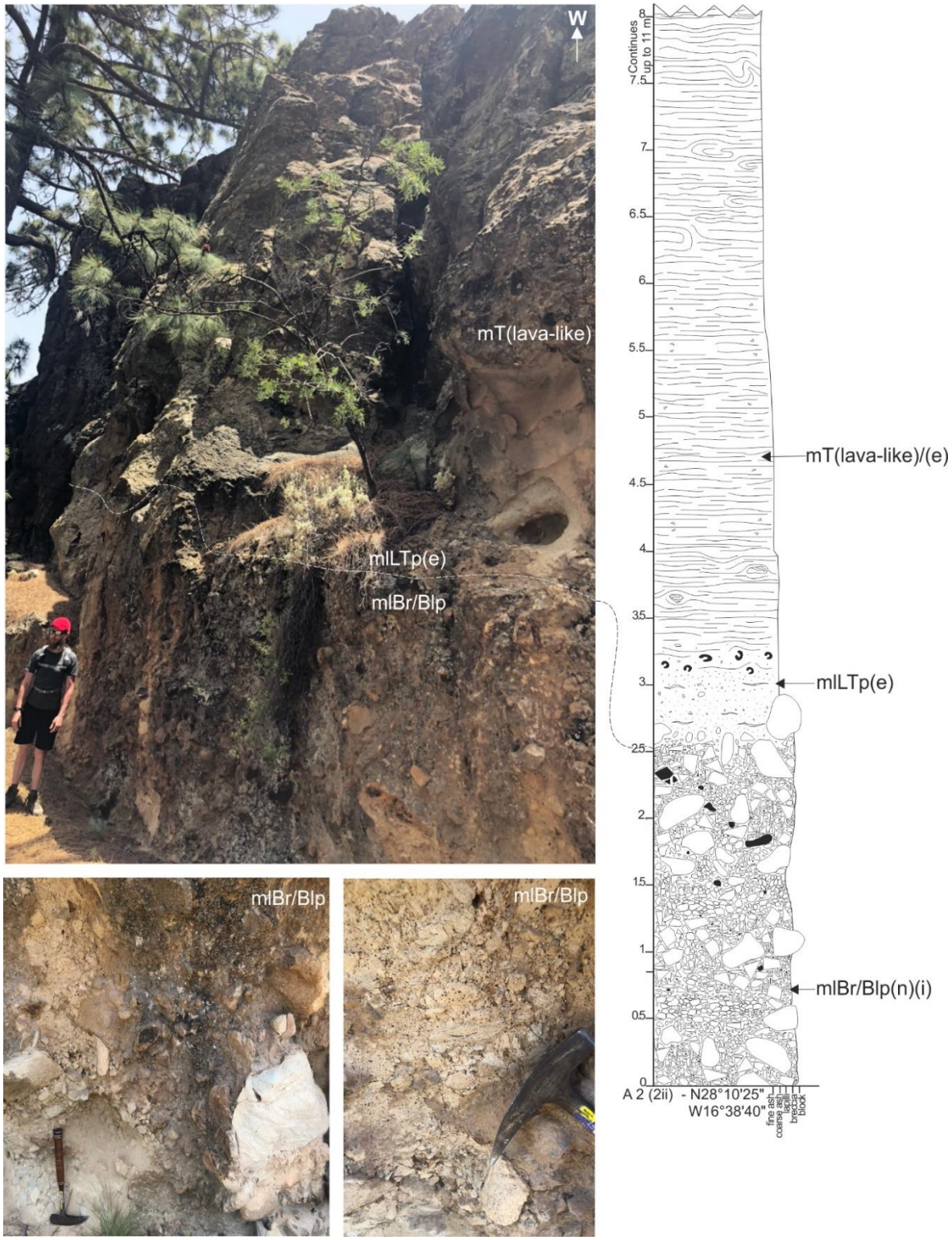


**Figure 4–10.** Atravesado Mb Unit 2 base exposed at roadside locality at (N28°10'25 W16°38'40). Lithic breccia exhibiting normal grading, with a gradual increase in welding into an intensely welded and lava-like lithofacies (Vertical scale in metres).

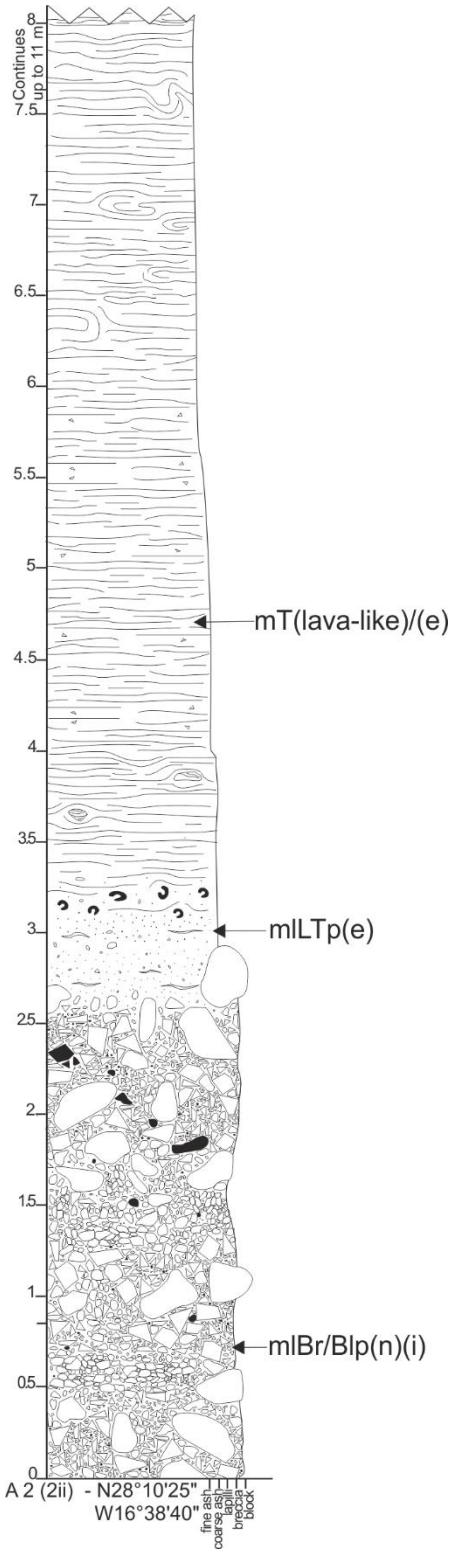


| Lithofacies description |
|---|
| Orange, crystal-poor, clast-poor, massive, lava-like tuff with a planar, persistent base-parallel fabric, exhibiting rare tight isoclinal folds and is strongly columnar jointed. No discernible vitroclastic textures are visible. This facies continues to approximately 11 m. |
| Welding intensity increasing upwards, with progressively stretched and elongated pumice fiamme, grading into a predominantly lava-like lithofacies, with no visible vitroclastic textures. |
| Heavily pock-marked horizon, large (up to 0.5 m) prolate lithophysae as facies increases in welding intensity. Fabric is stretched and deformed around lithophysae, which becomes more developed with height. Welding intensity also increases with height, as the grain size decreases. Fiamme in the underlying eutaxitic lapilli tuff are slightly inclined, displaying variable lateral imbrication. |
| Creamy white, predominantly non-welded, pumice rich (>80%) breccia, with blocks of pumiceous and lava-like material. Clasts are subangular and angular, pumiceous, welded and lava-like and basic material (<5%). Very poorly sorted. Occasional blocks of pumice-rich material, up to 0.75 m. |

**Figure 4–11.** Lithofacies description of stratigraphic log at base of Atravesado Mb Unit 2 (log 2ii) (Vertical scale in metres).

**Figure 4–12.** Atravesado Mb Unit 2 (N28°10'28.5 W16°38'54.9) - horizon of very poorly sorted lithic-rich breccia with angular clasts and blocks (predominately altered, spherulitic welded and lava-like material, and weathered-out pumice material) within the welded facies. Appearing bluish green due to chlorite (vapor phase) alteration. Matrix is a fine grained, crystal poor, flow-banded lava-like tuff.

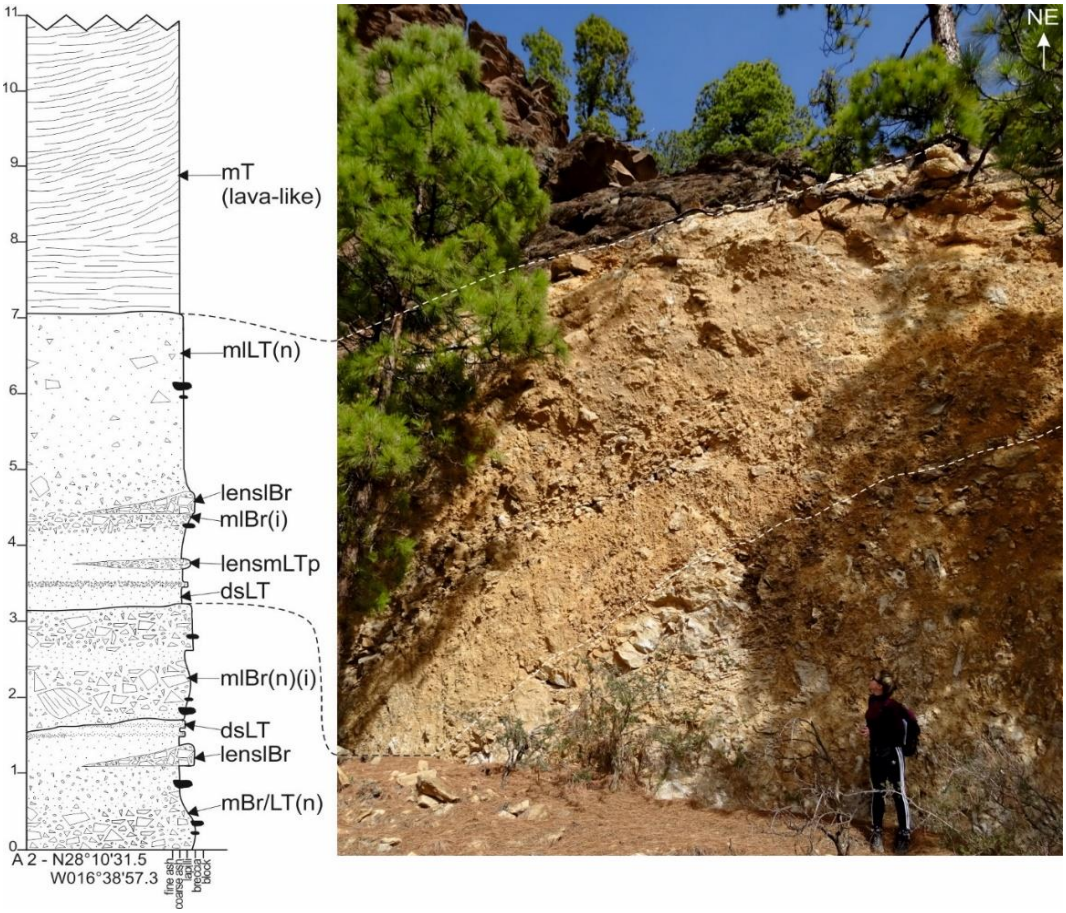


**Figure 4–13.** Atravesado Mb Unit 2: stratigraphic log (vertical scale in metres) and photograph of uppermost non-welded, stratified stratigraphy, overlain by Unit 3 (N28°10'31.5" W16°38'57.3")

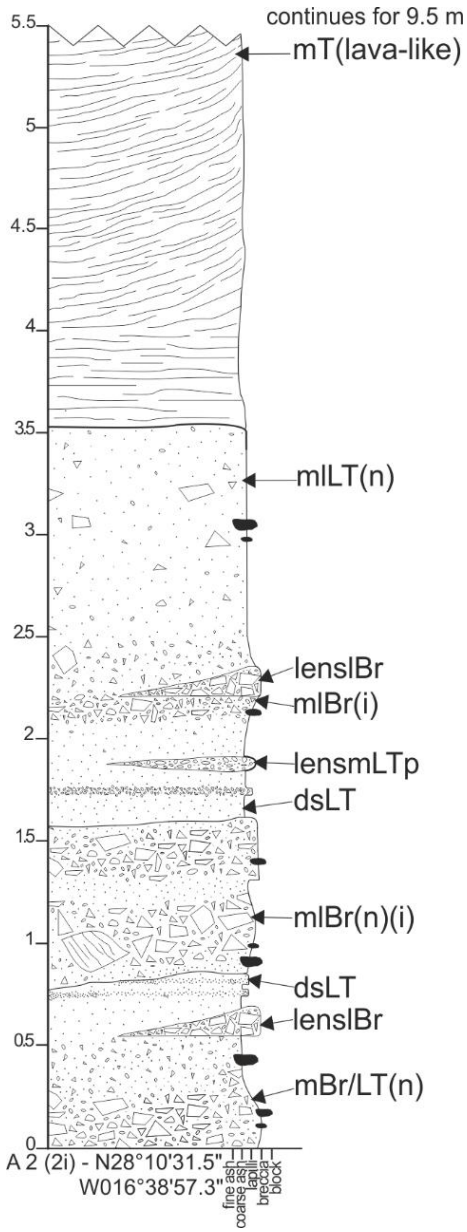


**Lithofacies description**

Base of Atravesado Unit 3: Clast- and crystal- poor lava-like tuff with persistent base-parallel fabric, locally ramping up to the SE. Lithofacies continues up to 15.5 m.

Sharp, predominantly planar, locally erosional contact (not a gradational contact).

Occasional blocks of pumice lapilli. Lithic lapilli are pumiceous and lava-like material.

Fabric - 084 34 ° SE

Occasional blocks of pumice lapilli.

Fabric - 090 34 ° SE

Lithic lapilli are lava-like and pumiceous material with occasional blocks of pumice lapilli.

Highly erosive, irregular contact
Discontinuous, irregular, clast-supported, pumice-rich breccia, grading into a diffuse stratified lapilli tuff.
Very poorly sorted with lithic lapilli of lava-like and pumiceous material.

**Figure 4–14.** Lithofacies description of stratigraphic log of the uppermost stratigraphy of Atravesado Mb Unit 2, underlying Unit 3 (log 2i) (vertical scale in metres).

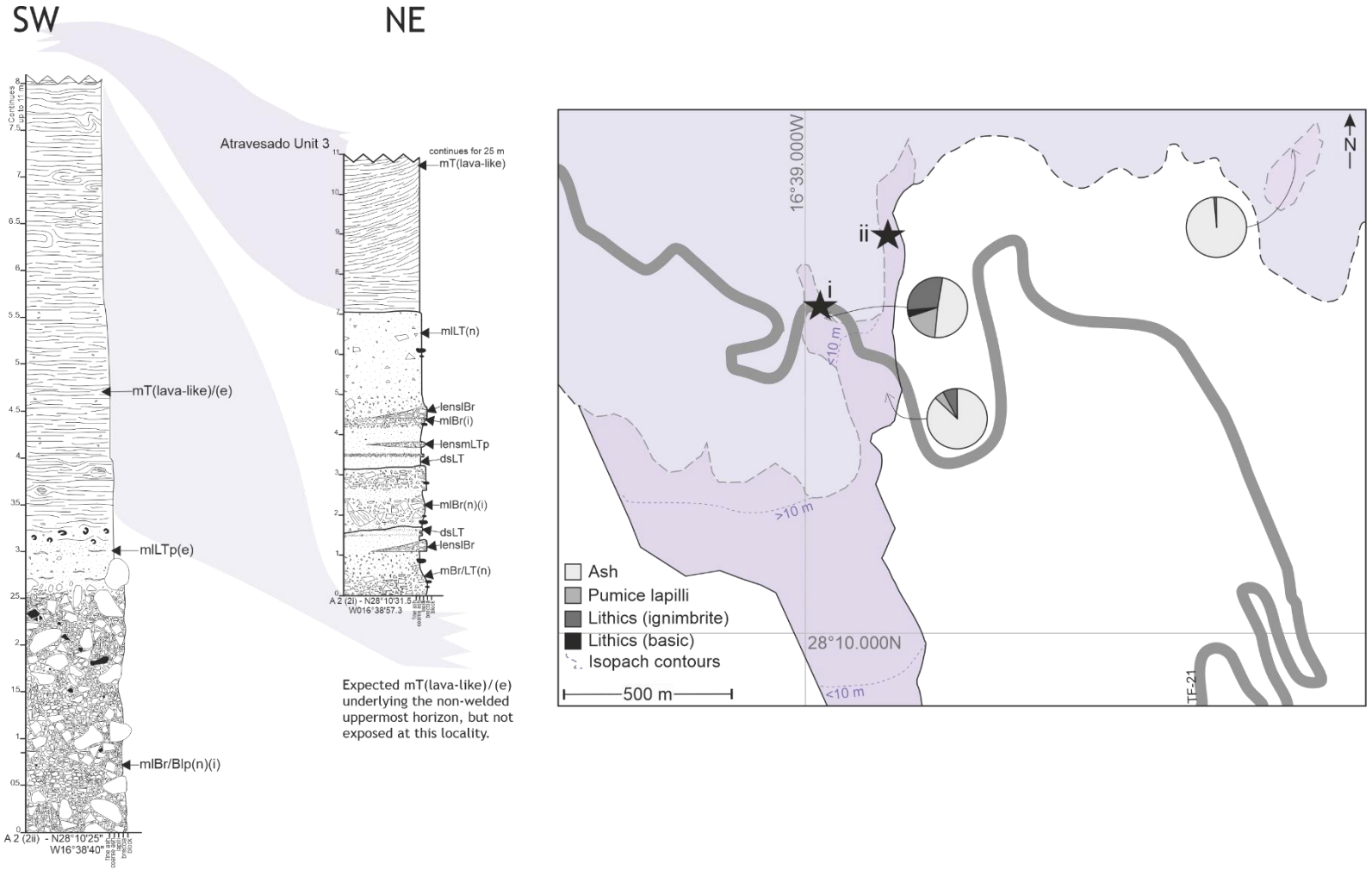


**Figure 4–15.** Correlation of the stratigraphic logs of Atravesado Mb Unit 2 (vertical scale in metres), showing variable upper stratigraphy that cannot be traced laterally in the deposit, perhaps as a result of irregular and inconsistent deposition, or erosion of material during the deposition of Unit 3. Isopach map displays both the mapped (dark shade) and expected exposure (light shade), displaying the distribution of grain size and lithic components. Black stars show log localities.

### 4.2.3. Atravesado Unit 3

Unit 3 is well exposed overlying Unit 2 from the roadside exposure at N28°10'28.5 W16°38'54.9 (Figure 4–5) and can be traced laterally along the Riscos Atravesados where it is bound by the El Pinalito lavas to the east, and poorly constrained to the west where it is overlain by Atravesado Unit 4.

Unit 3 is exposed along the Riscos Atravesados (approx ~80 m exposure) (Figure 4–16) although the base is undefined here due to onlapping El Pinalito lavas on the western edge of the unit, but can be observed in road side sections and traced northwards from N28°10'28.5 W16°38'54.9. The unit is reddish-orange and has a predominantly lava-like lithofacies from base to top, with spherulitic (1-2 mm) and lithophysic zones and horizons (lowermost exposed 5 m is heavily 'pock-marked') and localised brecciation and variation in welding, from lava-like to eutaxitic (typically less welded and much lighter in colour in clast-rich horizons/lenses, with green chlorite alteration (vapour phase).

Unlike the other units of the Atravesado Mb there is an absence of a non-welded basal stratigraphy and intense welding extends throughout the entire thickness of the Unit. The fabric in both Units 2 and 3 (pervasive planar fabric, parallel to depositional horizons) have a 30°-45° dip, with columnar jointing, orientated at 18-25°, indicating emplacement on sloped paleo-topography. Unit 3 displays a pervasive base-parallel (0-5°, sub-horizontal flow banding) fabric throughout, with localised tight isoclinal and chevron folding of the fabric, which progressively becomes irregular and undulating towards the upper surface, with inclined fabrics and very few folds in the upper domain (Figure 4–18).

Large scale ramping of the deposit is seen in the downslope oriented lobes of the deposit (Figure 4–16). There is a distinct secondary cleavage (230 21° NW) in the lower 15 m of the unit, which is not as developed towards the ramped and 'contorted' upper domains. The unit is prominently columnar jointed (5°-22°), and joints cut through the entirety of the unit, and extend down, penetrating in to Unit 2, where the contact is observed (e.g. steeply oriented columnar jointing at N28°10'29.8" W16°38'40.4" and roadside exposure at N28°10'28.5 W16°38'54.9), which indicate simultaneous cooling of these two deposits. A

concavity (shallow depression) observed in the uppermost section of unit 3 in the Riscos Atravesado exposure (Figure 4–16) is mimicked and traced by the pervasive base-parallel fabric, indicating emplacement and cooling in a paleo-valley or depression.


**Figure 4–16.** Atravesado Mb Unit 3 at Riscos Atravesado locality. Strongly columnar jointed, with slight variation(s) in welding intensity, as seen in the colour change, fluctuating through the central portion of the outcrop.

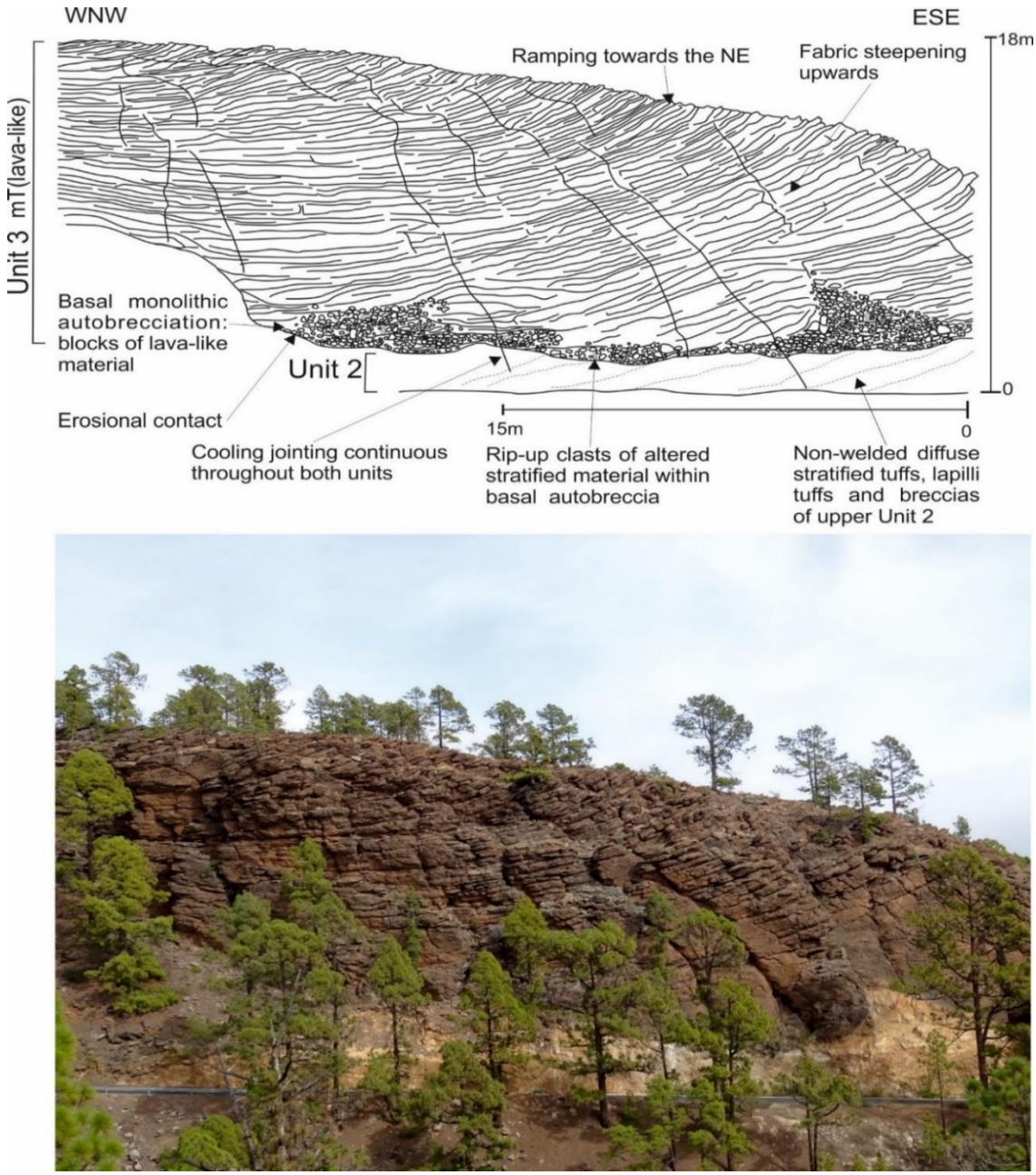


**Figure 4–17.** Annotated field sketch and photograph of the ramp structure in a lobe of Atravesado Mb Unit 3, overlying the non-welded uppermost stratigraphy of Unit 2, with inclined columnar jointing and ramping of fabrics towards the NE (roadside exposure at N28°10'28.5 W16°38'54.9)

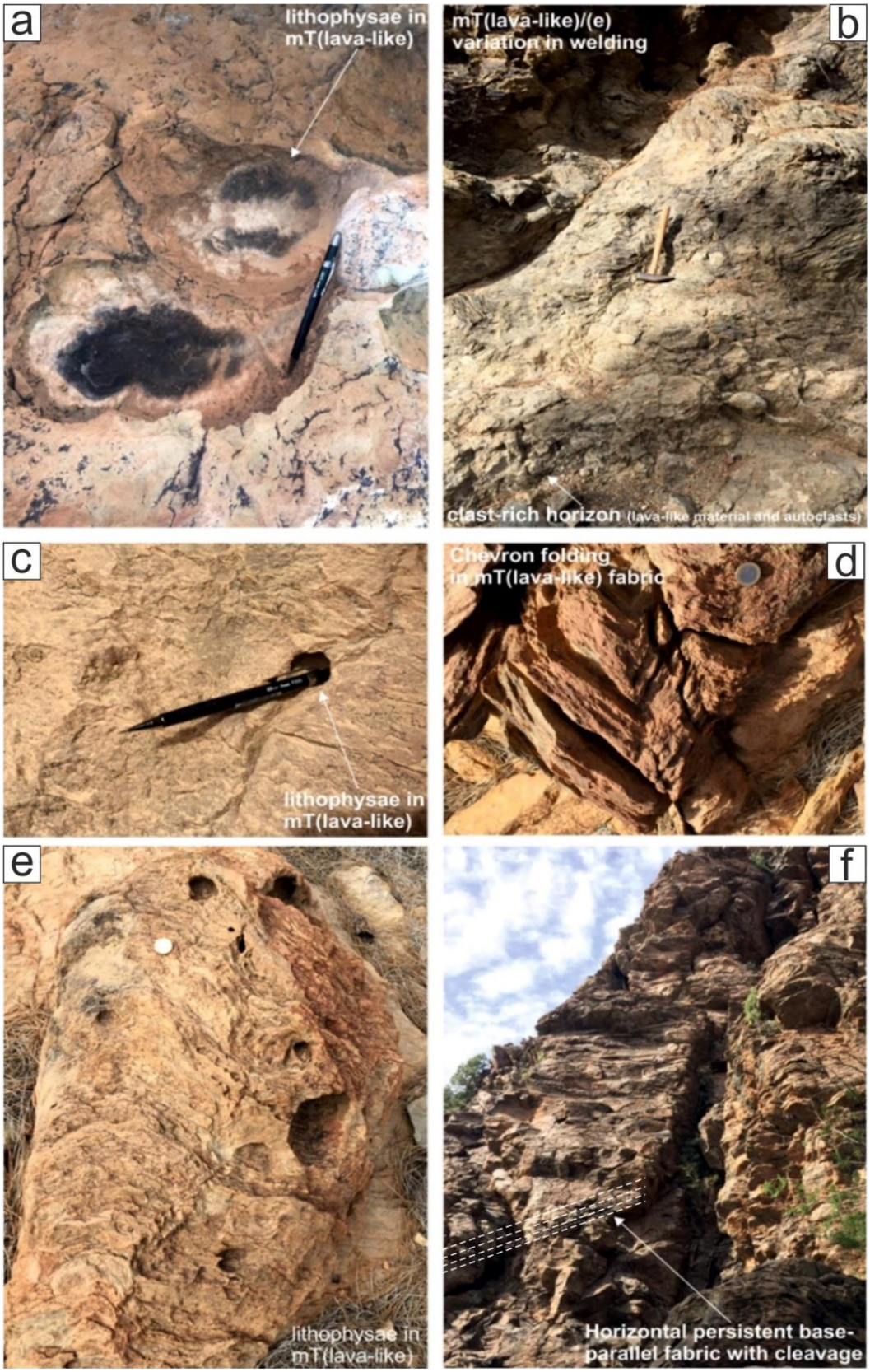


**Figure 4–18**. Overview of features observed in Atravesado Mb Unit 3 at Riscos Atravesado (at N28°33.8'15.5 W16°31.1'65.7): a) smooth, glassy lithophysae zones in aphyric lava-like facies; b) localised variation in welding, with rare 'pockets' of lighter-coloured, lithic-rich, pumiceous material; c) rare lithophysae within pervasive base-parallel planar fabric; d) localised small scale (10's cm) chevron-style folding of the fabric(s); e) localised 'pock-marked' texture, with deformation of the fabric(s) from lithophysae growth; f) pervasive, base-parallel, planar fabric with an inclined, secondary fabric (cleavage).

#### 4.2.3.1. Atravesado Unit 3: Riscos Atravesados localities

Northeast of the Riscos Atravesados, (N28°11'12 W16°38'35) Unit 3 overlies a highly localised series of non-welded variable, graded and stratified tuffs, lapilli tuffs, breccias and lava flows (Figure 4–19 - 4–23) that cannot be traced laterally, or observed at any other locality underlying Unit 3. Unit 3 thins (~ 15 m) over these deposits and continues to 'pool' or thickens downslope to both the west and south. The presence of mafic bombs, scoriaceous material, and basaltic clasts within the stratigraphy, and the lava flows suggest pre-Unit 3 scoria cone associated activity at this locality.

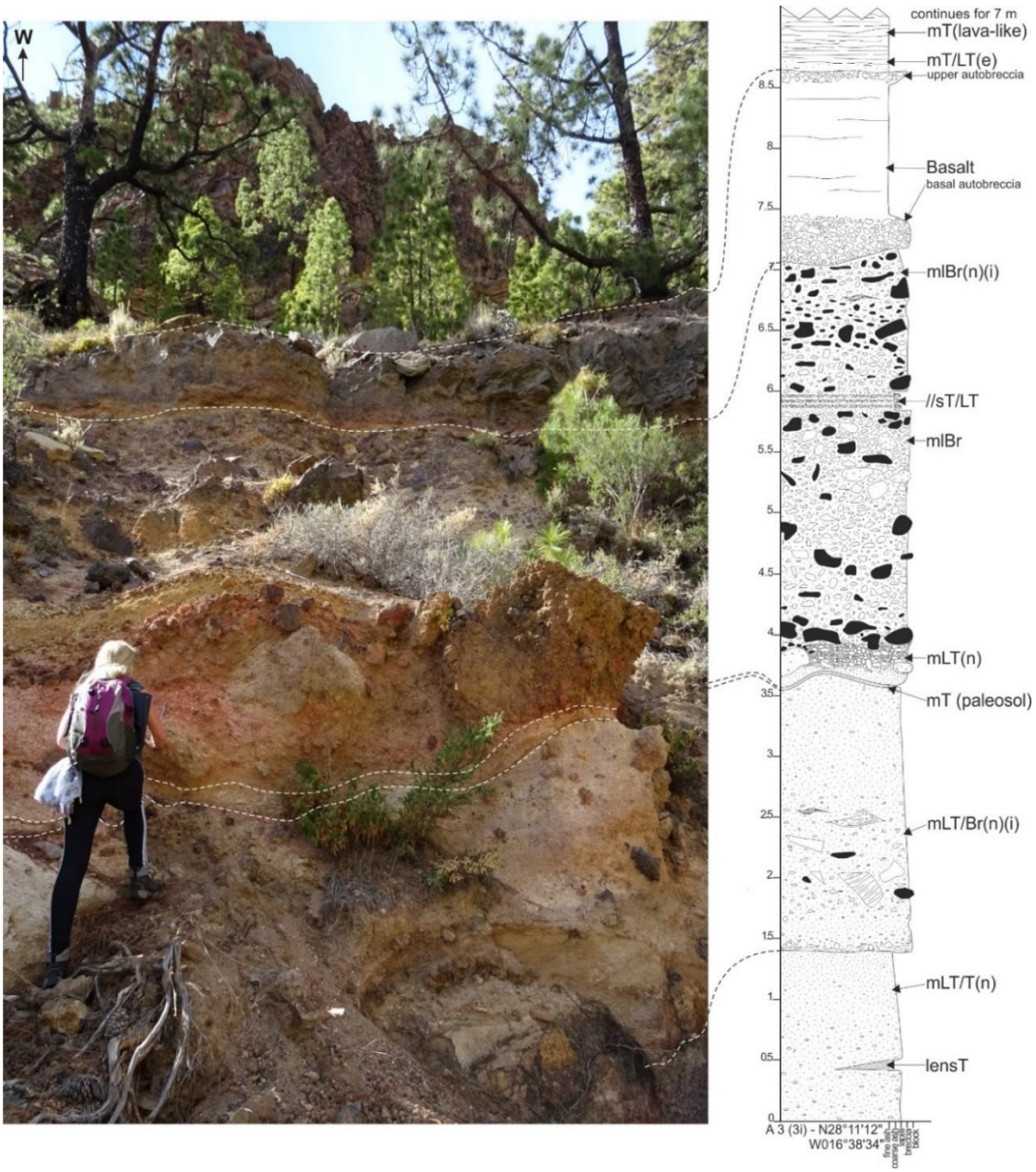


**Figure 4–19.** Pre-Atravesado Mb Unit 3 localised deposits (non-welded tuffs, lapilli tuffs, breccias and lava flow). Location of stratigraphic log 3i at N28°11'12 W16°38'34 (vertical scale in metres).

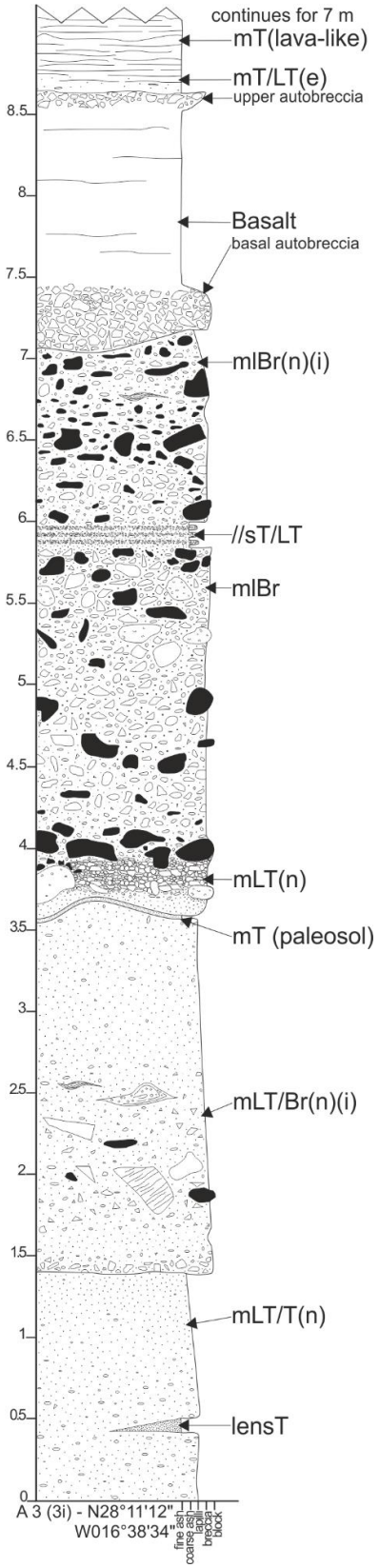


| Lithofacies description |
|---|
| Clast- and crystal- poor lava-like tuff with persistent base-parallel fabric. Lithofacies continues up to approximately 15.5 m. |
| Vesicular, porphyritic basalt lava with upper and auto-brecciation. |
| Pumice rich, ash matrix-supported, clast-compositionally stratified breccia with clast imbrication, mafic cow-pat bombs and localised fiamme with clasts of basic and pumiceous material. |
| Pumice rich, ash matrix-supported, poorly sorted breccia with blocks (up to 1.45 m) of pumiceous material. Clasts of basic and pumiceous material. |
| Highly vesicular mafic-bomb horizon (up to 18 cm across). Pumice rich, clast supported lapilli tuff with pumiceous blocks (up to 1.08 m across) .<br>Reddish brown highly undulating paleosol horizon. |
| Pumice rich, ash matrix supported breccia with clasts of pumiceous and tuff (autoclasts) material, scoriaceous bombs and angular lava-like material. |
| Pumice-rich, rounded clasts of pumice blocks, autoclasts and ignimbrite. |
| Discontinuous fine ash lens<br>(reappears 200 m west, but laterally discontinuous also). |

**Figure 4–20.** Lithofacies description of stratigraphic log of localised pre Atravesado Mb Unit 3 stratigraphy (log 3i) (vertical scale in metres).

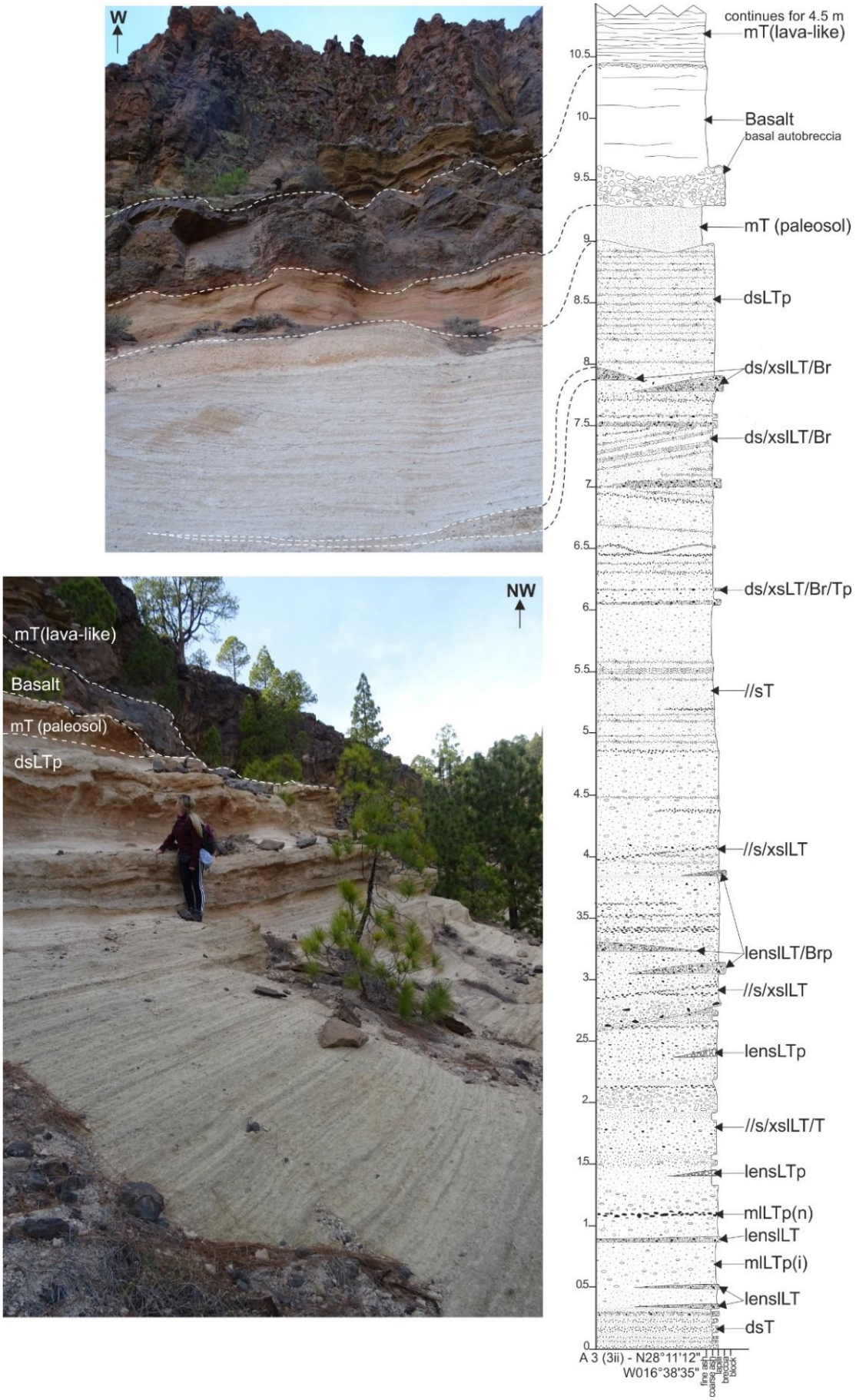


**Figure 4–21.** Pre-Atravesado Mb Unit 3 localised deposits (non-welded tuffs, lapilli tuffs, breccias and lava flow). Location of stratigraphic log 3ii at N28°11'12 W16°38'35 (vertical scale in metres).

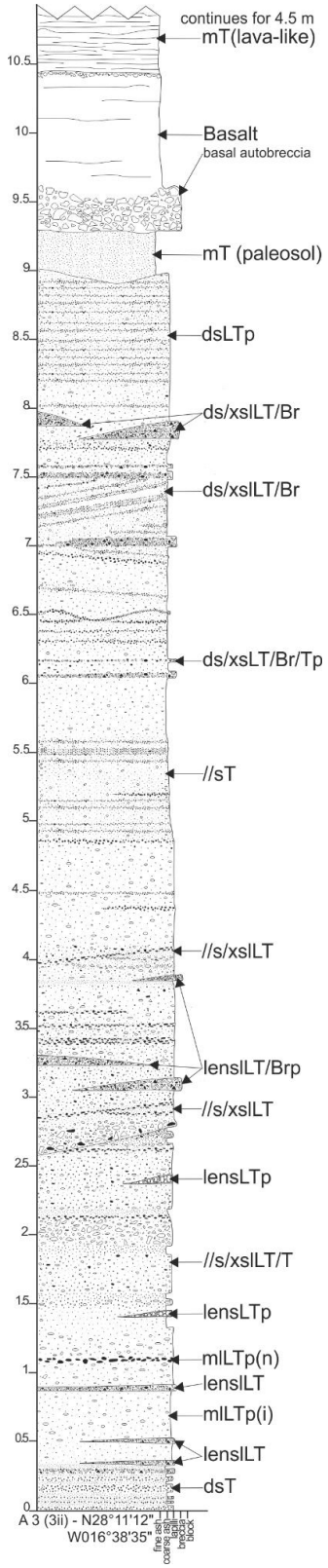


| Lithofacies description |
|---|
| Clast- and crystal- poor lava-like tuff with persistent base-parallel fabric. Lithofacies continues up to approximately 15 m.<br>Vesicular, porphyritic basalt lava with upper and auto-brecciation .<br>Reddish orange (possible paleosol). |
| Diffuse stratified lapilli tuff with regular, alternating bands of pumice-rich and basic-rich lithic lapilli. |
| Discontinuous lens of angular lithic lapilli (basic and pumiceous material). |
| Cross-stratification and erosional horizons throughout. |
| Discontinuous lenses of lithic lapilli, rich in angular clasts of basic and pumiceous material. |
| Imbricated lithic lapilli (basic clasts)<br>Lithic lapilli rich in basic material. |
| Alternating fine and course ash with occasional pumice lapilli. |

**Figure 4–22.** Lithofacies description of stratigraphic log of localised pre Atravesado Mb Unit 3 stratigraphy (log 3ii) (vertical scale in metres).

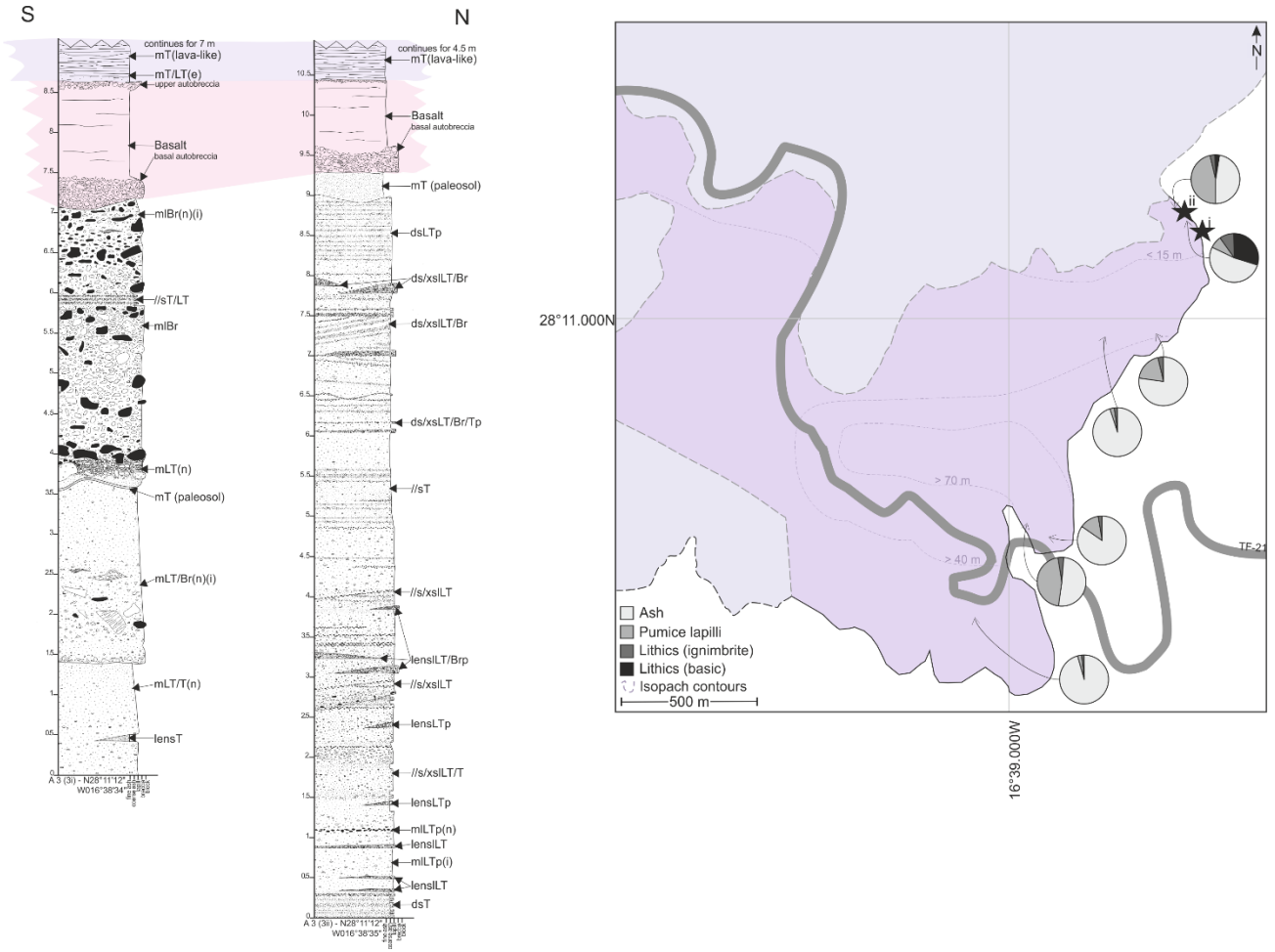


**Figure 4–23**. Correlation of the stratigraphic logs of the localised Atravesado Unit Mb 3 (vertical scale in metres), illustrating the highly variable and discontinuous lateral non-welded stratigraphy underlying a basaltic lava at the base of Unit 3 in the western Riscos Atravesado cliffs. Isopach map displays both the mapped (dark shade) and expected exposure (light shade), displaying the distribution of grain size and lithic components. Black stars show log localities. Colours used to tie stratigraphy are arbitrary.

### 4.2.4. Atravesado Unit 4

Unconformably overlying Unit 3, Unit 4 is a reddish-orange, predominantly lava-like to moderately welded and eutaxitic tuff, with clast-rich and brecciated horizons throughout. Where visible, it has an ~ 0.45 -2.75 m non-welded pumice lapilli base, which grades into lava-like lithofacies (Figure 4–24). The entire unit is of variable thickness between ~ 5 m and ~ 22.5 m thickness and can be traced across the Llana de Ucanca caldera wall from the base of Las Lajas (N28°11'27.4" W16°39'53.6", most westerly mapped area) to west of Roque de Encaje (N28°11'23.2" W16°37'43.2"), where it forms down-slope thickened lobes (Figure 4–26 and 4–27). Much of the unit is underlying younger units of the Retamares Mb and the later caldera-fed El Pinalito lavas (at Llano de la Mesas), although there are areas where it protrudes from the lava flows, forming 'islands' as the lavas have flowed around topographic highs (Figure 4–26 & 4–27).

The unit is steeply dipping (very variable, but SW average dip - foliation – 21° - 80°) in comparison to prior Atravesado units, with abundant lithics (fabric rotated around lithics, commonly sub-angular and sub-rounded lava-like and pumiceous material), crystals and globules (enclaves) (Figure 4–29) and spherulitic and lithophysic horizons and exhibits columnar jointing (15°-21°). The intermediately welded and lava-like component has a persistent base-parallel fabric and is heavily folded (much more so than in Atravesado Units 1 – 3), exhibiting a variety of folding (tight isoclinal, open curvilinear and chevron folding) of the fabric. Similarly to Units 1 and 2 of the Atravesado Mb, Unit 4 has a varying welding profile with a predominantly non-welded, stratified basal stratigraphy, which locally grades up into a welded and lava-like lithofacies (Figure 4–25 - 4–34).

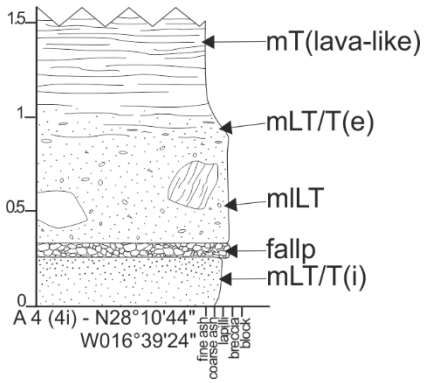


| Lithofacies description |
|---|
| Crystal-rich, clast poor with persistent base-parallel fabric (horizontal).<br><br>Gradational, undulating contact.<br>Ash with blocks of lava-like and basic material.<br>Pumice lapilli fall deposit (tapers out 2 m west).<br><br>Occasional pumiceous clasts (up to 2 cm). |

**Figure 4–24.** Lithofacies description of stratigraphic log of the base of Atravesado Unit 4 (log 4i) (vertical scale in metres).

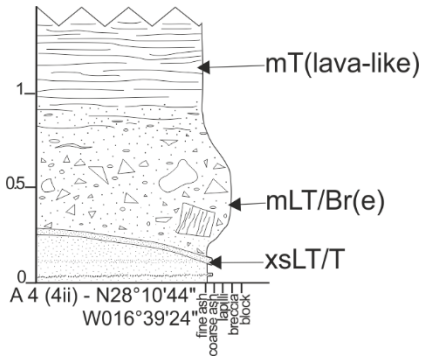


| Lithofacies description |
|---|
| Crystal-rich (lath plagioclase), clast poor with persistent base-parallel fabric (horizontal).<br><br>Gradational, undulating contact.<br>Greenish alteration (chlorite alteration).<br>Pumice lapilli matrix supported with clasts of pumiceous and lava-like material. |

**Figure 4–25.** Lithofacies description of stratigraphic log of the base of Atravesado Unit 4 (log 4ii). Both logs 4i and 4ii consist of an 0.45 m thick of non-welded ash matrix-supported, lithic-rich pumice lapilli with blocks grading up (over approx ~0.17 m) into mT(lava-like), (vertical scale in metres).


**Figure 4–26.** Atravesado Unit 4 overlying Unit 3, highlighting variable thickness, and localised down-slope thickened lobe. Much of the unit is overlain and bound by the El Pinalito basalt lavas at Llano de las Mesas. View from Riscos Atravesados at N28°11'12 W16°38'35.


**Figure 4–27.** Atravesado Mb Unit 4 field relationships with lower Atravesado stratigraphy and later caldera-fed El Pinalito lavas. Note irregular thickness and topography. View from Riscos Atravesados at N28°11'12 W16°38'35.


**Figure 4–28.** Atravesado Unit 4: non-welded, base (planar stratified tuffs and lapilli tuffs) grading up into lava-like lithofacies (N28°11'19.3" W16°39'25.0").

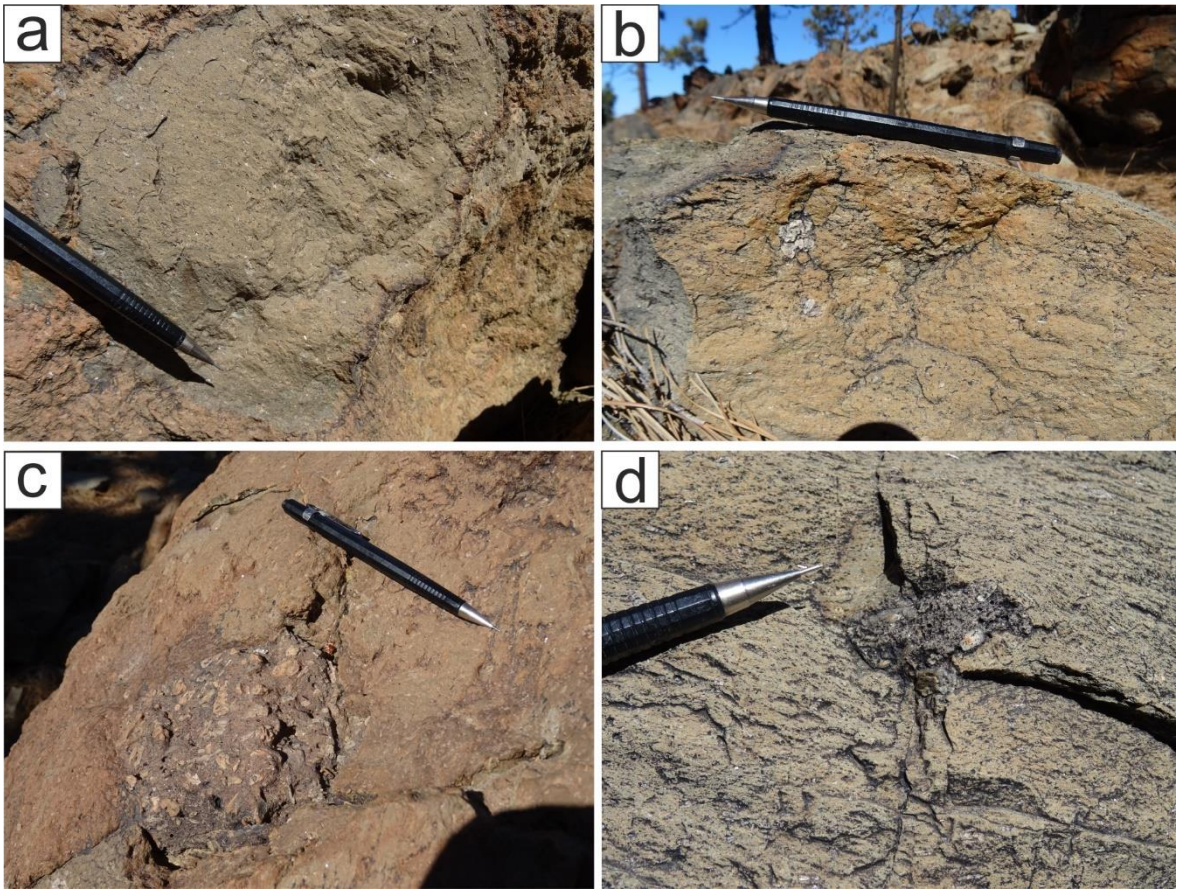


**Figure 4–29.** Crystals and inclusions within Atravesado Mb Unit 4: a) alignment of lath-shaped plagioclase and nepheline crystals (up to 0.5 cm, within the fabric; b) cluster of broken feldspar (sanidine and nepheline) crystals with fabric rotated and deformed around them; c) 10 cm syenite globule (enclave) with nepheline crystals up to 2 cm; d): finer grained, mica-rich, smaller globules (enclaves) (2.5 cm) with finer grained crystals (0.24 – 1 cm feldspars).

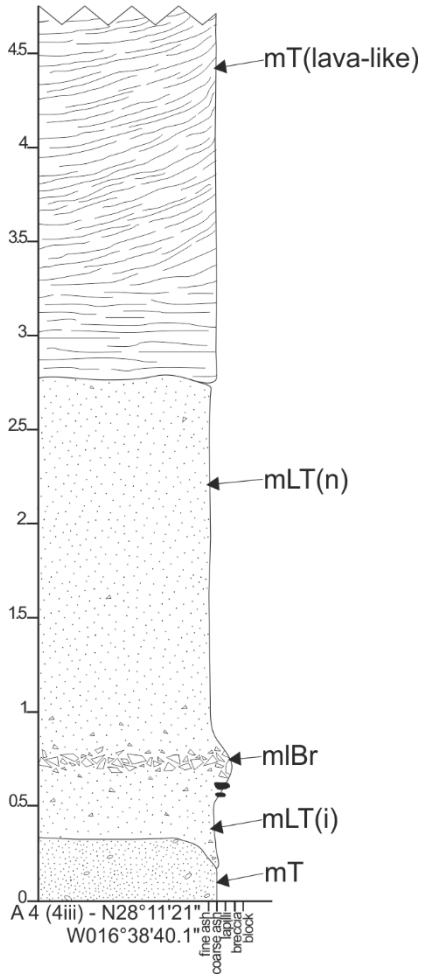


| Lithofacies description |
|---|
| Pervasive, planar (base-parallel) fabric for first metre and a half, which then immediately ramps up to the NW, with localised small (cm) scale folding (chevron and buckle folds) of the fabric. |
| Aphyric, lack of vitroclastic textures. Clast poor, crystal poor. |
| Sharp, undulating erosional contact. |
| Both ash matrix and clast supported.<br>Lithic lapilli are predominantly pumice and basic material, subangular and angular |
| Breccia is predominantly ash-matrix-supported with highly angular clasts of ignimbrite of varying degrees of welding. |
| Reddish pink in colour with occasional rounded orange-coated pumice lapilli (possible paleosol). |

**Figure 4–30.** Lithofacies description of stratigraphic log of the base of Atravesado Mb Unit 4 (log 4iii) (vertical scale in metres).

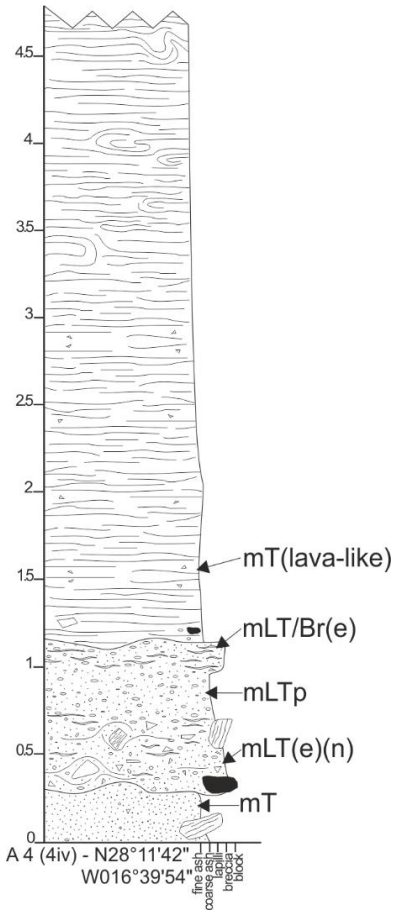


| Lithofacies description |
|---|
| Crystal-rich, clast-poor, lava-like lithofacies with a persistent base-parallel fabric, exhibiting tight isoclinal folding. Abundant mafic enclaves and globules. |
| Crystal-rich, welded (eutaxitic) with stretched and elongated pumice. |
| Clast-supported, pumice-rich. |
| Green (chlorite alteration) with strong, base-parallel fabric, rotated around clasts of lava-like material, pumice and basic material. Highly irregular and erosional contact between the lava-like tuff and the underlying eutaxitic breccia. |
| Crystal-rich ash tuff (imbricated crystals) with blocks of lava-like material. |

**Figure 4–31.** Lithofacies description of stratigraphic log of the base of Atravesado Mb Unit 4 (log 4iv) (vertical scale in metres).

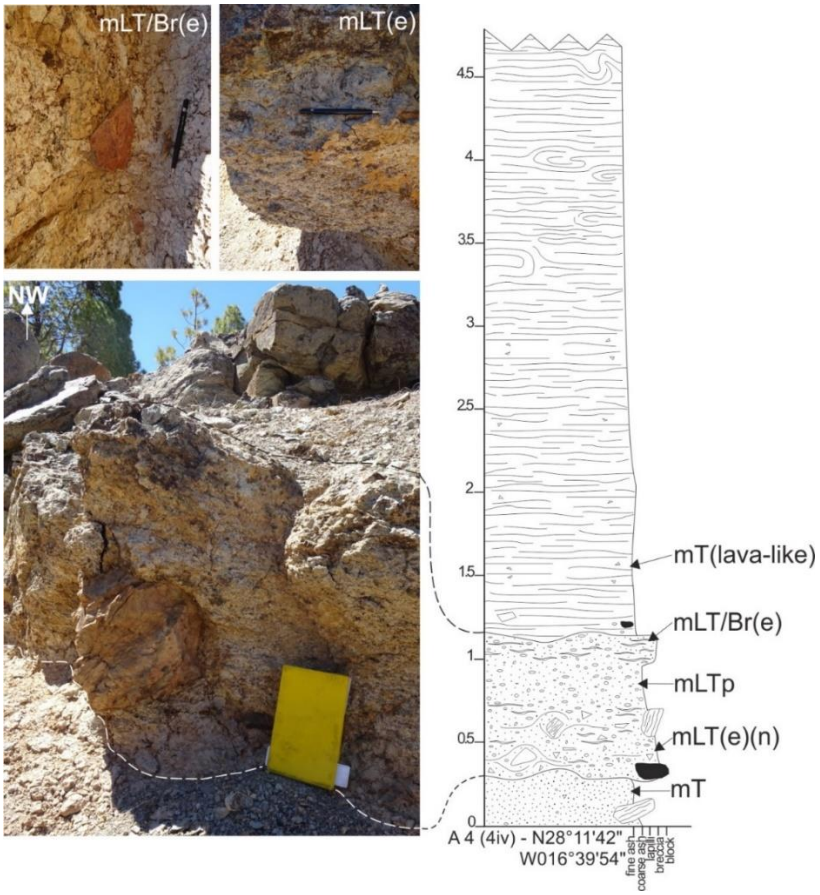


**Figure 4–32.** Atravesado Unit 4 (stratigraphic log 4iv) basal non-welded stratigraphy, grading up into a lava-like lithofacies (vertical scale in metres).

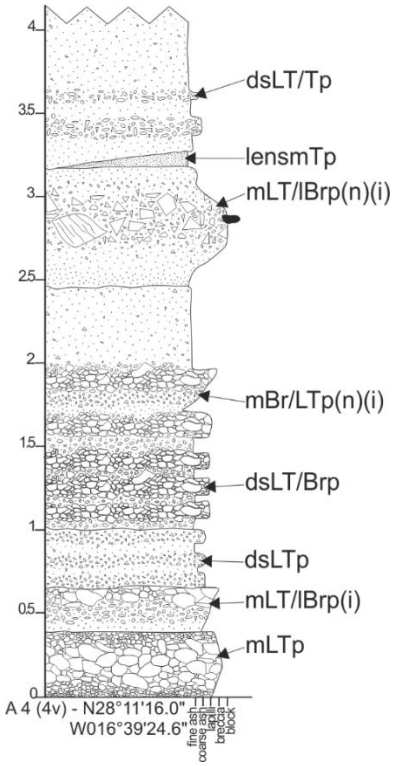


| Lithofacies description |
|---|
| Poorly sorted, pumice-rich, sub-rounded pumice and lithic (ignimbrite) lapilli.<br>120 32° SW. |
| Clast-supported breccia, rich in pumiceous and lava-like material with angular blocks of lava-like material. |
| Clast supported, pumice-rich breccia horizons.<br>Clast supported, pumice rich diffuse stratified lapilli tuff, with rounded, poorly sorted pumice lapilli.<br>Fabric - 120 28° SW.<br>Ash matrix supported; pumice rich with occasional clasts of lava-like material<br>Clast supported, pumice-rich<br>(average clast size: 2 cm). |

**Figure 4–33.** Lithofacies description of stratigraphic log of the base of Atravesado Mb Unit 4 (log 4v) (vertical scale in metres).

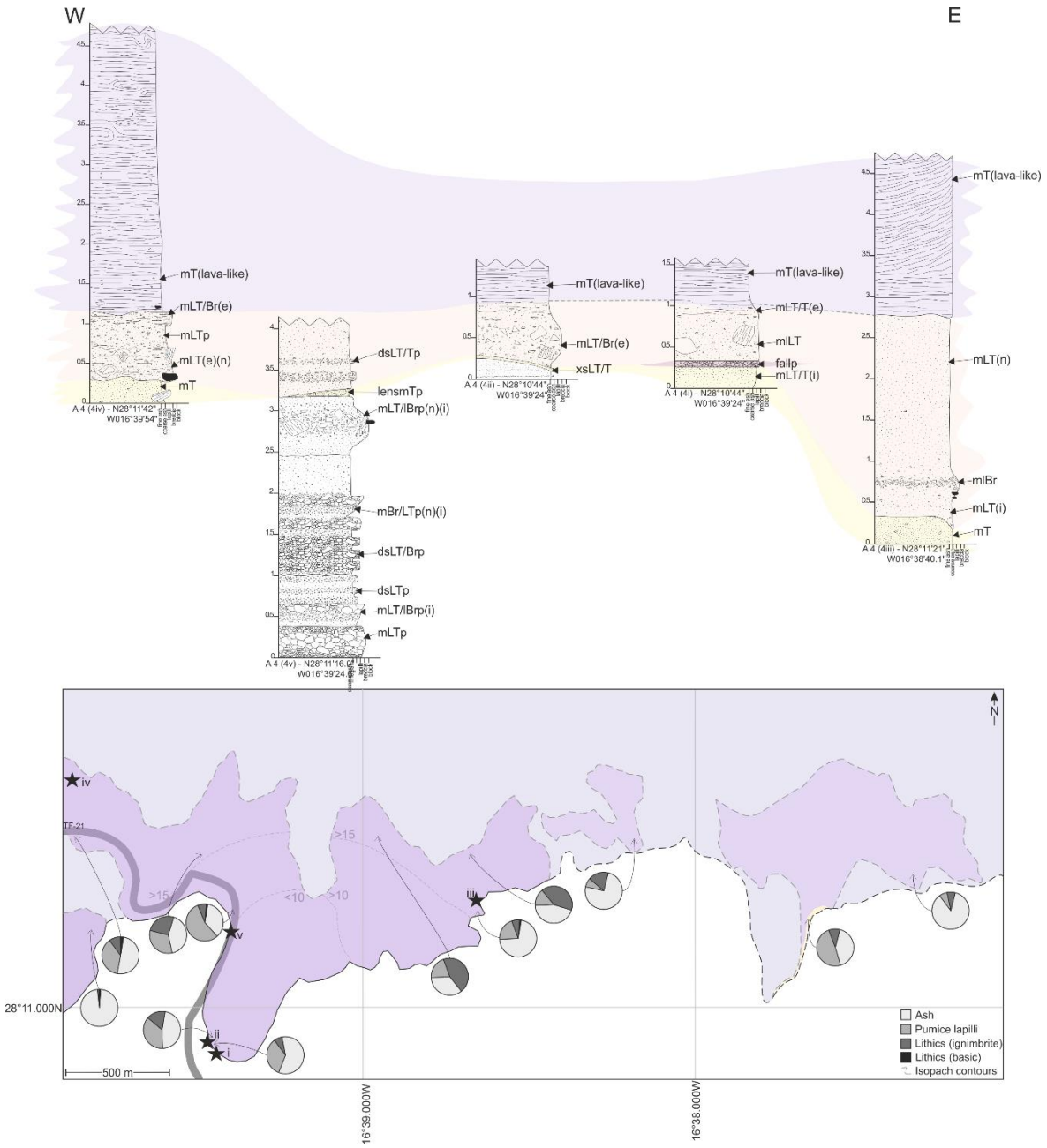


**Figure 4–34.** Correlation of the stratigraphic logs of Atravesado Mb Unit 4 (vertical scale in metres), with the coloured bands showing possible continuation of lateral facies. Colours used to tie stratigraphy are arbitrary. Isopach map displays both the mapped (dark shade) and expected exposure (light shade), displaying the distribution of grain size and lithic components. Black stars show log localities.

### 4.2.5. Interpretation

The four units of the Atravesado Member share a textural and structural resemblance, comprising a distinctly lava-like lithofacies with lesser degrees of welding typically seen at the base of the deposit(s), or localised lateral variations, in the form of pockets or lenses. The nature of the stratification (planar, cross, and diffuse) and erosive surfaces seen in the typically thinly-bedded, lesser welded basal stratigraphy, which increase both horizontally and laterally in welding indicates these units, are formed from sustained, but unsteady, predominantly traction-dominated pyroclastic density current(s), with the gradation and variability of welding intensity attributed to both syn- and post-depositional processes, discussed further in Chapters 5 and 7.

In comparison with the other members, these deposits are distinctly lithic-poor, with a lack of lithic-lapilli and blocks present in the lower-welded stratigraphy (with the exception of the basal stratigraphy of Unit 2), which suggests the sustained, high mass-flux output of ash-rich material is not associated with explosive, caldera-scale collapse and mass wasting events (e.g. Brown et al., 2008; Jordan et al., 2018; Smith & Kokelaar, 2013).

Lateral variations in depositional processes (e.g. from diffusely stratified to massive) (e.g. Figure 4–34) indicate highly variable depositional conditions with fluctuations between fluid escape- and traction-dominated FBZs. The presence of pumice rich, discontinuous lenses in the basal stratigraphy of Units 2, 3, and 4 supports a mechanism of variable and non-uniform deposition initiating each member. The lava-like lithofacies that represents much of each unit's thickness is attributed to rapid deposition from sustained PDC(s), whereby the intensity of welding is a result of both syn-depositional coalescence and welding of pyroclasts, and from both syn- and post-emplacement deformation and rheomorphism.

## 4.3. Retamares Member

The Retamares Mb consists of seven (A – G), eastward younging, low-aspect ratio, welded and lava-like tuffs with highly variable welding profiles, interbedded with periodic pumice- and ash-fall deposits. Units appear greenish blue in colour (vapour phase alteration, e.g. chlorite), are typically clast-rich (lithic and pumice lapilli) and are heavily flow banded, exhibiting a variety of fold structures, (indicative of both syn- and post-emplacement folding).

### 4.3.1. Retamares Unit A

Retamares Mb Unit A unconformably overlies Atravesado Unit 4 (Figure 4–35) and can be traced laterally from ~ 100 m north of Las Lajas (at N28°11'45.2" W16°39'47.6") to Llano de las Mesas (at N28°11'30.3" W16°38'28.3"), where it is overlain and obscured by subsequent Retamares Units and the later caldera-fed El Pinalito lavas. It extends to the north caldera wall boundary, underlying Unit B in the caldera wall stratigraphy.

The unit exhibits highly variable welding throughout, from non-welded, typically at the base, to lava-like with highly variable gradations in between (Figure 4–35 - 4–46). The base of the unit where observed, is comprised of non-welded, pumiceous, typically diffuse-stratified tuffs, lapilli tuffs and breccias, with a variable thickness of between ~ 1 m and ~ 4.5 m, with approximately 1 m of non-welded massive tuff (Figure 4–46). Localised interbedded pumiceous fall deposits within the basal stratigraphy (Figure 4–43 - 4–44) indicate associated Plinian activity, are laterally discontinuous within Unit A, and are host to horizons of scoriaceous bombs, up to 0.8 m in diameter. At this locality, the overlying lava-like/welded facies do not grade from a non-welded, nor stratified base, and remain welded from their base to the uppermost part of the deposit, with an erosional basal contact (Figure 4–43 & 4–44) streaked with obsidian (basal vitrophyre), and are lithic-poor.


**Figure 4–35.** Stacked sequence of Atravesado and Retamares Mb units looking north east from Sendero de Las Lajas. Note highly variable thickness of Unit 4, with two visible thickened lobes. Note differential weathering of Retamares A as a result of a pumiceous, predominantly non-welded basal stratigraphy, grading up into the more resistant, strongly welded – lava-like facies.

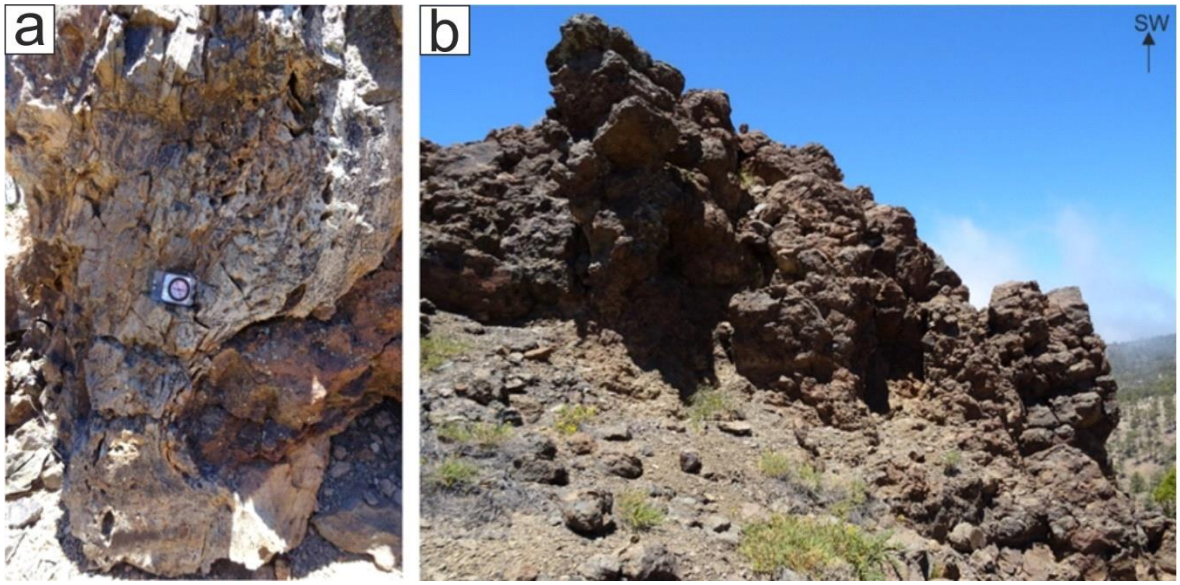


**Figure 4–36.** Variable welding, textures and weak columnar jointing observed in the predominantly lava-like lithofacies at the base of Retamares Mb Unit A (N28°11'26" W16°39'9"): a) Fabric is folded and rotated around a block of sub-rounded crystal-rich, lava-like material, and pock-marked appearance indicating lithophysae, which also contribute to the deformation of fabrics. b) Welding intensity increases vertically, and unit thickens northwards at this locality, where it 'pools' in a topographic depression. Weakly columnar jointed.

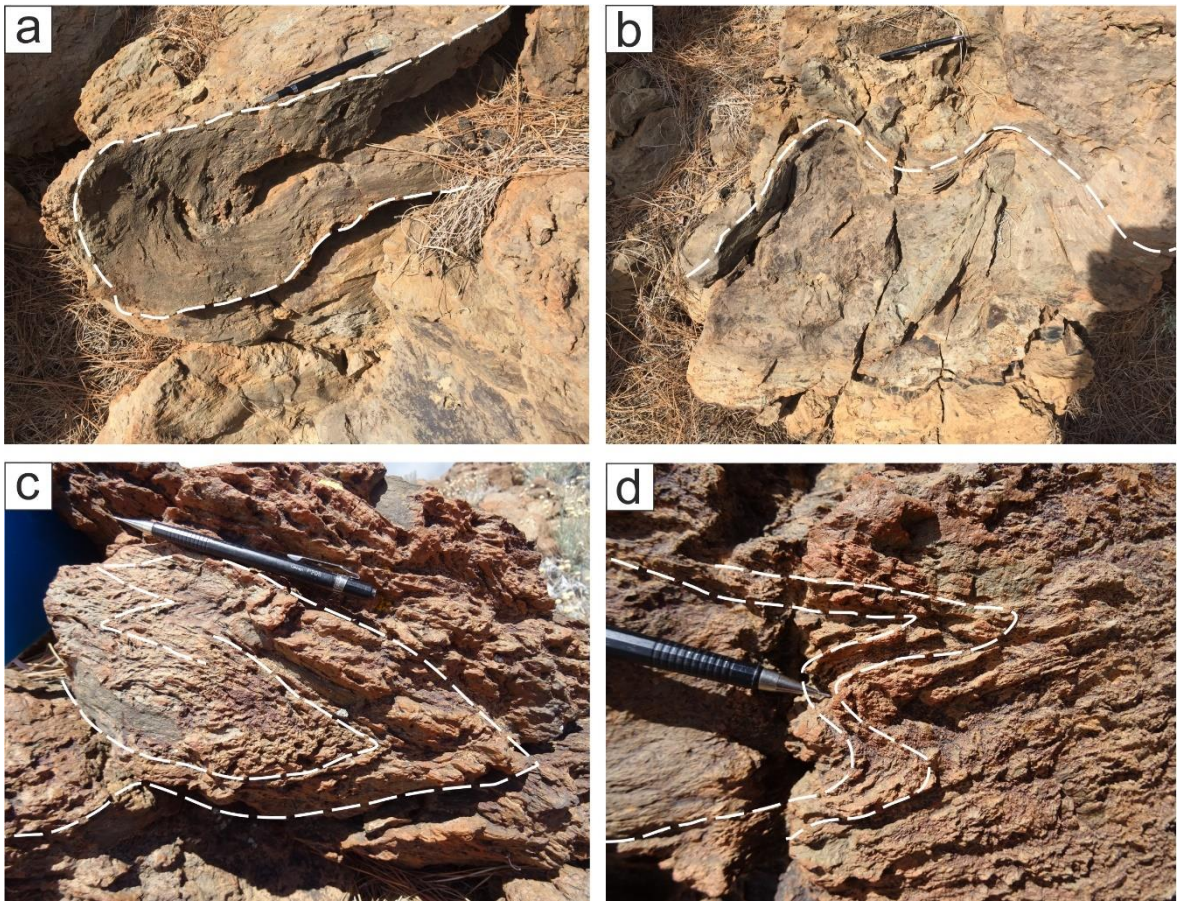


**Figure 4–37.** Folding in Retamares Mb Unit A. a) tight, closed isoclinal fold observed in lava-like lithofacies (N28°11'41.7" W16°39'29.8"); b) open, asymmetrical buckle fold in clast-rich eutaxitic lithofacies (N28°11'41.7" W16°39'29.8"); c) chevron folding within lava-like lithofacies (N28°11'26" W16°39'9"); d) loose buckle fold within lava-like lithofacies (N28°11'26" W16°39'9").

The intensely welded and lava-like lithofacies accounts for the majority of the thickness of Unit A, with a highly variable fabric and displays a range of folding, particularly around lithics (Figure 4–36 & 4–37). The unit is locally weakly columnar jointed (Figure 4–36) and welding varies at the base as it gradually increases up the stratigraphy, but also varies and decreases with clast and lithic content (i.e. decreases around higher clastic input and blocks, as seen in Figure 4–36).

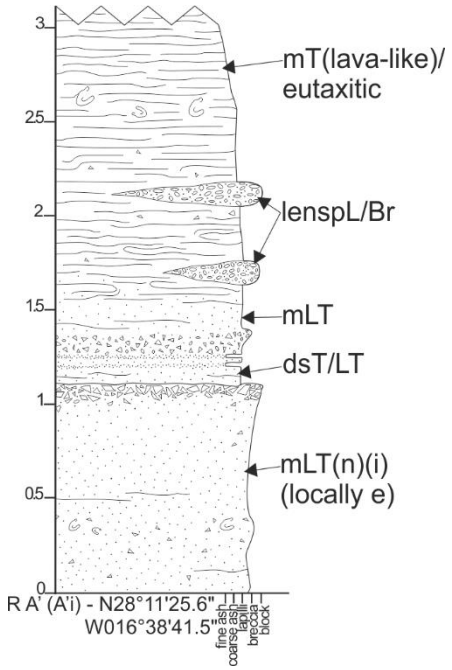


| Lithofacies description |
|---|
| Clast-rich, flow banded, glassy tuff with zones of lithophysae ('pock-marking') and prolate vesicles.<br><br>Variation in welding with a decrease in welding intensity associated with increase in lithic lapilli and occasional clasts. Welding intensity generally increases with height.<br>200 18° NE.<br>Matrix (ash) supported breccia with pumice and lithic lapilli (lava-like (Atravesado) ignimbrite).<br>Variably welded – with localised devitrified fiamme, prolate lithophysae and occasional lithic lapilli (lava-like ignimbrite). |

**Figure 4–38.** Lithofacies description of stratigraphic log of the base of Retamares Mb Unit A (log A'i) (vertical scale in metres).

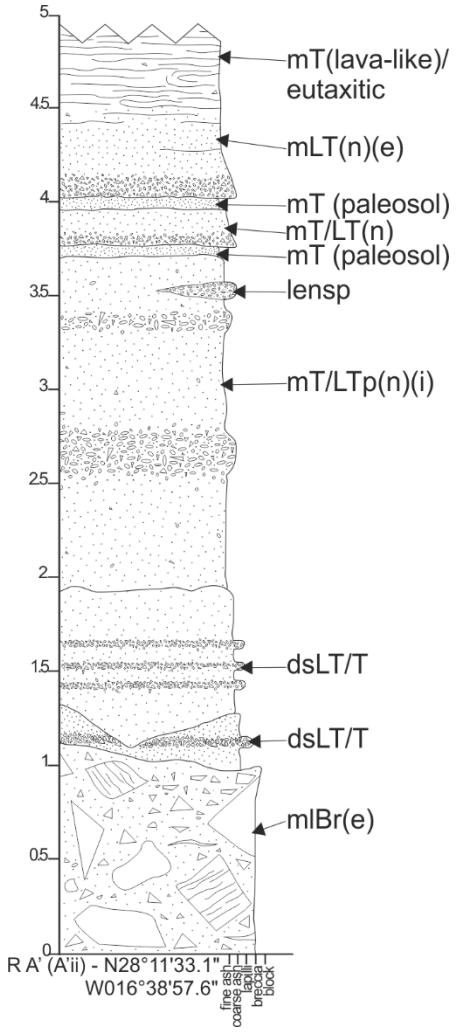


| Lithofacies description |
|---|
| Clast-rich, flow banded tuff with tight isoclinal and chevron folds. |
| Orange-pink fine ash horizon (paleosol). |
| Clast-supported, pumice-rich lithic lapilli band (VF16-S). |
| Pumice-rich. |
| Highly erosive, undulating contact. |
| Partially welded (sintered edges) bombs and blocks (up to 1.25m across). Clasts are lava-like material, basic and pumiceous, occasionally welded. Fine ash matrix supported. |

**Figure 4–39.** Lithofacies description of stratigraphic log of the base of Retamares Mb Unit A (log A'ii) (vertical scale in metres).

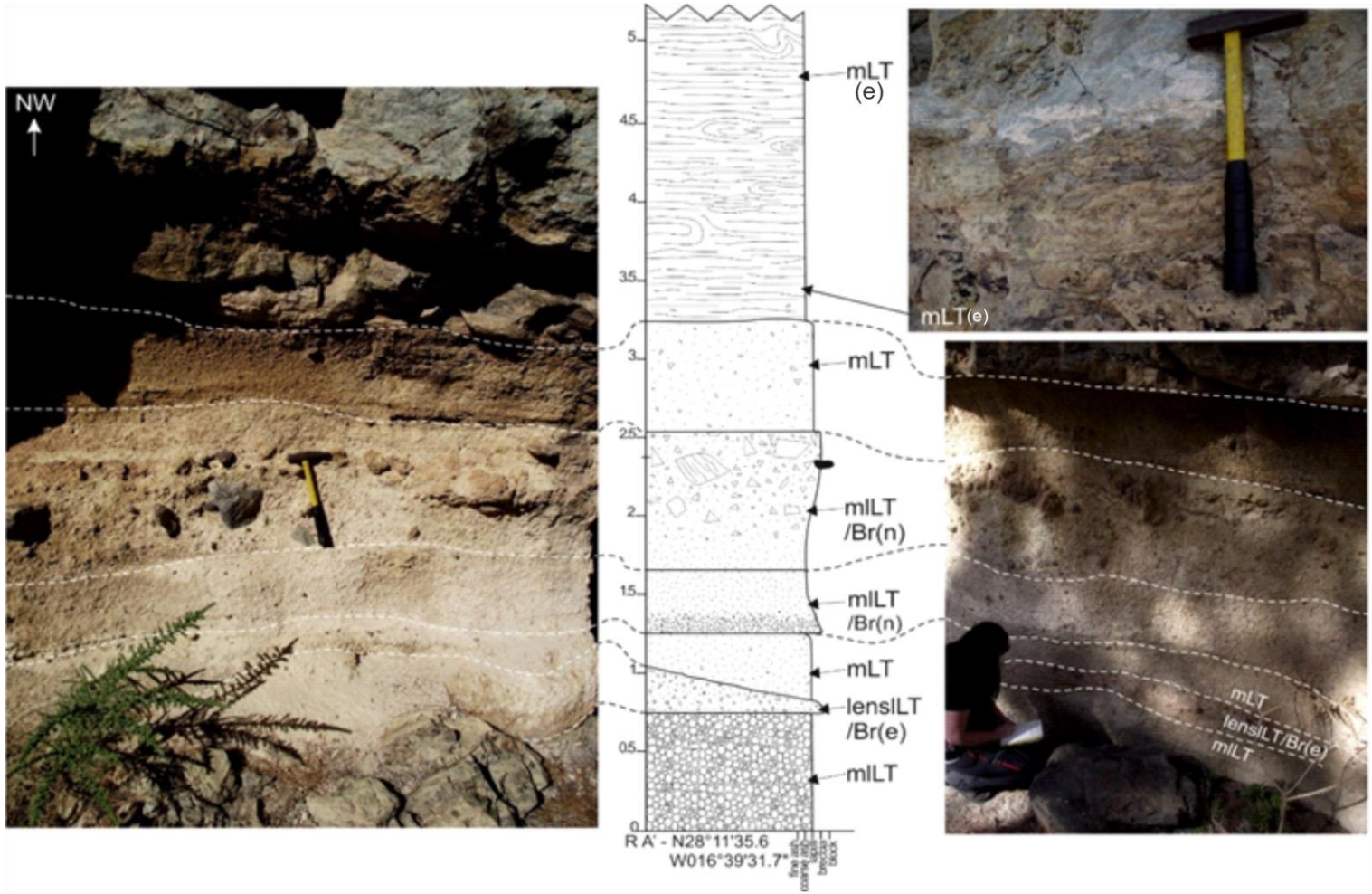


**Figure 4–40.** Lithofacies of the base of Retamares Mb Unit A (log A'II) (vertical scale in metres).

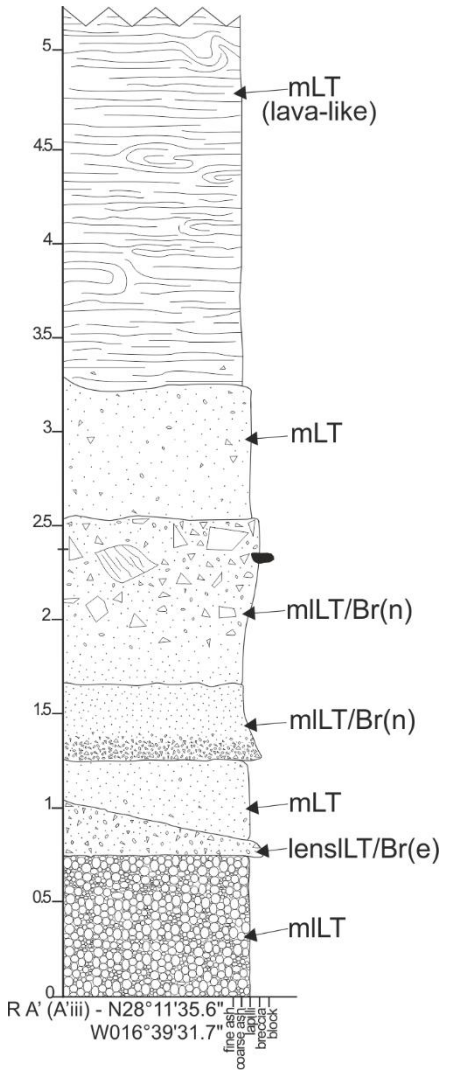


| Lithofacies description |
|---|
| Teal and orange banded, clast-rich, crystal-poor intensely welded and lava-like tuff with horizons of lithophysae throughout. Fabric is banded with tight closed and curvilinear folds. |
| Ash matrix-supported with occasional pumiceous clasts. |
| Ash matrix-supported with angular blocks of lava-like and eutaxitic material and rounded blocks of pinkish orange coated pumice lapilli. |
| Ash-matrix supported; pumice rich. |
| Clast and matrix supported with clasts of pumiceous material (pink coating), basic and lava-like clasts with fiamme. |
| Clast-supported, well sorted, pumice rich. |

**Figure 4–41.** Lithofacies description of stratigraphic log of the base of Retamares Mb Unit A (log A'iii) (vertical scale in metres).

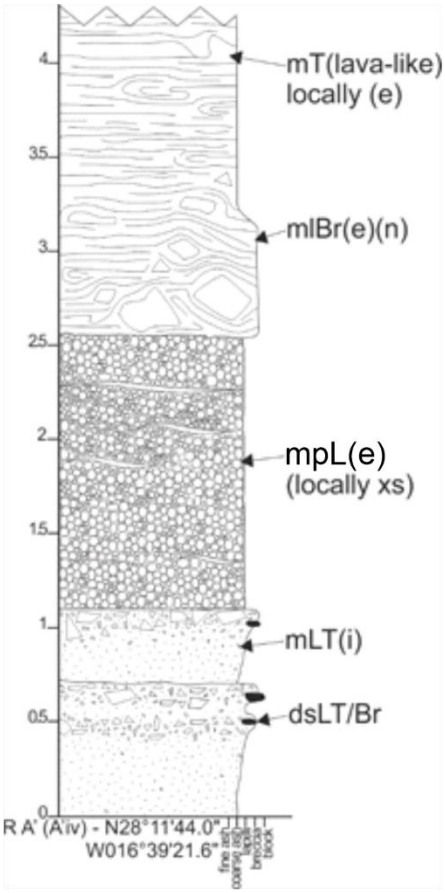


| Lithofacies description |
|---|
| Teal and orange, clast-rich, crystal-poor, banded, folded (tight isoclinal and curvilinear folds). |
| Ash-matrix supported with abundant fiamme and clasts of lava-like and pumiceous material. Fabric rotated around clasts/blocks. |
| Clast-supported, pumice rich tuff with abundant fiamme and sintered clasts edges. |
| Orange (devitrified) fiamme-rich horizons (stretched and deformed pumice). 'Ghost' cross stratification can be seen in the pumice-rich, welded fabric.<br>Lapilli matrix-supported with clasts of pumiceous and lava-like material. Occasional blocks of sub-rounded basic material. |
| Ash matrix supported with clasts of pumiceous and lava-like material. Blocks of sub-rounded basic material. |

**Figure 4–42.** Lithofacies description of stratigraphic log at the base of Retamares Mb Unit A (log A'iv) (vertical scale in metres).

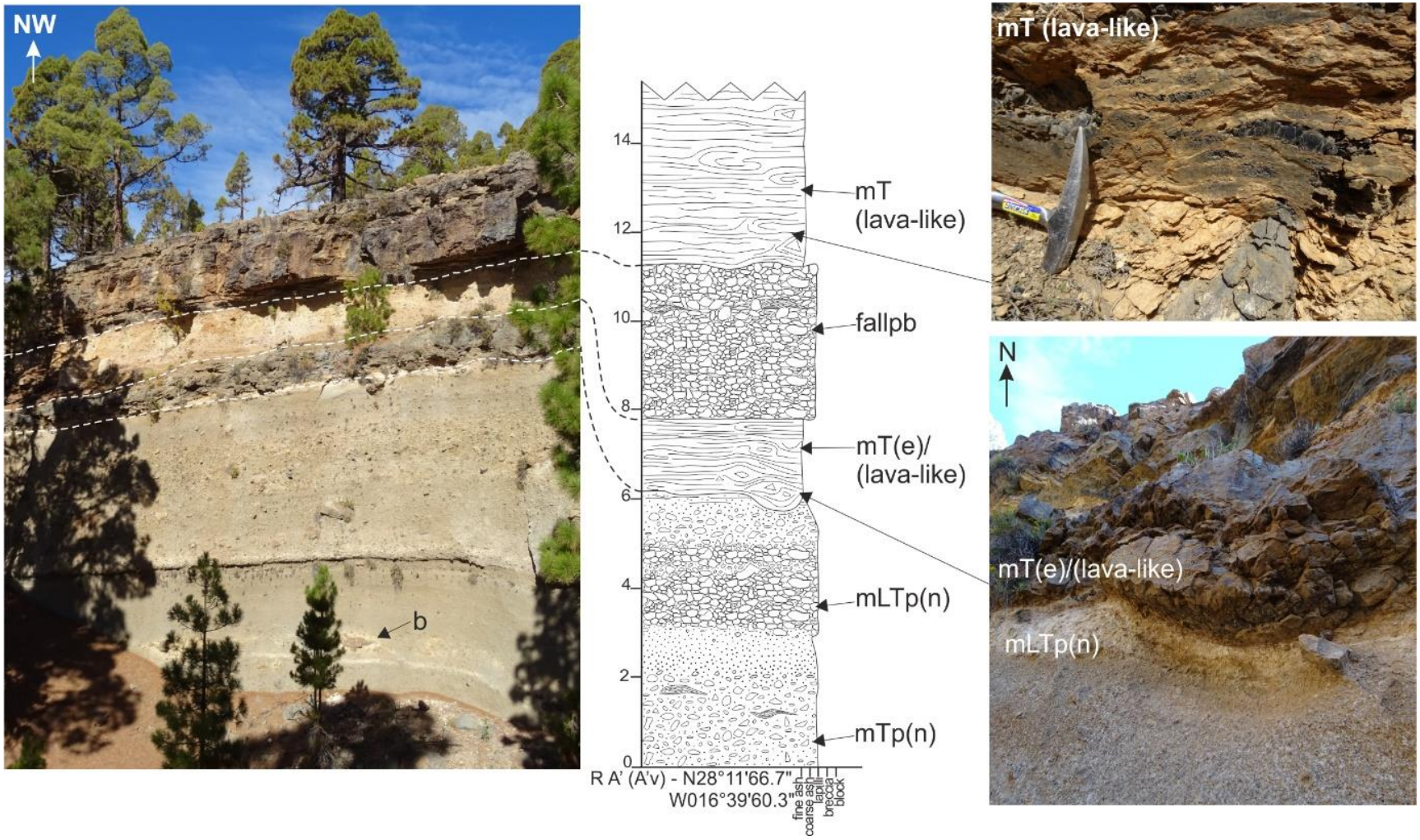


**Figure 4–43.** Lithofacies of the basal stratigraphy of: Retamares Mb Unit A (log A'v) (vertical scale in metres).

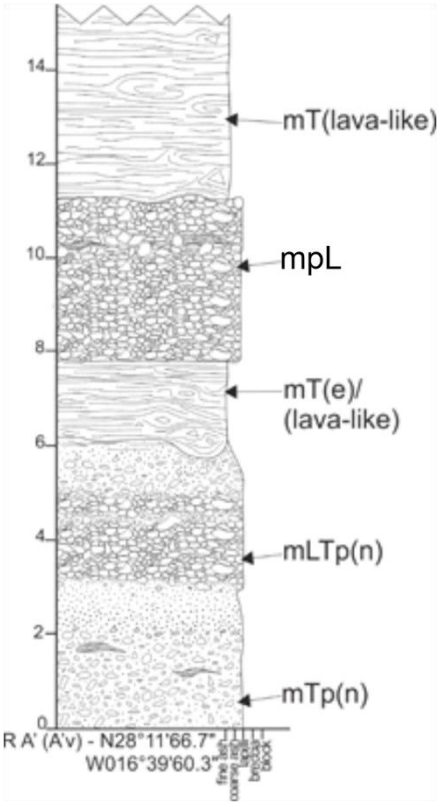


| Lithofacies description |
|---|
| Teal and orange, clast-rich and crystal poor. Heavily flow banded with tight isoclinal and curvilinear folding and fabric rotation around clasts. Obsidian-rich at the base (vitrified base). |
| Clast-supported pumice lapillistone with fluidal, scoriaceous bombs. Possible fall deposit. |
| Teal and orange, clast-rich and crystal poor. Heavily flow banded with tight isoclinal and curvilinear folding and fabric rotation around clasts. Obsidian-rich at the base (vitrified base). |
| Predominantly clast supported, poorly sorted pumice lapilli with fluidal, scoriaceous bombs.<br>Ash matrix-supported, pumice-rich with fluidal, scoriaceous bombs. |

**Figure 4–44.** Lithofacies description of stratigraphic log at the base of Retamares Mb Unit A (log A'v). Note change of scale of log (vertical scale in metres).

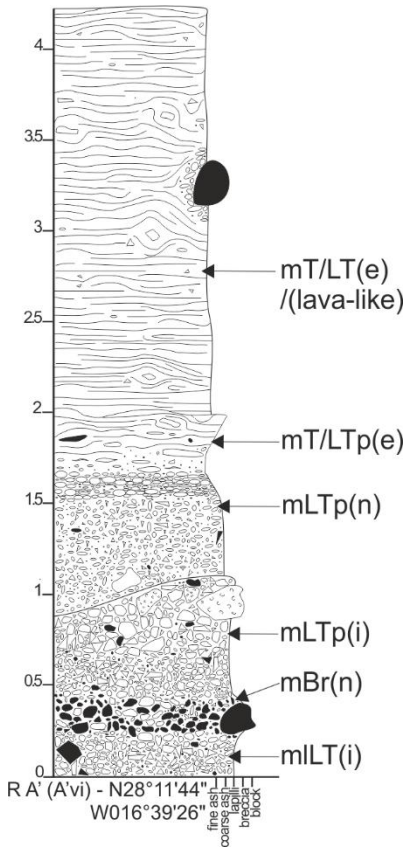


| Lithofacies description |
|---|
| Greenish blue and orange banded lava-like lithofacies, exhibiting variable welding (particularly around blocks and large clasts) and columnar jointing.<br><br>Pumice where visible is orange and altered. |
| Creamy green in colour, exhibiting base-parallel flow banding with stretched and elongated fiamme. Fabric rotated around clasts. |
| Highly irregular, erosional boundary.<br>Ash matrix-supported, gradually becoming pumice lapilli supported.<br>Ash and pumice lapilli supported, locally clast supported.<br>Compositionally stratified, non-welded.<br>Angular clasts of lava-like and basic material. |

**Figure 4–45.** Lithofacies description of stratigraphic log at the base of Retamares Mb Unit A (log A'vi) (vertical scale in metres).

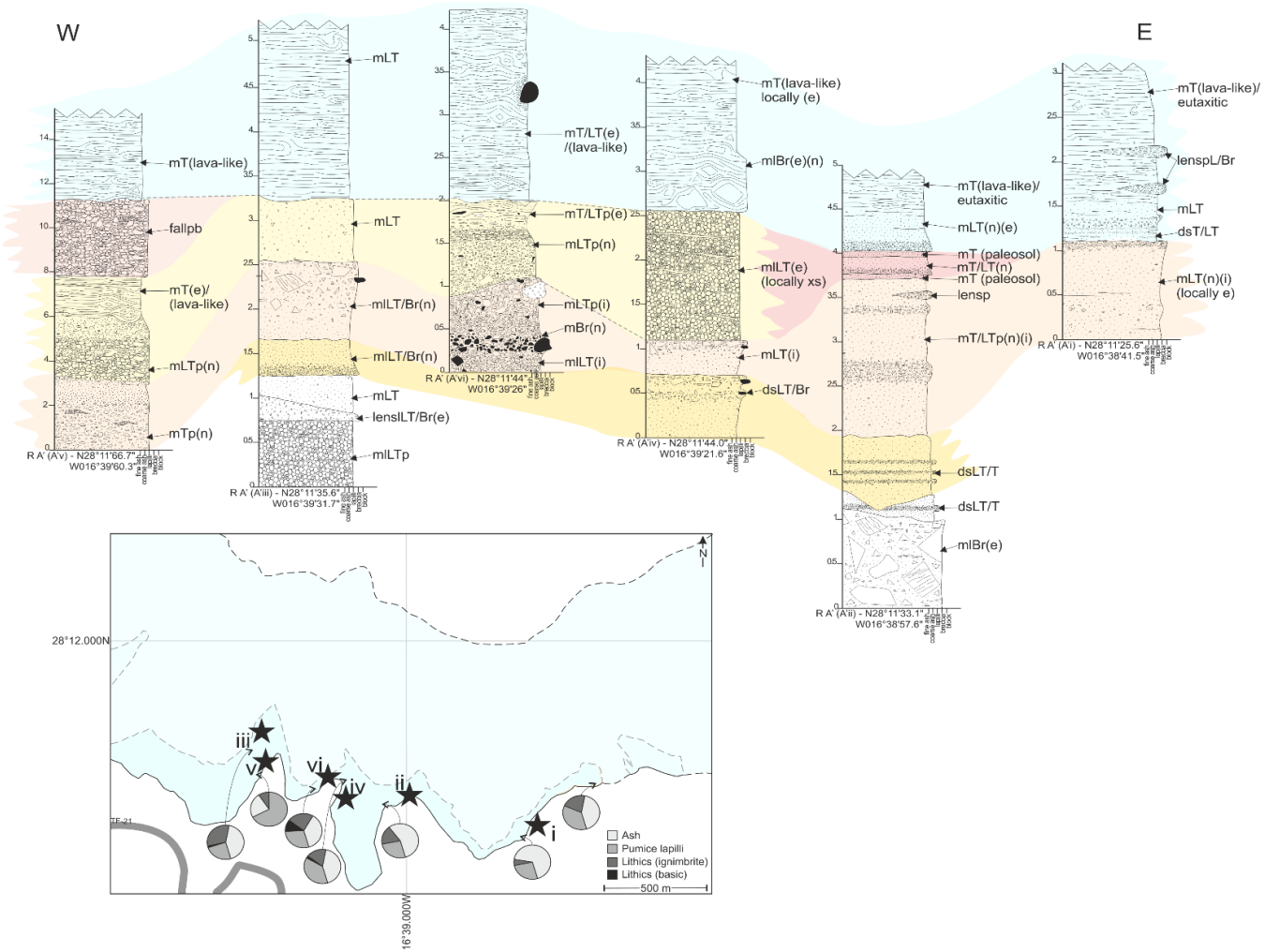


**Figure 4–46.** Correlation of the stratigraphic logs of Retamares Mb Unit A (vertical scale in metres), with the coloured bands showing possible continuation and variability of the lateral facies. Colours used to tie stratigraphy are arbitrary. Isopach map displays both the mapped (dark shade) and expected exposure (light shade), displaying the distribution of grain size and lithic components. Black stars show log localities.

### 4.3.2. Retamares Unit B

Similarly to Retamares Mb Unit A, the base of Unit B is distinctly defined by a non-welded, pumiceous base, up to ~5.5 m thickness which immediately (>0.2 m) grades up into intensely welded and lava-like lithofacies. It directly overlies Unit A, and is exposed 155 m north of Las Lajas (at N28°11'45.2" W16°39'47.6") and at the caldera wall, underlying Unit C at Llano de las Mesas (at N28°11'30.3" W16°38'28.3"), but much of the unit is overlain and obscured by the El Pinalito lavas and subsequent Retamares Units (Units C and D) (Figure 4–47). The unit is thinnest over topographic highs (3 – 4 m) and exposed at the caldera wall (approximately 9.5 m) which then thickens downslope, to the south.

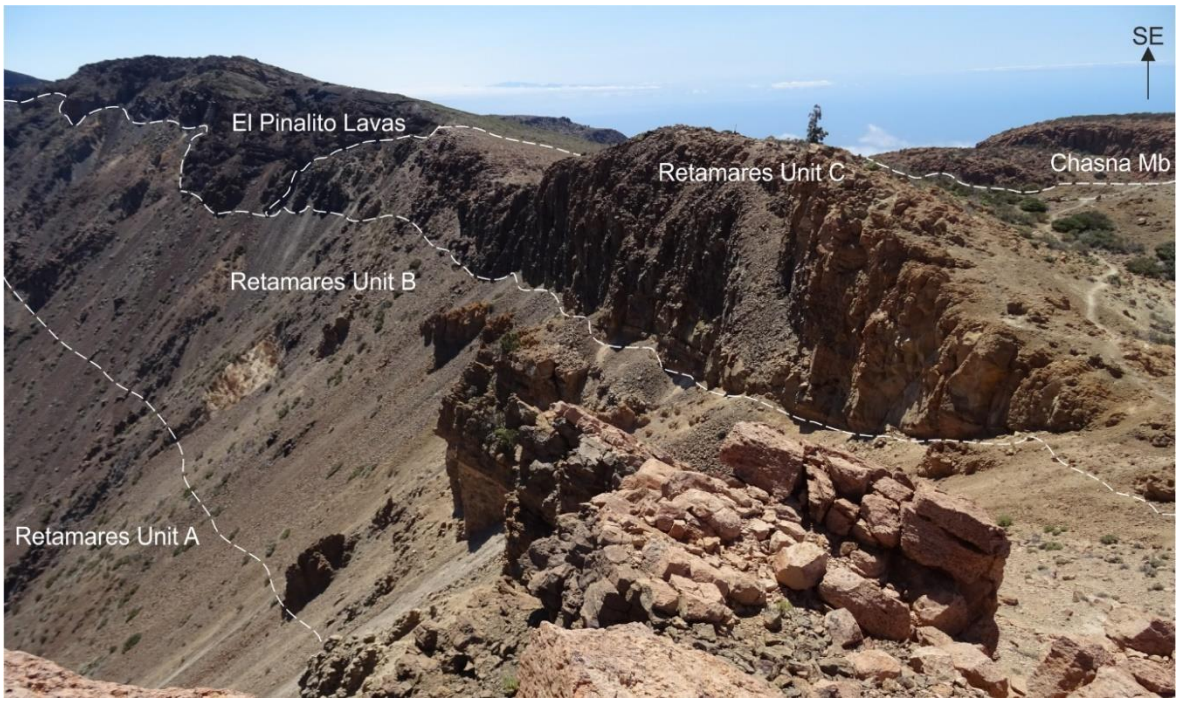


**Figure 4–47.** Field relationships of Unit B exposed on the caldera wall, Llano de las Mesas locality, overlying Unit A and underlying Unit C.

The basal stratigraphy of Unit B is predominantly diffuse and planar stratified tuffs and pumice-rich lapilli tuffs, overlain immediately by an intensely welded tuff (Figure 4–48 & 4–58). The basal stratigraphy of Unit B is exposed ~ 85 m east of Sombrero de Chasna in an erosional barranco, underlying Retamares Unit C ('mini-chasna') (Figure 4–53). Unit C thickens or topographically 'pools' downslope above these deposits, which are predominantly non-welded to welded lapilli tuffs and

breccias. A higher concentration of angular lithics (pumiceous and lava-like material) is observed at this locality, and the deposits here are distinctly less welded than observed elsewhere. Highly localised imbricate normal-listric faulting observed is observed in the upper stratigraphy at this locality, with 60°-75° NW trending faults which flatten out laterally to 35°-20°.

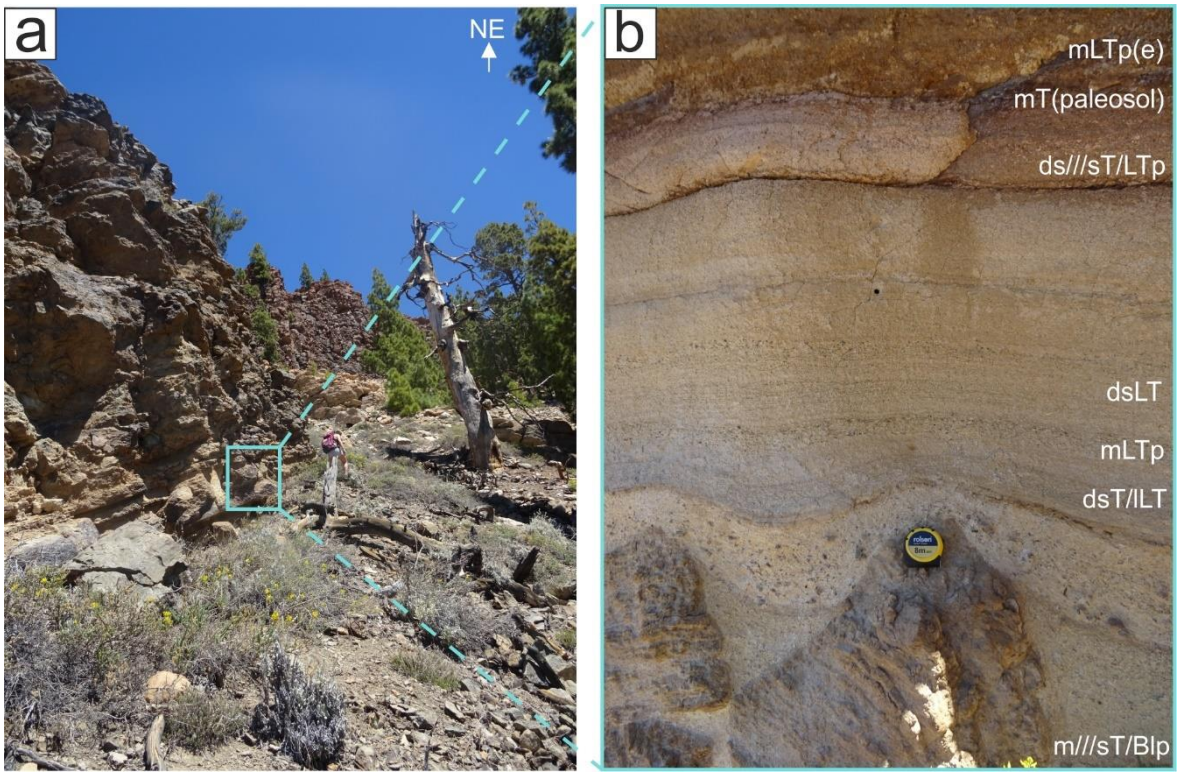


**Figure 4–48.** Basal stratigraphy of Retamares Mb Unit B (locality of log Biii) (a) (N28°11'39" W16°38'59") showing the non-welded lithofacies, grading up into the lava-like lithofacies (b). Unit thickness approximately 9 m at this locality.

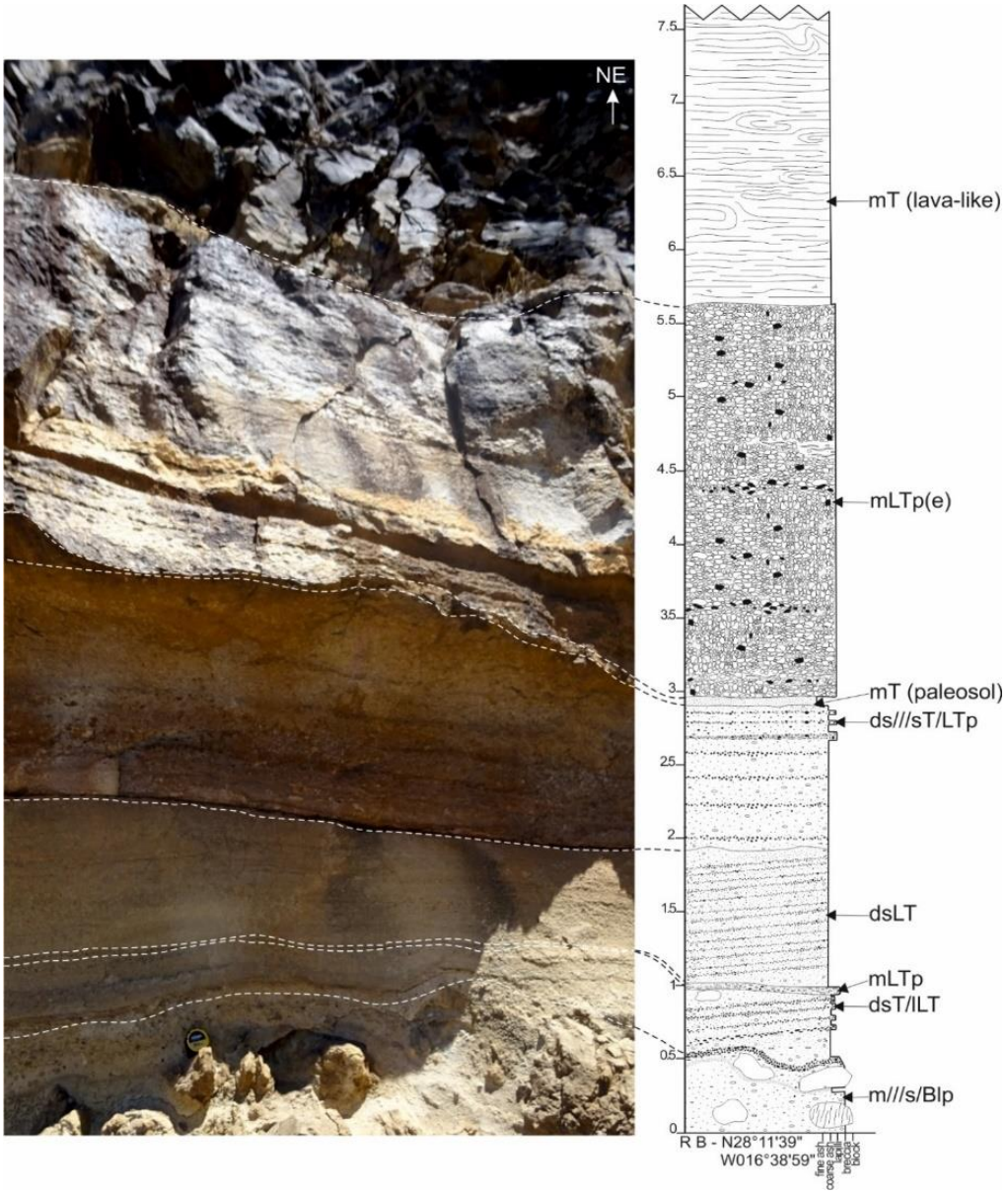


**Figure 4–49.** Basal stratigraphy and lithofacies of Retamares Mb Unit B (log Biii) (N28°11'39" W16°38'59") (vertical scale in metres).

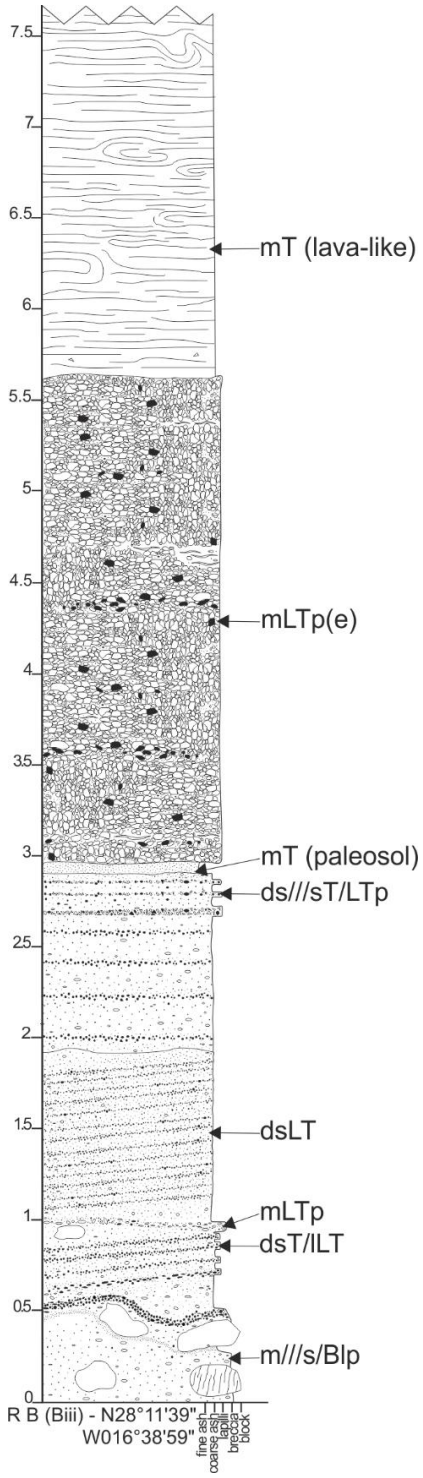


| Lithofacies description |
|---|
| Clast-poor, crystal-poor lava-like tuff with a persistent base-parallel fabric with folds (tight isoclinal and open, buckle folds) and locally wrapped around occasional clasts of lava-like material. |
| Welded red/orange pumice-rich, clast-supported, poorly-sorted lapilli tuff with pumice and lithic lapilli (obsidian, basalt, ignimbrite of varying degrees of welding) with bluish green (devitrified) fiamme throughout. Localised 'pockets' of ash-supported matrix, displaying weak stratification. |
| Orange very fine tuff (possible paleosol). |
| Non-welded alternating bands of pumiceous lapilli tuff and basic lithic lapilli. |
| Regular alternations of pumice-rich ash-supported and lapilli-supported lapilli tuff. |
| Alterations of ash-rich, pumice-rich and basic lithic lapilli tuff. |
| Fine ash tuff with blocks of pumiceous and lava-like material. Layers disrupted underneath blocks. |

**Figure 4–50.** Lithofacies description of stratigraphic log at the base of Retamares Mb Unit B (log Biii) (vertical scale in metres).

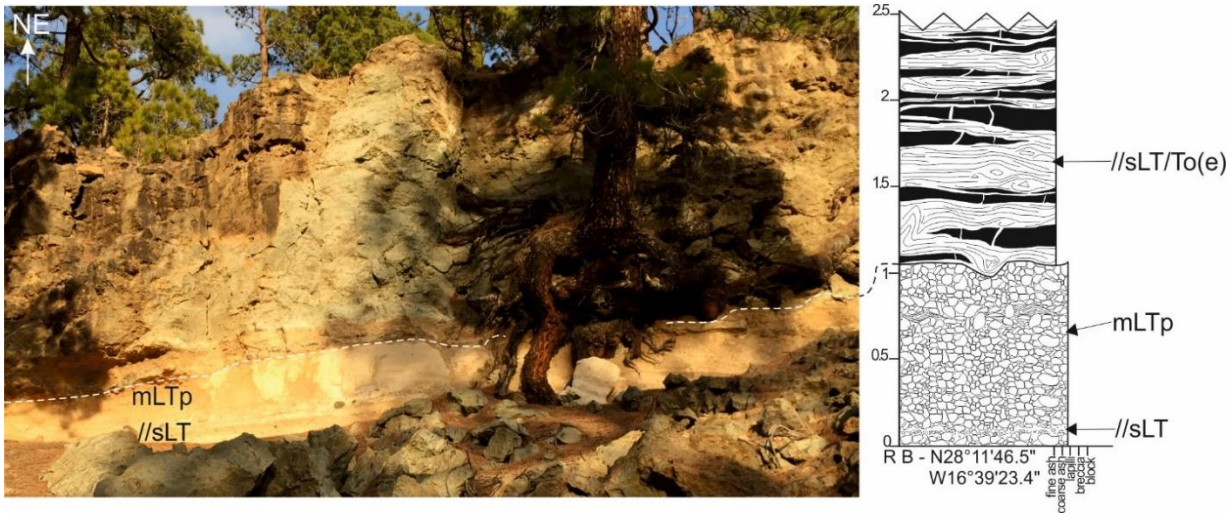


**Figure 4–51.** Basal stratigraphy of Retamares Mb Unit B (log Bii) (vertical scale in metres).

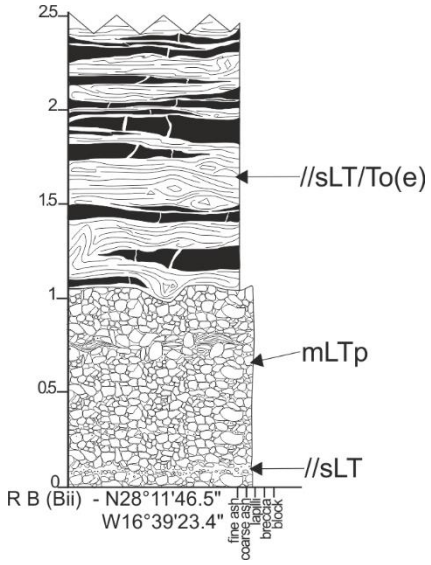


**Lithofacies description**

Teal and orange, banded, last-rich, crystal-poor welded lapilli tuff with discontinuous obsidian-rich fiamme (merged and forming continuous horizons).

Fabric folded (open and curvilinear folds) and rotated around clasts (lava-like and pumiceous material).
Highly erosive, undulating contact.
Well sorted, clast-supported pumice lapilli tuff with mafic cow-pat bombs throughout (possible fall deposit).

**Figure 4–52.** Lithofacies description of stratigraphic log at the base of Retamares Mb Unit B (log Bii) (vertical scale in metres).

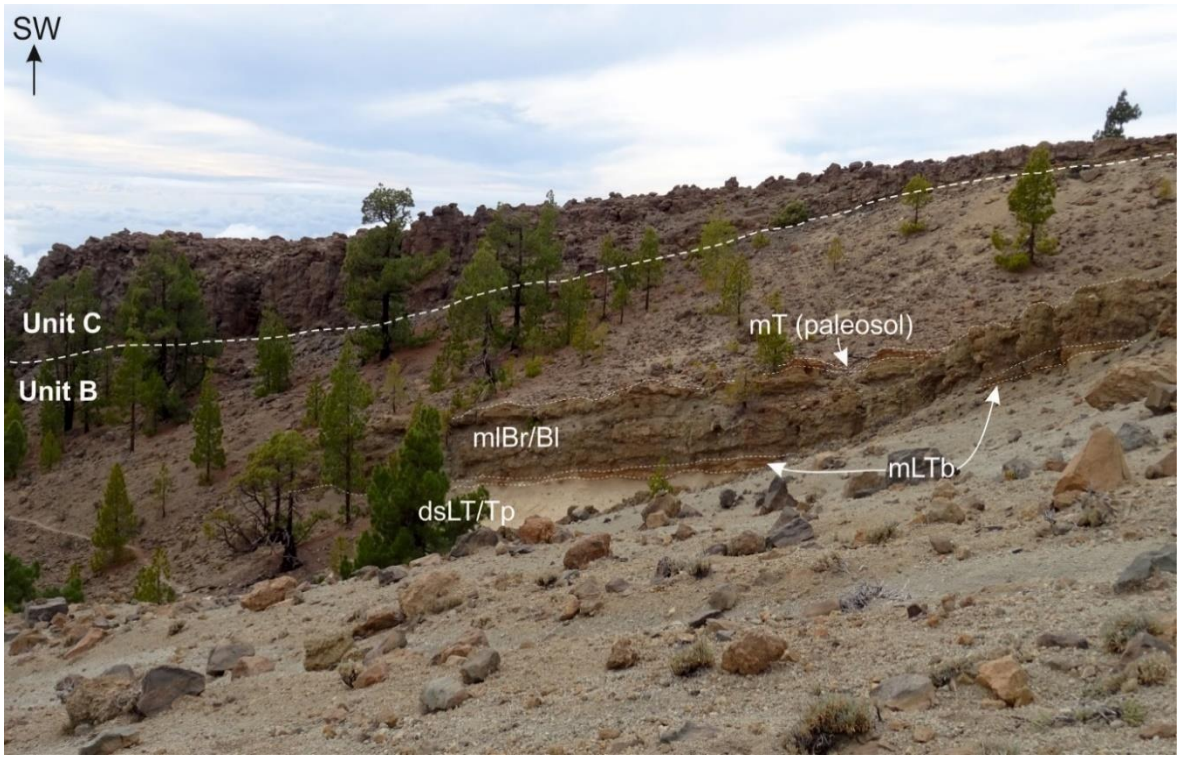


**Figure 4–53.** Uppermost stratigraphy of Retamares Mb Unit B, overlain by Unit C, looking southwest at N28°11'48.0" W16°38'58.1".

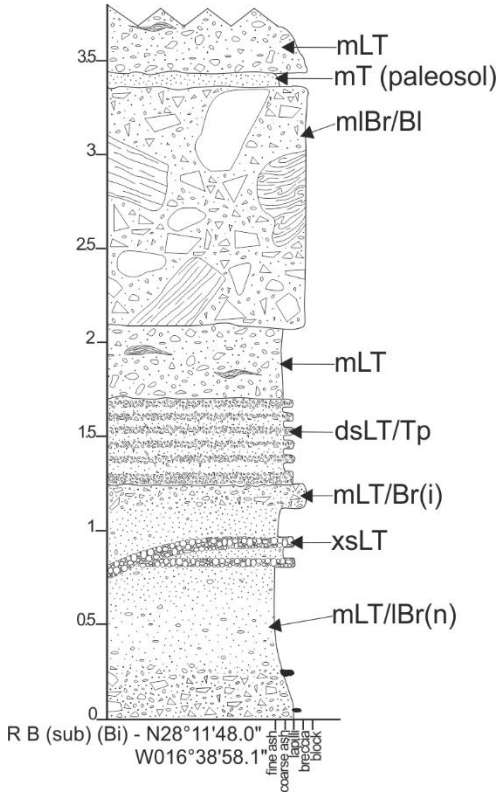


| Lithofacies description |
|---|
| Pinkish red fine ash – possible paleosol. |
| Ash matrix-supported with blocks up to 1.23 m across. Clasts are predominantly lava-like material with pumiceous material. Spatter-like bombs are also present, with fluidal and deformed boundaries. |
| Horizontal, planar contact (eroding deposit).<br>Pumice and clast-rich lapilli tuff with mafic cow-pat bombs throughout (with associated bomb sag etc). |
| Lapilli matrix-supported with clasts of vesicular basalt and lava-like material.<br>Lapilli matrix-supported breccia with clasts of obsidian, basic, tuff (auto-clasts), pumiceous and lava-like material and blocks of basic material. |

**Figure 4–54.** Lithofacies description of stratigraphic log at the uppermost stratigraphy of Retamares Mb Unit B (log Bi) (vertical scale in metres).

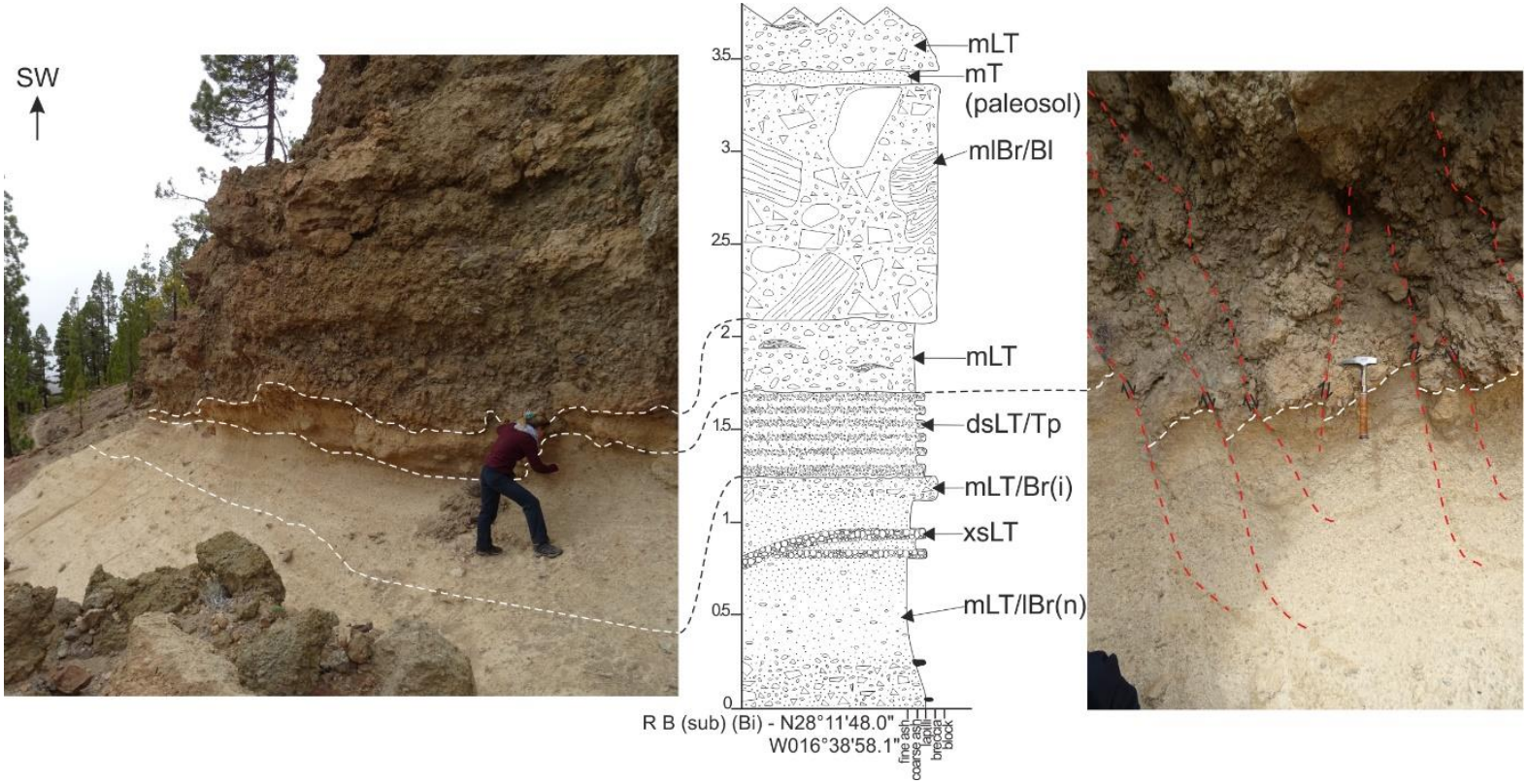


**Figure 4–55.** Uppermost stratigraphy of Retamares Mb Unit B (log Bi) (vertical scale in metres). Note the localised small-scale listric faulting in the contact between the mLT and mlBr. Faults are not traceable for any distance into the breccia with height and are presumably a result of the weight and compression of the overlying breccia, applied to the weaker, incoherent mLT, leading to localised extensional displacement.

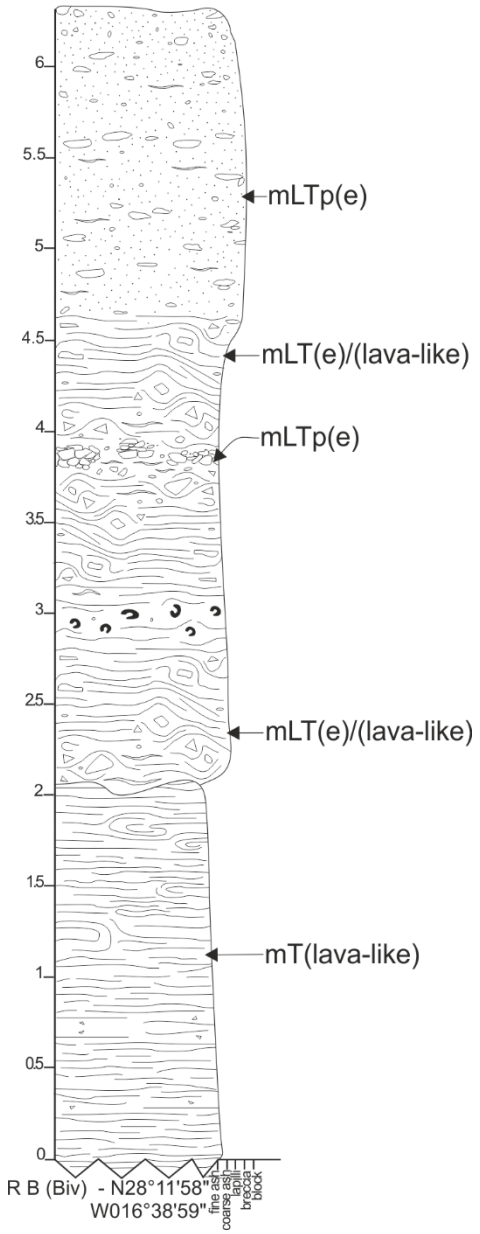


| Lithofacies description |
|---|
| Flattened, stretched, and elongated pumice, ash matrix supported. Creamy pink in colour. Upwards decrease in welding, with fiamme becoming absent and more intact clast boundaries towards the top of the section. |
| Planar fabric - 110 42° |
| Pockets of clast-supported pumice. Areas where pumice lapilli are concentrated is distinctly less welded. |
| Dark blue and orange banding, heavily pock-marked (lithophysae) horizon. |
| Bluish grey in colour, lithic-rich intensely welded, lava-like lithofacies. Persistent base-parallel fabric, rotated around clasts. |
| Red, strongly flow banded – persistent base-parallel fabric exhibiting tight isoclinal folding, and fabric rotated and folded around clasts. Clasts are pumiceous and lava-like material. |

**Figure 4–56.** Lithofacies description of the stratigraphic log at the uppermost stratigraphy of Retamares Mb Unit B (log Biv) (vertical scale in metres).


**Figure 4–57.** Uppermost section of Retamares Mb Unit B (displaying the upwards decrease in degree of welding) and lithofacies of log Biv (N28°11'58" W16°38'59").

The uppermost 2 to 3 m of Unit B stratigraphy exhibits a progressive decrease in welding intensity from the dominant lava-like lithofacies; with pumice clast boundaries gradually becoming more visible and less deformed and is a distinctly creamy pale pink colour (Figure 4-56 & 4-57).

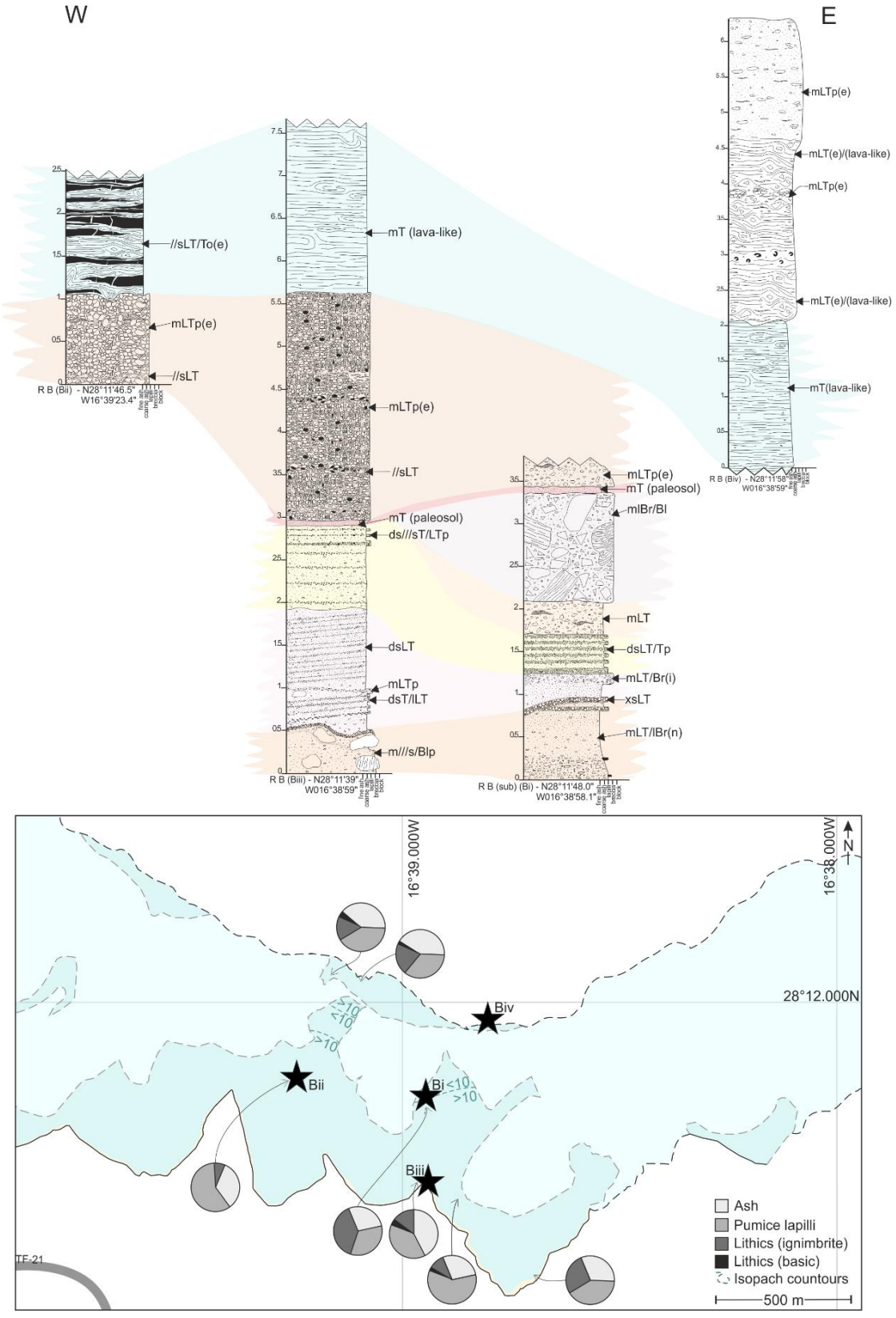


**Figure 4–58.** Correlation of the stratigraphic logs of Retamares Mb Unit B (vertical scale in metres), with the coloured bands showing possible continuation and variability of the lateral facies. Colours used to tie stratigraphy are arbitrary. Isopach map displays both the mapped (dark shade) and expected exposure (light shade), displaying the distribution of grain size and lithic components. Black stars show log localities.

### 4.3.3. Retamares Unit C

Overlying much of Unit B, Unit C is exposed in the caldera wall from the west at Roque los Almendros (at N28°12'0.2" W16°39'34")(Figure 4–60) to Llano de las Mesas in the caldera wall (Figure 4–59), with many lobe-like structures which extend downslope towards the south (Figure 4–61 & 4–62). Much of the unit is overlain by the younger Retamares units (Unit D), the Chasna Mb (directly at Roque los Almendros and the Sombrero de Chasna localities) and the El Pinalito caldera-fed lavas.

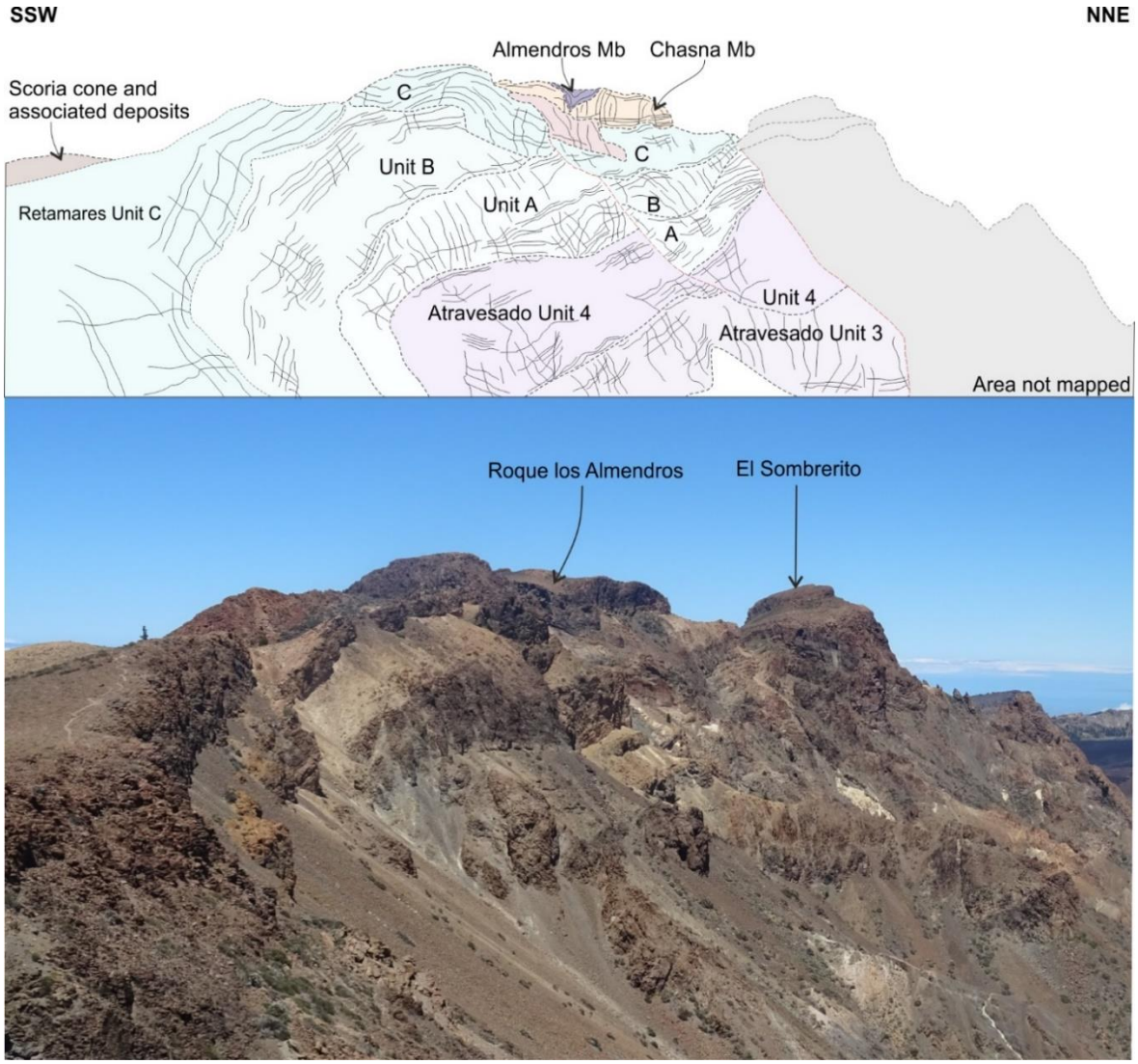


**Figure 4–59.** Field sketch and photograph of the field relationships of the Atravesado, Retamares and Chasna Members exposed in the central southern caldera wall stratigraphy, from Llano de las Mesas to Roque los Almendros.

Similarly to the previous Retamares Units, Unit C consists of non-welded basal stratigraphy, which grades up into an intensely welded and lava-like lithofacies

which accounts for most of the unit's thickness. The basal stratigraphy is highly variable across Unit C and consists of non-welded lithic breccias, localised, discontinuous fall deposits, stratified tuffs and lapilli tuffs and progressively grades into an intensely welded and lava-like lithofacies, with highly variable welding textures and gradations (Figure 4-63 - 4-70). This unit displays a variety of interesting welding textures, such as in the densely welded base of Unit C (Figure 4-65 & 4-66, log Ci), which contains blocks of pumice-rich massive lapilli tuff and breccia (typical of previous Retamares units) up to 2.15 m across. These blocks are surrounded by a ~4 - 25 cm 'halo' of non-welded, clast-supported, poorly-sorted pumice lapilli tuff with clast sintering and alteration (green, chlorite alteration) on the outer ~ 1 – 5 cm rim (occurring at the contact with the obsidian banded lava-like and eutaxitic tuff). These textures are discussed further in Chapter 7. The lava-like lithofacies extends to the top of the Unit, with a planar, persistent base-parallel fabric and exhibits columnar jointing throughout (dipping at 2 ° - 7 °).


**Figure 4–60.** Retamares Mb Unit C, exhibiting columnar jointing, exposed at the caldera wall, overlain by the Chasna Mb at Roque los Almendros locality (N28°12'0.2" W16°39'34").


**Figure 4–61.** Lobe of columnar jointed, lava-like lithofacies of Retamares Mb Unit C, which thickens downslope, overlying Unit B. View is looking west from Sendero 31 at Sombrero de Chasna.


**Figure 4–62.** Retamares Mb Unit C at locality of log Civ (N28°11'49" W16°39'51"), exhibiting a strong, pervasive, base-parallel fabric, weak columnar jointing and a vertical increase in welding intensity throughout the deposit, with a typically non-welded basal stratigraphy, which is thickest at the frontal lobe of the deposit, grading up into a lava-like lithofacies.

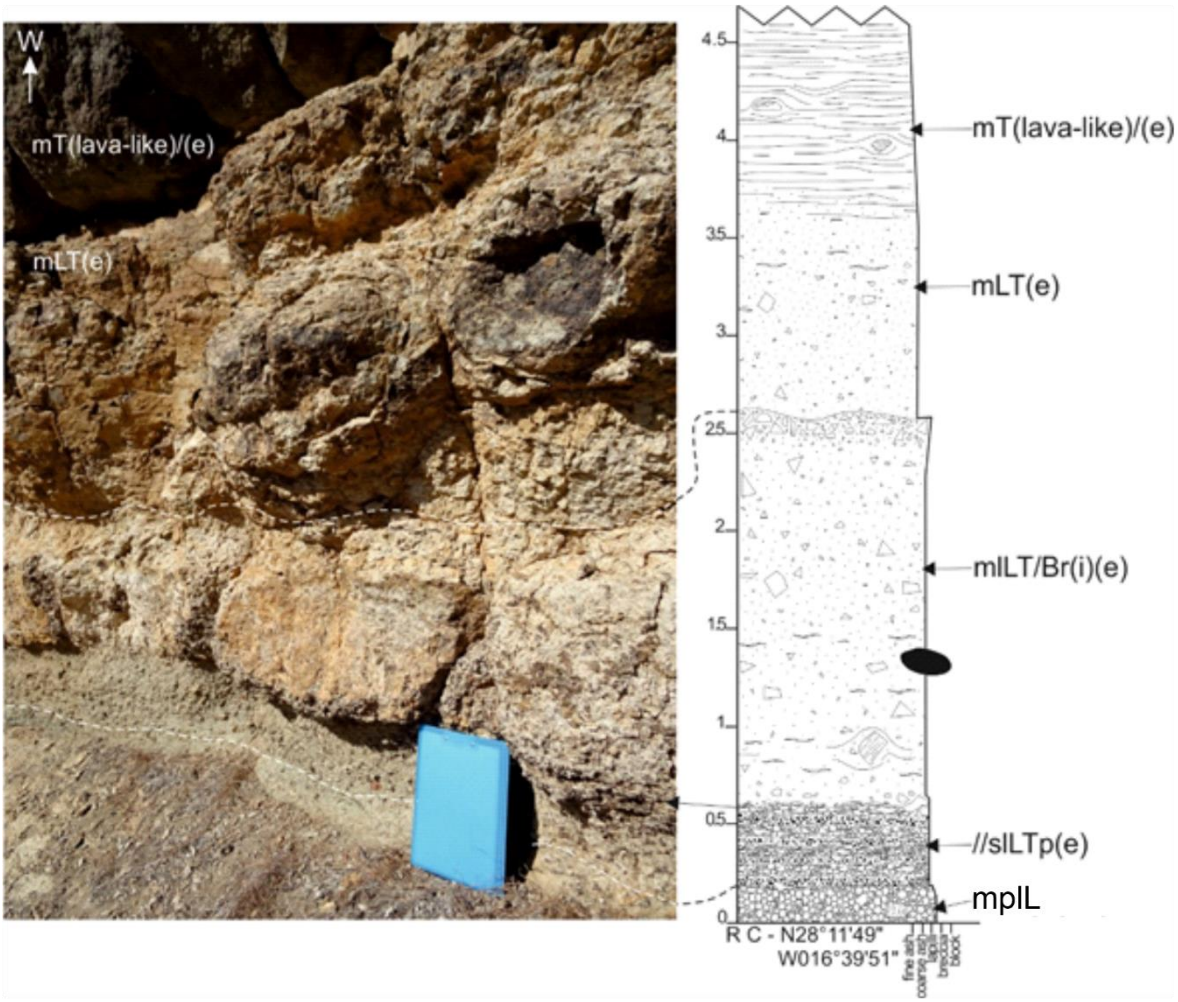


**Figure 4–63.** Basal stratigraphy of Retamares Mb Unit C (log Civ) (vertical scale in metres).

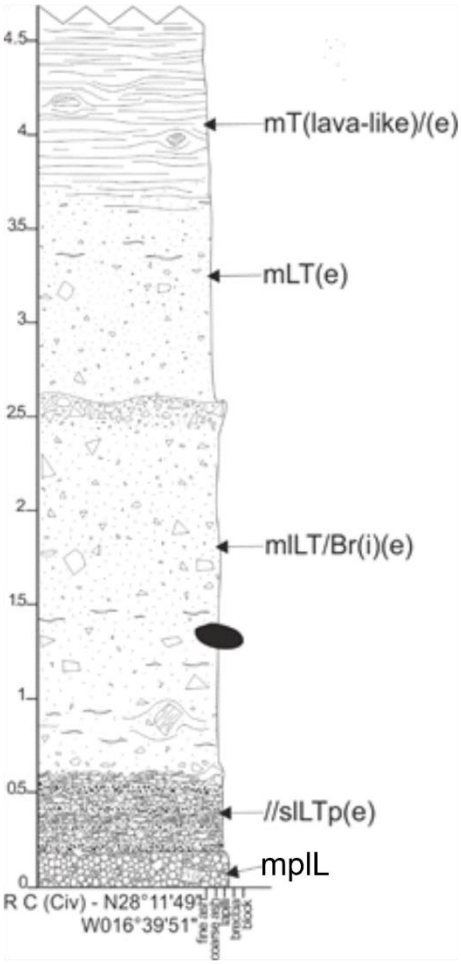


| Lithofacies description |
|---|
| Banded teal and orange, clast-rich, crystal poor predominantly lava-like, locally eutaxitic with a persistent base-parallel fabric which is folded (tight isoclinal) and rotated around clasts. |
| Occasional clasts of lava-like and pumiceous material. |
| Welded, pumice-rich lapilli tuff with sintered clast boundaries and fiamme, often concentrated in horizons. |
| Fabric locally rotated around clasts. Clasts of pumiceous, basic and lava-like material Sharp, gradational contact. |
| Welded alternating pumice-rich and basic material. |
| Pumice-rich, well sorted, clast supported horizon (possible fall deposit). |

**Figure 4–64.** Lithofacies description of the basal stratigraphy of Retamares Mb Unit C (log Civ) (vertical scale in metres).

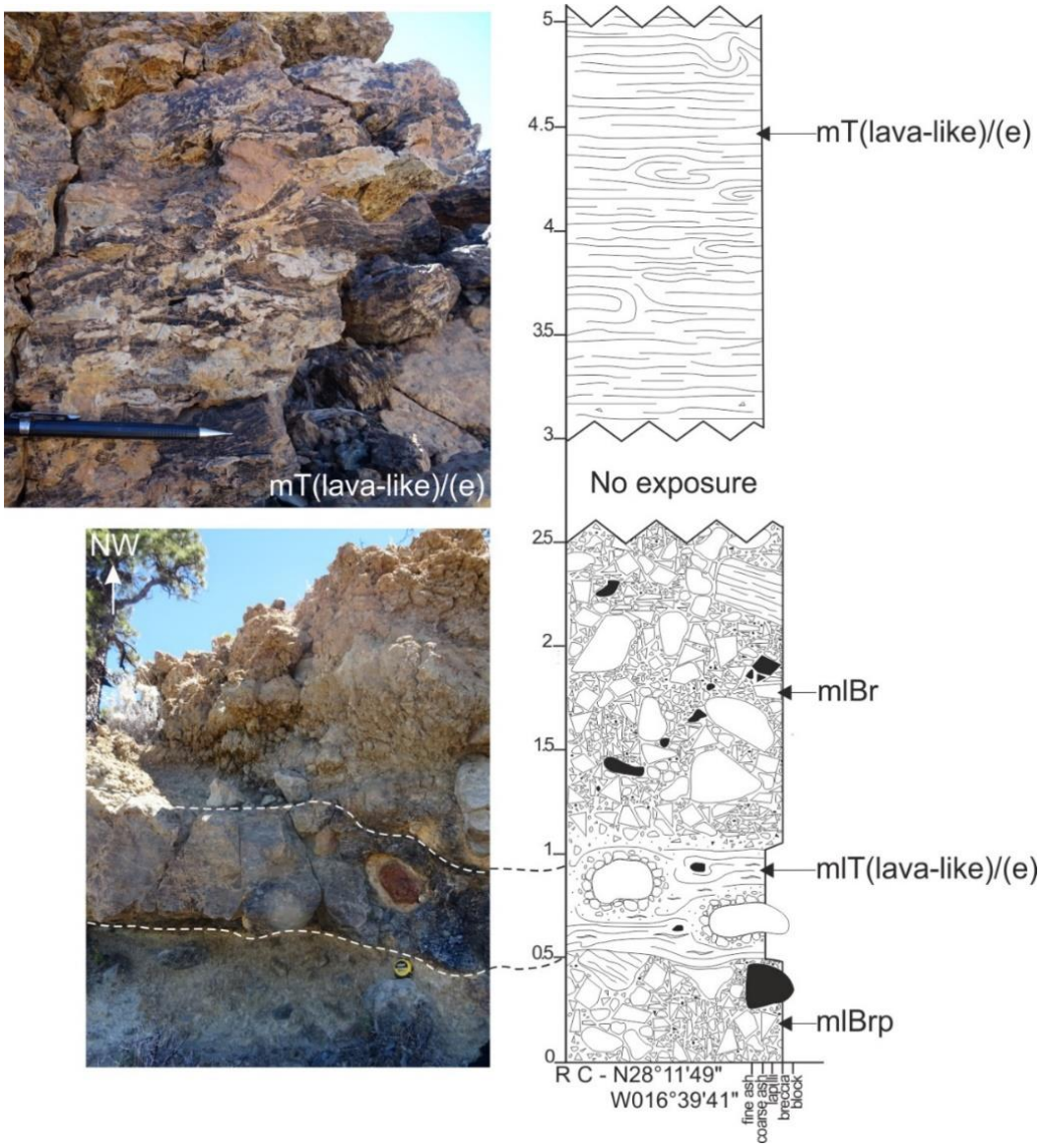


**Figure 4–65.** Basal stratigraphy and lithofacies of Retamares Mb Unit C at log Ci (vertical scale in metres).

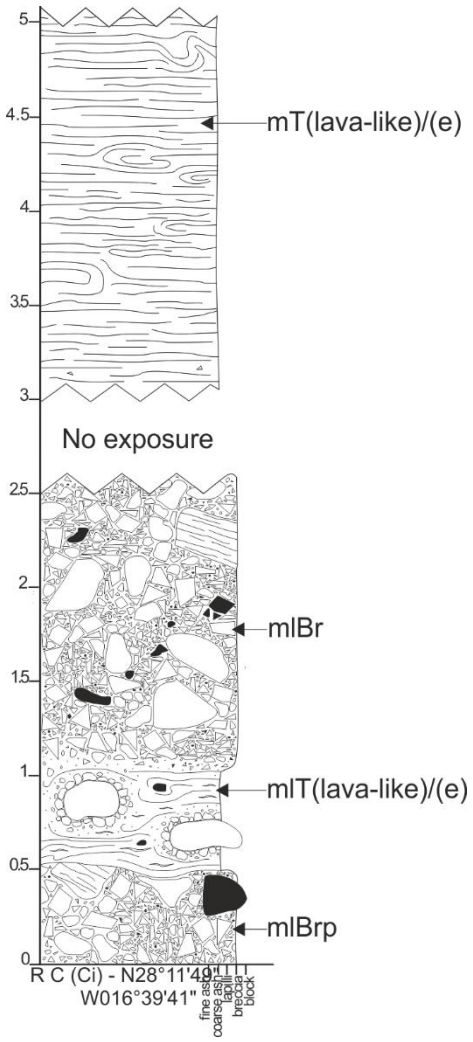


| Lithofacies description |
|---|
| Lava-like lithofacies extends up to 7.5 m.<br>Clast-poor, crystal-poor, predominantly lava-like with a persistent base-parallel fabric with folded (tight isoclinal and curvilinear folds) and rotated fabric around clasts and crystals. Clasts are of lava-like material. |
| 0.5 m of no exposure (scree slope). |
| Clast-supported, very poorly sorted breccia with clasts of obsidian, pumiceous, lava-like and non-welded ignimbrite material with local fiamme. |
| Sharp, gradational contact.<br>Obsidian-banded, predominantly lava-like, locally eutaxitic with blocks of lava-like material surrounded by a cooled pumiceous margin/halo discussed in Chapter 7. |
| Non-welded, clast-supported, very poorly sorted pumice-rich breccia with blocks of basic material. |

**Figure 4–66.** Lithofacies description of the basal stratigraphy of Retamares Mb Unit C (log Ci) (vertical scale in metres).

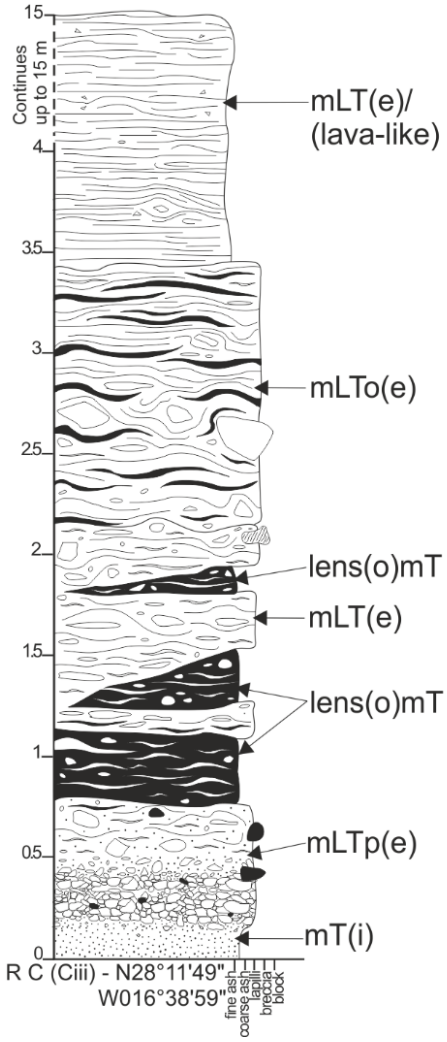


| Lithofacies description |
|---|
| Lava-like lithofacies continues up to approximately 15 m. Orange, clast-poor, crystal-poor, predominantly lava-like with a persistent base-parallel fabric exhibiting folding (tight isoclinal and curvilinear folds) and strongly columnar jointed. Much more porous where pumice has eroded out. Banded and streaked obsidian throughout. Greenish blue in colour with a flow banded pumiceous matrix and occasional blocks of lava-like material. Fabric - 210 18°. |
| Poorly sorted with sub-rounded to angular clasts. Pumice is deformed around clasts, with streaky obsidian lenses throughout. Pinkish cream in colour. |
| Black obsidian matrix (locally devitrified) with occasional clasts and fiamme, and greenish altered pumice. Pumice flattened and bent around lithics. Clasts are predominantly pumice with grey mafic material (basalt, scoria) and lava-like material. Non-welded up to 0.4 m with clear clast boundaries and welding increases upwards. Creamy white in colour, predominantly ash. |

**Figure 4–67.** Lithofacies description of the basal stratigraphy of Retamares Mb Unit C (log Ciii) (vertical scale in metres).

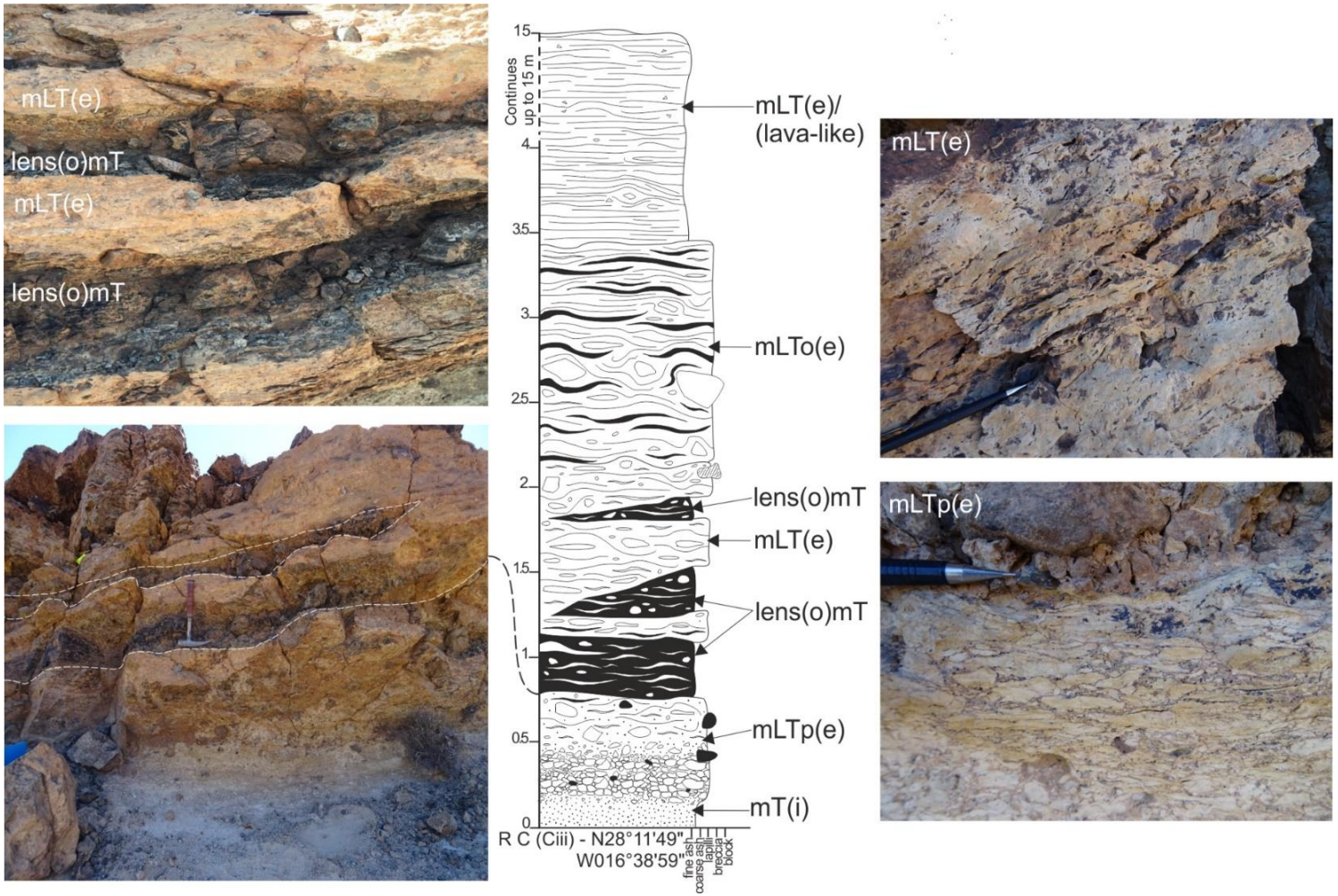


**Figure 4–68.** Lithofacies and welding profiles at the basal stratigraphy of Retamares Mb Unit C (log Ciii) (vertical scale in metres).

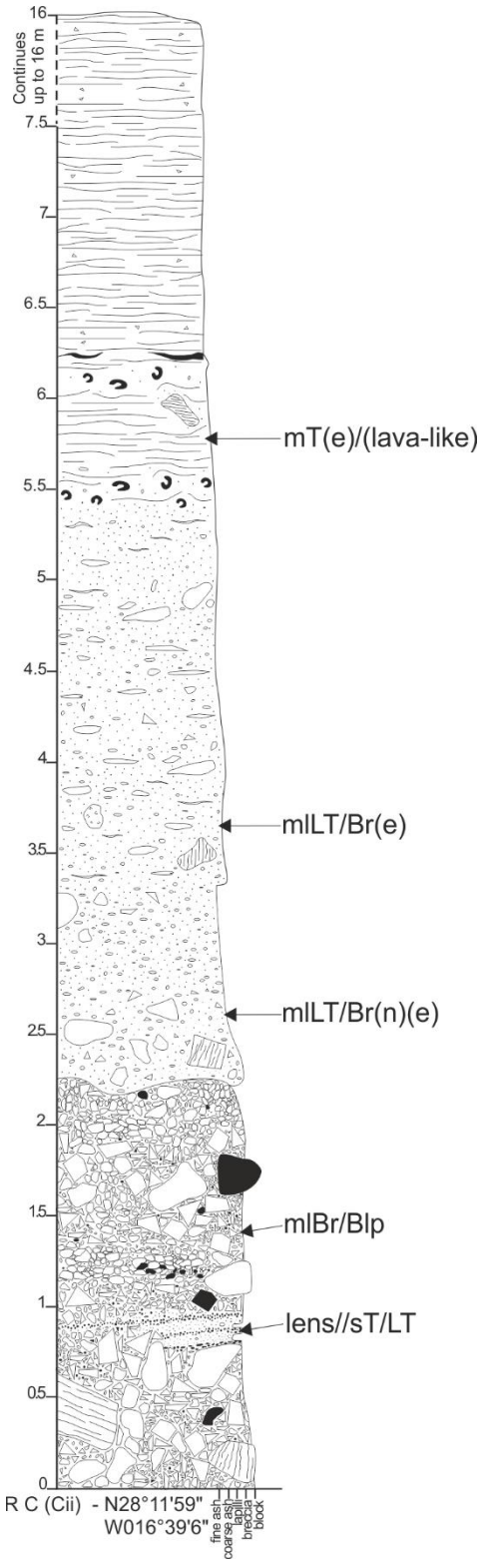


**Lithofacies description**

Lava-like lithofacies extends up to approximately 16 m. Clast-poor, crystal-poor, predominantly lava-like with a persistent base-parallel fabric with folded (tight isoclinal and curvilinear folds).

Obsidian fiamme, stretched and elongated pumice fiamme and lithophysae horizon. Occasional clasts and blocks of lava-like material.

Creamy green in colour. Ash and lapilli supported breccia, welded with stretched and elongated pumice and clasts with sintered boundaries. Clasts are predominantly pumiceous, lava-like and non-welded, stratified ignimbrite material.

Welding gradually increasing upwards. Light creamy grey in colour, predominantly clast and lapilli supported, fines poor. Sintered clast boundaries. Clasts are pumiceous, lava-like and non-welded, stratified ignimbrite material.

Clast size decreasing upwards with occasional blocks. Pale cream predominantly pumiceous material with clasts of lava-like material, non-welded ignimbrite material, obsidian bearing ignimbrite and basic (basalt) material. Incipiently welded (slight sintering of clast edges and cohesion of supporting ash matrix. Discontinuous lenses of planar stratified ash and lapilli.

**Figure 4–69**.. Lithofacies description of the basal stratigraphy of Retamares Mb Unit C (log Cii) (vertical scale in metres).

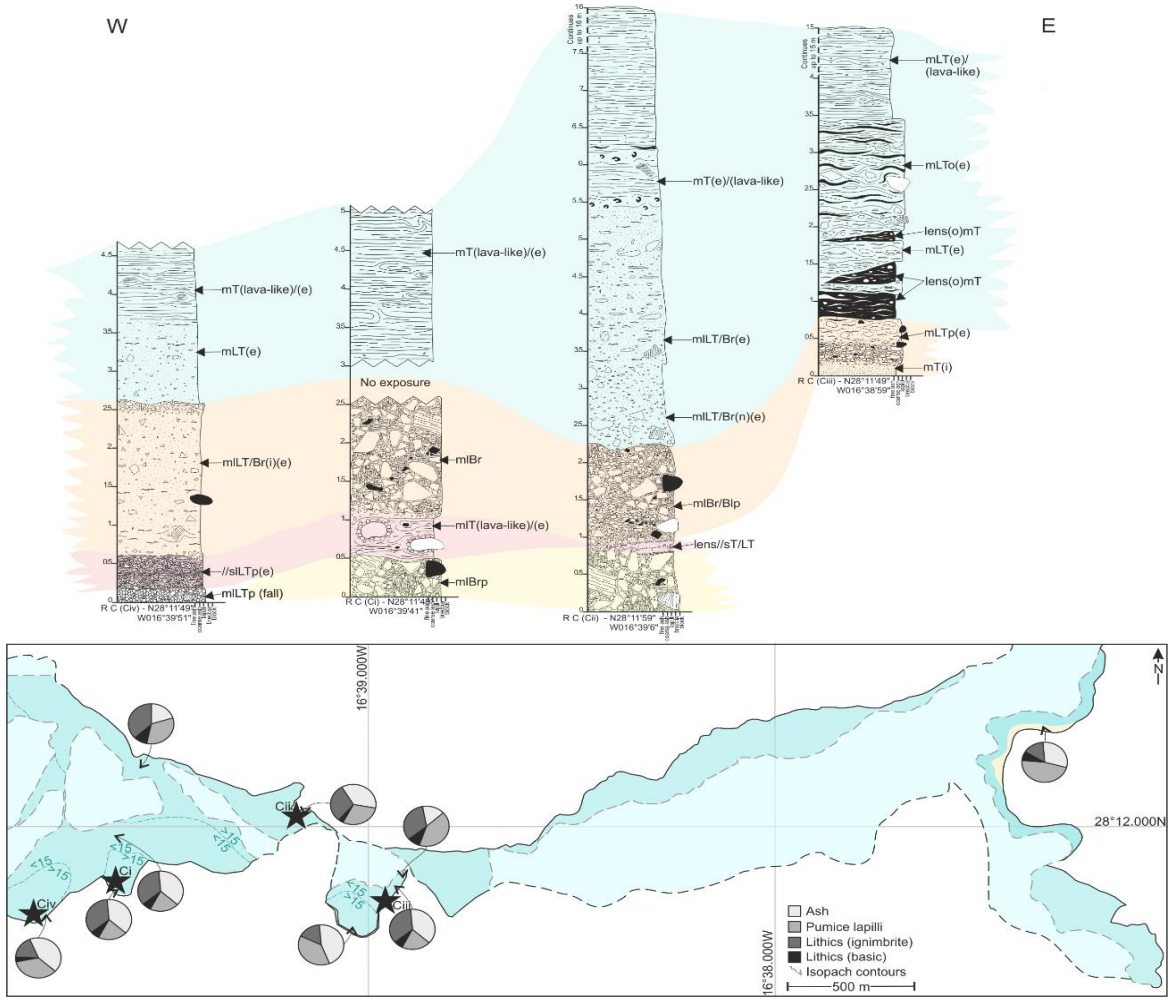


**Figure 4–70.** Correlation of the stratigraphic logs of Retamares Mb Unit C (vertical scale in metres), with the coloured bands showing possible continuation and variability of the lateral facies. Colours used to tie stratigraphy are arbitrary. Isopach map displays both the mapped and expected exposure, displaying the distribution of grain size and lithic components. Black stars show log localities.

### 4.3.4. Retamares Unit D

Extending from the Llano de Ucanca on the central caldera wall (N28°11'58.9" W16°38'19.2"), to Montaña Guajara and Roque de Encaje in the south (Figure 4–71), Unit D consists of a 4 – 12 m thick non-welded, stratified base (Figure 4–72 & 4–75), grading up into a strongly columnar jointed, clast-rich, intensely welded to lava-like lithofacies, which accounts for most of the unit's thickness (15 - 40 m thick) (Figure 4–73 & 4–74). Much of the unit is overlain by the caldera-fed El Pinalito lavas and the Chasna Mb at the Llano de las Mesas locality.

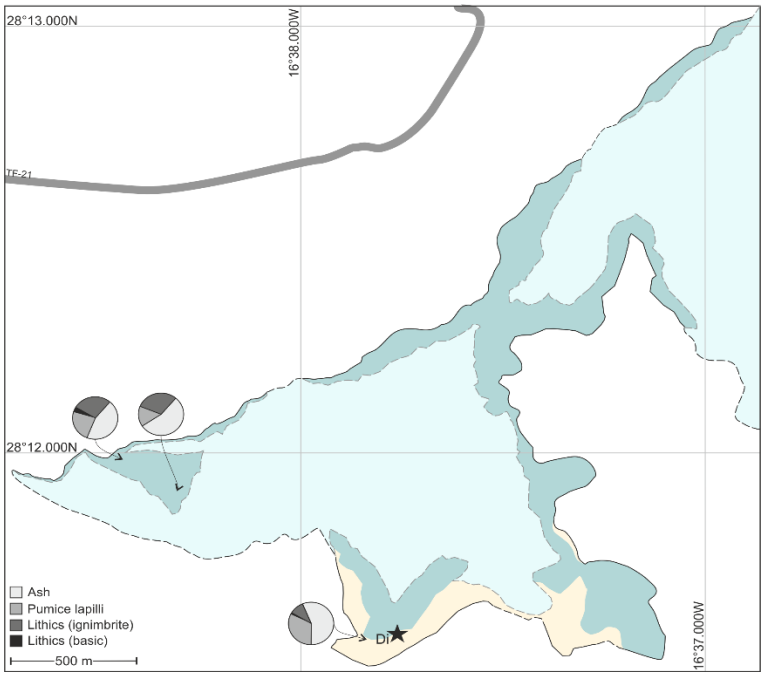


**Figure 4–71.** Retamares Mb Unit D mapped exposure (dark shade) and expected exposure (light shade) map, displaying distribution of grain size and lithic components. Cream colour indicates non-welded stratigraphy.

The lava-like and intensely welded lithofacies is abundant in angular to sub-rounded lithics, which can be stretched and deformed. Lithics are predominantly flow-banded lava-like and pumiceous material, and welding intensity varies (typically decreases) with increasing lithic content (Figure 4–74).


**Figure 4–72.** Field relationships of Retamares Unit D and the Chasna Mb at Llano de las Mesas locality. The unit consists of a thick (>12 m) non-welded basal stratigraphy which grades up into the aphyric, lava-like lithofacies, and is overlain by the Chasna Member. Note the faulting of the unit, displacing the stratified sequence. Log locality of Di is marked by the black star. View looking NE from the Galeria Agua Agria route.


**Figure 4–73.** Loosely columnar jointed, north-west dipping Retamares Unit D 'island' on the central sector of the caldera wall (N28°11'58.9" W16°38'19.2"), protruding from El Pinalito lava cover to the west, south and east.

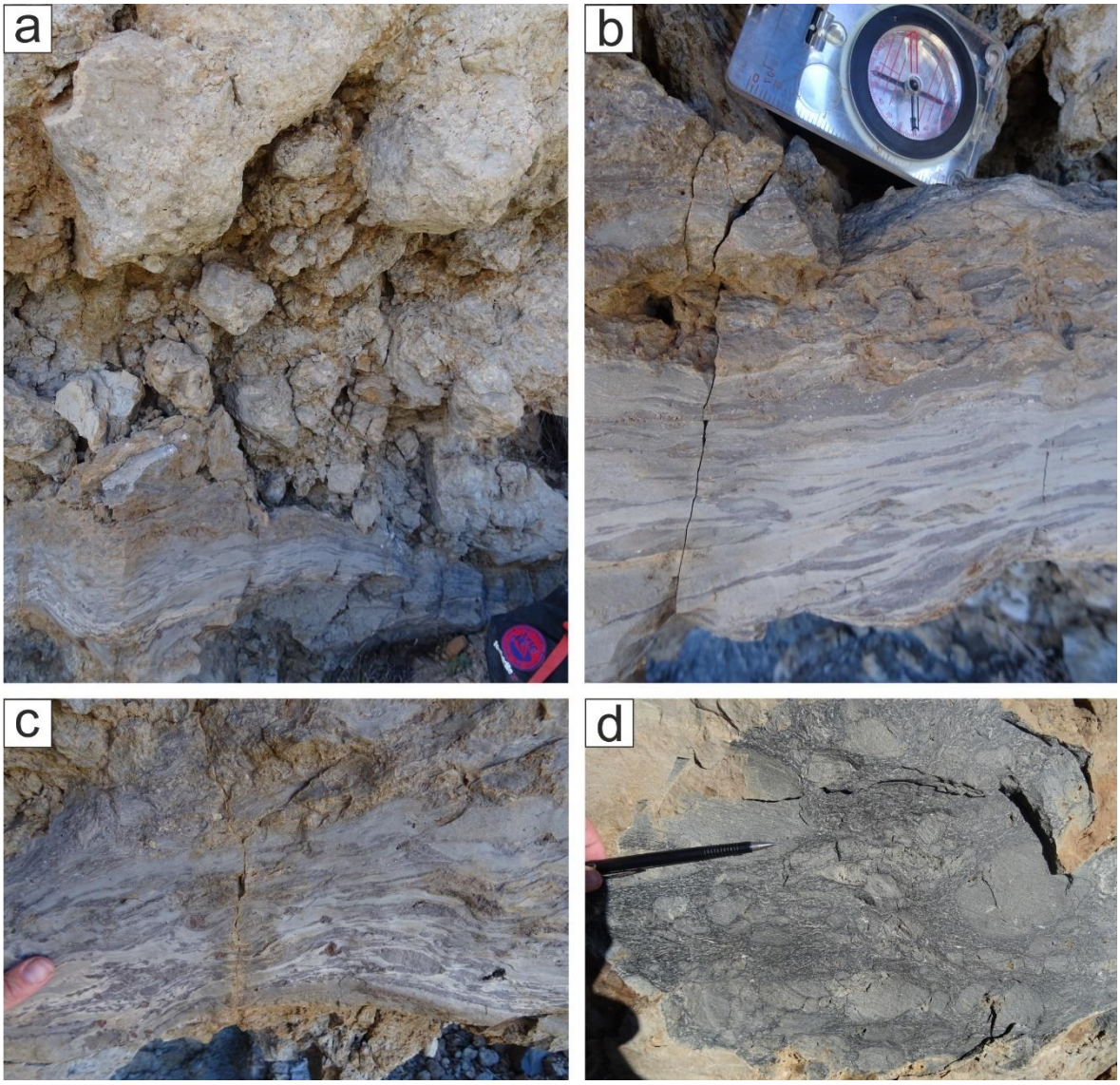


**Figure 4–74.** Features observed within Retamares Mb Unit D at caldera wall locality (N28°11'58.9" W16°38'19.2"): a) A decrease in welding intensity is seen from a flow banded, eutaxitic tuff to a massive breccia. Angular lithic blocks of pumiceous, welded and lava-like material are poorly sorted within the massive, inversely graded breccia. b) A transitional gradation is seen in the close up of the boundary between the flow banded tuff and the breccia. Fiamme are imbricated and boudinaged. C) Imbricate, deformed and boudinaged fiamme within the flow banded facies. The fabric is folded, rotated and wrapped around lithics (ignimbrite and scoria). d) 'Ghost' lithic lapilli and clasts and planar fabrics in the lava-like facies. No vitroclastic textures in between the lithics are visible, with a predominantly aphyric lava-like matrix of the clasts.

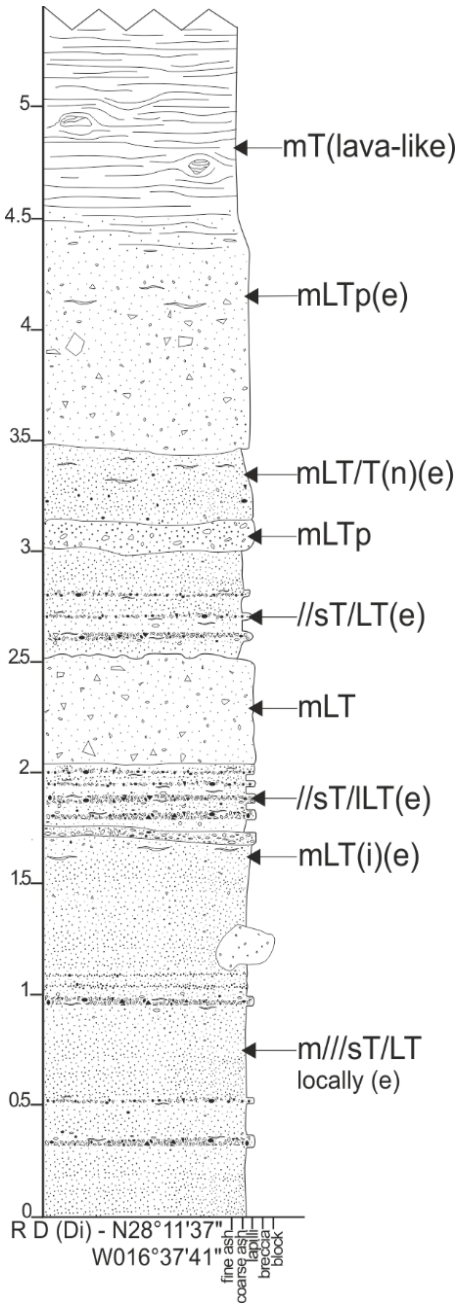


**Lithofacies description**

Clast-rich, crystal-poor, teal and orange banded, predominantly lava-like, locally eutaxitic with a persistent base-parallel fabric with tight isoclinal and open curvilinear folding and rotated fabric around occasional clasts of lava-like material. Lithofacies continues up to~ 18 m.

Pumice-rich partially welded grading up into lava-like lithofacies.

Non-welded at base grading into eutaxitic and distinctly welded facies.
Non-welded, pumice-rich.

Pumice-rich, basic lithic lapilli horizons.

Non-welded with occasional angular clasts of pumiceous and lava-like material. Partially welded with fiamme throughout
Partially welded, dark-brown resistant horizon.

Predominantly pumice-rich, non-welded LT with localised welding (eutaxitic) and coarser, lithic-lapilli rich horizons. Occasional blocks of pumiceous material. Tuff layers exhibit desiccation cracks (below) indicating a period(s) of hiatus between.

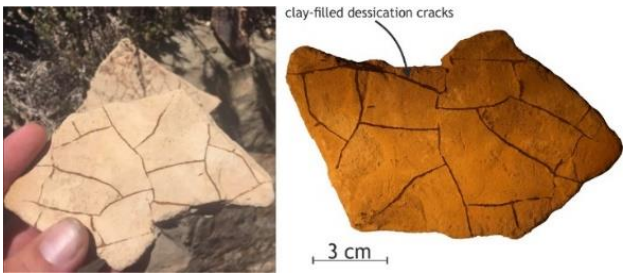


**Figure 4–75.** Lithofacies description of basal stratigraphy of Retamares Mb Unit D (Di) (vertical scale in metres).

### 4.3.5. Retamares Unit E

Unit E underlies much of Montaña Guajara (Guajara Units 1 – 4) (Figure 4–76) and younger Retamares Units (Units F and G) and extends westwards towards Llano de Ucanca on the eastern edge of the caldera wall. Unit E consists of a stratified, pumice-rich, non-welded lithic breccia base of variable thickness, with occasional blocks of lava-like material, which grades up into a predominantly lava-like lithofacies (Figure 4–84).

Much of Unit E is an intensely welded, strongly columnar jointed, lava-like tuff with a planar (horizontal, gently dipping), base-parallel fabric. The non-welded basal stratigraphy, consisting of tuffs, lapilli tuffs and breccias is continuous across the base of the Unit, but varies substantially in thickness and welding intensity, with thickness increasing towards the east (Figure 4–77 & 4–83).


**Figure 4–76.** Retamares Unit E at the base of the Montaña Guajara sequence, underlying the units of the Guajara Member. View looking SE from Galeria Riachuelos.


**Figure 4–77.** Retamares Mb Unit E on Sendero GR131 on Montaña Guajara (N28°12'53" W16°37'07") (log Eii). Strongly columnar jointed, which extends through both the lava-like lithofacies and the less welded (lighter coloured) basal stratigraphy.

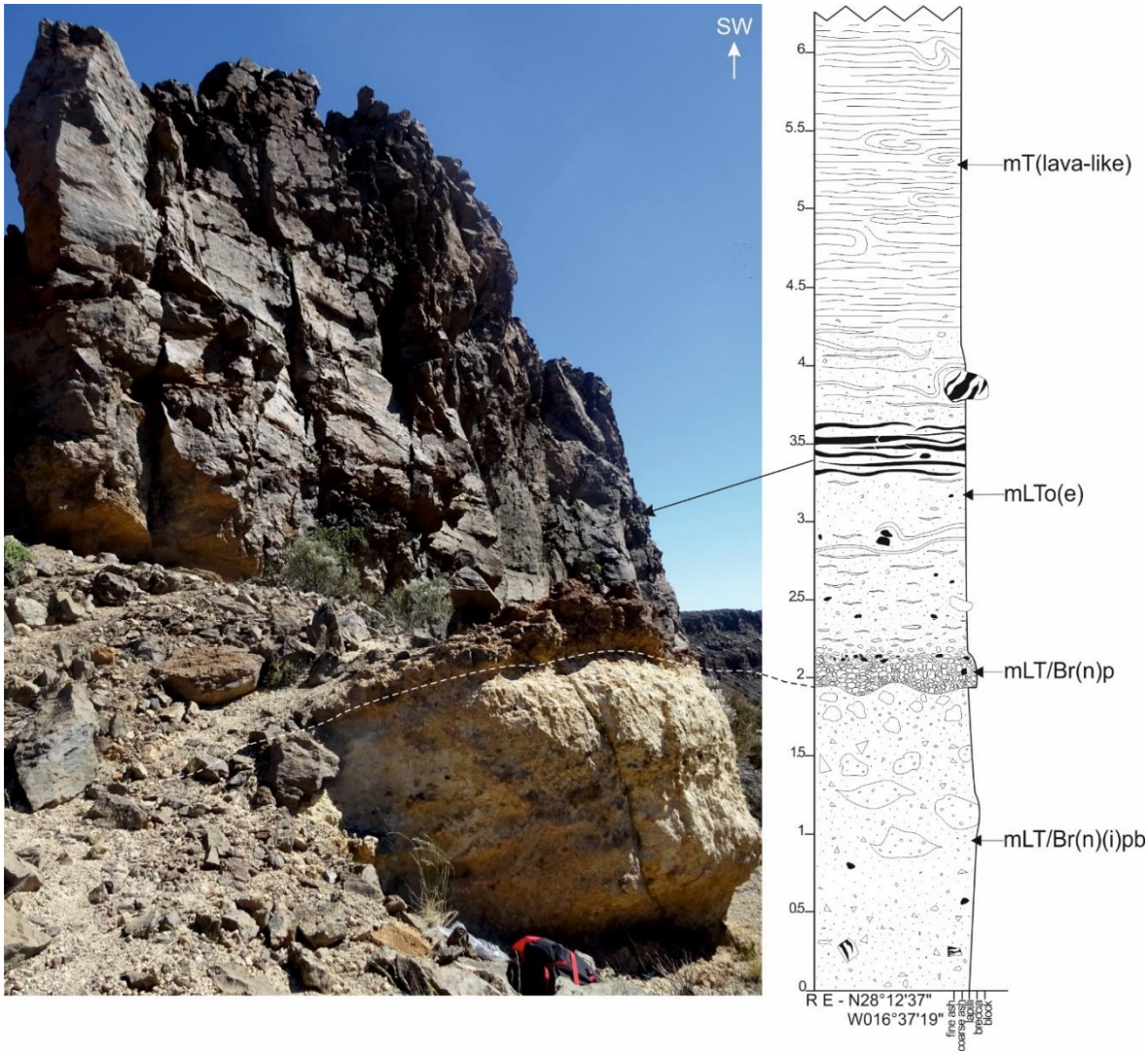


**Figure 4–78.** Basal stratigraphy of Retamares Mb Unit E (log Ei) (vertical scale in metres).

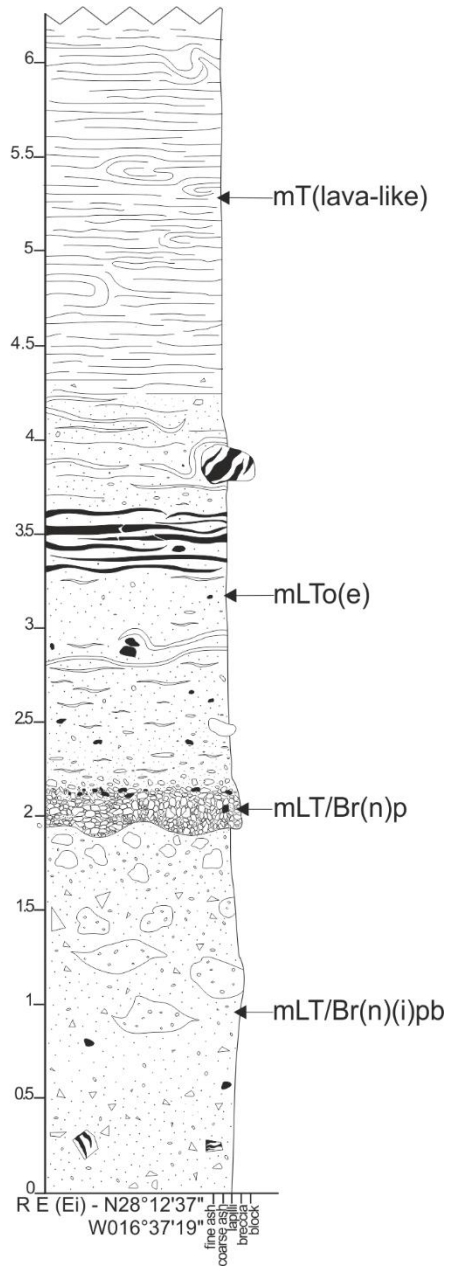


| Lithofacies description |
|---|
| Clast-rich, crystal-poor, predominantly lava-like, locally eutaxitic with a persistent base-parallel fabric with tight isoclinal and open curvilinear folding and rotated fabric around occasional clasts of lava-like material. |
| Blocks of obsidian rich (likely Retamares Mb).<br><br>Fabric - 120 28° SE. |
| Welded and strongly welded obsidian fiamme, forming entire horizons. |
| Fiamme gradually becoming glassier/ obsidian rich. |
| Greenish blue (chlorite) alteration<br>Partially welded, sintered clast edges and slight elongation becoming progressively flatter. |
| Pumice-rich, clast supported breccia with occasional lava-like and basic material and localised fiamme.<br>Ash matrix-supported breccia with bombs with lobate, fluidal edges, greenish blue (chlorite) alteration, localised fiamme and clasts of pumice, lava-like, obsidian-rich (Retamares Mb) and basic material. |

**Figure 4–79**. Lithofacies description of the basal stratigraphy of Retamares Mb Unit E (log Ei) (vertical scale in metres).

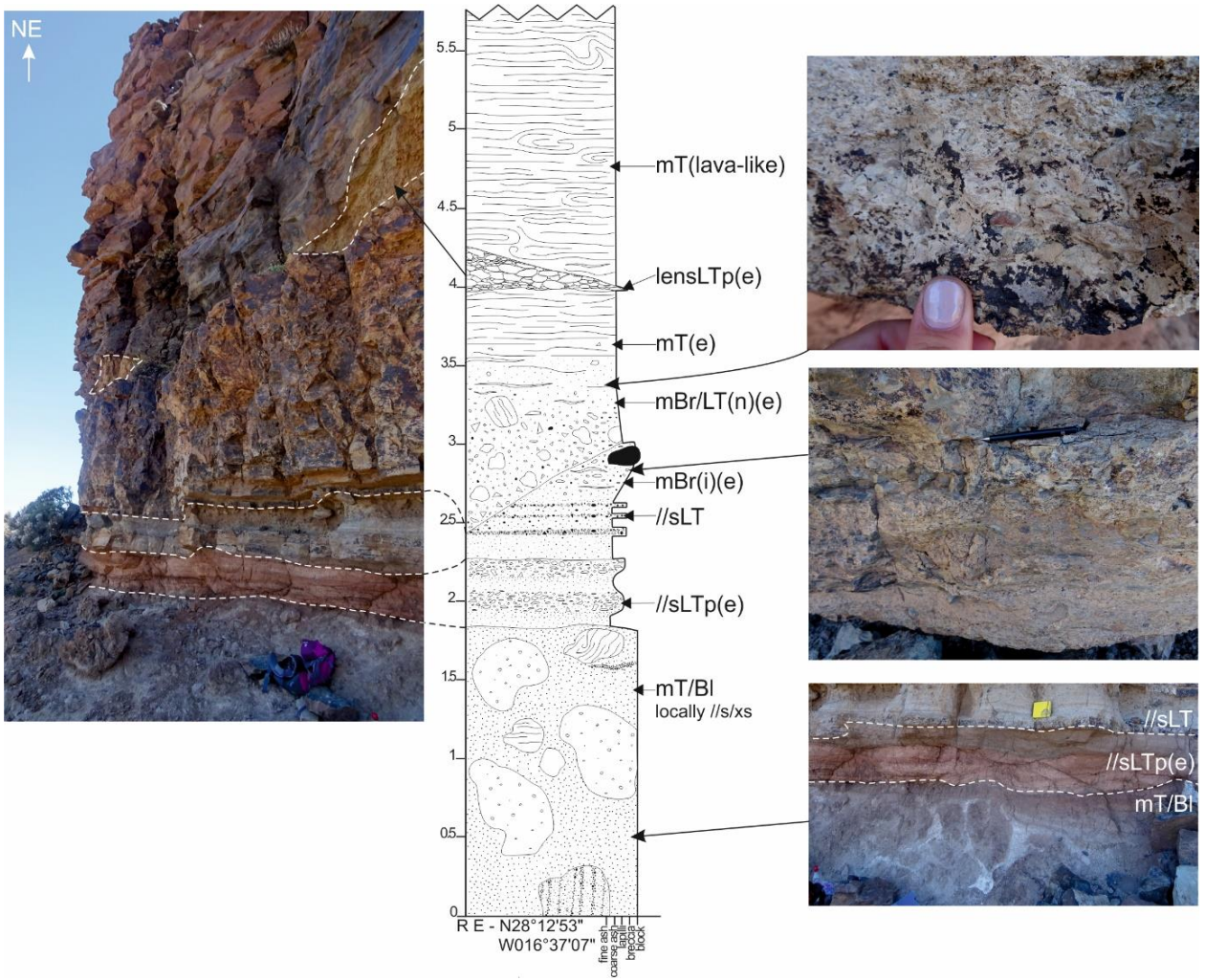


**Figure 4–80:** Basal stratigraphy of Retamares Mb Unit E (log Eii) (vertical scale in metres).

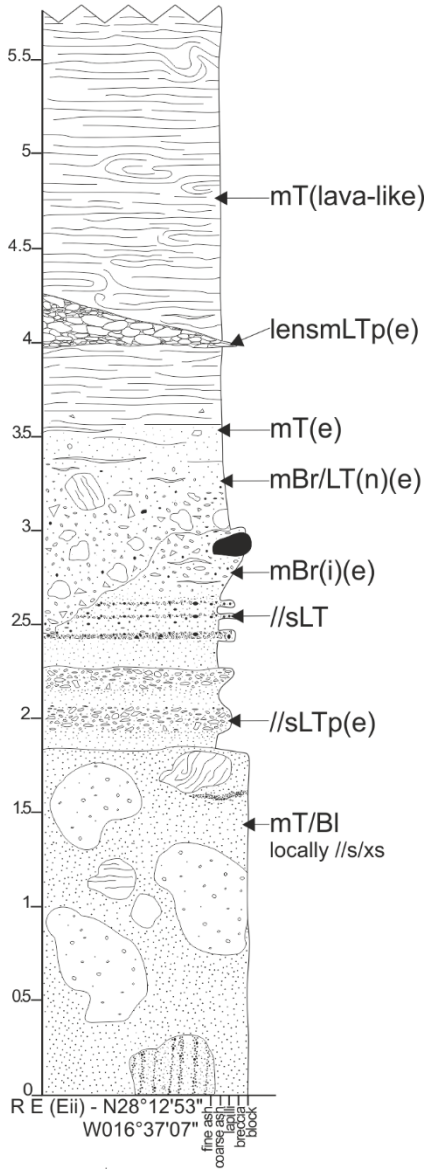


**Lithofacies description**

Lava-like lithofacies continues up to 10.25 m.

Clast-poor, crystal-poor, predominantly lava-like, locally eutaxitic with a persistent base-parallel fabric with tight isoclinal and open curvilinear folding and rotated fabric around occasional clasts of lava-like material.

Tapers out laterally to the west. Non-welded but slight sintered clast edges.

Welding increasing upwards, lapilli matrix-supported clasts of lava-like and pumiceous material. Clasts up to 55 cm across.

Ash matrix-supported breccia which thins out 220 m to the east.

Pumice-rich, reddish pink (possible paleosol). Partially welded pumice clasts.

Fine ash matrix-supported with blocks of lobate, fluidal pumiceous material, basic (scoriaceous) and altered lava-like material. Blocks up to 4 m across, predominantly sub-rounded.

**Figure 4–81.** Lithofacies description of the basal stratigraphy of Retamares Mb Unit E (log Eii) (vertical scale in metres).

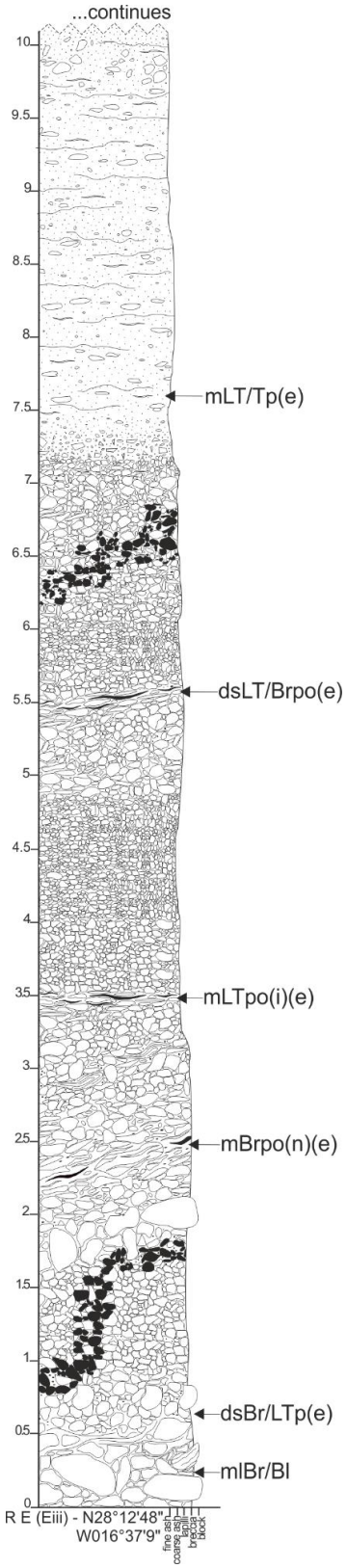


**Lithofacies description**

…continues overleaf.

Greenish blue, welding increases upwards. Very fine-grained green ash matrix. Flattened and deformed pumice, clast boundaries becoming sintered and undistinguishable. Very few lithics.

Weakly (compositionally) stratified. Pumice lapilli stratified by colour (black, grey and reddish orange). Predominantly non-welded.

Predominantly non-welded with localised deformed discontinuous horizons. Fines upwards and very poorly sorted.

Deformed fiamme, obsidian streaked horizon, stretched and discontinuous
Pumice lapilli matrix supported, imbrication (alignment of clasts).

Predominantly non-welded although there are horizons of stretched and elongated pumice and fiamme.

Loosely diffusely stratified (compositionally stratified). Clasts are predominantly pumice, welded and lava-like material, obsidian-bearing clasts, with three colours of pumice (brown, cream, green and reddish orange). Spatter-like fluidal pumice morphologies.

Eutaxitic, mildly welded with clast boundaries visible and vesicularity maintained.

Non-welded basal breccia. Blocks of pumice and welded and lava-like material.

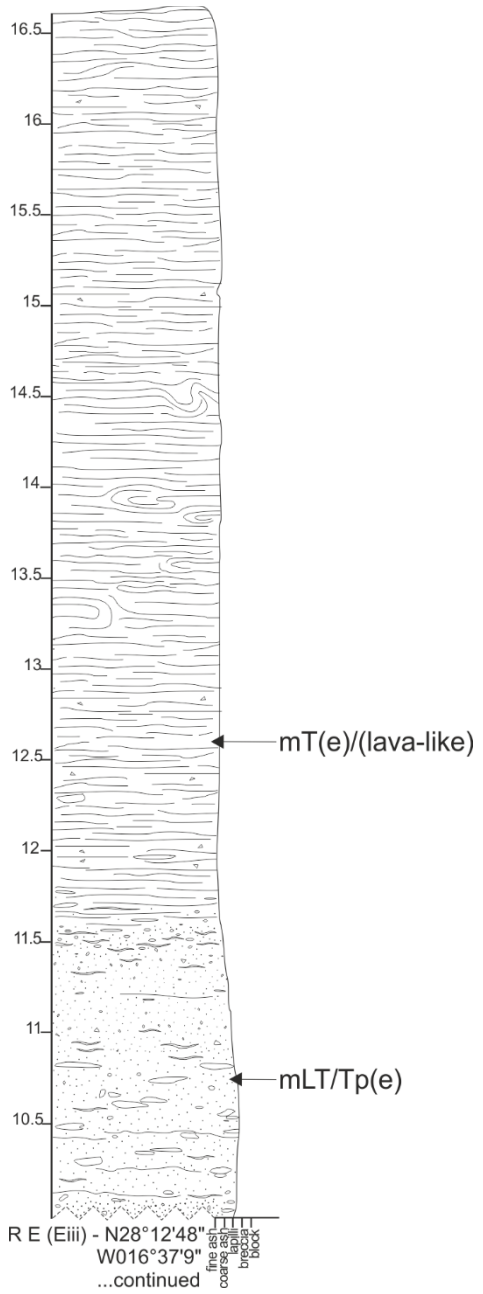


Clast-poor, crystal-poor orange lava-like lithofacies with a persistent, base-parallel fabric with tight isoclinal folds, exhibiting columnar jointing.

Decrease in lithics, increase in welding, pumice clasts and lapilli boundaries no longer visible.

Greenish ash matrix, eutaxitic with stretched and elongated pumice.

RE (Eiii) continued…
Welding continues to increase vertically, with a progressive loss of visible pyroclast boundaries, fewer lithic lapilli (and deformed pumice and fiamme).

**Figure 4–82**. Lithofacies description of the basal stratigraphy of Retamares Mb Unit E (log Eiii) (vertical scale in metres).

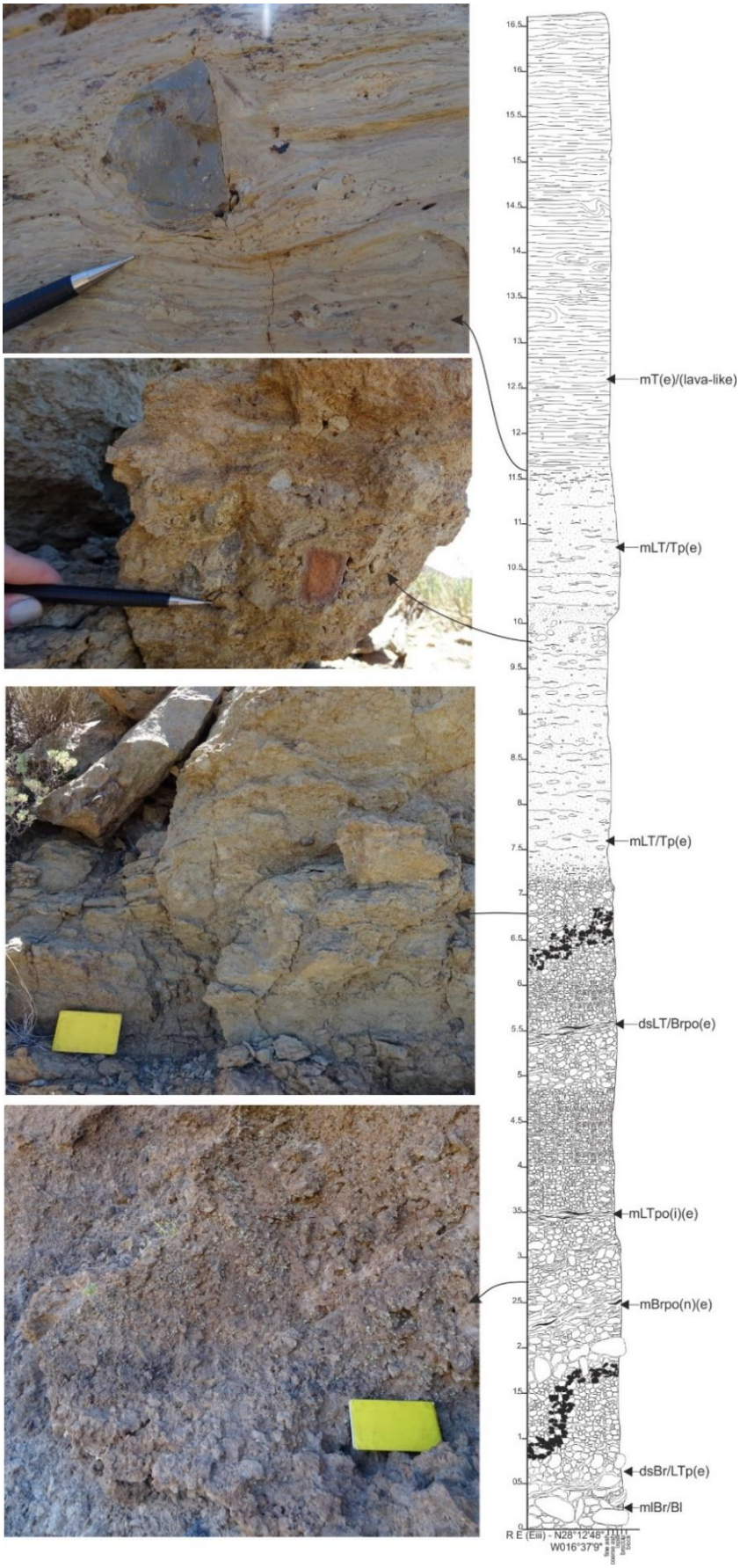


**Figure 4–83.** Lithofacies of the basal stratigraphy of Retamares Mb Unit E (log Eiii) (N28°12'48" W16°37'09") (vertical scale in metres).

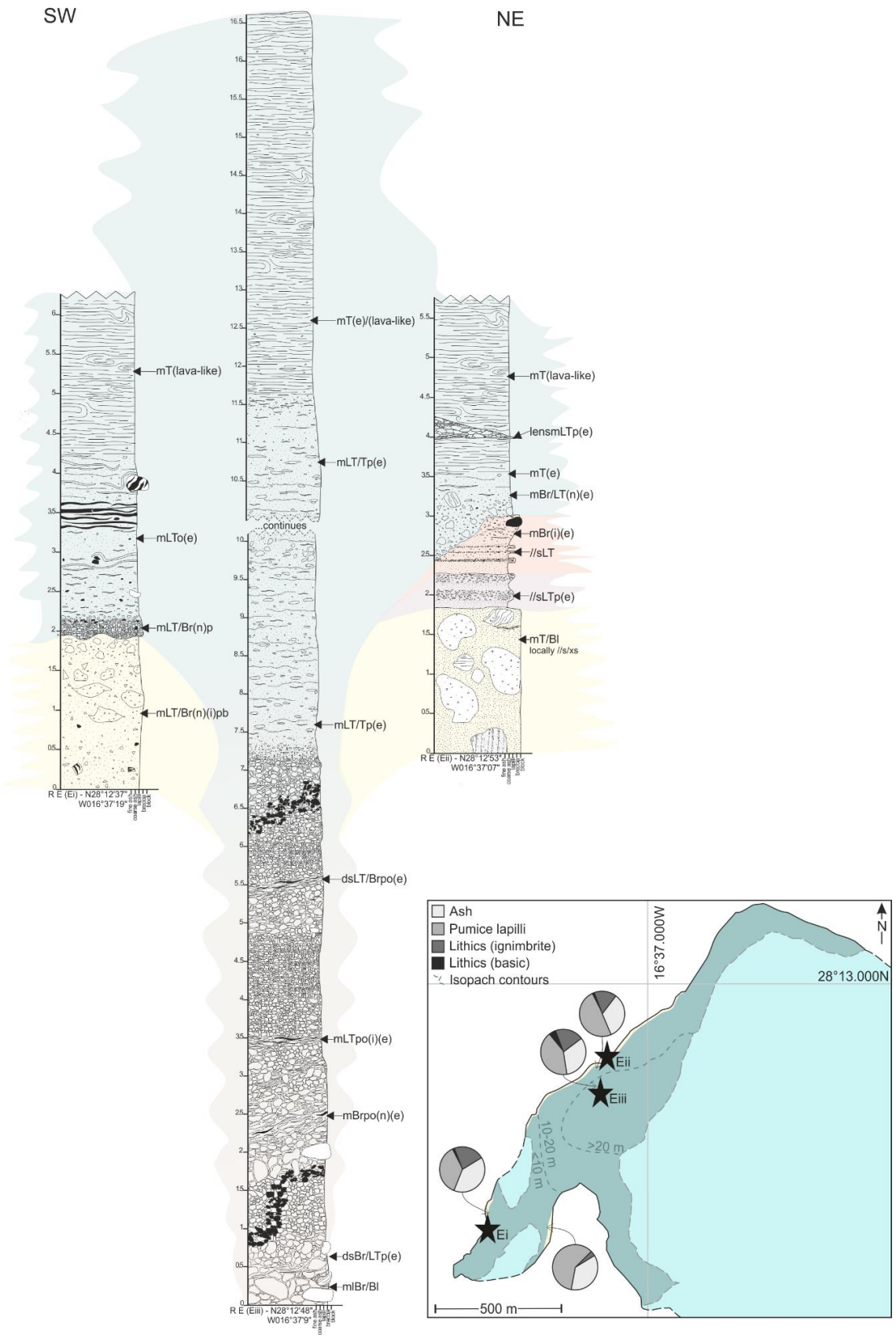


**Figure 4–84.** Correlation of the stratigraphic logs of Retamares Mb Unit E (vertical scale in metres), with the coloured bands showing possible continuation and variability of the lateral facies. Colours used to tie stratigraphy are arbitrary. Isopach map displays both the mapped (dark shade) and expected exposure (light shade), displaying the distribution of grain size and lithic components. Black stars show log localities.

### 4.3.6. Retamares Units F and G

Retamares Units F and G both overlie Unit E on the caldera wall in between Montaña Guajara and Llano de Ucanca (N28 12'26" W16 37'18") (Figure 4–85) and consist of small-scale, thin (<10 m) welded and lava-like units with a stratified, non-welded basal stratigraphy of variable thickness (5-12 m), consisting of planar and cross stratified tuffs and lapilli tuffs, with discontinuous lenses of pumice breccia. Unit F dips to the south east, and Unit G to the south has a north westerly dip, with an approximate thickness of 4.5 m (Figure 4–86). Unlike the other units of the Retamares Mb, they do not cover much distance laterally, nor are they seen at other localities overlying Unit E.

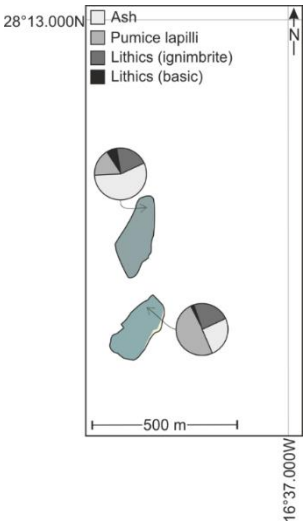


**Figure 4–85.** Retamares Mb Units F and G mapped exposure map, displaying distribution of grain size and lithic components.


**Figure 4–86.** Retamares Mb Unit F and Unit G overlying Unit E, west of Montaña Guajara.

### 4.3.7. Interpretation

The units of the Retamares Member are interpreted as the deposits of a series of highly unstable, topographically controlled pyroclastic density currents. The non-welded facies, and those exhibiting lower degrees of welding provide insights into the depositional structures, displaying a range of erosional surfaces, and lithofacies exhibiting grading (normal and reverse) and stratification (diffuse, cross, planar), with lithofacies often grading in to one another, suggesting highly variable and dynamic switching between FBZ conditions. Much of this insight is obscured and lost with the progressive increase in welding exhibited by the majority of the units.

As described in the stratigraphic profiles, these units display both vertical and lateral variation in thickness and oscillations in the intensity of welding, exhibiting far more variability and typically lesser degrees of welding intensities than the underlying Atravesado units. This variability in welding intensity is interpreted as the result of a combination of: i) variable deposit thickness, with units thinning over topographic highs and pooling of the deposits in valleys and downslope, both affecting the deposit's ability to retain heat following deposition; ii) temperature instability of the progressively aggrading current, which may be a factor of the column height; iii) variable lithic input, with lesser degrees of welding intensity associated with lithic-rich facies, which also may contribute to unstable emplacement temperatures.

## 4.4. Chasna Member

The Chasna Mb consists of three self-contained units across the southern central caldera wall, seen at three localities (from west to east): i) the Roque los Almendros; ii) the Sombrero de Chasna; and iii) the Llano de las Mesas.

The Chasna Mb overlies units (Units B, C and D) of the Retamares Member and shares common characteristics and lithofacies (Figure 4–101). Each is reddish orange in colour, proximal to the caldera wall boundary, distinctly columnar jointed, and rich in crystals, clusters of broken and rotated crystals and crystal-rich globules (enclaves).

### 4.4.1. Chasna Mb: Roque los Almendros locality

The Chasna Mb at this locality overlies Retamares Unit C on the south western edge of the caldera wall at Montaña Roque los Almendros (Figure 4–87) (N28°12'0.2" W16°39'34"). A thick (approximately ~ 22 m) discontinuous, non-welded to eutaxitic highly stratified ignimbrite forms the base of the Chasna Mb at the south and south-eastern face of Roque los Almendros (Figure 4–90 - 4–95), which grades up into a distinctly lava-like lithofacies, rich in crystals and globules (Figure 4–94).

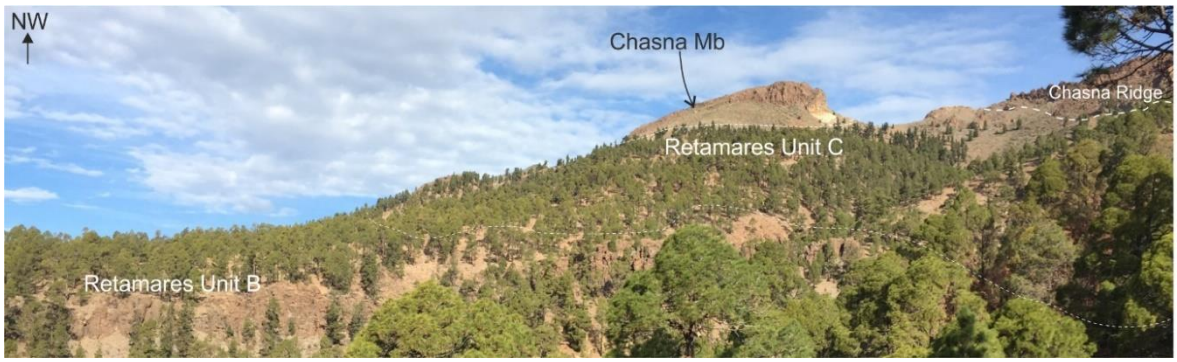


**Figure 4–87.** Field relationships of the Chasna Mb at Roque los Almendros locality, overlying Retamares Unit C (N28°12'0.2" W16°39'34").


**Figure 4–88.** Orange, columnar jointed Chasna Mb at Roque los Almendros, with the stratified non-welded basal stratigraphy.


**Figure 4–89.** Chasna Mb of Roque los Almendros locality showing field relationships in the caldera wall stratigraphy, with the lower Retamares Mb and the younger Almendros Mb**.**

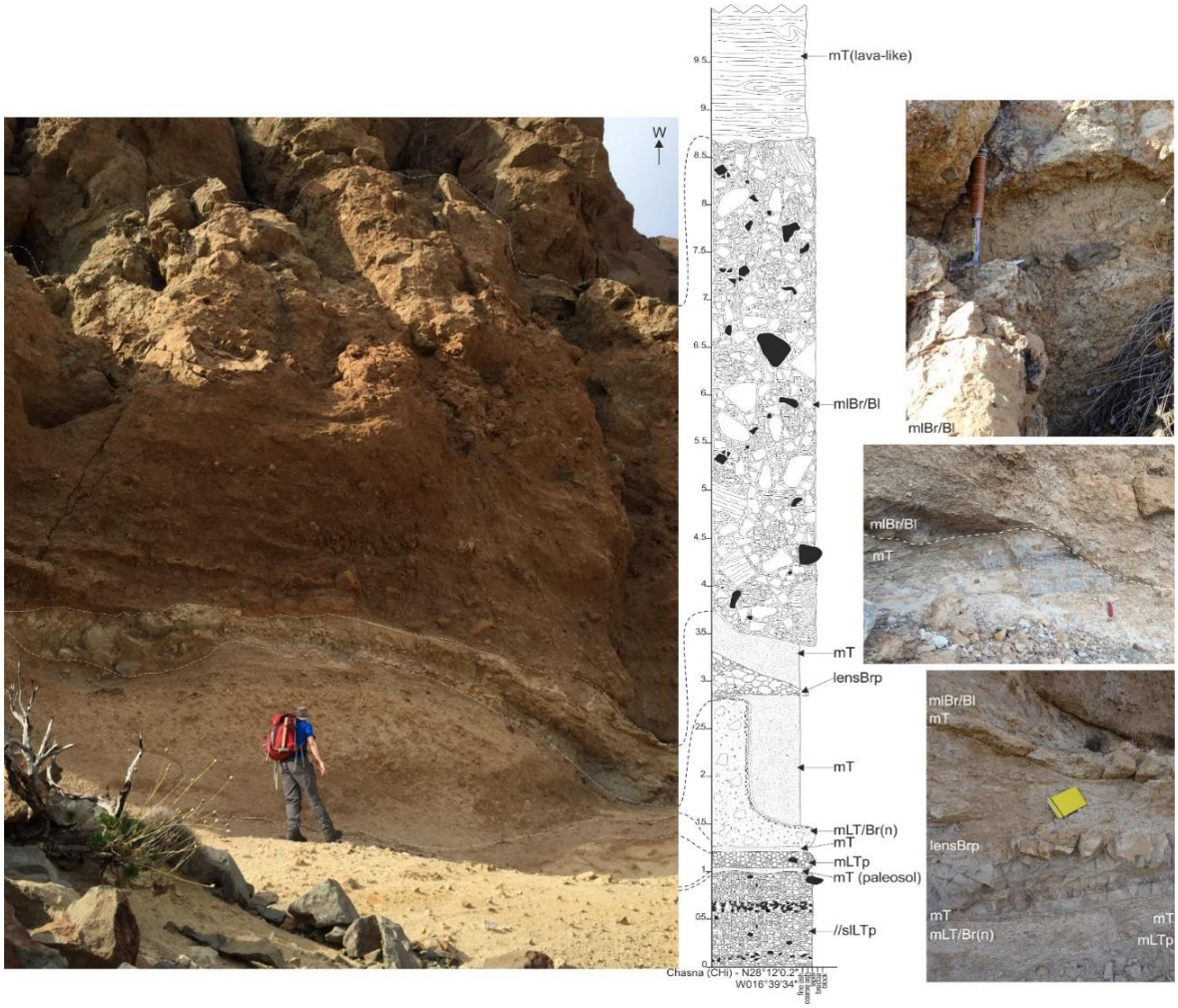


**Figure 4–90.** Basal stratigraphy of Chasna Mb at Roque los Almendros locality (log Chi) (vertical scale in metres).

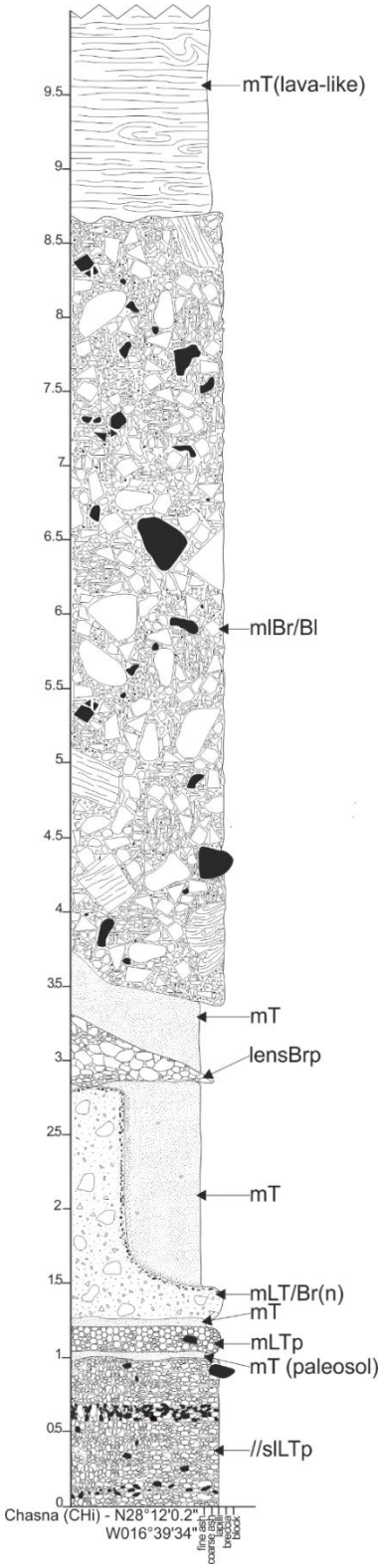


**Lithofacies description**

Crystal-rich, clast-rich, orange massive lava-like lithofacies with a persistent base-parallel fabric, with tight isoclinal folds. Columnar jointed.
Breccia does not show a gradual increase in welding, but immediately transitions in to the lava-like lithofacies. The contact is not obvious, nor is there evidence of erosion or autobrecciation of the material.

Massive, non-welded, reddish brown, clast-supported, very poorly sorted breccia (collapse/debris) with clasts of up to 2.08 m of obsidian-bearing material, pumiceous, lava-like, lapilli tuff and basic material. Lithic lapilli, breccia and blocks are very angular to angular, with minor sub-rounded pumice lapilli in the matrix. Matrix supported with minor pockets of tuff.

Light grey, very fine tuff/mudstone
Discontinuous pumice-rich, clast-supported lens, tapers out to the east.

Light grey, very fine tuff/ siltstone
Steep-sided, non-erosional contact (likely possible paleo-valley/depression fill)
Light grey, very fine tuff/mudstone.
Massive with no internal structure.
Pumice-rich, clast supported, poorly sorted lens, which tapers out to the north west.
Pinkish red alteration (possible paleosol) with occasional orange-coated pumice lapilli.
Pumice-rich, clast supported lithic lapilli tuff with blocks of obsidian. Lithic lapilli are compositionally stratified, with alternating bands of pumice-rich and basic-rich material, with minor ash.

**Figure 4–91.** Lithofacies description of basal stratigraphy of the Chasna Mb at Roque los Almendros locality (log CHi) (vertical scale in metres).

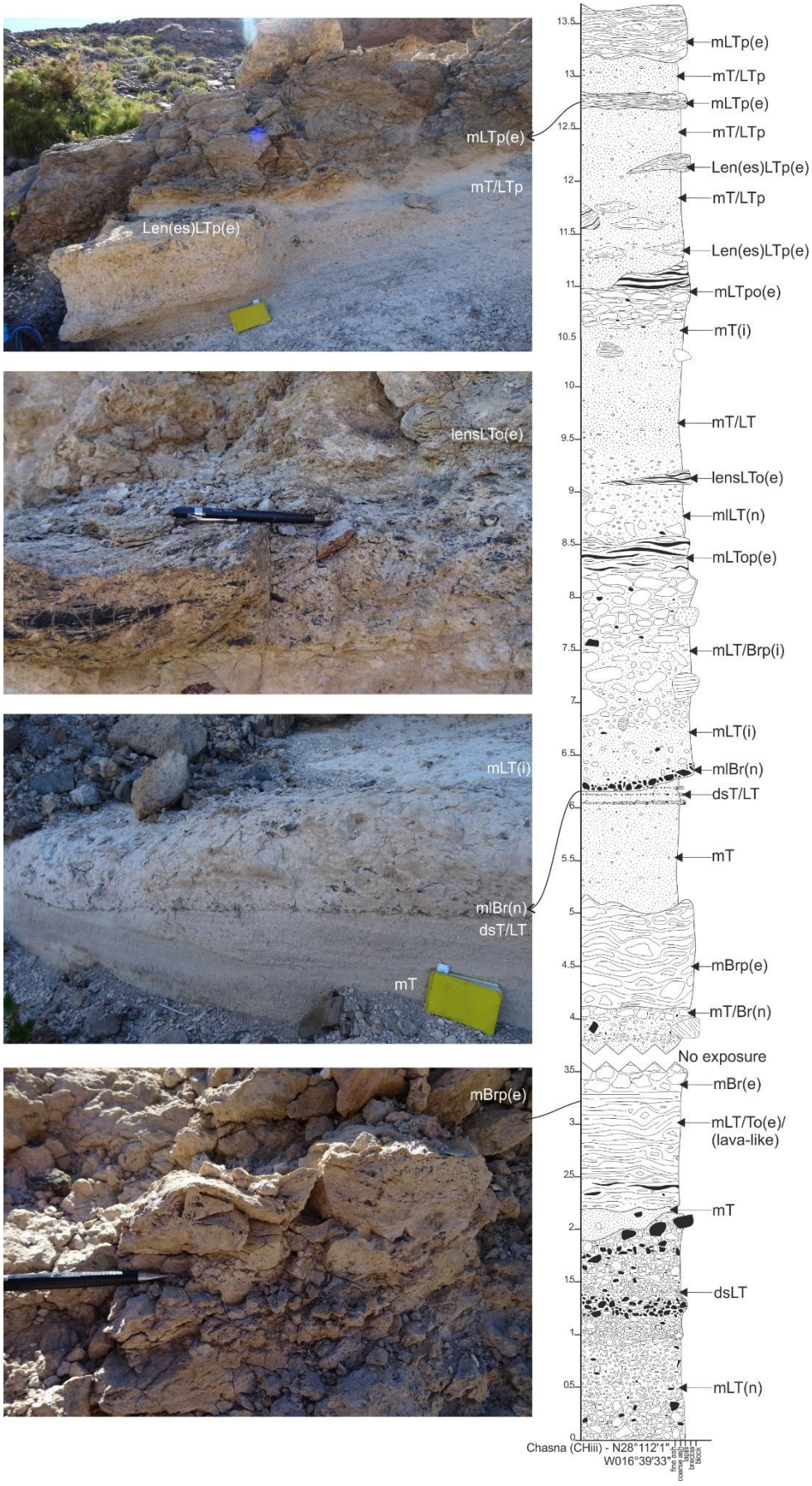


**Figure 4–92.** Lithofacies of the basal stratigraphy of the Chasna Mb at Roque los Almendros locality (log CHii) (vertical scale in metres).

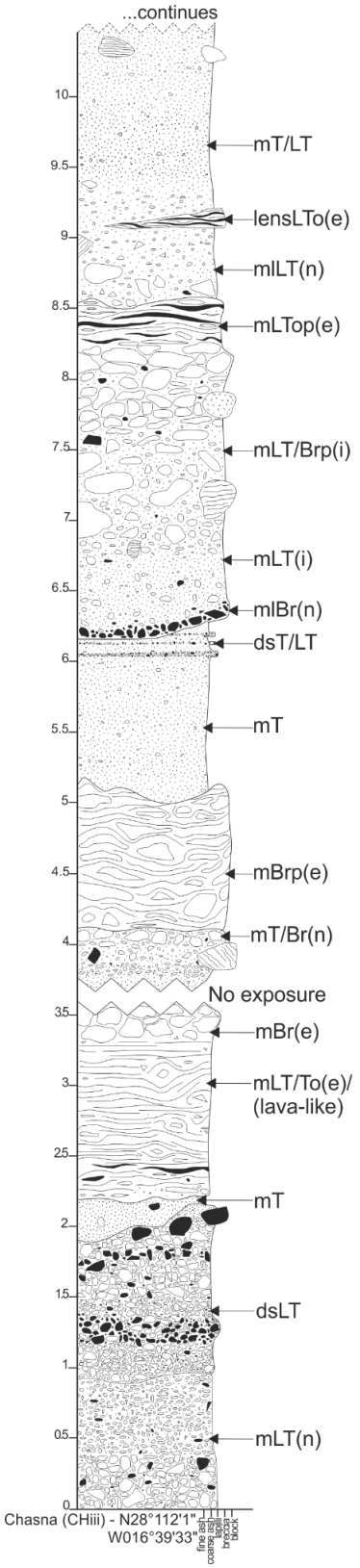


**Lithofacies description**

Non-welded, ash matrix supported, clasts are 95% pumiceous material, 5% obsidian bearing material.

Obsidian streaked horizon stretched and deformed spatter-like pumice clasts. Clasts are subangular, 90% pumiceous material, 5% lava-like material, 5% obsidian bearing material. Non-welded however pumiceous clast edged appear fluidal. Ash-matrix supported, becoming clast supported towards top of unit.

Highly erosional contact. Non-welded, clasts purely lava-like material
White grey, predominantly coarse ash with occasional pumice lapilli.

Welded pumiceous, clast-supported breccia, brown-grey. Pumice clasts are fluidal (spatter-bombs), welded edge.

Fabric - 180 24°.

Clasts are 90% pumiceous material, 5% obsidian bearing material and 5% basic material. Poorly sorted, ash matrix-supported.

Blue, flow banded with fabric folded and rotated around clasts, with streaky obsidian lenses (stretched and deformed pumice). Clasts are pumiceous and lava-like material. Non-welded, white ash horizon.

Compositionally stratified, horizons of imbricated basic material, very poorly sorted. Fabric - 182 24°.
Clasts very poorly sorted, predominantly pumiceous, lava-like and basic material.

**Figure 4–93.** Lithofacies description of the basal stratigraphy of Chasna Mb at the Roque los Almendros locality (log CHiii) (vertical scale in metres).

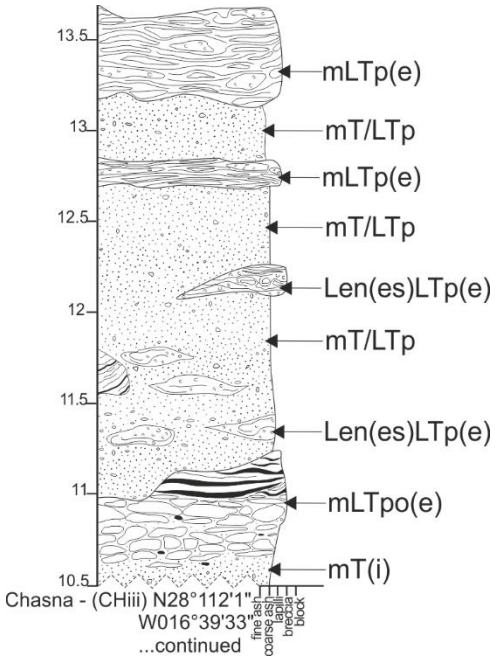


| Lithofacies description |
|---|
| Lenses of brown, spatter-like pumiceous material, with highly fluidal edges. Clast supported. |
| Discontinuous lenses of brown spatter-like pumiceous material, highly fluidal edges. |
| Brown, spatter-like material streaked with obsidian and stretched, deformed fiamme. |
| Pumice clast edges appear fluidal and spatter-like bombs. |

**Figure 4-93.** continued… (vertical scale in metres).

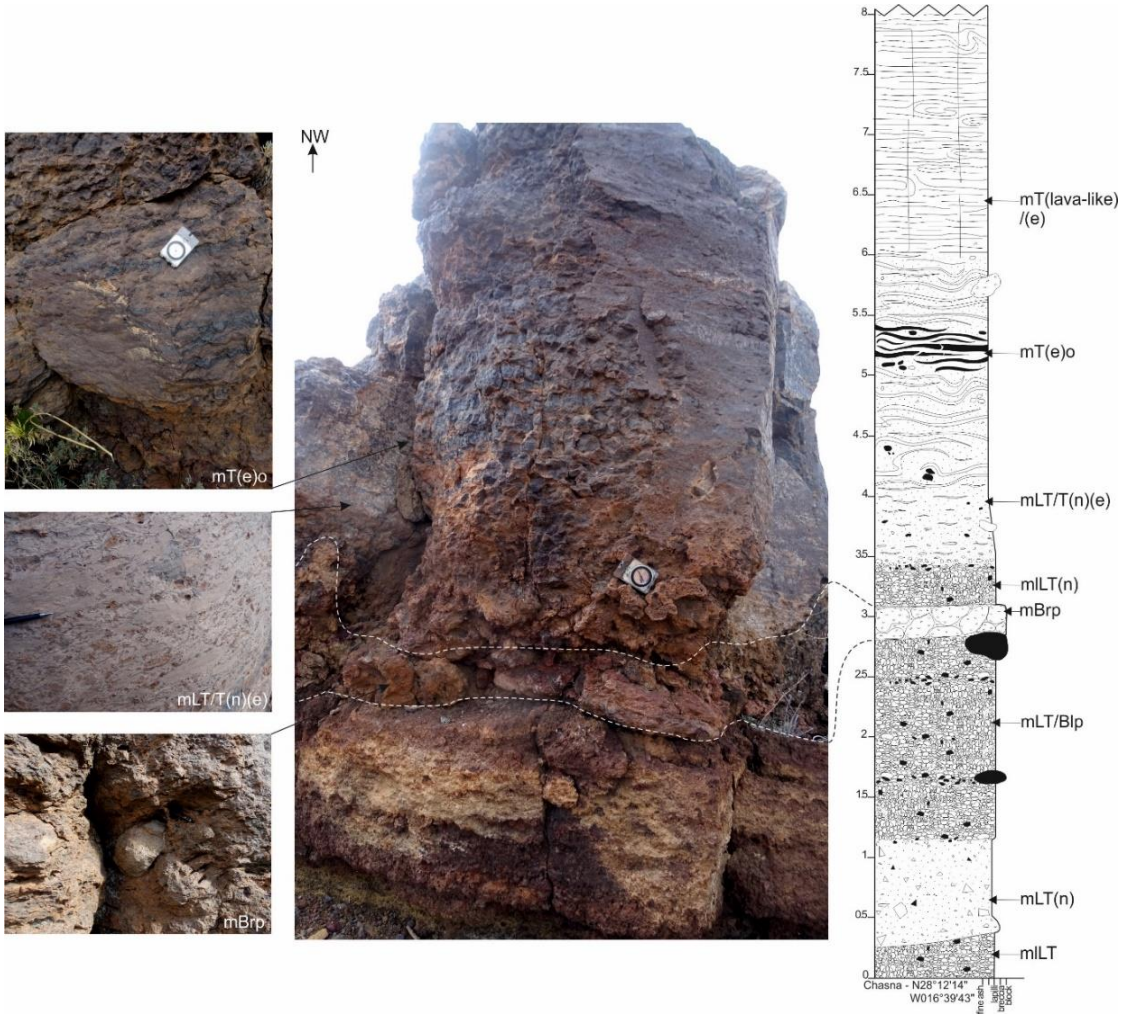


**Figure 4–94.** Lithofacies of the basal stratigraphy of the Chasna Mb at Roque los Almendros locality (log CHiv) (vertical scale in metres).

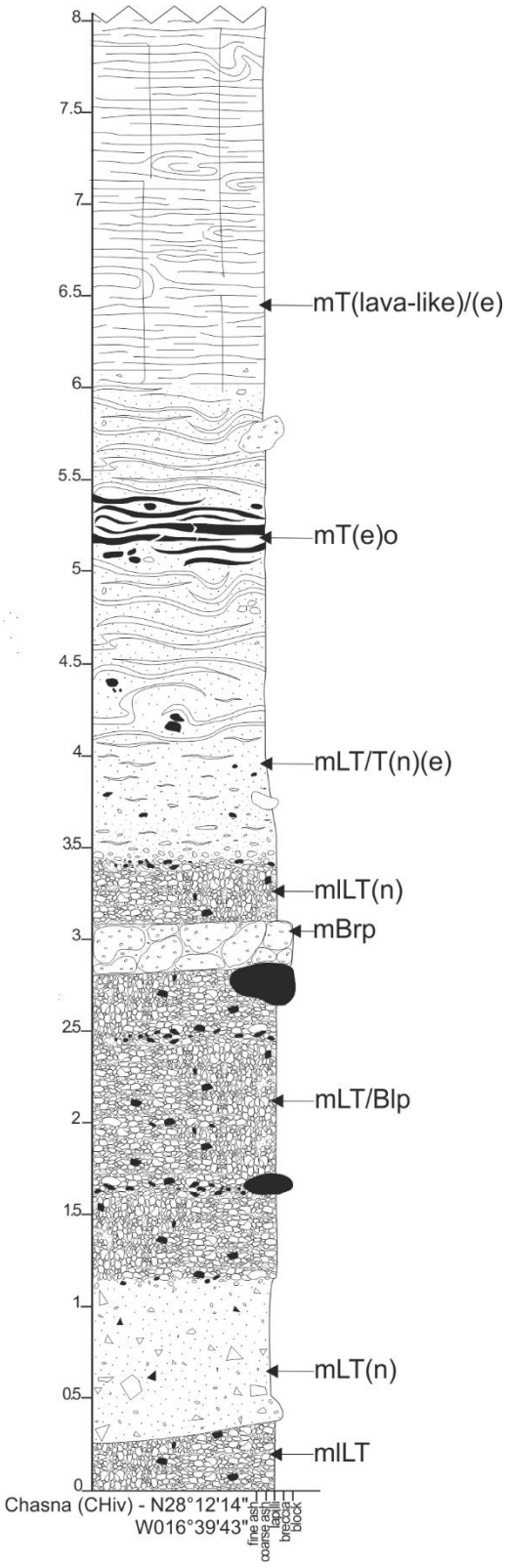


| Lithofacies description |
|---|
| Crystal-rich, clast poor predominantly lava-like, locally eutaxitic with a persistent base-parallel fabric with folds (tight isoclinal, closed curvilinear and buckle folds) and fabric rotated around crystals and occasional clasts. Strongly columnar jointed (87°). Fabric - 180 11° S. |
| Banded teal and orange, crystal-rich, strongly welded tuff with abundant fiamme (streaks) and blocks of pumiceous material. Obsidian-rich horizon (glassy fiamme) which extends throughout sequence. Fabric - 140 12° S. |
| Gradational increase in welding profile upwards with increasing fiamme Weakly welded (sintered boundaries) pumice-rich, clast supported lithic lapilli tuff. |
| Pink, pumice-rich, clast supported uniform breccia horizon. |
| Pumice-rich (pink with yellow alteration haloes around individual lapilli), clast supported lapilli tuff with horizons of imbricated basic lithic. |
| lapilli and blocks of basic material and obsidian up to 0.75 m across. |
| Ash matrix-supported, pumice rich with occasional lava-like and basic material lithic lapilli. |
| Pumice-rich, clast-supported with lithic lapilli of pumiceous, tuff (autoclasts) and basic material. |

**Figure 4–95.** Lithofacies description of the basal stratigraphy of the Chasna Mb at Roque los Almendros locality (log CHv) (vertical scale in metres).

### 4.4.2. Chasna Mb: Sombrero de Chasna locality

The Chasna Mb at the 'Sombrero de Chasna' locality forms a tear-shaped exposure which thickens downslope, overlying Unit B of the Retamares Member (Figure 4–96 & 4–97). The Chasna Mb here is intensely welded and lava-like from base to top, with a distinct lack of vitroclastic textures for the majority of the unit's thickness. At the base of the deposits, a strongly welded lithic block breccia grades up in to a clast-poor, crystal-rich lava-like tuff, which extends to the upper surfaces (Figure 4–98 & 4–99).

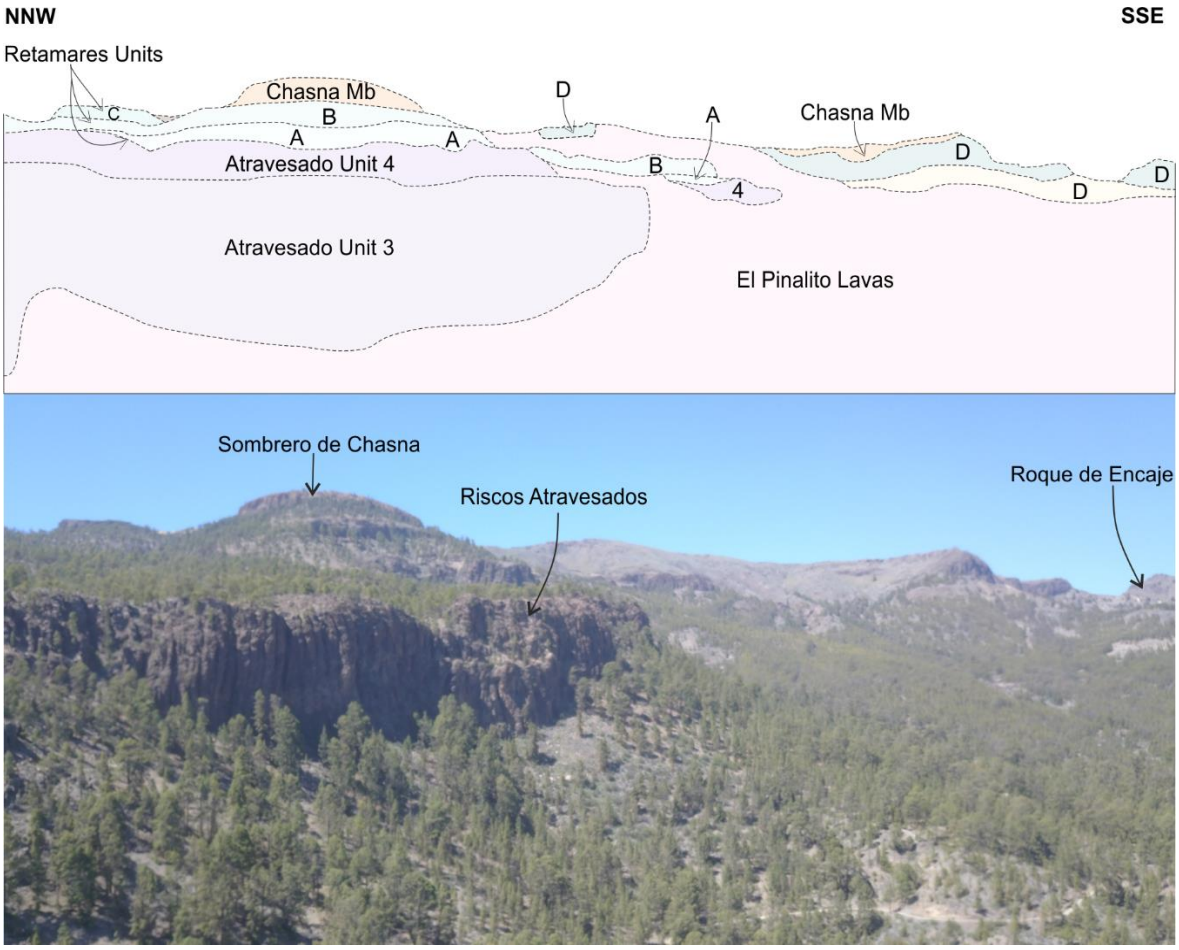


**Figure 4–96.** Field relationships of the Chasna Mb at the Sombrero de Chasna and Llano de las Mesas localities as seen in the landscape from Vilaflor.


**Figure 4–97.** Field relationships of the Chasna Mb at Sombrero de Chasna locality, overlying Retamares Mb Unit B and bound on the eastern side by the El Pinalito lavas.

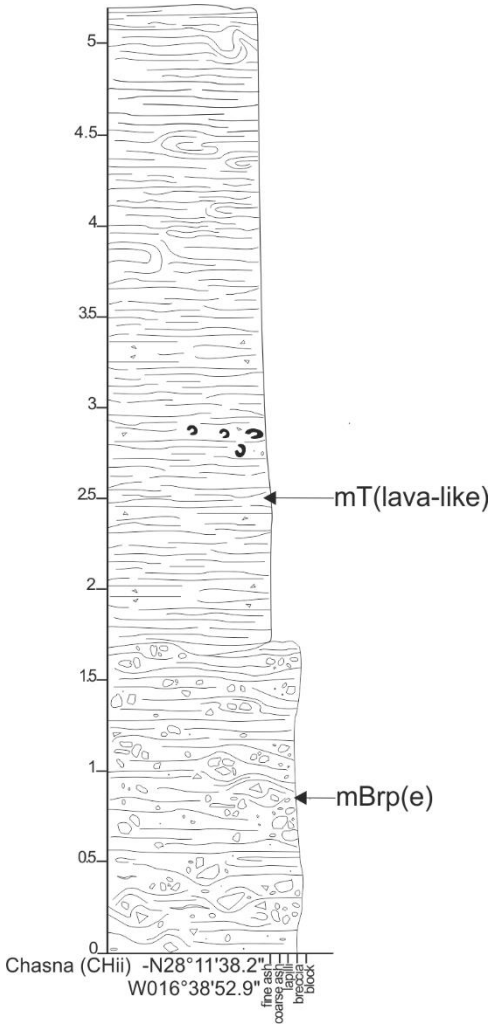


## Lithofacies description

Massive, crystal-rich, clast-poor lava-like lithofacies with a persistent base-parallel fabric with minor folds (tight and isoclinal). Strongly columnar jointed with discontinuous horizons and zones of lithophysae (pock-marked appearance).

Blue and orange banded, crystal-rich lava-like lithofacies.

Immediate gradation from banded, locally eutaxitic, clast-rich facies, into distinctly lava-like with distinct lack of vitroclastic textures.

Brownish red, very poorly sorted welded breccia. Matrix is crystal-rich, flow-banded lava-like tuff. Clasts are very angular, autoclasts (lava-like material) and altered pumiceous blocks (blue green in colour), with an a-axis up to 1.7 m. Localised green (devitrified0 stretched and elongated fiamme and eutaxitic textures.

**Figure 4–98.** Lithofacies description of the basal stratigraphy of the Chasna Mb at the Sombrero de Chasna locality (log CHi) (vertical scale in metres).

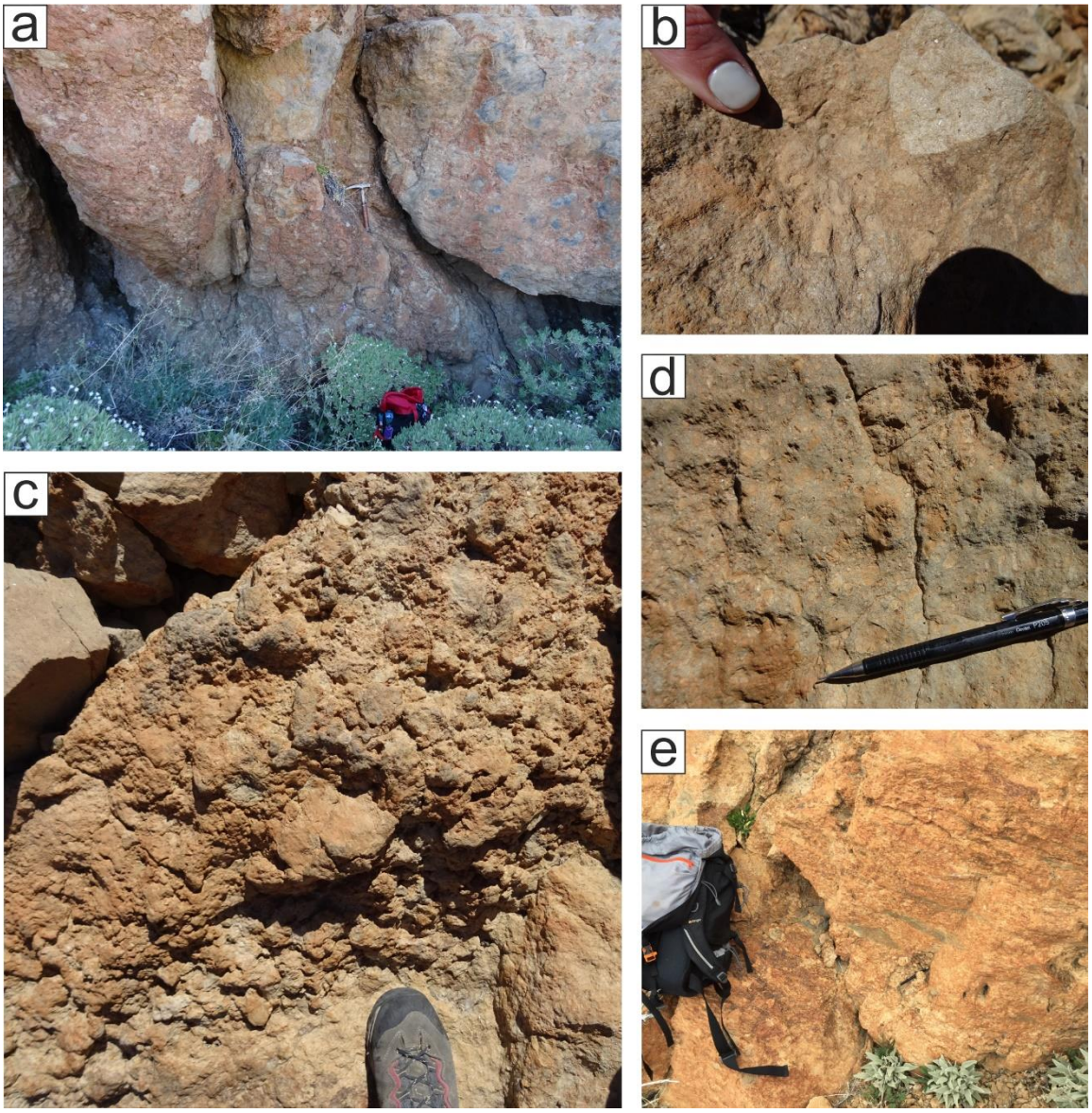


**Figure 4–99.** Characteristics of the basal welded breccia of the Chasna Member at the Sombrero de Chasna locality: a) mBrp(e) – columnar jointed, strongly welded (eutaxitic) crystal-rich, flow banded tuff matrix with angular clasts (predominantly lava-like and pumiceous material); b) clearly visible clast boundaries, with flattened and deformed pumice. Breccia is ash-matrix supported, with sub-angular to very angular clasts; c) localised clast-supported 'pockets' within the breccia, with sub-rounded to very angular clasts of ignimbrite (of varying degrees of welding) and pumiceous material; e) eutaxitic texture with elongated and stretched fiamme, with varying degrees of alteration and devitrification.

### 4.4.3. Chasna Mb: Llano de las Mesas locality

The Chasna Mb at this locality directly overlies Retamares Unit D (2350 m elevation) to the south of the deposit. However, its northern, eastern, and western boundaries are bound by, and obscured by the later caldera-fed El Pinalito lavas. Unlike the Chasna Mb at Roque los Almendros and the Sombrero de Chasna, the deposit here is intensely welded from base to top with no exposed non-welded

basal component and is lithic poor with very few clasts. Much of the unit is a very fine blue-grey, flow banded tuff, with large crystals. Aligned plagioclase feldspar and hornblende crystals, with mineral alignment parallel with the persistent base-parallel fabric, are present. There is a persistent, planar base-parallel fabric throughout, which is horizontal for most of the unit thickness, however towards the upper 2 m of the deposit, the fabric 'ramps up' and becomes highly irregular, ramping up towards the south east (Figure 4–100).

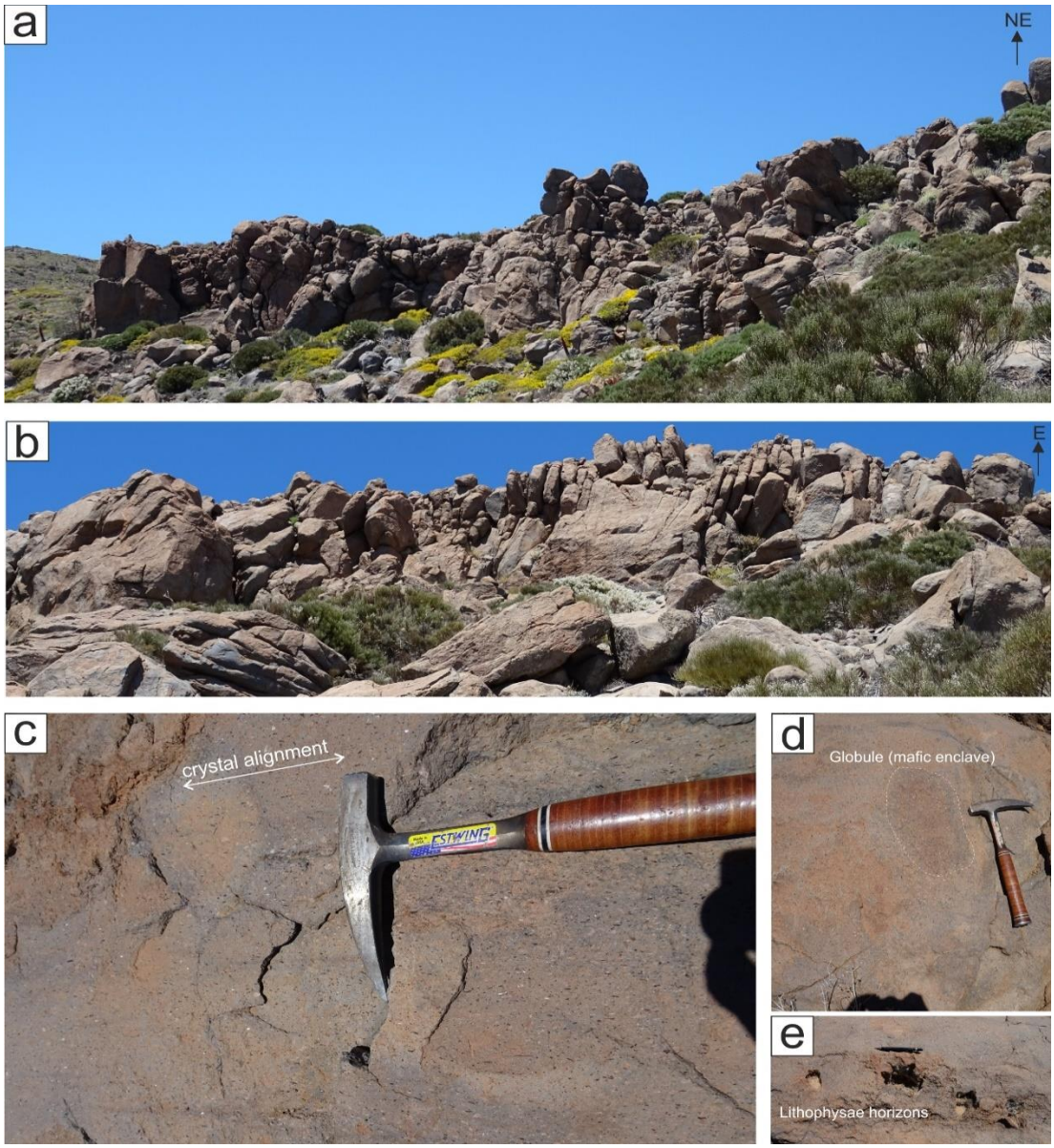


**Figure 4–100.** Features of the Chasna Member at Llano de las Mesas locality: a) columnar jointing observed on the western edge of the unit indicating deposition on a paleo-slope (12-15 °), with a steeply included fabric, ramping towards the northeast; b) steeply inclined and ramping of fabric towards the south east exposed face, dipping towards the southern face of the unit.; c) pervasive alignment of crystals (feldspathoids (up to 5 cm) and hornblende amphibole (up to 3 mm)) aligned 274 (E-W), parallel to the base-parallel (or ramped) fabric, and faint flow banding; d) 'ghost' globules (mafic enclave) with 'faded', indistinct boundaries; e) rare horizons of prolate and collapsed lithophysae.

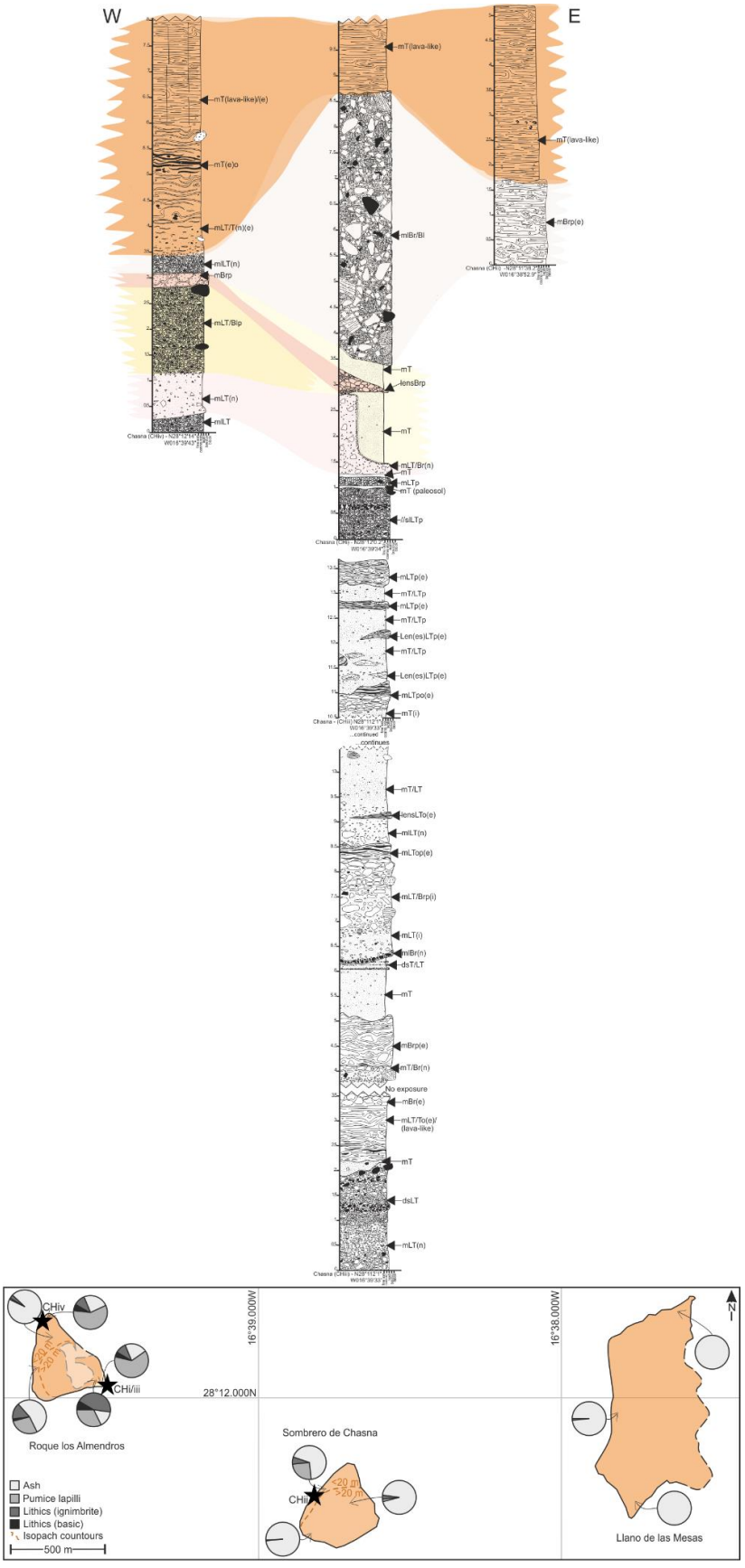


**Figure 4–101.** Correlation of the stratigraphic logs of the units of the Chasna Mb (vertical scale in metres), with the coloured bands showing possible continuation and variability of the lateral facies. Colours used to tie stratigraphy are arbitrary. Isopach map displays both the mapped (dark shade) and expected exposure (light shade), displaying the distribution of grain size and lithic components. Black stars show log localities.

### 4.4.4. Interpretation

The units of the Chasna Member share common morphological, textural, and structural characteristics, and are grouped into a collective member. Many similarities exist between these units and the units of the Atravesado Mb suggesting a similar emplacement mechanism but the units are more isolated and do not extend either down-slope or laterally over any significant distance (Figure 4–101).

They are interpreted as rheomorphic, lava-like ignimbrites, intensely welded from base to top, from a combination of both syn-depositional welding and rheomorphism, and post-depositional welding and down-slope rheomorphic slumping. As these units display distinctly lava-like facies, no original depositional textures remain, providing limited insight into the pre-welded nature of the material. The Sombrero de Chasna has been loosely referred to as a lava (Ridley, 1970) as well as a lava-coulee (Troll & Carracedo, 2016). However, the lack of a basal or upper autobreccia together with the occurrence of vitroclastic textures, the polymict graded breccia at the base of this unit, as well as the evidence of polyphase rheomorphism, supports the interpretation of this unit as a rheomorphic, lava-like ignimbrite.

Lithic-rich breccia and block horizons at the base of both the Sombrero de Chasna and Roque los Almendros localities suggests an explosive initiation of the eruption(s), followed by sustained, high-temperature, low column, ash-rich PDC(s). The base of both these deposits, associated with the high-lithic content, display lower intensities of welding, which both grade up into lava-like facies. The deposit at Llano de las Mesas exhibits a distinct lack of lithics or any vitroclastic textures, and is lava-like from base to top, which may represent a lower column, less explosive mechanism of eruption. A pervasive and base-parallel fabric, with the presence of imbricated, stretched and deformed fiamme in the lower portion of both the Sombrero de Chasna and Roque los Almendros units are attributed to syn-depositional deformation in a rheomorphic shear zone (e.g. Andrews & Branney, 2005). Evidence of downslope slumping, sliding and rheomorphism is seen in both the Sombrero de Chasna and Llano de las Mesas units, with

deformation of primary (syn-depositional) foliation and the development of large-scale ramp structures and ogives, discussed further in Chapter 7.

## 4.5. Almendros Member

The Almendros Member overlies the Chasna Member at Roque los Almendros, and is a comparatively very thin (<6 m), steeply inclined, low aspect ratio sheet, and the youngest mapped unit of the Ucanca Formation of the central caldera wall stratigraphy.

The unit consists of two steep-sided obsidian-rich, columnar jointed limbs, dipping in opposite directions inwards towards one and other, and onlapping the Chasna Member at Roque los Almendros (N28°12'10.6N W16°39'46.7) (Figure 4–102). Oscillations in welding are seen throughout the deposit, with obsidian-rich, eutaxitic and banded tuff alternating with weakly welded lapilli tuffs, with a base-parallel fabric developed in the more welded facies (Figure 4–103 & 4–104). Lithics are predominantly non-weakly welded stratified ignimbrite and welded, strongly foliated ignimbrite, presumably from the stratigraphy of the underlying Chasna Mb.


**Figure 4–102.** Field relationships of the Almendros Member overlying the Chasna Member, with the western limb steeply dipping to the SE and the eastern limb dipping NE. Note the columnar jointing indicating cooling on a steep paleo-slope.

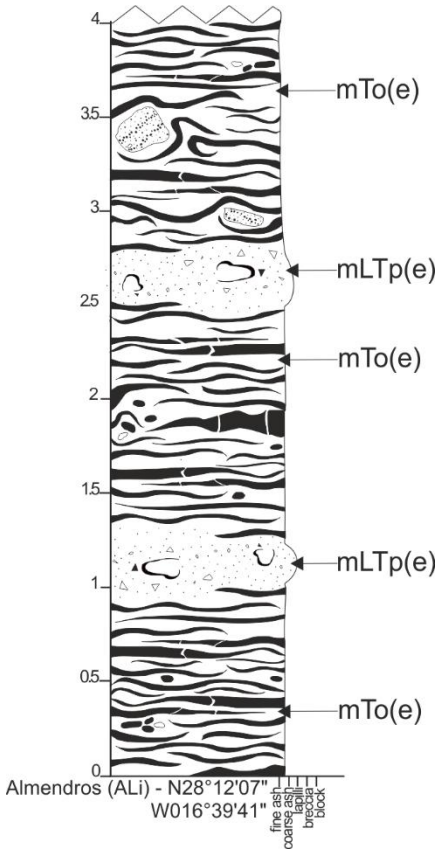


| Lithofacies description |
|---|
| Welded, obsidian-rich (glassy fiamme), crystal poor tuff with occasional pumiceous clasts and blocks of non-welded lapilli tuff. Fabric is folded (open curvilinear folds) and rotated around clasts. |
| Weakly welded, highly vesicular (prolate) lithophysae zones. |
| Weakly welded, highly vesicular (prolate) lithophysae zones. |
| Obsidian bands (glassy fiamme) up to 4 cm thickness, locally weathered red. Locally stratified which is churned up by the flow banding. |

**Figure 4–103.** Lithofacies descriptions of the basal stratigraphy of the Almendros Mb (western limb) (log ALi) (vertical scale in metres).


**Figure 4–104.** Lithofacies of the basal stratigraphy of the Almendros Mb (western limb) (log ALi) (vertical scale in metres).

### 4.5.1. Interpretation

The steep dip of the Almendros Member ('Los Almendros Mb' in Soriano et al., 2006) is attributed by Soriano et al., (2002; 2006) to rheomorphic flowage and draping of a welded fall back into the conduit structure, proposed to be located directly under the unit (Figure 3–6). However, given the localised nature of the deposit, and the depositional stratigraphy (Figure 4–103 & 4–104), this unit is interpreted as the result of a PDC, undergoing both syn- and post-depositional welding, with the former as the dominant welding process (further outlined in Chapter 5). The steep, inwardly dipping limbs can be attributed to the valley-filling nature of PDCs, with columnar jointing oriented at 25-42°, suggesting deposition and cooling against the walls of a paleo-valley of the underlying the Chasna Mb (also the 'Chasna Mb' of Soriano et al., 2006, but only at this locality). The Chasna Mb at the Roque los Almendros locality exhibits a centralised dip in foliation, albeit much shallower than the Almendros Mb (20°), also consistent with deposition in a paleo-valley, creating a v-shaped depression at the surface, which is then later filled by the Almendros Mb. Valleys and deeply incised barrancos are a common feature in the flanks of the Las Cañadas Caldera and even Mt. Teide volcano.

Furthermore, field investigation and views from inside the caldera show no indication of a vent structure located underneath Roque los Almendros, or the Almendros Mb. The unit appears to lie uncomfortably atop the mapped Chasna Mb, with no evidence of an intrusive feature associated with the deposit, being well exposed along the caldera wall (Figure 4–4).

## 4.6. El Pinalito lavas

At least eight individual porphyritic basalt lavas can be traced from the caldera wall, overlying Retamares units (A, B, C & D) at Llano de las Mesas, and all of the Atravesado units through El Pinalito to the northern town of Vilaflor. The most southern mapped exposure is 30 m south of El Pinalito Water Factory (28°10'18.3"N 16°38'22.1"W), but the lower limits remain undefined (Figure 4–105). The lavas display a porphyritic texture with phenocrysts of plagioclase feldspar, with mafic enclaves up to 10 cm abundant throughout (Figure 4–105 b). These lavas postdate

the Chasna Mb, as they flow down around the Chasna Mb at the Sombrero de Chasna locality.

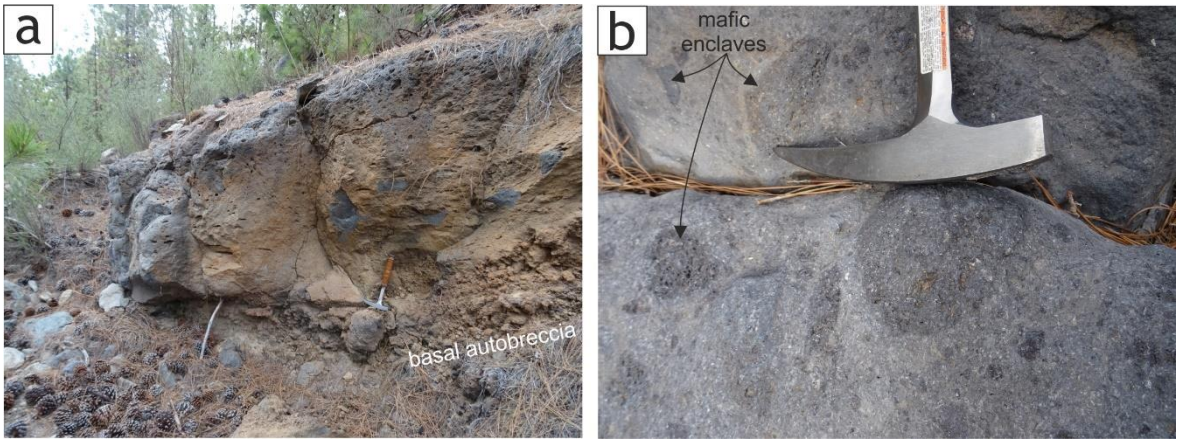


**Figure 4–105.** El Pinalito lavas south of Riscos Atravesado (28°11'01.2"N 16°38'21.6"W). a) Cross section through an individual unit, displaying basal autobreccia and prolate vesicles. b) Basalt displays a porphyritic texture with up to 0.5 cm plagioclase crystals, and rich in mafic enclaves.

## Guajara Formation

The account of the deposits of the Guajara Formation is not as detailed or comprehensive in comparison to that of the central caldera wall stratigraphy of the Ucanca Formation, and this section stands as a preliminary investigation and insight into the description, stratigraphy and nature of the deposits belonging to the Guajara Formation (Martí, 1971) overlying those of the Retamares Member at Montaña Guajara.

### 4.7. Guajara Mb

The Guajara Mb is a series of at least four, thick, stacked, downwards (southern) sloping, distinctly columnar jointed, predominantly lava-like units, punctuated by thick sequences of fall deposits, which form Montaña Guajara (Figure 4–106). Each unit typically consists of a non-weakly welded lithic block-rich breccia at the base, which grades up into an intensely welded and lava-like lithofacies. Each unit appears to form a crescent-shaped wedge, onlapping the unit below, and thinning distally to the south from a central point, near the peak or summit of the mountain, suggesting a ‘cone-building’ morphology (Bryan, 1998), as opposed to

the radial, sheet-like (e.g. Walker, 1973) distribution of the members of the Ucanca Formation.


**Figure 4–106.** Stratigraphy of Montaña Guajara (Guajara Units 1, 2, 3 and 4) overlying the Ucanca Fm (Retamares Unit E).

### 4.7.1. Guajara Unit 1

Unit 1 directly overlies Retamares Unit E and forms a wedge-like exposure at the northern face of Guajara, where it thins laterally where it is overlain to the east and west by the subsequent Guajara Mb units. A non-welded lithic-rich basal bedded stratigraphy grades up into the predominant lava-like lithofacies of the unit and can be traced across the base with variable thickness (Figure 4–107, log G1).

### 4.7.2. Guajara Units 2 & 3

Units 2 and 3 are exposed on the northern face of Montaña Guajara and both thin downslope to the south, underlying Guajara Mb Unit 4. Both units form 65-80 m steep cliff faces, which proved problematic to both sampling and facies analysis as the base of each unit is largely inaccessible. Lava-like lithofacies account for the majority of each unit's thickness, with well-developed sub-vertical columnar jointing.

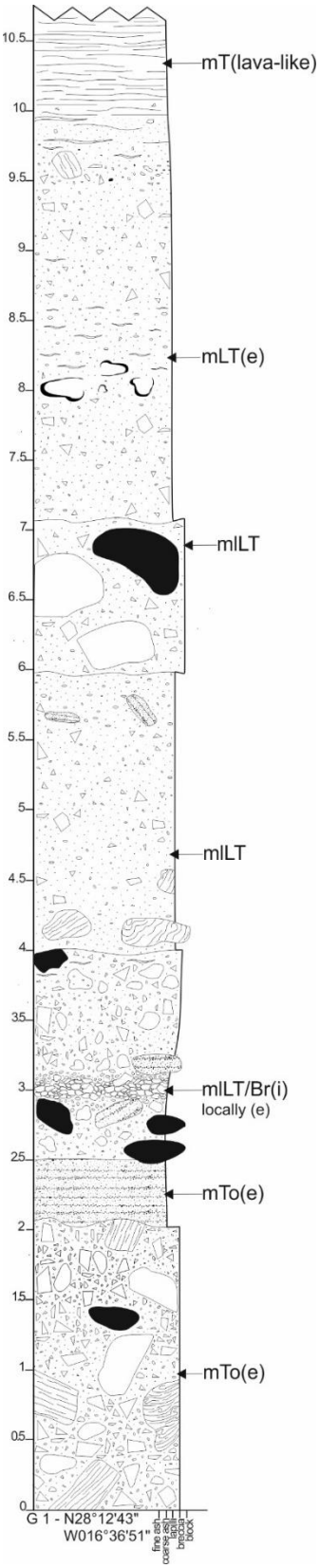


**Lithofacies description**

Grading upwards into a crystal-rich, clast poor predominantly lava-like, locally eutaxitic with a persistent base-parallel fabric with folds (tight isoclinal, closed curvilinear and buckle folds) and fabric rotated around crystals and occasional clasts.

Strongly columnar jointed (87°).

Horizon of welded (eutaxitic) pumice around zone of lithophysae (prolate vesicles).

Non-welded, ash matrix-supported with sub-rounded and rounded blocks of basic and lava-like material.

Pumice-rich ash matrix-supported with blocks and clasts of non-welded mLT (autoclasts) and rounded lava-like material.

Predominantly non-welded, locally eutaxitic, ash matrix-supported, locally clast-supported (pumice) with blocks basic and lava-like material.

Alternating layers of coarse and fine ash.

Clast-supported, locally ash matrix supported with predominantly angular clasts of basic, pumiceous, lava-like and obsidian-rich material.

**Figure 4–107.** Lithofacies description of the basal stratigraphy of Guajara Unit 1 (G1) (vertical scale in metres).

### 4.7.3. Guajara Unit 4

The youngest of the Guajara Mb, Unit 4 is exposed on the peak of Montaña Guajara and extends down slope from the summit and is overlain by the Areñas Member and later scoria cone and associated deposits to the south. A lithic-rich block breccia basal stratigraphy underlies much of the lava-like lithofacies which dominates the unit (Figure 4–108, log G4). The unit appears to be normally faulted, forming a steep (85°) contact between the northern and southern extents of the deposit, forming an eroded valley through the otherwise steep cliffs on either side, which is exploited by the summit ascent path (GR131) and provides good exposure up through the basal non-welded stratigraphy which grades in to the lava-like facies.

Northbound of the fault, the unit appears lava-like from base to top, overlying a thick sequence of non-welded stratified pumice fall. South of the fault, the deposit displays the same thickness of lava-like lithofacies, with the stratigraphy seen in log G4, with alternating massive and diffuse-and planar stratified tuffs, lapilli tuffs and block-rich breccia, grading into the lava-like facies from a welded, massive lithic-rich breccia (mlBr). The deposit thins considerably southwards towards Montaña Areñas, and displays large-scale ramping of the planar fabrics, with a highly contorted and deformed upper ‘skin’ of the deposit (Figure 4–109).

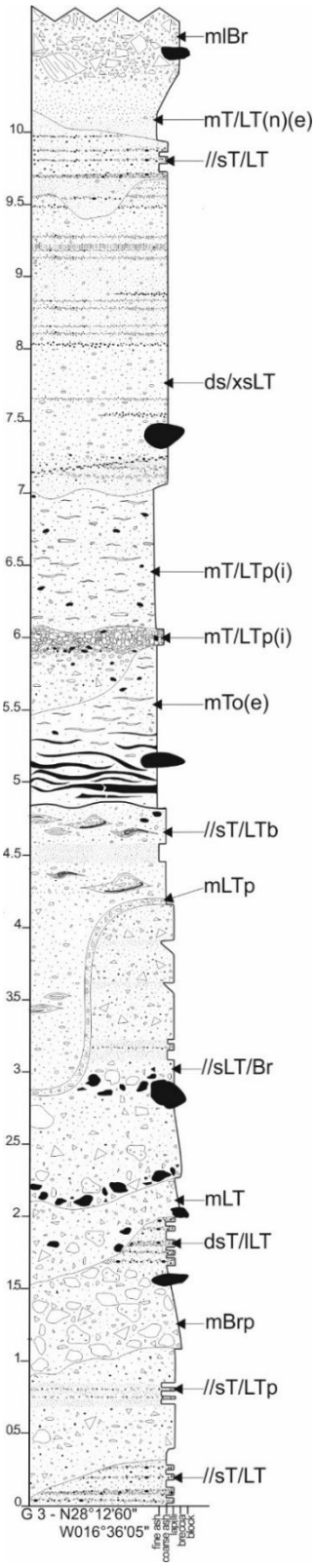


| Lithofacies description |
|---|
| Welded, dark orange, obsidian rich eutaxitic ash matrix supported breccia. |
| Highly erosional, undulating contact with brown staining on upper 0.45 cm. |
| Non-welded diffuse and cross stratified pumice lapilli alternating with basic, angular lithic lapilli<br>Welded, eutaxitic, locally lava-like with faint, weak columnar jointing. |
| Pumice-rich, non-welded lens of variable thickness<br>Welded, eutaxitic, locally lava-like with faint columnar jointing. Rare obsidian (glassy fiamme). |
| Highly erosive, erosional contacts between lithic-rich lapilli and breccias, with display inverse grading.<br>Eutaxitic, obsidian-rich horizon, with obsidian clasts, and stretched and deformed obsidian fiamme, which grades up into white/green devitrified fiamme. |
| Bomb rich horizon. Brownish orange scoriaceous bombs, occasionally obsidian-rich, with fluidal, lobate edges (cow-pat bombs) and bread crusted boundaries. Non-welded with occasional fiamme (altered green, chlorite). |
| Non-welded, stratified pumice-rich with clasts of lava-like and basic material. Highly irregular, erosive contact. Wide variation in lithic composition (basic material, obsidian, banded obsidian, ignimbrite of varying degrees of welding). |
| Pumice rich with occasional basic and lava-like blocks<br>Massive, locally planar stratified pumice-rich with occasional clasts of lava-like material. |
| Alternating bands of pumice-rich and basic-rich lithic lapilli. |

**Figure 4–108.** Lithofacies description of the basal stratigraphy of Guajara Unit 4 (log G3) (vertical scale in metres).

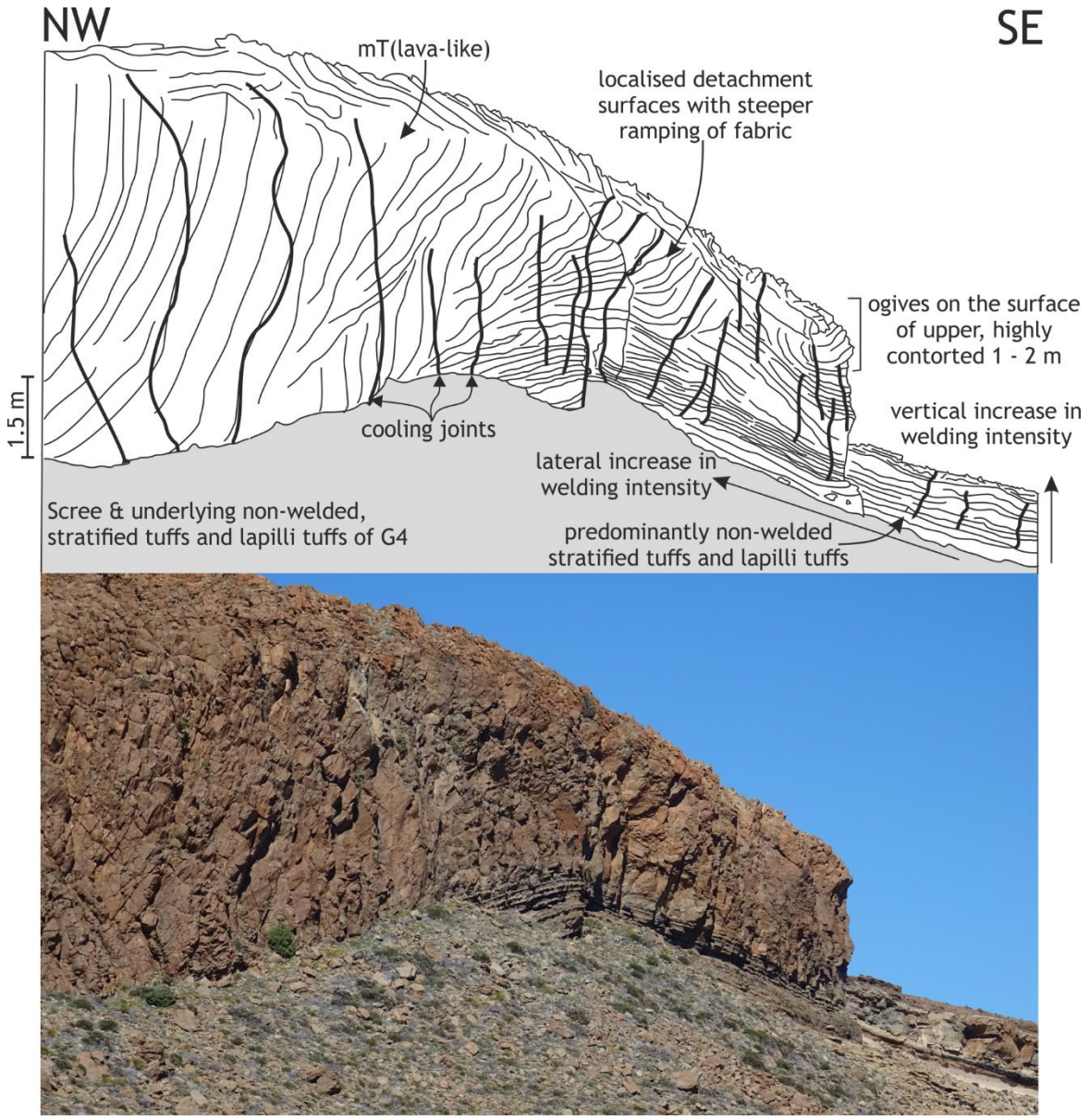


**Figure 4–109.** Annotated field sketch and photograph of the post-depositional rheomorphic ramp structure in Guajara Unit 4. The deposit thins southwards at of Montaña Guajara towards of Montaña Areñas at (28°20.4'75.7"N 16°60.6'08.0"W).

### 4.7.4. Interpretation and discussion

Similarly to the units of the underlying Ucanca Fm, the units of the Guajara Fm are interpreted as welded and lava-like ignimbrites, deposited from vent-proximal, high-temperature, boil-over style eruptions, punctuated by periodic Plinian activity, giving rise to thick, interbedded fall deposits. The deposits share characteristics and structures with those of the Atravesado Member, but have a distinctly different morphology, and thin downslope as opposed to pool or thicken, suggesting very different rheological behaviours of the material.

The highly variable facies of the basal stratigraphy suggest fluctuating and abrupt changes of depositional regimes, between turbulent, traction dominated FBZs, giving rise to the planar and cross stratification in tuffs and lapilli tuffs, and also locally within ash-supported components of breccias; and rapid fluid escape flow boundary zones, rich in ash and pumice, resulting in the massive tuffs, lapilli tuffs and pumice breccias. The deformation, rotation and stretching of fluidal bombs and spatter-like material is consistent with shear-driven processes, taking place at the depositional boundary of a progressively aggrading current. It is difficult to attribute the range of textures, features and kinematic indicators present in the non- and lesser welded basal stratigraphy to load compaction welding of fall and spatter.

The presence of lithic block-rich and coarse breccias within the basal stratigraphy of Units 1 and 4 suggest initial highly explosive, perhaps 'vent-clearing' phases of eruptive activity, which then transitions into sustained, ash-rich, lithic-poor PDCs, with intense welding taking place syn-depositionally, giving rise to the aphyric, lava-like facies. Structures relating to post-depositional rheomorphism is not as clearly defined as in the Atravesado, Retamares and Chasna members, with a lack of evidence of rheomorphic remobilisation (e.g. folding, slumping, ramping and pooling downslope), with the exception of the upper surface of Unit 4.

The 'clastogenic lava' described by Bryan et al (1998) on the summit of Guajara is interpreted in this study to be the upper rheomorphic domain of Guajara Mb Unit 4, with steeply inclined foliation and flow banding as a result of rheomorphic flow, slumping and settling of the deposit following emplacement. There is no evidence of a distinct boundary, nor autobreccia associated with this deposit, as expected with the flow of a phonolitic lava, and an upwards gradation welding is seen from the lava-like facies of Unit 4 (Guajara Welded Unit (GWU) of Bryan, 1998), in support of this interpretation. The clastic nature of the deposit is better explained by the presence of lithic-lapilli and clasts, which are not as susceptible to intense welding during deposition as the pumice and ash component of the deposit, giving rise to a distinctly lava-like facies, rich in lithic lapilli. Flow directions as determined by folding and inclined ramps are in agreement with Bryan (1998), with downslope flow to both the east and west from the central

peak of Guajara, supporting post-depositional settling and slumping of the deposit from a central high point.

Furthermore, Unit 4 is described as two distinct units by Bryan (1988), with the deposit north of the fault described as the Guajara Welded Unit (GWU), and the deposit to the south as an 'aphyric lava-like unit'. These are distinguished as such by textural differences (with the latter being distinctly aphyric and lava-like), with minor haüyne 'phenocrysts', and a basal partially welded stratigraphy consisting of 'fall and lag breccias'. Both of these apparent distinctions can be attributed to differential welding profiles as a result of a combination of syn-emplacement welding processes, and post-depositional rheomorphism, both influenced by unit thickness and topographical constraints. The lack of a non-welded counterpart exposed in the unit northbound of the fault (seen in Figures 3-8 and 4-4-) could be attributed to the proximity to the vent, with hotter material allowing for more intense welding to take place. The unit appears to onlap the underlying dipping Unit 3, and thickens downslope, in contrast to Units 1-3, and it may be that due to the steep nature of the contact, the non-welded stratigraphy only accumulated on the flatter, southern flanks, with either intense welding or erosion of any prior deposition taking place. The interpretation of Unit 4 (GWU) as a pyroclastic density current deposit is also proposed by Richard (2015), based on thermal analysis and geospeedometry of glasses present in the banded, obsidian-rich facies at the base of the unit.

## 4.8. Areñas Member

The youngest deposits overlying the Guajara Units (1-4) are described in Bryan (1998) as the Guajara Spatter Cone Complex (GSCC), representing products of a proposed vent towards the southern side of Guajara peak, consisting of a welded ignimbrite, welded spatter-pumice fall and non-welded pumice fall. Both the welded ignimbrite and the welded spatter-pumice are interpreted here as topographically controlled lithic-rich ignimbrites, belonging to the proposed Areñas Member.

The Areñas Member consists of two thin (5-10 m), variably welded, pumice-rich deposits which overlie Unit 4 of the Guajara Member at two localities on the summit of Montaña Guajara.

### 4.8.1. North-west Guajara summit locality

The first unit is a very thin (5-6 m) isolated unit, exposed north of the southern unit, north-west of the peak of Guajara, forming an elongated crescent-shaped deposit overlying Guajara Mb Unit 4. It exhibits weak, sub-vertical columnar jointing, and a eutaxitic texture from base to top, with gradations in lithic size, from lapilli up to block throughout the deposit's thickness (Figure 4–110). Pumice is stretched and deformed, forming a largely planar fabric, which displays localised imbrication, and the fabric is wrapped and rotated around lithics, forming a 'swirly' banded appearance, with rare obsidian-rich fiamme and blebs.

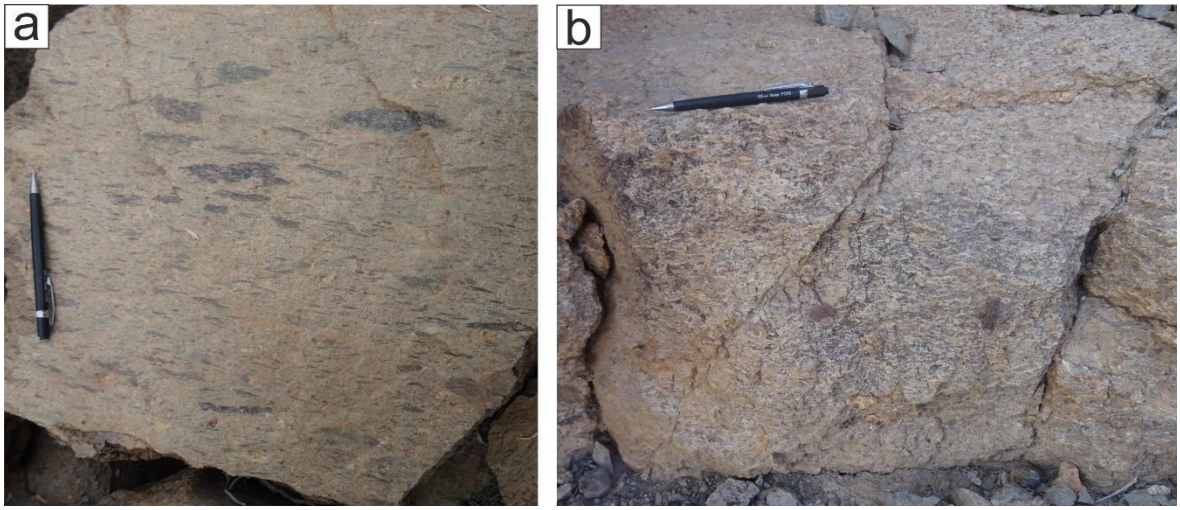


**Figure 4–110.** Areñas Mb at north-west Guajara summit locality: a) pervasive eutaxitic texture, with climbing, imbricated fiamme, often glassy with raggedy edges; b) crude flow banding, with a base-parallel planar fabric wrapped and rotated around occasional lithics (scoria and ignimbrite).

### 4.8.2. Southern Guajara summit locality

The Areñas Member to the south of Montaña Guajara summit onlaps Unit 4 of the Guajara Mb, 100 m south of the northern face of Montaña Guajara, forming a radially (predominantly to the south east) dipping, crescent shaped deposit. The unit is between 5.5 - 10.5 m thick and exhibits a range of welding textures, grading up to a lava-like lithofacies (Figure 4–111 & 4–112).

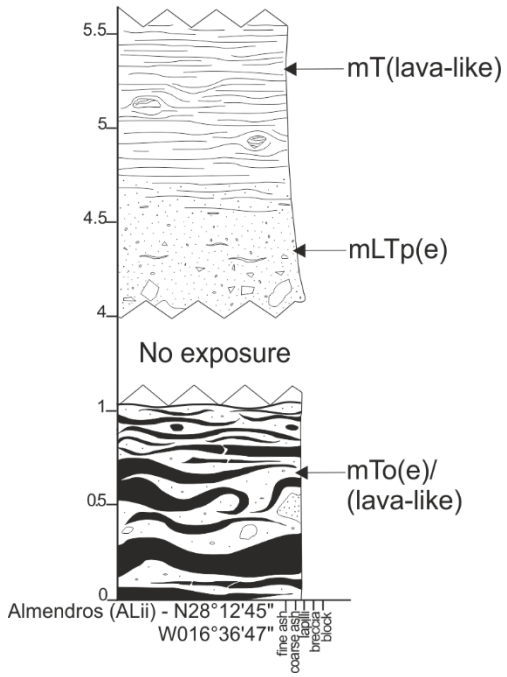


| Lithofacies description |
|---|
| Non-welded, locally eutaxitic pumice-rich, grading upwards into a crystal-rich, clast poor predominantly lava-like tuff, locally eutaxitic with a persistent base-parallel fabric with folds (tight isoclinal, closed curvilinear and buckle folds) and fabric rotated around crystals and occasional clasts.<br>Planar fabric - 042 56 °S.<br>~ 3 m of no exposure (scoriaceous scree). |
| Flow banded, bluish green and orange, predominantly lava-like, obsidian rich with occasional clasts of pumice (occasionally fiamme) and lava-like material. |

**Figure 4–111.** Lithofacies description of the basal stratigraphy of the Areñas Mb at the southern Montaña Guajara summit locality (log ALii) (vertical scale in metres).

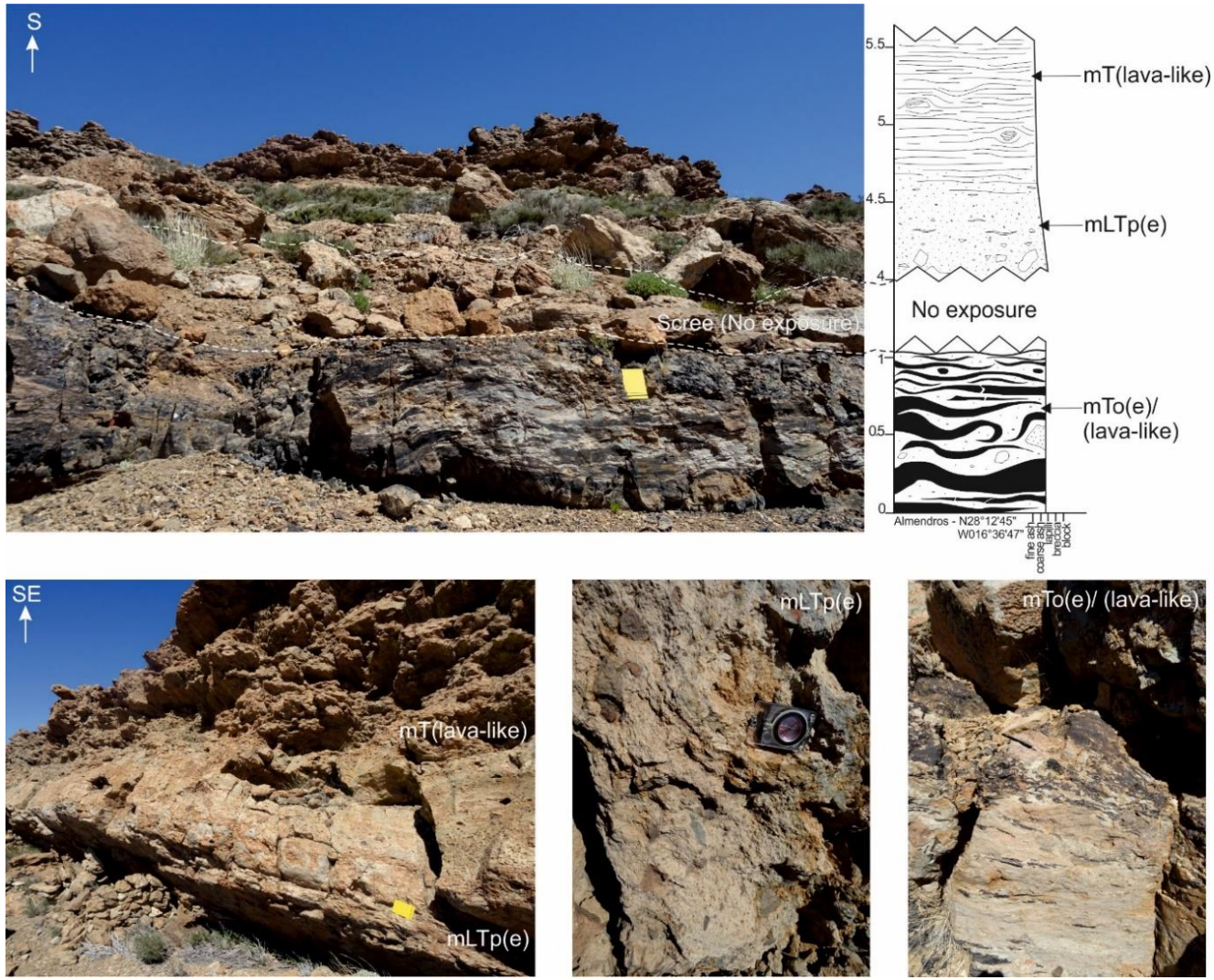


**Figure 4–112.** Lithofacies of the basal stratigraphy of the Areñas Mb at the southern Montaña Guajara summit locality (vertical scale in metres).

### 4.8.3. Interpretation

The Areñas Member differs in characteristics, thickness, and facies from the deposits of the Guajara Mb. The unit displays many similarities with the Almendros Mb of the Ucanca Formation, having similar thicknesses, lithofacies gradations and obsidian banded horizons, but are geographically and temporally unrelated, albeit they may have resulted from similar eruptive processes, towards the end of caldera-forming eruptive cycles.

The nature of the grading (of grain size and lithic components), sedimentological features, kinematic indicators (wrapped and rotated fabrics, flow banding, folds) lead to the conclusion that both units of the Areñas Member are both high-grade ignimbrites, with variable welding as a result of instability of a syn-depositional shear zone, resulting in gradations between moderately and strongly welded zones. This emplacement model would account for the variety of welding observed throughout the deposit, particularly the southern locality.

# Chapter 5

## 5. Mapping welding intensity

This chapter outlines the methodology used in the semi-quantitative mapping and description of welding intensity through the documented Las Cañadas stratigraphy, across both individual units and packages of units. This was achieved through field observations and determinations of welding (petrographic and fabric analysis, oblateness of pyroclasts…etc), cross referenced with the physical properties of the deposits, specifically porosity, density and rock strength.

As detailed in Chapter 2, welding is the progressive deformation of hot, glassy pyroclasts, from all stages of sintering, compaction and flattening, to complete obliteration and cohesion of the material (e.g. Smith, 1960i; Ross & Smith, 1961; Cas & Wright, 1987; Quane & Russell, 2003; 2005). Meaningful comparisons and categorisation of welding intensity across welded pyroclastic deposits remains problematic, with no widely accepted, standardised methodology or scheme to do so. A number of welding classification schemes exist (e.g. Smith, 1960ii; Smith & Bailey, 1966; Sheridan & Ragan, 1976; Peterson, 1979; Streck & Grunder, 1995; Wilson & Hildreth, 2003; Quane & Russell, 2003; 2005; Mundula, 2009), attempting to semi-quantitively describe welding intensities based primarily on qualitative field data, petrographic analysis and physical properties.

The measurement of rock strength (Section 5.1) of pyroclastic deposits and ignimbrites emplaced at temperatures around the glass transition ($T_g$) has potential to be used as an analogue in determining the intensity of welding (Quane & Russell, 2003, 2005), providing a semi-quantitative means of recording and tracking variations in the degree of welding throughout a deposit. Porosity and density (Section 5.2) are often used to measure and quantify welding of ignimbrites (e.g. Ragan & Sheridan, 1972; Streck & Grunder, 1995; Ross & Smith, 1980; Wilson & Hildreth, 2003) alongside more traditional field determinations, such as flattening ratios (length/width) of fiamme (e.g. Smith & Bailey, 1996; Smith, 1979; Ross & Smith, 1980) (Figure 5–1), oblateness and fabric angle (e.g. Quane & Russell, 2005). With increasing welding intensity, there is an observed reduction in primary porosity, associated with increased density and progressive

development of foliation (e.g. Ragan & Sheridan, 1972; Streck & Grunder, 1995; Rust & Russell, 2000), reflecting the accumulated strain immediately following deposition (Ross & Smith, 1961; Quane et al., 2004). The time spent above the material's $T_g$ (e.g. Giordano et al., 2000; Russell & Quane, 2004, Giordano, 2005), as well as the load effect of the overlying column(s) is reflected in the intensity of welding (e.g. Smith, 1960a; Ross & Smith, 1961) particularly for deposits attributed to an en masse depositional model (e.g. Sparks, 1976; Sheridan & Ragan, 1976; Wright & Walker, 1981). The extent of volume strain, and in turn welding, of a singular deposit can therefore vary systematically with stratigraphic position (e.g. deposit thickness and lateral extent) as it is a factor of the porosity loss during compaction.

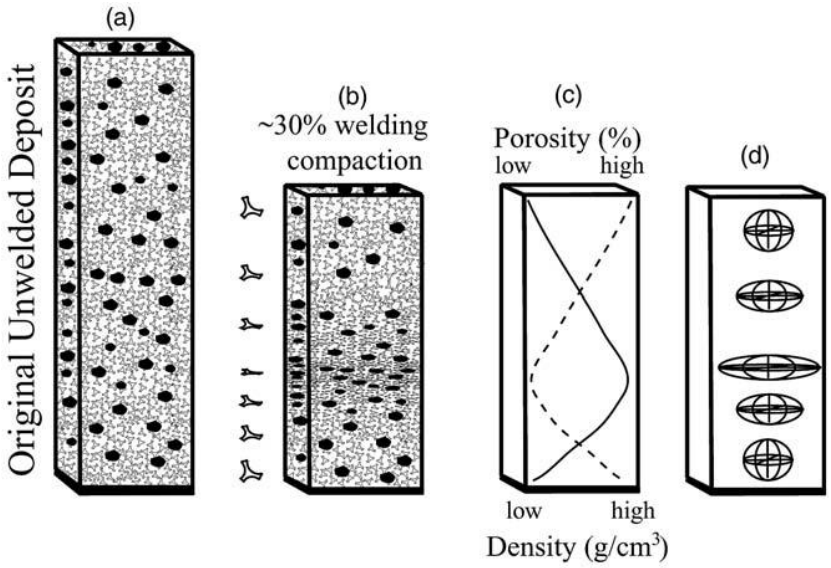


**Figure 5–1.** Quane & Russell's (2003) schematic representation of post-depositional welding of an originally unwelded ignimbrite (a), with subspherical pumice lapilli (black dots) and Y-shaped ash shards. After 30% of welding compaction the pumice and shards within the deposit undergo flattening (b). A decrease in porosity (%) and increase in density (g/cm$^2$) typically occurs in the lowest third of a deposit (e.g. Ragan & Sheridan, 1972) (c), and corresponds with the highest degree of flattening in (b). (d) shows a schematic representation of the strain ellipses of the pumice lapilli under the welding regime.

For high-grade and lava-like ignimbrites deposited as a result of progressive aggradation in high-temperature eruptions (e.g. Branney & Kokelaar, 1992; Sumner & Branney, 2002; Andrews & Branney, 2011), as discussed in Chapter 2, syn-emplacement welding and agglutination of glassy pyroclasts occurs, commonly coupled with post-emplacement rheomorphism (e.g. Schmincke & Swanson, 1967; Walker & Swanson, 1968; Wolff & Wright, 1981; Branney & Kokelaar, 1992;

Kobberger & Schmincke, 1999; Sumner & Branney, 2002; Andrews & Branney, 2011; Mundula, 2013; etc) so the resulting deposits are typically devoid of the systematic variations resulting from solely volume compaction. As well as post-depositional deformation, secondary crystallisation and vapour-phase alteration (e.g. lithophysae and spherulites: Streck & Grunder, 1995) may impact the measured physical properties in higher-grade and lava-like deposits. Minor cases of vitrification and secondary crystallisation, where vitroclastic textures remain, are documented to have little to no impact on the physical properties (e.g. Wilson & Hildreth, 2003; Quane & Russell, 2005), highlighting the importance of combining field observations with the metrics of welding intensity.

## 5.1. Measuring rock strength

### 5.1.1. The point load index test

The point load index test (PLT) is an accepted method in rock mechanics, predominantly used in the geotechnical industry, to calculate and determine the strength of a rock or geomaterial. The test is done by applying a vertical, increasingly concentrated load (σ 1) to a sample held in the apparatus, inducing tensile stresses, which result in a failure parallel to the loading pressure. The failure load is used to calculate the point load strength index (Broch & Franklin, 1972; ISRM, 1985) and can be used to estimate the uniaxial (or unconfined) compressive strength (UCS), an indirect measurement of the compressive or tensile strength of a rock. UCS measurements are more standardised in rock mechanics literature (Broch & Franklin, 1972; Hoek & Brown, 1980), and are typically a more robust, yet costly means of classifying rock strength. Direct UCS values are a measurement of the strength of a geomaterial under a uniformly distributed axial stress and are the most common metric of determining the strength of a geomaterial. As PLTs are more practical and inexpensive, with less sample preparation and the ability to collect measurements in the field, attempts are made here to establish a better relationship between PLT measurements and the widely used UCS classification.

Point load index testing can be undertaken on rock cores or on hand specimens or blocks of material (Figure 5–2). Experimentally measured values are dependent on

the sample size, shape and orientation, and each testing style (axial, diametral or irregular lump) has specific geometric and size restrictions. The failure strength index ($I_S$) for axial and diametral testing of rock cores is determined using the formula $P/D^2$, where P is the force required to cause failure (kN) and D is the distance (mm) between the hardened points at the moment of failure.

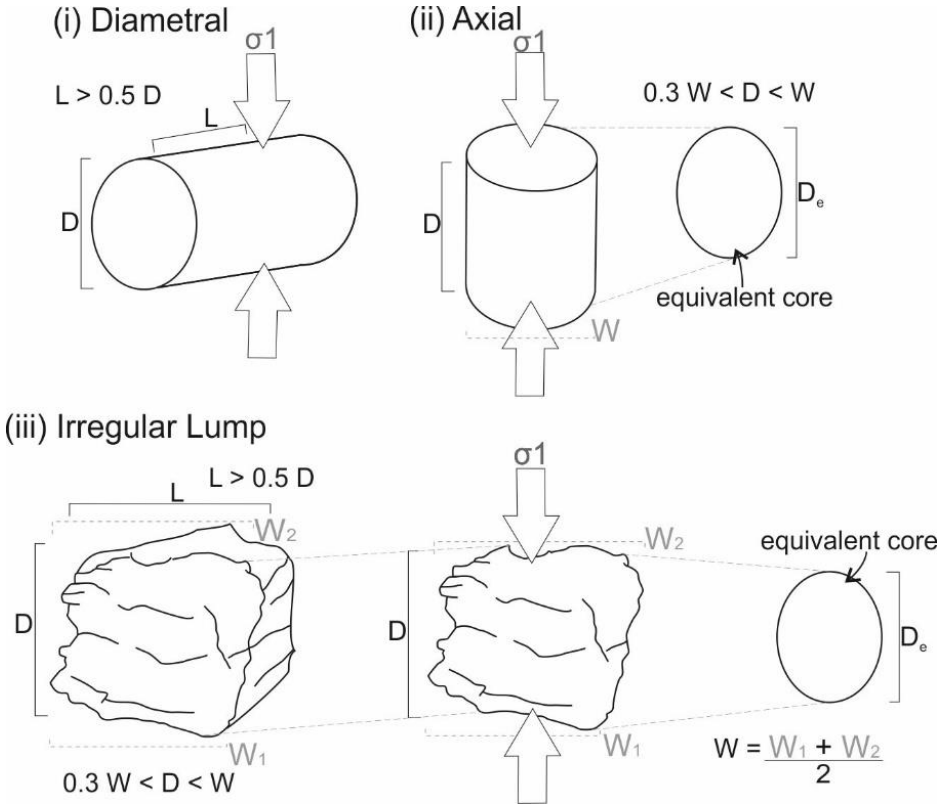


**Figure 5–2.** Point load index testing styles according to sample shape and orientation: (i) diametral and (ii) axial point load measurements on rock cores, and measurements of (iii) irregular lumps, or blocks of irregular sized material (modified after Quane & Russell, 2003; ISRM, 1985).

Irregular lump (IL) testing (Figure 5–2) is carried out on irregular blocks or hand specimens of material, approximately 50 mm in diameter. ILs should be cut or sawed to where the length/diameter ratio of the sample is between 0.3 and 1.0. The uncorrected failure strength index ($I_S$) for ILs is determined using the formula $P/D_e^2$, where $D_e$ is a coefficient to correct the measured load at failure to that of an equivalent rock core during a diametral test (Rusnak & Mark, 2000) (Figure 5–2 (i)). The shortest width of the sample is measured in the direction perpendicular to W, the loading direction and P, the force required to cause failure. The loading direction, W, is calculated using: $0.5 \cdot (W_1 + W_2)$ as per Figure 5–2 (iii).

Size corrections are then applied to the PLT strength measurements, correcting them to a standard (50 mm) core diameter ($I_{S50}$) using the formula:

$$I_{S50} = F \cdot I_S$$

F, the size correction factor is calculated using: $F = (D_e/50)^{0.45}$ (ISRM, 1985).

### 5.1.2. PLT – UCS conversion

Conversion factors (k) from PLT measurements to the widely accepted UCS values typically differ depending on the properties (i.e. strength, porosity, compositional and textural inhomogeneity, extent of weathering) and the type of rock. A PLT-UCS strength conversion of 24 times the measured PLT value ($I_S$), for a standard size of 50 mm ($I_{S50}$), was initially proposed by Broch & Franklin (1972), and subsequent studies (Table 5-1) have attempted to better account for these relationships, particularly for softer geomaterials. Variations of the equation:

$$UCS = k \cdot I_{S50} + b$$

for point load to uniaxial strength conversion are documented in the literature, with widely varying k factors (Table 5-1). ISRM (1985) outlined a universal conversion factor of 20-25 times for all lithologies, but many studies describe a strong linear correlation between the point load index and UCS strengths, with a broad range of ratios from 8 – 29 (Table 5-1), and typically propose smaller k factors, between 8 – 15, and non-linear equations for weak, weathered and soft rocks (Table 5-1). It is agreed that there is no single k value that is applicable to all lithologies and geomaterials, and values are commonly particular to the rock type, or subdivision of the rock type(s).

For pyroclastic rocks, which vary in strength across singular deposits, Quane & Russell (2003) proposed a non-linear PLT-UCS conversion equation for 'weak' rocks < 5 MPa and a linear equation for 'strong' rocks > 4 MPa, and recommend taking an average of the two predicted values for rocks of strengths that fall between these determinations (between 4 and 5 MPa):

$UCS = 24.4 \cdot I_{S50}$ for PLT values of > 4 MPa;

$UCS = 3.86 \cdot I_{S50^2} + 5.6 \cdot I_{S50}$ for PLT values of < 5 MPa.

Quane and Russell's (2003) models are a good fit to the strength data of pyroclastic rocks, which are typically < 50 MPa, and a variety of lithologies. The linear equation for 'strong' materials, with PLT values of 4 – 14 MPa (and UCS values of 100 – 325 MPa), is consistent with the range most commonly proposed in the literature (Table 5–1), and the standard ISRM (1985) conversion ratio (20 – 25). For weak rocks, with measured PLT values of 0 – 5 MPa (or measured UCS values of 0 – 125 MPa) a non-linear model is commonly used.

### 5.1.3. Methodology

Point load testing of samples was carried out at Terra Tek Ltd, Airdrie, a UKAS/ Mcerts accredited laboratory. Samples were prepared and tested as irregular lumps (IL), following the standardised procedure according to ISRM Commission on Testing Methods (ISRM, 1985; Brown, 1981). A total of 53 samples were tested across 19 individual units, with between one and four samples per unit representing the basal, middle, or uppermost regions of the deposits. Samples were dried at 100°C prior to testing to remove absorbed moisture, which can lower strength values (ISRM, 1985; Ghweir, 1995) and tested at ambient room temperature.

Index readings were obtained from a digital PLT experimental apparatus (Impact PLA 002 Digital Point Load Tester) (Figure 5–3) consisting of a secured crosshead load frame, two point load platens with hardened conical points to secure the sample, a manual hydraulic jack with a pump handle to apply the load (of up to 55kN) to the sample, and a digital pressure gauge to display the applied load. Samples were loaded on to the apparatus in contact with the two platens (Figure 5–3) and the platen pointer measures the distance between the two standard conical points on the platens, which are composed of hardened steel to limit deformation during testing (ISRM, 1985).

| Reference source | Lithologies | UCS-PLT equation (k) |
|---|---|---|
| D'Andrea et al. (1964) | various lithologies | $UCS = 16.3 + 15.3 \cdot I_{S50}$ |
| Deere & Miller (1966) | various lithologies | $UCS = 20.7 \cdot I_{S50} + 29.6$ |
| Broch & Franklin (1972) | various lithologies | $UCS = 24 \cdot I_{S50}$ |
| Bieniawski (1975) | sandstone, quartzite, norite | $UCS = 24 \cdot I_{S50}$ |
| Brook (1980) | sandstone, dolerite, limestone, siltstone | $UCS = 24 \cdot I_{S50}$ |
| Read *et al.* (1980) | limestone, sandstone, siltstone | $UCS = 16 \cdot I_{S50}$ |
| Read *et al.* (1980) | basalt | $UCS = 20 \cdot I_{S50}$ |
| Hassani *et al.* (1980) | limestone, sandstone | $UCS = 29 \cdot I_{S50}$ |
| Singh (1981) | Sandstone, shale | $UCS = 18.7 \cdot I_{S50}$ |
| Forster (1983) | dolerite, sandstone, felsite, greenstone | $UCS = 14.5 \cdot I_{S50}$ |
| Gunsallus & Kulhawy (1984) | dolostone, sandstone, limestone | $UCS = 16.5 \cdot I_{S50}$ |
| ISRM (1985) | all rock types | $UCS = 20 \cdot I_{S50} \rightarrow 25 \cdot I_{S50}$ |
| Rao *et al.* (1987) | sandstone | $UCS = 9.5 - 1.5 \cdot I_{S50}$ |
| O'Rourke (1989) | limestone, sandstone, anhydrite, halite | $UCS = 21.8 \cdot I_{S50}$ |
| Vallejo *et al.* (1989) | shale | $UCS = 8.6 \cdot I_{S50} \rightarrow 16 \cdot I_{S50}$ |
| Cargill & Shakoor (1990) | - | $UCS = 23 \cdot I_{S50}$ |
| Mehrotra *et al.* (1991) | slate, quartzite, basalt, gneiss, shale | $UCS = 26 \cdot I_{S50}$ |
| Ghosh & Srivastava (1991) | granite | $UCS = 16 \cdot I_{S50}$ |
| Grasso *et al.* (1992) | - | $UCS = 9.3 \cdot I_{S50} + 20.04$ or, $UCS = 25.67 \cdot I_{S50^{0.57}}$ |
| Ulusay *et al.* (1994) | sandstone | $UCS = 19 \cdot I_{S50}$ |
| Chau & Wong (1996) | granite, tuff | $UCS = 12.5 \cdot I_{S50}$ |
| Chau & Wong (1996) | theoretical model | $UCS = 14.9 \cdot I_{S50}$ |
| Wiesner & Gillate (1997) | sandstone, basalt | $UCS = 18.6 \cdot I_{S50}$ |
| Smith (1997) | limestone, siltstone, sandstone | $UCS = 12.5 \cdot I_{S50}$ |
| Tuğru & Zarif (1999) | granite | $UCS15.25 \cdot I_{S50}$ |
| Rusnak & Mark (2000) | shale, sandstone and limestone | $UCS(psi) = 1970 + 17.6 \cdot I_{S50}$ or, $UCS\ (MPa) = 21 \cdot I_{S50}$ |
| Kahraman (2001) | carbonate, sandstone, diabase, serpentinite | $UCS = 23.6 \cdot I_{S50} - 9.51$ |
| Kahraman (2001) | marl, limestone | $UCS = 8.4 \cdot I_{S50} + 9.51$ |
| Look & Griffiths (2001) | tuff | $UCS = 18 \cdot I_{S50}$ |
| Quane & Russell (2003) | non-welded to partially welded ignimbrites | $UCS = 24 \cdot I_{S50}$ (PLT > 4 MPa)<br>$UCS = 3.86 \cdot I_{S50^2} + 5.6 \cdot I_{S50}$ (PLT <5 MPa) |
| Tsiambaos & Sabatakakis (2004) | limestone<br>marlstone<br>sandstone | $UCS = 13 \cdot I_{S50}$<br>$UCS = 20 \cdot I_{S50}$<br>$UCS = 28 \cdot I_{S50}$ |
| Palchik & Hatzor (2004) | chalk | $UCS = 8 \cdot I_{S50} \rightarrow 18 \cdot I_{S50}$ |
| Fener *et al.* (2005) | basalt, granite, andesite, metagabbro, granodiorite, quartzite, marble, limestone, travertine | $UCS = 9.08 \cdot I_{S50} + 39.32$ |
| Akram & Bakar (2007) | sandstone, siltstone, limestone, dolomite | $UCS = 22.792 \cdot I_{S50} + 13.295$ |
| Akram & Bakar (2007) | sandstone, limestone, marl | $UCS = 11.0761 \cdot I_{S50}$ |
| Binal (2009) | non-welded to moderately welded ignimbrites | $UCS = 9 \cdot I_{S50}$ |
| Kaya & Karaman (2016) | Pyroclastic, volcanic & plutonic rocks<br>sedimentary rocks<br>metamorphic rocks | $UCS = 12.98 \cdot I_{S50} \rightarrow 17.68 \cdot I_{S50} \rightarrow 15.32 \cdot I_{S50}$<br>$UCS = 18.55 \cdot I_{S50} \rightarrow 13.51 \cdot I_{S50}$<br>$UCS = 14.26 \cdot I_{S50} \rightarrow 16.24 \cdot I_{S50}$ |

**Table 5–1.** A non-exhaustive compilation of PLT-UCS conversion equations and relationships (linear, non-linear, power etc) for a variety of lithologies. Units for both UCS (uniaxial compressive strength) and $I_{S50}$ (point load index test, standardised to 50 mm core diameter) are MPa. Arrow (→) denotes range of values.

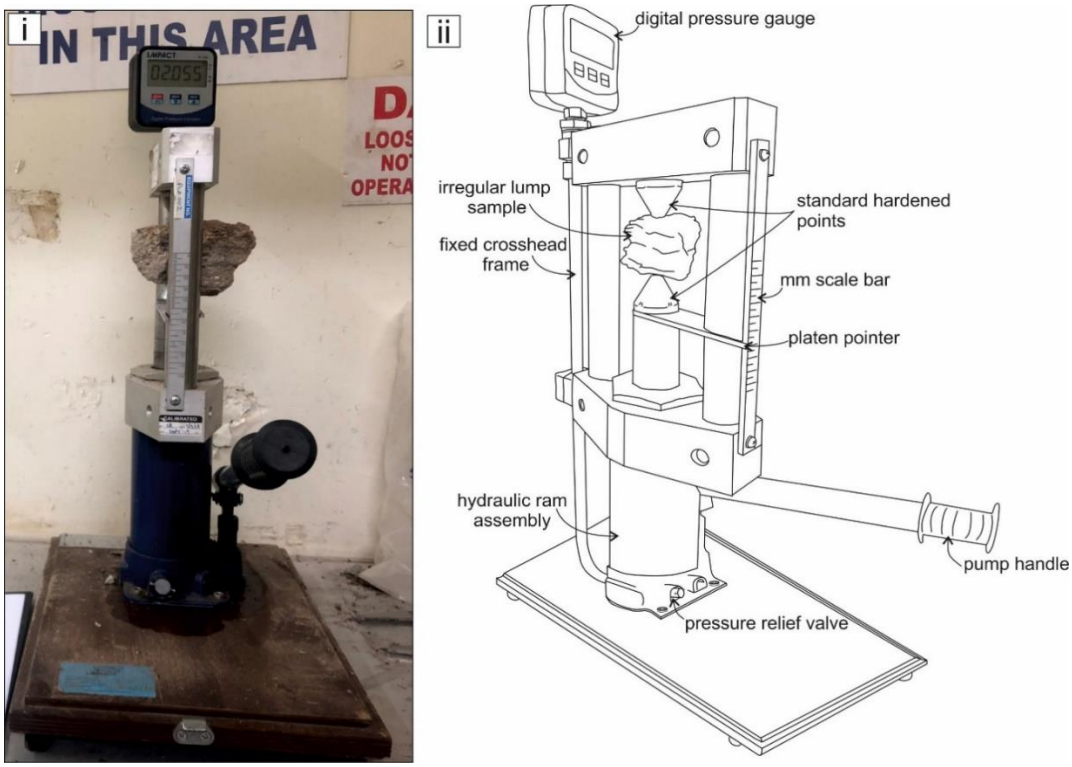


**Figure 5–3.** Digital PLT experimental apparatus (Impact Digital Point Load Tester), Terra Tek Ltd Laboratory: (i) photograph and (ii) annotated illustration of an irregular lump sample held in the PLT apparatus, prior to being tested.

PLT measurements were made so that $\sigma 1$ and the platen contact was perpendicular to any foliation, lineations, crystal alignment, fabrics or flow banding present in the samples (ISRM, 1985), to ensure that the results related to the same material property. A load is then applied manually and gradually increased until the sample breaks for between 10-60 seconds. The validity of the test is confirmed only if the fracture surface extends between the two conical points. In order to account for discrepancies and inhomogeneity of samples (i.e. lithophysae, voids, uneven crystal distribution, etc), PLT measurements were repeated a minimum of five times per sample. Values were obtained by discarding the lowest and highest measurements and calculating a mean value, following the procedure outlined by ISRM (1985) and Quane and Russell (2003).

### 5.1.4. Results

The range of measured PLT ($PLT_m$) values for the samples (Table 5–2) fall between 0.19 and 12.98 MPa, with the predicted UCS ($UCS_p$) values ranging from 1.2 - 316.63 MPa, spanning the full suite of rock strength classifications, from extremely weak to extremely strong (Table 5–3).

| Sample | $PLT_m$ (MPa) | $UCS_p$ (MPa) | Rock Strength Rating (GSEGWP, 1970) | Member & Unit | |
|---|---|---|---|---|---|
| **TN-48** | 6.24 | 152.13 | Very strong | 1 | Atravesado |
| **TN-47** | 3.82 | 77.79 | Strong | | |
| **TN-24** | 5.19 | 126.64 | Very strong | | |
| **TN-46** | 9.07 | 221.39 | Extremely strong | 2 | |
| **TN-32** | 3.04 | 52.85 | Strong | | |
| **TN-45** | 0.42 | 3.02 | Very weak | | |
| **TN-33** | 10.28 | 250.91 | Extremely strong | 3 | |
| **TN-35** | 10.31 | 251.65 | Extremely strong | | |
| **TN-01** | 5.29 | 128.99 | Very strong | 4 | |
| **TN-23** | 4.23 | 97.98 | Strong | | |
| **TF-04** | 2.94 | 50.07 | Moderately strong - strong | | |
| **TN-44** | 0.24 | 1.58 | Very weak - weak | | |
| **TN-40** | 11.96 | 291.91 | Extremely strong | A | Retamares |
| **TN-10** | 5.08 | 124.03 | Very strong | | |
| **TN-02** | 0.58 | 4.61 | Weak | | |
| **TN-03** | 4.25 | 98.61 | Strong | | |
| **TN-05** | 5.68 | 138.51 | Very strong | B | |
| **TN-41** | 2.93 | 49.76 | Moderately strong | | |
| **TF-03** | 1.90 | 24.67 | Moderately weak – moderately strong | | |
| **VF-16/1** | 4.45 | 104.97 | Very strong | | |
| **TF-02** | 3.53 | 68.15 | Strong | C | |
| **TN-43** | 1.14 | 11.46 | Moderately weak | | |
| **TN-06** | 2.31 | 33.73 | Moderately strong | | |
| **TN-09** | 1.66 | 19.95 | Moderately strong | | |
| **TN-42** | 11.30 | 275.60 | Extremely strong | D | |
| **TF-01** | 7.46 | 182.02 | Very strong | | |
| **TN-14** | 6.72 | 164.05 | Very strong | E | |
| **TN-22** | 9.63 | 235.03 | Extremely strong | | |
| **TN-15** | 2.29 | 33.19 | Moderately strong | | |
| **TF-09** | 4.95 | 121.49 | Very strong | | |
| **TN-19** | 1.48 | 16.82 | Moderately weak | F | |
| **TN-20** | 4.63 | 110.83 | Very strong | | |
| **TN-21** | 0.39 | 2.82 | Weak | | |
| **TN-17** | 1.23 | 12.79 | Moderately weak | G | |
| **TN-18** | 0.19 | 1.21 | Very weak | | |
| **VF-16/2** | 2.82 | 46.63 | Moderately strong | SdC | Chasna |
| **TN-08** | 2.94 | 50.07 | Moderately strong – strong | | |
| **TN-07** | 4.31 | 100.72 | Strong – very strong | | |
| **TN-38** | 5.56 | 135.75 | Very strong | RlA | |
| **TN-36** | 8.63 | 210.49 | Very strong – extremely strong | | |
| **VF-16/3** | 7.34 | 179.18 | Very strong | | |
| **TF-06** | 3.49 | 66.73 | Strong | | |
| **TN-12** | 3.2 | 57.53 | Strong | LdlM | |
| **TN-04** | 2.19 | 30.96 | Moderately strong | | Almendros |
| **TF-05** | 0.71 | 5.99 | Weak – moderately weak | | Chasna ridge |
| **VF-16/4** | 4.05 | 92.61 | Strong | | |
| **TN-11** | 4.16 | 95.80 | Strong | | |
| **TF-08** | 1.86 | 23.93 | Moderately weak – moderately strong | 2 | Guajara |
| **TN-30** | 4.53 | 107.78 | Very strong | 3 | |
| **TN-28** | 4.41 | 103.69 | Very strong | | |
| **TN-29** | 12.98 | 316.63 | Extremely strong | | |
| **TN-27** | 4.77 | 111.47 | Very strong | SW | Areñas |
| **TN-26** | 1.74 | 21.58 | Moderately weak – moderately strong | | |
| **TN-25** | 2.92 | 49.41 | Moderately strong | | |

**Table 5–2.** Measured point load index test values ($PLT_m$) are the mean value of all measurements taken, discarding the lowest and highest value. Members and units are listed from oldest to youngest. The predicted uniaxial compressive strength ($UCS_p$) are calculated using both Quane & Russell's (2003) linear and non-linear conversion equation for 'weak' rocks (< 5 MPa $PLT_m$) and for 'strong' rocks (> 4 MPa $PLT_m$) retrospectively. An average was taken of the results of both formulas for rocks of strengths that fall between these determinations.

| Rock strength rating | UCS (MN/m$^2$) | UCS (MPa) | PLT (MPa) | Rating | UCS (MPa) | PLT (MPa) |
|---|---|---|---|---|---|---|
| (GSEGWP, 1970) | | (Hoek & Brown, 1980) | | | (Hoek & Brown, 1997 | |
| Extremely strong | > 200 | >200 | >8 | 15 | > 250 | > 10 |
| Very strong | 100 – 200 | 100 – 200 | 4 - 8 | 12 | 100 – 250 | 4 – 10 |
| Strong | 50 – 100 | 50 – 100 | 2 - 4 | 7 | 50 – 100 | 2 – 4 |
| Moderately strong | 12.5 – 50 | 25 – 50 | 1 - 2 | 4 | 25 – 50 | 1 – 2 |
| Moderately weak | 5 – 12.5 | 10 – 25 | - | 2 | 5 - 25 | - |
| Weak | 1.25 – 5 | 3 – 10 | - | 1 | 1 – 5 | - |
| Very weak | < 1.25 | 1 - 3 | - | 0 | 0.25 1 | - |

**Table 5–3.** Descriptive terminology for rock strength ratings of uniaxial compressive strength (UCS) and point load index test (PLT). Values are not typically present for PLT < 25 MPa in standard classifications. Distinguishing between weak and extremely weak is likely to result in ambiguous values (after Deere & Miller, 1966; Hoek & Brown, 1997; 1980; ISRM, 1985).

## 5.2. Porosity and density determination

### 5.2.1. Methodology

Rock testing to obtain porosity (pore volume) and density (bulk volume) values of the samples was undertaken at MATtest Limited, a UKAS accredited laboratory. Samples were tested using the Saturation and Buoyancy method following the ISRM's (1981) suggested methods.

A total of 53 samples were tested across 19 individual units, with between one and four samples per unit representing the basal, middle or uppermost regions of the deposits. Where possible, each sample was broken or sawed into 10 lumps of irregular geometry, each having a mass of at least ~ 50 g for standard testing. Non-standard testing was done on samples with between 5 and 9 irregular lumps due to lack of available material.

Samples are then washed with water to remove any dust or sediment obtained during preparation. Each sample was then saturated by water immersion within a vacuum vessel, which is maintained at 0.8 kPA, for approximately an hour (Figure 5–4 i). The samples are then transferred in a container of water to a submerged wire basket to measure the saturated-submerged mass (Figure 5–4 ii). The mass is then measured again after the submerged samples have been removed from the water and gently dried with a moist cloth to remove the surface water. The samples are then fully dried in an oven set at 105±3 °C for 24 hours and the oven dried mass of the sample is measured. The full observations and list of calculations

to determine pore volume and dry density for each sample tested is listed in Appendix II.


**Figure 5–4.** Apparatus used in porosity and density determination at MATtest Limited laboratory, Glasgow: i) samples submerged in water in the vacuum vessel, prior to weighing in (ii) the submerged wire basket in an immersion bath to determine the saturated-submerged mass

### 5.2.2. Results

The results from porosity and density determination from samples representing the base, middle and uppermost horizons of nineteen individual units, across the six proposed members is presented in Table 5–4. Values of dry bulk rock density range from between 870 and 2630 kg/m$^3$. A wide range of porosity values are also seen, ranging from 0.9 to 53 %.

| Sample | Test | Dry density (kg/m$^3$) | Porosity % | Φ | Member & Unit | |
|---|---|---|---|---|---|---|
| **TN-48** | Non-standard | 2520 | 3.9 | 0.04 | 1 | Atravesado |
| **TN-47** | Non-standard | 2400 | 2.3 | 0.02 | | |
| **TN-24** | Non-standard | 2320 | 9.3 | 0.09 | | |
| **TN-46** | Non-standard | 2550 | 3.6 | 0.04 | 2 | |
| **TN-32** | Non-standard | 2390 | 11.6 | 0.12 | | |
| **TN-45** | Non-standard | 2420 | 11.2 | 0.11 | | |
| **TN-33** | Non-standard | 3440 | 4 | 0.04 | 3 | |
| **TN-35** | Non-standard | 2530 | 2.6 | 0.03 | | |
| **TN-01** | Standard | 2500 | 1.5 | 0.02 | 4 | |
| **TN-23** | Standard | 2210 | 9 | 0.09 | | |
| **TF-04** | Standard | 2560 | 1 | 0.01 | | |
| **TN-44** | Non-standard | 870 | 53 | 0.53 | | |
| **TN-40** | Non-standard | 2630 | 3.4 | 0.03 | A | Retamares |
| **TN-10** | Non-standard | 2190 | 5.8 | 0.06 | | |
| **TN-02** | Non-standard | 1610 | 30.4 | 0.30 | | |
| **TN-03** | Non-standard | 2440 | 4.4 | 0.04 | | |
| **TN-05** | Non-standard | 2360 | 2.8 | 0.03 | B | |
| **TN-41** | Standard | 1980 | 16.8 | 0.17 | | |
| **TF-03** | Standard | 2100 | 12.3 | 0.12 | | |
| **VF-16/1** | Standard | 2180 | 7.4 | 0.07 | | |
| **TF-02** | Standard | 2330 | 3.6 | 0.04 | C | |
| **TN-43** | Non-standard | 2040 | 15 | 0.15 | | |
| **TN-06** | Standard | 2190 | 13.1 | 0.13 | | |
| **TN-09** | Standard | 2280 | 1.1 | 0.01 | | |
| **TN-42** | Non-standard | 2590 | 2.3 | 0.02 | D | |
| **TF-01** | Standard | 2500 | 1.3 | 0.01 | | |
| **TN-14** | Non-standard | 2500 | 5.2 | 0.05 | E | |
| **TN-22** | Non-standard | 2470 | 4.9 | 0.05 | | |
| **TN-15** | Non-standard | 2050 | 10.8 | 0.11 | | |
| **TF-09** | Standard | 2240 | 5.5 | 0.06 | | |
| **TN-19** | Non-standard | 1970 | 24.4 | 0.24 | F | |
| **TN-20** | Standard | 2230 | 11.1 | 0.11 | | |
| **TN-21** | Non-standard | 1060 | 43.2 | 0.43 | | |
| **TN-17** | Non-standard | 2020 | 20.6 | 0.21 | G | |
| **TN-18** | Non-standard | 1160 | 40.6 | 0.41 | | |
| **VF-16/2** | Standard | 2100 | 11.8 | 0.12 | S | Chasna |
| **TN-08** | Non-standard | 2200 | 9.9 | 0.10 | | |
| **TN-07** | Non-standard | 1860 | 13.6 | 0.14 | | |
| **TN-38** | Non-standard | 2340 | 2.5 | 0.03 | R | |
| **VF-16/3** | Non-standard | 2370 | 2.8 | 0.03 | | |
| **TF-06** | Non-standard | 2450 | 4.8 | 0.05 | | |
| **TN-12** | Non-standard | 2630 | 2.7 | 0.03 | 2.0 | |
| **TN-04** | Non-standard | 2320 | 10 | 0.10 | | Almendros |
| **TF-05** | Standard | 2160 | 11.8 | 0.12 | | Chasna ridge |
| **VF-16/4** | Standard | 2160 | 9.1 | 0.09 | | |
| **TF-08** | Standard | 1890 | 16.8 | 0.17 | 2 | Guajara |
| **TN-30** | Non-standard | 2350 | 3.7 | 0.04 | | |
| **TN-28** | Non-standard | 2250 | 9.4 | 0.09 | 3 | |
| **TN-29** | Non-standard | 2610 | 1.3 | 0.01 | | |
| **TN-27** | Non-standard | 2330 | 4.9 | 0.05 | SW | Areñas |
| **TN-31** | Non-standard | 2440 | 0.9 | 0.01 | | |
| **TN-26** | Non-standard | 2150 | 15.2 | 0.15 | | |
| **TN-25** | Non-standard | 2100 | 13.9 | 0.14 | | |

**Table 5–4.** Results of density and porosity determination using the saturation and buoyancy method (ISRM 1981). Standard testing followed the ISRM (1981) procedure, using a minimum of ~ 500 g of sample, consisting of 10 irregular lumps, each weighing ~ 50 g. Non-standard testing was carried out with between 5 and 9 irregular lumps of material, each weighing ~ 50 g.

## 5.3. Oblateness of pumice lapilli

The extent of welding deformation can be derived from measuring features such as pyroclast 'flattening' or oblateness. Oblateness is considered a direct measure of welding intensity and can provide insights into the extent of welding in rocks that have undergone subsequent alteration, which may have impacted and overprinted other metrics of welding (i.e. strength and porosity) but where vitroclastic textures remain (Quane & Russell, 2005).

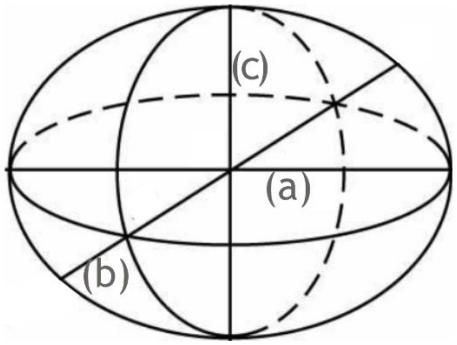


**Figure 5–5.** Deformed pumice lapilli behave like flattened ellipsoids, with two equatorial axes: (a) and (b), and a polar axis (c).

Pumice lapilli progressively deform to form fiamme (Sheridan & Ragan, 1976; Peterson 1979), which behave like flattened ellipsoids (Figure 5–5), with shortening of the polar axis, or height (c-axis), and a paired changed observed in the equatorial axes (a- and b-axis) (Ragan & Sheridan, 1972). Flattening is typically measured as the ratio of fiamme length to height (a:c), however oblateness measures the full extent of deformation, assuming that both a- and b- axes are equal, using the equation:

$$OB = 1 - \frac{c}{a}$$

The closer the oblateness value is to 1, the more deformation, and therefore a greater intensity of welding can be inferred.

### 5.3.1. Methodology

Where possible, the oblateness of pumice lapilli present in samples was measured from field observations, collected samples and petrographic analysis. Similarly to

the method outlined in Quane and Russell (2005), the reported values of oblateness are the mean of 20 measurements on pumice lapilli with a minimum area of 2 $mm^2$. Some facies were too limited in pumice lapilli to be accurately measured, and it was not possible to use this method in facies exhibiting such high intensity welding, where vitroclastic textures were obliterated completely.

### 5.3.2. Results

The measured mean oblateness values from 39 samples are presented in Table 5-5, with values ranging from 0.33 to 0.92. The full dataset of measurements taken from each sample is available is found in Appendix III.

| Sample | Mean OB | Member & Unit | |
|---|---|---|---|
| **TN-47** | 0.88 | 1 | Atravesado |
| **TN-24** | 0.33 | | |
| **TN-46** | 0.92 | 2 | |
| **TN-32** | 0.75 | | |
| **TN-45** | 0.27 | | |
| **TN-35** | 0.92 | 3 | |
| **TF-04** | 0.65 | 4 | |
| **TN-44** | 0.42 | | |
| **TN-40** | 0.84 | A | Retamares |
| **TN-10** | 0.65 | | |
| **TN-02** | 0.63 | | |
| **TN-03** | 0.44 | | |
| **TN-05** | 0.92 | B | |
| **TN-41** | 0.54 | | |
| **TF-03** | 0.58 | | |
| **VF-16/1** | 0.53 | | |
| **TF-02** | 0.91 | C | |
| **TN-43** | 0.79 | | |
| **TN-06** | 0.62 | | |
| **TN-09** | 0.70 | | |
| **TF-01** | 0.81 | D | |
| **TN-22** | 0.84 | E | |
| **TN-15** | 0.83 | | |
| **TF-09** | 0.57 | | |
| **TN-20** | 0.64 | F | |
| **TN-21** | 0.34 | | |
| **TN-18** | 0.65 | G | |
| **TN-07** | 0.69 | S | Chasna |
| **VF-16/3** | 0.85 | R | |
| **TF-06** | 0.77 | | |
| **TN-04** | 0.83 | | Almendros |
| **TF-08** | 0.75 | 2 | Guajara |
| **TN-27** | 0.93 | SW | Areñas |
| **TN-31** | 0.83 | | |
| **TN-26** | 0.64 | | |
| **TN-25** | 0.91 | | |

**Table 5–5.** Results of oblateness measurements taken on each sampled facies.

## 5.4. Discussion

Strong correlations are observed in the relationships between rock strength (PLTm and UCSp) and measured dry density and porosity (Figure 5–6) when plotted against stratigraphic position, providing indication that strength determination may be an effective, semi-quantitative means of welding classification for these units. Rock strength determination is considered an indirect measure of welding intensity compared to density and porosity due to higher uncertainties in comparisons with the other metrics (Quane & Russell, 2003; 2005).

Post-emplacement processes in pyroclastic deposits (e.g. pervasive secondary crystallisation) is likely to impact the strength, and thus its application as a metric of welding intensity (e.g. Streck & Grunder, 1995; Quane & Russell, 2005). Both the bulk composition of the magma and post-emplacement processes (e.g. secondary crystallisation, vapour phase alteration, lithophysae etc), as discussed previously, can also influence the effectiveness of density as a metric of welding intensity, but high correlation co-efficient values with the other metrics (Table 5–6) provide confidence in its application for this study. Porosity also has the potential to be impacted by post-emplacement processes and alteration (e.g. secondary porosity via vapour phase alteration, secondary crystallisation, rheomorphism etc) and measures were taken to mitigate these effects, through selective and consistent sampling and only measuring bulk porosity. The relationship between porosity and density is near linear (Figure 5–7 i; Table 5–6), with high correlation coefficients, indicating that the welding of these units is accomodated by porosity loss.

As porosity and density have almost perfect correlation, the relationship between rock strength and porosity shows the least amount of variance (~ 0.5) in the r values seen across the relationships between the measured physical properties of the deposits (Table 5–6). Slightly higher, but ultimately low variance is shown in the values for UCS vs. density and density vs. porosity, ~ 0.6 and 0.8, respectively. Rock strength and density have a non-linear relationship, with a gradual increase in both strength and density up until ~2.6 g/cm$^3$, then strength continues to increase with very little change in density. Similar relationships are observed in previous studies (e.g. in the Yucca Mt. Tuff - Price & Bauer, 1985; the Bandelier

Tuff - Quane & Russell, 2003; 2005) but with much lower values of both metrics, and are attributed to progressive mechanical strengthening of the pyroclastic material after a certain amount of densification has taken place. As glassy particles sinter and weld under progressive densification, the contact area of individual ash particles increases, leading to an increase in the strength of the material.

Relatively weaker correlations are seen in the oblateness of pyroclastics with the measured physical properties (Figure 5-7 v & vi). In the relationship between density and oblateness, there is a sharp trend in flattening with increasing density up to ~ 2.1 g/cm$^3$, and then above this, a range of oblateness values are seen, associated with very little change in density, similar to the trend shown by density and rock strength. Progressive densification accounts for the initial flattening of pumice lapilli taking place, however the limited change in density between ~2.3 – 2.6 g/cm$^3$ indicates flattening is still taking place. During welding, deformation of pumice lapilli occurs at a faster rate than the surrounding ash matrix (Sheridan & Ragan, 1976; Streck & Grunder, 1995), which is able to maintain porosity longer, having up to ~10% when a total loss of porosity is seen in the pumice lapilli (Sheridan & Ragan, 1976; Streck & Grunder, 1995). The fundamental differences between these two components, and even between just the pumice lapilli component of a deposit (e.g. differences in initial porosity, chemical composition and bulk density) could explain the observed decoupling of welding processes (Streck & Grunder, 1995; Quane & Russell, 2005), particularly between porosity and oblateness, as well the effect of emplacement temperature, as discussed in Chapter 7.

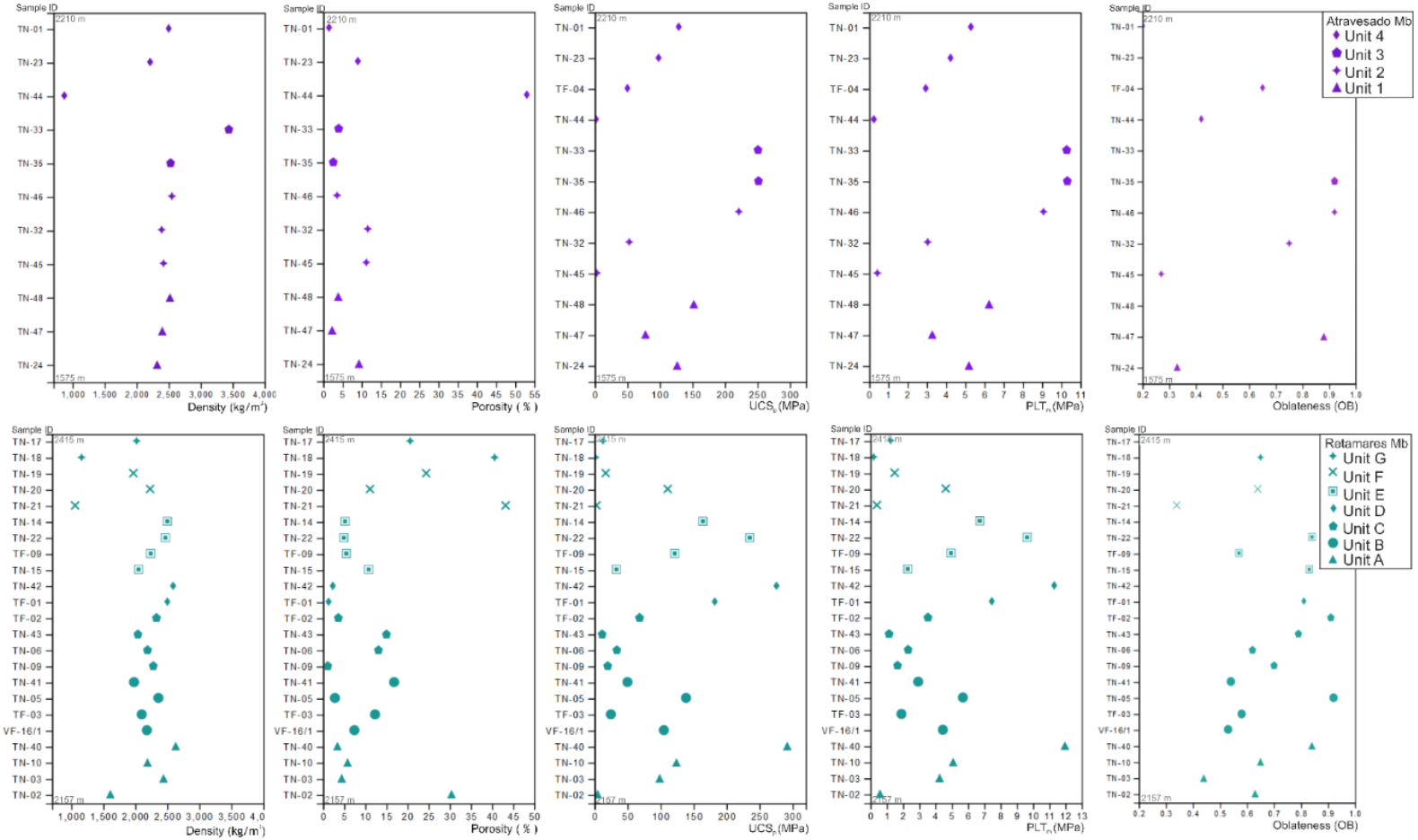


Continues overleaf

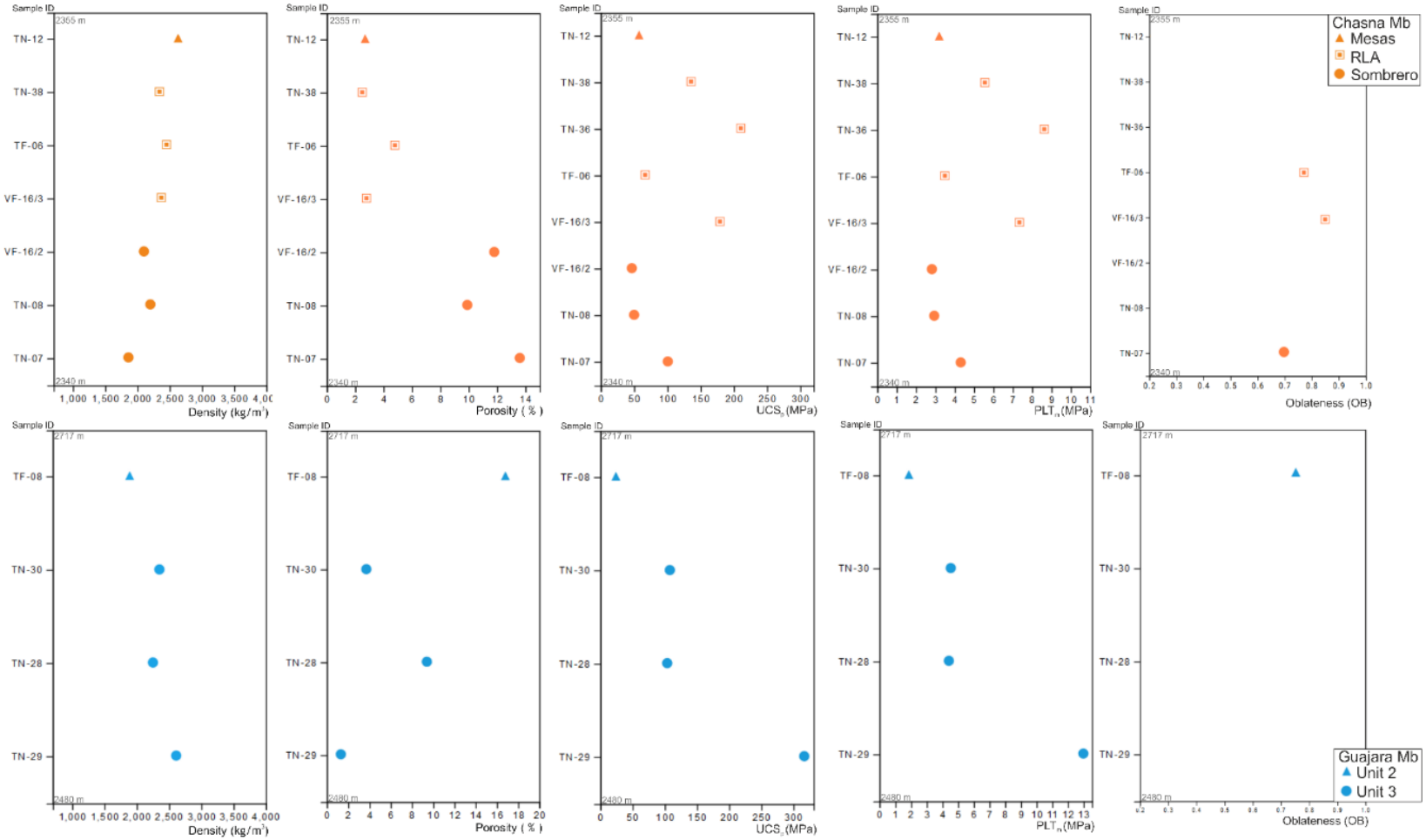


Continues overleaf

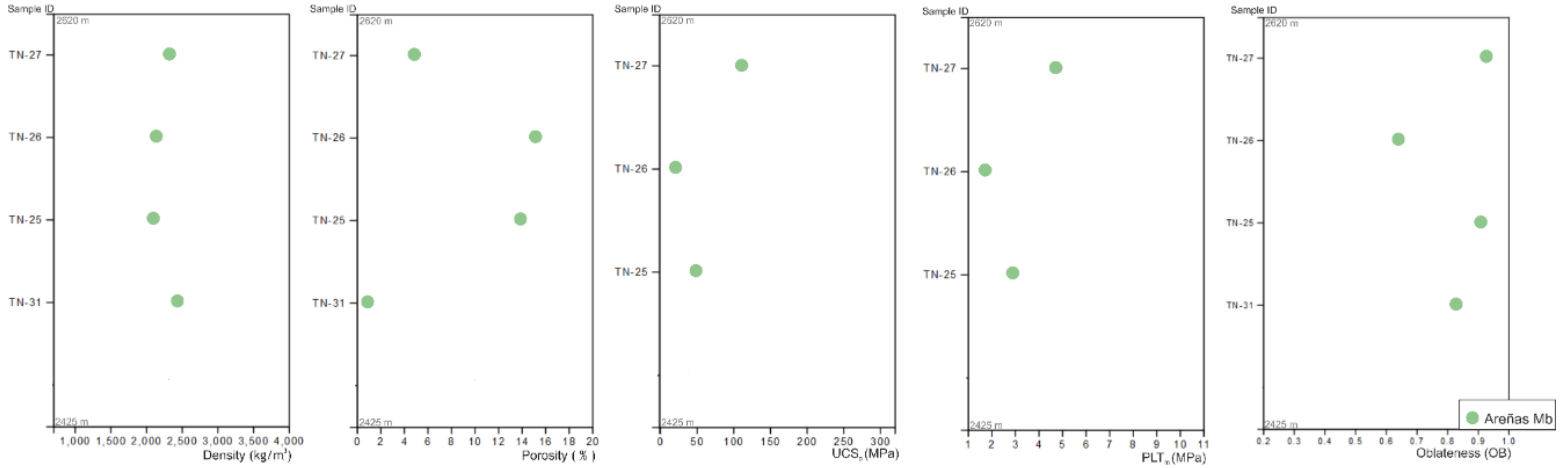


**Figure 5–6.** The physical properties (density, porosity, strength and oblateness) results of samples, plotted from the base to the top of the stratigraphy of each Member. The function of elevation is not given due to the topographically controlled nature and uneven thicknesses of the deposits, but the basal and upper-most sample elevations (in metres) are marked on each plot for reference.

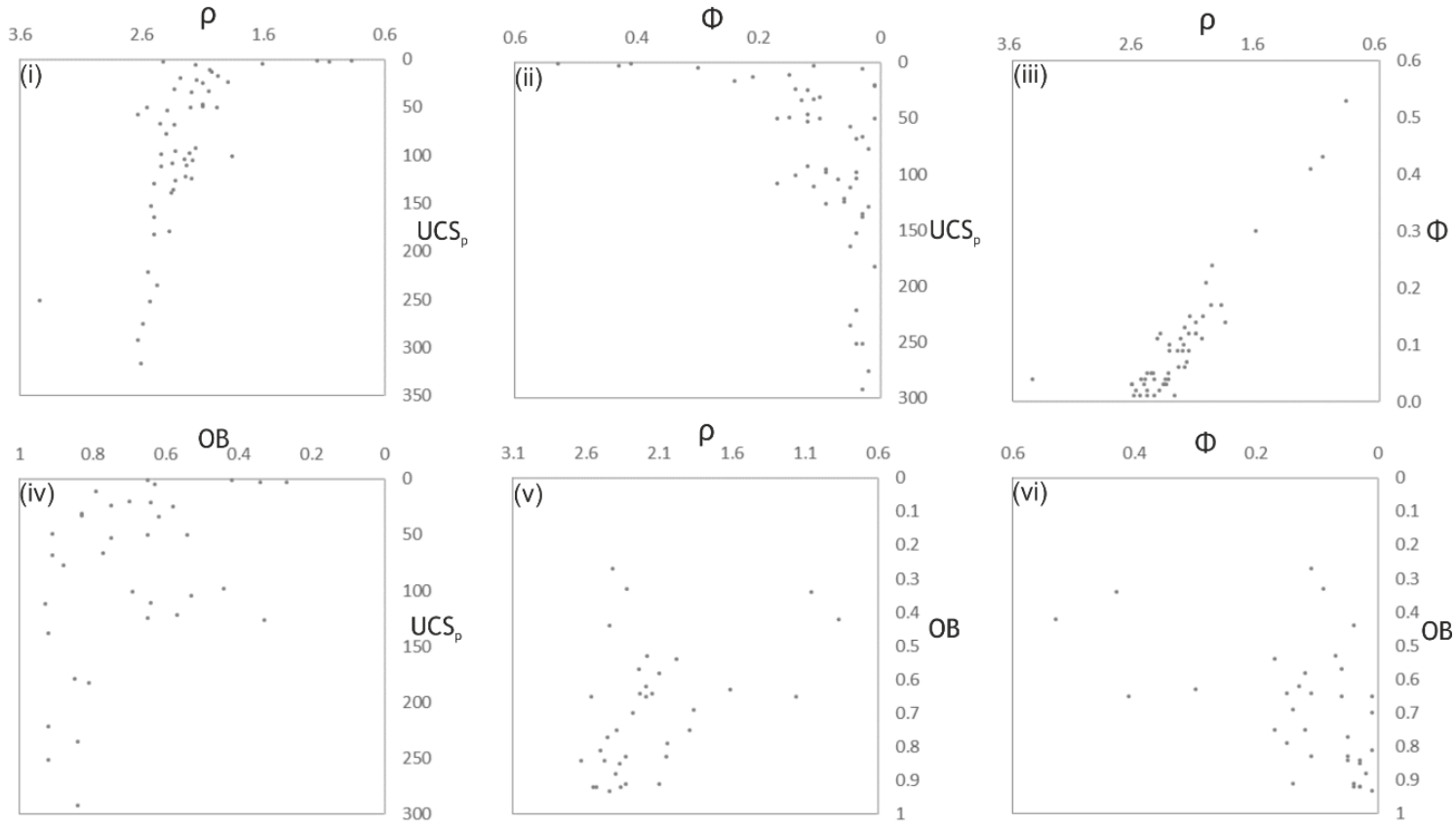


**Figure 5–7.** Relationships between the metrics: density (ρ), porosity (Φ), rock strength ($UCS_p$), and oblateness of pumice lapilli (OB). Strong, near linear relationships are shown by density vs. both strength (i) and porosity (iii), and porosity with strength (ii). Weaker, more sporadic relationships are seen with oblateness vs. strength (iv), density (v) and porosity (vi).

| Member | Unit | $UCS_p$ - ρ $r$ | $UCS_p$ - Φ $r$ | ρ - Φ $r$ | OB - $UCS_p$ $r$ | OB - ρ $r$ | OB - Φ $r$ |
|---|---|---|---|---|---|---|---|
| Atravesado | 1 | 0.44 | 0.39 | -0.65 | -1 | 1 | -1 |
| | 2 | 0.92 | -0.96 | -0.99 | 0.84 | 0.57 | 0.70 |
| | 3 | -1 | -1 | 1 | - | - | - |
| | 4 | 0.97 | -0.97 | -0.99 | - | - | - |
| Retamares | A | 0.85 | -0.73 | -0.94 | 0.68 | 0.20 | 0.07 |
| | B | 0.85 | -0.87 | -0.99 | 0.70 | 0.85 | -0.75 |
| | C | 0.73 | -0.41 | -0.87 | 0.57 | 0.24 | -0.29 |
| | D | 1 | 1 | 1 | - | - | - |
| | E | 0.91 | -0.88 | -0.81 | 0.10 | 0.08 | 0.39 |
| | F | 0.75 | -0.88 | -0.98 | 0.07 | 0.70 | -0.54 |
| | G | 1 | -1 | -1 | - | - | - |
| Chasna | Mesas | - | - | - | - | - | - |
| | RLA | -0.79 | -0.87 | 0.99 | 0.89 | -1 | -1 |
| | Sombrero | -0.94 | 0.83 | -0.97 | - | - | - |
| Almendros | GUA | 0.87 | -0.98 | 0.98 | 0.78 | 0.24 | -0.44 |
| | RLA | - | - | - | - | - | - |
| Guajara | 2 | - | - | - | - | - | - |
| | 3 | 0.97 | -0.74 | -0.89 | - | - | - |

**Table 5–6.** The correlation coefficients ($r$ values) for the measured physical properties (density, porosity and strength determination) for each unit throughout the stratigraphy.

### 5.4.1. Correlation with field observations

There is a strong correlation in the relationships between measured density, porosity, and rock strength and our field determined welding intensity, providing confidence in the use of these metrics as analogues for semi-quantitatively mapping welding intensity. Field-based welding classification based solely on observations, lithofacies categorisation and extensive logging of deposits, alongside flatness ratios and oblateness measurements, represents a spectrum of welding intensities across the units, which can vary wildly in scale, from one end member to another across a few centimetres to tens of metres.

Generalised welding profiles based on qualitative field determinations of welding intensity for each Member, alongside schematic sections, is presented in Figure 5-8, using the terminology outlined in Chapter 2, from non-welded to lava-like.

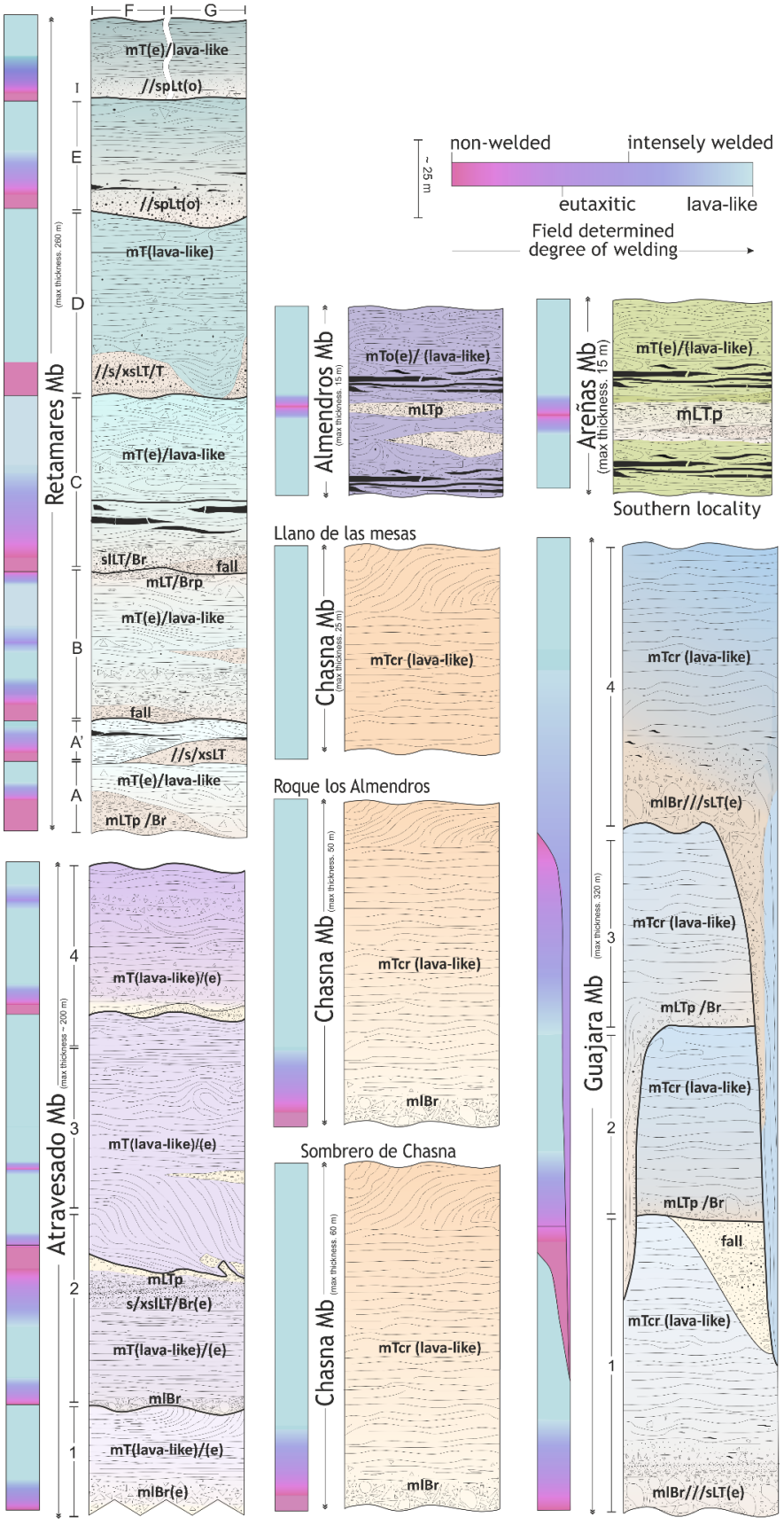


**Figure 5–8.** Schematic, generalised welding profiles for mapped units based solely on field observations. Field relationships are simplified to present welding profiles for each unit, see Figure 4-3 in Chapter 4 for more detailed stratigraphic representation.

#### 5.4.1.1. Atravesado Member

Each unit of the Atravesado Mb exhibits a general increase in oblateness and ρ from base to top, coupled with a decrease in Φ, but this trend is not followed by Unit 3, which shows homogeneity throughout the deposit, with only a marginal (<2%) change in Φ from base to top (Figure 5–6). Strength measurements largely follow these trends, increasing upwards, with again the exception of Unit 3, with little change seen throughout, and Unit 1 where there is an observed loss in strength in the middle of the unit. An upwards progressive increase in welding intensity, from non-welded at the base, to predominantly lava-like is seen in Units 1, 2, and 4 (Figure 5–8, 4–15 – 4–34), consistent with the trends in the measured physical properties. Unit 3, the thickest of the Atravesado units, shows little variation in welding intensity, with a lava-like lithofacies from base to top (Figure 5–8, 4–16 - 4–23), consistent with the homogeneity shown in the measured metrics. Although there is evidence of post-emplacement rheomorphism in the lava-like lithofacies in these units (e.g. Figure 4–17) the metrics closely align with welding intensity, with increases in ρ, strength and OB, and a loss in Φ. The loss in strength observed in the lava-like lithofacies of Unit 1 could be attributed to post-emplacement deformation, as ramping up and folding in the fabric may have impacted the properties of the deposit.

#### 5.4.1.2. Retamares Member

The units of the Retamares Mb exhibit more complex and variable profiles of welding intensity (Figure 5–8), which can oscillate back and forth between the end members within individual units (e.g. Figure 4–46, 4–58, 4–70, & 4–84) and welded lithofacies can be punctuated by lenses and discontinuous horizons of lesser and non-welded material (e.g. Figure 4–38, 4–39, 4–67, & 4–81). There is a clear correlation between the field determined and the measured metrics of welding intensity. All units, with the exception of Units B, C, and F, show general increases in ρ from base to top, coupled with a decrease in Φ and increases in strength and oblateness (Figure 5–6), nicely aligning with the schematic welding profiles in Figure 5–8, from non-welded at the base to intensely welded and lava-like. More variable welding is shown by Unit B, which is non-welded at the base and uppermost regions of the deposit, and predominantly lava-like for most of its

thickness, but interfingered with lenses of lesser welded pumice lapilli (Figure 4–38). This is reflected in the metrics trends, with the highest values of ρ, oblateness and strength, and lowest Φ seen towards the centre of the unit where the welding is most intense. Unit C displays more variable trends despite having a similar welding profile to the majority of the units. A minor loss in ρ, coupled with increasing Φ is observed in the lower three quarters of the unit, with the highest ρ and lowest Φ seen at the uppermost horizon of the unit. However, strength and oblateness progressively increase throughout, mirroring the observed welding profile. The disparity between the metrics here may be a result of lithophysae growth (e.g. Figure 4–56), which could impact the density and increase the porosity of the deposit. The metrics of welding for Unit F also largely follow those classified in the field with the exception of those in the uppermost horizon. A progressive increase in strength and ρ is observed, followed by much lower values at the top of the unit, and as expected the opposite trend is observed in the Φ values. However, oblateness shows a continual increase throughout, suggesting that again, alteration (e.g. post-depositional processes, rheomorphism) of the physical properties has occurred, but has not completely overwritten the fabric and textures, with faint 'ghost' vitroclastic textures remaining.

#### 5.4.1.3. Chasna Member

The units of the Chasna Mb are predominantly lava-like with a progressive increase in welding, from non- to partially welded at the base, to lava-like, as observed in both the Roque los Almendros and Sombrero de Chasna localities (Figure 5–8). There is not as strong a correlation with the measured metrics in these units as with those seen in the Atravesado and Retamares Members. In the RLA locality, there is little to no change observed in ρ throughout the deposit, with variable, negatively paired Φ and strength. An initial increase in density is seen by the unit at SdC locality, with the highest ρ value in the middle of the unit, and decreases again towards the top, which inversely correlates with Φ values. Rheomorphism is observed towards the uppermost regions of these units, with prolate vesicles and ramping of the fabric (e.g. Figure 4–100), which explains the loss of density and increased porosity observed towards the top of each unit, rather than an inferred decrease in welding intensity.

The unit at the Llano de las Mesas locality is lava-like from base to top with little to no observed variation in welding intensity. Due to a lack of material suitable for testing, results from only the top of this deposit are available, which shows the highest ρ values observed across all of the localities, paired with low Φ and relatively very low strength compared to the others. A lack of flattened pyroclasts, fiamme or textures observed in the lava-like lithofacies across the units meant that establishing oblateness values was not possible.

#### 5.4.1.4. Almendros Member

The Almendros Mb display a generalised increase in welding from base to top, with much variability in welding intensity seen in the lowermost third of the units, from non- to densely welded, grading up in to a predominantly lava-like lithofacies (Figure 5–8, 4–103 & 4–104). Only the base of the was tested due to lack of available material, so trends are not established for this unit, but it plots within the same range as the basal sample from Areñas Mb.

#### 5.4.1.5. Guajara Member

Units 2 and 3 of the Guajara Mb both display a progressive increase in welding, from a predominantly non-welded breccia basal region, grading up into a thick, lava-like tuff (Figure 5–8 & 4–107). The measured metrics of Unit 3 show an initial reduction in density and strength, with very little change observed between the mid and uppermost horizons of the unit, inversely correlated with Φ. The inhomogeneity of the transition between lower intensities of welding and the lava-like lithofacies which dominates much of the thickness of the unit may account for the initial decrease in strength and Φ. Oblateness values are not established due to the intense nature of welding. The uppermost horizon of Unit 2 shows lower ρ and strength values, and higher Φ than those of Unit 3.

#### 5.4.1.6. Areñas Member

The Areñas Mb (southwestern locality) exhibits an initial loss, and then progressive increase in both ρ and strength values, negatively paired with Φ. Oblateness is more variable but generally aligns with the field classifications of welding, oscillating from 0.6 to 0.93 (Figure 5–8).

### 5.4.2. Limitations and further work

More sampling at closer intervals, both throughout individual units and across the stratigraphy would have allowed for more frequency and detail in tracking the changes throughout the deposits and the relationships between the physical properties of the ignimbrites, especially in the Almendros and Guajara Members, where more sampling and data is needed for a complete, comprehensive insight into the welding variation. Sampling vertical profiles at different locations within the same deposit would allow welding intensities to be tracked laterally, and at different thicknesses, providing deeper insights to the effects of deposit thickness and topography on the welding process.

Ideally, sampling would have allowed for more standardised testing, especially in the porosity and density determination, and a higher volume of material would have been tested. The saturation and buoyancy method (ISRM, 1985) used in this study was selected due to the low cost and the ability to do the testing on chips or gravel of material, which allowed the same samples to undergo multiple testing (to determine strength, $\Phi$ and $\rho$) . Other methods to determine matrix density, unconnected (isolated) porosity and skeletal porosity (i.e. The Saturation and Caliper method: ISRM, 1985; helium pycnometry: Rust et al., 1999), may provide better insights to the nature of these metrics, to allow more comprehensive comparisons with other published data on welded ignimbrites.

## 5.5. A framework for welding classification

Quane & Russell (2003) initially proposed four initial welding zones (I-IV), with a suggested range of PLT values, from 0 MPa, for very weak to weak rocks, to a maximum of 1.95 MPa for moderately weak to moderately strong, to account for unwelded up to moderately welded facies, as welding intensities and lithofacies beyond 'moderately welded' are not observed in the Bandelier Tuff. This was later adapted to a ranking scheme of six welding zones (I-VI) (Table 5-7), based on further data from the Bandelier Tuff combined with published physical property data and characteristics of progressively welded pyroclastic deposits (Figure 5-9), with PLT values spanning from 0.59 MPa to a maximum of 6.4 MPa, accounting for higher intensity welding of pyroclastic deposits (Quane & Russell, 2005). This

widely accepted classification scheme (e.g. Lesti et al., 2011; Heap et al., 2014) aligns with the terminology used in previous schemes to rank welding intensities (e.g. Smith, 1960ii; Streck & Grunder, 1995; Wilson & Hildreth, 2003), providing a basis for consistency.

The units of the Ucanca and Guajara Fm, as outlined in Chapter 4, exhibit a wide range of welding intensities and profiles, both within individual units and throughout the stratigraphy. The nature of the welding variation of these units, particularly when localised to particular horizons, and the smooth transitions of both increasing and decreasing welding intensity, indicates welding is not only dominantly syn-depositional, but a result of a combination of both syn- and post-emplacement processes, as discussed in Chapter 4. A wide range of measured PLTs from 0.19 to 12.98 MPa are seen across these deposits. 20 % of the $PLT_m$ values, and 48 % of the $UCS_p$ lie within the 'densely welded' rank of Quane and Russell's scheme (2005), with the maximum recorded strength being over double that of the maximum measured strength in their study.

Furthermore, a far wider range of strengths in our results lie out with the ranking range than within it, and with $UCS_p$ of up to 316.63 MPa, it is problematic to group so much variety in strength as well as the other physical parameters into one welding rank (VI). The use of 'densely welded' in this case is also too vague and broad a term, largely underestimating the spectrum and extent of welding observed beyond rank VI, as discussed in Section 5.4.1. A variety of textures and characteristics, both in the field and in petrographic analysis, as well in the measured physical properties is seen across the deposits which fall within rank VI. The lower observed and measured welding intensities from these units align with the parameters of the first five welding zones (I-V), and suggested ranges of the physical properties (PLT, φ, ρ, OB) (Table 5–7) proposed by Quane and Russell (2005). This provides confidence in the use of these parameters, particularly rock strength, as a semi-quantitative method of classifying welding intensity in deposits whereby welding is largely a result of syn-depositional processes. However, rheomorphism and secondary crystallisation, on the other hand, proves to be problematic for the use of this scheme, whereby the physical properties are affected by subsequent deformation, alteration and rheomorphic flowage of material.

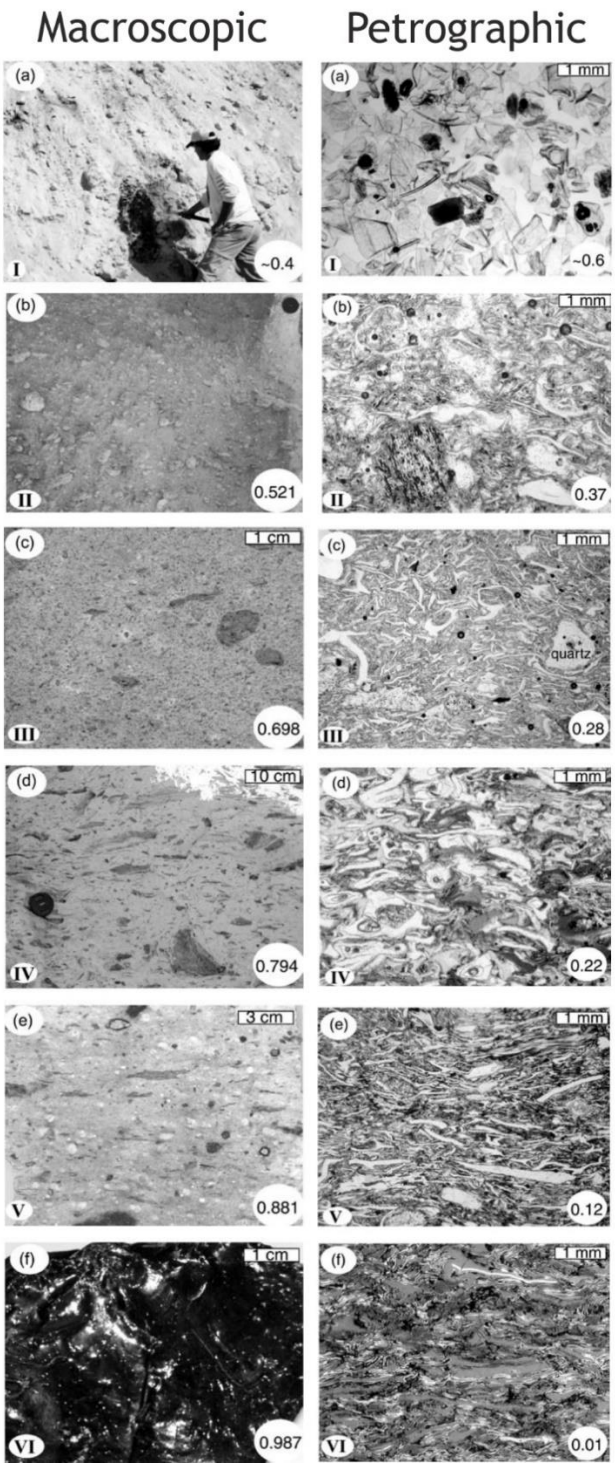


**Figure 5–9.** Characteristics in Quane & Russell's (2005) ranking scheme (I-V), based on both macroscopic features (a-f) and petrographic characteristics (a-f). Normalised density values are shown in the bottom right corner of the macroscopic photos, and porosity values on the bottom right corner of the petrographic photomicrographs. Rank I (nonwelded) shows both unconsolidated pumice in an ash matrix, and undeformed glass shards, showing no deformation. Ash is consolidated in Rank II (incipiently welded), showing incipient adhesion of largely undeformed ash shards. Rank III (partially welded) displays deformation of ash shards around crystal(s) with a largely undeformed matrix, with incipiently flattened and crudely aligned pumice lapilli, with eutaxitic textures beginning to develop. Both fiamme and moderately flattened pumice lapilli appear in Rank IV (moderately welded), with a weak development of foliation in the ash shard matrix. Stronger foliation is seen in Rank V (partially to densely welded) with extensively flattened ash shards, with fully collapsed pumice lapilli, exhibiting a total loss of porosity. Rank VI (densely welded) shows adhesion of ash shards, giving rise to a glassy, massive texture, with close to zero porosity.

As a means of representing the variable and higher intensities of welding observed across the units, and the weighting of measurements beyond the boundaries of the existing scheme, a further three zones are proposed. Using a combination of physical properties, petrographic analysis and macroscopic characterisation, these ranks accommodate higher intensity welding and account for post-depositional processes.

The ranges of the metrics and characteristics of the deposits in these proposed ranks is outlined in Table 5–8 and 5–9, respectively. The upper limits of 'densely welded' (VI) have been adjusted according to our data, with the addition of 'intensely welded' (VII) followed by an end-member 'lava-like' rank (VIII), whereby the welding is so extreme that it is largely indistinguishable from a lava. A third rank (IX), 'lava-like$^{taph}$' (abbreviation of 'taphanomic') is proposed to account for the variability seen in the physical properties as a result of post-depositional processes and alteration, but the deposit remains distinctly 'lava-like'. Taphanomic processes are those which take place post-emplacement (e.g. devitrification and vapour-phase alteration, lithophysae and spherulitic growth, and rheomorphism) resulting in changes to both the appearance and character of the ignimbrite (Andrews, 2006).

As discussed in Section 5.4, post-depositional rheomorphism typically leads to losses in ρ, and increased Φ, coupled with higher OB and strength values as compaction and strain intensifies (e.g. Quane & Russell, 2005). A summary of the welding descriptors and rank, using both schemes, for each Member is presented in Table 5–10.

| Quane & Russell (2005) | | | | | | | Rock strength ratings | |
|---|---|---|---|---|---|---|---|---|
| Rank | Welding intensity (Descriptive) | $PLT_m$ (MPa) | $UCS_p$ (MPa) | Φ | ρ | OB | GSEGWP (1970) | Hoek & Brown (1980) |
| I | nonwelded | <0.59 | <4.4 | >0.42 | <1.45 | <0.58 | 0 | very weak to weak |
| | | 0.19-0.42 | 1.21-3.02 | 0.53-0.11 | 0.87-2.42 | 0.22-0.65 | | |
| II | 'incipiently welded' or 'sintered' | 0.28-1.13 | 1.8-9.8 | 0.50-0.34 | 1.25-1.65 | 0.46-0.67 | 1 | weak to moderately weak |
| | | 0.58 | 4.61 | 0.3 | 1.61 | 0.63 | | |
| III | 'Partially' or 'poorly' welded | 1.4-1.6 | 15.2-19.1 | 0.34-0.25 | 1.65-1.85 | 0.67-0.74 | 2 | moderately weak to moderately strong |
| | | 1.14-1.86 | 11.46-23.93 | 0.21-0.01 | 1.89-2.28 | 0.64-0.79 | | |
| IV | 'Moderately welded' or 'partially welded with fiamme' | 2.15-4.6 | 21.4-53.2 | 0.25-0.13 | 1.85-2.15 | 0.74-0.8 | 4 | moderately strong |
| | | 1.48-4.25 | 24.67-98.61 | 0.24-0.01 | 1.98-2.56 | 0.44-0.91 | | |
| V | 'Partially welded' to 'densely welded' | 4.6-6.4 | 53.2-80.2 | 0.13-0.07 | 2.15-2.3 | 0.8-0.82 | 7 | Strong |
| | | 4.45-5.19 | 68.15-126.64 | 0.11-0.02 | 1.86-2.44 | 0.33-0.91 | | |
| VI | densely welded | >6.4 | >80.2 | <0.07 | >2.3 | >0.82 | | |
| | | 5.29-12.98 | 128.99-316.63 | -0.05-0.01 | 2.50-3.44 | 0.81-0.92 | | |

**Table 5–7**. Comparison of the ranges of physical properties associated with the welding ranks outlined by Quane & Russell (2005) in the grey fields, with the data from this study (the white fields), aligned with the rock strength ratings (purple fields).

| This study | | | | | | | Rock strength ratings | |
|---|---|---|---|---|---|---|---|---|
| Rank | Welding intensity (Descriptive) | $PLT_m$ (MPa) | $UCS_p$ (MPa) | Φ | ρ | OB | GSEGWP, 1970 | Hoek & Brown, 1980 |
| VI | densely welded | 5.29-7.46 | 128.99-182.02 | 0.05-0.01 | 2.34 -2.5 | 0.84-0.92 | 7 | Strong |
| VII | intensely welded | 8.63-9.63 | 210.49-235.03 | 0.05-0.04 | 2.47-2.55 | 0.84-0.92 | 12 | Very strong |
| VIII | lava-like | 10.28-12.98 | 250.91-316.63 | 0.03-0.01 | 2.53-3.44 | >0.92 | 15 | Extremely strong |
| *IX* | *lava-like*$^{taph}$ | *2.82-4.77* | 46.63-111.47 | 0.09-0.01 | 2.1-2.63 | >0.93 | 4-7 | Moderately strong to strong |

**Table 5–8.** Proposed welding ranks and range of physical properties as an extension of Quane & Russell's (2005) scheme, based on higher intensity welding observed in this study, aligned with rock strength ratings (purple fields).

| Rank | Welding intensity (Table 5-8) | Welding intensity characteristics | |
|---|---|---|---|
| | | Field observations | Petrographic observations |
| **VI** | densely welded | Variable welding with oscillations between eutaxitic, with zones of stretched and deformed pyroclasts and a banded, lava-like lithofacies. Fabric is stretched and deformed around juveniles, and pyroclast boundaries remain largely visible, although deformed to various extents. Weak development of a base-parallel fabric. | Variable degrees of welding and adhesion between components but dominated by 'ghost' eutaxitic textures and strongly flattened, aligned and foliated fabric with ash shards remaining visible, although evidence of adhesion between shards. Fabric wrapped and rotated around crystals. |
| **VII** | intensely welded | Largely massive, with localised evidence of 'ghost' vitroclastic textures, commonly concentrated in bands associated with obsidian and rare glassy fiamme. Clear development of a base-parallel fabric, with or without presence of folding. | Strongly foliated and banded, with glassy lenses common. Faint 'ghost' fiamme and boundaries of ash shards can be picked out. |
| **VIII** | lava-like | Distinctly massive or crystalline in appearance, typically very fine to medium grained, with or without crystals. Strongly pervasive base-parallel fabric, with or without secondary cleavage, with little to no evidence of ghost fiamme or vitroclastic textures. | Vitroclastic textures are largely absent or difficult to detect. Crystals are common and typically aligned with the base-parallel fabric. |
| **IX** | Lava-like$^{taph}$ | Lava-like in appearance, with a distinct lack of vitroclastic textures with extensive evidence of post-emplacement rheomorphism, including but not limited to: lithophysae, spherulites, folded and deformed fabric (open, loose and buckle folds) with common macro-scale (10s m) ramping. | Vitroclastic textures are largely absent or difficult to detect. Crystals are common and typically aligned with the base-parallel fabric, and folding of fabric is common. |

**Table 5–9.** Welding intensity descriptors for each proposed zone for higher intensity welding, based on field observations across all units from this study.

| Mb | Unit | Sample ID | Elevation (m) | Position | $PLT_m$ (MPa) | $UCS_p$ (MPa) | Φ | ρ | OB | Summary of welding descriptors | | Welding Scheme | |
|---|---|---|---|---|---|---|---|---|---|---|---|---|---|
| | | | | | | | | | | Field observations | Petrographic observations | Rank[1] | Rank[2] |
| Atravesado | 1 | **TN-48** | 1840 | upper | 6.24 | 152.13 | 0.04 | 2.52 | - | mT(lava-like). v. fine grained, distinctly massive crystal- & clast-poor, with planar, persistent base-parallel fabric, with occasional crystals (plagioclase feldspar). | - | VI | |
| | | **TN-47** | 1805 | mid-unit | 3.82 | 77.79 | 0.02 | 2.4 | 0.88 | mT(e). intensely welded, v. fine grained, massive crystal- & clast poor, with weak base-parallel fabric. Presence of stretched and elongated pumice, fiamme and ghost fiamme. Fabric rotated around occasional lithics and crystals | Strongly foliated fabric with localised eutaxitic texture. Ash shards largely visible. Rare crystals. | V | |
| | | **TN-24** | 1575 | base | 5.19 | 126.64 | 0.09 | 2.32 | 0.33 | m///sLT/Tp. predominantly non welded with randomly oriented pumice, with rare localised flattened pumice. | Strongly foliated, banded fabric with pervasive eutaxitic texture. Ash shards and pumice boundaries largely visible. | V | |
| | 2 | **TN-46** | - | upper | 9.07 | 221.39 | 0.04 | 2.55 | 0.92 | mT(lava-like). v. fine grained, distinctly massive crystal- & clast-poor with planar, persistent base-parallel fabric, exhibiting tight isoclinal folding, with occasional crystals (plagioclase feldspar). | Weak fabric, largely massive with faint visible fiamme. Fabric rotated around crystals. | VI | VII |
| | | **TN-32** | 1825 | mid-unit | 3.04 | 52.85 | 0.12 | 2.39 | 0.75 | mlLTp(e). partially welded with eutaxitic texture, with stretched and elongated pumice (fiamme) and zones of prolate lithophysae. | Developed eutaxitic texture, with obsidian-like fiamme and clearly visible pumice, although flattened. | IV | |
| | | **TN-45** | 1810 | base | 0.42 | 3.02 | 0.11 | 2.42 | 0.27 | mlBr/Blp. predominantly non-welded with slight evidence of clast sintering. | Ash shards and pumice largely undeformed with localised adhesion between, and slight flattening of, pumice. | I | |
| | 3 | **TN-33** | 1890 | upper | 10.28 | 250.91 | 0.04 | 3.44 | - | mT(lava-like). v-fine grained, distinctly massive, crystal- & clast-poor, with persistent base parallel fabric with macro-scale (10s m) ramp structures | No visible boundaries between ash or pumice components. Strongly foliated (very planar). | VI | VIII |
| | | **TN-35** | 1800 | mid-unit | 10.31 | 251.65 | 0.03 | 2.53 | 0.92 | mT(lava-like). v-fine grained, distinctly massive crystal- & clast-poor, with persistent base parallel fabric, displaying chevron and tight isoclinal folding. Occasional zones of lithophysae and secondary cleavage. | - | VI | VIII |
| | | **TN-34** | 1875 | base | - | - | - | - | - | mT(lava-like). intensely welded to lava-like with clast-rich (autoclasts) horizons, with persistent base-parallel fabric and occasional folding around clasts. | Strongly banded, with alignment and segregation of crystals. Faint 'ghost' fiamme can be detected. | - | VII* |
| | 4 | **TN-01** | 2210 | upper | 5.29 | 128.99 | 0.02 | 2.5 | - | mT(lava-like). crystal rich, clast poor, intensely welded to lava-like with persistent base-parallel fabric, with folding throughout (tight isoclinal, open curvilinear and chevron). | Strongly foliated fabric exhibiting folding, particularly around crystals. Pervasive fiamme, flattened to varying degrees. | VI | |

| | | | | | | | | | | | | |
|---|---|---|---|---|---|---|---|---|---|---|---|---|
| | | **TN-23** | 2140 | upper | 4.23 | 97.98 | 0.09 | 2.21 | - | mT(lava-like). crystal rich, clast poor, intensely welded to lava-like with persistent base-parallel fabric, with folding throughout (tight isoclinal, open curvilinear and chevron). | Distinctly massive 'fuzzy' appearance with no visible boundaries between shards. Weak fabric, which is rotated around crystals. | V | IX |
| | | **TF-04** | 2060 | mid-unit | 2.94 | 50.07 | 0.01 | 2.56 | 0.65 | mT(e). intensely welded, locally lava-like with lithic-rich horizons particularly associated with areas of lesser welding intensities (i.e. eutaxitic and moderately welded). Strong persistent base-parallel fabric with stretched and elongated pumice and occasional folding (tight isoclinal, open curvilinear and chevron). | - | IV | |
| | | **TN-44** | 2040 | base | 0.24 | 1.58 | 0.53 | 0.87 | 0.42 | m///sLT/Brp. predominantly non-welded, with slight sintering and deformation of pumice. | - | I | |
| **Retamares** | A | **TN-40** | 2265 | upper | 11.96 | 291.91 | 0.03 | 2.63 | 0.84 | mT(lava-like)/(e). v.fine grained, clast- & crystal-rich, locally eutaxitic, glassy, planar flow-banded with zones with tight folding (isoclinal, chevron and curvilinear). | Strongly foliated with rare faint fiamme, but lack of visible shard and pumice boundaries. Fabric locally rotated around crystals. | VI | VIII |
| | | **TN-10** | 2230 | mid-unit | 5.08 | 124.03 | 0.06 | 2.19 | 0.65 | mT(lava-like)/(e). v.fine grained, clast- & crystal-rich, moderately welded to lava-like, locally eutaxitic with planar flow-banded with zones of prolate lithophysae and tight fabric folding (isoclinal, chevron and curvilinear), particularly around clasts/blocks. | Highly banded with a folded and variable fabric, twisted and folded around lithics with alteration haloes. Fiamme persistent with rare glassy bands. | V | |
| | | **TN-02** | 2175 | base | 0.58 | 4.61 | 0.3 | 1.61 | 0.63 | m/ds/xsLT/T. predominantly non-welded with localised areas of partial welding (sintering of pumice pyroclast edges). | Highly vesicular, largely undeformed pumice with rare localised adhesion between pumice. | II | |
| | | **TN-03** | - | base | 4.25 | 98.61 | 0.04 | 2.44 | 0.44 | m/ds/xsLT/T. predominantly non-welded with localised areas of partial welding (sintering of pumice pyroclast edges), but with occasional scoriaceous bombs present. | - | IV | |
| | B | **TN-05** | 2440 | upper | 5.68 | 138.51 | 0.03 | 2.36 | 0.92 | mT(lava-like). v.fine grained, massive, flow banded locally vitrified (glassy) with local eutaxitic and lesser degrees of welding focussed around blocks and clasts. | - | VI | |
| | | **TN-41** | 2350 | upper | 2.93 | 49.76 | 0.17 | 1.98 | 0.54 | mLT. Partially welded, locally eutaxitic, pumice lapilli-supported with flattened, stretched and elongated pumice. Only partial sintering and welding of pyroclasts seen towards the uppermost horizon. | Flattening and stretching of pumice, but vesicularity largely remains. Ash matrix is deformed with total adhesion between shards, rotated around lithics. | IV | |
| | | **PP02** | 2350 | mid-unit | - | - | - | - | - | mT(lava-like)/(e). v.fine grained, clast-, crystal- & obsidian-rich, base-parallel flow banded with stretched and elongated pumice (fiamme). Fabric is folded and rotated around lithics. | - | - | V* |

| | | | | | | | | | | | | |
|---|---|---|---|---|---|---|---|---|---|---|---|---|
| | | **TF-03** | 2350 | mid-unit | 1.9 | 24.67 | 0.12 | 2.1 | 0.58 | mT(e)/(lava-like). v.fine grained, clast-, crystal- & obsidian-rich, base-parallel flow banded with stretched and elongated pumice (fiamme). Fabric is folded and rotated around lithics. | Distinctly eutaxitic, with flattened ad stretched pumice. Wavy, persistent fabric with deformed and aligned ash matrix. | IV | |
| | | **VF-16/1** | 2300 | mid-unit | 4.45 | 104.97 | 0.07 | 2.18 | 0.53 | mT(e)/(lava-like). v.fine grained, clast-, crystal- & obsidian-rich, base-parallel flow banded with stretched and elongated pumice (fiamme). Fabric is folded and rotated around lithics. | Strongly foliated, eutaxitic texture with stretched and elongated pumice. Fabric is wavy and folded around crystals and lithics. | V | |
| | | **TF-10** | 2290 | base | - | - | - | - | - | ds/xslT/LT. predominantly non-welded, with no evidence of pyroclast deformation at base, grading up rapidly to eutaxitic, partially welded tuff. | Highly variable welding over short scale. Pumice remains vesicular, with areas of non-deformed ash shards, and glassy fiamme and banding. | - | I* |
| | C | **TF-02** | 2400 | upper | 3.53 | 68.15 | 0.04 | 2.33 | 0.91 | mT(lava-like)/(e). v.fine grained, crystal-poor, clast-rich, locally eutaxitic with base-parallel fabric locally rotated around lithics. | Eutaxitic with a 'fuzzy' homogenous deformed ash matrix, folded and rotated around crystals. | V | |
| | | **TN-43** | - | mid-unit | 1.14 | 11.46 | 0.15 | 2.04 | 0.79 | mT(e). clast-rich, crystal-poor, moderately welded with sintered pyroclast boundaries, and concentrated zones of fiamme (variable welding). Weak fabric locally rotated around lithics. | Variable welding, from 'fuzzy' banded ash matrix to glassy banded fiamme. Weak fabric rotated around crystals and abundant lithics. | III | |
| | | **TN-06** | 2460 | base | 2.31 | 33.73 | 0.13 | 2.19 | 0.62 | mlLTp(e). lithic-rich, variations between non-welded and partially welded with pumice flattened and bent around clasts. Ash supported with localised eutaxitic texture. | - | IV | |
| | | **TN-09** | 2400 | base | 1.66 | 19.95 | 0.01 | 2.28 | 0.7 | mlLT/Brp(e). lithic-rich, predominantly non-welded with slight evidence of partial sintering between pyroclasts and rare fiamme. | - | III | |
| | D | **TN-42** | 2450 | upper | 11.3 | 275.6 | 0.02 | 2.59 | - | mT(lava-like). v.fine grained, distinctly massive, crystal-poor, lithic lapilli-rich, predominantly lava-like with 'ghost' fiamme. Persistent base-parallel fabric exhibiting tight isoclinal and open curvilinear folding. | - | VI | VIII |
| | | **TF-01** | 2450 | mid-unit | 7.46 | 182.02 | 0.01 | 2.5 | 0.81 | mLTp(e). pumice-rich, moderately to intensely welded with prevalent eutaxitic texture, locally grading up to lava-like. Crystal-poor, clast-rich, with stretched and elongated pumice. | Weakly banded, locally eutaxitic with altered 'fuzzy 'deformed pumiceous lenses. Abundant fiamme with a homogenous, largely deformed ash matrix. | VI | |
| | | **TN-13** | 2310 | mid-unit | - | - | - | - | - | mLTp(e). pumice-rich, moderately to intensely welded with prevalent eutaxitic texture, locally grading up to lava-like. Crystal-poor, clast-rich, with stretched and elongated pumice. | - | - | IV* |
| | | **TF-07** | 2275 | base | - | - | - | - | - | m///sT/LT. predominantly non welded, locally partially welded with occasional flattened and deformed pumice, | Banded, streaky fabric with varying degrees of welded and flattened pumice. Rare glassy fiamme. | - | II* |

| | | | | | | | | | | | | |
|---|---|---|---|---|---|---|---|---|---|---|---|---|
| | E | **TN-14** | 2430 | upper | 6.72 | 164.05 | 0.05 | 2.5 | - | mT(lava-like). clast-rich, crystal-poor, distinctly massive with a pervasive base-parallel fabric and occasional folding (tight isoclinal and open curvilinear folding). | Predominantly homogenous, 'fuzzy' deformed ash matrix, rotated around lithic lapilli, with faint stretched 'ghost' fiamme. | VI | |
| | | **TN-22** | 2440 | mid-unit | 9.63 | 235.03 | 0.05 | 2.47 | 0.84 | mLTo(e). densely to intensely welded with banded obsidian and glassy fiamme. Crystal-poor, lithic rich with weak fabric wrapped and rotated around clasts. | Distinctly homogenous matrix with total adhesion of ash. Weak fabric with localised fiamme. | VI | VII |
| | | **TN-15** | 2430 | base | 2.29 | 33.19 | 0.11 | 2.05 | 0.83 | mLT/Brp. predominantly non-welded with localised horizons of partial welding (sintering and deformation of pumice). | Highly banded, eutaxitic with developed fabric, locally rotated and deformed around lithics. Pumice are flattened and stretched. | IV | |
| | | **TF-09** | 2420 | base | 4.95 | 121.49 | 0.06 | 2.24 | 0.57 | mLT/Brp. predominantly non-welded with localised horizons of partial welding (sintering and deformation of pumice). | Streaky banding with clear pumice lapilli and clast boundaries, showing varying degrees of deformation. | V | |
| | F | **TN-19** | 2440 | upper | 1.48 | 16.82 | 0.24 | 1.97 | - | mT(e). clast-rich, crystal-poor, moderately welded to lava-like with weak fabric locally rotated around lithics. | Weak, streaky fabric twisted and rotated around moderately vesicular pumice and abundant lithic lapilli. | IV | |
| | | **TN-20** | 2435 | mid-unit | 4.63 | 110.83 | 0.11 | 2.23 | 0.64 | mT(e)€/(lava-like). clast-rich, crystal-poor, with a pervasive base-parallel fabric and occasional folding (tight isoclinal and open curvilinear folding). | Folded and wavy, streaky banding with clear pumice lapilli and clast boundaries, showing varying degrees of deformation. Fabric rotated around lithics. | V | |
| | | **TN-21** | 2430 | base | 0.39 | 2.82 | 0.43 | 1.06 | 0.34 | //s/xs/T/LT. predominantly non-welded with no evidence of welding or deformation. | - | I | |
| | G | **TN-17** | 2415 | upper | 1.23 | 12.79 | 0.21 | 2.02 | - | mT(e). clast-rich, crystal-poor, moderately welded to lava-like with weak fabric locally rotated around lithics. | Weak, streaky fabric twisted and rotated around moderately vesicular pumice and abundant lithic lapilli. | III | |
| | | **TN-18** | 2410 | base | 0.19 | 1.21 | 0.41 | 1.16 | 0.65 | //s/xs/T/LT. predominantly non-welded with no evidence of welding or deformation. | Highly vesicular and unaltered pumice and ash shards with little evidence of deformation. | I | |
| **Chasna** | SdC | **VF-16/2** | 2405 | upper | 2.82 | 46.63 | 0.12 | 2.1 | - | mT(lava-like). crystal-rich, clast-poor, distinctly massive with a persistent base-parallel fabric exhibiting minor folds (tight and isoclinal) with localised zones of lithophysae. | No visible vitroclastic textures. Homogenous, 'fuzzy' and crystal-rich, with strong, base-parallel alignment of crystals. | IV | IX |
| | | **TN-08** | 2370 | mid-unit | 2.94 | 50.07 | 0.1 | 2.2 | - | mT(lava-like). crystal-rich, clast-poor, distinctly massive with a persistent base-parallel fabric exhibiting minor folds (tight and isoclinal) with localised zones of lithophysae. | No visible vitroclastic textures. Homogenous, 'fuzzy' and crystal-rich, with strong, base-parallel alignment of crystals. | IV | IX |
| | | **TN-07** | 2340 | base | 4.31 | 100.72 | 0.14 | 1.86 | 0.69 | mBRp(e). moderately to densely welded, crystal-& clast-rich and flow banded with altered, stretched and deformed pumice. | Strongly foliated with 'fuzzy', largely homogenous ash matrix, deformed around lithic lapilli and clasts | V | |

| | | | | | | | | | | | | |
|---|---|---|---|---|---|---|---|---|---|---|---|---|
| | RLA | **TN-38** | 2525 | upper | 5.56 | 135.75 | 0.03 | 2.34 | - | mT(lava-like). v.fine grained, distinctly massive with pervasive base-parallel fabric occasionally exhibiting tight isoclinal folds. | Distinctly massive, with only very faint, rare evidence of 'ghost' fiamme. Aligned, abundant crystals. | VI | |
| | | **TN-36** | 2520 | mid-unit | 8.63 | 210.49 | - | - | - | mLTop(e). moderately welded to densely welded, with glassy fiamme and banded with obsidian. Clast-rich, crystal poor with discontinuous lenses of highly fluidal spatter-like material. | Strongly foliated with a base-parallel fabric, with stretched and elongated deformed fiamme, rotated around lithic lapilli, and rare crystals. | VI | VII |
| | | **VF-16/3** | 2475 | base | 7.34 | 179.18 | 0.03 | 2.37 | 0.85 | m/dsLT/T. variable welding from non-welded to eutaxitic, with localised stretched and deformed pumice lapilli. | Highly banded, streaky and eutaxitic with developed fabric, locally rotated and deformed around lithics. Pumice are flattened and stretched. | VI | |
| | | **TF-06** | 4475 | base | 3.49 | 66.73 | 0.05 | 2.45 | 0.77 | m/dsLT/T. variable welding from non-welded to eutaxitic, with localised stretched and deformed pumice lapilli. | Eutaxitic and foliated with visible pumice boundaries and occasional crystal. Pumice is variable stretched and flattened. | IV | |
| | LdlM | **TN-12** | 2355 | upper | 3.2 | 57.53 | 0.03 | 2.63 | - | mT(lava-like). Crystal-rich, clast-poor, distinctly massive with a persistent base-parallel fabric exhibiting a macro ramp-structure. | Distinctly massive, with no visible vitroclastic textures. Crystal rich (up to 0.7 cm) which show base-parallel alignment. | IV | IX |
| | | **TN-16** | 2450 | base | - | - | - | - | - | mT(lava-like). Crystal-rich, clast-poor, distinctly massive with a persistent base-parallel fabric. | - | - | IX* |
| **Almendros** | | **TN-39** | 2465 | upper | - | - | - | - | - | mTo(e). moderately to densely welded, crystal-poor, clast-rich with glassy fiamme and banded with obsidian. Weak fabric is folded (open curvilinear) and rotated around lithics. | Highly banded, streaky and eutaxitic with developed fabric, and evidence of disintegration of the fabric, which is locally rotated and deformed around lithics. | - | VI* |
| | | **TN-37** | 2515 | mid-unit | - | - | - | - | - | mLTp(e). pumice-rich, partially welded with pyroclasts boundaries largely intact, with zones of stretched prolate lithophysae. | Strongly eutaxitic and foliated with stretched and elongated fiamme. | - | VI* |
| | | **TN-04** | 2525 | base | 2.19 | 30.96 | 0.05 | 2.33 | 0.83 | mTo(e). moderately to densely welded, crystal-poor, clast-rich with glassy fiamme and banded with obsidian. Localised stratification which is churned up by flow banding. | Wavy, base-parallel foliation, rotated and stretched around lithics, with variable degrees of welding. | IV | |
| **Guajara** | 2 | **TF-08** | 2717 | upper | 1.86 | 23.93 | 0.17 | 1.89 | 0.75 | mT(lava-like). crystal-rich, clast-rich, densely welded to lava-like with zones of prolate and stretched lithophysae. | Wavy and undulating base-parallel foliation, rotated and stretched around lithics, with variable degrees of welding and rare glassy fiamme. | III | |
| | 3 | **TN-30** | 2480 | upper | 4.53 | 107.78 | 0.04 | 2.35 | - | mT(lava-like). crystal-rich, clast-poor, distinctly massive with persistent base-parallel fabric, exhibiting tight isoclinal folding. | - | V | IX |

| | | | | | | | | | | | | |
|---|---|---|---|---|---|---|---|---|---|---|---|---|
| | | **TN-28** | 2480 | mid-unit | 4.41 | 103.69 | 0.09 | 2.3 | - | mT(lava-like). crystal-rich, clast-poor, distinctly massive with persistent base-parallel fabric, exhibiting tight isoclinal folding and ghost fiamme. | No visible vitroclastic textures. Homogenous, 'fuzzy' and crystal-rich, with strong, base-parallel alignment of crystals. | V | IX |
| | | **TN-29** | 2480 | base | 12.98 | 316.63 | 0.01 | 2.6 | - | mT(lava-like). crystal-rich, clast-poor, distinctly massive with persistent base-parallel fabric, exhibiting tight isoclinal folding. | - | VI | VIII |
| **Areñas** | | **TN-27** | 2620 | upper | 4.77 | 111.47 | 0.01 | 2.44 | 0.93 | mT(lava-like). clast-poor, crystal-rich with persistent base-parallel fabric exhibiting minor folding (tight isoclinal and buckle folds). | - | V | IX |
| | | **TN-26** | 2615 | mid-unit | 1.74 | 21.58 | 0.15 | 2.15 | 0.64 | mLTp(e). predominantly non-welded, pumice-rich with some slight deformation and flattening of pumice. | - | III | |
| | | **PP-01** | 2615 | mid-unit | - | - | - | - | - | mLTp(e). predominantly non-welded, pumice-rich with some slight deformation and flattening of pumice and glassy fiamme. | - | - | III* |
| | | **TN-25** | 2610 | base | 2.92 | 49.41 | 0.14 | 2.1 | 0.91 | mTo(e)/(lava-like). densely welded to lava-like, distinctly flow banded with obsidian and glassy fiamme. | - | IV | |
| | | **TN-31** | 2610 | base | - | - | - | - | - | mTo(e)/(lava-like). densely welded to lava-like, distinctly flow banded with obsidian and glassy fiamme. | - | - | IV* |

**Table 5–10.** Summary of measured physical properties: strength (PLT & $UCS_p$), porosity (Φ), density (ρ) and oblateness (OB), with a summary of the welding intensity in both field and petrographic observations. Rank[1] welding intensities are based on the parameters outlined in Quane & Russell (2005). Rank[2] are the proposed welding intensities, outlined in Table 5–9. One value is provided where both ranking schemes agree. *denotes the expected rank based on comparisons of field and petrographic observations with lithofacies of similar characteristics.

## 5.6. Summary

The variable welding of the mapped deposits can be attributed to polyphase prosses: syn-emplacement agglutination, coalescence and rheomorphism of pyroclasts during sedimentation; and post-emplacement rheomorphism, with the former being the most dominant. Using a combination of detailed field observations, petrographic textural analysis and measuring the physical properties of the deposits, a framework to semi-quantitively track welding intensities through the stratigraphy has been established (Figure 5–10).

The strong correlations and relationships observed between these metrics provides validity to their ability to track sensitive variations in welding, across both individual units, and entire packages of ignimbrites. Building upon the widely accepted welding intensity ranking scheme (I-VI) of Quane & Russell (2005), a further three ranks are proposed, accounting for the higher intensities and polyphase welding experienced by high grade, lava-like ignimbrites, summarised in Figure 5–11.

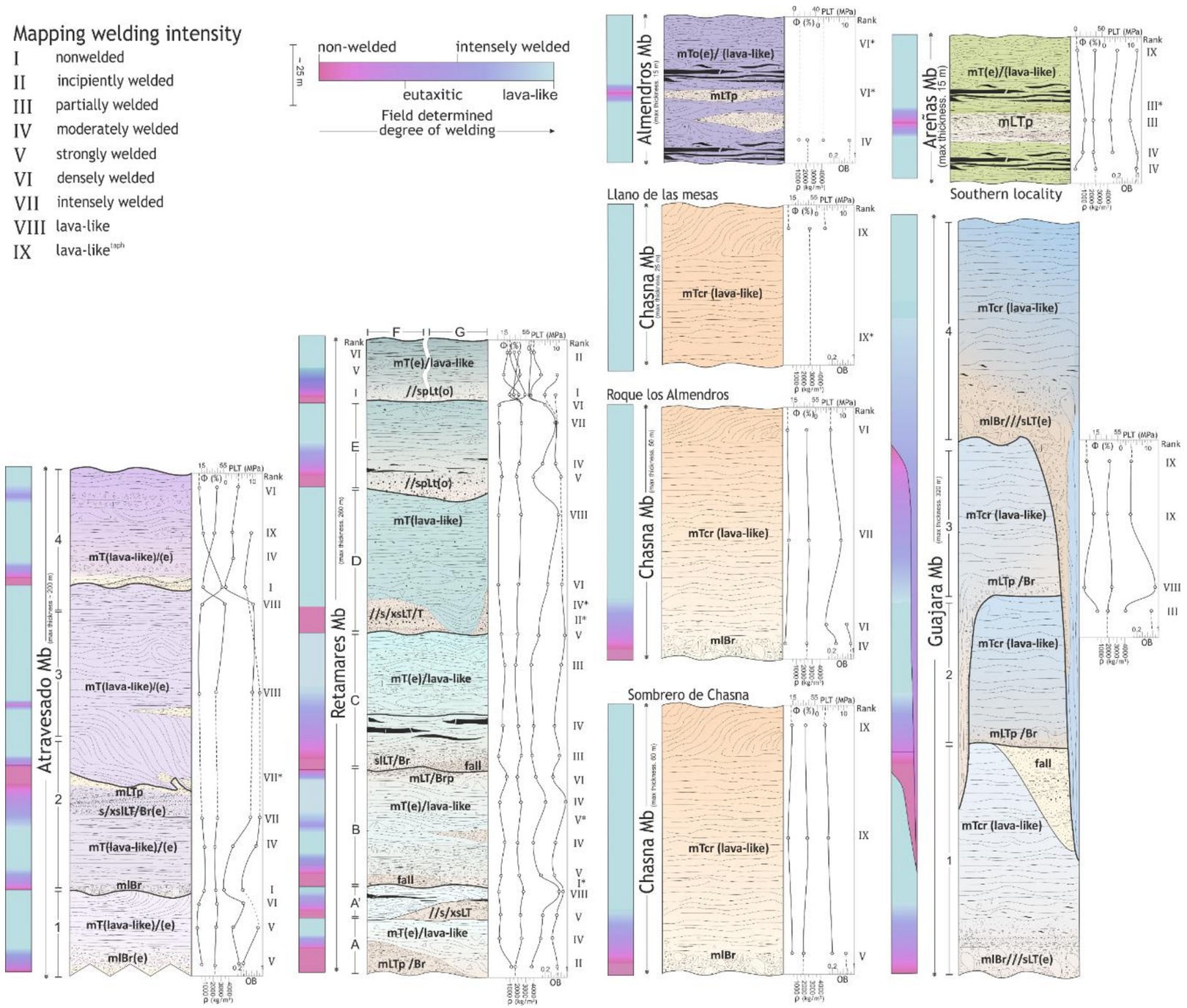


**Figure 5–10.** Combined field-determined and proposed ranking of welding intensities, based on the measured physical properties, throughout the stratigraphy of the mapped Las Cañadas deposits. Lines between data points are inferred.

| Rank | Descriptor | Metric parameters | | Characteristics: Field | Characteristics: Petrographic |
|---|---|---|---|---|---|
| I | nonwelded<br>Unconsolidated with no evidence of adhesion or deformation of pyroclasts. | $PLT_m$ | <0.59 |  | 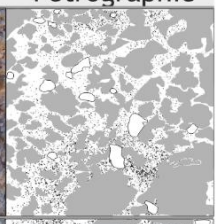 |
| | | $UCS_p$ | <4.4 | | |
| | | Φ | >0.42 | | |
| | | ρ | <2.42 | | |
| | | OB | <0.65 | | |
| II | incipiently welded<br>Coherent with slight adhesion of shards. Pyroclasts remain undeformed, maintaining porosity. | $PLT_m$ | 0.28 - 1.13 |  | 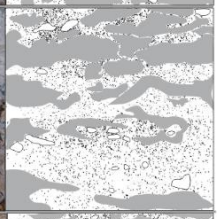 |
| | | $UCS_p$ | 1.8 - 9.8 | | |
| | | Φ | 0.50 - 0.34 | | |
| | | ρ | 1.25 - 1.65 | | |
| | | OB | 0.46 - 0.67 | | |
| III | partially welded<br>Slight deformation and partial flattening of pyroclasts. Evidence of coalescence of ash shards. | $PLT_m$ | 1.4 - 1.6 |  | 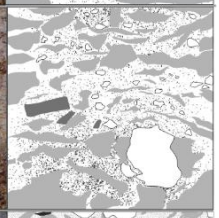 |
| | | $UCS_p$ | 11.46 - 23.93 | | |
| | | Φ | 0.34 - 0.01 | | |
| | | ρ | 1.65 - 1.85 | | |
| | | OB | 0.67 - 0.74 | | |
| IV | moderately welded<br>Flattening and deformation of pumice and pyroclasts. Development of eutaxitic textures and collapsed fiamme. Pyroclast boundaries clearly visible. | $PLT_m$ | 1.86 - 4.6 |  | 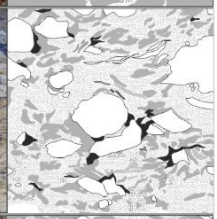 |
| | | $UCS_p$ | 21.4 - 98.61 | | |
| | | Φ | 0.25 - 0.01 | | |
| | | ρ | 1.85 - 2.15 | | |
| | | OB | 0.74 - 0.80 | | |
| V | strongly welded<br>Strongly foliated with a distinct fabric and developed eutaxitic texture. Obsdian common. Pyroclasts are deformed and strongly adhered to one another. | $PLT_m$ | 4.6 - 5.20 | 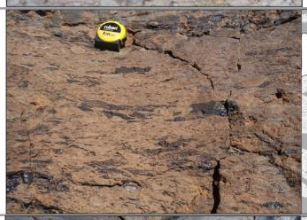 | 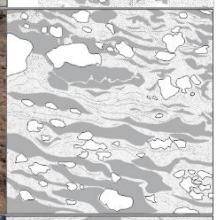 |
| | | $UCS_p$ | 98.61 - 126.64 | | |
| | | Φ | 0.13 - 0.02 | | |
| | | ρ | 2.15 - 2.34 | | |
| | | OB | 0.8 - 0.82 | | |
| VI | densely welded<br>Variability in welding from eutaxitic to lava-like. Fabric stretched and deformed around juveniles, with pyroclast boundaries remaining slightly visible. | $PLT_m$ | 5.29 - 7.46 |  |  |
| | | $UCS_p$ | 128.99 - 182.02 | | |
| | | Φ | 0.05 - 0.01 | | |
| | | ρ | 2.34 - 2.50 | | |
| | | OB | 0.82 - 0.92 | | |
| VII | intensely welded<br>Largely massive, with localised evidence of 'ghost' and altered fiamme. Strong foliation and banding common. | $PLT_m$ | 8.63 - 9.63 |  | 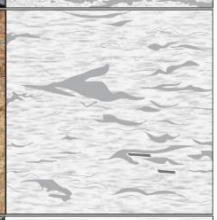 |
| | | $UCS_p$ | 210.43 - 235.03 | | |
| | | Φ | 0.05 - 0.04 | | |
| | | ρ | 2.50 - 2.55 | | |
| | | OB | 0.84 - 0.92 | | |
| VIII | lava-like<br>Distinctly massive or crystalline in appearance, with little to no evidence of vitroclastic textures. Pervasive base-parallel fabric common. | $PLT_m$ | 10.28 - 12.98 |  |  |
| | | $UCS_p$ | 250.91 - 316.63 | | |
| | | Φ | 0.03 - 0.01 | | |
| | | ρ | 2.55 - 3.44 | | |
| | | OB | >0.92 | | |
| IX | lava-like$^{rheom}$<br>Lava-like in appearance, with little to no evidence of vitroclastic textures, with extensive evidence of post-emplacement rheomorphsism. | $PLT_m$ | 2.82 - 4.77 |  |  |
| | | $UCS_p$ | 46.63 - 111.47 | | |
| | | Φ | 0.09 - 0.01 | | |
| | | ρ | 2.1 - 2.63 | | |
| | | OB | >0.93 | | |


**Figure 5–11.** Mapping welding intensity**:** a summary of the characteristics (field photographs and petrographic illustrations – discussed further in Chapter 6) and metric parameters of each rank of welding intensity in this study, adapted from Quane & Russell's (2005) I-VI scheme. Field characteristics: I – Atravesado Mb Unit 1 base; II – Retamares Mb Unit C base; III – Retamares Mb Unit C base; IV – Retamares Unit C base; V – Almendros Mb base; VI – Retamares Mb Unit D mid-unit; VII – Atravesado Mb Unit 3 base; VIII – Atravesado Mb Unit 4 mid-unit; IX – Chasna Mb LdlM locality mid-unit. Petrographic illustrations: I – Retamares Mb Unit G base (TN-18); II – Retamares Mb Unit D base (TF-07); III – Guajara Mb Unit 2 upper (TF-08); IV – Retamares Mb Unit B upper (TN-41); V – Retamares Mb Unit B base (TF-09); VI – Almendros Mb mid-unit (TN-37); VII – Chasna Mb RLA locality mid-unit (TN-36); VIII – Atravesado Mb Unit 3 upper (TN-33); IX – Guajara Mb Unit 3 mid-unit (TN-28).

# Chapter 6

# Geochemistry and Petrography

## 6.1. Geochemical insights

With the aim of investigating both the nature and presence of any chemical zoning or stratification throughout the units, samples from the top, mid and base of each unit, across the six proposed members, were processed for bulk rock X-ray fluorescence spectrometry (XRF) analysis. Fresh glasses present in three of the members underwent Electron-Microprobe (EMP) analysis to compare the composition of the obsidian fiamme and lenses with that of the bulk rock determined by XRF.

### 6.1.1. XRF analysis

#### 6.1.1.1. Methodology

Samples were analysed for 10 major and 14 trace elements at the School of Geosciences, University of Edinburgh, using a Philips PW2404 wavelength-dispersive, sequential X-ray fluorescence spectrometer (XRF), fitted with a Rh anode end-window X-Ray tube. 54 samples representing each unit across the six members, the Chasna Ridge conduit, and the El Pinalito lavas were prepared for bulk rock XRF analysis. Where possible, each ignimbrite unit was sampled at the base, middle and upper horizons of the deposit, to track any vertical changes through the stratigraphy. To ensure only the juvenile material was analysed, samples were initially crushed using a jaw crusher into ~ 3 mm gravel shards in order to remove the lithic components, and the remaining shards were then ground to a fine powder using a disc mill and sieved to ~ 6 µm. Sample powders were then divided to make glass discs for major oxide analysis and pressed powder pellets for trace element analysis.

#### 6.1.1.2. Glass disc preparation

For major element analysis, fused glass discs were prepared at the University of Edinburgh using a similar methodology to the one outlined in Norrish and Hutton (1969). The powders were initially dried overnight in an oven at 110 °C. The mass

loss on ignitions (LOI) are calculated from the difference in mass after igniting 10 g of the dried powder at 400 °C overnight, however due to the peralkaline nature of the ignimbrites, a modified method to determine LOIs was employed separately to prevent the sample powders fusing at ignition temperatures. 1 g of dried powder was weighed into a Pt90Au10 crucible and ignited in a muffle furnace at 1100 °C for 20 minutes and then reweighed after cooling to room temperature in a glass desiccator to determine the percentage weight loss (LOI).

0.95 g aliquots of the dried powder were weighed into a Pt90Au10 crucible and mixed with borate flux (Johnson and Matthey Spectroflux 105), measured to have a 5:1 (flux: sample) dilution ratio, which were then fused in the muffle furnace for 15 minutes at 1500 °C. The mass loss measured following ignition is made up by a further addition of flux and then fused over a Meker burner. The mixture is swirled over the burner for a couple of minutes to ensure complete homogeneity before it is cast on a graphite plate atop on a hotplate (220 °C). An aluminium plunger is used to press the molten globule into a glass disc which is left for ten minutes to anneal on the hotplate before removing to cool and label.

#### 6.1.1.3. Pressed powder pellet preparation

For trace element analysis, pressed powder pellets were prepared at the University of Edinburgh. 8 g aliquots of dried powder were measured into a beaker along with 8 drops of a binding agent, a 2 % aqueous solution of polyvinyl alcohol and thoroughly mixed to homogenise the sample with the binding agent, which was then distributed into tapered aluminium pellet cups. The cups are assembled within a steel mould, underneath a polished tungsten carbide disc and then compressed within a hydraulic press at 8 tons to produce a smooth ~ 40 mm diameter pellet.

#### 6.1.1.4. Calibration

Calibration of the XRF spectrometer for both major and trace element analyses was done using international standards in Govindaraju (1994). See Appendix IV for comparison against measured standards. The instrumental settings (Appendix IV) are optimised to achieve accuracy and resolution.

### 6.1.1.5. Results

Results are reported in Tables 6.1–1 to 6.1–4 of major and trace element analysis from samples belonging to each mapped Member. Glass discs were analysed for $SiO_2$, $Al_2O_3$, $Fe_2O_3$, MgO, CaO, $Na_2O$, $K_20$, $TiO_2$, MnO, and $P_2O_5$; and pressed powder pellets for Zn, Cu, Ni, Cr, V, Ba, Sc, La, Ce, Nd, Sr, U, Rb, Th, Pb, Nb, Zr and Y.

| | **Atravesado** | | | | | | | | | | | |
|---|---|---|---|---|---|---|---|---|---|---|---|---|
| Unit | 1 | | | 2 | | | 3 | | | 4 | | |
| | TN-24 | TN-47 | TN-48 | TN-45 | TN-32 | TN-46 | TN-34 | TN-35 | TN-33 | TN-44 | TF-04 | TN-01 |
| $SiO_2$ | 63.52 | 63.51 | 59.48 | 63.94 | 63.54 | 63.51 | 63.24 | 61.37 | 63.30 | 62.70 | 62.32 | 58.92 |
| $Al_2O_3$ | 17.66 | 17.66 | 19.11 | 17.56 | 16.71 | 17.66 | 16.76 | 18.52 | 17.74 | 18.25 | 17.52 | 17.98 |
| $Fe_2O_3$ | 4.22 | 4.10 | 5.35 | 3.79 | 4.42 | 4.10 | 4.25 | 3.76 | 4.03 | 3.91 | 4.66 | 7.76 |
| MgO | 0.23 | 0.30 | 0.33 | 0.18 | 0.46 | 0.30 | 0.45 | 0.22 | 0.32 | 0.16 | 0.35 | 0.26 |
| CaO | 0.21 | 0.29 | 0.99 | 0.18 | 0.48 | 0.29 | 0.48 | 0.67 | 0.14 | 0.15 | 0.39 | 0.68 |
| $Na_2O$ | 6.48 | 6.49 | 7.33 | 6.75 | 6.89 | 6.49 | 6.62 | 7.93 | 6.21 | 6.59 | 6.66 | 7.32 |
| $K_2O$ | 5.291 | 5.182 | 5.267 | 5.346 | 5.190 | 5.182 | 5.166 | 5.368 | 5.254 | 5.252 | 5.204 | 5.211 |
| $TiO_2$ | 0.802 | 0.822 | 0.796 | 0.729 | 0.839 | 0.822 | 0.820 | 0.698 | 0.771 | 0.764 | 0.904 | 0.783 |
| MnO | 0.195 | 0.136 | 0.236 | 0.211 | 0.252 | 0.136 | 0.248 | 0.270 | 0.190 | 0.278 | 0.269 | 0.267 |
| $P_2O_5$ | 0.035 | 0.063 | 0.075 | 0.051 | 0.090 | 0.063 | 0.054 | 0.038 | 0.053 | 0.013 | 0.035 | 0.057 |
| LOI | 1.17 | 1.23 | 1.00 | 1.15 | 0.99 | 1.23 | 1.24 | 1.13 | 1.48 | 1.85 | 1.37 | 0.66 |
| Total | 99.81 | 99.78 | 99.97 | 99.90 | 99.87 | 99.78 | 99.33 | 99.97 | 99.49 | 99.92 | 99.68 | 99.90 |
| Zn | 115 | 118 | 122 | 158 | 143 | 149 | 183 | 178 | 192 | 192 | 191 | 181 |
| Cu | 7.2 | 6.8 | 6.3 | 8.6 | 12 | 6.5 | 4.3 | 5.6 | 7.6 | 17 | 4.2 | 27 |
| Ni | n. d | n. d | n.d. | n.d. | n.d. | n.d. | n.d. | n.d. | n.d. | 25 | 0 | 3.2 |
| Cr | 10.9 | 8.7 | 2.3 | 8.7 | 7.3 | 11 | 7.6 | 18 | 17 | 91 | 24 | 32 |
| V | 28 | 31 | 122 | 29 | 33 | 22 | 22 | 30 | 29 | 26 | 29 | 29 |
| Ba | 244 | 318 | 919 | 259 | 252 | 252 | 235 | 273 | 262 | 165 | 66 | 80 |
| Sc | 2.1 | 1.1 | 16 | 2.4 | 2.8 | n.d. | 1.9 | 1.2 | 1.5 | 4 | 1.4 | n.d. |
| La | 113 | 142 | 108 | 102 | 141 | 249 | 79 | 145 | 173 | 193 | 172 | 214 |
| Ce | 192 | 229 | 193 | 202 | 224 | 316 | 226 | 266 | 264 | 302 | 287 | 293 |
| Nd | 81 | 97 | 112 | 68 | 108 | 164 | 67 | 99 | 112 | 160 | 115 | 89 |
| Sr | 16 | 71 | 1165 | 27 | 18 | 16 | 15 | 58 | 64 | 100 | 66 | 81 |
| U | 2.7 | 4 | 3.1 | 5.8 | 2.4 | 3.7 | 4.1 | 3.7 | 3.3 | 4.1 | 3.2 | 7.9 |
| Rb | 106 | 96 | 37 | 97 | 102 | 97 | 97 | 99 | 101 | 113 | 107 | 177 |
| Th | 17 | 17 | 6.4 | 11 | 17 | 17 | 19 | 16 | 16 | 18 | 18 | 37 |
| Pb | 10 | 10 | 5.2 | 6.7 | 9.8 | 9.4 | 9.6 | 9 | 10 | 10 | 11 | 19 |
| Nb | 252 | 250 | 116 | 188 | 252 | 252 | 271 | 234 | 243 | 254 | 256 | 401.9 |
| Zr | 878 | 842 | 378 | 735 | 901 | 845 | 870 | 807 | 832 | 963 | 875 | 1706 |
| Y | 34.5 | 32 | 63 | 35 | 46 | 94 | 38 | 62 | 96 | 112 | 75 | 85 |

**Table 6.1–1.** XRF whole rock data of the units (1-4) of the Atravesado Member.

| | Retamares | | | | | | | | | | | | | |
|---|---|---|---|---|---|---|---|---|---|---|---|---|---|---|
| Unit | A | | | B | | | C | | | D | | | E | |
| | TN-03 | TN-10 | TN-40 | TF-10 | VF-16/1 | TN-41 | TN-06 | TN-43 | TF-02 | TF-07 | TF-01 | TN-42 | TN-14 | TN-15a |
| $SiO_2$ | 61.09 | 58.06 | 62.05 | 59.94 | 62.53 | 60.29 | 61.90 | 62.28 | 62.67 | 58.55 | 59.77 | 62.28 | 61.34 | 61.47 |
| $Al_2O_3$ | 18.94 | 18.98 | 16.94 | 18.73 | 16.40 | 20.28 | 17.46 | 16.78 | 17.88 | 17.90 | 19.21 | 16.78 | 16.13 | 17.46 |
| $Fe_2O_3$ | 3.96 | 4.83 | 5.16 | 4.94 | 5.26 | 3.48 | 5.24 | 5.37 | 3.51 | 6.64 | 5.38 | 5.37 | 6.04 | 5.02 |
| MgO | 0.25 | 0.26 | 0.40 | 0.31 | 0.35 | 0.31 | 0.28 | 0.41 | 0.35 | 0.36 | 0.34 | 0.41 | 0.51 | 0.47 |
| CaO | 0.64 | 0.62 | 0.41 | 0.61 | 0.37 | 1.07 | 0.26 | 0.53 | 0.72 | 0.37 | 1.00 | 0.53 | 0.58 | 0.60 |
| $Na_2O$ | 6.96 | 6.66 | 6.57 | 5.75 | 7.47 | 6.14 | 6.53 | 6.38 | 7.14 | 4.86 | 7.36 | 6.38 | 6.23 | 5.70 |
| $K_2O$ | 5.271 | 5.037 | 5.009 | 4.581 | 5.209 | 5.100 | 5.108 | 5.109 | 5.263 | 5.987 | 5.293 | 5.109 | 5.080 | 4.275 |
| $TiO_2$ | 0.716 | 0.696 | 0.976 | 1.028 | 0.946 | 0.874 | 0.982 | 0.956 | 0.751 | 1.176 | 0.800 | 0.956 | 1.054 | 0.970 |
| MnO | 0.255 | 0.325 | 0.319 | 0.309 | 0.301 | 0.226 | 0.331 | 0.396 | 0.243 | 0.384 | 0.238 | 0.396 | 0.395 | 0.398 |
| $P_2O_5$ | 0.036 | 0.025 | 0.073 | 0.050 | 0.038 | 0.088 | 0.028 | 0.053 | 0.121 | 0.052 | 0.075 | 0.053 | 0.039 | 0.108 |
| LOI | 1.65 | 4.27 | 2.34 | 3.61 | 1.01 | 2.07 | 1.78 | 1.56 | 0.81 | 3.39 | 0.14 | 1.56 | 2.17 | 3.21 |
| Total | 99.77 | 99.77 | 100.25 | 99.86 | 99.90 | 99.91 | 99.92 | 99.81 | 99.46 | 99.67 | 99.60 | 99.81 | 99.57 | 99.68 |
| Zn | 191 | 315 | 202 | 293 | 231 | 186 | 210 | 198 | 116 | 278 | 121 | 126 | 328 | 165 |
| Cu | 16 | 13 | 7.8 | 13 | 9 | 15 | 10 | 54 | 5.9 | 20 | 22 | 26 | 7.3 | 16 |
| Ni | 1.3 | n.d. | n.d. | n.d. | 1.3 | n.d. | n.d. | 85 | n.d. | 7.9 | 12 | n.d. | n.d. | n.d. |
| Cr | 25 | 8.8 | 17 | 14 | 31 | 9.7 | 13 | 252 | 24 | 34 | 65 | 17 | 12 | 18 |
| V | 24 | 32 | 24 | 31 | 30 | 6.3 | 32 | 31 | 18 | 40 | 27 | 31 | 38 | 36 |
| Ba | 76 | 50 | 54 | 224 | 38 | 49 | 48 | 87 | 334 | 44 | 327 | 574 | 39 | 152 |
| Sc | n.d. | 2.5 | 0.5 | 2.6 | 2.8 | 2 | 1.8 | 1.8 | n.d. | 1.7 | n.d. | n.d. | 2.8 | 3 |
| La | 212.8 | 228 | 201 | 184 | 175 | 214 | 147 | 160 | 125 | 274 | 158 | 173 | 274 | 163 |
| Ce | 293.3 | 385 | 336 | 376 | 308 | 347 | 352 | 297 | 204 | 480 | 254 | 296 | 432 | 308 |
| Nd | 92.4 | 155 | 128 | 131 | 119 | 148 | 106 | 103 | 74 | 178 | 78 | 92 | 175 | 132 |
| Sr | 83.1 | 27 | 80 | 16 | 34 | 21.5 | 19 | 33 | 27 | 22 | 78 | 250 | 107 | 27 |
| U | 7.8 | 5.8 | 5 | 5 | 3.2 | 3.9 | 3.8 | 3.4 | 3.4 | 6.7 | 5.9 | 5.6 | 5.5 | 4.1 |
| Rb | 171.2 | 124 | 125 | 192 | 120 | 111 | 119 | 128 | 103 | 177 | 143 | 125 | 137 | 85 |
| Th | 35.3 | 24 | 22 | 22 | 20 | 20 | 24 | 21 | 15 | 34 | 25 | 22 | 28 | 18 |
| Pb | 16.4 | 13 | 13 | 12 | 12 | 14 | 12 | 13 | 10 | 20 | 13.6 | 12 | 18 | 12 |
| Nb | 394.1 | 352 | 312 | 374 | 293 | 330 | 342 | 302 | 189 | 475 | 292 | 281 | 387 | 260 |
| Zr | 1703.9 | 1286 | 1098 | 1070 | 1085 | 1118 | 1233 | 1139 | 724 | 1740 | 1056 | 977 | 1378 | 952 |
| Y | 118.4 | 109 | 84 | 78 | 82 | 94 | 68 | 41 | 44 | 115 | 49 | 51 | 132 | 81 |

**Table 6.1–2.** XRF whole rock data of the units (A-E) of the Retamares Member.

| | Retamares | | | | | Chasna | | | | | | | |
|---|---|---|---|---|---|---|---|---|---|---|---|---|---|
| Unit | F | | | G | | Unit | Sombrero | | | RLA | | | 2.0 | |
| | TN-21 | TN-20 | TN-19 | TN-17 | | | TN-07 | TN-08 | VF-16/2 | TF-06 | TN-36 | TN-38 | TN-16 | TN-12 |
| $SiO_2$ | 63.65 | 61.02 | 60.80 | 60.92 | | $SiO_2$ | 59.74 | 59.51 | 60.12 | 59.86 | 63.09 | 62.24 | 55.73 | 58.26 |
| $Al_2O_3$ | 16.01 | 16.85 | 17.36 | 17.37 | | $Al_2O_3$ | 20.57 | 20.06 | 20.05 | 18.74 | 18.11 | 18.31 | 17.46 | 19.05 |
| $Fe_2O_3$ | 4.69 | 6.05 | 6.02 | 5.63 | | $Fe_2O_3$ | 3.83 | 3.55 | 3.33 | 6.03 | 3.58 | 3.70 | 8.21 | 5.09 |
| MgO | 0.53 | 0.38 | 0.27 | 0.36 | | MgO | 0.17 | 0.09 | 0.16 | 0.29 | 0.32 | 0.36 | 2.25 | 1.28 |
| CaO | 0.65 | 0.42 | 0.31 | 0.56 | | CaO | 0.72 | 0.78 | 0.68 | 0.65 | 0.61 | 0.67 | 5.26 | 4.12 |
| $Na_2O$ | 0.69 | 5.96 | 6.20 | 4.93 | | $Na_2O$ | 5.45 | 6.49 | 6.61 | 6.55 | 7.30 | 6.99 | 4.89 | 5.37 |
| $K_2O$ | 2.389 | 5.163 | 5.085 | 4.940 | | $K_2O$ | 5.133 | 5.241 | 5.31 | 5.369 | 5.352 | 5.193 | 3.419 | 3.966 |
| $TiO_2$ | 0.943 | 1.095 | 1.069 | 1.012 | | $TiO_2$ | 0.642 | 0.578 | 0.54 | 0.798 | 0.757 | 0.800 | 1.873 | 1.209 |
| MnO | 0.105 | 0.405 | 0.397 | 0.324 | | MnO | 0.281 | 0.254 | 0.26 | 0.260 | 0.254 | 0.265 | 0.181 | 0.166 |
| $P_2O_5$ | 0.057 | 0.064 | 0.052 | 0.078 | | $P_2O_5$ | 0.029 | 0.067 | 0.06 | 0.026 | 0.100 | 0.102 | 0.554 | 0.589 |
| LOI | 9.94 | 2.59 | 2.23 | 3.77 | | LOI | 3.04 | 3.00 | 2.78 | 1.05 | 0.57 | 1.20 | 0.10 | 0.67 |
| Total | 99.66 | 100.00 | 99.79 | 99.89 | | Total | 99.61 | 99.61 | 99.89 | 99.62 | 100.04 | 99.84 | 99.94 | 99.78 |
| Zn | 154 | 230 | 250 | 258 | | Zn | 168 | 174 | 155 | 188 | 172 | 154 | 69 | 63 |
| Cu | 9 | 15 | 13 | 21 | | Cu | 8.2 | 13 | 4.1 | 28 | 10 | 12 | 28 | 17 |
| Ni | n.d. | 2.8 | 25 | 1.3 | | Ni | n.d. | n.d. | n.d. | 4.8 | n.d. | n.d. | 15 | 1.1 |
| Cr | 13 | 23 | 70 | 11 | | Cr | 11 | 15 | 26 | 36 | 19 | 16 | 61 | 15 |
| V | 11 | 45 | 42 | 31 | | V | 31 | 31 | 26 | 29 | 23 | 25 | 73 | 59 |
| Ba | 3 | 39 | 33 | 128 | | Ba | 104 | 50 | 45 | 50 | 89 | 113 | 689 | 815 |
| Sc | 2.4 | 2.5 | 1.7 | 1.9 | | Sc | n.d. | 0.2 | n.d. | 0.2 | n.d. | 0.1 | 5.4 | 2.6 |
| La | 168 | 220 | 236 | 184 | | La | 172 | 172 | 155 | 169 | 181 | 170 | 88 | 125 |
| Ce | 199 | 430 | 447 | 410 | | Ce | 265 | 265 | 249 | 304 | 291 | 301 | 149 | 202 |
| Nd | 115 | 148 | 158 | 136 | | Nd | 69 | 73 | 64 | 81 | 81 | 78 | 58 | 71 |
| Sr | 53 | 24 | 23 | 38 | | Sr | 54 | 64 | 46 | 59 | 60 | 76 | 928 | 835 |
| U | 2.6 | 4.8 | 5.3 | 4.4 | | U | 4.2 | 6.1 | 5.9 | 5.6 | 7.5 | 6.5 | 6.3 | 6.9 |
| Rb | 126 | 150 | 138 | 147 | | Rb | 135 | 136 | 135 | 201 | 178 | 170 | 113 | 126 |
| Th | 18 | 28 | 28 | 26 | | Th | 27 | 26 | 26 | 37 | 35 | 34 | 22 | 24 |
| Pb | 7.2 | 20 | 19 | 15 | | Pb | 13 | 14 | 13 | 18 | 17 | 16 | 11 | 11 |
| Nb | 263 | 401 | 397 | 351 | | Nb | 323 | 312 | 306 | 409 | 385 | 380 | 158 | 162 |
| Zr | 950 | 1358 | 1404 | 1284 | | Zr | 1255 | 1144 | 1150 | 1798 | 1599 | 1652 | 706 | 783 |
| Y | 60 | 103 | 114 | 70 | | Y | 45 | 52 | 45 | 62 | 71 | 66 | 36 | 38 |

**Table 6.1–3.** XRF whole rock data of the units (F-G) of the Retamares Member, and the Chasna Member localities.

| Almendros | | | |
|---|---|---|---|
| | TN-04 | TN-37 | TN-39 |
| $SiO_2$ | 62.59 | 60.58 | 61.63 |
| $Al_2O_3$ | 18.59 | 18.63 | 17.12 |
| $Fe_2O_3$ | 3.53 | 4.01 | 4.80 |
| MgO | 0.23 | 0.21 | 0.70 |
| CaO | 0.42 | 0.75 | 0.67 |
| $Na_2O$ | 6.35 | 6.89 | 6.94 |
| $K_2O$ | 5.268 | 5.316 | 5.243 |
| $TiO_2$ | 0.769 | 0.757 | 0.887 |
| MnO | 0.209 | 0.263 | 0.318 |
| $P_2O_5$ | 0.132 | 0.066 | 0.074 |
| LOI | 1.71 | 2.25 | 1.22 |
| Total | 99.80 | 99.71 | 99.59 |
| Zn | 112 | 11 | 123 |
| Cu | 8.3 | 9.7 | 6 |
| Ni | n.d. | n.d. | n.d. |
| Cr | 8.3 | 29 | 24 |
| V | 22 | 16 | 16 |
| Ba | 330 | 351 | 366 |
| Sc | n.d. | n.d. | 0.2 |
| La | 304 | 126 | 133 |
| Ce | 282 | 220 | 228 |
| Nd | 145 | 78 | 82.6 |
| Sr | 27 | 12 | 12 |
| U | 3.6 | 3.9 | 4.2 |
| Rb | 110 | 105 | 101 |
| Th | 17 | 17 | 17 |
| Pb | 12 | 11 | 11 |
| Nb | 206 | 202 | 210 |
| Zr | 787 | 766 | 790 |
| Y | 74 | 412 | 45 |

| Areñas | | | | |
|---|---|---|---|---|
| | TN-25 | TN-26 | TN-27 | TN-31 |
| **$SiO_2$** | 59.89 | 61.05 | 59.94 | 62.22 |
| **$Al_2O_3$** | 19.88 | 19.35 | 18.77 | 18.06 |
| **$Fe_2O_3$** | 3.78 | 3.71 | 3.82 | 4.49 |
| **MgO** | 0.21 | 0.18 | 0.24 | 0.20 |
| **CaO** | 0.65 | 0.51 | 1.14 | 0.17 |
| **$Na_2O$** | 5.39 | 6.22 | 7.29 | 6.30 |
| **$K_2O$** | 5.259 | 5.347 | 5.226 | 5.427 |
| **$TiO_2$** | 0.761 | 0.757 | 0.741 | 0.870 |
| **MnO** | 0.279 | 0.275 | 0.284 | 0.213 |
| **$P_2O_5$** | 0.070 | 0.033 | 0.052 | 0.034 |
| **LOI** | 3.18 | 2.11 | 2.35 | 1.76 |
| **Total** | 99.35 | 99.55 | 99.85 | 99.76 |
| **Zn** | 170 | 159 | 156 | - |
| **Cu** | 15 | 8.6 | 8.2 | - |
| Ni | n.d. | n.d. | 5.6 | - |
| Cr | 17 | 13 | 4 | - |
| V | 22 | 24 | 20 | - |
| Ba | 154 | 55 | 80 | - |
| Sc | n.d. | n.d. | n.d. | - |
| La | 176 | 173 | 166 | - |
| Ce | 313 | 276 | 277 | - |
| Nd | 96 | 97 | 92 | - |
| Sr | 39 | 27 | 63 | - |
| U | 5.7 | 4.7 | 5.3 | - |
| Rb | 132 | 135 | 134 | - |
| Th | 24 | 23 | 24 | - |
| Pb | 11 | 12 | 12 | - |
| Nb | 294 | 285 | 293 | - |
| Zr | 996 | 988 | 1015 | - |
| Y | 58 | 77 | 56 | - |

| Guajara | | | | |
|---|---|---|---|---|
| **Unit** | | | | |
| | TF-08 | TN-29 | TN-28 | TN-30 |
| $SiO_2$ | 60.83 | 61.66 | 59.74 | 61.11 |
| $Al_2O_3$ | 19.66 | 19.37 | 19.74 | 18.66 |
| $Fe_2O_3$ | 3.57 | 3.29 | 3.67 | 3.82 |
| MgO | 0.28 | 0.13 | 0.24 | 0.37 |
| CaO | 0.83 | 0.54 | 1.15 | 1.17 |
| $Na_2O$ | 5.08 | 7.82 | 5.49 | 7.18 |
| $K_2O$ | 5.101 | 5.400 | 4.911 | 4.760 |
| $TiO_2$ | 0.727 | 0.645 | 0.835 | 0.842 |
| MnO | 0.315 | 0.231 | 0.201 | 0.254 |
| $P_2O_5$ | 0.087 | 0.066 | 0.131 | 0.105 |
| LOI | 3.02 | 0.81 | 3.43 | 2.00 |
| Total | 99.50 | 99.97 | 99.53 | 100.27 |
| Zn | 165 | 128 | 142 | 122 |
| Cu | 6.8 | 8.6 | 22 | 7 |
| Ni | n.d. | n.d. | n.d. | n.d. |
| Cr | 12 | 12 | 17 | 25 |
| V | 32 | 38 | 25 | 30 |
| Ba | 200 | 405 | 882 | 400 |
| Sc | n.d. | 0 | n.d. | n.d. |
| La | 192 | 152 | 170 | 203 |
| Ce | 313 | 245 | 270. | 259 |
| Nd | 103 | 75 | 93 | 94 |
| Sr | 75 | 146 | 161 | 23 |
| U | 6 | 5 | 4.2 | 5.1 |
| Rb | 113 | 123 | 104 | 141 |
| Th | 21 | 22 | 19 | 25 |
| Pb | 10 | 123 | 11 | 13 |
| Nb | 306 | 264 | 258 | 270 |
| Zr | 977 | 898 | 830 | 956 |
| Y | 65 | 40 | 53 | 53 |

| El Pinalito | |
|---|---|
| | TN-49 |
| $SiO_2$ | 44.99 |
| $Al_2O_3$ | 20.11 |
| $Fe_2O_3$ | 12.33 |
| MgO | 2.33 |
| CaO | 5.46 |
| $Na_2O$ | 2.57 |
| $K_2O$ | 1.855 |
| $TiO_2$ | 3.705 |
| MnO | 0.259 |
| $P_2O_5$ | 1.522 |
| LOI | 4.32 |
| Total | 99.45 |
| Zn | 190 |
| Cu | 14 |
| Ni | n.d. |
| Cr | 14 |
| V | 30 |
| Ba | 309 |
| Sc | 1.2 |
| La | 180 |
| Ce | 282 |
| Nd | 120 |
| Sr | 108 |
| U | 3.8 |
| Rb | 102 |
| Th | 16 |
| Pb | 10 |
| Nb | 246 |
| Zr | 856 |
| Y | 83 |

**Table 6.1–4.** XRF whole rock data of the units of the Almendros, Areñas and Guajara Members and the El Pinalito lavas.

## 6.1.2. EMPA work

### 6.1.2.1. Methodology

Seven samples of fresh interstitial glass (obsidian) belonging to units of the Retamares (Units A, B and C), Almendros, Chasna (RLA locality) and Areñas members were analysed at the Electron-Microprobe Lab, Department of Earth & Environmental Sciences at Ludwig-Maximilians-Universität (LMU), Munich. Sample chips of fresh glass were mounted for analysis of major element chemistry using a Cameca SX100 electron probe microanalyser (EMPA).

The measurements on the glass groundmass mounts were taken using a 15 kV accelerating voltage and 5 nA beam current. See Appendix IV for analysis parameters of the microanalyser. In order to prevent the volatilisation of the mobile Na and K elements within the glass groundmass during the measurements, a defocused electron beam (10 μm) with a counting time of 10 seconds was implemented.

Results were standardised against characterised minerals: albite (Na, Si), periclase (Mg), orthoclase (Al, K), apatite (P), wollastonite (Ca), Rutile (Ti), hematite ($Fe_2O^3$) (Fe), eskolaite ($Cr_2O_3$) (Cr), bustamite (Mn), vanadinite (Cl), and anhydrite (S). See Appendix IV for compositional data on standards used. Water content of the glasses is approximated by measuring the mass loss during heating samples up to 1300 °C using a Netzsch ® STA 449C instrument, outlined in Chapter 7, Section 7.3.2., which combines thermogravimetry and differential scanning calorimetry (DSC).

### 6.1.2.2. Results

The results of major element chemistry (SiO2, $TiO_2$, $Al_2O_3$, $Fe_2O_3$, $Na_2O$, $K_2O$, MgO, CaO, $Cr_2O_3$, MnO, $P_2O_5$, $SO_3$ and Cl) of the seven interstitial obsidian samples are presented in Table 6.1–5.

| | Retamares Mb | |
|---|---|---|
| Unit | B | C |
| | PP-02 | TN-09 |
| $SiO_2$ | 62.22 | 61.87 |
| $TiO_2$ | 0.94 | 0.95 |
| $Al_2O_3$ | 16.41 | 16.30 |
| $Fe_2O_3$ | 4.72 | 5.05 |
| $Na_2O$ | 8.76 | 9.30 |
| $K_2O$ | 5.25 | 5.10 |
| MgO | 0.53 | 0.47 |
| CaO | 0.52 | 0.48 |
| $Cr_2O_3$ | 0.03 | 0.02 |
| MnO | 0.25 | 0.33 |
| $P_2O_5$ | 0.09 | 0.08 |
| $SO_3$ | 0.14 | 0.16 |
| Cl | 0.15 | 0.18 |
| Total | 100.02 | 100.29 |

| | Almendros Mb | | | |
|---|---|---|---|---|
| Unit | RLA | | | |
| | TN-37 | TN-39 | PP-01 | TN-31 |
| $SiO_2$ | 62.60 | 62.65 | 61.27 | 60.86 |
| $TiO_2$ | 0.73 | 0.74 | 0.75 | 0.75 |
| $Al_2O_3$ | 18.04 | 18.14 | 19.04 | 18.95 |
| $Fe_2O_3$ | 3.18 | 3.13 | 3.47 | 3.49 |
| $Na_2O$ | 7.97 | 7.95 | 9.20 | 9.45 |
| $K_2O$ | 5.80 | 6.04 | 5.32 | 5.34 |
| MgO | 0.46 | 0.47 | 0.34 | 0.34 |
| CaO | 0.76 | 0.75 | 0.60 | 0.58 |
| | 0.01 | 0.01 | 0.02 | 0.02 |
| MnO | 0.23 | 0.18 | 0.27 | 0.25 |
| $P_2O_5$ | 0.11 | 0.10 | 0.08 | 0.07 |
| $SO_3$ | 0.05 | 0.05 | 0.05 | 0.04 |
| Cl | 0.18 | 0.19 | 0.26 | 0.24 |
| Total | 100.11 | 100.40 | 100.67 | 100.38 |

| | Chasna Mb |
|---|---|
| Unit | RLA |
| | VF-16/3 |
| $SiO_2$ | 62.88 |
| $TiO_2$ | 0.74 |
| $Al_2O_3$ | 18.13 |
| $Fe_2O_3$ | 3.05 |
| $Na_2O$ | 7.91 |
| $K_2O$ | 5.83 |
| MgO | 0.42 |
| CaO | 0.76 |
| | 0.03 |
| MnO | 0.20 |
| $P_2O_5$ | 0.12 |
| $SO_3$ | 0.09 |
| Cl | 0.18 |
| Total | 100.33 |

**Table 6.1–5.** Results of major element chemistry from EMPA on glasses from four units across the Retamares, Almendros and Chasna Members.

## 6.1.3. Discussion

### 6.1.3.1. Classification

In studies outlining ignimbrite geochemistry, particularly where the focus is on chemical stratification or zonation of deposits, the analysis of fresh pumice, or fiamme (e.g., Hildreth & Wilson, 2007) is preferred to whole rock samples. However, such materials cannot be extracted from ignimbrites with welding intensities beyond rank V (Chapter 5). In these samples, post-depositional processes, such as devitrification, secondary crystallisation and vapour-phase alteration are likely to have altered and masked the original magmatic concentrations of major and trace elements (Hildreth & Mahood, 1985).

The five members plot within the trachyte field on the TAS diagram (Figure 6.1–1), as do many of the phonolitic rocks of the Las Cañadas caldera of ages >0.2 Ma (e.g. Zafrilla, 2001; Bryan et al., 2002; Soriano et al., 2009; Smith, 2012) due to alkali depletion as a result of weathering, devitrification and vapour-phase alteration (Zafrilla, 2001; Bryan et al., 2002). Vapour phase alteration in particular is prevalent throughout the units, and this is likely behind the scattered MgO, CaO and alkali concentrations (e.g. Bryan, 2006). The leaching of alkalis in felsic glasses, due to post-depositional alteration and hydration (Scott, 1971), makes TAS diagrams (Figure 6.1–1) largely unreliable for classification of these units.

The Winchester and Floyd (1977) classification diagram, modified by Pearce (1996) (Figure 6.1–2), uses elements less likely to be affected by fractionation and

alteration, and plots the ignimbrites largely as phonolitic, with some units bordering on trachytic composition, with the exception of the Chasna Mb at the Llano de las Mesas locality which has a more intermediate composition, plotting within the tephriphonolite field.

The results of the interstitial obsidian samples provide an insight into the approximate magmatic composition, plotting largely within the phonolitic field, and at the boundary between the trachytic and phonolitic fields on the TAS diagram, in alignment with whole rock samples belonging to the same units on the Zr/Ti vs. Nb/Y diagram. The glass compositions can be considered to represent the least altered composition of each sampled unit, recording a composition prior to any subsequent alteration by weathering, secondary crystallisation, and devitrification.

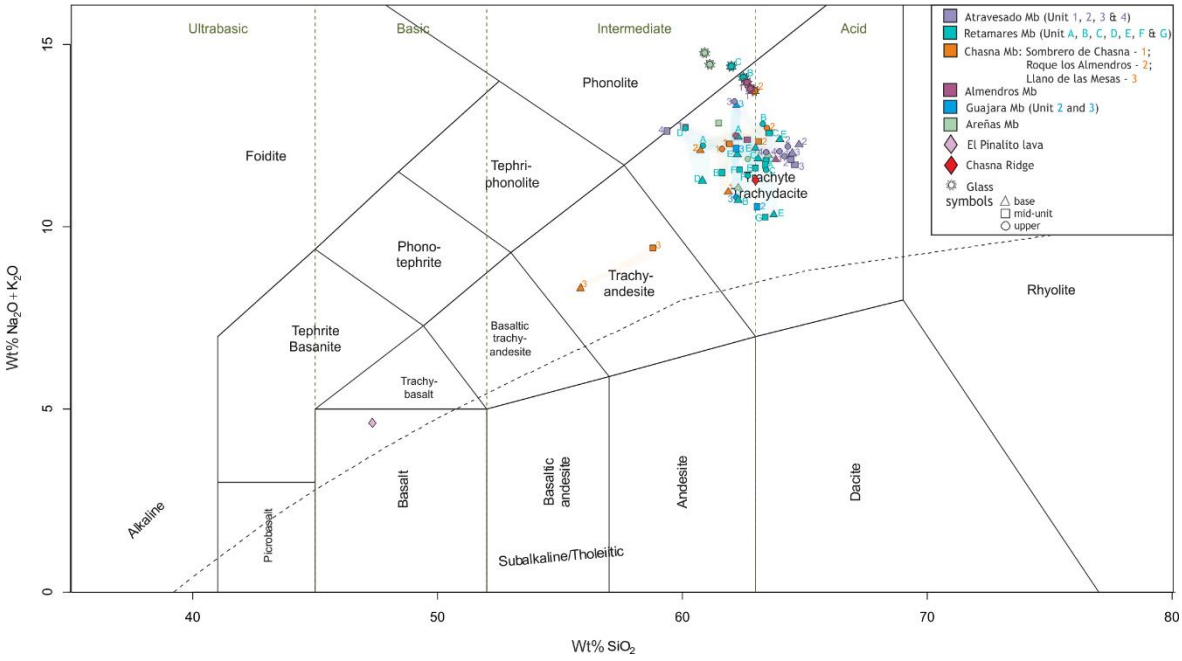


**Figure 6.1–1.** Total alkali ($Na_2O$ + $K_20$ wt. %) vs. silica ($SiO_2$) plot (TAS) (Le Bas et al., 1986) for whole rock XRF data for each Member and EMPA glass compositions. Symbols indicate the stratigraphic position of each unit (i.e. the base, middle and uppermost horizon).

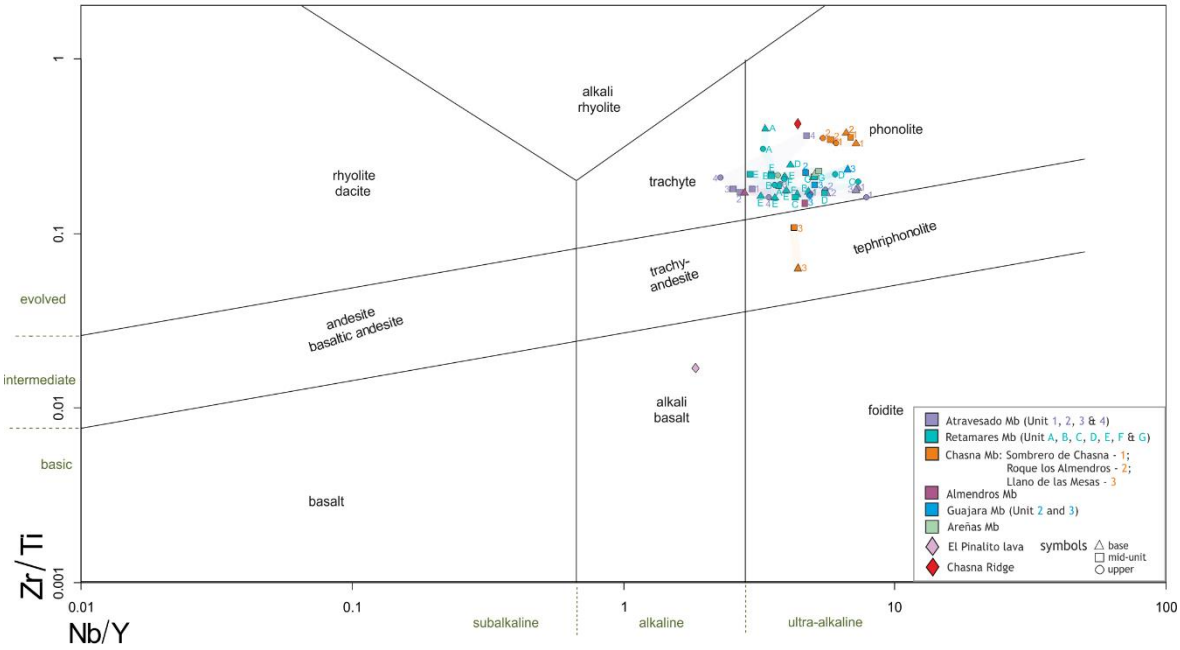


**Figure 6.1–2.** Zr/Ti vs. Nb/Y classification diagram of Winchester and Floyd (1977) modified by Pearce (1996) for whole rock XRF data for each Member. Symbols indicate the stratigraphic position of each unit (i.e. the base, middle and uppermost horizon).

Wider studies into the geochemistry of Tenerife phonolites, mostly focussed on the deposits in the south of the island, show that the pyroclastic deposits are geochemically similar, attributing fractional crystallisation as the dominant process behind phonolitic magma production (e.g. Wolff, 1984; Wolff & Storey, 1984; Palacz & Wolff, 1989; Bryan et al., 2002; Bryan, 2006). From this study, there is no distinct difference in the compositions between those of the Ucanca and Guajara Formations.

### 6.1.3.2. Cryptic zonation

Zoning or chemical stratification in caldera-forming eruptions is well documented, (e.g. Smith & Bailey, 1966; Conrad, 1984; Civetta et al., 1997; Milner et al., 2003; Hildreth & Wilson, 2007; Hernando et al., 2019) and the nature of which is dependent on the eruption dynamics and the style of magma withdrawal from a reservoir (e.g. Blake, 1981; Blake & Ivey 1986i; 1986ii). Normal zoning in pyroclastic deposits, from an initial more evolved basal composition, to a generally less evolved composition toward the uppermost horizons of the deposit (e.g. Hildreth, 1979, 1981; Wolff & Storey, 1984; Wörner & Schmincke 1984i, 1984ii; Druitt & Bacon, 1986; Duffield et al., 1995) is considered to represent an

inverse reflection of a portion of a compositionally zoned shallow reservoir. This has also been noted in the Poris Formation on Tenerife, albeit from two potentially petrogenetically distinct magma batches, observed in both the proximal (Smith & Kokelaar, 2013) and distal deposits (Edgar et al., 2002; Brown & Branney, 2004).

Although there is no distinct differences in the compositions of the units within each member, with the exception of the Chasna Mb, the units exhibit complex vertical chemical variations, in both major and trace element concentrations, with larger excursions seen in the latter. In the Ucanca Fm, there is a slight trend from slightly more evolved compositions in the youngest Atravesado and Retamares units, to more intermediate compositions in the Chasna members, with the Chana Mb at the Llano de Ucanca representing the least evolved composition of all units, with $SiO_2$ concentrations of 56 - 58 wt. %. $SiO_2$ concentrations in all other units range from 59 - 64 wt. %, with scatter shown by the alkalis and more mobile elements (Figure 6.1–3), which can be attributed to the discussed post-depositional alteration processes. There is very minimal vertical chemical zonation of major elements shown by individual units or members, typically between 2 and 3 wt. % $SiO_2$.

The immobile trace elements (Ba, Nb, Zr and Th), which are less likely to be affected by alteration, do not display the extent of scatter seen by most elements, and display incremental gradations when plotted against the stratigraphy, and indirectly, height (Figure 6.1–5). Zr has been used in both the Harker plots (Figure 6.1–4) and against the stratigraphy as it is a key index element typically used in studies of geochemical variation of pyroclastic rocks on Tenerife (e.g. Wolff et al., 2000; Edgar et al., 2002; Smith, 2012; Schwartz-Mesa, 2016) due to its incompatibility in the Tenerife magma series and that it remains unaffected during subsequent hydrous alteration (Wolff et al., 2000; Edgar et al., 2002). The units are considered high-Zr (Edgar et al., 2002) with concentrations ranging between 705 – 2707 ppm.

Vertical variations in the enrichment and depletion of immobile trace element (Zr, Nb, and Th) concentration (Figure 6.1–5) generally show smooth trends, with considerably more variation observed in the units of the Atravesado and Retamares Members. The units of the Atravesado Mb show an incremental, but

overall enrichment in immobile trace elements, with the lowest values seen in the base of each unit, and the highest values seen at the top. Zr concentrations show an increase from 878 ppm to 1706 ppm from the base of Unit 1 to the uppermost horizon of Unit 4, with the lowest value observed at the base of Unit 2. A more complex, 'zig-zagging' pattern in enrichment and depletion of immobile trace elements is seen in the units of the Retamares Mb. The highest values in immobile trace elements are seen at the base of Unit A and the uppermost horizon of Unit F, with 'zig-zagging' oscillations between enrichment or depletion from the base to top of each unit, with marked changes in concentrations seen at the boundary between each unit. All units show an up-sequence enrichment in immobile trace elements, with the exception of Units A and C, which show a reverse cryptic zonation, in a gradual decrease in element concentrations from base to top, atypical of compositional zoning in pyroclastic deposits. Very little variation is seen in the immobile trace element concentrations from base to top in the Units of the Chasna, Almendros, Guajara and Areñas Member units, with only minor up sequence enrichment of Zr (maximum: 200 ppm).

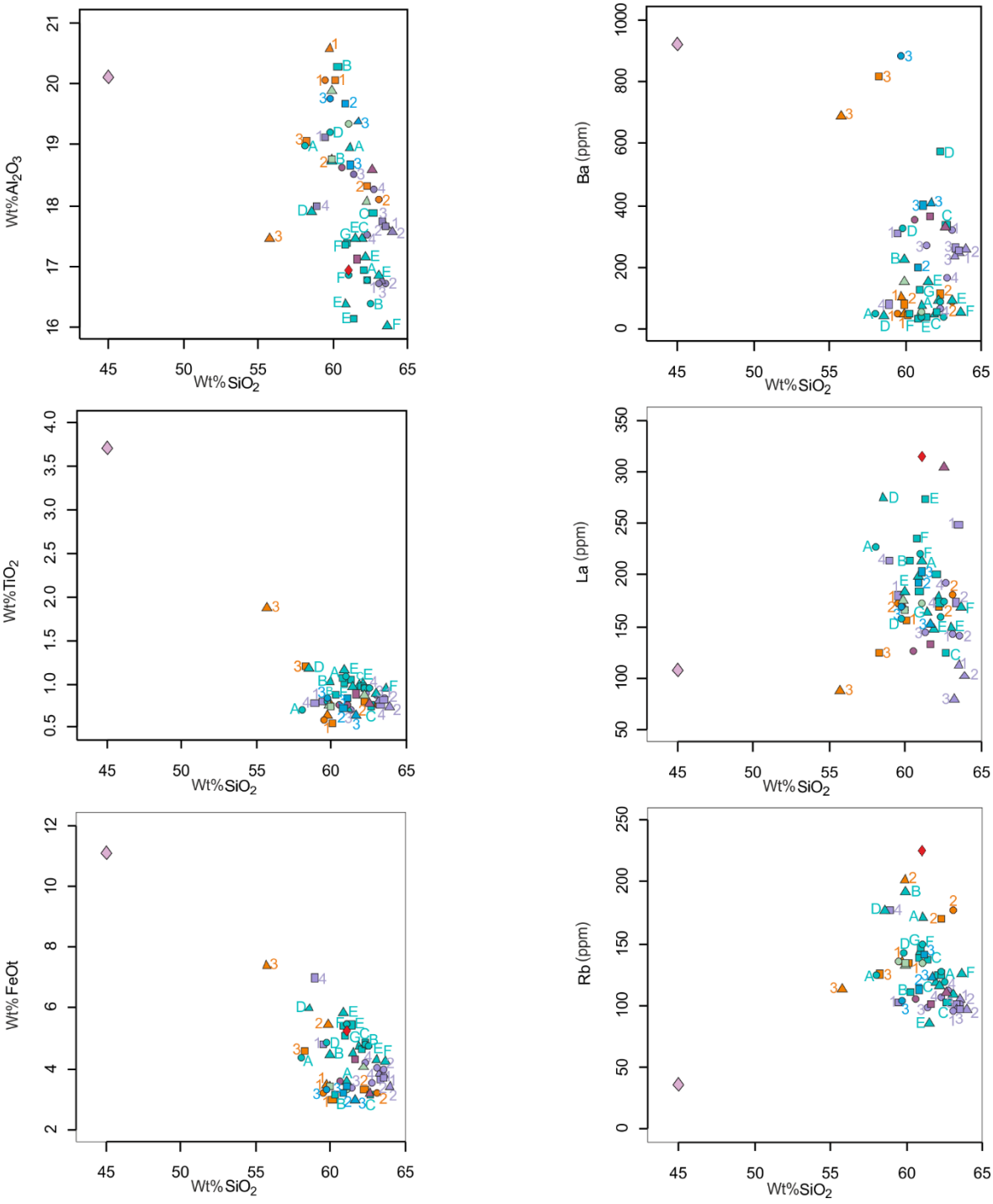


Continues overleaf

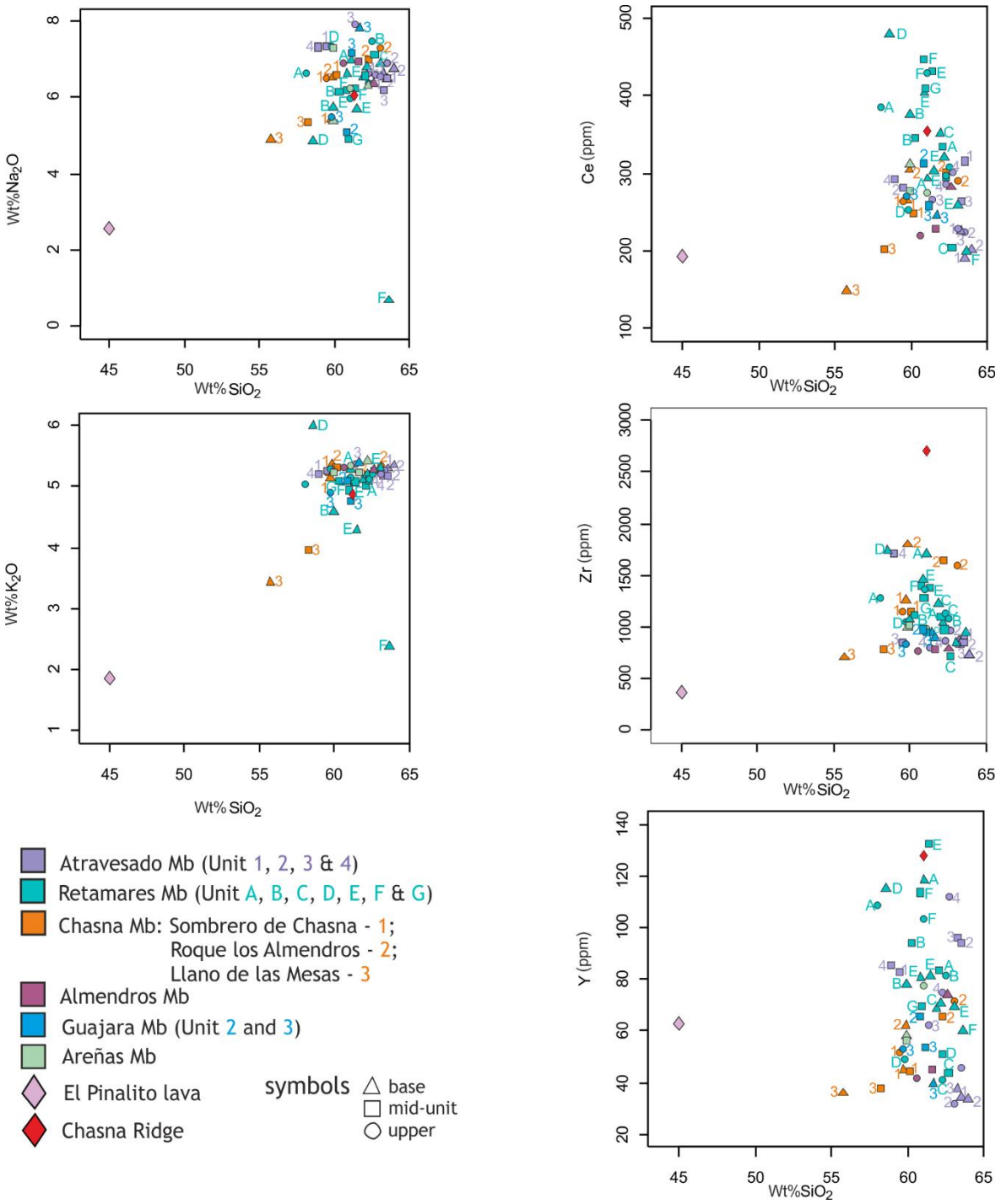


**Figure 6.1–3.** Selected major and trace element variation plots (Harker diagrams) against $SiO_2$ for whole rock (XRF) data for each mapped unit throughout the stratigraphy. Harker diagrams for $SiO_2$ against full suite of elements is presented in Appendix IV.

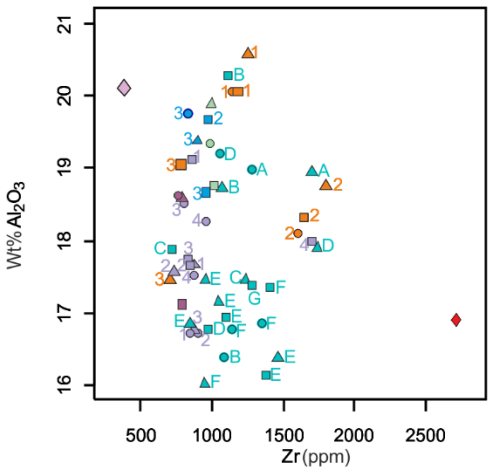


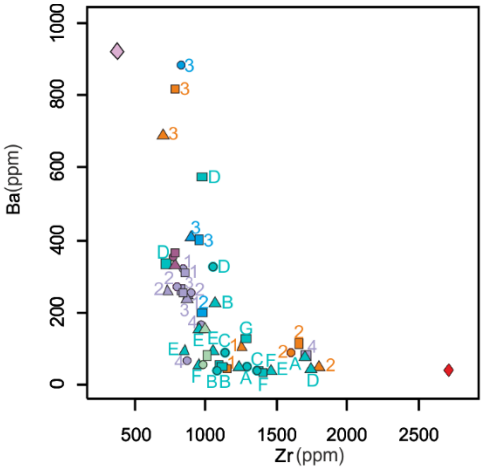


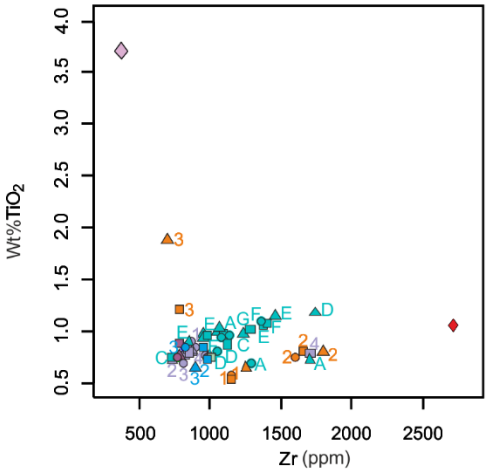


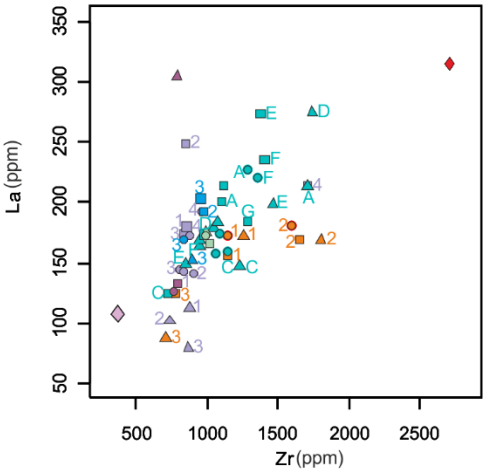


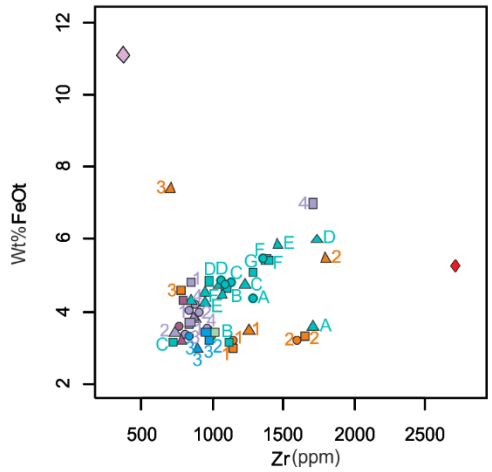


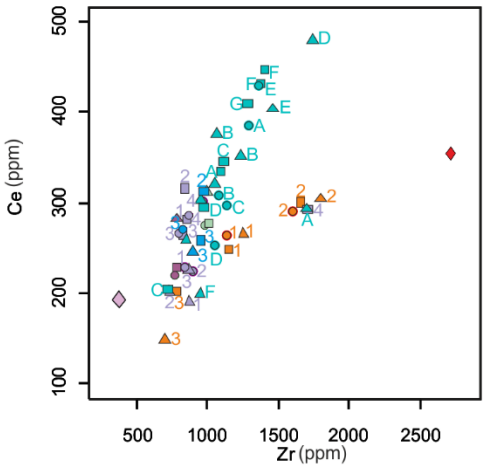


Continued overleaf.

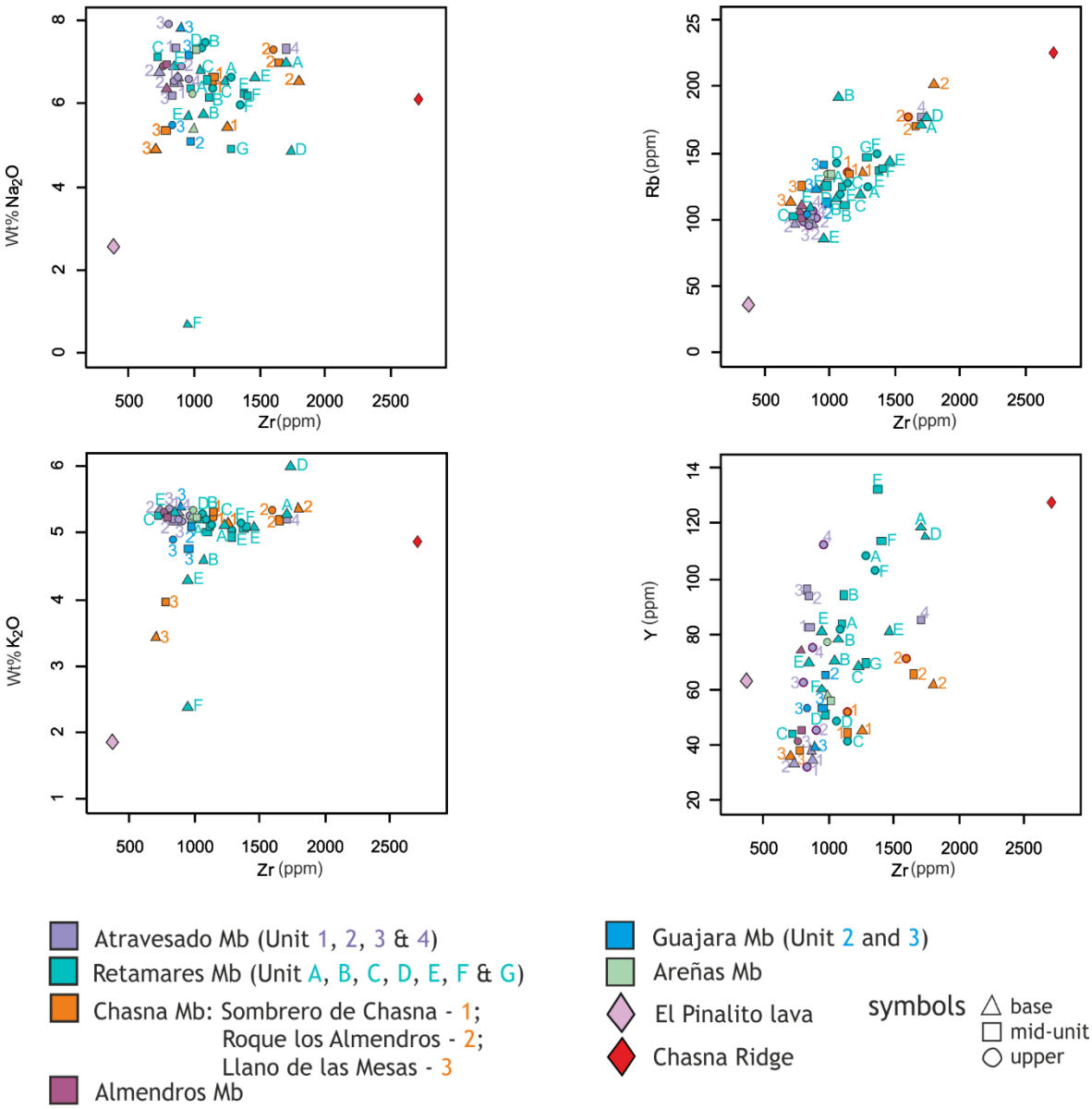


**Figure 6.1–4.** Selected major and trace element variation plots (Harker diagrams) against Zr for whole rock (XRF) data for each mapped unit throughout the stratigraphy. Harker diagrams for Zr against full suite of measured elements is presented in Appendix IV.

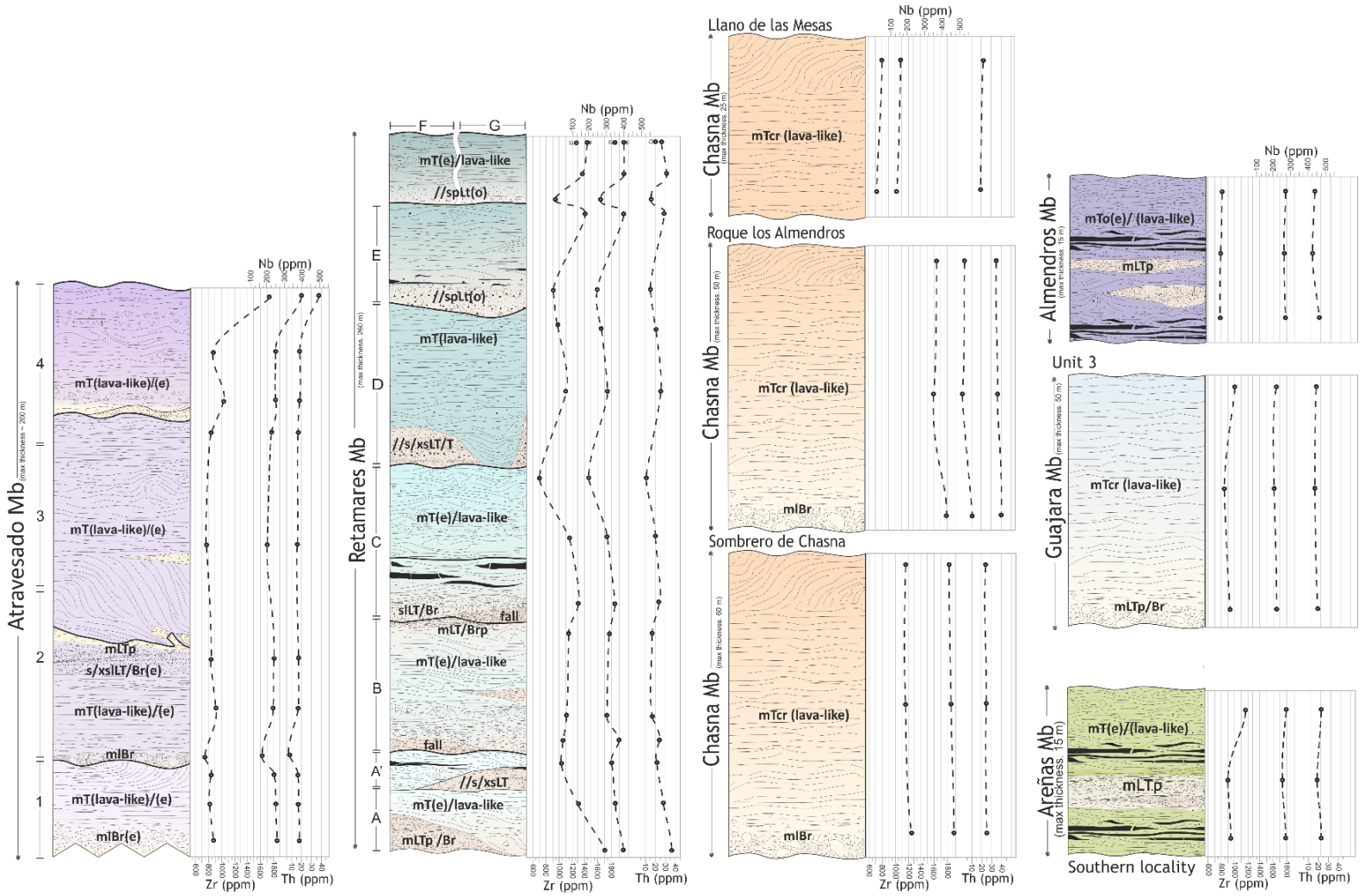


**Figure 6.1–5.** Stratigraphic position of samples from each unit of the mapped members vs. Zr (left trace), Nb (middle trace) and Ba (right trace) ppm concentrations. Dashed lines indicate presumed and inferred variation of Zr, Nb and Ba, but this may vary with more data collected.

#### 6.1.3.2.1. Discussion on visible zoning

The occurrence of colour variations and stratification in both pumice and the matrix component with the non-welded to partially welded lithofacies (I-IV) in many of the units is described in Chapter 4 (e.g. Figure 4–19, 4–20, 4–82, 4–83). Colour variation in fresh pumice can be attributed to differences in major element composition, differential scattering of light due to vesicularity, or the presence of microcrysts within the pumice groundmass (Fisher & Schmincke, 1984; Klug & Cashman, 1994). Post-depositional secondary mineral growth (Honnorez, 1969; Capaccioni & Coniglio, 1995; Carrasco-Núñez et al., 2012), such as $Fe^{3+}$ -rich oxide microcrysts (Paulick & Franz, 1997) have also been attributed to colour variation seen in pumice within the same deposits.

Variation in chemical composition was investigated in the base of Unit E of the Retamares Mb, which shows distinct colour variation in pumice horizons in the basal stratigraphy. Four pumice samples were analysed from the non- to weakly-welded base, outlined in Figure 4–82 and 4–83. As described, the unit vertically and incrementally grades up in welding intensity, from non-welded, to lava-like for much of the unit's thickness. Cream, olive green, dark brown and rusty orange pumice form distinct horizons and also appear variably mixed in horizons and lenses (Figure 6.1–6). The stratigraphy and spatter-like, fluidal, and blobby morphology of the pumice boundaries indicate that this deposit belongs to the same eruption phase(s), with no reworking or sorting of the pumice having taken place.

Results show there is no distinct nor wholly convincing compositional difference between the coloured pumice samples (Table 6.1–6) to suggest the apparent colour stratification indicates tapping of different compositions or magma mixing event(s). Variations in Zr, Nb, and Th concentrations between the samples further indicate weak, incremental, cryptic chemical zoning at the base of the unit. The observed colour variation may be a result of differential hydrothermal alteration (e.g. Donoghue, et al., 2008) or weathering of the deposit, perhaps due to the minor chemical differences, and ultimately requires further investigation to shed light on the multi-coloured deposit.

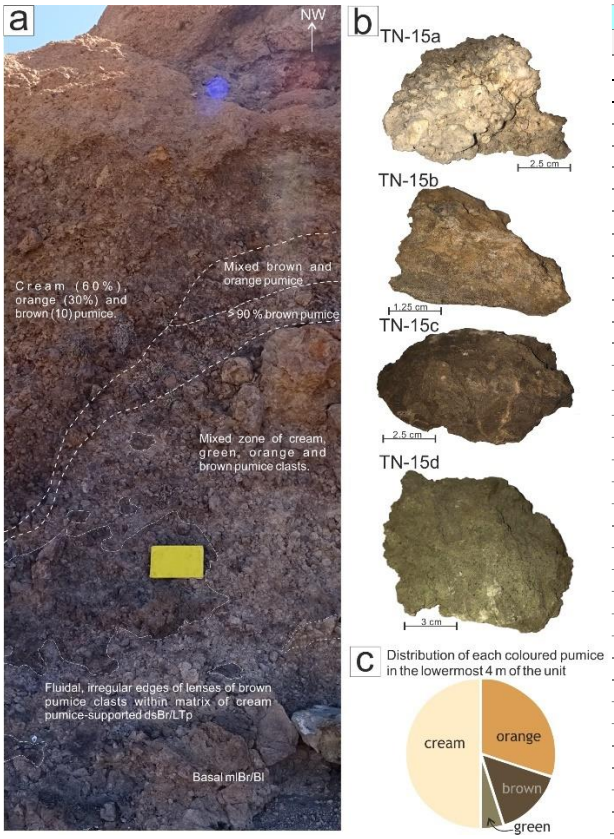


| Retamares Mb | | | | |
|---|---|---|---|---|
| Unit E | | | | |
| | TN-15a | TN-15b | TN-15c | TN-15d |
| $SiO_2$ | 61.47 | 63.05 | 62.17 | 60.86 |
| $Al_2O_3$ | 17.46 | 16.85 | 17.15 | 16.38 |
| $Fe_2O_3$ | 5.02 | 4.77 | 5.23 | 6.48 |
| MgO | 0.47 | 0.24 | 0.36 | 0.35 |
| CaO | 0.60 | 0.23 | 0.40 | 0.36 |
| $Na_2O$ | 5.70 | 6.89 | 6.82 | 6.62 |
| $K_2O$ | 4.275 | 5.316 | 5.187 | 5.096 |
| $TiO_2$ | 0.970 | 0.888 | 0.996 | 1.153 |
| MnO | 0.398 | 0.250 | 0.310 | 0.414 |
| $P_2O_5$ | 0.108 | 0.069 | 0.102 | 0.060 |
| LOI | 3.21 | 1.16 | 1.37 | 1.93 |
| Total | 99.68 | 99.70 | 100.09 | 99.71 |
| | | | | |
| Zn | 165 | 165 | 198 | 220 |
| Cu | 16 | 22 | 19 | 9.3 |
| Ni | n.d. | 15 | n.d. | n.d. |
| Cr | 18 | 54 | 18 | 4.9 |
| V | 36 | 24 | 36 | 52 |
| Ba | 152 | 91 | 92 | 39 |
| Sc | 3 | 2.5 | 3.4 | 3.6 |
| La | 163 | 148 | 179 | 199 |
| Ce | 303 | 258 | 321 | 403 |
| Nd | 132 | 103 | 125 | 137 |
| Sr | 27 | 16 | 17 | 14 |
| U | 4.1 | 4.2 | 3.8 | 3.5 |
| Rb | 85 | 109 | 116 | 143 |
| Th | 18 | 17 | 20 | 27 |
| Pb | 12 | 20 | 24 | 16 |
| Nb | 259 | 250 | 280 | 317 |
| Zr | 952 | 851 | 1049 | 1461 |
| Y | 81 | 70 | 71 | 81 |
| Sr | 24 | 14 | 16 | 12 |
| Rb | 85 | 110 | 118 | 146 |

**Figure 6.1–6.** Basal 4 m of Retamares Unit E at N28 12’48” W016 37’9”. See Figure 4–83 for log Eiii and description. a) Annotated basal stratigraphy displaying distribution of coloured pumice in the basal massive to diffuse stratified lapilli tuff and breccia. b) Photographs of each coloured pumice sample. c) Pie-chart of overall distribution of the pumice varieties.

**Table 6.1–6.** Results of XRF analysis of the four coloured pumice samples at the base of Retamares Unit E. TN-15a: cream pumice; TN-15b: orange pumice; TN-15c: dark brown pumice; TN-15d: olive green pumice.

## 6.2. Petrography and textures

An overview of the mineralogy and textures from optical microscopy and SEM (Scanning Electron Microscopy) analysis is presented, providing further insights into the nature of welding (as summarised in Table 5–10), deposition, cooling, and post-depositional alteration of the deposits. Polished thin sections were prepared and analysed at the School of Geographical and Earth Sciences, University of Glasgow.

### 6.2.1. Ucanca Formation

As outlined in this chapter, the mapped deposits of the Ucanca Formation are predominantly peralkaline phonolites, with a more trachytic composition seen in the Chasna Member at Llano de las Mesas. The crystal-rich units (Atravesado and Chasna Members) contain abundant crystals (up to 3 cm) of anorthoclase, hornblende amphibole, Na-augite, Fe-Ti oxides, nepheline, and minor biotite (Araña, 1971).

#### 6.2.1.1. Atravesado Member

The units of the Atravesado Member are rich in crystals (up to 3 cm) of octahedral and circular leucite crystals and euhedral sanidine, which often appear broken and fragmented, in a 'fuzzy' matrix of finer grained feldspathoids, sanidine and anorthoclase (Figure 6.2–1). The welded (>V) facies which dominates much of each unit's thickness, displays a trachytic texture with varying degrees of devitrification and recrystallisation, resulting in this 'fuzzy' and blurred texture due to pervasive bowtie and axiolitic spherulite growth (Figure 6.2–1 c). Evidence of original pyroclast boundaries are largely absent, with 'ghost' remnants of deformed pumice lapilli and fiamme seen in cloudy and raggedy colour variations and occasional partial faint outlines, which are largely overgrown by spherulites (Figure 6.2–1 a). Spherulites are up to 3 μm in diameter and associated with minor Fe- and Ti-oxide nanolites in the boundaries and void space between crystals (Figure 6.2–1 e & f). A clear fabric, occasional banding, and an alignment of euhedral sanidine is shown by each unit, with minor wrapping of the fabric around crystals.

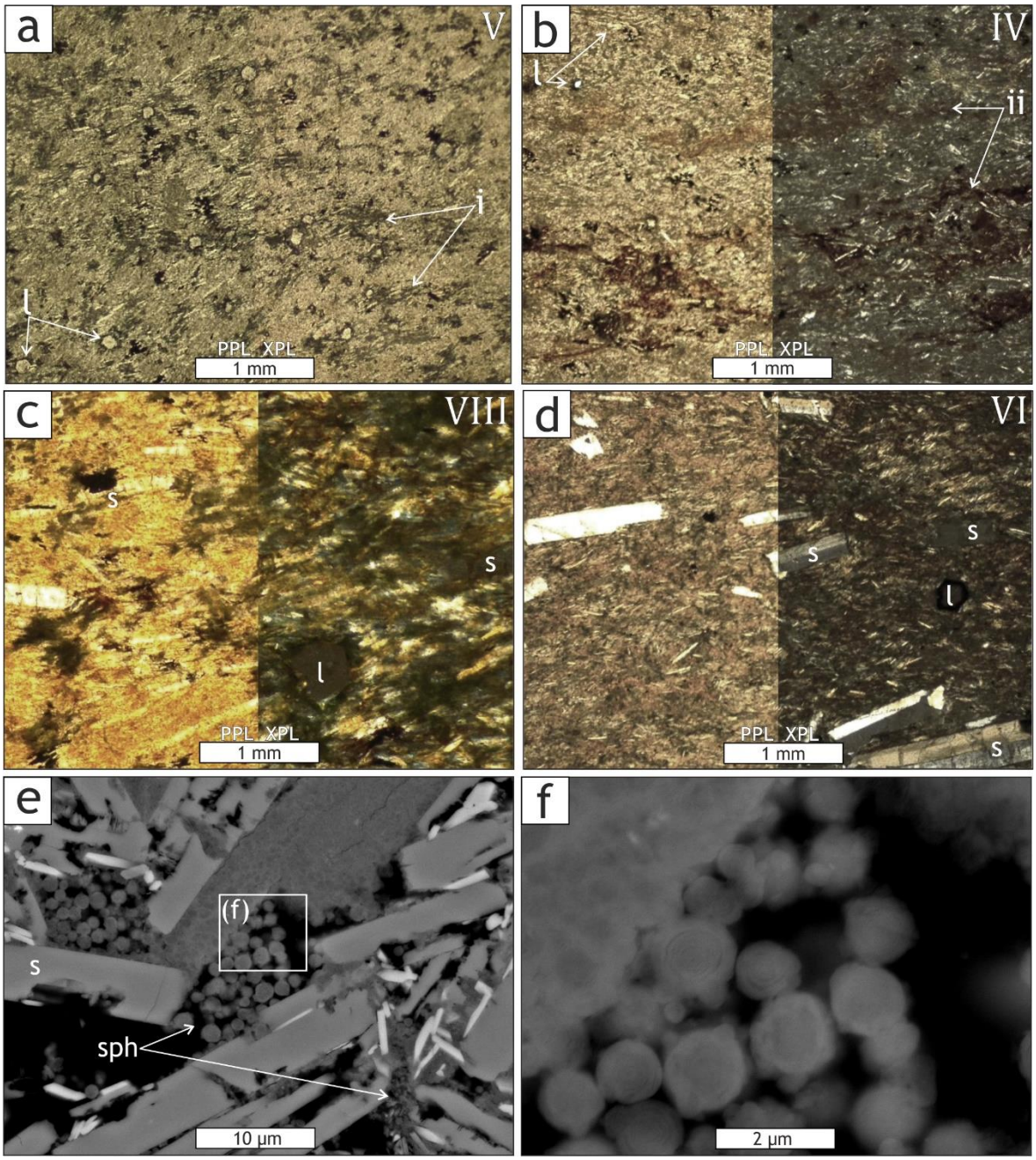


**Figure 6.2–1.** Photomicrographs of the units belonging to the Atravesado Member. Welding ranks (as determined in Chapter 5) are denoted on the top right corner. Both plane-polarised light (PPL) and cross polarised light (XPL) are shown where indicated. Abbreviations: l=leucite; s=sanidine; sph=spherulites. a) Strongly welded base of Unit 1 (TN-24) with a matrix of aligned sanidine crystals and nepheline crystals. Faint 'ghost' raggedy fiamme and banding of darker and lighter patches (marked by i) are seen, parallel to crystal alignment. Pyroclast and deformed pumice lapilli boundaries are largely visible. b) Moderately welded middle region of Unit 2 (TN-32), with visible altered and deformed pyroclast boundaries and raggedy fiamme. ii – highlights altered and stretched fiamme. c) Coarse grained, devitrified upper region of Unit 3 (TN-33) displaying a 'fuzzy' trachytic texture, with aligned tabular sanidine crystals. d) Densely welded upper domain of Unit 4 (TN-01) with a lesser extent of devitrification than (c), with aligned sanidine crystals (up to 3 cm) and leucite, in a matrix of trachytic texture predominantly of anorthoclase and sanidine. 'Ghost' pumice lapilli and fiamme is visible as brown/red patches. e) SEM image of Unit 3 (c) from section TN-33, highlighting concentric spherical spherulitic growth in voids between sanidine crystals and feldspathoids, with (f) showing a closer view of the concentrically ringed spherulites.

### 6.2.1.2. Retamares Member

The units of the Retamares Member display a wide range of welding intensities and thus microscale welding textures, from non-welded to lava-like, displaying various phases and extents of alteration, rheomorphism and recrystallisation. Higher welding intensities display more pervasive devitrification (e.g. Figure 6.2–2 b), and an upwards in increase in welding intensity (and devitrification) can be seen comparing the middle and upper regions of Units A (Figure 6.2–2 a-b).

Crystals are not as abundant as in the units of the Atravesado and Chasna members and are typically smaller (up to 1 mm) (Figure 6.2–2 g & j), with rare leucite, sanidine, anorthosite and biotite. However, ash-grade lithic fragments are common, forming entire bands and graded lenses (Figure 6.2–2 h) of lithic fragments comprising of ignimbrite displaying varying welding intensities and basalt (Figure 6.2–2 d).

The matrix of the majority of the welded (>V) facies display 0.5 – 3 mm elongated and glassy fiamme, some of which display imbrication with planar fabrics (Figure 6.2–2 f), and are devitrified to varying degrees. Flow banding and planar fabrics are common, with alternating fine (glassy) and coarser (coarse ash or lithic lapilli) areas (Figure 6.2–2 b, c, f, h and i) interpreted to be controlled by the original sedimentological grain size variation (e.g. stratification) of material. This is supported by the erosional surface preserved in the mm-scale cross bedding in the moderately welded base of Unit E (Figure 6.2–2 h), further supporting the interpretation of these deposits as deposits of pyroclastic density currents, discussed further in Chapter 7.

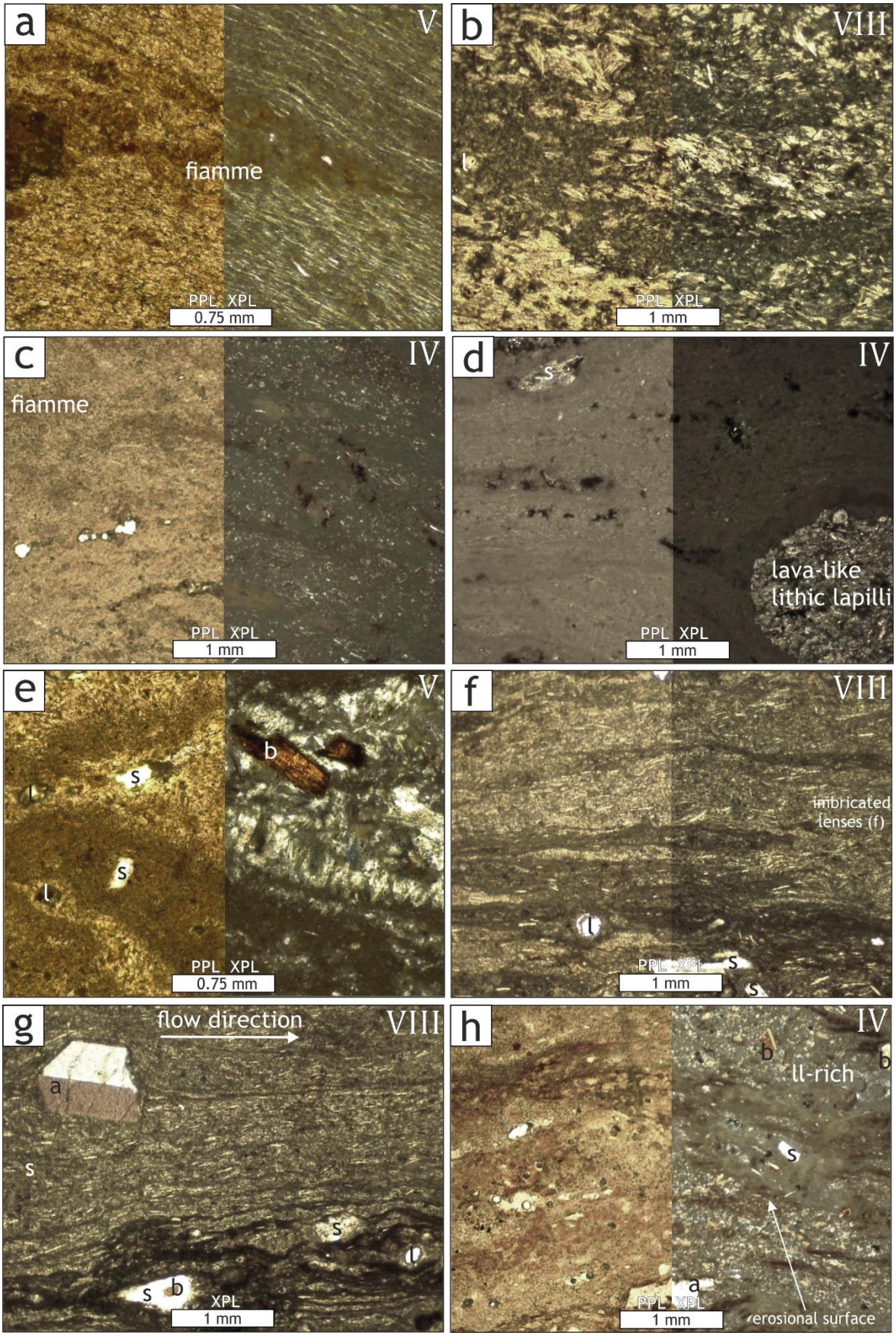


Continued overleaf

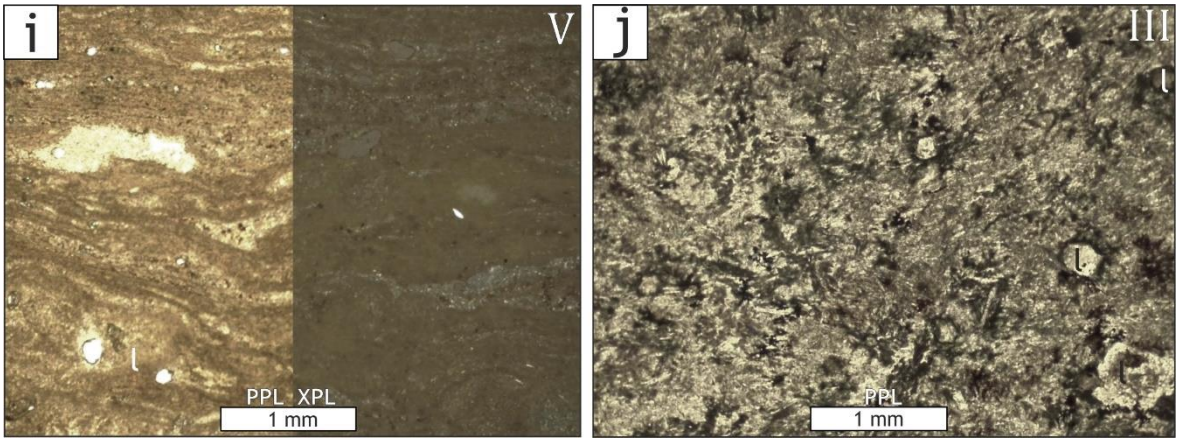


**Figure 6.2–2.** Photomicrographs of the units belonging to the Retamares Member. Welding ranks (as determined in Chapter 5) are denoted on the top right corner. Both plane-polarised light (PPL) and cross polarised light (XPL) are shown where indicated. Abbreviations: l=leucite; s=sanidine; a=anorthosite; b=biotite; ll=lithic lapilli; f=fiamme. a) Strongly welded middle region of Unit A (TN-10) with a very well-defined fabric with banding and alignment of euhedral sanidine crystals and stretched fiamme. b) Differential devitrification of the lava-like facies of the upper region of Unit A (TN-40), with 'fuzzy' trachytic texture and spherulitic growth alternating with finer grained, lithic fragments (of ash-grade) bands. Note the upwards increase in welding from middle (a) to the upper region of Unit A. c) Banded and folded fabric of the moderately welded, crystal-poor middle region of Unit B (TF-03) with flattened and deformed pumice and fiamme. d) The upper crystal-poor moderately welded facies of Unit B (TN-41) displaying weak banding around crystals and lithic lapilli. Pyroclast boundaries are largely visible, with an alternation of grain size. e) Highly devitrified upper domain of the strongly welded and banded Unit C (TF-02) with alternating bands of finer grained darker (glassier) material and highly devitrified and fizzy lighter bands, with crude trachytic texture and a 'fuzzy' appearance due to bowtie spherulitic growth between crystals. f) Flow banded lava-like facies of the upper region of Unit D (TN-42) with alternating bands and lenses of glassy (darker coloured) finer material and the lighter bands rich in fine grained aligned sanidine crystals. Imbrication and climbing of the darker coloured bands is seen, indicating syn-depositional shearing of planar fabrics. g) Flow banded lava-like facies of the upper region of Unit D (TN-42) again displaying alternating glassy (dark) and light bands, with fabrics wrapped and deformed around crystals, indicative of the flow direction. h) Moderately welded base of Unit E with visible sedimentary features, showing cross stratification in mm-scale tuff and lapilli tuff, with occasional sanidine and leucite crystals. i) Strongly welded middle region of Unit F (TN-20) showing flow banding and wrapping of fabrics around fiamme and elongated and stretched pumice fragments. j) Partial welded upper domain of Unit G (TN-17) with visible pyroclast and shard boundaries, but moderate spherulite growth, particularly on the borders of leucite crystals, resulting in a 'fuzzy' and grainy texture.

### 6.2.1.3. Chasna Member

Devitrification and extensive alteration is displayed by the intensely welded and lava-like lithofacies in the units of the Chasna Member. Prevalence of spherulitic growth shows a correlation with grade of welding, which typically increases up section, with the upper contorted domains, associated with the ogives and ramping (as discussed in Chapter 4) displaying distinctly 'fuzzy' and altered textures (Figure 6.1–1 a-b & e-f). There is no trace of vitroclastic textures largely due to recrystallisation of the glassy matrix, but there is evidence of two-stage rheomorphism with the development of a weak crenulation and imbrication of sanidine crystals (Figure 6.2–3 d).

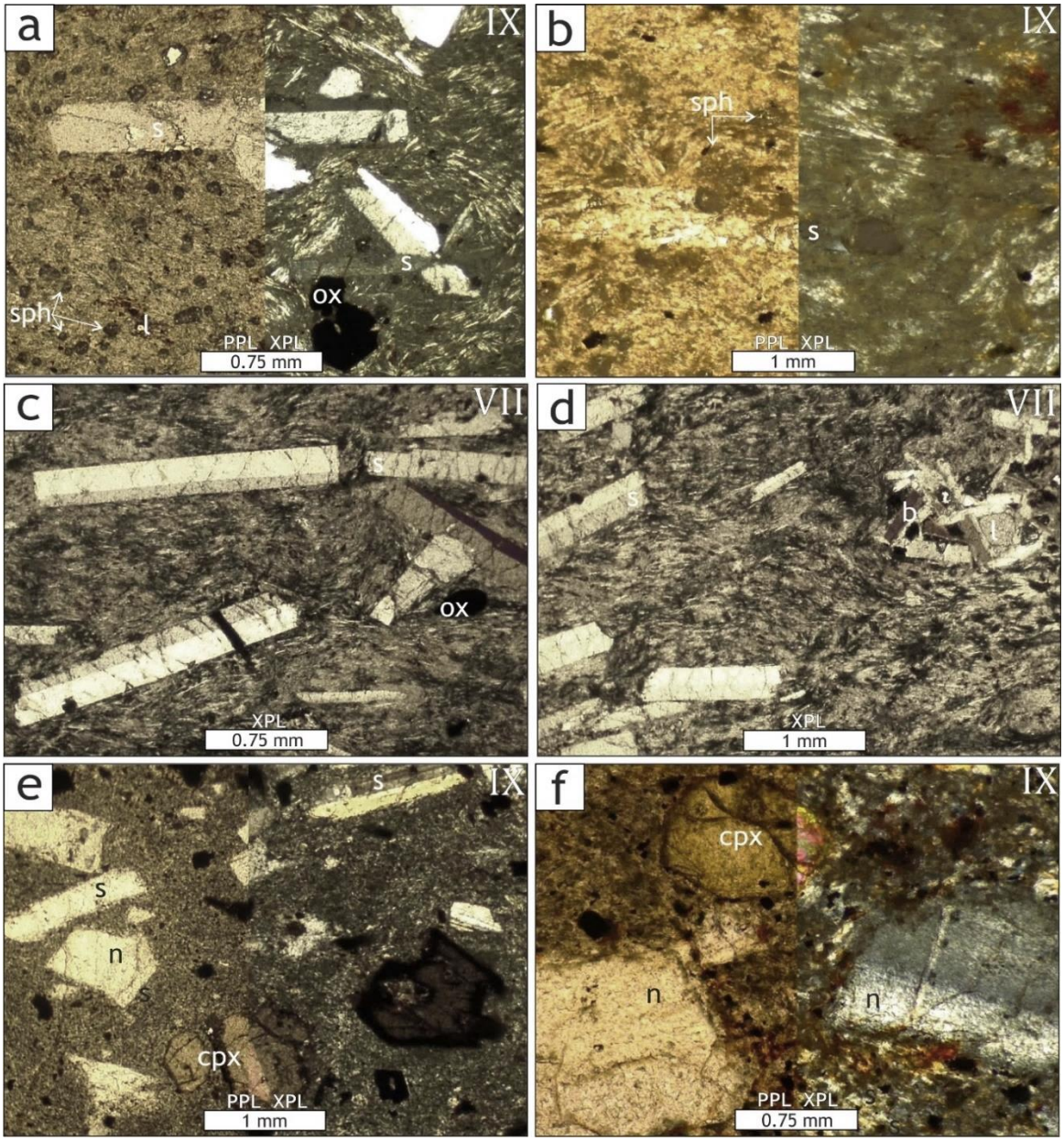


**Figure 6.2–3.** Photomicrographs of the units belonging to the Chasna Member. Welding ranks (as determined in Chapter 5) are denoted on the top right corner. Both plane-polarised light (PPL) and cross polarised light (XPL) are shown where indicated. Abbreviations: l=leucite; s=sanidine; cpx=clinopyroxene; n= nepheline; ox=oxides (opaques); b=biotite; sph=spherulites. a) Lava-like lithofacies of the middle region of the crystal-rich Chasna Mb at the Sombrero de Chasna (TN-08), with pervasive spherulite growth, both as concentrically ringed brown circular growths, and interstitial fibrous (bowtie) growth in the trachytic textured matrix. A highly deformed and folded fabric is visible, which is wrapped and rotated around coarse (up to 3 cm) sanidine crystals. b) More pervasive spherulitic growth and devitrification is seen towards the upper domain of the crystal-rich lava-like Chasna Mb at the Sombrero de Chasna (VF-16/2), with a 'fuzzy' and grainy appearance to the trachytic textured matrix, with altered and broken crystals. c) & d) Intensely welded and lava-like lithofacies of the middle region of the Chasna Mb at Roque los Almendros (TN-36), displaying a strong fabric throughout, and a hint of a secondary cleavage (d). Fabrics are wrapped and rotated around euhedral sanidine crystals, which are crudely aligned, parallel to secondary cleavage planes (d). e) Lava-like lithofacies of the middle region of the Chasna Mb at Llano de las Mesas (TN-16), with a largely aphyric, fine grained glassy matrix, with large crystals of sanidine, nepheline and clinopyroxene. No evidence of vitroclastic textures or flow banding present. f) Highly altered and devitrified upper domain of the Chasna Mb at Llano de las Mesas (TN-12), with a 'fuzzy' and grainy matrix due to pervasive spherulitic growths throughout, particularly around crystal edges. Crystals are more broken and altered than is seen in (e).

### 6.2.1.4. Almendros Member

Despite exhibiting relatively lower intensities of welding (moderately to densely welded) than the Chasna and Atravesado Members, the Almendros Mb has undergone vapour-phase alteration, producing pervasive spherulitic growth around the margins of both glassy banding crystals (Figure 6.2–4 a & b). Crystals are relatively poor, with rare broken sanidine crystals, associated with 1-2 mm dark brown spherulitic rims in the ash-rich base of the unit. The presence of alternating glassy banding with lithic fragments of ash-grade (Figure 6.2–4 d) is interpreted to represent the original pre-welding sedimentological nature of the material.

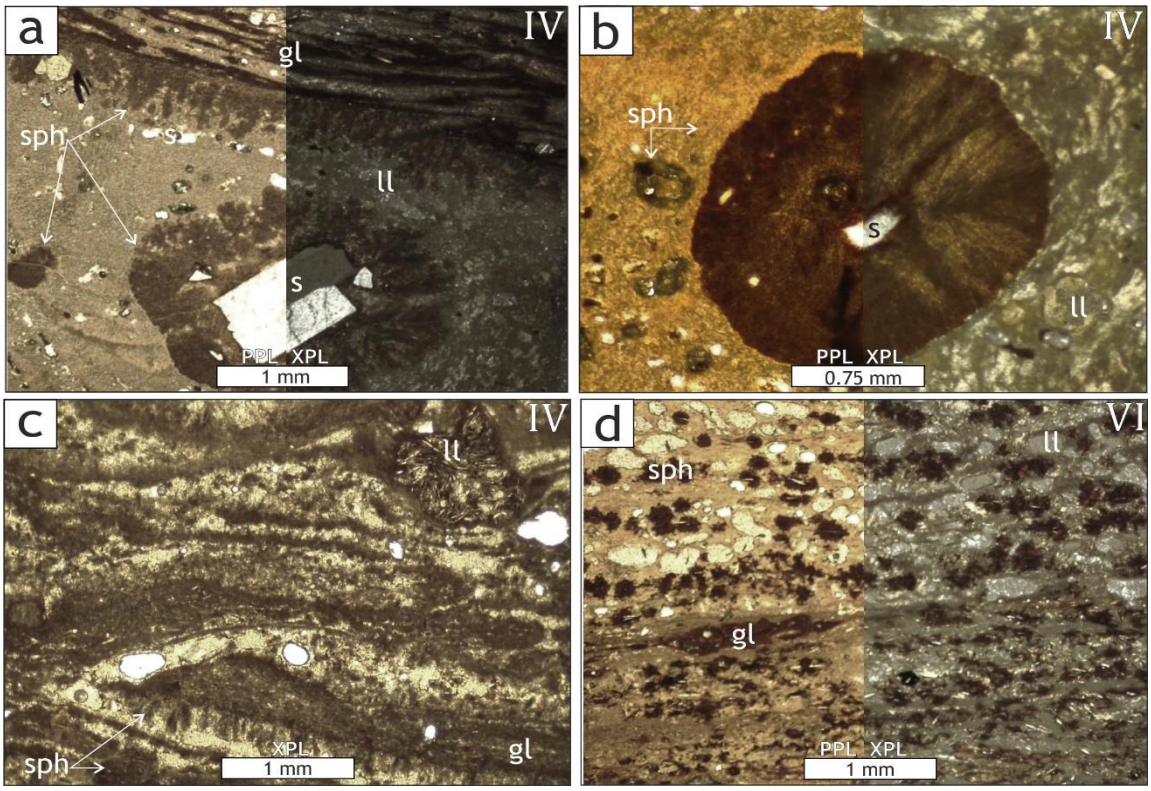


**Figure 6.2–4.** Photomicrographs of the Almendros Member. Welding ranks (as determined in Chapter 5) are denoted on the top right corner. Both plane-polarised light (PPL) and cross polarised light (XPL) are shown where indicated. Abbreviations: s=sanidine; sph=spherulites; ll=lithic lapilli; gl=glass. a) Moderately welded base of Almendros Mb (TN-04) with spherical and plumose spherulitic growth nucleating around a broken lath-shaped sanidine crystal; as well as a boarder of plumose fans along the glassy banding towards the top right corner. Very small (0.1-0.3 mm) circular spherulites are common in the tuff matrix. Grading from tuff to lapilli tuff is seen in the matrix. b) Another example of a 1-2 mm spherical spherulitic rim around a broken sanidine crystal, with brown spherulites common in the surrounding matrix, giving rise to a 'fuzzy' trachytic texture with common rounded lithic lapilli. c) Glassy (dark brown) banding in the base of the Almendros Mb (TN-04), displaying sheath folds in the fabric, further indicating syn-depositional shear of the material. Fan and plumose spherulitic growth lines the borders of the glassy bands. d) grain size stratification in the densely welded middle region of the Almendros Mb, alternating between welded fine ash, coarse ash and very rounded lithic lapilli (towards the top of the image). Isolated spherulitic growth (brown) overprints much of the slide.

## 6.2.2. Guajara Formation

The Guajara Formation is similar in terms of mineralogy to that of the Ucanca Formation, has been described as more porphyritic, containing 'phenocrysts' of haüyne crystals, rather than nepheline (Martí et al., 1994).

### 6.2.2.1. Guajara Member

Both Unit 2 and 3 of the Guajara Member share similarities to the crystal-rich, lava-like units of the Atravesado and Chasna members, exhibiting glassy, banded fabrics, alignment of euhedral sanidine crystals and flow-banding and trachytic textures in the upper domains, which are typically more effected by post-depositional rheomorphism (e.g. ramping, slumping and ogives, as discussed in Chapter 4).

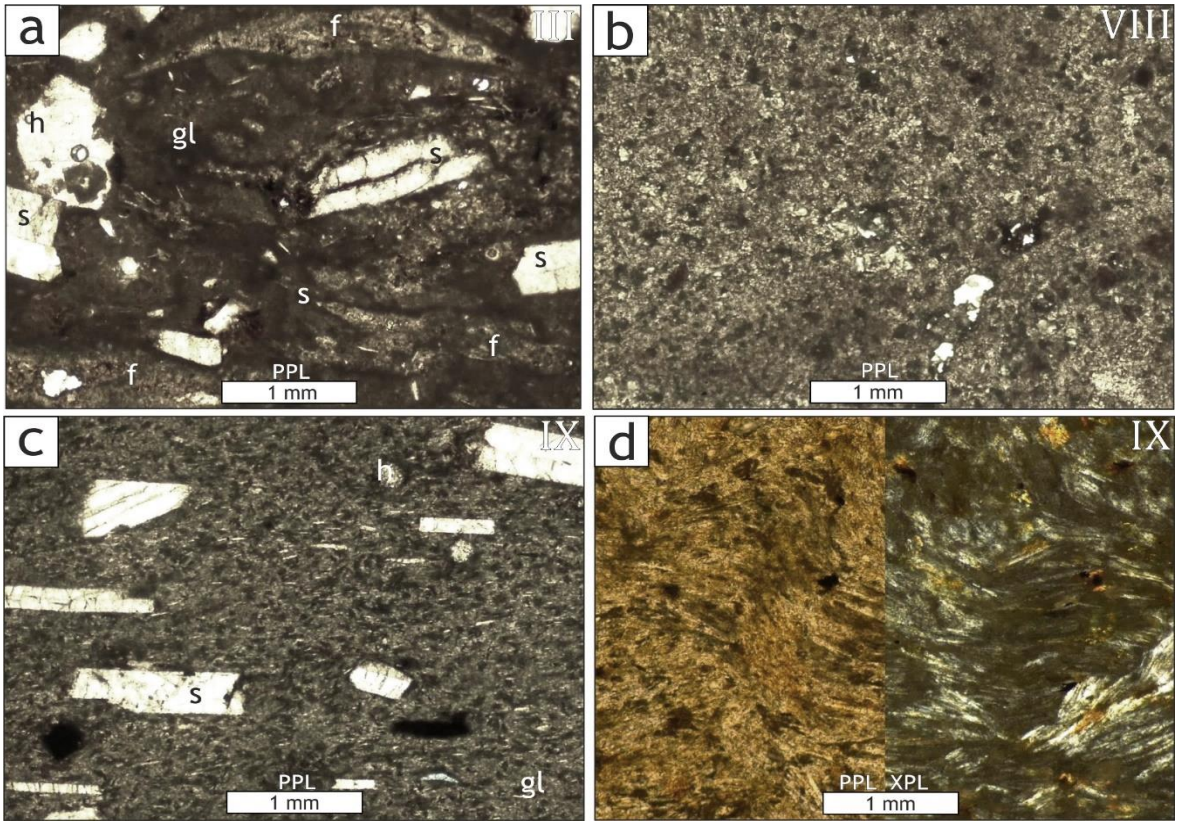


**Figure 6.2–5.** Photomicrographs of the units belonging to the Guajara Member. Welding ranks (as determined in Chapter 5) are denoted on the top right corner. Both plane-polarised light (PPL) and cross polarised light (XPL) are shown where indicated. Abbreviations: s=sanidine; h= haüyne; gl=glass; f=fiamme. a) Upper domain of the variably welded (partially welded to lava-like) Unit 2, with fiamme and a deformed glassy fabric wrapped around crystals of haüyne and sanidine. b) Largely aphyric and devitrified base of Unit 3, with small scale (0.1-0.3 mm) spherulites throughout. c) Lava-like lithofacies of the middle region of Unit 3, with aligned euhedral sanidine crystals in a devitrified glassy matrix. d) The contorted and folded (post-depositional rheomorphism) upper domain of Unit 3, which has a largely aphyric trachytic texture and pervasive devitrification.

### 6.2.2.2. Areñas Member

The southwestern locality of the Areñas Member is distinctly crystal poor, with very rare sanidine crystals, no greater than 1 mm in size. Lithic fragments of ash-grade are common in the banded, devitrified glassy matrix, with the fabrics wrapped and rotated around sub-rounded to very rounded ignimbrite (lava-like) lithic lapilli. Deformed fiamme in the basal stratigraphy display small-scale (0.5 – 1 mm) displacements, localised only to the glassy fiamme, suggesting brittle deformation of the glass, surrounded by largely fluidal textures (Figure 6.2–6 c). This interpretation is further supported by the spherulitic growth extending around both the deformed margins of the fiamme and along the fault itself.

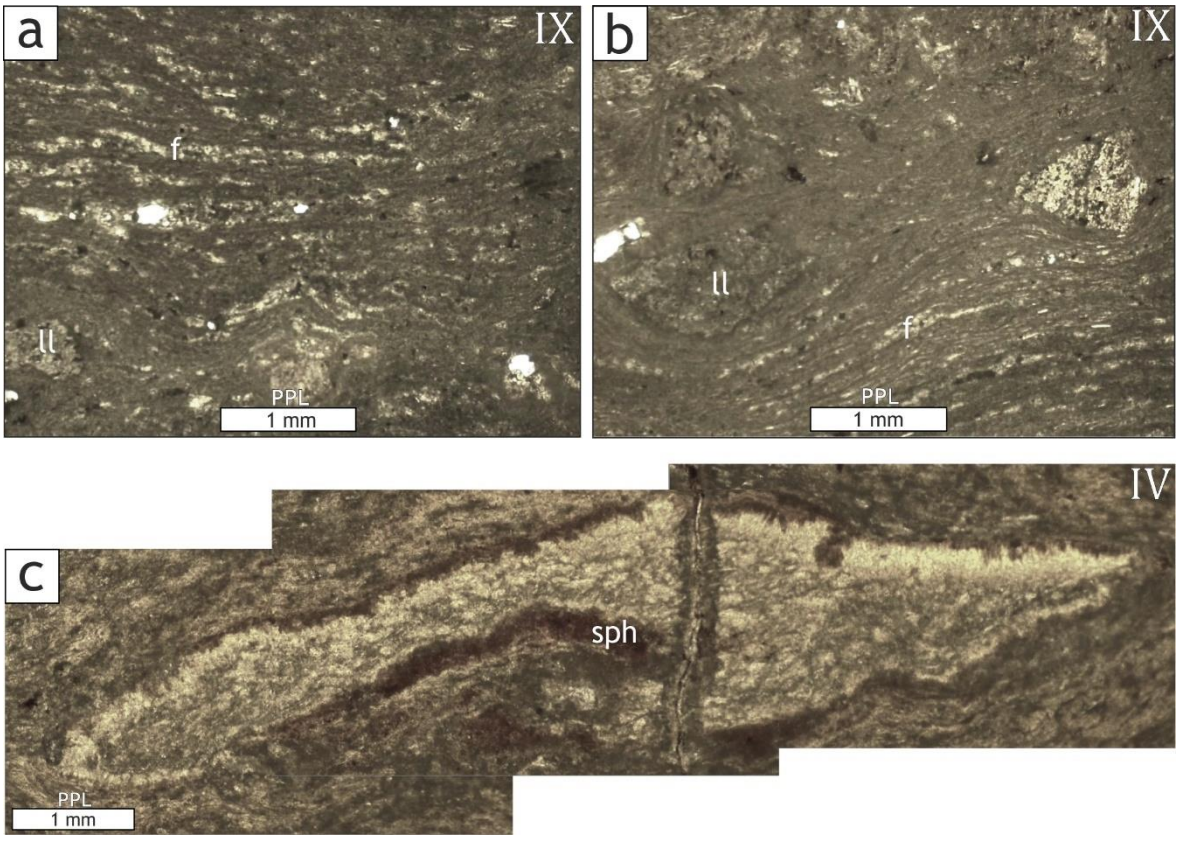


**Figure 6.2–6.** Photomicrographs of the Areñas Member at the southwestern locality. Welding ranks (as determined in Chapter 5) are denoted on the top right corner. Images are taken in lane-polarised light (PPL). Abbreviations: f=fiamme; ll=lithic lapilli; sph=spherulites. a) Lava-like, flow-banded lithofacies of the upper glassy region of the Areñas Mb (TN-27), with fabrics wrapped around sub-rounded lithic lapilli (lava-like material, likely from the underlying Guajara units). b) Rotation and deformation of fabrics in the glassy lava-like lithofacies of the upper region of the Areñas Mb (TN-27). c) Devitrified and faulted fiamme in the moderately welded base of the Areñas Mb. The curled tail of the fiamme and the apparent thickening to the right-hand side of the small-scale (2 mm) fault suggests syn-depositional faulting, which doesn't extend into the surrounding fine grained trachytic textured matrix, suggest a left to right flow direction. A 0.5 mm plumose and fan-shaped spherulitic growth mark the border of the fiamme.

## 6.3. Implications and future work

Microscopic textures record a progression of welding across many of the units, but many of these examples highlight the problems in determining the original sedimentological nature of the deposit, even in deposits of lower welding intensities where pyroclast boundaries should be discernible in theory, but are not due to pervasive vapour phase crystallisation and spherulitic growth. A range of spherulitic textures and morphologies are exhibited across the deposits, from isolated spherical or circular concentrically ringed morphologies, to bowtie, axiolitic and fan-shaped morphologies which commonly nucleate on the margins of crystals, lithics and fiamme. Pervasive spherulitic growth gives rise to a blurry and 'fuzzy' texture, due to the fibrous interstitial nature of growth in the void space. The cooling histories and occurrence of vapour phase alteration is discussed further in Chapter 7.

In terms of the geochemical insights, there appears to be no relationship between the cryptic zonation in element concentrations with the extent of welding and intensity of each unit, outlined in Chapter 5. This suggests that there is no chemical control on the welding processes, such as lower viscosities associated with particular chemistries (e.g. higher Na and K values) (Wilson, 1986), which may facilitate the deformation and flattening of pumice more readily.

However, post-emplacement rheomorphism may be a factor in the homogenisation of the material, accounting for the lack of variation seen in the trace elements of the Chasna and Almendros members, and also in Unit 3 of the Atravesado Member and Unit 2 of the Guajara Member. As discussed in Chapters 4 & 5, these units are distinctly lava-like (VI and IX), from base to top, with little variation in welding intensity and extensive evidence of rheomorphic flow and ramping. Post-depositional slumping and flowage may have contributed to the mobilisation and mixing of material, obscuring any cryptic zoning present.

The oscillating reverse-to-normal cryptic zonation (e.g. Wolff & Storey, 1984; Bryan et al., 2002; Bryan, 2006) observed particularly in the Atravesado and Retamares Members indicates that the units do not represent simple, downward discharge(s) from a simple, compositionally zoned reservoir. Reverse cryptic

zoning seen in the Granadilla Member (600 ka) from the Las Cañadas edifice is attributed to *in situ* (sidewall) fractionation (Chen & Turner, 1980; Langmuir, 1989) within a vertically and laterally zoned shallow reservoir (Bryan, 2006). Interactions between highly fractionated phonolite and the underling tephriphonolite give rise to a hybrid magma, which accounts for the disparities in composition from the products of eruption(s) at different vents from the same reservoir (Wolff & Storey, 1984; Bryan et al., 1998i; Bryan, 2006). A similar model of reservoir configuration could help explain the cryptic zoning seen in the units of the Ucanca Formation, with different vents across the caldera wall tapping in to phonolitic magmas of differing extents of fractionation. The tephriphonolitic composition of the Chasna Mb at the Llano de las Mesas locality, one of the youngest units of the Ucanca Formation, represents the least evolved composition of the eruptive sequence, indicating the depletion of phonolitic compositions, and tapping of a less evolved, deeper source of magma.

Establishing geochemical profiles and variation in a detailed stratigraphic framework provides insights into the nature of the magma reservoir, but highlights the need for further investigation, particularly involving detailed mineral analysis (e.g. stable isotope analysis to investigate the extent of wall rock interaction; or elemental analysis to determine the extent of equilibrium between crystals and surrounding liquids as a proxy for mixing of magma types) to shed light on the magma chamber conditions and configuration.

This study also lays the groundwork for investigations into correlating the proximal mapped units of the Ucanca and Guajara Formations with their distal counter parts (e.g. Smith & Kokelaar, 2013; Bryan, 1998i). Stratigraphic correlation between proximal and distal deposits of the Ucanca and Guajara Formations alone is a near impossible task due to the extent and variation of welding in the proximal deposits. Each ‘unit’ mapped (Chapter 4) may represent a series of units, or entire packages of units, but evidence for which has been obliterated in the welding processes (e.g., Jutzeler, 2010), with correlations largely reliant on geochemical or other signatures (e.g. isotopic or dating techniques) to make meaningful connections.

# Chapter 7

# 7. Insights into emplacement

The units, exhibiting strongly welded (> rank V) and lava-like welding facies, are interpreted as high grade ignimbrites deposited from high-particle concentration pyroclastic density currents, undergoing syn-depositional welding and rheomorphism, coupled with post-depositional rheomorphism and settling. A review of the defining criteria and discussion of evidence from both field observations and petrographic analysis for both mechanisms of rheomorphism are outlined in this Chapter, as well as presenting insights into the physical controls of welding processes: emplacement temperatures, deformation history, and eruptive behaviour of the deposits, based on textural, structural and thermal analysis and modelling.

## 7.1. Syn-depositional processes

The typically non-welded basal stratigraphy, of many of the units within the Ucanca and Guajara Formation, as described in Chapter 4, which laterally and horizontally grade in welding intensity, provides insight into the internal architecture of the deposits. There is extensive evidence of erosional surfaces and sedimentary features, including but not limited to normal and reverse grading; imbrication of lithic components, and planar-, cross- and diffuse-stratification, in many of the lesser welded counterparts of predominantly lava-like units, which is contradictory to their previous interpretations as welded fall deposits (e.g. Soriano, 2002; 2006; Bryan, 1998). Fall deposits do occur throughout the Retamares Member stratigraphy, but there is no occurrence of a syn-depositionally welded fall deposit, nor evidence to suggest that the fall deposits grade into the lava-like lithofacies.

The nature of the welding and textures observed across the units and described in Chapters 4 and 5 supports a model of syn-depositional agglutination and coalescence of material from a progressively aggrading current (Branney & Kokelaar, 1992). The gradation in welding intensities can be gradual (over 2 – 5 m) or very abrupt (0.02 – 0.5 m) in some areas, with a complex interaction

between the varying intensities. The lateral and vertical variation in welding intensity, in units that exhibit welding profiles, display a range of complex textures and morphologies suggesting variable and chaotic processes at the depositional boundary and suggests temperature heterogeneities during emplacement.

As the units that are welded from base to top do not provide a 'snap shot' of the internal architecture as units with more variable welding intensities do, the criteria listed in Table 7–1 outlines the diagnostic syn-depositional features and textures they exhibit, in support of their interpretation as the deposits of pyroclastic density currents. Diagnostic features include: i) the basal contacts of units that exhibit higher intensities of welding (>V) displaying irregular, erosional contacts with the underlying substrate (e.g. Table 7–1 G), particularly if the underlying material is less consolidated (e.g. Table 7–1 H); ii) the presence of pervasive, base-parallel, sub-horizontal fabrics in welding intensities in rank V and above is common in all units, and occasionally associated with localised, minor tight isoclinal and sheath folding of the fabric (e.g. Table 7–1 A & B); iii) imbricated fiamme and oblique fabrics within the transition from predominantly non-welded to welded facies (e.g. Table 7–1 D), and; iv) the stretching and deformation of fabrics locally around lithics, blocks and crystals. The underlying substrate, as well as lithics and blocks can often appear 'baked' at the contact with the welded deposit, and blocks occasionally exhibit fragmented margins and evidence of thermal spalling (e.g. Table 7–1 E) indicating rapid heating and brittle deformation. Many of the macro-scale textures and features associated with syn-depositional rheomorphism are seen in the micro-scale (Chapter 6), and a summary is presented in Table 7–2.

In the intensely welded and lava-like deposits, such as in the units of the Atravesado and Chasna Member, that typically lack any evidence of 'primary' welding, distinguishing between syn-emplacement rheomorphism, and rheomorphism that occurs following transportation and deposition could be problematic, as both rheomorphic processes may occur in conjunction with one and other, as the particulate component of the current may be in transportation as slumping and settling of the non-particulate current is taking place (e.g. Branney at al., 1992). There is also the possibility, discussed further in Section

7.4, that these intensely welded deposits may represent a series of deposits, with the boundaries of each obscured by the degree of welding, with potentially multiple overlaps of syn- and post-rheomorphic processes taking place during emplacement.

Imbricated fiamme and oblique fabrics (Table 7–1 D), showing an alignment of the orientations of matrix-supported fiamme or flattened and deformed pyroclasts, oblique to that of the planar-foliation of the inferred depositional boundary (e.g. Schmincke & Swanson, 1967; Wolff & Wright, 1981ii), or bedding surface, where there is visible evidence in deposits of lower welding intensities, are attributed to shear deformation of fluidal pyroclasts (e.g. Schmincke & Swanson, 1967; Chapin & Lowell, 1979; Wolff & Wright, 1981ii) at the depositional boundary during sustained deposition from a progressively aggrading current (Branney & Kokelaar, 1992; Figure 7–10). These fabrics are commonly visible in the 'transition zones' from low welding intensities (I-IV) grading up into strongly welded and above (>V), and as they are source-ward dipping, are indicators of transport direction.

The inferred transport directions of the deposits of Chapter 4 (averaged in Figure 4–4), taken from the measurements of the axes of sheath and curvilinear folding within the fabric and the imbrication and elongation of fiamme, where present, vary substantially throughout the deposits, with many of them spreading out radially, and often appearing unrelated to the dip of the underlying palaeo-slope, as indicated by the angle of the columnar jointing.

This supports a more complex mechanism of both transport and rheomorphism in these deposits, and discredits the simple down-slope, gravity-driven transport described by Soriano et al. (2002; 2006) and Bryan (1998). The variation could be attributed to both local and temporal heterogeneities with the shear zone of a progressively aggrading current, akin to the variation in transport direction seen in the ductile shear zone of the Grey's Landing ignimbrite (Andrews & Branney, 2005).

| Observations | Interpretation |
|---|---|
| **Sheath and isoclinal folding**<br> 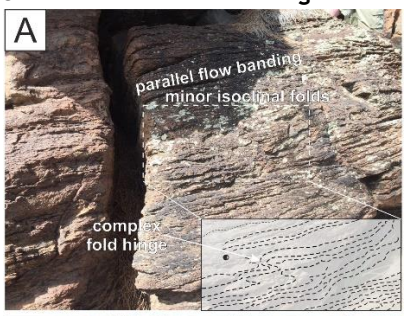 <br>  | Localised, minor curvilinear, sheath, and isoclinal folds within the largely planar fabric of densely welded to lava-like facies are likely a result of a combination of progressive stretching and hinge rotation of initial flow-perpendicular folds (A), into fabric-parallel sheath folds (B) and, deformation around flow perturbations (e.g. Andrews & Branney, 2005) (such as a crystal, lithic lapilli or block as seen in E and F) within the shear zone of a progressively aggrading PDC(s). As the minor folds are restricted to localised 'areas' of the deposit, and not laterally contemporaneous, this suggests the latter as the likely dominant mechanism of fold development. |
| **Base-parallel fabrics and flow banding**<br> 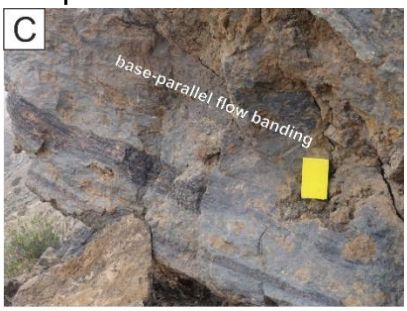 <br> 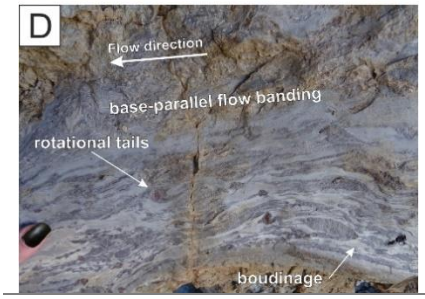 | The majority of the units above rank V exhibit a pervasive base-parallel fabric and evidence of flow banding (C) for much of their thickness and extent, with or without the presence of minor folds (A and B). Where welding grades horizontally, the progressive development of this fabric can be tracked, with evidence of stretching, shearing and boudinage of fiamme and eutaxitic textures and ductile flow around pyroclasts (D). The gradual, pervasive fabric and textures are consistent with progressive agglutination and coalescence of pyroclasts, undergoing extensive and progressive shear and imbrication, in line with Branney & Kokelaar's (1992) depositional model. |
| **Fabric rotated around crystals, lithics & blocks**<br>  <br> 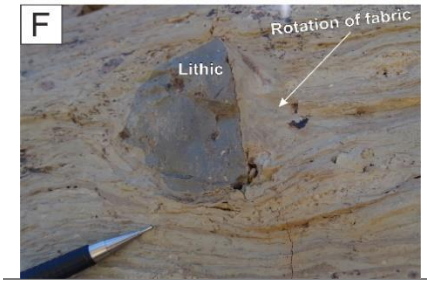 | The presence of a 'swirly' flow banding occurs in welded facies with high lithic content, suggesting simple shear flow, corresponding to that of the pervasive fabrics and flow banding (D). Pumice has undergone collapse with stretched, deformed and imbricated fiamme present (D), but lithic lapilli and lithic blocks remain largely intact, displaying dextral shear, perpendicular to the pervasive fabric present (E & F) (similar to the rotated crystals discussed in Section 6.2) which is indicative of the transport direction (Branney & Kokelaar, 1992; Andrews & Branney, 2005) and are good shear sense indicators (Pioli, 2002). |

**Erosional Surfaces**

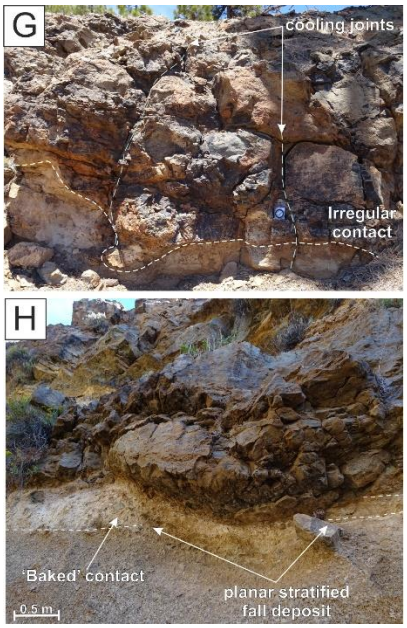


Where deposits are welded (>rank V) from base to top, a highly undulating and irregular basal contact with the underlying deposit is suggestive of a remnant erosional contact, as opposed to deposition of a planar fall deposit (as interpreted by previous workers: Soriano, 2002; 2006), or from deposition on irregular topography, which would be reflected in base-parallel flow banding that would mimic such underlying topography. Cooling joints that extend from the welded facies into the underlying deposit(s) are also indicative that the contact is erosional and concurrent, rather than irregular paleo-topography.

**Table 7–1.** A non-exhaustive overview of the macro-scale evidence of syn-depositional welding and rheomorphic features and textures across the mapped units above rank V in welding intensity, in support of their interpretation as deposits from PDCs, and the interpretation for each. Unit and localities of examples used: A) Atravesado Unit 3 – N28° 10'58.8" W16° 38' 36.9"; B) Retamares Unit A at N28° 11'41.7" W16° 39'29.8"; C) Atravesado Mb, RLA locality at N25° 12'06.7" W16° 39'40.3"; D) Retamares Mb Unit D at N28° 11'57" W16° 38'16"; E) Retamares Mb Unit A at N28° 11'26" W16° 39'9"; F) Retamares Mb Unit F at N28° 12'27" W16° 37'19"; G) Retamares Mb Unit B at N28° 11'31" W16° 39'9"; H) Retamares Mb Unit A' at N28° 11'40.4" W16° 39'35.5".

| Observations | Interpretation |
|---|---|
| **Planar fabrics**<br> 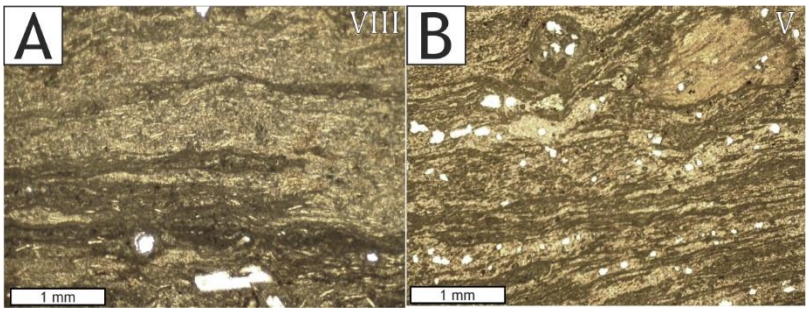 | Planar fabrics (A) and flow banding (B) is common in units >V across all of the members. These fabrics are consistent with progressive coalescence of depositing pyroclasts in a ductile shear zone. |
| **Kinematic indicators**<br> 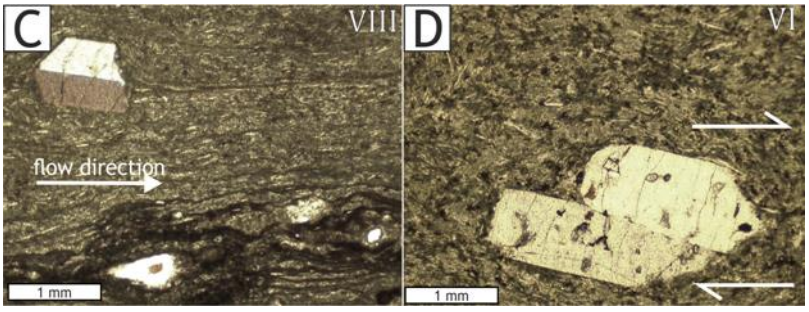 | Broken and rotated crystals are common, indicative of transport direction (Branney & Kokelaar, 1992; Andrews & Branney, 2005) and are good shear sense indicators (Pioli, 2002), consistent with deposition in a ductile shear zone. |

| | | |
|---|---|---|
| stretching lineations and folding of fabrics | | |
| 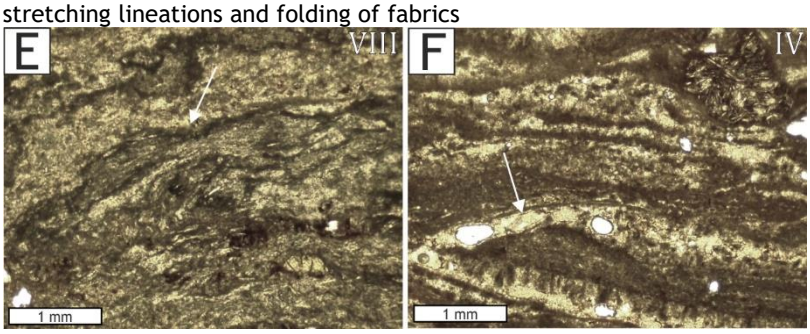 | | Stretching lineations and boudinaged fiamme (E) indicate elongation and shear deformation. (F) shows mm-scale isoclinal folding of fabrics, parallel to planar fabrics, consistent with deposition with a ductile shear zone. |

**Table 7–2.** A summary of the micro-scale evidence of syn-depositional welding and rheomorphic features and textures across the mapped units above rank V in welding intensity, in support of their interpretation as deposits from PDCs. Photomicrographs are in plain polarised light. Units and localities of examples used: A) Upper horizon of Retamares Mb Unit D (TN-42); B) Flow banding in the base of Retamares Member Unit E (TF-09); C) Upper horizon of Retamares Mb Unit D (TN-42); D) Upper horizon of Retamares Mb Unit E (TN-14); E) Upper horizon of Retamares Unit D (TN-42); F) Base of Almendros Mb (TN-04).

### 7.1.1. ‘Snowball’ blocks: insights to temperature variations

An example of lateral variation in welding intensity can be seen in the basal stratigraphy of Retamares Unit C (Figure 7–1), where the degree of welding varies extensively over 0.25 m, from (III) to (VI). The deposit is a 0.5 m thick, obsidian banded, predominantly lava-like, locally eutaxitic, lithic-rich tuff, overlying and underlain by massive pumice- and lithic- rich breccias with abundant blocks of strongly foliated lava-like material, likely belonging to the underlying Retamares and Atravesado units. The boundaries are highly irregular and marked by sharp gradation (0.02 m) in welding intensity.

Within the mT(lava-like) lithofacies at locality Ci (Figure 7–1 B, D & E and Figure 4–66), an interesting gradient in welding intensity is seen around a block of lava-like material within the deposit. This is interpreted as the result of the interaction between an extremely high-grade PDC and a cold block of material.

The interference to the temperature gradient within the flow boundary zone, caused by the incorporation of the ‘snowball’ block into the current, prevented local agglutination and coalescence of the depositing pyroclasts, creating a ‘chilled margin’ or ‘halo’ of progressively lesser welded pyroclasts towards the block (Figure 7–2). The exterior of the block is coated in an unstructured 2 - 4 mm shell of very fine ash, which is interpreted as resulting from ash aggregation around the block as it passes through the finer, upper horizons of a density

stratified current, picking up a coating of the finest material as it enters the current.

As fine ash shards coalesce and deform more readily, the shell may represent the initial stages of the 'chilled margin', as larger pyroclasts require more heat in order for agglutination between them to take place. Pumice lapilli have then accumulated around the block, largely remaining undeformed, until the thickness of the deposit, and thus heat transfer, reaches the point whereby welding around the block begins to take place. Fragmented and rotated autoclasts of eutaxitic and welded (III-IV) pumice lapilli and tuff from around the rim of the block indicate that there is rotation of the block, which is syn-depositionally fragmenting and shearing the outer welding crust, perhaps due to gravity-driven, down-slope momentum with the transporting current, or due to rotational shear, driven by the overriding current. This is also apparent in the fabric of the surrounding glassy, densely welded deposit, which is wrapped and rotated around the block. The presence of cooling joints, radiating out from the block also support the existence of a temperature contrast between the block and the deposit.

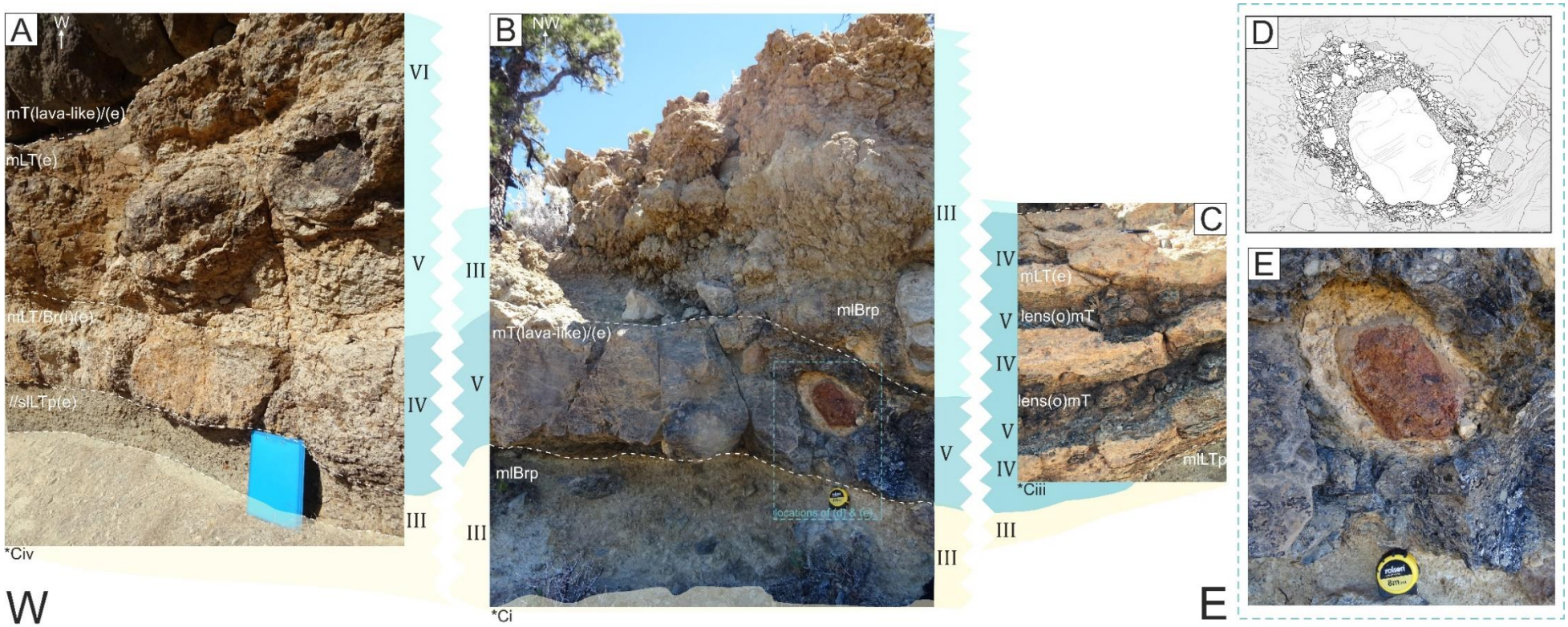


**Figure 7–1.** Variable welding intensities and thicknesses in the correlated basal stratigraphy of Retamares Unit C. Log localities (*C) correspond to those in Chapter 4. Welding Ranks (I-V) correspond to the classification scheme outlined in Figure 5-11 in Chapter 5. (A) Basal stratigraphy of Unit C at N28°11'49" W16°39'51". Note the spheroidal weathering within the welded mLT(e) lithofacies (B) Basal stratigraphy of Unit C at N28°11'49" W16°39'41", with the locality of D & E highlighted with the blue dashed box. (C) Basal stratigraphy of Unit C at N28°11'49" W16°38'59". (D) Field sketch of the variable gradation in welding intensity around a block of welded ignimbrite. (E) Photo of the variable gradation in welding intensity around a block of welded ignimbrite.

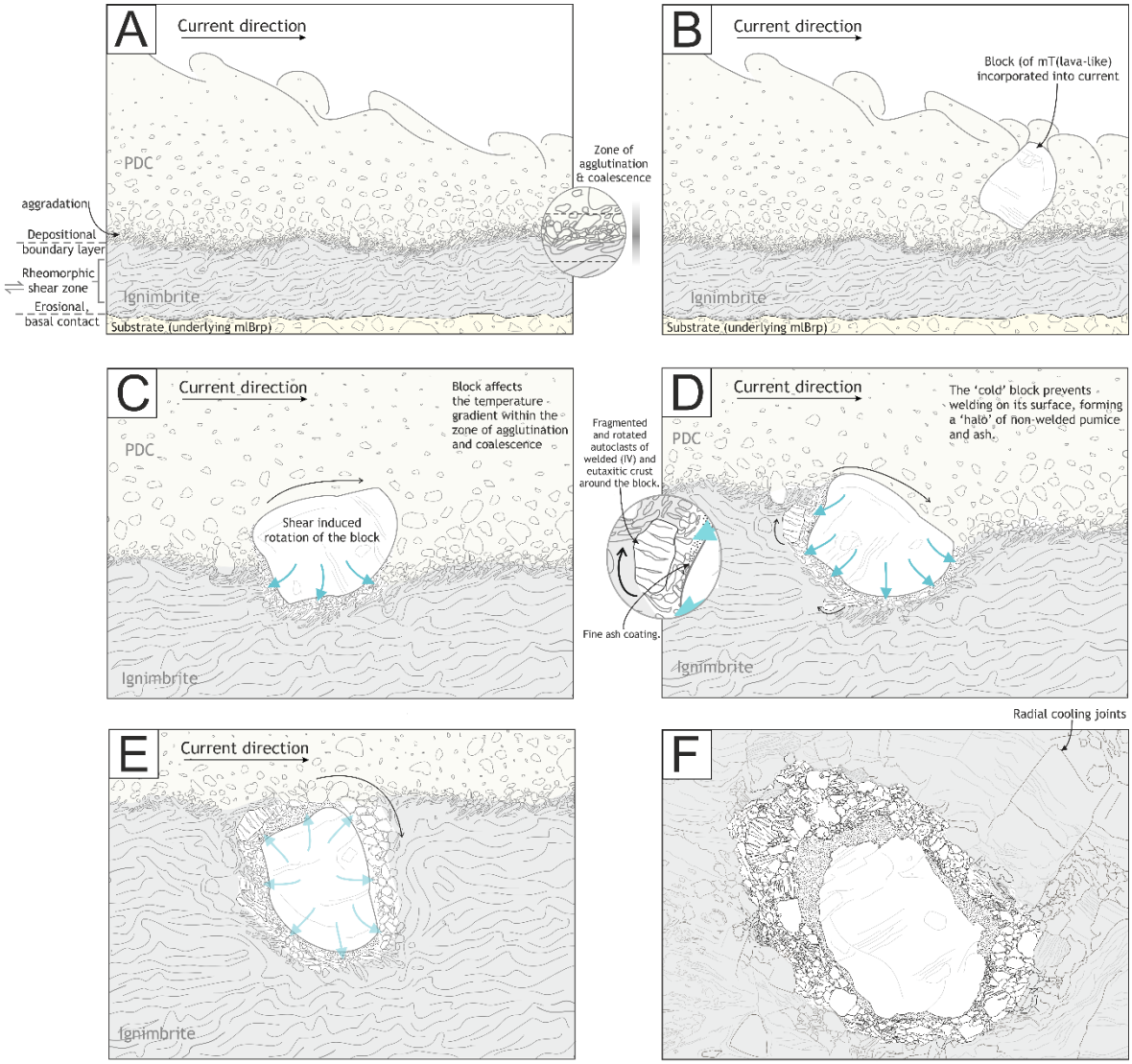


**Figure 7–2.** Schematic model of the interaction of the PDC with the 'snowball' block. Not to scale. A) Emplacement of a progressively aggrading, high-temperature, extremely high-grade ignimbrite. Adapted from Branney & Kokelaar (1992) and Andrews (2006). B) Incorporation of a block of mT(lava-like) block to the (typically lithic-poor) transporting current. C) The block effects the temperature gradient within the zone of agglutination and coalescence, providing a 'chilled margin' (blue arrows) effect, preventing the pyroclasts around the block from undergoing welding at the FBZ. Rotation of the block occurs due to shear of the overriding current. D) Block continually rotates, resulting in a coating of fine ash. The 'cold' block locally interferes with the welding process at the FBZ, forming an immediate 'halo' of non-welded material, which gradually increases in welding intensity away from the surface. The eutaxitic and welded crust around the block undergoes fragmentation during rotational shear, resulting in autoclasts of welded (IV) material. E) Growth of the non-welded 'halo' as the block rotates and is buried in the deposit. F) The cooled deposit, displaying radial cooling joints around the block, with flow banding exhibiting rotation around the block.

A similar, isolated texture and gradation in welding intensity, although not as stark a contrast, is seen around a lithic-rich 'pocket' within the strongly welded facies of Retamares Unit A, consisting of flow banded and eutaxitic massive breccia grading into a flow banded lithic-rich tuff. The pocket occurs in the basal welded facies (Figure 7–3) with a decrease in welding intensity from strongly welded (V) to incipiently welded (II), where pyroclast boundaries are largely visible and intact and good pumice porosity is maintained. A similar model as that outlined for the 'snowball' block (Figure 7–2) can be applied, whereby the interaction with relatively 'cold' lithics and blocks inhibits welding on a very local scale, again supporting the conclusion that syn-depositional welding is largely temperature dependent.

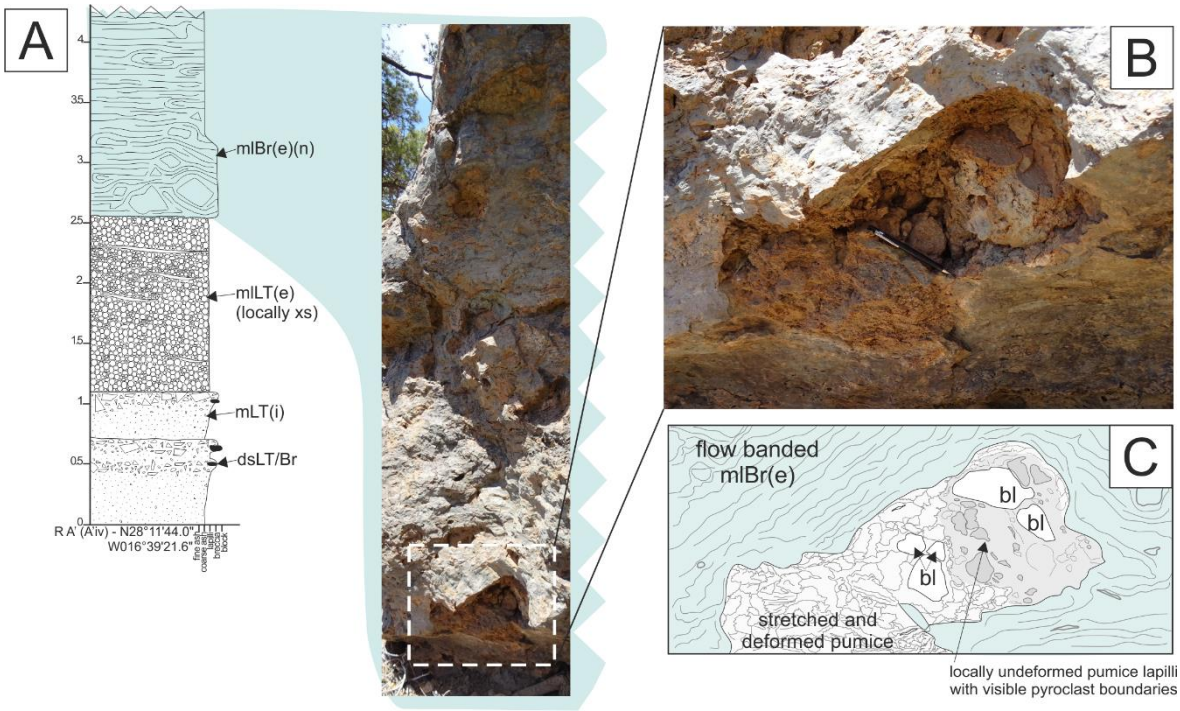


**Figure 7–3.** Variable welding observed in a 'pocket' of lithic blocks in the strongly welded flow banded mlBr/T(e) of Unit A of the Retamares Mb. A) The 'pocket' is located within the lithic-rich breccia at the base of the facies. Other blocks are present but not associated with a decrease in welding intensity. B) Photograph of the ellipsoid-shaped 'pocket'. Pencil for scale. C) A simplified field sketch of the 'pocket', highlighting the variable welding. The flow banded mlBr(e) grades immediately (1-1.5 cm) in to a stretched and deformed pumice, with largely visible deformed pumice and pyroclast boundaries. Towards the lithic blocks (lava-like material), welding intensity decreases, where undeformed pumice lapilli and clearly visible pyroclast boundaries can be seen (in the darker grey shaded area).

### 7.1.2. Spatter-like bombs and obsidian spirals

The presence of lithic-rich horizons, spatter-like bombs, and obsidian-rich, fluidal pumice lenses within the basal stratigraphy of both the Chasna Mb at the Roque los Almendros locality (Figure 4–91 to 4–95), and Unit E of the Retamares Mb (Figure 4–78 to 4–84 and discussed in Chapter 6) are interpreted as the result of alternating magmatic and phreatomagmatic activity, with evidence of the presence of localised ephemeral lakes.

The inwardly dipping, very fine, light grey mT in the basal stratigraphy of the Chasna Mb (RLA locality) is interpreted as a reworked volcaniclastic mudstone. The mudstone onlaps underlying non-welded tuffs and lapilli tuffs and tapers out to the northwest (Figure 4–90 & 4–91). This deposit is also interpreted as lacustrine by Soriano et al. (2009), with the overlying lithic-rich horizons (mlBr in this study, Figure 4–90) interpreted as the products of phreatomagmatic activity, arising from water entering into the conduit-vent during the early stages of eruption.

However, the occurrence of spatter-rich, fluidal, obsidian-bearing pumice within the deposits is not described by previous workers. These occur in both the underlying stratigraphy, as well as above, on the north face of Roque Los Almendros (interpreted as PDCs in this study, associated with lithic block horizons and very fine ash), and suggest the localised interaction of PDC(s) with a shallow lake or ground water, immediately followed by horizons of fluidal, spatter-like bombs and obsidian-bearing lenses and fiamme. This is highly localised to the north and north-eastern faces of the Roque Los Almendros, and there is no convincing evidence of phreatomagmatic activity elsewhere at this locality, or at the other Chasna Mb localities. This is also supported by the presence of a localised glassy ‘obsidian spiral’ within this deposit (Figure 7–4) interpreted as the result of the disturbance of a stratified ash-rich layer from the impact of a block of ignimbrite, leading to mobilisation and deformation of the ‘detached’ segments. The presence of steam within the PDC may have may have reduced the melting points of the juvenile fragments, and combined with the shear of the overring current, leading to glassy fiamme and lenses (e.g. McBirney, 1968), due to the collapse and deformation of the porous pumice (e.g. Fisher & Schmincke, 1984). In contrast to the spatter-like bombs, the obsidian lenses and fiamme

within the folded and rotated detached segments resulted from load pressure and shear, and not the instantaneous agglutination of hot material during deposition. The intensity of welding of the layer (//sT/LTp) from which it was detached shows no evidence of fiamme, obsidian or localised welding above rank III, other than in the mobilised 'glassy spiral'.

Local horizons of spatter-like bombs and fluidal pumice are also seen in the basal stratigraphy of Retamares Unit E, described in Figure 4–78 to 4–84, which again suggests highly localised phreatomagmatic activity. This may also account for the colour variation observed in the pumice (discussion in Section 6.1.3.2.1.). Within the predominantly non-welded stratigraphy on the northern face of the deposit (Figure 4–75), clay-filled desiccation cracks are observed within the very fine ash horizons (mT) of Retamares Unit D, further indicating the presence of ephemeral lakes in the paleo-landscape.

### 7.1.3. Block and lithic clast variations

Lithic lapilli and blocks are typically composed of ignimbrite, exhibiting variations of welding, but predominantly comprising the characteristic strongly foliated lava-like facies. Clast composition variation with height through the deposits may suggest vent clearing or vent widening phases, with the lava-like material originating from the earlier Ucanca Fm deposits, or picked up by the current(s) from the underlying substrate (e.g. Sumner & Branney, 2002). The basaltic/ basic lithics may represent the pre-Ucanca basalt flows, which may have been exposed in the early caldera wall at the time of eruption. There is evidence in some of the deposits (e.g. the pre-Atravesado Unit 3 localities) that erosion of early scoria cones and associated deposits took place, either actively by the eroding current(s), or being picked up as loose material (accidental lithics) as the current travelled across the topography, resulting in horizons rich in scoriaceous material and angular basaltic lithics (e.g. Figure 4–19 to 4–23). Lithic and pumice breccias are a component within the basal stratigraphy, typically associated with blocks of ignimbrite of varying degrees of welding, of many of the units, and may suggest initial 'vent clearing' phases or collapse events associated with the generation of PDCs.

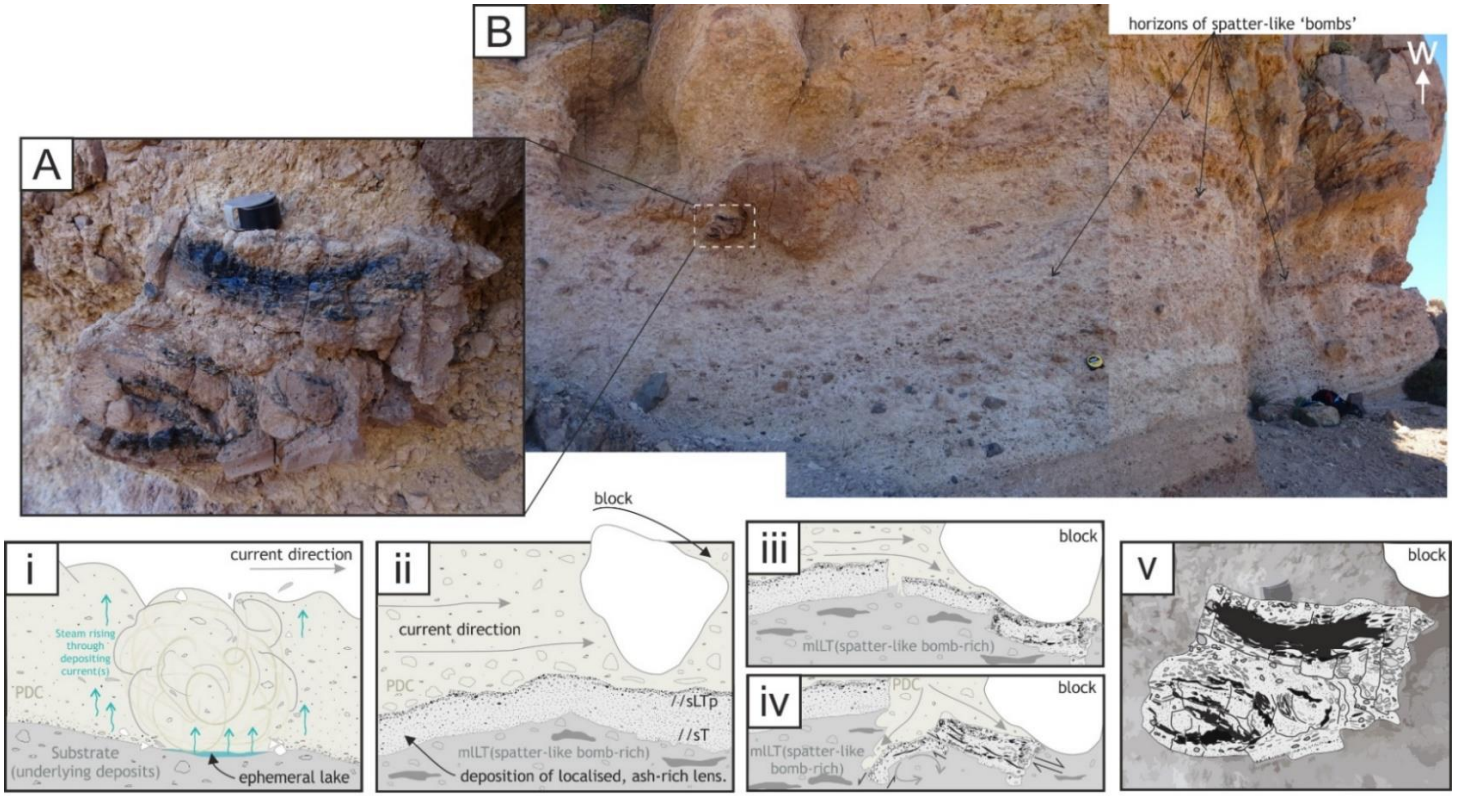


**Figure 7–4.** Schematic model of the obsidian spiral within the basal stratigraphy of the Chasna Mb at Roque Los Almendros locality, at N28°12'14" W16°39'43". Scale not intended. A) Photograph of the obsidian spiral. Hand lens for scale. B) The outcrop of the basal weakly welded (I – III) stratigraphy of the Chasna Mb, highlighting location of the obsidian spiral. Lithofacies are described in Figure 4–92Figure 4–95. Note horizons rich in spatter-like bombs. i) Highly localised phreatomagmatic activity as a result of interaction between PDC(s) and ground water, leading to very fine ash and lithic-rich horizons, fragmentation of material. Horizons of spatter-like bombs and fluidal pyroclasts directly below and above indicate the localised nature of this activity, with immediate transition back to magmatic activity. ii) Incorporation of lithic block into current; iii) block disturbs underlying ash-rich layer, consisting of a planar stratified tuff, grading up to a planar stratified lapilli tuff rich in pumice lapilli. Detachment of the ash layer occurs underneath the block, encouraging highly localised compression and deformation of pumice. iv) The detached segments become rotated and deformed, driven by the shear of the overriding current. Localised compressional and shear-induced deformation occurs within the pumice-rich component of the detached segments. One segment is rotated and folded underneath the under. v) Field sketch of the final configuration of the rotated, detached obsidian-rich segment.

## 7.2. Post-depositional processes and rheomorphism

Across the intensely welded and lava-like units, there is evidence of distinct phase(s) of secondary deformation, associated with the contortion of original and planar fabrics, including: i) open, loose and buckle folding of fabrics; ii) large scale ramping of the upper horizons of units; and iii) localised rheomorphic gravity driven flow, producing a secondary deformation foliation (cleavage) and mineral alignment, as described in Chapter 4. These extensional and compressional structures are attributed to localised post-depositional remobilisation, deflation, and gravity-driven slumping of hot-state deposits.

Post-depositional rheomorphic structures tend to be restricted to only the deposits exhibiting higher welding intensities (rank VI and above), and do not affect the entirety of the deposit. Areas of open, buckle and kink folding are typically concentrated to the thickest, upper surfaces of the deposit, associated with the ramping or contortion of previous fabrics. They are highly localised, and non-pervasive, in contrast to the fabrics and folds attributed to syn-depositional processes. A secondary deformational fabric (a secondary cleavage) can be seen in these rheomorphic zones, often accompanied by randomly oriented small-scale kink and bucking folding of the fabric. Table 7–3 provides an overview of the structures and features attributed to post-depositional rheomorphism, and the interpretation behind their development.

The units that do not exhibit the distinctive 'post-depositional' rheomorphic structures (Table 7–3), such as the majority of units belonging to the Retamares Mb, tend to be considerably thinner and exhibit more variable, and lesser intensities of welding, both overall, and throughout individual deposits, which may be factors inhibiting the insulation of the deposit, and thus the hot-state post-emplacement mobilisation.

Ramping of the foliation is seen in the southern faces of both the Chasna Mb at Llano de las Mesas and locally within a lobe of Unit 3 of the Atravesado (Table 7–3 E & F), associated with a source-ward dipping curvature and steepening (up to 90° in the Chasna Mb) of the formerly planar foliation.

| Observations | Interpretation |
|---|---|
| **Deformation of primary fabrics**<br> 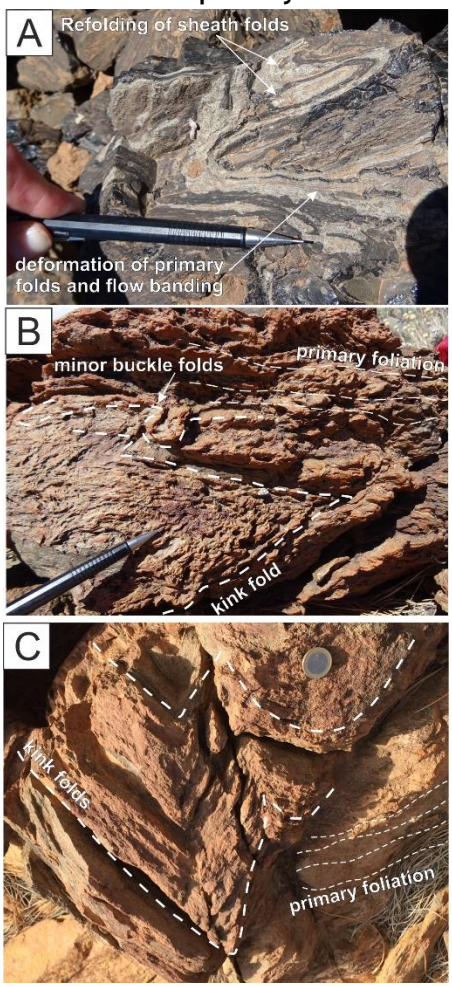 | Minor folding (open, curvilinear, buckle, and kink folding (B & C) and refolding of primary folding (A)) of primary base-parallel fabrics occurs towards the upper horizons of welded deposits > rank VI. These folds are typically isolated, within a primary base-parallel foliation, and do not form pervasive horizons or domains. 'Primary' fabrics and features are those attributed to syn-depositional processes (Table 7-1). These folds record the deformation and refolding of these 'primary' structures and features, from a combination of: rheomorphic mobilisation and flowage of material, giving rise to refolding and rotation of foliation-parallel sheath folds, and; deflation and gravity-driven down-slope slumping of the deposit following cessation of transport. Kink folds (B and C) as well as buckle folds and localised development of a strong cleavage (D), are common in the Atravesado Mb, and indicate flexural slip between base-parallel foliation, and coaxial shortening (Ramsey, 1967), perhaps associated with down-slope slumping of the deposit. |
| **Secondary foliation**<br> 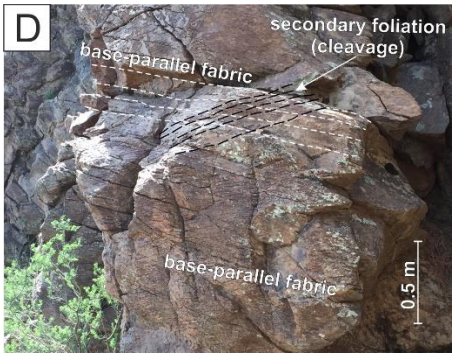 | The development of a secondary foliation (cleavage) is localised within the Atravesado Member units, and is not a common feature, nor pervasive throughout the deposits. It is associated with the ramp structure of Atravesado Unit 3 (E), as well as in the Atravesado cliff section, associated with the downslope, hot state 'plug flow' style of rheomorphism (see below). |
| **Ramp structures**<br> 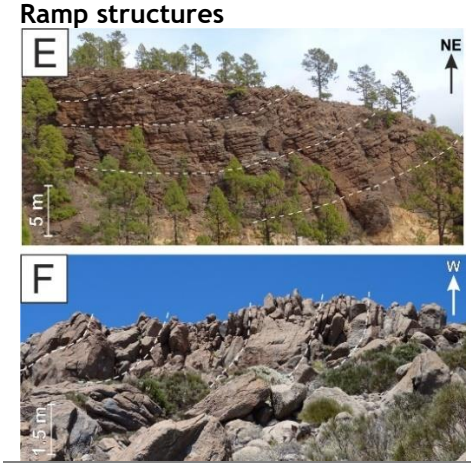 | Macro-scale ramping is seen on the southern faces (lobes) of both Atravesado Mb Unit 3 (E) and the Chasna Mb at Llano de las Mesas locality (F). Both units exhibit a downwards 'ramping' of the formerly, sub-horizontal foliation, attributed to compressional hot-state sliding of the upper surface of the deposit, whereby the upper part of the current continues to slide, detaching from the underlying material, in a partial plug-flow style mechanism. |

| Crystal alignment and lineations | |
|---|---|
|  | Restricted to the units of the Chasna Member, mineral alignments parallel with foliation or ramping (at Llano de las Mesas) and trachytic textures (Figure 6.2–3), whereby 'ghost' flow banding is visible, with alignment of sanidine and hornblende crystals (G). |

**Table 7–3.** An overview of features associated with post-depositional deformation and rheomorphism across the mapped units above rank V in welding intensity, and interpretation of their development. Unit and localities of examples used: A) Almendros Mb – Guajara locality at N28°12'44.6" W16°36'45.9"; B) Retamares Mb Unit A at N28°11'26" W16°39'9"; C) Atravesado Mb Unit 3 at N28°10'59.8" W16°38'37.0"; D) Atravesado Mb Unit 3 at N28°10'56.5" W16°38'36.5"; E) Atravesado Mb Unit 3 seen at N28°10'28.5" W16°38'54.9"; F) Chasna Mb at Llano de las Mesas locality at N28°11'40" W16°37'46"; G) Chasna Mb at Llano de las Mesas locality at N28°11'40" W16°37'46".

The Chasna Mb also displays curved, concentric ridges, or ogives (Fink, 1980) on the upper surface of the deposit (Figure 4–100), similar to those described in rhyolitic lavas (e.g. MacDonald, 1972; Loney, 1968; Fink, 1980) and are concave source-wards, indicating down-slope flow. Due to good exposure of both the surface and a cross-sectional view of the deposit, it is clear they are surface expressions of the ramping of the deposit, as opposed to surface folding. These may be a feature associated with the ramping of Atravesado Unit 3 but are not visible in the field. The stepped, down-slope steepening of foliation in both structures suggests incremental hot-state gravitational sliding, with shortening occurring along compressional rheomorphic shear zones (e.g. Sumner & Branney, 2002), which can be traced laterally, with the development of the secondary cleavage at the Riscos Atravesados locality (Table 7–3 D). As the rheomorphic transport of the deposit ceases, frontal compression is driven by the weight of the material behind being thrust against the leading face. The inclination of cooling joints within the Atravesado Unit 3 shallow down slope towards the lobe front, from sub-vertical, 85-90°, to approx. 40-50° which may indicate the topography-controlled cessation of the deposit, terminating, and pooling against a paleo-topographic barrier.

The basal contact between Atravesado Unit 3 and the underlying 'baked', predominantly non-welded stratigraphy of Unit 2 is highly irregular, with localised basal autobrecciation (Figure 4–17) and deformation of the underlying material.

Due to the extent of the 'baking', little remains of the dipping, stratified sedimentary features that are visible 1-2 m below the contact. A flame-like wedge of baked material is seen towards the southern face of the ramp structure, indicating the deformation, displacement, and compaction of the underlying material as the sticky rheomorphic mass tracks over the surface. Similar load-and-flame structures associated with late-stage rheomorphism are seen in deposits in Gran Canaria (e.g. Leat & Schmincke, 1993; Sumner & Branney, 1993). The continuation of cooling joints throughout both the deposits of Units 2 and 3 suggests Unit 2 was still hot, and perhaps unconsolidated, allowing for ease of manipulation and deformation.

### 7.2.1. Cooling dynamics and alteration

Autobrecciation, common in rheomorphic and lava-like ignimbrites (e.g. Henry & Wolff, 1992; Branney et al., 1992; Sumner & Branney, 2002) is generally not a feature associated with the base or the upper surfaces of the rheomorphic deposits, suggesting largely fluidal and ductile deformation, and the ability of the deposits to maintain lower viscosities via effective insulation long after transport ceases. The lack of basal autobreccias may be due in part to the rapid syn-depositional welding taking place at the base of the deposit, that are then chilled rapidly against the cooler substrate, and forming a basal vitrophyre in units which are intensely welded and lava-like from base to top.

Many of the units of the Retamares Mb exhibit a streaky turquoise-green tint, due to devitrification processes (e.g. Smith, 1960; Henry & Wolff, 1992; Manley, 1995; Kobberger & Schmincke, 1999), common throughout the units, giving rise to colourful 'swirly' banded orange-brown and green facies. This may be the effect of welding variation, with an initially finer grained, glassy component alongside a coarser grained, more lithic or more crystal-rich component, which did not undergo the same extent of devitrification during vapour-phase alteration. The banding may then reflect the pre-welding architecture and sedimentology of the ignimbrite, which has been obscured in the welding process, and further altered by post-emplacement processes.

More pervasive devitrification is very common in the densely welded facies and above (>V), as seen in the 'fuzzy' interstitial trachytic textures seen in the plagioclase and sanidine crystals, as well as the presence of spherulites (Figure 6.2–2) as discussed in Chapter 6.

Zones rich in lithophysae are common throughout many units with welding intensities above rank IV and are irregularly distributed throughout the deposits. These range in size from millimetre scale to stretched and prolate vesicles, forming cavities over a metre in size, with evidence of deformation of the surrounding fabric. This indicates that their formation and growth is post-development of syn-depositional fabrics, but likely occurring while the deposit remained in a hot ductile state, as the smooth, plastically deformed nature of the cavity walls suggests that the material maintained low enough viscosities in order for surface tension to be maintained (e.g. Sumner & Branney, 2002).

A combination of these processes will have further obscured and altered much of the evidence of the original sedimentary features, as well as affecting the physical properties of the units following both post-depositional rheomorphism and cooling of the deposits. The IX$^{th}$ welding rank (lava-like$^{taph}$), outlined in Chapter 5 takes into the consideration the change in physical properties associated with the post-depositional rheomorphism and alteration of the deposit, resulting in reduced rock strength and density, and increased porosity as the structural integrity of the rock is reduced, due to the deformation of primary fabrics; development of secondary foliations (Table 7–3); lithophysae growth and devitrification.

## 7.3. Controls on welding

Thermal analysis was undertaken on fresh glasses present in six of the units, belonging to the Retamares, Chasna, Almendros and Areñas members, with the initial aims of establishing glass transition ($T_g$) temperatures as well as to determine rates of cooling, to provide insights into emplacement and the processes and constraints associated with welding (e.g. viscosity, chemical composition and magmatic water content at the glass transition) within these units.

### 7.3.1. Glass Transition

Glass is an amorphous material exhibiting a non-crystalline atomic structure, disordered at the atomic level compared to their crystalline counterparts (Figure 7–5). The formation of volcanic glass from a melt is a factor of the melt composition and dissolved volatile content, the temperature-dependence of viscosity, and the cooling history. The conditions best suited to the formation of glass are unfavourable conditions to crystallisation, in that glass is not a constituent of a fully crystallised magma.

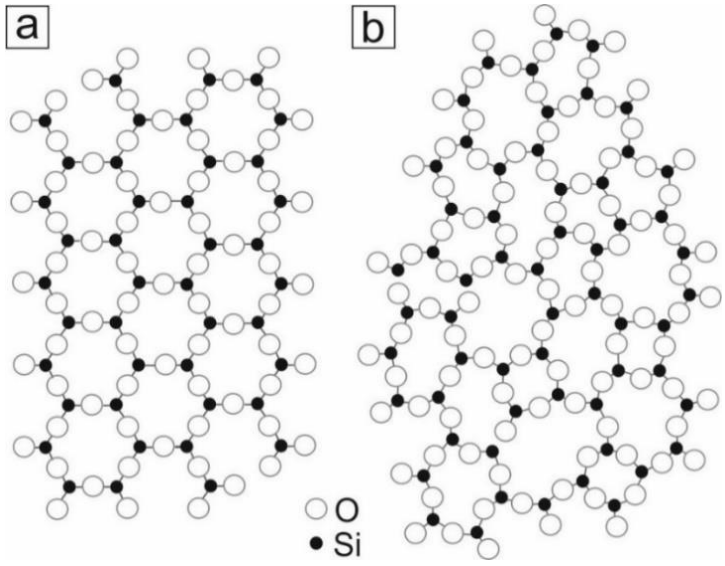


**Figure 7–5.**Schematic illustration of the 2-dimensional atomic structure of (a) crystalline quartz ($SiO_2$); and (b) amorphous glass of the same composition ($SiO_2$). Figure adapted from Kingery et al (1976).

Volcanic glass displays a glass transition ($T_{g)}$ when heated towards the liquid state. $T_g$ is an important temperature interval in the welding process of volcanic deposits, as it is the glass particle component within a deposit that undergoes welding (Giordano et al., 2005). Welding of pyroclasts occurs when the viscosity of the fragments is sufficiently low to allow significant deformation and sintering across the time-temperature paths governed by the cooling and loading history of a deposit. Above the $T_g$, glass particles undergo viscous deformation, facilitating welding in pyroclastic rocks (e.g. Smith, 1979; Ross & Smith, 1980; Cas & Wright, 1987; Gottsman & Dingwell, 1999; Giordano et al., 2000), but below the $T_g$ the particles behave elastically in response to stresses, preventing welding (Dingwell & Webb 1990). Thus, the welding intensity of a deposit is considered a factor of both the load compaction of the overlying deposit and the time spent at temperatures above the $T_g$ (Ross & Smith, 1980; Riehle et al., 1995). Silicic deposits typically have emplacement temperatures within a closer range to their minimum welding temperature than deposits of more basic compositions, leading to slower crystal growth rates and increased potential for glass preservation. Therefore, the emplacement temperature, as a function of composition, coupled with the rates of both crystallisation and cooling controls the material's ability to weld or crystallise, and whether a glassy phase will be preserved in the rock.

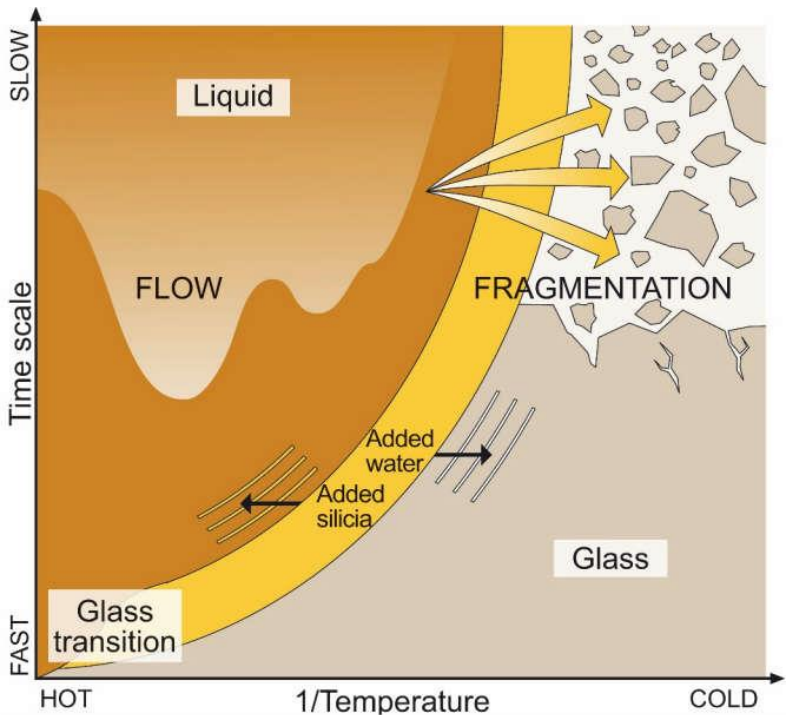


**Figure 7–6.** Deformation of magma along the glass transition between glass and a liquid (Dingwell, 1996).

The transition of glass from a liquid to a solidus state for natural silicate melts occurs across a confined temperature range of ~100 – 150 °C, the $T_g$, during cooling or due to compression (Hansen & McDonald, 2006). When considering the cooling histories of silicate melts, from eruption temperatures of up to ~1200 °C, to ambient surface temperatures, the glass transition is a significant temperature interval in the understanding of many volcanic processes, representing the kinetic boundary between the liquid-like (viscous) and solid-like (elastic) response of a melt to applied stresses (e.g. Dingwell & Webb, 1990). This boundary is the transition between flow and fragmentation (Figure 7–6), ultimately controlling the eruption style (i.e. explosive or effusive); and the behaviour of a volcanic flow (i.e. motion or deposition).

### 7.3.2. Thermal analysis

Simultaneous thermal analysis (STA) combines both thermogravimetry (TG) and differential scanning calorimetry (DSC) simultaneously on a sample. The cooling history influences the structure frozen within a cooled glass, whether volcanic or synthetic. The cooling rate history can be determined via geospeedometry, by controlled reheating cycles across the glass transition in a calorimeter, relaxing the glass structure back to equilibrium, producing heat capacity curves based on the kinetic parameters. The heat capacity values can then be modelled across the $T_g$ interval and the relaxation of enthalpy, indicating the cooling rate across the $T_g$ interval (Wilding et al., 1996i).

### 7.3.3. Methodology

Samples of obsidian glass were prepared and analysed at the Department of Earth & Environmental Sciences at Ludwig-Maximilians-Universität (LMU), Munich, using a Netzsch ® STA 449C instrument that combines DSC with TGA. Glass samples were hand crushed, to select the most pristine looking mm-scale chips for analysis. Approximately 20 mg of crushed glass was hand selected, rinsed with acetone and oven dried at 110 C for 1 hour, before shards are placed in a platinum crucible and analysed within an argon atmosphere. The temperature calibration was based on the melting points of Indium, Zinc, Ba-carbonate, and gold. Each sample is

then heated at a known rate (10 K $min^{-1}$), with between two and three heating cycles through the glass transition to quantify the glass transition temperature.

#### 7.3.3.1. Sample characterisation

Glasses present in units B and C of the Retamares Mb, the Almendros Mb, the Chasna Mb and the Areñas Mb were obtained via samples collected at various log localities (Table 7–4). The results of EMPA analysis of the glass chips is presented in Chapter 6, Section 6.1.2. The phonolite glasses of each member exhibit minor differences in major element concentrations and have been categorized into three groups accordingly: the Retamares Member, the Areñas Member at Montaña Guajara (southern locality); and the Almendros and Chasna members at Roque los Almendros. Each group shows minor variations in concentrations of $SiO_2$, $Al_2O_3$, $Fe_2O_3$, $Na_2O$, CaO, $P_2O5$, $SO_2$ and Cl, with the Areñas Member at Montaña Guajara exhibiting different trends in terms of correlations between major elements, than is shown by the other groups (e.g. positive correlations between $SiO_2$ with MgO, CaO and K, and negative correlations between $SiO_2$ with $TiO_2$, $Al_2O_3$, $Fe_2O_3$, and $Na_2O$ (Table 6.1–5).

| Mb | Unit | Sample | Stratigraphy | Description | Interpretation | Field Photograph |
|---|---|---|---|---|---|---|
| Retamares | B | PP-02 | 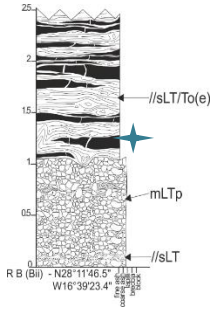 | **//SLT/To(e)**<br>Obsidian fiamme (merged and forming continuous horizons) within a teal and orange flow-banded, clast-rich, crystal-poor strongly (*V) welded lapilli tuff. Fabric exhibits minor folding (open and curvilinear folds) and is locally rotated around minor lithic clasts of predominantly lava-like and pumiceous material. | The banded obsidian and welded lapilli tuff are interpreted to reflect, and be a factor of, the original pre-welding grainsize (obsidian = v. fine), with the finer particle size being more readily deformed. This stratigraphy may represent a planar stratified tuff and lapilli tuff. A highly erosive contact with the underlying, predominantly non-welded, pumice-rich lapilli tuff supports the interpretation of being deposited from a PDC. |  |
| | C | TN-09 | 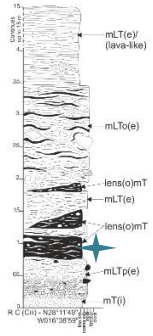 | **mTo**<br>Sporadic and discontinuous streaky, flow-banded obsidian horizons and lenses from 0.8 m to 3.5 m which grades from partially welded (III) up into a eutaxitic to strongly welded (V) tuff with occasional lithic clasts (predominantly lava-like material) and localised green deformed and largely devitrified pumice. | The localised and discontinuous vitric lenses could be attributed to both temperature fluctuation and differential grain size. Lithic lapilli and clasts are largely undeformed but no fiamme or pumice (via clasts or lapilli) is present, suggesting total collapse of pumice and ash components. The discontinuous and sporadic occurrence suggests temperature variability. An irregular, erosional contact with the mLT below also supports the interpretation as the result of a PDC. | 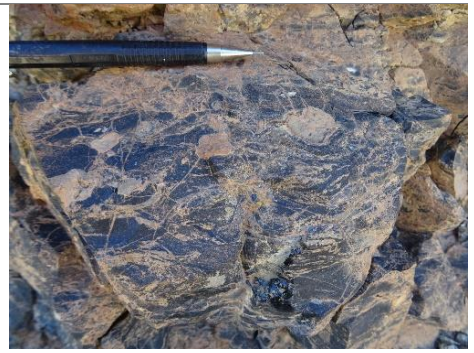 |
| Chasna | RLA | VF-16/3 | Log continues up…<br> 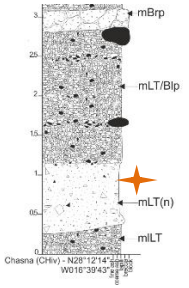 | **mLT(n)**<br>Thin, (< 0.2 m) discontinuous lens rich in obsidian fiamme within the basal 1 m of the deposit, consisting of brown predominantly clast-supported, locally LT-supported, rich in pumiceous lapilli with laterally variable welding, from non-welded to distinctly welded (I-VI). | The highly localised nature may indicate an irregular flux in temperature or viscosity of the depositing material. The imbrication of obsidian fiamme (see photo), relative to the planar bedding suggests the initiation of a shear zone within the depositing current, giving rise to localised coalescence and welding of material, which may then dissipate due to instability. |  |

| | | | | | |
|---|---|---|---|---|---|
| Almendros | TN-37 | 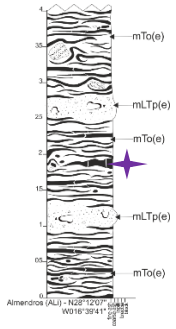 | **mTop(e)**<br>Obsidian bands (glassy fiamme) are up to 4 cm in thickness, and locally weathered a brownish red colour. Planar stratification can be seen in the densely welded (VI) matrix surrounding obsidian bands, which is churned up and deformed by flow banding. Fabric is also deformed around minor lithics (predominantly lava-like and welded ignimbrite material). | Obsidian fiamme and bands (amalgamated fiamme) are stretched and boudinaged, and weakly imbricated, oblique to the planar bedding surfaces, indicating shear-induced deformation. The vitric lenses are likely a result of differential material viscosity, perhaps representing lower viscosity pumice that are more easily deformed, than as a product of differential devitrification, since pyroclast boundaries are more visible in the welded tuff matrix. |  |
| | TN-39 | 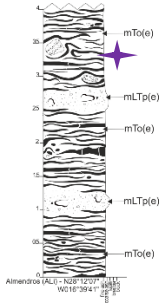 | **mTo(e)**<br>Obsidian-rich (glassy fiamme) are extensive throughout a crystal poor densely welded (VI) tuff with occasional fiamme green coloured devitrified fiamme, and blocks of lesser welded material. Flow banded obsidian and orange, devitrified material exhibits a planar, that is locally folded and rotated around occasional clasts (predominantly lava-like material). | The obsidian banding is laterally extensive throughout the deposit, may again, reflect, or be a factor of the original grainsize or particle component (smaller grained, or less viscous pyroclasts, more readily deformed). However, due to the extent of the welding intensity, it is not possible to rule out the contribution of differential devitrification to the banding. |  |
| *Arenas* | GUA<br>(south)<br>TN-31 | 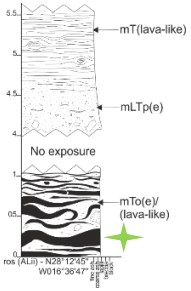 | **mTo(e)/(lava-like)**<br>Obsidian fiamme, and concentrations of fiamme forming vitric horizons within the basal ~ 1 m of a predominantly flow-banded bluish-green (devitrified) and orange, moderately welded (IV) tuff with occasional lithic lapilli and minor clasts (pumiceous and lava-like material). | The fiamme horizons are stretched and elongated, partly parallel with a base-parallel fabric, but also displaying imbrication, oblique to the planar fabric, consistent with syn-depositional shearing. Differential extents of devitrification seem to give rise to the banded nature of the deposit, with the 'fresh' black obsidian vs. the blue-green devitrified tuff. |  |

| | | | | | |
|---|---|---|---|---|---|
| GUA (south) | PP-01 | 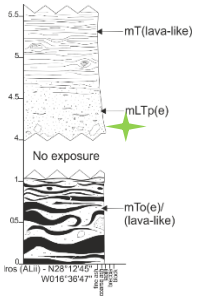 | **mLTp(e)**<br>Rare high-aspect (low flattening) ratio obsidian fiamme, and irregular shaped 'blebs' within the 'foamy' textured predominantly non-welded to partially welded (III), locally eutaxitic pumice-rich lapilli tuff, with occasional lithic clasts (pumiceous and lava-like material). Very poorly sorted with a weak planar fabric, which gradually becomes more pronounced. | The low flattening ratios and weak fabric of this unit suggest the glassy 'blebs' within this horizon are the result of remobilisation of a much lower viscosity material, relative to the surrounding depositing material, rather than the result of intense coalescence. Due to the rarity and morphology of obsidian 'blebs', it is unlikely that they are a result of fluidal spatter or spatter-like bombs. |  |

**Table 7–4.** Outline of the glass samples measured by both EMPA and STA analysis, including stratigraphic position within the unit, relationship to the horizon in which is belongs, and interpretation. Star symbols on stratigraphic logs mark the vertical position from where the sample was collected. Welding intensities (I-IX) are based on the criteria of both visual characteristics and measured properties (described in Chapter 5). Full descriptions of the logs and lithofacies symbols used here are outlined in Chapter 4.

### 7.3.4. Results

All of the glasses, with the exception of the sample from Unit B of the Retamares Mb (PP-02), displayed pronounced annealing behaviour, indicated by differences in peak shapes between the first and second heating runs (Figure 7–7). Each sample displays two peaks, the 1st on initial heating, associated with a higher temperature, and a 2nd reproducible peak, which is the $T_g$ of the glass. Insignificant mass loss (<0.05 wt. %) during TG 1st heating indicates that the samples are fresh and largely unweathered, with the exception of TN-09 which recorded a loss of 0.3 wt. %, indicating alteration of the glass. $T_g$ is broadly correlated with the peralkalinity of the samples (Tables 6.1–2, 6.1–3, & 6.1–4), with TN-09 and PP-02 (Retamares Mb Unit B) having the lowest $T_g$ temperatures.

### 7.3.5. Discussion

The residence of the material at temperatures close to and around the $T_g$ contributes to changes in the nature and structure of the glass, as well as lowering the cooling rate. Annealing may be the reflection of very slow cooling rates, whereby a lower equilibrium has become 'frozen' within the structure or from reheating of a quenched glass to within the annealing temperature (the fictive temperature, $T_f$), which can be maintained until structural relaxation of the glass (Wilding et al., 1996ii). This could be the result of thermal alteration during continuous deposition of hot material above, within the same unit, as in the Almendros Members, where they are the youngest deposits, or from the thermal influence of subsequent overlying deposits, which could have occurred at any stage during the deposit's cooling. It is not possible to determine either the extent of annealing, or how many thermal events the deposits have endured, or the cooling rates associated with the measurements.

A cooling rate of 10 K/min ± 5 can be approximated for Retamares Unit B (Figure 7–7 a), indicating rapid cooling with the subsequent depositing material being below the $T_g$, and experiencing no subsequent heating towards the $T_g$. The deposit is considerably thinner at this locality (<3 m) (Table 7–4) with the average thickness of Unit B being 15 m. The unit thins over a topographic high at this locality and is not overlain by the younger Retamares units. It also indicates that

the underlying Unit A was sufficiently cooled, which is further supported by the presence of localised non-welded pumice fall deposits between Units A and B observed at other localities, indicating a hiatus between the emplacement of Units A and B. The presence of banded obsidian or glassy fiamme is not a common feature throughout Unit B, and as it is largely restricted to where the unit thins over the underlying topography, suggesting the deposit cooled through the $T_g$ at this locality at a faster rate than the thicker accumulated mass, due to a limited capacity for the deposit to stay insulated.

An exothermic trend from 815°C seen in the heat flux curve of TN-09 (Retamares Unit C) (Figure 7–7 b) is interpreted to represent the onset of partial melting, when melt droplets start to appear. This falls within the range of magmatic temperatures determined by Soriano et al. (2002), based on iron-titanium oxide pairs from the densely welded and lava-like lithofacies of Montaña Pasajirón, which are between 751-847°C, and are also in the same realm of those estimated by Wolff & Storey (1983), Ablay et al. (1995), and Bryan (1998).

The Almendros Mb and Chasna Mb at Roque los Almendros (TN-37, TN-37, and VF-16/3) (Figure 7–7 c, d & e) display similarities in both position and height of the $2^{nd}$ $T_g$ peak, indicating a shared thermal history. The Almendros Mb overlies the Chasna Mb at this locality and is interpreted as the deposit of a topographically controlled PDC in a paleo-depression, leading to steeply inclined, inwardly dipping limps. Due to the nature of the cooling joints and the morphology in the underlying Chasna Mb, the concavity is also likely a result of deposition in a paleo-valley, rather than an erosional feature of the Chasna Mb following emplacement and cooling. Their shared thermal history suggest that the Chasna Mb was still hot while the Almendros Mb was emplaced, which may have contributed to the annealing of both units, as they were able to maintain higher temperature for longer periods of time. The densely welded (VI) facies of the relatively thin (<15 m) Almendros Mb may be both a function of syn-depositional rheomorphism, with the underlying deposit providing both heat and insulation, coupled with a prolonged residence within the welding interval following deposition.

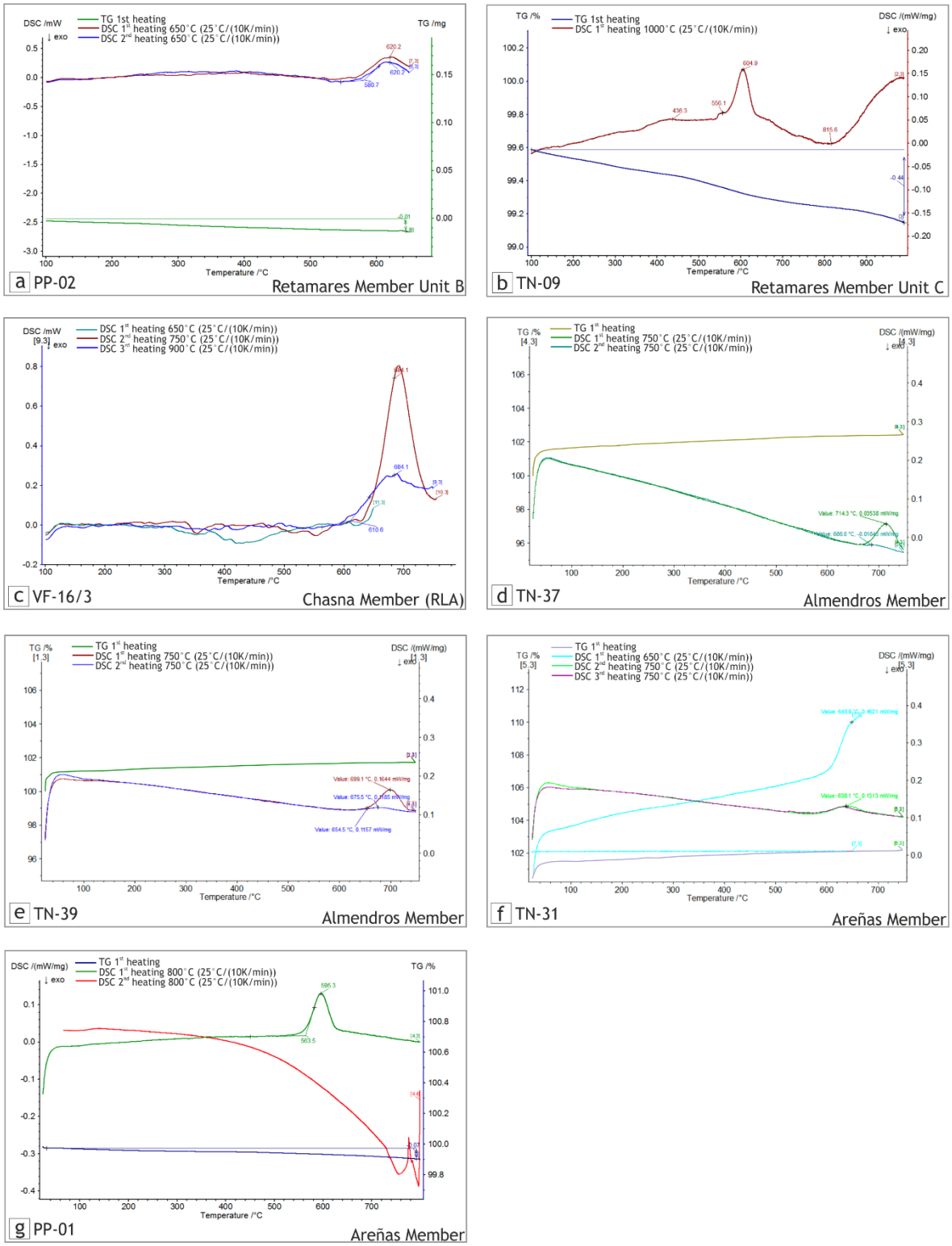


**Figure 7–7.** Heat flux and mass loss curves from calorimetry (DSC) and thermogravimetry (TG). The baseline has not been subtracted from samples TN-31, TN-37, and TN-39. The $T_g$ temperatures are annotated on each peak for each sample, and presented in Table 7–5.

### 7.3.6. Viscosities and degassing

The morphology, behaviour and welding textures of volcanic deposits is controlled by shear viscosity, which itself is a factor of the chemical composition, $H_2O$, bubble and crystal content, and stress (Gottsmann, 2002). As viscosity is the measure of a material's ability to resist ductile deformation, the eruptive behaviour of a material is largely controlled by the viscosity of the material at different stages of emplacement. The magmatic viscosity is proposed to reflect the degree of silicate polymerisation in the melt, with high viscosities from thoroughly polymerised melts having the most resistance to flow (Webb & Dingwell, 1990). The viscosity and viscous deformation during the welding process can be described by Maxwell's (1867) law of linear viscoelasticity:

$$\tau = \frac{\eta_N}{G_\infty}$$

The relaxation time(s) ($\tau$) is dependent on the shear (rigidity) modulus ($G_\infty$), at infinite frequency, and the Newtonian shear viscosity of the liquid ($\eta_N$). Newtonian viscosities across $T_g$ are dependent on the cooling history, as structural relaxation is thermally activated, with the $T_g$ being crossed as a result of exponential temperature loss related to the thermal diffusivity of components in the liquid. This 'freezing' of the liquid into a glass has an effect on a variety of processes (e.g. viscous flow, the nucleation and growth of crystals and bubbles) taking place during emplacement.

Using the Gottsmann et al. (2002) model, the calorimetric $T_g$ temperature (of the 2nd peak) can be converted into viscosity data, providing a determination of shear viscosity at the $T_g$ interval (Table 7–5), using the following equation:

$$\log_{10} \eta \left(T_g\right) = K - \log_{10} |q|$$

For this equation, mildly oxidised conditions are assumed, with a $K$ value based on a 75:25 ratio of $Fe^{2+}/Fe^{3+}$. The $K$ value is the shift factor as a function of the excess oxides in the melt composition:

$$K = 10.321 - 0.175 \times \ln x$$

$x =$ the molar percentage of excess oxides ($Fe^{2+}$:$Fe^{3+}$ - 75:25 ratio)

The total iron content ($Fe_2O_3$) was measured from EMPA (Table 6.1–5) but the ratio between reduced iron ($Fe^{2+}$) or oxidised iron ($Fe^{3+}$) is unknown. To account for this, both the excess oxides (EXox, assuming all Fe as $Fe^{3+}$) and excess oxide (EXred, assuming all Fe as $Fe^{2+}$) was calculated, and the NBO/T value was determined for each (Table 7–5). NBO/T is the ratio of tetrahedrally coordinated cations (T) to non-bridging oxygen (NBO) ions. The ratio gives a measure of the degree of interruption, or polymerisation of the structure: i.e. the smaller the ratio, the more polymerised the melt is. It is a useful parameter in the semiquantitative determination of viscosity, but as the composition also influences the transport properties, it can be used to indicate the composition-dependence of mineral-melt element partitioning (Jana & Walker, 1997; Walter & Thibault, 1995; Toplis & Corgne, 2002; Mysen & Richet, 2019). Minor differences are observed on comparison between the NBO/T and K values assuming both oxidised (EXox) and reduced (EXox) conditions, providing confidence in the assumption of reduced conditions in the model. The quench rate (q), measured in DSC, is a constant in the equation, set at 0.78 K/s (10K/min).

The viscosity at $T_g$ is dependent on the cooling history of the glass, and independent of water content and composition (Giordano et al., 2000). Predicted viscosities of the glasses at $T_g$ are within the range of $\log_{10}$ 10.88 – 10.96 Pa·s and are within the range of the viscosity values derived from applying the Giordano et al. (2008) (GRD) model to the glass compositions (Table 7–5). Although cooling rates cannot be extracted from these samples due to the extent of annealing experienced by the glasses, insights into the thermal and cooling histories can be inferred by drawing comparisons with the Giordano et al. (2008) model (Table 7–5). The temperature-dependence of viscosity (η) at $T_g$ is modelled using the VFT equation) (Vogel, 1921; Fulcher, 1925; Tammann & Hesse, 1926):

$$\log \eta = \mathrm{A} + \frac{B}{T(K) - C}$$

Where the parameters of B and C are the compositional dependencies, and A is a constant, representing the high temperature limit to silicate melt viscosities.

The disparity between the calorimetrically determined $T_g$ and the GRD predicted $T_g$ can be attributed to the variability in water content. Through modelling of the $H_2O$ concentrations (wt. %), to align the determined and predicted $T_g$s, the extent of degassing can be inferred for each sample. Both TN-09 and PP-01 do not exhibit a defined 2nd peak on reheating, so the $T_g$ from the first peak cannot be compared with the GRD model, so $H_2O$ values cannot be estimated for these glasses. Each of the assigned groups show similarities in $H_2O$ concentrations, and thus extent of degassing.

Unit B of the Retamares Mb and the Areñas Mb show higher concentrations of excess water, 0.17 and 0.14 wt. % respectively, in comparison to very low values of 0.03 – 0.06 wt. % estimated in the Roque los Almendros localities of the Chasna and Almendros Mb. Both of these units at RLA are highly degassed, indicating that these units resided within the welding interval, or in residence close to the $T_g$, for longer periods of time, and a significantly slower cooling rate for these deposits can be assumed, relative to the other deposits. This is supported by higher degrees of depolymerisation of the glasses, with lower NBO/T values in the highly degassed deposits, consistent with prolonged periods spent at higher temperatures. Higher water content in the Retamares Mb Unit B and Areñas Mb at Montaña Guajara can be associated with faster rates of cooling, with less time for efficient degassing to take place. This is in line with the approximated cooling rate (10 K/min ± 5) via geospeedometry for Retamares Unit B. The presence of obsidian within both deposits is associated with highly vesicular 'foamy' pumice lapilli within the variably welded facies (III-V), which may further inhibit the efficiency of degassing.

| Member | Unit | Sample | Thermal gravimetry wt. % | $T_g$ 1st peak °C | $T_g$ 2nd peak °C | EXox | NBO/T | EXred | NBO/T | 50:50 $Fe^{2+}$: $Fe^{3+}$ | K | 75:25 $Fe^{2+}$: $Fe^{3+}$ | K | log η ($T_g$) Pa·s | $T_g$ GRD °C | $H_2O$ GRD wt.% |
|---|---|---|---|---|---|---|---|---|---|---|---|---|---|---|---|---|
| Retamares | B | PP-02 | <0.05 | 620.20 | 620.20 | 1.99 | 0.04 | 7.91 | 0.17 | 4.95 | 10.04 | 3.47 | 10.10 | 10.88 | 662 | 0.17 |
| | C | TN-09 | -0.30 | 604.90 | - | 2.26 | 0.05 | 8.59 | 0.19 | 5.42 | 10.03 | 3.84 | 10.09 | 10.87 | 652 | - |
| Chasna | RLA | VF-16-3 | <0.05 | 690.00 | 680.00 | - | - | - | - | - | - | - | - | - | - | 0.06 |
| Almendros | RLA | TN-37 | <0.05 | 714.30 | 686.00 | 1.25 | 0.03 | 5.26 | 0.11 | 3.26 | 10.11 | 2.25 | 10.18 | 10.96 | 689 | 0.03 |
| | | TN-39 | <0.05 | 699.10 | 680.00 | - | - | - | - | - | - | - | - | - | - | 0.04 |
| Areñas | GUA | TN-31 | <0.05 | 650.00 | 638.00 | 1.34 | 0.03 | 5.78 | 0.12 | 3.56 | 10.10 | 2.45 | 10.16 | 10.94 | 672 | 0.14 |
| | | PP-01 | <0.05 | 595.00 | - | - | - | - | - | - | - | - | - | - | - | - |

**Table 7–5.** Summary of results from STA analysis and the model parameters and outcomes of both Gottsmann et al. (2002) and Giordano et al. (2008) (GRD) models. The 2nd peak is the physical property of the glass, as used in the models. EXox, assumes all Fe as Fe3+; and EXred, assumes all Fe as Fe2+. NBO/T: ratio between non-bridging oxygens and isolated tetrahedron cations. Calculations for each sample is included in Appendix V.

The resulting welding intensities of these deposits can be therefore be attributed in part as a factor of the time spent within the welding interval, correlated with the extent of degassing. The longer the time spent within temperatures near to, or in the realm of the $T_g$, facilitates more effective degassing, leading to more effective welding of pyroclastics, resulting in both the annealing of the material, and the higher intensities of welding seen in the highly degassed Chasna and Almendros Members at Roque los Almendros. The Retamares and Areñas Mb both displaying lower, and more variable intensities of welding (III-V), spent less time within this zone respectively, with limited time for degassing and welding to take place, and cooling at a faster rate. As the rank of welding intensity can be broadly correlated with these parameters (Figure 7–8), it may provide a pseudo-quantifiable analogue of cooling rate.

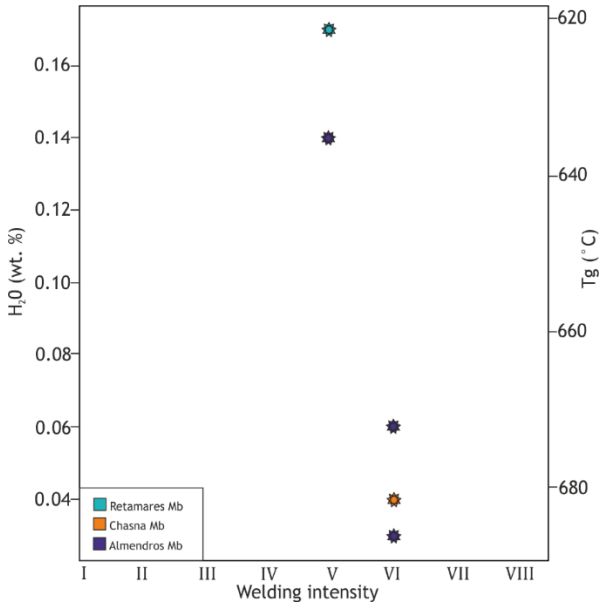


**Figure 7–8.** Rank of welding intensity (as outlined in Chapter 5) vs. the $T_g$ (2nd peak) and the modelled magmatic $H_2O$ concentrations of the glasses.

### 7.3.7. Implications for emplacement

The localised nature of the glasses present within the deposits, associated with variable thicknesses (e.g. thinning) in the case of the Retamares Members, indicates differential cooling of individual deposits, producing variable thermal histories across singular units, dependant on, but not limited to, the deposit

thickness, the remnant heat associated with the underlying deposit(s), and the thermal alteration provided by overlying material and subsequent deposit(s).

Thicker accumulations of hot material have the capacity to stay insulated for longer periods, which may contribute to the higher intensities of welding in the thickest deposits. However, as discussed in this chapter, welding intensity is both a product of syn-depositional processes coupled with post-depositional processes, and the cooling rate, which may or may not contribute to the further deformation and welding of pyroclasts. This is true for the significantly thinner units, particularly those of the Almendros and Retamares members which display high intensities of welding, as a result of predominantly syn-depositional processes, as demonstrated by their relatively rapid cooling rates.

The absence of glass preserved at welding intensities <V and >VI may suggest a combination of higher crystal content, or faster cooling rates for lower welding intensities below the $T_g$, preventing the formation of glass, and significantly slower cooling pathways for intensely welded glassy deposits, which leads to the devitrification and crystallisation of glasses present. The devitrified intensely welded and lava-like facies of the crystal-rich Atravesado and Chasna Members, suggests these deposits cooled slowly through the $T_g$, promoting crystal phases and spherulitic growth (e.g. Figure 6.2–1 & 6.2–3).

### 7.3.8. Further work

Further analysis of glassy phases from other localities within individual units of variable thickness may provide further insights into the thermal history and cooling dynamics of singular deposits. The correlation with welding intensity is based on modelling of only a handful of glass samples, and more data may elucidate this relationship.

Some of the endothermic trends may be related to a change in crystal phases of sub-micron crystals that may be present within the glass (microlites (>0.6 μm wide) and nanolites (<0.6 μm wide)) (Sharp et al., 1996). Investigation into the presence and nature of sub-micron crystals using scanning electron microscopy or Raman spectroscopy is planned for future work.

## 7.4. Discussion

The Ucanca and Guajara Formations were interpreted as welded fallout deposits by previous workers (Soriano, et al. 2002; 2006 & Bryan, 1998), who described a simplified vertical welding profile as the result of initial Plinian activity, followed by fountain-fed spatter, which then undergoes post-depositional rheomorphic flowage and detachment (Figure 7–9), with similarities to other models of rhyolitic and phonolitic welded air-fall tuffs (e.g. Tuberville, 1992; Sparks & Wright, 1979; Stevenson & Wilson, 1997; Wright, 1980).

Agglutination of low-viscosity spatter is proposed to occur in situ, on landing, and the flattening is attributed to both low viscosities and the effects of loading (Soriano, et al., 2002; 2006; Bryan, 1998). The emplacement temperature is estimated to be 740 °C, with the progressive collapse of the eruption column leading to higher temperatures and lower viscosities, and thus resulting in the upward increase in welding intensity (Soriano, et al. 2002; 2006; Bryan, 1998).

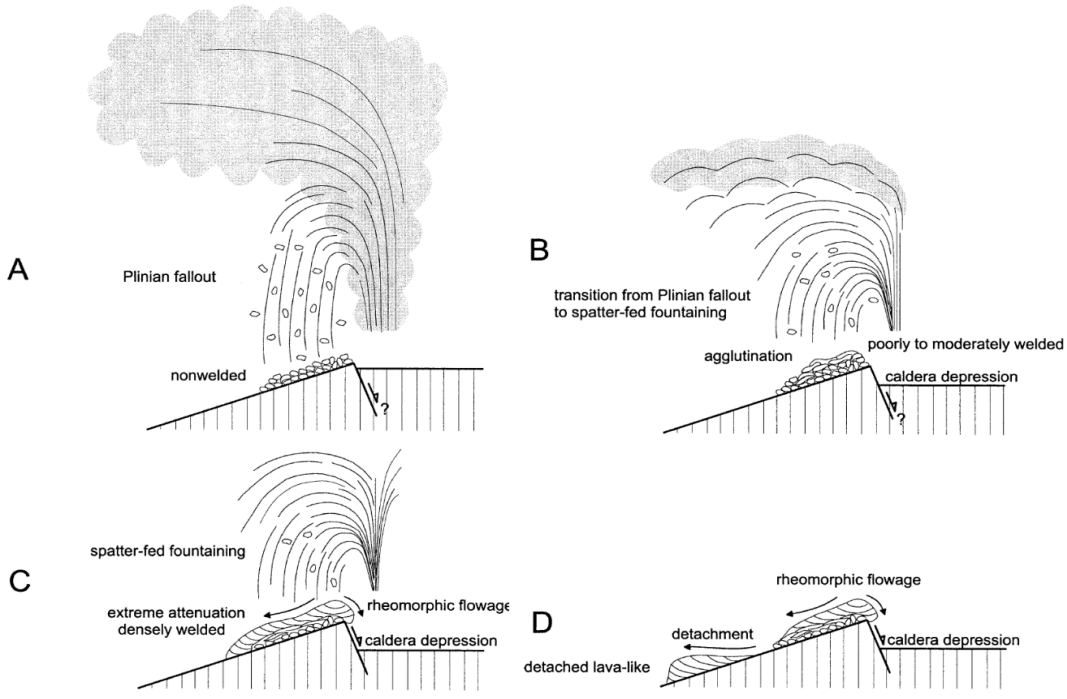


**Figure 7–9.** The emplacement model of Soriano et al. (2006) for the welded and lava-like deposits of the Las Cañadas Caldera wall, interpreted as welded fallout. A) A rising plume of Plinian columns, generating fallout, giving rise to an initially non-welded deposit. B) Transition from Plinian activity to a lower column fountaining leads to spatter accumulation, whereby agglutination of material occurs, leading to the homogenisation of material. C) Spatter-fed fountaining continues leading to a densely welded facies and extreme attenuation, leading to down-slope rheomorphism of the material. D) Detachment of the rheomorphic, hot material occurs post-depositionally down slope, and there is slumping of the material back into the caldera depression.

This emplacement model is both problematic and highly contradictory to the findings of this study, established through field analysis, including isopach and facies mapping, and detailed stratigraphic analysis (Chapter 4) of the deposits. It does not account for the range and extent of syn-depositional sedimentary and depositional features (e.g. grading; imbrication of lithics; planar-, cross- and diffuse-stratification) and the prevalence of fine-coarse tuffs in the basal stratigraphy, as detailed in Chapter 4, nor the evidence for syn-depositional or polyphase rheomorphism exhibited across many of the units. The in-situ welding mechanism fails to explain the diversity in erosional and original sedimentary features diagnostic of deposition from pyroclastic density currents.

Furthermore, welding profiles exhibit substantial complexity in gradients, both vertically, laterally, and irregularly throughout individual deposits, giving rise to a host of unusual textures and intensities of welding, discussed in Chapter 5 and this Chapter. While some outcrop faces of the deposits do exhibit the gradational up-section transition from nonwelded to lava-like facies, as described by Soriano et al., (2002), this does not represent the entirety of the units, and presents an oversimplified and passive description of the welding facies, using only three purely descriptive classifications: nonwelded, densely welded and lava-like.

The proposed detachments in Soriano et al's model (2002), although not attributed to a particular Unit or field description, aims to account for the highly variable thickness of the proposed fall deposit. No field evidence is found for detachment of the rheomorphic ignimbrites. The variable thickness of the units, which pool in paleo-topographic lows, both as a result of original depositional thickness and thinning over topographic highs (e.g. Figure 4–84), as well as the result of compressional thickening of the rheomorphic deposits (e.g. Figure 4–53), can be better explained by the topographically controlled nature of PDCs. This interpretation accounts for both distal thickening seen in some units, and thinning observed in others. Syn-depositional flow foliations of welded units can be base-parallel, consistent with syn-depositional transportation, but often with disregard to the slope of the underlying substrate, and responsible for the pervasive shear fabrics, such as the elongation, imbrication, and deformation of fiamme. These structures cannot be explained by simple welding compaction, followed by down-slope rheomorphism.

The $T_g$ temperatures estimated by Soriano et al. (2002) associated with the densely welded Montaña de Pasajiron proposed fall succession is 740 °C, which focusses on the contribution of deposit thickness on heat retention, using the model by Thomas and Sparks (1992) that predicts the fraction of initial heat retained as both a function of particle grain size and height of fallout. Cooling rates associated with these calculated emplacement temperatures are then based on comparison of $T_g$ estimates of other glasses present in the Las Cañadas Caldera (e.g. Gottsmann & Dingwell, 2001; Wilding et al., 1996i). This model assumes that the material deposited furthest from the vent therefore has the lowest emplacement temperatures. This is not only problematic from a lack of field evidence (e.g. no welding intensity or textural basis for a distal variation in emplacement temperature), but as calculations are based on a particle grain size parameter, estimations become progressively less accurate with increasing welding intensity.

Furthermore, while deposit thickness and rate of accumulation plays a role in the capacity of the material to stay insulated and retain heat (e.g. Walker, 1973; Sparks and Wright, 1979; Mahood, 1984; Riehle et al., 1995; Stevenson and Wilson, 1997; Kobberger and Schmincke, 1999), as shown in this study, for some units (Unit B of the Retamares Member, the Areñas Member and the Almendros Member) it does not play the dominant role. It is difficult to ascertain how pumice fall, particularly lithic-rich, would be able to accumulate at such a rate to maintain these temperatures. The interaction of lithics (lapilli and block) in PDCs leads to a reduction in the temperature of the current (e.g. Martí et al., 1991). Soriano et al. (2002) proposes that the presence of lithic material in the densely welded facies contributes to higher emplacement temperatures, as larger clasts allow for more effective heat retention, both contributing to and accelerating the welding processes. This is contradictory to the findings of this study, where lower intensities of welding intensities are associated with higher lithic input, as well as the variety of welding textures associated with the interaction of currents with lithic lapilli and blocks (e.g. 'Snowball' blocks of section 7.1.1.).

### 7.4.1. Interpretation as PDCs

The interaction of PDCs with the underlying substrate can lead to erosional contacts and scouring (e.g. Walker et al., 1980; Sparks et al., 1997), gravity-driven loading (e.g. Cole et al., 1993), or deformation by the impact or shear of the current (e.g. Sparks et al., 1985). The nature of the erosional features and those associated with deformation, both during and following deposition is in strong agreement with the interpretation of the units of the Ucanca and Guajara Formations as deposits of pyroclastic density currents.

The variability in welding intensities and textures observed throughout the deposits, both vertically and laterally, does not fit the typical model attributed to vertical welding profiles, whereby burial compaction is the primary welding control, associated with differential cooling rates at the basal and lower extents of an initially isothermal hot deposit (e.g. Smith, 1960; Ragan & Sheridan, 1972; Peterson, 1979; Riehle et al., 1995) (Figure 7–11). Deposit thickness does not appear to be a primary factor of welding intensity across the units, with no systematic relationship between welding intensity and deposit thickness, particularly in the units of the Retamares Member, nor is there evidence for a reduction in welding intensity towards the upper margins of the deposit, with the exception of a local decrease in welding intensity towards the upper limits of Retamares Unit B (Figure 4–53 & 4–54). The contribution of load compaction in these deposits is minimal, and associated with post-depositional processes (Figure 7–10), as it does not affect the entirety of the deposits, nor does it account for the variety of welding profiles within individual units, particularly those exhibiting intense and pervasive welding from base to top.

Extensive evidence exists in support of a model whereby rapid welding occurs syn-depositionally (Figure 7–10 b), within a high-temperature progressively aggrading current, with agglutination and coalescence occurring between low-viscosity pyroclasts (e.g. Branney & Kokelaar, 1992; Branney et al., 1992; Freundt & Schmincke, 1995; Freundt, 1998), with minimal impact from load compaction (e.g. Gibson, 1970; Mahood, 1984) (Figure 7–10 b), resulting in highly variable, non-systematic welding profiles, from non-welded to intensely welded and lava-like.

The occurrence of imbricated fiamme and oblique fabrics is interpreted as a result of initial imbrication during the process of sedimentation, paired with syn-depositional shear-induced rheomorphism, due to the gravity of the accumulating mass, coupled with shear stress of the overriding PDC. Curvilinear and sheath folds are likely a result of the progressive stretching and hinge rotation of folds initially perpendicular to the flow direction or stretching and nucleation around obstacles in the flow (e.g. lithic lapilli, lithic blocks, and crystals) (e.g. Figure 7–10 b).

While the possibility of compound cooling units within these intensely welded and lava-like facies (e.g. Retamares Unit 3; Chasna Mb at RLA & LdlM) exists, and may account for the observed irregularities in welding profiles, particularly in Retamares Unit 3, these irregularities are discontinuous however, and do not extend any great length throughout the deposit. Evidence of stacked or compound ignimbrites would be discernible in units of lower welding intensities (<V), and units display gradations and irregularities in welding, but no evidence of boundaries between different units.

A model whereby welding intensity is attributed to both variable emplacement temperatures and differential cooling histories would account for the variation in welding intensity seen across the units of lower welding intensities (<V). Temperature instability within the progressively aggrading current would account for the localised welding variation and textural phenomena associated with lithic component interactions. As demonstrated, there is a relationship between welding intensity and interaction with lithic lapilli and blocks (e.g. Sections 7.1.1 to 7.1.3.), suggesting a strong influence of the lithic input to the thermal stability of the current. The volume and physical properties of the incorporated material (e.g. porosity, permeability, density), are controlled by the degree of welding of the lithic ignimbrite material itself, the degree of sorting, and vesicularity, all of which influence the volatile exsolution and/or resorption during agglutination of the material (e.g. Sparks et al., 1999; Sumner & Branney, 2002). Furthermore, lithic components within a largely welded matrix display various degrees of compositional sorting and grading in size, from lithic lapilli up to blocks, providing an insight into the former stratification and zoning of the units, much of which has been obscured by the welding process.

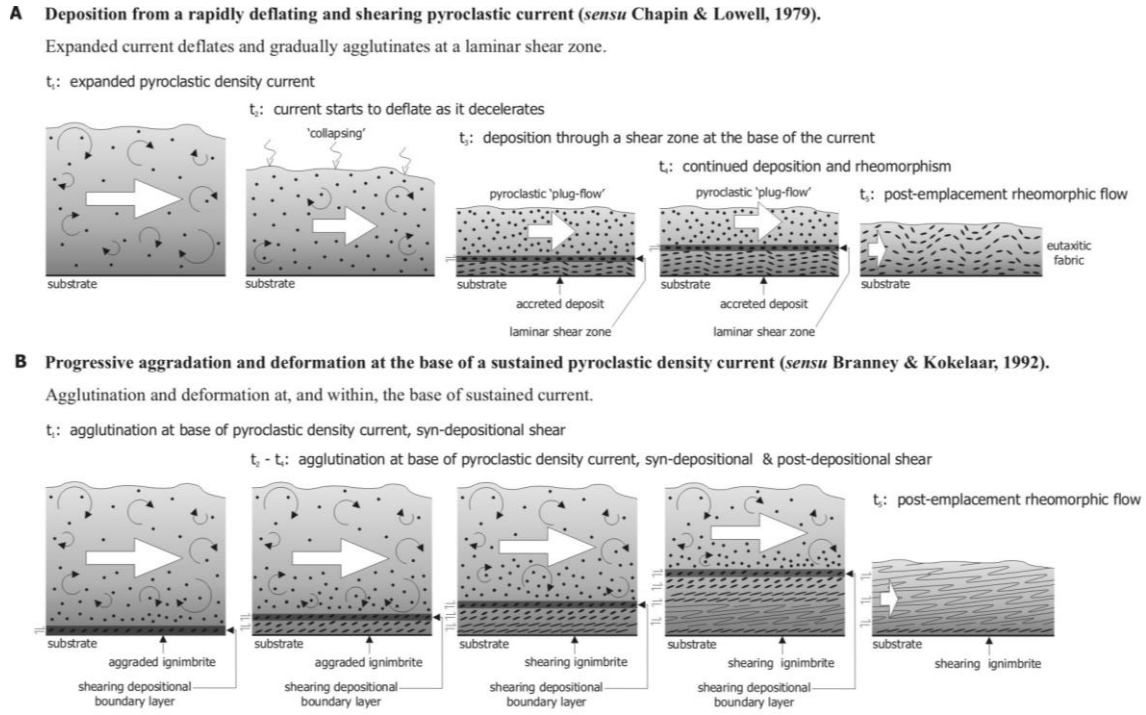


**Figure 7–10.** Models of syn-emplacement dominated welding and rheomorphism (Andrews, 2006). In (A) Chapin & Lowell (1979) describe 'plug-flow' ($t_3$) of a deflated current ($t_1$-$t_2$), which undergoes rapid welding and deformation ($t_4$-$t_5$) in a boundary-layer regime of plane strain and non-coaxial shear, enabling deformation to occur after plug-flow has ceased. In (B) Branney & Kokelaar (1992) outline progressive aggradation from a sustained, inflated current ($t_1$-$t_3$)t, with progressive shearing at the boundary layer. This in turn leads to progressive deformation within the deposit, enabling deformation to continue after transportation of the current has ceased ($t_4$-$t_5$).

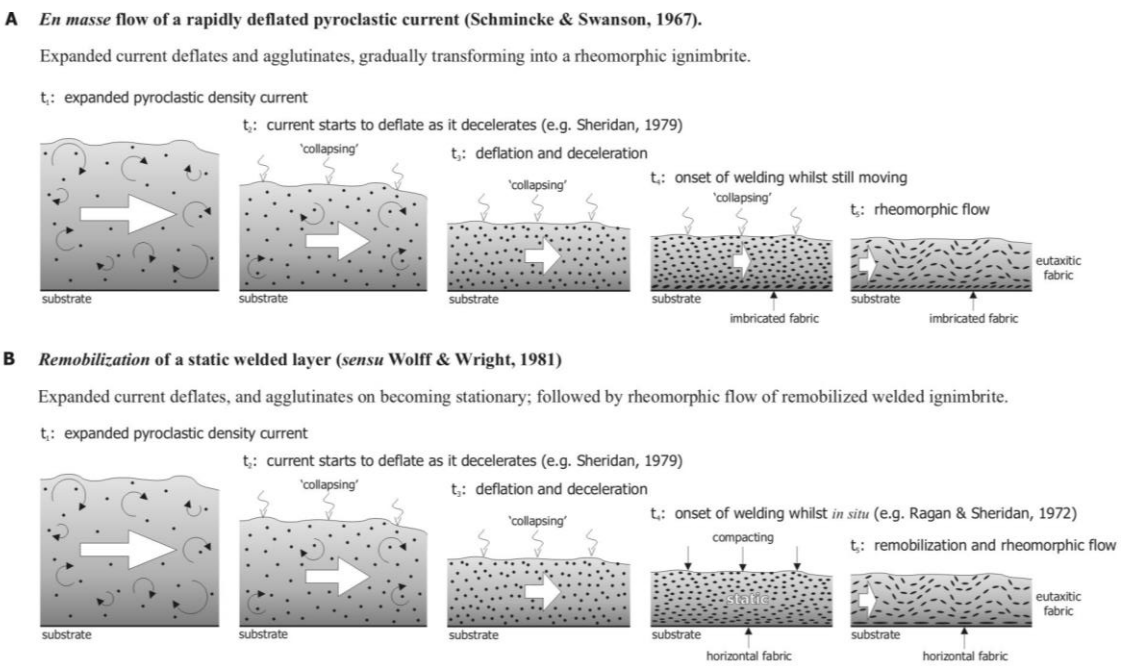


**Figure 7–11.** Models of post-emplacement dominated welding and rheomorphism (Andrews, 2006). In *en masse* rheomorphic flow (Schmincke & Swanson, 1967), shown by (A), welding immediately precedes rheomorphism ($t_4$-$t_5$) giving rise to a basal fabric and imbricated fiamme ($t_5$), after gradual deceleration and deflation of the current, from particulate to non-particulate ($t_1$-$t_3$). In the model described by Wolff & Wright (1981), shown in (B), there is a pause between deposition ($t_1$-$t_2$) and deflation ($t_3$), with welding occurring after transport has ceased. Welding occurs in situ (e.g. Ragan & Sheridan, 1972) prior to rheomorphism and remobilisation of the welded material ($t_5$). As welding does not occur during the transport of the current, there is no imbrication, with a largely horizonal fabric instead.

The progression from moderately and strongly welded to higher intensities and pervasive lava-like facies is likely a result of the progressive coalescence of fluidal pyroclasts during deposition, leading to the destruction and total obliteration of vitroclastic textures. Post-depositional hot-state rheomorphism may also play a smaller, secondary role in the destruction of any remaining vitroclastic textures, contributing to a homogeneous lava-like facies. A lack of lithics in the lava-like facies further supports the role of lithic content on welding capacity, as it is unlikely that larger lithic clasts and those of basic compositions, and thus higher melting temperatures, would be fully incorporated into the coalesced mass. The extent of the lava-like facies to the upper surfaces, where cooling would have been rapid, with the least compressional load indicates that coalescence plays the dominant role in the welding process.

The welding intensities observed throughout the deposits is therefore largely syn-depositional and a reflection of: i) the emplacement temperature, related to the viscosity, volatile content, and porosity of pyroclasts, and the ability of the current to maintain high temperatures; ii) the input and interaction with lithic clasts; iii) the extent of shear stress as a result of both gravity and that of the overriding current(s); iv) the time spent within the shear zone of a sustained current, which is a factor of sedimentation rate; and v) the time spent at temperatures above the $T_g$ (Figure 7–12).

The evidence for post-depositional rheomorphism, restricted to the thickest deposits exhibiting the highest welding intensities (Figure 7–12) suggests localised gravity-driven slumping and settling, in part due to their gravitational instability, and their ability to maintain higher temperatures and lower viscosities for longer durations. A model of down-slope mobilisation of material accounts for the development of secondary fabrics, ramp structures and ogives due to compressional deformation and thickening at the frontal faces of deposits. Localised minor folding and refolding of fabrics attributed to syn-depositional rheomorphism, indicates the presence of two distinct phases of deformation: a pervasive syn-depositional rheomorphism, affecting much of the unit's thickness; and highly localised rheomorphism attributed to post-depositional processes, although the exact timing and boundaries of each remains largely indistinguishable.

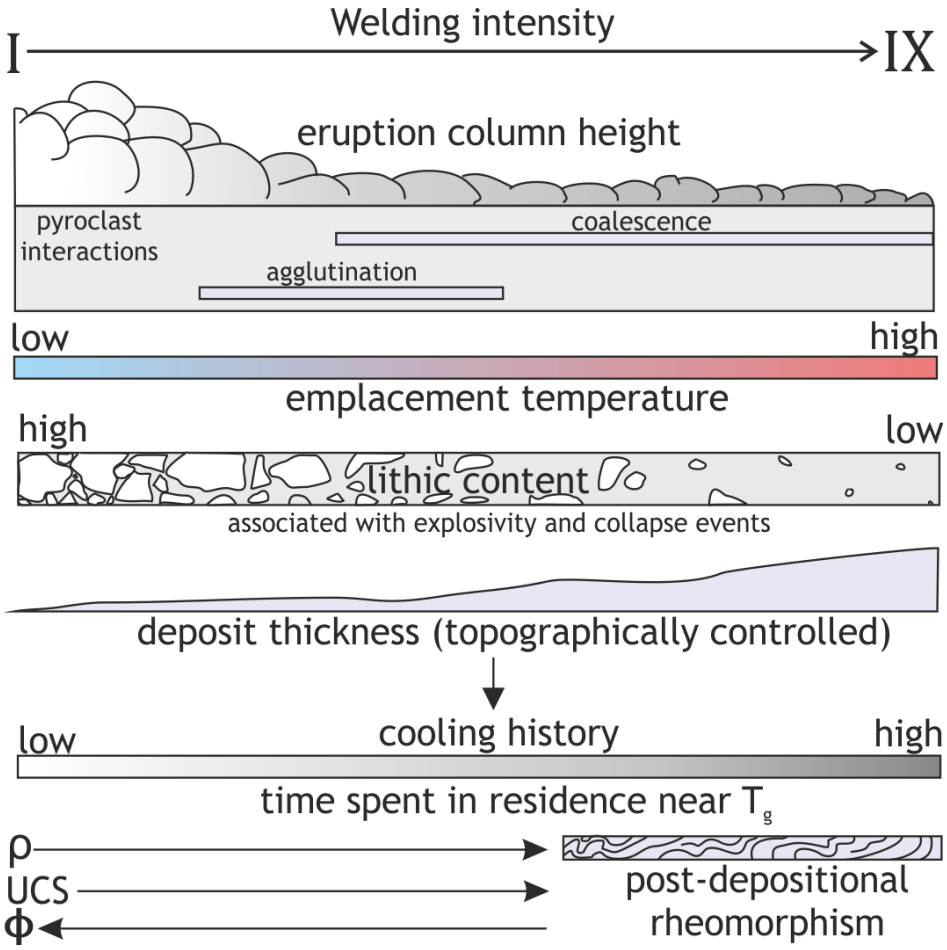


**Figure 7–12**. A summary of the factors and processes responsible for the welding intensity of the units. See text for details.

Peralkaline compositions (Chapter 6) and high magmatic temperatures are also factors contributing to the apparent ease of welding, as low magmatic viscosities, and lower eruption columns, are capable of maintaining higher temperatures and insulating suspended pyroclasts (Schmincke, 1974; Mahood, 1984). The ability of the deposit to retain high temperatures (Figure 7–12) is favoured by deposit thickness and both rapid and high accumulation rates (Smith, 1960; Friedman et al., 1963; Walker, 1973).

Although there is no distinct compositional difference between units which exhibit intensely welded and lava-like facies from lesser welded units, such as those of the Retamares Mb, the presence of globules and mafic enclaves in those exhibiting the highest intensities of welding (Atravesado and Chasna Members) may suggest the discharge of magma from deeper within the reservoir, associated with higher temperatures. These units are not associated with a variation in welding and are

intensely welded and lava-like from top to bottom. They are typically crystal rich, with aligned feldspar and hornblende crystals. The more intermediate composition of the Chasna Mb at Llano de las Mesas may represent tapping of a deeper, and thus hotter source within the reservoir, reflected in both the high intensity of welding and composition.

## 7.5. Summary

In light of the review of field evidence and investigation into the nature, dynamics and mechanisms of emplacement, the welded and lava-like deposits of the Ucanca and Guajara Formations are interpreted as a series of pyroclastic density currents, with the following findings and implications:

- This section outlines the extensive evidence from both field observations and petrographic analysis, in support of the ignimbrites of the Ucanca and Guajara Formation as deposits of PDCs.

- A review of the structures and textures observed in the ignimbrites, combined with the measured physical properties (Chapter 5) demonstrates that shear-driven, syn-depositional welding is the dominant process controlling the welding intensity.

- Deposits that have undergone extensive syn-depositional welding display evidence of post-depositional flow and deformation, suggesting that thick, intensely welded deposits are more susceptible to post-depositional rheomorphism, as they remain in a hot, plastic state for longer periods of time.

### 7.5.1. Emplacement models

Drawing upon the findings from detailed field investigation (Chapter 4 and this Chapter), geochemical, petrographical, thermal, and textural analysis (Chapter 6), and measurements of the physical properties and welding classification (Chapter 5), schematic models illustrating the emplacement and post-depositional processes of each mapped member is summarised in Figures 7–13 to 7–18.

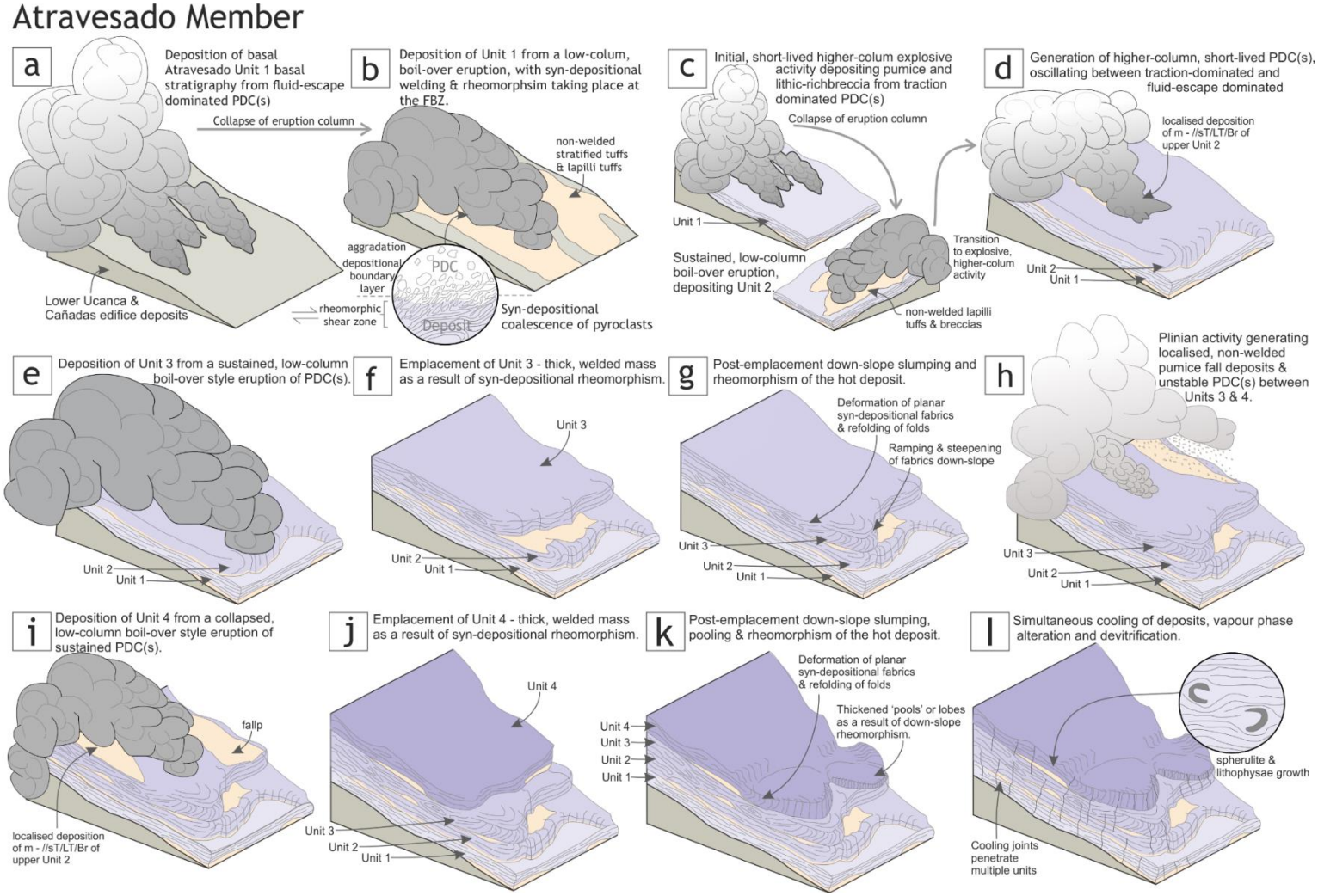


**Figure 7–13.** Schematic illustration of the emplacement of units (1-4) of the Atravesado Member. No scale intended. Note: Plinian activity may have been ongoing throughout all stages of eruptive activity, and was only recorded when current activity paused for a sufficient time period. These images are not attempting to depict any possible bypass and/or erosion that may have occurred both between and within units.

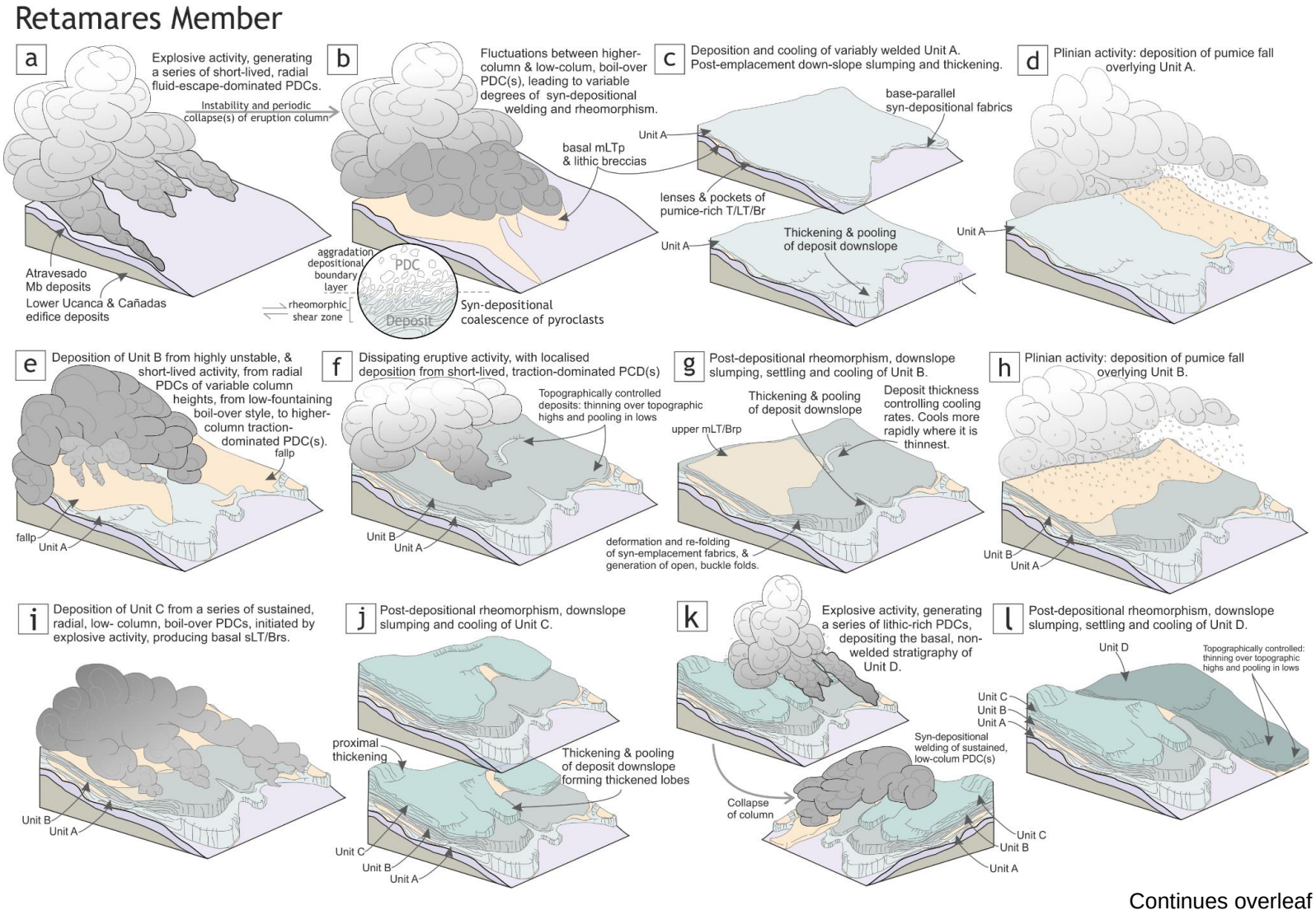


Continues overleaf

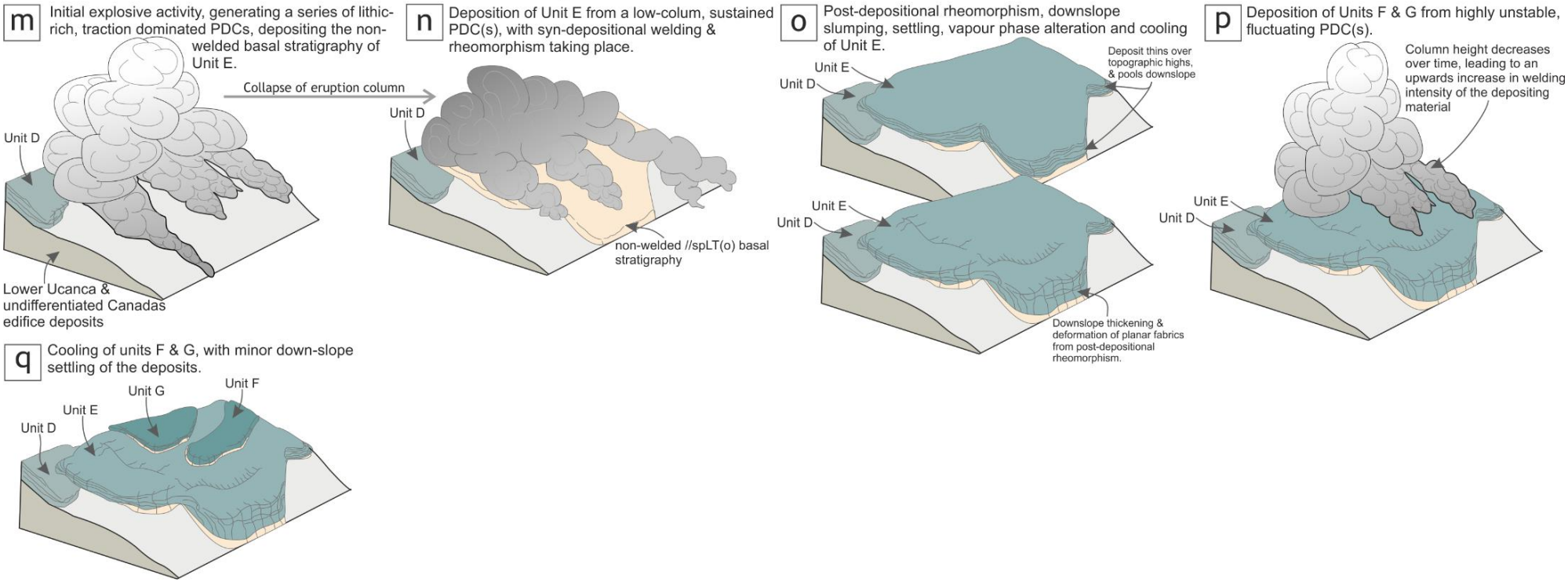


**Figure 7–14.** Schematic illustration of the emplacement of units A-G of the Retamares Member. No scale intended. Note: Plinian activity may have been ongoing throughout all stages of eruptive activity, and was only recorded when current activity paused for a sufficient time period. These images are not attempting to depict any possible bypass and/or erosion that may have occurred both between and within units.

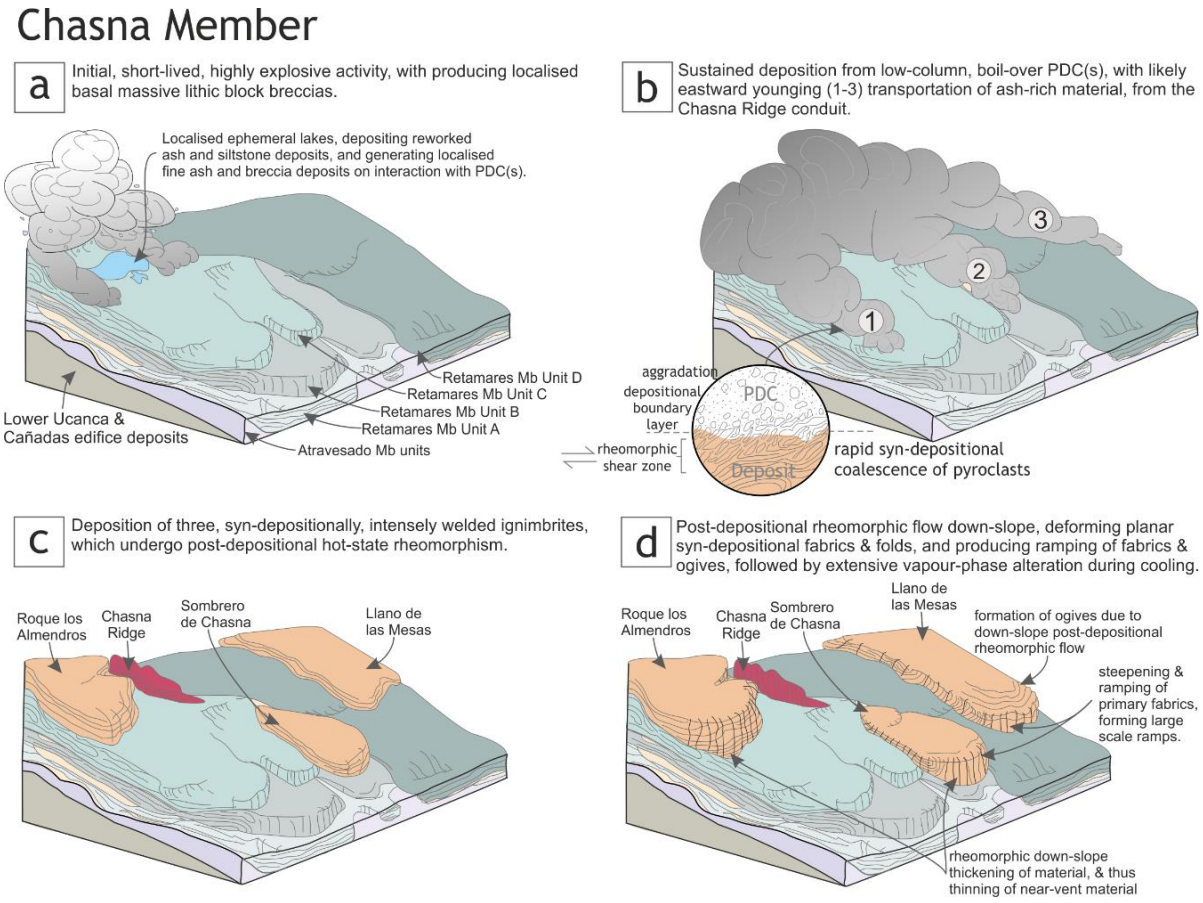


**Figure 7–15.** Schematic illustration of the emplacement of the three units of the Chasna Member. No scale intended. Note: Plinian activity may have been ongoing throughout all stages of eruptive activity, and was only recorded when current activity paused for a sufficient time period. These images are not attempting to depict any possible bypass and/or erosion that may have occurred both between and within units.

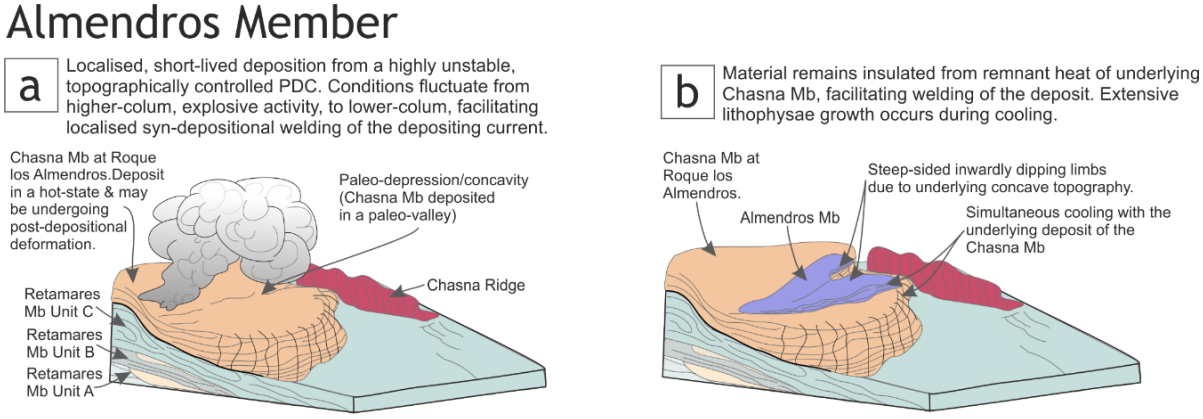


**Figure 7–16.** Schematic illustration of the emplacement of the Almendros Member on Roque los Almendros. No scale intended. Note: Plinian activity may have been ongoing throughout all stages of eruptive activity, and was only recorded when current activity paused for a sufficient time period. These images are not attempting to depict any possible bypass and/or erosion that may have occurred both between and within units.

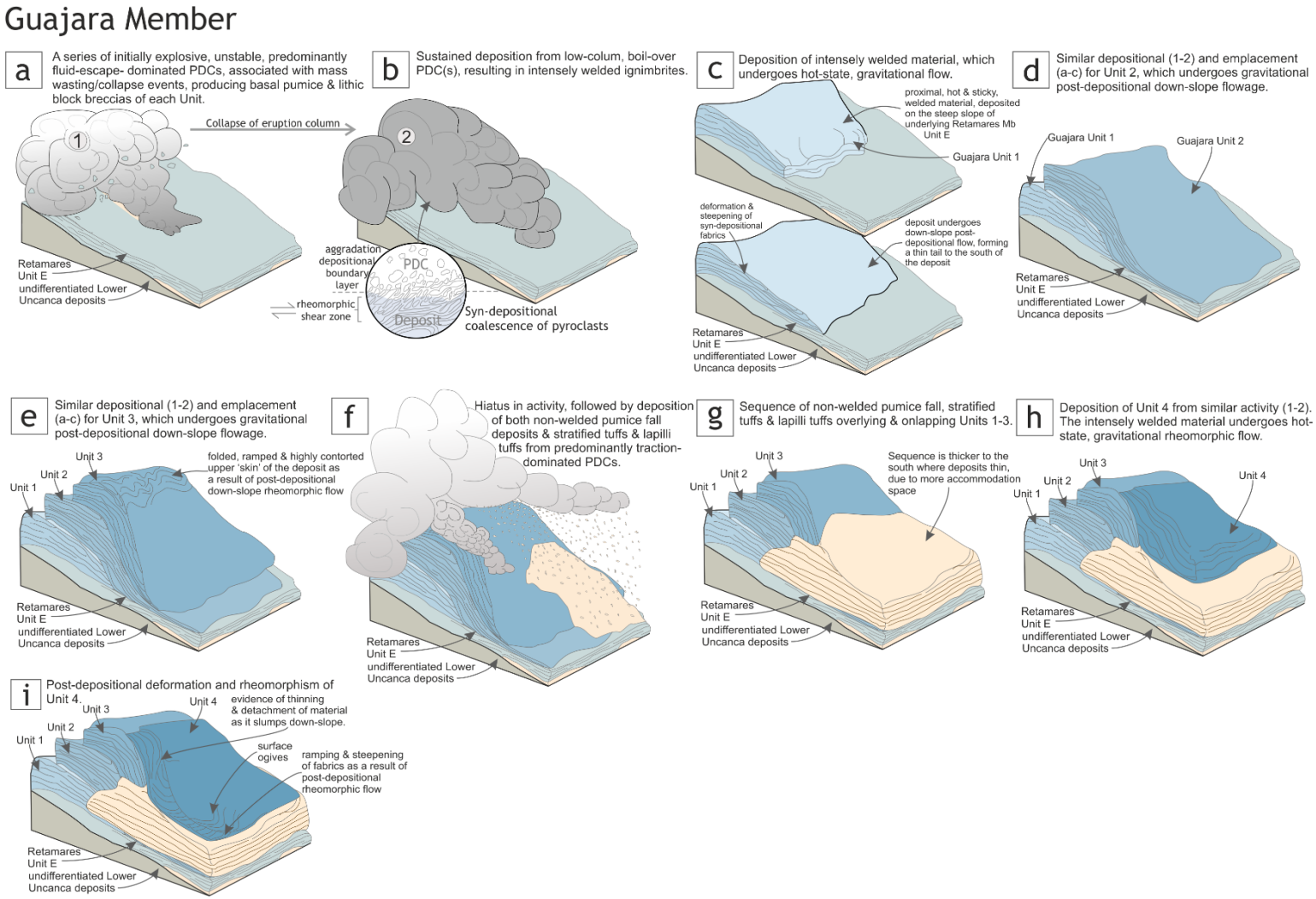


**Figure 7–17.** Schematic illustration of the emplacement of the units of the Guajara Member. No scale intended. Note: Plinian activity may have been ongoing throughout all stages of eruptive activity, and was only recorded when current activity paused for a sufficient time period. These images are not attempting to depict any possible bypass and/or erosion that may (and likely) have occurred both between and within units.

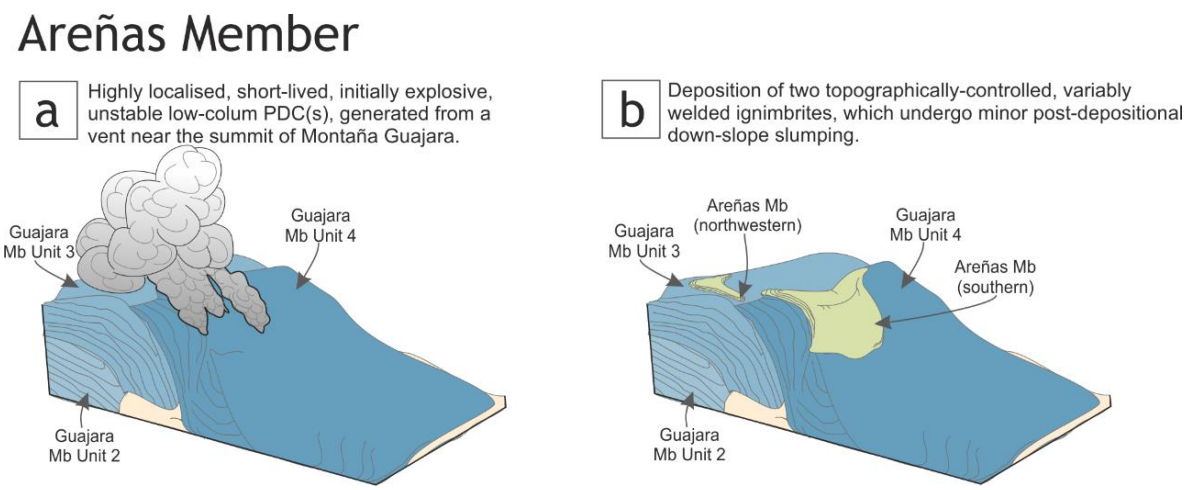


**Figure 7–18.** Schematic illustration of the emplacement of the units of the Areñas Member. No scale intended. Note: Plinian activity may have been ongoing throughout all stages of eruptive activity, and was only recorded when current activity paused for a sufficient time period. These images are not attempting to depict any possible bypass and/or erosion that may (and likely) have occurred both between and within units.

# Chapter 8

# 8. Conclusions and further work

The findings of this project elucidate our understanding of the deposits of the Ucanca and Guajara Formations, and their role in the construction of the Las Cañadas Caldera. Welded deposits by their very nature obscure much of the record of evidence used by traditional interpretive and analytical approaches in understanding the depositional mechanisms of ignimbrites. The variability in welding intensity exhibited by many of the deposits of the Ucanca and Guajara Formations allows for valuable insights into the pre-welding architecture of the deposit, and their interpretation as ignimbrites opens up opportunities in further understanding of welding processes and the behaviour of proximal high-grade PDCs. This chapter discusses and summarises the key findings of the work and the behaviour and emplacement of vent-proximal welded and lava-like ignimbrites

## 8.1. Stratigraphy of proximal ignimbrites

The documentation and description of the deposits provide an updated, revised and more complete stratigraphy and eruptive history of the Ucanca and Guajara Formations, and the relationship between the two, which was largely absent from the literature and stratigraphy of Tenerife. Where possible, the organisation of units and naming of the proposed members respects the work previously established to allow for a uniform and transferrable classification of units, again previously lacking from documentation of these deposits.

Based on extensive evidence presented in this thesis, the interpretation of the welded and lava-like units as deposits from PDCs is significant in both understanding the vent-proximal processes of high-magnitude caldera-forming eruptions (discussed further in Section 8.2) and the formation of the Las Cañadas depression. A range of sedimentological, textural and morphological evidence is presented in support of their interpretation as PDCs, further affirmed by the structural and textural evidence of poly-phase rheomorphism exhibited by many of the deposits, which indicated that syn-depositional shear of the depositing current(s) was the prevailing method of welding in the deposits.

The hazards associated with PDCs are considerably greater than those of vent-proximal spatter, fallout and particularly lava flows, due to their ability to travel great distances (>100 km) in extremely short timeframes (seconds to hours). In addition, many of the deposits (e.g. units of the Retamares Member) display evidence of highly irregular and radial PDC pathways, expanding outwards in fan-like morphologies from a centralised source, thinning over topographic highs and thickening in barrancos and valleys. These aspects of PDC behaviour, combined with the lack of understanding surrounding high-grade eruptions highlight an area where hazards associated with these types of environments, specifically volcanism related to the Canary Islands system, may be significantly underestimated. The revised interpretation also opens possibilities in correlating vent-proximal and distal deposits, discussed further in Section 8.3.

The significance of the lithic breccia horizons associated with each of the eruptive packages supports the model of caldera formation associated with high-frequency, incremental, multi-cyclic collapse and wasting events (e.g. Martí, 1994; 1995; 1997), as opposed to isolated, singular events. Lithic-rich horizons are common at the base of the ignimbrites, but also form concentrated horizons throughout, indicating episodes of conduit wall erosion or instability, and perhaps collapse events themselves (e.g. Buesch, 1992; Bryan et al., 1998). The absence of changes in fabrics or grain size grading associated with this lithic input is indication that these breccias are not associated with increasing rates of deposition or the erosion or entrainment of material from the substrate (e.g. Bryan et al., 1998). This suggests that continuous collapse and mass wasting was a prevalent and persistent component throughout the eruptive cycles of the Ucanca and Guajara Formations.

## 8.2. The nature of vent-proximal welding processes

Detailed description and textural categorisation of the ignimbrites combined with a methodological sampling approach for the determination of the physical rock properties allowed for a sensitive record of welding intensity throughout each deposit to be established. Welding profiles and variation display considerably more complexity than is described elsewhere, and this study uncovered the following key findings:

i) Syn-depositional shear-driven rheomorphism played the dominant role in the welding process, with little evidence of any contribution by means of load welding. This was particularly prevalent in thin (<10 m) units that exhibit facies that are strongly welded (>V) and above.

ii) A relationship between deposit thickness, the intensity (or rank) of welding and the extent of post-depositional rheomorphism is demonstrated, with the thickest units more capable of retaining heat for longer periods of time, facilitating the welding process where temperatures are within range of the $T_g$, allowing plastic deformation of the hot material and post-depositional flow and slumping.

iii) Lithic input and collapse events lead to temperature instability at the flow boundary zone, providing a cooling effect leading to a reduction in welding intensity, with both lateral and localised examples. The occurrence of lithics is perhaps associated with a higher column, more explosive activity, or collapse events leading to a higher input of 'cold' material.

iv) The most extreme welding and rheomorphism is seen in the youngest deposits representing the end of the eruptive cycle (for both the Ucanca and Guajara Formations), perhaps a factor of tapping of deeper, hotter areas of the magma reservoir, as reflected by the eastwards transition to a less evolved composition seen in the Chasna Mb at Llano de las Mesas.

These findings lead to the description of new and exciting welding textures (e.g. the 'snowball block' and 'obsidian swirls' of Section 7.1.1. & 7.1.2.), further indicating the important relationship of lithic input and current stability on temperature variability and welding. This investigation also led to the development of an updated framework, based on a semi-quantitative methodology, for describing and classifying higher welding intensities in ignimbrites, including those that have undergone post-emplacement rheomorphism and alteration. This accounts for the reduction of strength and density, and the increase in porosity of units following the development of post-depositional deformation (lithophysae development, spherulitic growth,

recrystallisation and vitrification) and rheomorphism (e.g. buckle folds, secondary foliation). The possible applications of this scheme are discussed further in Section 8.3.

## 8.3. Future work

The following areas arose over the course of the project as avenues to explore relevant to this research:

- Much of the early Ucanca Formation exposed on the western margins of the caldera wall, largely consisting of welded and lava-like units, remain undifferentiated beyond the El Sombrerito, which is partially mapped as predominantly welded fallout by Soriano et al. (2006). Work is required here to provide a detailed account of the most westerly Ucanca Formation deposits, for further insight into the nature and emplacement of these deposits, and their place in the early construction of the Ucanca caldera. The units of the Retamares and Chasna Members likely continue westwards in this direction, and good exposure on the southern flank of the Las Cañadas wall allows for a more complete stratigraphic record of the proximal record of the Ucanca Fm, and correlation with the members described in this study. A similar situation exists with the units of the Guajara Formation, the stratigraphy of which remains largely incomplete and undocumented eastwards of Montaña Guajara. The lower caldera wall consisting of units of the Lower group also remains undifferentiated. These units represent the pre-caldera configuration, and there are proposed correlations with these units and the highly intruded units exposed at the Roques de Garcia.

- Due to previous approaches and interpretations of the units of the Ucanca Formation, correlations with their distal counterparts has not been a consideration. The interpretation of these units as ignimbrites opens the opportunity for correlation with undifferentiated ignimbrites to the south of Tenerife. The detailed lithofacies analysis, stratigraphic context, and geochemical analysis here lays the groundwork for efforts in making these correlations between proximal, medial, and distal exposures.

- There is the possibility that other intensely welded and lava-like deposits are misinterpreted, as in the case of the Ucanca and Guajara Formations. The proposed scheme to map and track welding intensity (Chapter 5) and classify high-grade deposits in other environments may be applied to sensitively track welding in deposits that similarly fall collectively under the rank of 'lava-like' despite exhibiting considerable variation and textural diversity. These insights allow for detailed cross-referencing with other features and textures, as demonstrated in this study, which may assist in unravelling the emplacement dynamics and controls on welding here and in other volcanic settings. Further investigation with other high grade, lava-like ignimbrites (e.g., Ignimbrite 'TL', Gran Canaria: Sumner & Branney, 2002; Grey's Landing ignimbrite: Andrews & Branney, 2011), as well as more ancient examples (e.g., the Bad Step Tuff: Branney et al., 1992; the Sgurr of Eigg: Brown & Bell, 2013) would be useful comparisons to test the applicability and durability of this scheme.

# List of References

Abdurachman, E. K., Bourdier, J. -L. & Voight. 2000. Nuées ardentes of 22 November 1994 at Merapi volcano, Java, Indonesia. Journal of Volcanology and Geothermal Research. 100 (1), 345-361

Ablay, G.J., Ernst, G.G.J., Martí, J., & Sparks, R.S.J. 1995. The 2 ka subplinian eruption of Monta*ñ*a Blanca, Tenerife: Bulletin of Volcanology, 57, 337–355

Ablay, G. J. & Hürlimann, M. 2000. Evolution of the north flank of Tenerife by recurrent giant landslides. Journal of Volcanology and Geothermal Research. 103 (1-4), 135-159

Ablay, G. J. & Keary, P. 2000. Gravity constraints on the structure and volcanic evolution of Tenerife, Canary Islands. Journal of Geophysical Research. 105 (B3), 5783-5796

Akram, M. & Bakar, M. Z. A. 2007. Correlation between uniaxial and point load index for Salt-Range rocks. Pakistan Journal of Engineering and Applied Sciences, Volume 1

Allan, R. 1988. False pyroclastic textures in altered silicic lavas, with implications for volcanic-associated mineralization. Economic Geology. 83, 1424–1446

Allen, S. R. & McPhie, J. 2002. The Eucarro Rhyolite, Gawler Range Volcanics, South Australia: A >675 $km^3$, compositionally zoned lava of Mesoproterozoix age. GSA Bulletin. 114 (12), 1582-1609

Ancochea, E., Fúster, J. M., Ibarrola, E., Cendrero, A., Coello, J., Hernán, F., Cantagrel, J. M & Jamond, C. 1990. Volcanic evolution of the island of Tenerife (Canary Islands) in the light of new K–Ar data. Journal of Volcanology and Geothermal Research. 44, 231–249.

Ancochea, E., Huertas, M. J., Cantagrel, J. M., Coello, J., Fúster, J. M., Arnaud, N., Ibarrola, E. 1991. Evolution of the Cañadas edifice and implications for

the evolution of the Cañadas caldera (Tenerife, Canary Islands) Journal of Volcanology and Geothermal Research. 88, 177-199

Ancochea, E. , Huertas, M.J., Cantagrel, J.M. Coello, J., Fúster, J. M., Arnaud, N. & Ibarrola E. 1999. Evolution of the Cañadas edifice and its implications for the origin of the Cañadas Caldera (Tenerife, Canary Islands). Journal of Volcanology and Geothermal Research. 88, 177-199

Anderson, C. A. & Flett, J. S. 1903. Report on the eruptions of the Soufriére in St. Vincent in 1902, and on a visit to Montagne Pelée, in Martinique, Part I: Royal Sociey of London Philosophical Transactions. A, 200, 353-553

Andrews, G. 2006. The emplacement and deformation of high-temperature tuffs: a structural analysis of the Grey's Landing ignimbrite, Snake River Plain, Idaho. Unpublished PhD Thesis, University of Leicester

Andrews, G. & Branney, M. J. 2011. Emplacement and rheomorphic deformation of a large, lava-like rhyolitic ignimbrite: Grey's Landing, southern Idaho. GSA Bulletin. 123, 725-743

Andrews, G. D. M. & Branney, M. J. 2005. Folds, fabrics, and kinematic criteria in rheomorphic ignimbrites of the Snake River Plain, Idaho: insights into emplacement and flow. In: Pederson J, D. C. (ed.) Interior Western United States: GSA Field Guide 6, 310-328

Andrews, G.D.M., Branney, M.J., Bonnichsen, B. & McCurry M. 2008. Ignimbrites in the Rogerson Graben, southern Snake River Plain volcanic province: volcanic stratigraphy, eruption history, and basin evolution. In: Leeman, B. & McCurry. 2008. (eds) Volcanism and petrogenesis of anorogenic rhyolites. Bulletin of Volcanology. 70, 269-291

Anguita, F. & Hernan, F. 1975. A propagating fracture model versus hotspot origin for the Canary Islands. Earth and Planetary Science Letters. 27, 11-19

Auker, M. R., Sparks, R. S. J., Siebert, L., Crosweller, H. S. & Ewert, J. 2013. A statistical analysis of the global historical volcanic fatalities record. Journal of Applied Volcanology. 2(2)

Arnaud, N. O. Huertas, M.J. Cantagrel, J.M. Ancochea, E. Fúster J. 2001. Edades 39Ar/40Ar de los depósitos de Roques de García (Las Cañadas, Tenerife) Geogaceta, 29, 19-22

Araña, V. 1971. Litología y estructura del edificio Cañadas, Tenerife (Islas Canarias). Estudios Geológicos. 27, 95–137

Araña, A. & Brändle, J. L. 1969. Variation trends in the alkaline salic rocks of Tenerife. Bulletin Volcanologique. 33, 1145 – 1165

Bachmann, O., Dungan, M. & Lipman, P. 2000. Voluminous lava-like precursor to a major tuff: pyroclastic eruption of the Pagosa Peak Dacite, San Juan volcanic field, Colorado. Journal of Volcanology and Geothermal Research. 98, 153-171

Bacon, C. R., 1987. Mount Mazama and Crater Lake caldera, Oregon: Geological of America Centennial Field Guide. 1, 301-306

Baer, E. M., Fisher, R. V., Fuller, M. & Valentine, G. 1997. Turbulent transport and deposition of the Ito pyroclastic flow: determinations using anisotropy of magnetic susceptibility. Journal of Geophysical Research. 102, 22565-22586

Bagdassarov, N. S. & Dingwell, D. B. 1992. A rheological investigation of vesicular rhyolite. Journal of Volcanology & Geothermal Research. 50, 307-322

Bagdassarov, N. S. & Dingwell, D. B. 1993. Deformation of foamed rhyolites under internal and external stresses: an experimental investigation. Bulletin of Volcanology. 55, 147-154

Barberi, F., Innocenti, F. Lirer, L, Munno, R., Pescatore, T. & Santacroce, R. 1978. The campanian ignimbrite: a major prehistoric eruption in the Neapolitan area (Italy). Bulletin Volcanologique. 41, 10-31

Barclay, J., Carroll, M. R., Houghton, B. F. & Wilson, C. J. N. 1996. Pre-eruptive volatile content and degassing history of an evolving peralkaline volcano. Journal of Volcanology and Geothermal Research. 74(1-2), 75-87

Bardintzeff, J. M. 1984. Merapi volcano (Java, Indonesia) and Merapi-type nueé ardente. Bulletin of Volcanology. 47, 433-446

Beddoe-Stephens, B. & Millward, D. 2000. Very densely welded, rheomorphic ignimbrites of homogeneous intermediate calc-alkaline composition from the English Lake District. Geology Magazine. 137, 155-173

Belousov, A. 1996. Deposits of the 30 March 1956 blast at Bezymianny volcano, Kamchatka, Russia. Bulletin of Volcanology. 57, 649-662

Belousov, A., Voight, B., Belousova, M. 2007. Directed blasts and blast-currents: a comparison of the Bezymianny 1956, Mount St Helens 1980, and Soufrière Hills, Montserrat 1997 eruptions and deposits. Bulletin of Volcanology. 69, 701–740

Bieniawski, Z. T. 1975. The point-load test in geotechnical practice. Engineering Geology, 9, 1–11

Bindeman I. N. & Valley J. W. 2003. Rapid generation of both high- and low $\delta^{18}O$, large-volume silicic magmas at the Timber Mountain / Oasis Valley caldera complex, Nevada. Geological Society of America Bulletin. 15, 581-595

Blake, S. 1981. Eruptions from zoned magma chambers, Journal of the Geological Society, London, 138, 281 287

Blake, S. & Ivey, G. N. 1986i. Magma-mixing and the dynamics of withdrawal from stratified reservoirs, Journal of Volcanology and Geothermal Research, 27, 153-178

Blake, S. & Ivey, G. N. 1986ii. Density and viscosity gradients in zoned magma chambers, and their influence on withdrawal dynamics, Journal of Volcanology and Geothermal Research, 30, 201-230

Bogoyavlenskaya, G. E., Braitseva, O. A., Melekestsev, I. V., Kirianov V. Y. & Miller, C. D. 1985. Catastrophic eruptions of the directed-blast type at Mount St. Helens, Bezymianny and Shiveluch volcanoes. Journal of Geodynamics. 3, 189–218

Bonnichsen, B., & Citron, G. P. 1982. The Cougar Point Tuff, southwestern Idaho and vicinity, in Cenozoic Geology of Idaho, Idaho Bureau of Mines and Geology Bulletin. 26, 255– 281

Bonnichsen, B. & Kauffman, D. F. 1987. Physical features of rhyolite lava flows in the Snake River Plain volcanic province, south- western Idaho. In: Fink, J. H. (ed) The emplacement of silicic domes and lava flows. Geological Society of America Special Paper. 212, 119-145

Booth, B. 1973. The Granadilla pumice deposit of southern Tenerife, Canary Islands. Proceedings of the Geological Association. 84, 353-370

Bottinga, Y. 1994. Rheology and rupture of homogeneous silicate liquids at magmatic temperatures. Journal of Geophysical Research. 99, 9415-9422

Boudon, G., Camus, G., Gourgaud, A. & Lajoie, J. 1993. The 1984 nuée-ardente deposits of Merapi volcano, Central Java, Indonesia: stratigraphy, textural characteristics, and transport mechanisms. Bulletin of Volcanology. 55, 327-342

Boulesteix, T. Hildenbrand, A. Gillot, P.Y. & Vicente Soler, V. 2012. Eruptive response of oceanic islands to giant landslides: New insights from the geomorphologic evolution of the Teide–Pico Viejo volcanic complex (Tenerife, Canary) Geomorphology. 138, 61-73

Bouma, A. H. 1962. Sedimentology of some Flysch deposits: a graphic approach to facies interpretation. (ed). Elsevier, Amsterdam

Buesch, D. C. 1992. Incorporation and redistribution of locally derived lithic fragments within a pyroclastic flow. Geological Society of America Bulletin. 104, 1193-1207

Branney M.J, Barry, T.L. & Godchaux, M.M. 2004. Sheath folds in rheomorphic ignimbrites. Bulletin of Volcanology, 66, 485-491

Branney, M. J., Bonnichsen, B., Andrews, G. D. M., Barry, T. L. & McCurry, M. 2008. 'Snake River (SR)-type' volcanism at the Yellowstone hotspot track: distinctive products from unusual, high-temperature silicic super-eruptions. Bulletin of Volcanology. 70, 293-314

Branney, M. J. & Kokelaar, P. B. 1992. A Reappraisal of Ignimbrite Emplacement - Progressive Aggradation and Changes from Particulate to Non-particulate Flow during Emplacement of High-Grade Ignimbrite. Bulletin of Volcanology, 54, 504-520

Branney, M. J. & Kokelaar, P. 1997. Giant bed from a sustained catastrophic density current flowing over topography: Acatlán ignimbrite, Mexico. Geology. 25, 115-118

Branney, M. J. & Kokelaar, B. P. 2002. Pyroclastic density currents and the sedimentation of ignimbrites. Geological Society of London Memoir. 27, 143

Branney, M. J., Kokelaar, P. B. & McConnell, B. J. 1992. The Bad Step Tuff: a lava-like rheomorphic ignimbrite in a calc-alkaline piecemeal caldera, English Lake District. Bulletin of Volcanology. 54, 187-199

Branney, M. J. & Sparks, R. S. J. 1990. Fiamme formed by diagenesis and burial-compaction in soils and subaqueous sediments. Journal of the Geological Society. 147, 919-922

Breitkreuz, C. 2013. Spherulites and lithophysae—200 years of investigation on high-temperature crystallization domains in silica-rich volcanic rocks. Bulletin of Volcanology. 75, 1-16

Briggs, R. M., Gifford, M., Moyle, A. R., Taylor, S. R., Norman, M. D., Houghton, B. F. & Wilson, C. J. N. 1993. Geochemical zoning and eruptive mixing in ignimbrites from Mangakino volcano, Taupo Volcanic Zone, New Zealand. Journal of Volcanology and Geothermal Research. 56 (3), 175-203

Broch, E. & Franklin, J. A. 1972. The point-load strength test. International Journal of Rock Mechanics and Mining Science 9, 669-693

Brook, N. 1980. Shape and size effects in point load testing. In: Summers, D. D. (Editor) The state of the art in rock mechanics. Proceedings in the annual symposium on Rock Mechanics, Balkema, United States, 556-563

Brown, D. J. and Bell, B. 2013. The emplacement of a large, chemically zoned, rheomorphic, lava-like ignimbrite: The Sgurr of Eigg Pitchstone, NW Scotland. Journal of the Geological Society. 170(5), 753-767

Brown, E. T. 1981. Rock characterization and monitoring. International Society for Rock Mechanics (ISRM). Suggested Methods. Pergamon Press. Oxford, 1981

Brown, R. J. & Andrews, G. D. M. 2015. Deposits of Pyroclastic Density Currents. In: Sigurdsson, H., Houghton, B., Rymer, H., Stix, J. & McNutt, S. (eds) Encyclopaedia of Volcanoes, Second Edition. Academic Press, San Diego. 631-648

Brown, R. J., Barry, T. L., Branney, M. J., Pringle, M. S. & Bryan, S. E. 2003. The Quaternary pyroclastic succession of southeast Tenerife, Canary Islands; explosive eruptions, related caldera subsidence, and sector collapse. Geology Magazine. 140, 265–288

Brown, R. J. & Branney, M. 2004i. Bypassing and diachronous deposition from density currents: Evidence from a giant regressive bed form in the Poris ignimbrite, Tenerife, Canary Islands. Geology. 32, 445-448

Brown, R. J. & Branney, M. J. 2004ii. Event-stratigraphy of a caldera-forming ignimbrite eruption on Tenerife: the 273 ka Poris Formation. Bulletin of Volcanology. 66, 392-416

Bryan, S. E. 2006. Petrology and geochemistry of the Quaternary caldera-forming, phonolitic Granadilla eruption, Tenerife (Canary Islands). Journal of Petrology. 47, 1557–1589

Bryan, S., E. 1998. Volcanology and Petrology of the Granadilla Member, Tenerife, (Canary Islands): Constraints on the eruption dynamics, ignimbrite emplacement and caldera evolution. Unpublished PhD Thesis, Monash University, Clayton, Victoria

Bryan, S. E., Martí, J. & Cas, R. A. F. 1998. Stratigraphy of the Bandas del Sur Formation: an extracaldera record of Quaternary phonolitic explosive eruptions from the Las Cañadas edifice, Tenerife (Canary Islands). Geological Magazine, 135, 605-636

Bryan, S. E., Martí, J. & Leosson, M. 2002. Petrology and geochemistry of the Bandas del Sur Formation, Las Cañadas edifice, Tenerife (Canary Islands). Journal of Petrology. 43, 1815–1856.

Bull, K. F. & McPhie, J. 2007. Fiamme textures in volcanic successions: Flaming issues of definition and interpretation. Journal of Volcanology and Geothermal Research. 164, 205-216

Bursik, M. I. & Woods, A. W. 1996. The dynamics and thermodynamics of large ash flows. Bulletin of Volcanology. 58, 175-193

Calder, E. S., Lavallée, Y, Kendrick, J. E. & Bernstein, M. 2015. Lava dome eruptions. In: Sigurdsson, H., Houghton, B., Rymer, H., Stix, J. & McNutt, S. (eds) Encyclopaedia of Volcanoes, Second Edition. Academic Press, San Diego

Calderone, G. M. 1988. The Krafla air-fall, welded tuff layer, North Iceland. Internal Report, Nordic Volcanological Institute, University of Iceland

Cantagrel, J. M., Arnaud, N. O., Acochea, E., Fúster, J.M. & Huertas, M. J. 1999. Repeated debris avalanches on Tenerife and genesis of the Las Cañadas caldera wall (Canary Islands). Geology, 27, 739-742

Capaccioni, B. & Coniglio, S. 1995. Varicolored and vesiculated tuffs from La Fossa Volcano, Vulcano Island (Aeolian Archipelago, Italy): evidence for syndepositional alteration processes. Bulletin of Volcanology, 57, 61–70

Capaccioni, B. & Cuccoli, F. 2005. Spatter and welded air fall deposits generated by fire-fountaining eruptions: cooling of pyroclasts during transport and deposition. Journal of Volcanology and Geothermal Research. 145, 263-280

Cargill, J.S. & Shakoor, A. 1990. Evaluation of empirical methods for measuring the uniaxial compressive strength of rock. International Journal of Rock Mechanics and Mining Sciences and Geomechanics Abstracts, 27, 495-503

Carr, R. G. 1981. A scanning electron microscope study of post-depositional changes in the Matahina Ignimbrite, North Island, New Zealand. New Zealand Journal of Geology and Geophysics. 24 (3), 429-434

Carracedo, J-C. 1975. Estudio paleomagnético de la isla de Tenerife. Unpublished PhD Thesis. Universidad Complutense de Madrid

Carracedo, J-C. 1994. The Canary Islands: an example of structural control on the growth of large ocean-island volcanoes. Journal of Volcanology and Geothermal Research. 60, 225-41

Carracedo, J.C., Rodríguez-Badiola, E., Guillou, H. Paterne, M. Scaillet, S. Pérez-Torrado, F.J. Paris, R. Fra-Paleo, U. & Hansen, A. 2007. Eruptive and structural history of Teide volcano and rift zones of Tenerife, Canary Islands. Geological Society of America Bulletin. 119, 1027-1051

Carracedo, J. C., Rodriguez-Gonzalez, A., Pérez-Torrado, F. J., Fernandez-Turiel J. L., Paris, R., Rodríguez-Badiola, E., Pestana-Pérez, G., Troll, V. R. & Wiesmaier, S. 2013. Geological Hazards in the Teide Volcanic Complex. In: Carracedo JC & Troll VR (eds.) Teide Volcano: Springer Berlin Heidelberg, 978, 249-272

Carrasco-Núñez, G., McCurry, M., Branney, M.J., Norry, M. & Willcox, C. 2012. Complex magma mixing, mingling and withdrawal associated with an intra-

Plinian ignimbrite at a large silicic caldera volcano: Los Humeros of central Mexico. Geological Society of America, 124, 1793-1809

Cas, R. A. F. & Wright, J. V. 1987. Volcanic successions: Modern and Ancient - a geological approach to processes, products and successions. Allen and Unwin, London. 528 pages

Cas, R. A. F., Wright, H. M. N., Folkes, C. B., Lesti, C., Porreca, M., Giordano, G. & Viramonte, J.G. 2011. The flow dynamics of an extremely large volume pyroclastic flow, the 2.08-Ma Cerro Galán Ignimbrite, NW Argentina, and comparison with other flow types. Bulletin of Volcanology. 73, 1583–1609

Chapin, C. E. & Elston, W. E. 1979. Ash-flow Tuffs. Geological Society of America. Special Paper 180

Chapin, C. E. & Lowell, G. R. 1979. Primary and secondary flow structures in ash-flow tuffs of the Gribbles Run paleovalley, central Colorado. Special Paper - Geological Society of America.137-154

Chau, K. T. & Wong, R. H. C. 1996. Uniaxial compressive strength and point load strength. International Journal of Rock Mechanics and Mining Science, 33, 183–188

Chen, C. F. & Turner, J. S. 1980. Crystallization in a double diffuse system. Journal of Geophysical Research. 85, 2573-2593

Civetta, L. Orsi, G., Pappalardo, L., Fisher, R. V., Heiken, M. & Ort, M. 1997. Geochemical zoning, mingling, eruptive dynamics and depositional processes – the Campanian Ignimbrite, Campi Flegrei caldera, Italy. Journal of Volcanology and Geothermal Research, 75, 183-219

Cloos, E. 1957. Lineation: a critical review and annotated bibliography. Geological Society of America Memoirs. 18, 136 pages

Cole, P. D., Calder, E. S., Sparks, R. S. J., Clarke, A. B., Druitt, T. H., Young, S. R., Herd, R. A. Harford C. L. & Norton, G. E. Deposits from dome-collapse

and fountain-collapse pyroclastic flows at Soufrière Hills Volcano, Montserrat. Geological Society of London Memoirs. 21, 231-262

Conrad, W. 1984. The Mineralogy and petrology of compositionally zoned ash flow tuffs, and related silicic volcanic rocks, from the McDermitt Caldera Complex, Nevada-Oregon. Journal of Geophysical Research, 89, 8639-8664

Crisci, G., Rosa, R., Esperanca, S., Mazzuoli, R. & Sonnino, M., 1991.Temporal evolution of a three component system: the Island of Lipari (Aeolian arc, southern Italy). Bulletin of Volcanology. 53, 207–221

Crisp, J. A. & Spera, F. J. 1987. Pyroclastic flows and lavas of the Mogan and Fataga Formations, Tejeda Volcano, Gran Canaria, Canary Islands: mineral chemistry, intensive parameters, and magma chamber evolution. Contributions to Mineralogy and Petrology. 96, 503- 518

D'Andrea, D. V., Fischer, R. L. & Fogelson, D. E. 1964. Prediction of compression strength from other rock properties. Colorado School of Mines Quarterly 59(4b), 623-640

Dadd, K., 1992i. The Middle to Late Devonian Eden–Comerong–Yalwal Volcanic zone of Southeastern Australia: an ancient analogue of the Yellowstone–Snake River Plain region of the USA. Tectonophysics. 214, 277–291

Dadd, K. 1992ii. Structures within large volume rhyolite lava flows of the Devonian Comerong volcanics, south-eastern Australian, and the Pleistocene Ngongotaha lava dome, New Zealand Journal of Volcanology and Geothermal Research. 54, 33–51

Dade, W. D. & Huppert, H. E. 1996. Emplacement of the Taupo ignimbrite by a dilute, turbulent flow. Nature. 381, 509-512

Deere, D. U. & Miller, R. P. 1966. Engineering classification and index properties for intact rock. Air Force Weapons Lab. Tech. Report, AFWL-TR 65–116, Kirtland Base, New Mexico

Dell'Erba, L. 1892. Considerazioni sulla gene piperno: Gior. Mineralogica, Cristallografia and grafia. 3, 23-53

Dingwell, D. B. 1998i. Recent experimental progress in the physical description of silicic magma relevant to explosive volcanism. In: Gilbert, J. S. & Sparks, R. S. J. (eds). The physics of explosive volcanic eruptions. Geological Society of London Special Publications. 145, 9-26

Dingwell, D. B. 1998ii. Magma degassing and fragmentation: recent experimental advances. Developments in volcanology, Elsevier, Amsterdam, 4, 1-23

Dingwell, D. B. 1996 Volcanic Dilemma: Flow or Blow? Science, 237, 1054-1055

Dingwell D. B. & Hess K. U. 1998. Melt viscosities in the system Na-Fe-Si-O-F-Cl: contrasting effects of F and Cl in alkaline melts. American Mineralogist. 83, 1016-1021

Dingwell, D.B. & Webb, S.L. 1989. Structural relaxation on silicate melts and non-Newtonian melt rheology in geologic processes. Physics and Chemistry of Minerals, 16, 508–516

Dingwell, D. B & Webb, S. L. 1990. Relaxation in silicate melts: European Journal of Mineralogy, 2, 427-449

Donoghue, E., Troll, V. R., Harris, C., O'Halloran, A., Walter, T. R. & Pérez Torrado, F. J. 2008. Low-temperature hydrothermal alteration of intra-caldera tuffs, Miocene Tejeda caldera, Gran Canaria, Canary Islands. Journal of Volcanology and Geothermal Research, 176 (4), 551-564

Druitt, T. H. 1992. Emplacement of the 18 May 1980 lateral blast deposit ENE of Mount St. Helens, Washington. Bulletin of Volcanology. 54, 554-572

Druitt, T. H. 1998. Pyroclastic density currents. In: Gilbert, J. S. & Sparks, R. S. J. (eds) The Physics of Explosive Volcanic Eruptions. Geological Society, London, Special Publications. 145, 145-182

Druitt, T. H. & Bacon, C. R. 1986. Lithic Breccia and Ignimbrite Erupted During the Collapse of Crater Lake, Oregon. Journal of Volcanology and Geothermal Research, 29, 1-32

Duffield, W. A., Ruiz, J. & Webster, J. D. 1995. Roof-rock contamination of magma along the top of the reservoir for the Bishop Tuff. Journal of Volcanology and Geothermal Research. 69, 187-195

Edgar, C.J., Wolff, J.A., Nichols, H.J., Cas, R.A.F. & Martí, J., 2002. A complex Quaternary ignimbrite-forming phonolitic eruption: the Poris member of the Diego Hernandez Formation (Tenerife, Canary Islands). Journal of Volcanology and Geothermal Research. 118 (1-2), 99-130

Edgar, C.J. Wolff, J.A. Olin, P.H.. Nichols, H.J Pittari, A. Cas, R.A.F. Reiners, P.W. Spell, T.L. & Martí, J. 2007. The late Quaternary Diego Hernandez Formation, Tenerife: a cycle of voluminous explosive phonolitic eruptions. Journal of Volcanology & Geothermal Research. 160, 59-85

Edgar, C. J., Cas, R. A. F., Olin, P. H., Wolff, J. A., Martí, J. & Simmons, J. M. 2017. Causes of complexity in a fallout dominated Plinian eruption sequence: 312 ka Fasnia Member, Diego Hernández Formation, Tenerife, Spain. Journal of Volcanology and Geothermal Research. 345, 21-45

Ekren, E. B., McIntyre, D. H. & Bennett, E. H. 1984. High-temperature, large-volume, lavalike ash-flow tuffs without calderas in southwestern Idaho. US Geological Survey Professional Paper. 1272

Elburg, M. A. 1996. U–Pb ages and morphologies of zircon in micrograniteoid enclaves and peraluminous host granites: evidence for magma mingling. Contributions to Mineralogy and Petrology. 123, 177-189

Elston, W.E. 1979. (Ed.), Ash Flow Tuffs. Geological Society of America Special Paper 180, 137-154

Elston, W. E. & Smith, E. I. 1970. Determination of flow direction of rhyolitic ash-flow tuffs from fluidal textures. Geological Society of America Bulletin. 81, 3393-3406

Favela, J. & Anderson, D. L. 2000. Extensional tectonics and global volcanism. In: Boschi, E., Ekstrom, G., Morelli, A. (ed) Problems in geophysics for the new millennium. Editrice Compositori, Bologna. 463-498

Fener, M., Kahraman, S., Bilgil, A. & Gunaydin, O. 2005. A comparative evaluation of indirect method to estimate the compressive strength of a rock. Rock Mechanics and Rock Engineering, 38, 329-343

Fenner, C. N. 1948. Incandescent tuff flows in Southern Peru. Geological Society of America Bulletin, 59, 879-893

Fink, J. H. 1990. Lava Flows and Domes: Emplacement Mechanisms and Hazard Implications. IAVCEI Proceedings in Volcanology. Springer-Verlag Berlin Heidelberg

Fink, J.H. 1980. Surface folding and viscosity of rhyolite flows. Geology. 8, 250-254

Fisher, R. V. 1990. Transport and Deposition of a Pyroclastic Surge across an Area of High Relief - the 18 May 1980 Eruption of Mount St-Helens, Washington. Geological Society of America Bulletin. 102, 1038-1054.

Fisher, R. V. 1966. Mechanism of deposition from pyroclastic flows. American Journal of Science. 264, 350-363

Fisher, R. V., Orsi, G., Ort, M. & Heiken, G. 1993. Mobility of a Large-Volume Pyroclastic Flow - Emplacement of the Campanian Ignimbrite, Italy. Journal of Volcanology and Geothermal Research. 56, 205-220

Fisher, R. V. & Schmincke, H-U. 1984. Pyroclastic rocks .Springer-Verlag. Berlin, Federal Republic of Germany, 472 pages

Flinn, D. 1962. On folding during three-dimensional progressive deformation. Quarterly Journal of the Geological Society of London. 118, 385-428

Forni, F., Bachmann, O., Mollo, S., De Astis, G. Gelman, S. E. & Ellis, B. S. 2016. The origin of a zoned ignimbrite: Insights into the Campanian Ignimbrite magma chamber (Campi Flegrei, Italy). Earth and Planetary Science Letters. 449, 259-271

Forster, I. R. 1983. The influence of core sample geometry on the axial point-load test. International Journal of Rock Mechanics and Mining Sciences and Geomechanics Abstracts, 20, 291-295

Freundt, A. 1998. The formation of high-grade ignimbrites, Part I: Experiments on high- and low-concentration transport systems containing sticky particles. Bulletin of Volcanology. 59, 414-435

Freundt, A. 1999. Formation of high-grade ignimbrites - Part II. A pyroclastic suspension current model with implications also for low-grade ignimbrites. Bulletin of Volcanology, 60, 545-567

Freundt, A., & Bursik, M. I. 1998. Pyroclastic flow transport mechanism. In: Freundt, A. Rosi, M. (eds) From Magma to Tephra: Modelling Physical Processes of Explosive Volcanic Eruptions. 173– 246, Elsevier, New York

Freundt, A. & Schmincke, H-U. 1995. Eruption and emplacement of a basaltic welded ignimbrite during caldera formation on Gran Canaria. Bulletin of Volcanology. 56, 640-659

Freundt, A. & Schmincke, H. U. 1992. Mixing of rhyolite, trachyte and basalt magma erupted from a vertically and laterally zoned reservoir, composite flow P1, Gran Canaria. Contributions to Mineralogy and Petrology. 112, 1-19

Friedman, I., Long, W. & Smith, R.L. 1963. Viscosity and water content of rhyolitic glass. Journal of Geophysical Research, 68, 6523-6535

Fulcher, G.S. 1925. Analysis of recent measurements of the viscosity of glasses. Journal of the American Ceramic Society, 8, 339–355

Fúster, J.M., Araña, V., Brandle, J.L., Navarro, J.M., Alonso, U. & Aparicio, A. 1968. Geology and volcanology of the Canary Islands: Tenerife. Inst. Lucas Mallada, CSIC, Madrid. 218

Ghosh, D.K. & Srivastava, M. 1991. Point-load strength; an index for classification of rock material. Bulletin of the International Association of Engineering Geology, 44, 27-33

Ghweir, M. 1995. Point load strength index of Yucca Mountain tuff at elevated temperatures. Master's Thesis, New Mexico, Institute of Mining & Technology, Socorro, NM, 78

Gibson I. L. 1974. Blister caves associated with an Ethiopian ash-flow tuff. Studies in Speleology. 2(6), 225-232

Gibson, I. L. 1970. A Pantelleritic Welded Ash-flow Rift from the Ethiopian Rift Valley. Contributions to Mineralogy and Petrology. 28, 89–111

Gilbert, C. M. 1938: Welded Tuff in Eastern California. Bulletin of the Geological society of America. 49, 1829-1861

Giordano, D., Dingwell D. B. & Romano, C. 2000. Viscosity of a Teide phonolite in the welding interval. In: Martí, J. & Wolff, J. A. (eds) The geology and geophysics of Tenerife. Elsevier, Amsterdam

Giordano, D., Nichols, A. R. L. & Dingwell, D. B. 2005. Glass transition temperatures of natural hydrous melts: a relationship with shear viscosity and implications for the welding process. Journal of Volcanology and Geothermal Research. 142, 105-118

Gómez-Tuena, A. and Carrasco-Núnez, G. 1999. Fragmentation, transport and deposition of a low-grade ignimbrite: The Citlaltépetl Ignimbrite, Eastern México. Bulletin of Volcanology. 60, 448–464

Gottsmann, J. Camacho, A.G. Martí, J. Wooller, L. Fernández, J. García, A. & Rymer, H. 2008. Shallow structure beneath the Central Volcanic complex of Tenerife from new gravity data: implications for its evolution and recent reactivation. Physics of the Earth and Planetary Interiors. 168, 212-230

Gottsmann, J. & Dingwell, D.B. 1999. The cooling of welded fallout deposits; calorimetric geospeedometry applied to Montaña Blanca phonolites on Tenerife, Canary Islands, AGU 1999 fall meeting. Eos, Trans., American Geophysical Union, Washington, DC, United States, 1189

Gottsmann, J., & Dingwell, D.B. 2001. Cooling dynamics of spatter-fed phonolite obsidian flows on Tenerife, Canary Islands: Journal of Volcanology and Geothermal Research, 105, 323–342

Gottsmann, J., Giordano, D. & Dingwell, D. B. 2002. Predicting shear viscosity during volcanic processes at the glass transition: a calorimetric calibration. Earth and Planetary Science Letters. 198, 417–427

Govindaraju, K. 1994. 1994 compilation of working values and sample description for 383 geostandards. Geostandards Newsletter 18: Special Issue, 1994

Grasso, P., Xu, S., Mahtab, A. 1992. Problems & promises of index testing of rocks. In: Tillerson, J. R. & Wawersik, W. R. (Editors), Proceedings of the 33rd U.S. symposium on Rock Mechanics, Balkema, United States, 879-888

Grunder, A. L. & Russell, J. K. 2005. Welding processes in volcanology: insights from the field, experimental, and modelling studies. Journal of Volcanology and Geothermal Research, 142, 1-9

GSEEGWP. 1970. Geological Society Engineering Group Working Party Report on the logging of rock cores for engineering purposes. Quarterly Journal of Engineering Geology, 3, 1-24

Gunsallus, K.L. & Kulhawy, F.H. 1984. A comparative evaluation of rock strength measures. International Journal of Rock Mechanics and Mining Sciences and Geomechanics Abstracts, 21, 233-248

Hansen, J. & McDonald, I. R. (2006) Theory of simple liquids, 3rd Edition. Elsevier

Hassani, F. P., Scoble, M. J. & Whittaker, B. N. 1980. Application of point load index test to strength determination of rock and proposals for new size-correction chart. In: Summers, D.A. (ed.) Proceedings of the 21st US Symposium on Rock Mechanics. University of Missouri Press, Rolla, 543–564.

Hargrove, H. Petro-Lewis, D. & Sheridan, M. 1984. Welded tuffs deformed into megarheomorphic folds during collapse of the McDermitt Caldera, Nevada-Oregon. Journal of Geophysical Research. 89(B10), 8629-8638

Hay, R. L., Hildreth, W. & Lambe, R. N. 1979. Globule ignimbrite of Mount Suswa, Kenya. In: Chapin, C. E. & Elston, W. E. 1979. Ash-Flow Tuffs. Geological Society of America Special Papers. 180

Heap, M. J., Kolzenburg, J. K., Russell, J. K., Campbell, M. E., Welles, J., Farquharson, J. I & Ryan, A. 2014. Conditions and timescales for welding block-and-ash flow deposits. Journal of Volcanology and Geothermal Research, 289, 202-209

Henry, C. D., Price, J. G., Rubin, J. N., Parker, D. F., Wolff, J. A., Self, S., Franklin, R. & Barker, D. S. 1988. Widespread, lava-like volcanic rocks of Trans-Pecos Texas. Geology. 16, 509-512

Henry, C. D., Price, J. G., Rubin, J. N. & Laubach, S. E. 1990. Case study of an extensive silicic lava: the Bracks Rhyolite, Trans-Pecos Texas. Journal of Volcanology and Geothermal Research. 43, 113-132

Henry, C.D. & Wolff, J.A., 1992. Distinguishing strongly rheomorphic tuffs from extensive silicic lavas: Bulletin of Volcanology. 54, 171–186

Hernando, I. R., Petrinovic, I. A., Gutiérrez, D. A., Bucher, J. Fuentes, T. G. & Aragón, E. 2019. The caldera-forming eruption of the quaternary Payún Matrú volcano, Andean back-arc of the southern volcanic zone. Journal of Volcanology and Geothermal Research. 384, 15-30

Hildreth, W. 1979. The Bishop Tuff: Evidence for the origin of compositional zonation in silicic magma chambers. Geological Society of North America, 180, 43-75

Hildreth, W. & Wilson, C. 2007. Compositional Zoning of the Bishop Tuff. Journal of Petrology, 48 (5), 951-999

Hoblitt, R. P. 1986. Observations of the eruptions of July 22 and August 7, 1980, at Mount St. Helens, Washington. U.S. Geological Survey Professional Paper 1335, 44 pages

Hoek, E. & Brown, E. T. 1997. Practical estimates of rock mass strength. International Journal of Rock Mechanics and Mining Sciences. 34, 1165-1186

Hoek, E. & Brown, E. T. 1980. Underground excavations in rock. Institute of Minerals and Metallurgy, London, UK, 527

Hoernle, K. & Schmincke, H. -U. 1993. The role of partial melting in the 15-Ma geochemical evolution of Gran Canaria: a blob model for the Canary hotspot. Journal of Petrology. 34, 599-626

Honnorez, J. 1969. Sur l'origine artificielle de la coloration vertedu verre basaltique alteré des hyaloclastites de Palagonia (Si-cile). Schweizerische Mineralogische und Petrographische Mitteilungen (Swiss Bulletin of Mineralogy and Petrology), 49, 65–75

Huertas, M. J., Arnaud, N. O. Ancochea, E., Cantagrel, J. M. & Fúster, J.M. 2002. $^{40}Ar/^{39}Ar$ stratigraphy of pyroclastic units from the Cañadas Volcanic Edifce (Tenerife, Canary Islands) and their bearing on the structural evolution. Journal of Volcanology and Geothermal Research, 115, 351-365

Hughes, S. R. & Druitt, T. H. 1998. Particle fabric in a small, type-2 ignimbrite flow unit (Laacher See, Germany) and implications for emplacement dynamics. Bulletin of Volcanology. 60, 125-136

International Society for Rock Mechanics (ISRM), C.o.T.M, USA. 1985. Suggested method for determining point load strength. International Journal of Rock Mechanics and Mining Sciences and Geomechanics Abstracts, 22, 51-60

Jana, D. & Walker, D. 1997. The influence of silicate melt composition on distribution of siderophile elements among metal and silicate liquids. Earth and Planetary Science Letters, 150, 463-472

Jutzeler, M., Schmincke, H. & Sumita, M. 2010. The incrementally zoned Miocene Ayaguares ignimbrite (Gran Canara, Canary Islands). Journal of Volcanology and Geothermal Research, 196, 1-19

Kahraman, S. 2001. Evaluation of simple methods for assessing the uniaxial compressive strength of rock. International Journal of Rock Mechanics and Mining Sciences, 38, 981–994

Kamata, H. & Mimura, K. 1983. Flow directions inferred from imbrication in the Handa pyroclastic flow deposit in Japan. Bulletin Volcanologique. 46, 277-282

Kamata, H., Suzuki-Kamata, K. & Bacon, C. R. 1993. Deformation of the Wineglass Welded Tuff and the timing of caldera collapse at Crater Lake, Oregon. Journal of Volcanology and Geothermal Research. 56 (3), 253-265

Kaya, A. & Karaman, K. 2016. Utilizing the strength conversion factor in the estimation of uniaxial compressive strength from the point load index. Bulletin of Engineering Geology and the Environment, 75, 351-357

Kingery, D. W., Bowen, H. K., & Uhlmann, D. R. 1976. Introduction to Ceramics, 2nd Edition. Wiley

Kirstein L. A., Hawkesworth C. J. & Garland F. G. 2001. Felsic lavas or rheomorphic ignimbrites: is there a chemical distinction? Contributions to Mineralogy & Petrology. 142, 309-322

Klug, C. & Cashman, K. V. 1994. Vesiculation of May 18, 1980, Mount St. Helens magma. Geology, 22, 468–472

Knight, M. D. & Walker, G. P. L. 1988. Magma flow directions in dikes of the Koolau Complex, Oahu, determined from magnetic fabric studies. Journal of Geophysical Research. 4301-4319

Kobberger, G. & Schmincke, H-U. 1999. Deposition of rheomorphic ignimbrite D (Mogán Formation), Gran Canaria, Canary Islands, Spain. Bulletin of Volcanology. 60, 465-485

Kokelaar, P., Königer, S. 2000. Marine emplacement of welded ignimbrite: the Ordovician Pitts Head Tuff, North Wales. Journal of the Geological Society of London, 157, 517-536

Lacroix, A. 1903. L'eruption de la Montagne Pelée en janvier 1903. Académie des Sciences (Paris). Competes Rendus. 136, 442-224

Lacroix, A. 1904. La Montagne Pelée et ses éruptions. Paris, Masson et Cie. pp. 662

Lagmay, M. A., Pyle, D. M., Dade, B. & Oppenheimer, C. 1999. Control of crater morphology on flow path direction of Soufriere-type pyroclastic flows. Journal of Geophysical Research. 104, 7169-7181

Lange, R. L. 1994. The effect of H2O, CO2 and F on the density and viscosity of silicate melts. Mineralogical Society of America Review. 24, 331-369

Langmuir, C. H. 1989. Geochemical consequences of in situ crystallization. Nature. 340, 199-205

Leat, P. T. & Schmincke, H-U. 1993. Large-scale rheomorphic shear deformation in Miocene peralkaline ignimbrite E, Gran Canada. Bulletin of Volcanology. 55, 155-165

Le Bas, M. J., Le Maitre, R. W., Streckeisen, A., Zanettin, B. 1986. A chemical classification of volcanic rocks based on the total alkali-silica diagram. IUGS Subcommission on the systematics of igneous rocks. Journal of petrology 27(3), 745–750

Lesti, C., Porreca, M., Giordano, G., Mattei, M., Cas, R. A. F., Wright, H. M. N., Folkes, C. B. & Viramonte, J. 2011. High-temperature emplacement of the Cerro Galán and Toconquis Group ignimbrites (Puna plateau, NW Argentina) determined by TRM analyses. Bulletin of Volcanology, 73, 1535-1565

Look, B. G. & Griffiths, S. 2001. An engineering assessment of the strength and deformation properties of Brisbane Rocks. Australian Geomechanics Journal. 36, (3) 17,30

Loney, R. A. 1968. Flow structure and composition of the Southern Coulee, Mono Craters, California - A pumice rhyolite flow. In: Coats, R.A., Hay, R.L. & Anderson, C.A. (Eds.), Studies in Volcanology, Geological Society of America Memoirs, 116, 415-440

Lowenstern, J. B. & Mahood, G. A. 1991. New data on magmatic H2O contents of pantellerites, with implications for petrogenesis and eruptive dynamics at Pantelleria. Bulletin of Volcanology. 54, 78-83

Loughlin, S. C., Calder, E. S., Clarke, A. B., Cole, P.D., Luckett, R., Mangan, M., Pyle, D., Sparks, R. S. J., Voight, B. & Watts, R. B. 2000. Pyroclastic flows and surges generated by the 25 June 1997 dome collapse, Soufriere Hills Volcano, Montserrat. In: Druitt, T. H. & Kokelaar, B. P. (eds) The Eruption of Soufriere Hills Volcano, Montserrat, From 1995 to 1999. Geological Society, London, Memoirs. 21, 191-210

McArthur A.N., Cas R.A.F. & Orton G.J., 1998: Distribution and significance of crystalline, perlitic and vesicular textures in the Ordovician Garth Tuff (Wales), Bulletin of Volcanology. 60, 260-285

McBirney, A.R. 1968. Second additional theory of origin to fiamme in ignimbrites: Nature, 217, 938

McBirney, A. R. & Murase, T. 1984. Rheological properties of magmas. Annual Review of Earth and Planetary Sciences. 12, 337-357

MacDonald, G. A. 1972. Volcanoes. A discussion of volcanoes, volcanic products, and volcanic phenomena. Pretice-Hall International, Englewood Cliffs, New Jersey

Mahood, G. A. 1984. Pyroclastic Rocks and Calderas Associated with Strongly Peralkaline Magmatism. Journal of Geophysical Research. 89, 8540-8552

Mahood, G. A. & Hildreth, W. 1986. Geology of the peralkaline volcano at Pantelleria, Strait of Sicily. Bulletin of Volcanology. 48, 143-173

Manley, C. R. 1995. How voluminous rhyolite lavas mimic rheomorphic ignimbrites: Eruptive style, emplacement conditions, and formation of tuff-like textures. Geology, 23(4), 349-352

Marshall, P. 1935. Acid rocks of the Taupo-Rotorua volcanic district. Transactions of the Royal Society of New Zealand. 64, 323-366

Maxwell, J. C. 1867. On the dynamical theory of gases: Philosophical Transactions of the Royal Society of London, 157, 49-88

Means, W. D. 1976. Stress and Strain. Springer Verlag. New York

Mehrotra, V.K., Mitra, S., Agrawal, C.K. 1991. Need of long-term evaluation of rock parameters in the Himalaya. In: “Proceedings; Seventh international congress on Rock mechanics” 289-292

Milner, D. M., Cole, J. & Wood, C. P. 2003. Mamaku Ignimbrite: A caldera-forming ignimbrite erupted from a compositionally zoned magma chamber in Taupo Volcanic Zone, New Zealand. Journal of Volcanology and Geothermal Research. 122 (3), 243-264

Milner, S. C., Duncan, A. R. & Ewart, A. 1992. Quartz latite rheoignimbrite flows of the Etendeka Formation, north-western Namibia. Bulletin of Volcanology. 54, 200-219

Mukhopadhyay, J., Ray, A., Ghosh, G., Medda, R. A., Bandyopadhyay, P. P. 2001. Recognition, characterization and implications of high-grade silicic ignimbrite facies from the Palaeoproterozoic Bijli rhyolites, Dongargarh Supergroup, central India. Gondwana Research, 4, 519-527

Mundula, F., Cioni, R. & Mulas, M. 2013. Rheomorphic diapir in densely welded ignimbrites: The Serra di Paringianu ignimbrite of Sardinia, Italy. Journal of Volcanology and Geothermal Research. 258, 12-23

Mundula, F., Cioni, R. & Rizzo, R. 2009. A simplified scheme for the description of textural features in Welded Ignimbrites: the example of San Pietro Island (Sardinia, Italy). Italian Journal of Geoscience. 128, 615-627

Mysen, B. & Richet, P. 2019. Silicate Glasses and Melts (Second Edition). Elsevier, 2019

Newhall, C. & Bronto, S., Alloway, B. Banks, N.G. & Bahar, I. & del Marmol, M. & Hadisantono, R.D. Holcomb, R.T., McGeehin, J., Miksic, J., & Rubin, M., Sayudi, S. D., Sukhyar, R., Andreastuti, S., Tilling, R., Torley, R. & Trimble, D. & Wirakusumah, A. D. 2000. 10,000 Years of explosive eruptions of Merapi Volcano, Central Java: Archaeological and modern implications. Journal of Volcanology and Geothermal Research. 100, 9-50

Norrish, K. & Hutton, J. T. 1969. An accurate X-ray spectrographic method for the analysis of a wide range of geological samples. Geochimica et Cosmochimica Acta 33, 431-53

O'Rourke, J.E. 1989. Rock index properties for geoengineering in underground development. Minerals Engineering, 41, 106-110

Palacz, Z. A. & Wolff, J. A. 1989. In: Saunders, A. D. & Norry, M. J. (eds). Magmatism in the Ocean Basins. Special Publications of the Geological Society of London. 42, 147-59

Palchik, V. & Hatzor, Y. H. 2004. The influence of porosity on tensile and compressive strength of porous chalk. Rock Mechanics and Rock Engineering, 37 (4), 331–41

Pallister, J., Wessels, R., Griswold, J., McCausland, W., Kartadinata, N., Gunawan, H., Budianto, A., Primulyana, S. 2019. Monitoring, forecasting collapse events, and mapping pyroclastic deposits at Sinabung volcano with satellite imagery. Journal of Volcanology and Geothermal Research. 282, 149-163

Parker, D. F. & White, J. C. 2008. Large-scale silicic alkalic magmatism associated with the Buckhorn Caldera, Trans-Pecos Texas, USA: comparison with Pantelleria, Italy. Bulletin of Volcanology. 70, 403-415

Passchier, C. W. & Trouw, R. A. J. 1995. Microtectonics. Second Edition. Springer-Verlag Berlin Heidelberg. 366 pages

Paulick, H. & Franz, G. 1997. The colour of pumice: Case study on a trachytic fall deposit, Meidob volcanic field, Sudan. Bulletin of Volcanology, 59, 171-185

Pearce, J. A. 1996. A users guide to basalt discrimination diagrams. In – Wyman, D. A. (ed.), Trace Element Geochemistry of Volcanic Rocks: Applications for Massive Sulphide Exploration. Short Course Notes. Geological Association of Canada, 12, 79-113

Peterson, D. W. 1979. Significance of the flattening of pumice fragments in ash flow tuffs. In: Chapin, C. E. & Elston, W. E. (eds) Ash-flow tuffs. Geological Society of America Special Paper, Boulder, Co. 180, 195-204

Piña-Varas, P. Ledo, J. Queralt, P. Marcuello, A. Bellmunt, F. Ogaya, X. Pérez, N. & Rodriguez-Losada J. A. 2015. Vertical collapse origin of Las Cañadas

caldera (Tenerife, Canary Islands) revealed by 3-D magnetotelluric inversion. Geophysical Research Letters. 42, 1710-1716

Pioli, L. 2002. High-grade ignimbrites from the Sulcis volcanic district (SW Sardinia, Italy): the example of Nuraxi tuff. Unpublished PhD Thesis. Dipartimento di Scienze della Terra, University of Pisa

Pioli, L. & Rosi, M. 2005. Rheomorphic structures in a high-grade ignimbrite: the Nuraxi Tuff, Sulcis volcanic district (SW Sardinia, Italy). Journal of Volcanology & Geotherm Research. 142, 11-28

Pittari, A., Cas, R. A. F. & Martí, J. 2005. The occurrence and origin of prominent massive, pumice-rich ignimbrite lobes within the late Pleistocene Abrigo ignimbrite, Tenerife, Canary Islands. Journal of Volcanology and Geothermal Research. 139, 271–293

Pittari, A., Cas, R. A. F., Edgar, C. J., Nichols, H. J., Wolff, J. A. & Martí, J. 2006. The influence of palaeotopography on facies architecture and pyroclastic flow processes of a lithic-rich ignimbrite in a high gradient setting: the Abrigo Ignimbrite, Tenerife, Canary Islands. Journal of Volcanology and Geothermal Research. 152, 273–315

Price, R. H. & Bauer, S. J. 1985. Analysis of the elastic and strength properties of Yucca Mountain Tuff, Nevada. Research and engineering applications in rock masses (1). United States, AA Balkema Publications

Quane, S., L. & Russell, J. K. 2003. Rock strength as a metric of welding intensity in pyroclastic deposits. European Journal of Mineralogy. 15, 855-864

Quane, S. L. & Russell, J. K. 2004. Welding: insights from high-temperature analogue experiments. Journal of Volcanology and Geothermal Research,

Quane, S. L. & Russell, J. K 2005. Ranking welding intensity in pyroclastic deposits. Bulletin of Volcanology. 67, 129-143

Mahood, G. A. 1984. Pyroclastic rocks and calderas associated with strongly peralkaline magmatism. Journal of Geophysical Research. 89 (B10)

Martí, J. & Ablay, G. J. 1994. Origin and significance of welded pyroclastic rocks from Tenerife, Canary Islands. IAVCEI International Volcanology Congress, Ankara, 1994. Abstract Programme.

Martí, J., Mitjavila, J. & Araña, V. 1994. Stratigraphy, structure and geochronology of Las Cañadas caldera (Tenerife, Canary Islands). Geology Magazine. 131, 715-727

Martí, J. & Gudmundsson, A. 2000. The Las Cañadas caldera (Tenerife, Canary Islands): an overlapping collapse caldera generated by magma-chamber migration. Journal of Volcanology and Geothermal Research. 103(1-4), 161-173

Martí, J., Mitjavila, J. & Villa, I. 1990. Stratigraphy and K-Ar ages of the Cañada de Diego Hernández. Their significance on the Las Cañadas Caldera formation (Tenerife, Canary islands). Terranova. 2. 148-153

Martí, J. Mitjavila, J. & Araña V. 1994. Stratigraphy, structure and geochronology of the Las Cañadas caldera (Tenerife, Canary Islands). Geology Magazine. 131, 715-727

Martí, J., Hurlimann, M., Ablay, G. J. & Gudmundsson, A. 1997. Vertical and lateral collapses on Tenerife (Canary Islands) and other volcanic ocean islands. Geology. 25, 879-882

Martí, J. Geyer, A. Folch, A. & Gottsmann J. 2008. A review on collapse caldera modelling. In: Gottsmann, J. & Martí J. (Eds.): Caldera Volcanism: Analysis, Modelling and Response, Elsevier, Amsterdam, 233-283

Martí, J. Soriano, C. Galindo, I. & Cas. R.A.F. Resolving problems with the origin of Las Cañadas caldera (Tenerife, Canary Islands): Los Roques de García Formation—Part of a major debris avalanche or an in situ, stratified, edifice-building succession? In: Groppelli, G. Viereck-Goette, L. (Eds.),

Stratigraphy and Geology of Volcanic Areas: Geological Society of America Special Paper, 464, 1-20

Navarro, J.M. & Coello, J. 1989. Depressions originated by landslide processes in Tenerife. ESF Meeting on Canarian Volcanism. 150–152

Ragan, D. M. & Sheridan, M. F. 1972. Compaction of the Bishop Tuff, California. Geological Society of America Bulletin, 83 (1), 95-106

Ramsay, J. G. 1967. Folding and fracturing in rocks. McGraw-Hill, New York, 568 pages

Ramsay, J. G. & Huber, M. I. 1983. The techniques of modern structural geology, volume 1: strain analysis. Academic Press, London, 307 pages

Rao, E. L. S, Venkatappa Rao, G. & Ramamurthy, T. 1987. Strength of sandstone in saturated and partly saturated conditions. Geotechnical Engineering, 18, 99–127

Read, J. R. L., Thornten, P. N. & Regan, W. M. 1980. A rational approach to the point load test. In: Proceedings of the Third Australian–New Zealand Geomechanics Conference. New Zealand Institution of Engineers, Wellington, Volume 2, 35–39

Reedman, A. J., Park, K. H., Merriman, R. J. & Kim, S. E. Welded tuff infilling a volcanic vent at Weolseong, Republic of Korea. Bulletin of Volcanology. 49, 541-546

Richard, D. 2015. Crossing the glass transition during volcanic eruptions: a matter of time scale and magma rheology. Unpublished PhD Thesis. Fakultät für Geowissenschaften, Ludwig-Maximilians-Universität, München

Ridley, W. I. 1970. The petrology of the Las Cañadas Volcanoes, Tenerife, Canary Islands. Contributions to Mineralogy and Petrology. 26, 124-160

Ridley, W. I. 1971. The origin of some collapse structures in the Canary Islands. Geological Magazine. 108, 477-484

Ridley, W. I. 1972. The field relations of the Las Cañadas volcanoes, Tenerife, Canary Islands. Bulletin of Volcanology. 35 (2), 318-334

Riehle, J. R. 1973. Calculated compaction profiles of rhyolitic ash-flow tuffs. Geological Society of America Bulletin. 84, 2194-2216

Riehle J. R., Miller T. F. & Bailey R. A. 1995. Cooling, degassing, and compaction of rhyolitic ash-flow tuffs: a computational model. Bulletin of Volcanology. 57, 319-336

Rodehorst, U., Schmincke, H-U. & Sumita, M. 1998. Geochemistry and Petrology of Pleistocene Ash layers Erupted at Las Cañadas Edifice (Tenerife). Proceedings of the Ocean Drilling Program. 157, 315-328

Ross, C. S. & Smith, R. L. 1961. Ash-flow tuffs; their origin, geologic relations, and identification. U. S. Geological Survey Professional Paper 366

Ross, C. S. & Smith, R. L. 1980. Ash-flow tuff; their origin, geologic relations & identification and zones and zonal variations in welded ash flows. In: Callender, J. F. (ed) Special Publication – New Mexico Geological Society, 9. Socorro, NM, United States

Rowley, P. D., Macleod, N. S., Kuntz, M. A. & Kaplan, A. M. 1985. Proximal bedded deposits related to pyroclastic flows of May 18, 1980, Mount St Helens, Washington. Geological Society of America Bulletin. 96, 1373-138

Rusnak, J. & Mark, C. 2000. Using the point load test to determine the uniaxial compressive strength of coal measure rock. *In:* Peng, S.S. & Mark, C. (eds) Proceedings, 19th International Conference on Ground Control in Mining, Morgantown, WV, 7–9 August. West Virginia University, Morgantown, West Virginia, 362–371

Russell, J. K. & Quane, S. L. 2005. Rheology of welding: inversion of field constraints. Journal of Volcanology and Geothermal Research. 142, 173-191

Rust, A.C. & Russell, J. K. 2000. Detection of welding in pyroclastic flows with ground penetrating radar; insights from field and forward modelling data. Journal of Volcanology & Geothermal Research, 95 (1–4), 23–34

Rust, A. C., Russell, J. K. & Knight, R. J. 1999. Dielectric constant as a predictor of porosity in dry volcanic rocks. Journal of Volcanology and Geothermal Research, 91(1), 79–96

Scharff, L., Hort, M. & Varley, N. R. 2019. First in-situ observation of a moving natural pyroclastic density current using Doppler radar. Scientific Reports. 9, 7386

Schmincke H-U. 1974. Volcanological aspects of peralkaline silicic welded ashflow tuffs. Bulletin of Volcanology, 38, 594-636

Schmincke, H-U. & Sumita, M. 1998. Volcanic evolution of Gran Canaria reconstructed from apron sediments: Synthesis of VICAP project drilling

Schmincke, H-U. & Swanson, D. A. 1967. Laminar viscous flowage structures in ash-flow tuffs from Gran Canaria, Canary Islands. Journal of Geology. 75 (6), 641-664

Schwartz-Mesa, A. C. 2016. Petrogenesis and Physical Volcanology of a compositionally zoned ignimbrite on Tenerife, Canary Islands, Spain. Unpublished MPhil Thesis, University of Leicester

Scott, R. B. 1971. Alkali exchange during devitrification and hydration of glasses in ignimbrite cooling units. The Journal of Geology. 79 (1)

Scott, W. E., Hoblitt, R. P., Torres, R. C., Self, S., Martinez, M. L. & Nillos, T. J. 1996. Pyroclastic flows of the June 15, 1991, climatic eruption of Mount Pinatubo. In: Newhall, C. G. & Punongbayan, S. (eds) Fire and Mud: Eruptions of Mount Pinatubo, Philippines. Philippine Institute Volcanology

and Seismology, Quezon City & University of Washington Press, Seattle, 545-570

Seville, J. P. K., Silomon-Pflug, H. & Knight, P. C. 1998. Modelling of sintering in high temperature gas fluidisation. Powder Technology. 97,160-169

Sharp, T. G., Stevenson, R. J. & Dingwell, D. B. 1996. Microlites and "nanolites" in rhyolitic glass: microstructural and chemical characterization. Bulletin of Volcanology, 57, 631-640

Sheikh, J. M., Naik, A. & Keluskar, T. 2020. Widespread rheomorphic and lava-like silicic ignimbrites overlying flood basalts in the north-western and northern Deccan Traps. Bulletin of Volcanology. 82, 41

Sheridan, M. F. 1979. Emplacement of pyroclastic flows: a review. In: Chapin, C. E. & Elston, W. E. (eds) Ash-flow Tuffs. Geological Society of America Special Paper. 180, 125-136

Sheridan, M. F. & Ragan, D. M. 1976. Compaction of ash-flow tuffs. In: Chilingarian, G. V. & Wolff, K. H. (eds) Compaction of coarse-grained sediments, II, Developments in Sedimentology. Elsevier, Amsterdam. 677-713

Sheridan, M. F. & Wang, Y. 2005. Cooling and welding history of the Bishop Tuff in Adobe Valley and Chidago Canyon, California. Journal of Volcanology and Geothermal Research. 142, 119-144

Singh, D.P. 1981. Determination of some engineering properties of weak rocks. In: "Weak rock; soft, fractured & weathered rock; Proceedings of the international symposium on weak rock; Volume. I." K. Akai, M. Hayashi & Y. Nishimatsu (Editors), A. A. Balkema, Rotterdam, Netherlands, 315-320

Smith, H. J. 1997. The point load test for weak rock in dredging applications. International Journal of Rock Mechanics and Mining Science 34 (3/4), 702

Smith, J. V. & Houston, E. C. 1994. Folds produced by gravity spreading of a banded rhyolite flow. Journal of Volcanology and Geothermal Research. 63 (1-2), 89-94

Smith, J. V. & Marshall, B. 1992. Patterns of folding and fold interference in oblique contraction of layered rocks of the inverted Cobar Basin, Australia. Tectonophysics. 215

Smith, N. J. 2012. Near-vent processes of the 273 ka Poris eruption (Tenerife). Unpublished PhD Thesis. University of Liverpool

Smith, R. L. 1960i. Ash flows. Geological Society of America Bulletin. 71 (6), 795-841

Smith, R. L. 1979. Ash-flow magmatism. In: Chapin, C.E. & Elston, W.E. (Editors), Ash-flow tuffs. Special Paper – Geological Society of America (GSA), Boulder, Co, United States. 5 - 27

Smith, R. L. 1960ii. Zones and zonal variations in welded ash flows. US Geological Survey, Professional Paper. 354-F, 149-159

Smith, R. L. & Bailey, R. A. 1966. The Bandelier Tuff – A study of ash-flow eruption cycles from zoned magma chambers. Bulletin of Volcanology. 29, 83-104

Smith, N. & Kokelaar, B. P. 2013. Proximal record of the 273 ka Poris caldera-forming eruption, Las Cañadas, Tenerife. Bulletin of Volcanology. 75, 768

Sommer, C. A., Fernandes de Lima, E., Machado, A., May Rossetti, L. M., Pierosan, R. 2013. Recognition and characterisation of high-grade ignimbrites from the neoproterozoicrhyolitic volcanism in southernmost Brazil, Journal of South American Earth Sciences. 47, 152-165

Soriano, C., Giordano, D., Galindo, I., Hürlimann, M. & Ardia, P. 2009. Giant gas bubbles in a rheomorphic vent fill at the Cañadas caldera, Tenerife (Canary Islands). Bulletin of Volcanology. 71, 919-932

Soriano, C., Galindo, G, Martí, J. & Wolff, J.A. 2006. Conduit-vent structures and related proximal deposits in the Las Cañadas caldera, Tenerife, Canary Islands. Bulletin of Volcanology, 69, 217-231

Soriano, C., Zafrilla, S. Martí, J. Bryan, S. Cas, R.A.F. & Ablay, G. 2002. Welding and rheomorphism of phonolitic fallout deposits from the Las Cañadas caldera, Tenerife, Canary Islands. Geological Society of America Bulletin. 114, 883-895

Sparks, R. S. J. 1976. Grain-Size Variations in Ignimbrites and Implications for Transport of Pyroclastic Flows. Sedimentology. 23, 147-188

Sparks, R.S.J., Francis, P.W., Hamer, R.D., Pankhurst, R.J., O'Callaghan, L.O., Thorpe, R.S. & Page, R. 1985. Ignimbrites of the Cerro Galan Caldera, NW Argentina. Journal of Volcanology and Geothermal Research, 24, 205-248

Sparks, R. S. J., Stasuik, M. V., Gardeweg M. & Swanson, D. A. 1993. Welded breccias in andesite lavas. Journal of the Geological Society of London. 150, 897–902

Sparks, R. S. J., Self, S. & Walker, G. P. L. 1973. Products of Ignimbrite Eruptions. Geology, 1, 115-118

Sparks R. S. J, Tait, S. R. & Yanev, Y. 1999. Dense welding caused by volatile resorption. Journal of the Geological Society of London, 156, 217-225

Sparks, R. S. J. & Wright, J. V. 1979. Welded Air-Fall Tuffs. In: Chapin CE, Elston WE (eds) Ash-flow tuffs. Geological Society of America Special Paper. 180, 155–166

Stevenson, D. S., Bagdassarov, N. S., Dingwell, D. B. & Romano, C. 1998. The influence of trace amounts of water on the viscosity of rhyolites. Bulletin of Volcanology. 60, 89-97

Stevenson, R. J., Briggs, R. M. & Hodder, P. W. 1993. Emplacement history of a low-viscosity, fountain-fed Pantelleritic lava-flow. Journal of Volcanology and Geothermal Research, 57(1), 39-56

Stevenson, R. J., Dingwell, D. B., Webb, S. L. & Sharp, T. G. 1996. Viscosity of microlite-bearing rhyolitic obsidians: an experimental study. Bulletin of Volcanology. 58, 298-309

Stevenson, R. J. & Wilson, L. 1997. Physical volcanology and eruption dynamics of peralkaline agglutinates from Panterlleria. Journal of Volcanology and Geothermal Research. 79 (1-2), 97-122

Streck, M. J. & Grunder, A. L. 1995. Crystallization and welding variations in a widespread ignimbrite sheet - the Rattlesnake Tuff, Eastern Oregon, USA. Bulletin of Volcanology. 57 (3), 151-169

Sumner, J. M. & Branney, M. J. 2002. The emplacement history of a remarkable heterogeneous, chemically zoned, rheomorphic and locally lava-like ignimbrite: `TL' on Gran Canaria. Journal of Volcanology and Geothermal Research. 115 (1-2), 109-138

Sumner, J. M. & Wolff, J. 2003. Petrogenesis of mixed-magma, high-grade, peralkaline ignimbrite 'TL' (Gran Canaria): diverse styles of mixing in a replenished, zoned magma chamber. Journal of Volcanology and Geothermal Research. 126, 109–26

Tammann, G.& Hesse, W. 1926. Die Abhängigkeit der Viscosität von der Temperatur bie unterkühlten Flüssigkeiten (En: The dependence of the viscosity on the temperature of supercooled liquids). Zeitschrift für anorganische und allgemeine Chemie, 156(1), 245-257

Thomas R. M. E. & Sparks R. S. J. 1992. Cooling of tephra during fallout from eruption columns. Bulletin of Volcanology, 54, 542-553

Topal, T. 2000. Problems faced in the applications of the point load index test. Geological Engineering Journal, 24, 73–86

Toplis, M.J. & Corgne, A. 2002. An experimental study of element partitioning between magnetite, clinopyroxene and iron-bearing silicate liquids with particular emphasis on vanadium. Contributions to Mineralogy and Petrology, 144, 22-37

Troll, R. & Carracedo, J. C. 2016. The Geology of Tenerife. In: The Geology of the Canary Islands. Elsevier. Ch 5, 227-355

Tsiambaos, G. & Sabatakakis, N. 2004. Considerations on strength of intact sedimentary rocks. Engineering Geology, 72, 261–273

Tuberville, B. N. 1992. Tephra fountaining, rheomorphism, and spatter flow during emplacement of the Pitigliano Tuffs, Latera caldera, Italy. Journal of Volcanology and Geothermal Research. 53 (1-4), 309-327

Tuğru, A. & Zarif, I. H. 1999. Correlation of mineralogical and textural characteristics with engineering properties of selected granitic rocks from Turkey. Engineering Geology. 51, 303-317

Twiss, R. J, Moores, E. M. 1992. Structural geology. Freemen Press, New York, 532 pages

Ui, T, Matsuwo, N. Sumita, M. & Fujinawa, A. 1999. Generation of block and ash flows during the 1990-1995 eruption of Unzen Volcano, Japan. Journal of Volcanology and Geothermal Research. 89 (1-4), 123-137

Ulusay, R., Tureli, K., Ider, M.H. 1994. Prediction of engineering properties of a selected litharenite sandstone from its petrographic characteristics using correlation & multivariate statistical techniques. Engineering Geology, 38, 135-157

Vallejo, L. E., Welsh, R. A. & Robinson, M. K 1989. Correlation between unconfined compressive and point load strengths for Appalachian rocks. Rock Mechanics as a Guide for Efficient Utilization of Natural Resources: Proceedings of the 30th U.S. Symposium, Morgantown, Balkema, 461-468

Vogel, D.H. (1921) Das Temperaturabhängigkeits gesetz der Viskosität von Flüssigkeiten (En: The temperature-dependency law of viscosity of liquids). Physikalische Zeitschrift, 22, 645–646

Voight, B. Constantine, E. K., Siswowidjiyo, S. & Torley, R. 2000. Historical eruptions of Merapi Volcano, Central Java, Indonesia, 1768-1998. Journal of Volcanology and Geothermal Research. 100 (1-4), 69-138

Vogelsang, H. 1872. Ueber die Systematikder Gesteinslehre und die Eintheilung dergemengten Silikatgesteine.Zeitschrift der Deutschen Geologischen Gesellschaft. Berlin. 24, 507–544

Wadge, G., Voight, B. & Sparks, R.S.J., Cole, P., Loughlin, S. & Robertson, R. 2014. An overview of the eruption of Soufrière Hills Volcano, Montserrat from 2000 to 2010.In: Wadge, G. (eds) The Eruption of Soufrière Hills Volcano, Montserrat from 2000 to 2010. Geological Society of London Memoir. 39, 1-39

Walker, G.P.L. 1973. Lengths of lava flows. Philosophical Transactions of the Royal Society London Series A (Mathematical, Physical and Engineering Sciences), 274,107-118

Walker, G. P. L., Self, S. & Froggatt, P. C. 1981. The ground layer of the Taupo ignimbrite; a striking example of sedimentation from a pyroclastic flow. Journal of Volcanology and Geothermal Research. 10, 1-11

Walker, G. W. & Swanson, D. A. 1968. Laminar flowage in a Pliocene soda rhyolite ash-flow tuff, Lake and Harney counties, Oregon. Geological Survey Research 1968, Chap. B. USGS Professional Papers, Reston, VA. B37-B47

Wallace, A. B., Drexler, J. W. Norman, K. G. & Noble, D. C. 1980. Icelandite and aenigmatite-bearing pantellerite from the McDermitt caldera complex, Nevada-Oregon. Geology. 8(8), 380-384

Walter, M. J. & Thibault, Y. 1995. Partitioning of tungsten and molybdenum between metallic liquid and silicate melt. Science, 270, 1186-1189

Watts, A.B. & Masson, D.G. 1995. A giant landslide on the north flank of Tenerife, Canary Islands. Journal of Geophysical Research. 100, 487–494

Webb, S. L. & Dingwell, D. B. 1990. Non-Newtonian rheology of igneous melts at high stresses and strain rates: experimental results for rhyolite, andesite, basalt, and nephelinite. Journal of Geophysical Research. 95, 15695-15701

Wiesner, E. & Gillate, S.J. 1997. An evaluation of the relationship between unconfined compressive strength & point load strength index. Bulletin of the International Association of Engineering Geology, 56, 115-118

Wilding, M., Webb, S., Dingwell, D., Ablay, G., & Martí, J. 1996i. Cooling rate variation in natural volcanic glasses from Tenerife, Canary Islands: Contributions to Mineralogy and Petrology, 125(2-3), 151-160

Wilding, M., Webb, S. & Dingwell, D. B. 1996ii. Tektite cooling rates: Calorimetric relaxation geospeedometry applied to a natural glass. Geochimica et Cosmochimica Acta, 60(6), 1099-1103.

Williams, R., Branney, M. J. & Barry, T. L. 2014. Temporal and spatial evolution of a waxing then waning catastrophic density current revealed by chemical mapping. Geology. 42(2), 107-110

Wilson, C. J. N. 1986. Pyroclastic flows and ignimbrites. Science Progress (1933, 70 (2), 171-207

Wilson, C. J. N. 1985. The Taupo Eruption, New-Zealand: The Taupo Ignimbrite. Philosophical Transactions of the Royal Society of London Series Mathematical Physical and Engineering Sciences. 314, 229

Wilson, C. J. N. & Hildreth, W. 2003. Assembling an ignimbrite: mechanical and thermal building blocks in the Bishop Tuff, California. Journal of Geology. 111, 653–670

Wilson, C. J. N. & Walker, G. P. L. 1982. Ignimbrite depositional facies the anatomy of a pyroclastic flow. Journal of the Geological Society, London. 139, 581-592

Wilson, C. J. N. & Hildreth, W. 2003. Assembling an ignimbrite: mechanical and thermal building blocks in the Bishop Tuff, California. Journal of Geology. 111, 653-670

Winchester, J. A. & Floyd, P. A. (1977) Geochemical discrimination of different magma series and their differentiation products using inmobile elements. Chemical Geology, 20, 325-343

Wolff J. A. 1985. Zonation, mixing and eruption of silica-undersaturated alkaline magma: a case study from Tenerife, Canary Islands. Geology Magazine. 122, 623-640

Wolff, J. A., Grandy, J. S. & Larson, P. B. 2000. Interaction of mantle-derived magma with island crust? Trace element and oxygen isotope data from the Diego Hernandez Formation, Las Cañadas, Tenerife. Journal of Volcanology & Geothermal Research. 103 (1-4), 343-366

Wolff, J.A. & Storey, M. 1983. The volatile component of some pumice-forming alkaline magmas from the Azores and Canary Islands: Contributions to Mineralogy and Petrology, 82, 66–74

Wolff, J.A. & Storey, M. 1984. Zoning in highly alkaline magma bodies. Geological Magazine, 121, 563-575

Wolff J. A. & Wright, J.V. 1981i. Formation of the Green Tuff of Pantelleria. Bulletin of Volcanology, 44, 681-690

Wolff, J. A. & Wright, J. V. 1981ii. Rheomorphism of welded tuffs. Journal of Volcanology and Geothermal Research. 10, 13-34

Wörner, G. & Schmincke, H-U. 1984i. Mineralogical and chemical zonation of the Laacher See tephra sequence (East Eifel, FRG). Journal of Petrology, 25, 805–835

Wörner, G. & Schmincke, H-U. 1984ii. Petrogenesis of the Zoned Laacher See Tephra. Journal of Petrology, 25 (4), 836-851

Wright, J. V. 1980. Stratigraphy and geology of the welded air-fall tuffs of Pantelleria, Italy. Geologische Rundschau. 69, 263–291

Wright, J. V. 1981. The Rio Caliente ignimbrite: analysis of a compound intraplinian ignimbrite from a major late Quaternary Mexican eruption. Bulletin of Volcanology. 44, 189-212

Wright, J. V. & Walker, G. P. L. 1981. Eruption, transport and deposition of ignimbrite - a case-study from Mexico. Journal of Volcanology and Geothermal Research. 9, 111-131

Yamamoto, T., Takarada, S. & Suto, S. 1993. Pyroclastic flows from the 1991 eruption of Unzen volcano, Japan. Bulletin of Volcanology. 55, 166-175

Zafrilla, S. 2001. Relationships between Magmatic Evolution and Phonolitic Volcanic Activity in the Las Cañadas Edifice, Tenerife, Canary Islands. Unpublished PhD Thesis. Universitat de Barcelona

Zambonini, F. 1919. Il tufo pipernoide della Campania e i suoi minerali: Italy R. Comitato Geologico Memoirs. 7, 2, 1-130

# Appendices

## Appendix I

Record of each unit's sample field location, elevation and the data obtained from each sample.

Abbreviations - XRF: X-Ray Fluorescence Spectrometry at the University of Edinburgh (Chapter 7); EMPA Electron Micro-Probe analysis at *Ludwig-Maximilians*-Universität (LMU), Munich (Chapter 7); Petrographic analysis: optical microscopy & Scanning Electron Microscopy of thin sections prepared at the University of Glasgow) (Chapter 7); TA: thermal analysis via Differential Scanning Calorimetry at LMU (Chapter 7) ; PLT: point load strength testing at Terra Tek Laboratory, Airdrie (Chapter 5); ϕ & ρ: porosity and density determination at MATtest Ltd, Glasgow (Chapter 5).

| Sample | Member & Unit | Grid Reference | Elevation (m) | Stratigrapy | XRF | EMPA | Petrographic | TA | PLT | φ & ρ |
|---|---|---|---|---|---|---|---|---|---|---|
| TN-24 | Atravesado 1 | N28°9'40" W016°38'46" | 1575 | base | ✓ | - | ✓ | - | ✓ | ✓ |
| TN-47 | Atravesado 1 | N28°10'25" W016°38'40" | 1805 | mid-unit | ✓ | - | ✓ | - | ✓ | ✓ |
| TN-48 | Atravesado 1 | N28°10'25" W016°38'40" | 1840 | upper | ✓ | - | ✓ | - | ✓ | ✓ |
| TN-45 | Atravesado 2 | N28°10'35" W016°38'44" | 1810 | base | ✓ | - | ✓ | - | ✓ | ✓ |
| TN-32 | Atravesado 2 | N28°10'27" W016°38'50" | 1825 | mid-unit | ✓ | - | ✓ | - | ✓ | ✓ |
| TN-46 | Atravesado 2 | N28°10'35" W016°38'45" | - | upper | ✓ | - | ✓ | - | ✓ | ✓ |
| TN-34 | Atravesado 3 | N28°10'30" W016°38'53" | 1875 | base | ✓ | - | ✓ | - | - | - |
| TN-35 | Atravesado 3 | N28°10'13" W016°38'55" | 1800 | mid-unit | ✓ | - | - | - | ✓ | ✓ |
| TN-33 | Atravesado 3 | N28°10'30" W016°38'53" | 1890 | upper | ✓ | - | ✓ | - | ✓ | ✓ |
| TN-44 | Atravesado 4 | *N28°9'14" W016°40'4"* | 2040 | base | ✓ | - | ✓ | - | ✓ | ✓ |
| TF-04 | Atravesado 4 | N28°11'21.9" W016°39'34.7" | 2060 | mid-unit | ✓ | - | ✓ | - | ✓ | ✓ |
| TN-23 | Atravesado 4 | N28°11'7" W016°39'53" | 2140 | upper | - | - | ✓ | - | ✓ | ✓ |
| TN-01 | Atravesado 4 | N28°11'41" W016°39'56" | 2210 | upper | ✓ | - | ✓ | - | ✓ | ✓ |
| TN-02 | Retamares A | N28°11'45" W016°39'53" | 2175 | base | - | - | ✓ | - | ✓ | ✓ |
| TN-03 | Retamares A | N28°11'50" W016°39'5" | - | base | ✓ | - | - | - | ✓ | ✓ |
| TN-10 | Retamares A | N28°11'44" W016°39'26" | 2230 | mid-unit | ✓ | ✓ | ✓ | ✓ | ✓ | ✓ |
| TN-40 | Retamares A | N28°11'26" W016°39'9" | 2265 | upper | ✓ | - | ✓ | - | ✓ | ✓ |
| TF-10 | Retamares B | N28°11'33.1" W016°38'57.6" | 2290 | base | ✓ | - | ✓ | - | ✓ | - |
| VF-16/1 | Retamares B | N28°11'41.3" W016°39'00.0" | 2300 | mid-unit | ✓ | - | - | - | ✓ | ✓ |
| PP-02 | Retamares B | *N28°11' 40" W016°39'03"* | 2350 | mid-unit | - | ✓ | - | ✓ | - | - |
| TF-03 | Retamares B | N28°11' 40" W016°39'03" | 2350 | mid-unit | - | - | ✓ | - | ✓ | ✓ |
| TN-05 | Retamares B | N28°11'58" W016°38'59" | 2440 | upper | - | - | - | - | ✓ | ✓ |
| TN-41 | Retamares B | N28°11'45" W016°38'60" | 2350 | upper | ✓ | - | ✓ | - | ✓ | ✓ |
| TN-06 | Retamares C | N28°12'2" W016°39'12" | 2460 | base | ✓ | - | - | ✓ | - | ✓ |
| TN-09 | Retamares C | N28°11'49" W016°38'59" | 2400 | base | - | ✓ | - | ✓ | ✓ | ✓ |
| TN-43 | Retamares C | N28°11'31" W016°39'7" | - | mid-unit | ✓ | - | ✓ | - | - | ✓ |
| TF-02 | Retamares C | N28°12'02.6" W016°39'30" | 2400 | upper | ✓ | - | - | ✓ | - | ✓ |
| TF-07 | Retamares D | N28°11'37" W016°37'41" | 2275 | base | ✓ | - | ✓ | - | - | - |
| TF-01 | Retamares D | N28°11' 57" W016°38'18" | 2450 | mid-unit | ✓ | - | ✓ | - | ✓ | ✓ |
| TN-42 | Retamares D | N28°11'57" W016°38'16" | 2450 | upper | ✓ | - | ✓ | - | ✓ | ✓ |
| TN-13 | Retamares D | N28°11'36" W016°37'47" | *2310* | (mid) | - | - | - | - | - | - |
| TN-15 | Retamares E | N28°12'48" W016°37'9" | 2430 | base | ✓ (4) | - | ✓ (A) | - | ✓ (A) | ✓ |
| TF-09 | Retamares E | N28°12'37" W016°37'19.0" | 2440 | base | - | - | ✓ | - | ✓ | ✓ |
| TN-22 | Retamares E | N28°12'50" W016°37'9" | 2440 | mid-unit | - | - | ✓ | - | ✓ | ✓ |
| TN-14 | Retamares E | N28°12'48" W016°37'9" | 2420 | upper | ✓ | - | ✓ | - | ✓ | ✓ |
| TN-21 | Retamares F | N28°12'37" W016°37'19" | 2430 | base | ✓ | - | - | - | ✓ | ✓ |
| TN-20 | Retamares F | N28°12'34" W016°37'19" | 2435 | mid-unit | ✓ | - | ✓ | - | ✓ | ✓ |
| TN-19 | Retamares F | N28°12'35" W016°37'19" | 2440 | upper | ✓ | - | ✓ | - | ✓ | ✓ |
| TN-18 | Retamares G | N28°12'29" W016°37'18" | 2410 | base | ✓ | - | ✓ | - | ✓ | ✓ |
| TN-17 | Retamares G | N28°12'26" W016°37'18" | 2415 | upper | ✓ | - | ✓ | - | ✓ | ✓ |

| Sample | Member & Unit | Grid Reference | Elevation (m) | Stratigrapy | XRF | EMPA | Petrographic | TA | PLT | φ & ρ |
|---|---|---|---|---|---|---|---|---|---|---|
| TN-07 | Chasna (Sombrero) | N28°11'42" W016°38'48" | 2340 | base | ✓ | - | ✓ | - | ✓ | ✓ |
| TN-08 | Chasna (Sombrero) | N28°11'42" W016°38'48" | 2370 | mid-unit | ✓ | - | ✓ | - | ✓ | ✓ |
| VF-16/2 | Chasna (Sombrero) | N28°11'35.1" W016°38'42.8" | 2405 | upper | ✓ | - | - | - | ✓ | ✓ |
| VF-16/3 | Chasna (RLA) | N28°12'02.6" W016°39'43.7" | 2475 | base | - | ✓ | ✓ | ✓ | ✓ | ✓ |
| TF-06 | Chasna (RLA) | N28°12'02.6" W016°39'43.7" | 2475 | base | ✓ | - | ✓ | - | ✓ | ✓ |
| TN-36 | Chasna (RLA) | N28°12'02.8" W16°39'43.0" | 2520 | mid-unit | ✓ | - | ✓ | - | ✓ | - |
| TN-38 | Chasna (RLA) | N28°12'2" W016°39'35" | 2525 | upper | ✓ | - | ✓ | - | ✓ | ✓ |
| TN-16 | Chasna (LdlM) | N28°12'16" W016°37'34" | 2450 | base | ✓ | - | - | - | - | - |
| TN-12 | Chasna (LdlM) | N28°11'40" W016°37'46" | 2355 | upper | ✓ | - | ✓ | - | ✓ | ✓ |
| TF-05 | Chasna Ridge | N28°19.9'26.1" W016°65.4'29.9" | 2350 | - | - | - | - | - | ✓ | ✓ |
| VF-18/4 VF-16/4 | Chasna Ridge | N28°11'58.6" W016°39'17.0" | 2445 | - | - | - | ✓ | - | - | ✓ |
| TN-11 | Chasna Ridge | N28°12'3" W016°39'29" | 2350 | - | ✓ | - | - | - | ✓ | - |
| TN-04 | Almendros (RLA) | N28°12'1" W016°39'42" | 2525 | base | ✓ | - | ✓ | - | ✓ | ✓ |
| TN-37 | Almendros (RLA) | N28°12'6" W016°39'40" | 2515 | mid-unit | ✓ | ✓ | - | ✓ | - | - |
| TN-39 | Almendros (RLA) | N28°12'7" W016°39'40" | 2465 | upper | ✓ | ✓ | ✓ | ✓ | - | - |
| TN-31 | Areñas (southern) | N28°12'44" W016°36'47" | 2610 | base | - | - | - | ✓ | - | ✓ |
| TN-25 | Areñas (southern) | N28°12'44" W016°36'47" | 2610 | base | ✓ | ✓ | ✓ | - | ✓ | ✓ |
| PP-01 | Areñas (southern) | N28°12'44" W016°36'47" | 2615 | mid-unit | - | - | - | ✓ | - | - |
| TN-26 | Areñas (southern) | N28°12'44" W016°36'47" | 2615 | mid-unit | ✓ | ✓ | ✓ | - | ✓ | ✓ |
| TN-27 | Areñas (southern) | N28°12'44" W016°36'47" | 2620 | upper | ✓ | ✓ | ✓ | - | ✓ | ✓ |
| TF-08 | Guajara 2 | N28°13'03" W016°36'42" | 2717 | upper | ✓ | - | ✓ | - | ✓ | ✓ |
| TN-29 | Guajara 3 | N28°12'41" W016°36'55" | 2480 | base | ✓ | - | ✓ | - | ✓ | ✓ |
| TN-28 | Guajara 3 | N28°12'44" W016°36'51" | 2480 | mid-unit | ✓ | - | ✓ | - | ✓ | ✓ |
| TN-30 | Guajara 3 | N28°12'49" W016°36'50" | 2480 | upper | ✓ | - | ✓ | - | ✓ | ✓ |
| TN-49 | El Pinalito lava | N28°10'39.8" W16°38'43.2" | 1800 m | - | ✓ | - | ✓ | - | - | - |

# Appendix II

Data set and results from Point load Testing (PLT), (and conversion to UCS) of samples carried out at Terra Tek Laboratory, Airdrie.

| | | | | | | | | | | | | Quane & Russell (2003) | | | |
|---|---|---|---|---|---|---|---|---|---|---|---|---|---|---|---|
| Sample | Member & Unit | Grid Reference | Stratigrapy | Point Load Testing | Dimension A | Dimension B | Load | Is | Corrected Is(50) | Averaged Corrected Is(50) | Resistance to a point load classification | PLTm to UCSp | PLTm to UCSp | PLTm to UCSp | PLTm to UCSp |
| | | | | Irregular lump | mm | mm | kN | MN/m² | MN/m² | MN/m² | Garnica et al, (1997) | MPa | MPa | MPa | MPa |
| | | | | | | | | Mpa | MPa | MPa | Carol (2008) | > 4 MPa (linear) | < 5 MPa (non-linear) | Averaged (2.5 - 6.5 MPa) | Final |
| TN-48 | Atravesado Mb 1 | N28°10'25" W016°38'40" | Upper | Yes | 41.0 | 20.0 | 9.7 | 9.29 | 7.63 | 6.24 | Very high | 152.13 | 185.29 | 168.71 | 152.13 |
| | | | | | 38.0 | 20.0 | 4.1 | 4.24 | 3.42 | | | | | | |
| | | | | | 43.0 | 15.0 | 7.3 | 8.89 | 6.92 | | | | | | |
| | | | | | 30.0 | 40.0 | 11.9 | 7.79 | 6.97 | | | | | | |
| TN-47 | Atravesado Mb 1 | N28°10'25" W016°38'40" | Mid | Yes | 20.0 | 20.0 | 2.5 | 4.91 | 3.34 | 3.82 | Very high | 93.13 | 77.79 | 85.46 | 77.79 |
| | | | | | 30.0 | 23.0 | 3.9 | 4.25 | 3.39 | | | | | | |
| | | | | | 32.0 | 36.0 | 7.8 | 5.32 | 4.72 | | | | | | |
| TN-24 | Atravesado Mb 1 | N28°9'40" W016°38'46" | Base | Yes | 58.5 | 22.0 | 7.1 | 4.33 | 3.94 | 5.19 | Very high | 126.64 | 133.30 | 129.97 | 126.64 |
| | | | | | 55.0 | 12.0 | 5.0 | 5.95 | 4.66 | | | | | | |
| | | | | | 25.0 | 26.0 | 7.4 | 8.94 | 6.97 | | | | | | |
| TN-46 | Atravesado Mb 2 | N28°10'35" W016°38'45" | Upper | Yes | 58.0 | 15.0 | 11.1 | 10.02 | 8.34 | 9.07 | Very high | 221.39 | 369.04 | 295.21 | 221.39 |
| | | | | | 45.0 | 20.0 | 10.9 | 9.51 | 7.98 | | | | | | |
| | | | | | 35.0 | 35.0 | 18.9 | 12.12 | 10.90 | | | | | | |
| TN-32 | Atravesado Mb 2 | N28°10'27" W016°38'50" | Mid | Yes | 49.0 | 25.0 | 2.4 | 1.54 | 1.38 | 3.04 | Very high | 74.18 | 52.85 | 63.51 | 52.85 |
| | | | | | 38.0 | 32.0 | 5.0 | 3.23 | 2.90 | | | | | | |
| | | | | | 31.0 | 42.0 | 8.8 | 5.31 | 4.84 | | | | | | |
| TN-45 | Atravesado Mb 2 | N28°10'35" W016°38'44" | Base | Yes | 37.0 | 25.0 | 0.1 | 0.08 | 0.07 | 0.42 | Very low | 10.17 | 3.02 | 6.60 | 3.02 |
| | | | | | 43.0 | 15.0 | 0.1 | 0.12 | 0.09 | | | | | | |
| | | | | | 76.0 | 28.0 | 2.9 | 1.07 | 1.09 | | | | | | |
| TN-33 | Atravesado Mb 3 | N28°10'30" W016°38'53" | Upper | Yes | 39.0 | 15.0 | 7.8 | 10.47 | 7.97 | 10.28 | Extremely high | 250.91 | 466.28 | 358.60 | 250.91 |
| | | | | | 31.0 | 15.0 | 10.7 | 18.07 | 13.07 | | | | | | |
| | | | | | 28.0 | 30.0 | 12.7 | 11.87 | 9.81 | | | | | | |
| TN-35 | Atravesado Mb 3 | N28°10'13" W016°38'55" | Mid | Yes | 36.0 | 24.0 | 8.0 | 7.27 | 6.05 | 10.31 | Extremely high | 251.65 | 468.84 | 360.24 | 251.65 |
| | | | | | 27.0 | 18.0 | 6.0 | 9.70 | 7.08 | | | | | | |
| | | | | | 29.0 | 30.0 | 23.7 | 21.40 | 17.81 | | | | | | |
| TN-01 | Atravesado Mb 4 | N28°11'41" W016°39'56" | Upper | Yes | 43.0 | 44.0 | 10.6 | 4.40 | 4.36 | 5.29 | Very high | 128.99 | 137.75 | 133.37 | 128.99 |
| | | | | | 67.0 | 48.0 | 26.0 | 6.35 | 7.10 | | | | | | |
| | | | | | 75.0 | 74.0 | 24.6 | 3.48 | 4.40 | | | | | | |
| TN-23 | Atravesado Mb 4 | N28°11'7" W016°39'53" | Upper | Yes | 45.0 | 45.0 | 13.8 | 5.35 | 5.39 | 4.23 | Very high | 103.13 | 92.84 | 97.98 | 97.98 |
| | | | | | 55.0 | 45.0 | 7.9 | 2.51 | 2.64 | | | | | | |
| | | | | | 58.0 | 54.0 | 16.7 | 4.19 | 4.65 | | | | | | |
| TF-04 | Atravesado Mb 4 | N28°11'21.9" W016°39'34.7" | Mid | Yes | 60.0 | 25.0 | 4.7 | 2.46 | 2.31 | 2.94 | High | 71.82 | 50.07 | 60.94 | 50.07 |
| | | | | | 54.0 | 24.0 | 3.9 | 2.36 | 2.15 | | | | | | |
| | | | | | 29.0 | 34.0 | 6.4 | 5.10 | 4.37 | | | | | | |
| TN-44 | Atravesado Mb 4 | N28°9'14" W016°40'4" | Base | Yes | 47.0 | 25.0 | 0.2 | 0.13 | 0.12 | 0.24 | Low | 5.86 | 1.58 | 3.72 | 1.58 |
| | | | | | 46.0 | 25.0 | 0.1 | 0.07 | 0.07 | | | | | | |
| | | | | | 39.0 | 44.0 | 1.2 | 0.55 | 0.53 | | | | | | |
| TN-40 | Retamares Mb A | N28°11'26" W016°39'9" | Upper | Yes | 31.0 | 24.0 | 6.5 | 6.86 | 5.52 | 11.96 | Extremely high | 291.91 | 620.04 | 455.97 | 291.91 |
| | | | | | 18.0 | 28.0 | 12.6 | 19.63 | 14.46 | | | | | | |
| | | | | | 21.0 | 40.0 | 20.6 | 19.26 | 15.91 | | | | | | |
| TN-10 | Retamares Mb A | N28°11'44" W016°39'26" | Inter | Yes | 43.0 | 35.0 | 7.6 | 3.97 | 3.74 | 5.08 | Very high | 124.03 | 128.46 | 126.25 | 124.03 |
| | | | | | 44.0 | 30.0 | 8.6 | 5.12 | 4.68 | | | | | | |
| | | | | | 51.0 | 36.0 | 16.2 | 6.93 | 6.83 | | | | | | |
| TN-02 | Retamares Mb A | N28°11'45" W016°39'53" | Base | Yes | 69.0 | 48.0 | 2.0 | 0.47 | 0.53 | 0.58 | Moderate | 14.23 | 4.61 | 9.42 | 4.61 |
| | | | | | 66.0 | 40.0 | 1.2 | 0.36 | 0.38 | | | | | | |
| | | | | | 65.0 | 48.0 | 3.0 | 0.76 | 0.84 | | | | | | |
| TN-03 | Retamares Mb A | N28°11'50" W016°39'5" | Base | Yes | 47.0 | 30.0 | 3.9 | 2.17 | 2.02 | 4.25 | Very high | 103.62 | 93.61 | 98.61 | 98.61 |
| | | | | | 38.0 | 24.0 | 8.5 | 7.32 | 6.16 | | | | | | |
| | | | | | 30.0 | 28.0 | 5.9 | 5.52 | 4.56 | | | | | | |
| TN-05 | Retamares Mb B | N28°11'58" W016°38'59" | Upper | Yes | 78.0 | 34.0 | 5.9 | 1.75 | 1.87 | 5.68 | Very high | 138.51 | 156.46 | 147.49 | 138.51 |
| | | | | | 73.0 | 28.0 | 8.5 | 3.27 | 3.30 | | | | | | |
| | | | | | 38.0 | 36.0 | 22.4 | 12.86 | 11.86 | | | | | | |
| TN-41 | Retamares Mb B | N28°11'45" W016°38'60" | Upper | Yes | 30.0 | 25.0 | 5.2 | 5.45 | 4.39 | 2.93 | High | 71.55 | 49.76 | 60.66 | 49.76 |
| | | | | | 56.0 | 44.0 | 4.2 | 1.34 | 1.41 | | | | | | |
| | | | | | 55.0 | 30.0 | 3.5 | 1.67 | 1.60 | | | | | | |
| TF-03 | Retamares Mb B | N28°11' 40" W016°39'03" | Mid | Yes | 56.0 | 48.0 | 13.8 | 4.03 | 4.33 | 1.90 | High | 46.36 | 24.67 | 35.51 | 24.67 |
| | | | | | 81.0 | 38.0 | 7.5 | 1.91 | 2.12 | | | | | | |
| | | | | | 814.0 | 34.0 | 7.8 | 0.22 | 0.40 | | | | | | |
| | | | | | 90.0 | 68.0 | 19.2 | 2.46 | 3.18 | | | | | | |
| VF-16/1 | Retamares Mb B | N28°11'41.3" W016°39'00.0" | Mid | Yes | 90.0 | 38.0 | 19.1 | 4.39 | 4.97 | 4.45 | Very high | 108.50 | 101.45 | 104.97 | 104.97 |
| | | | | | 75.0 | 34.0 | 10.5 | 3.23 | 3.43 | | | | | | |
| | | | | | 75.0 | 64.0 | 24.7 | 4.04 | 4.94 | | | | | | |
| TF-02 | Retamares Mb C | N28°12'02.6" W016°39'30" | Upper | Yes | 79.0 | 65.0 | 21.0 | 3.21 | 3.99 | 3.53 | Very high | 86.21 | 68.15 | 77.18 | 68.15 |
| | | | | | 83.0 | 70.0 | 19.8 | 2.68 | 3.42 | | | | | | |
| | | | | | 77.0 | 85.0 | 20.3 | 2.44 | 3.19 | | | | | | |
| TN-43 | Retamares Mb C | N28°11'31" W016°39'7" | Mid | Yes | 69.0 | 50.0 | 3.3 | 0.75 | 0.85 | 1.14 | High | 27.82 | 11.46 | 19.64 | 11.46 |
| | | | | | 68.0 | 58.0 | 2.8 | 0.56 | 0.65 | | | | | | |
| | | | | | 64.0 | 72.0 | 9.3 | 1.59 | 1.92 | | | | | | |
| TN-06 | Retamares Mb C | N28°12'2" W016°39'12" | Base | Yes | 56.0 | 26.0 | 6.1 | 3.29 | 3.08 | 2.31 | High | 56.45 | 33.73 | 45.09 | 33.73 |
| | | | | | 55.0 | 28.0 | 5.1 | 2.60 | 2.46 | | | | | | |
| | | | | | 63.0 | 65.0 | 6.2 | 1.19 | 1.40 | | | | | | |
| TN-09 | Retamares Mb C | N28°11'49" W016°38'59" | Base | Yes | 46.0 | 20.0 | 1.8 | 1.54 | 1.30 | 1.66 | High | 40.42 | 19.95 | 30.19 | 19.95 |
| | | | | | 44.0 | 20.0 | 2.0 | 1.78 | 1.49 | | | | | | |
| | | | | | 23.0 | 25.0 | 2.1 | 2.87 | 2.18 | | | | | | |
| TN-42 | Retamares Mb D | N28°11'57" W016°38'16" | Upper | Yes | 47.0 | 28.0 | 11.5 | 6.86 | 6.27 | 11.30 | Extremely high | 275.60 | 556.26 | 415.93 | 275.60 |
| | | | | | 13.0 | 32.0 | 10.5 | 19.82 | 13.98 | | | | | | |
| | | | | | 31.0 | 26.0 | 8.6 | 8.38 | 6.86 | | | | | | |
| | | | | | 31.0 | 34.0 | 27.9 | 20.79 | 18.07 | | | | | | |
| TF-01 | Retamares Mb D | N28°11' 57" W016°38'18" | Mid | Yes | 57.0 | 32.0 | 15.5 | 6.67 | 6.56 | 7.46 | Very high | 182.02 | 256.96 | 219.49 | 182.02 |
| | | | | | 32.0 | 30.0 | 13.7 | 11.21 | 9.54 | | | | | | |
| | | | | | 62.0 | 45.0 | 20.6 | 5.80 | 6.28 | | | | | | |

| Sample | Member & Unit | Grid Reference | Stratigrapy | Point Load Testing | Dimension A | Dimension B | Load | Is | Corrected Is(50) | Averaged Corrected Is(50) | Resistance to a point load classification | Quane & Russell (2003) PLTm to UCSp | PLTm to UCSp | PLTm to UCSp | PLTm to UCSp |
|---|---|---|---|---|---|---|---|---|---|---|---|---|---|---|---|
| | | | | Irregular lump | mm | mm | kN | $MN/m^2$ | $MN/m^2$ | $MN/m^2$ | Garnica et al. (1997) | MPa | MPa | MPa | MPa |
| | | | | | | | | Mpa | MPa | MPa | Carol (2008) | > 4 MPa (linear) | < 5 MPa (non-linear) | Averaged (2.5 - 6.5 MPa) | Final |
| TN-14 | Retamares Mb E | N28°12'48" W016°37'9" | Upper | Yes | 67.0 | 48.0 | 22.9 | 5.59 | 6.25 | 6.72 | Very high | 164.05 | 212.47 | 188.26 | 164.05 |
| | | | | | 66.0 | 46.0 | 16.2 | 4.19 | 4.62 | | | | | | |
| | | | | | 56.0 | 65.0 | 37.5 | 8.09 | 9.30 | | | | | | |
| TN-22 | Retamares Mb E | N28°12'50" W016°37'9" | Mid | Yes | 60.0 | 35.0 | 23.1 | 8.64 | 8.77 | 9.63 | Very high | 235.03 | 412.57 | 323.80 | 235.03 |
| | | | | | 56.0 | 30.0 | 12.5 | 5.84 | 5.64 | | | | | | |
| | | | | | 50.0 | 25.0 | 11.8 | 7.41 | 6.70 | | | | | | |
| | | | | | 38.0 | 35.0 | 32.2 | 19.01 | 17.42 | | | | | | |
| TN-15A | Retamares Mb E | N28°12'48" W016°37'9" | Base | Yes | 34.0 | 16.0 | 2.5 | 3.61 | 2.70 | 2.29 | High | 55.88 | 33.18 | 44.53 | 33.18 |
| | | | | | 28.0 | 25.0 | 2.1 | 2.36 | 1.87 | | | | | | |
| | | | | | 44.0 | 28.0 | 4.0 | 2.55 | 2.30 | | | | | | |
| TF-09 | Retamares Mb E | N28°12'37" W016°37'19.0" | Base | Yes | 72.0 | 38.0 | 11.9 | 3.42 | 3.68 | 4.95 | Very high | 120.66 | 122.33 | 121.49 | 121.49 |
| | | | | | 50.0 | 38.0 | 12.0 | 4.96 | 4.92 | | | | | | |
| | | | | | 83.0 | 55.0 | 10.7 | 1.84 | 2.23 | | | | | | |
| | | | | | 43.0 | 50.0 | 24.0 | 8.77 | 8.95 | | | | | | |
| TN-19 | Retamares Mb F | N28°12'35" W016°37'19" | Upper | Yes | 65.0 | 38.0 | 3.4 | 1.08 | 1.14 | 1.48 | High | 36.11 | 16.82 | 26.46 | 16.82 |
| | | | | | 55.0 | 42.0 | 1.8 | 0.61 | 0.63 | | | | | | |
| | | | | | 42.0 | 46.0 | 6.6 | 2.68 | 2.67 | | | | | | |
| TN-20 | Retamares Mb F | N28°12'34" W016°37'19" | Mid | Yes | 40.0 | 16.0 | 6.3 | 7.73 | 6.01 | 4.63 | Very high | 112.89 | 108.77 | 110.83 | 110.83 |
| | | | | | 48.0 | 24.0 | 4.0 | 2.73 | 2.42 | | | | | | |
| | | | | | 27.0 | 28.0 | 6.5 | 6.75 | 5.45 | | | | | | |
| TN-21 | Retamares Mb F | N28°12'37" W016°37'19" | Base | Yes | 74.0 | 35.0 | 0.0 | 0.01 | 0.01 | 0.39 | Moderate | 9.60 | 2.82 | 6.21 | 2.82 |
| | | | | | 32.0 | 28.0 | 0.2 | 0.18 | 0.15 | | | | | | |
| | | | | | 39.0 | 32.0 | 1.8 | 1.13 | 1.02 | | | | | | |
| TN-17 | Retamares Mb G | N28°12'26" W016°37'18" | Upper | Yes | 51.0 | 189.0 | 4.9 | 0.40 | 0.57 | 1.23 | High | 30.01 | 12.79 | 21.40 | 12.79 |
| | | | | | 48.0 | 38.0 | 3.7 | 1.59 | 1.57 | | | | | | |
| | | | | | 50.0 | 45.0 | 4.3 | 1.50 | 1.55 | | | | | | |
| TN-18 | Retamares Mb G | N28°12'29" W016°37'18" | Base | Yes | 50.0 | 36.0 | 0.3 | 0.13 | 0.13 | 0.19 | Low | 4.64 | 1.21 | 2.92 | 1.21 |
| | | | | | 37.0 | 25.0 | 0.1 | 0.08 | 0.07 | | | | | | |
| | | | | | 72.0 | 65.0 | 1.8 | 0.30 | 0.37 | | | | | | |
| VF-16/2 | Chasna (Sombrero) | N28°11'35.1" W016°38'42.8" | Upper | Yes | 84.0 | 46.0 | 10.2 | 2.07 | 2.41 | 2.82 | High | 68.81 | 46.63 | 57.72 | 46.63 |
| | | | | | 50.0 | 48.0 | 7.8 | 2.55 | 2.67 | | | | | | |
| | | | | | 84.0 | 70.0 | 19.8 | 2.64 | 3.38 | | | | | | |
| TN-08 | Chasna (Sombrero) | N28°11'42" W016°38'48" | Mid | Yes | 58.0 | 48.0 | 8.1 | 2.29 | 2.47 | 2.94 | High | 71.82 | 50.07 | 60.94 | 50.07 |
| | | | | | 60.0 | 48.0 | 8.4 | 2.29 | 2.50 | | | | | | |
| | | | | | 62.0 | 55.0 | 14.8 | 3.41 | 3.86 | | | | | | |
| TN-07 | Chasna (Sombrero) | N28°11'42" W016°38'48" | Base | Yes | 27.0 | 16.0 | 1.8 | 3.27 | 2.33 | 4.31 | Very high | 105.25 | 96.19 | 100.72 | 100.72 |
| | | | | | 31.0 | 20.0 | 2.6 | 3.29 | 2.54 | | | | | | |
| | | | | | 24.0 | 26.0 | 8.3 | 10.45 | 8.07 | | | | | | |
| TN-38 | Chasna (RLA) | N28°12'2" W016°39'35" | Upper | Yes | 58.0 | 32.0 | 10.2 | 4.32 | 4.26 | 5.56 | Very high | 135.75 | 150.90 | 143.32 | 135.75 |
| | | | | | 49.0 | 24.0 | 8.1 | 5.41 | 4.82 | | | | | | |
| | | | | | 40.0 | 38.0 | 15.6 | 8.06 | 7.61 | | | | | | |
| TN-36 | Chasna (RLA) | N28°12'02.8" W16°39'43.0" | Mid | Yes | 42.0 | 25.0 | 10.8 | 8.08 | 7.02 | 8.63 | Very high | 210.49 | 336.00 | 273.25 | 210.49 |
| | | | | | 37.0 | 20.0 | 8.1 | 8.69 | 6.90 | | | | | | |
| | | | | | 42.0 | 35.0 | 23.9 | 12.77 | 11.96 | | | | | | |
| VF-16/3 | Chasna (RLA) | N28°12'02.6" W016°39'43.7" | Base | Yes | 62.0 | 35.0 | 17.1 | 6.19 | 6.33 | 7.34 | Very high | 179.18 | 249.64 | 214.41 | 179.18 |
| | | | | | 62.0 | 20.0 | 17.3 | 10.96 | 9.88 | | | | | | |
| | | | | | 58.0 | 56.0 | 21.5 | 5.20 | 5.82 | | | | | | |
| TF-06 | Chasna (RLA) | N28°12'02.6" W016°39'43.7" | Base | Yes | 98.0 | 30.0 | 14.0 | 3.74 | 4.10 | 3.49 | Very high | 85.16 | 66.73 | 75.94 | 66.73 |
| | | | | | 81.0 | 18.0 | 6.8 | 3.66 | 3.43 | | | | | | |
| | | | | | 74.0 | 60.0 | 8.8 | 1.56 | 1.87 | | | | | | |
| | | | | | 57.0 | 55.0 | 16.4 | 4.11 | 4.56 | | | | | | |
| TN-12 | Chasna (LdlM) | N28°11'40" W016°37'46" | Upper | Yes | 32.0 | 50.0 | 5.0 | 2.45 | 2.34 | 3.20 | Very high | 78.02 | 57.53 | 67.77 | 57.53 |
| | | | | | 42.0 | 25.0 | 3.5 | 2.62 | 2.27 | | | | | | |
| | | | | | 32.0 | 25.0 | 5.1 | 5.01 | 4.09 | | | | | | |
| | | | | | 53.0 | 48.0 | 12.5 | 3.86 | 4.09 | | | | | | |
| TF-05 | Chasna Ridge | N28°19.9'26.1" W016°65.4'29.9" | - | Yes | 58.0 | 35.0 | 1.1 | 0.43 | 0.43 | 0.71 | Moderate | 17.41 | 5.99 | 11.70 | 5.99 |
| | | | | | 72.0 | 20.0 | 1.9 | 1.04 | 0.97 | | | | | | |
| | | | | | 74.0 | 65.0 | 3.7 | 0.60 | 0.74 | | | | | | |
| VF-18/4 VF-16/4 | Chasna Ridge | N28°11'58.6" W016°39'17.0" | - | - | *81.0* | *50.0* | *12.8* | *2.48* | *2.92* | 4.05 | Very high | 98.90 | 86.32 | 92.61 | 92.61 |
| | | | | | *60.0* | *48.0* | *10.7* | *2.92* | *3.18* | | | | | | |
| | | | | | *70.0* | *66.0* | *29.4* | *5.00* | *6.06* | | | | | | |
| TN-11 | Chasna Ridge | N28°12'3" W016°39'29" | - | Yes | 44.0 | 10.0 | 2.5 | 4.46 | 3.19 | 4.16 | Very high | 101.42 | 90.18 | 95.80 | 95.80 |
| | | | | | 40.0 | 12.0 | 3.0 | 4.91 | 3.51 | | | | | | |
| | | | | | 28.0 | 36.0 | 8.6 | 6.70 | 5.77 | | | | | | |
| TN-04 | Almendros (RLA) | N28°12'1" W016°39'42" | Base | Yes | 32.0 | 25.0 | 3.2 | 3.14 | 2.57 | 2.19 | High | 53.52 | 30.96 | 42.24 | 30.96 |
| | | | | | 35.0 | 26.0 | 2.5 | 2.16 | 1.81 | | | | | | |
| | | | | | 57.0 | 56.0 | 8.0 | 1.97 | 2.20 | | | | | | |

| Sample | Member & Unit | Grid Reference | Stratigrapy | Point Load Testing | Dimension A | Dimension B | Load | Is | Corrected Is(50) | Averaged Corrected Is(50) | Resistance to a point load classification | Quane & Russell (2003) | | | |
|---|---|---|---|---|---|---|---|---|---|---|---|---|---|---|---|
| | | | | Irregular lump | mm | mm | kN | $NM/m^2$ | $MN/m^2$ | $MN/m^2$ | Garnica et al. (1997) | PLTm to UCSp | PLTm to UCSp | PLTm to UCSp | PLTm to UCSp |
| | | | | | | | | Mpa | MPa | MPa | Carol (2008) | MPa > 4 MPa (linear) | MPa < 5 MPa (non-linear) | MPa Averaged (2.5 - 6.5 MPa) | MPa Final |
| TF-08 | Guajara Mb 2 | N28°13'03" W016°36'42" | Upper | Yes | 70.0 | 48.0 | 2.8 | 0.65 | 0.74 | 1.86 | High | 45.47 | 23.93 | 34.70 | 23.93 |
| | | | | | 60.0 | 35.0 | 2.6 | 0.97 | 0.99 | | | | | | |
| | | | | | 62.0 | 55.0 | 14.8 | 3.41 | 3.86 | | | | | | |
| TN-30 | Guajara Mb 3 | N28°12'49" W016°36'50" | Upper | Yes | 37.0 | 22.0 | 4.1 | 3.96 | 3.24 | 4.53 | Very high | 110.61 | 104.94 | 107.78 | 107.78 |
| | | | | | 28.0 | 24.0 | 5.7 | 6.66 | 5.23 | | | | | | |
| | | | | | 54.0 | 24.0 | 9.3 | 5.64 | 5.13 | | | | | | |
| TN-28 | Guajara Mb 3 | N28°12'44" W016°36'51" | Mid | Yes | 37.0 | 20.0 | 1.2 | 1.27 | 1.02 | 4.41 | Very high | 107.52 | 99.85 | 103.69 | 103.69 |
| | | | | | 40.0 | 10.0 | 4.2 | 8.25 | 5.77 | | | | | | |
| | | | | | 23.0 | 26.0 | 6.4 | 8.41 | 6.43 | | | | | | |
| TN-29 | Guajara Mb 3 | N28°12'41" W016°36'55" | Base | Yes | 62.0 | 40.0 | 45.0 | 14.25 | 15.02 | 12.98 | Extremely high | 316.63 | 723.32 | 519.97 | 316.63 |
| | | | | | 60.0 | 40.0 | 45.0 | 14.73 | 15.41 | | | | | | |
| | | | | | 60.0 | 58.0 | 33.1 | 7.47 | 8.50 | | | | | | |

Data worksheets from testing carried out at MATtest Ltd laboratory, Glasgow for density and porosity determination of samples, using ISRM (1981) suggested methods.

**Calculations:**

Bulk volume $V = M_{sat} - M_{sub}/\rho_w$
Pore volume $V_v = M_{sat} - M_s/\rho_w$
Porosity $\eta = \left(\frac{V_v}{V}\right) * 100$
Dry Density $\rho_d = M_S/V$

**POROSITY/DENSITY - SATURATION & BUOYANCY**
**ISRM - SUGGESTED METHODS**

MATtest Limited

| | | | | | |
|---|---|---|---|---|---|
| Prepared By | GW | Date | 06/02/2020 | Project Number | 20/127 |
| Tested By | GW | Date | 07/02/2020 | | |
| Approved By | BH | Date | 07/02/2020 | | |

| | | | | |
|---|---|---|---|---|
| Borehole | | - | - | - |
| Sample | | TN-20 | TF-08 | VF-16/1 |
| Depth | m | - | - | - |
| Sample ID | | 1 | 2 | 3 |
| Initial sample mass | g | 497.50 | 498.10 | 480.80 |
| Vacuum start time | | 08:00 | 08:00 | 08:00 |
| Vacuum end time | | 09:00 | 09:00 | 09:00 |
| Submerged sample mass $M_{sub}$ | g | 289.60 | 279.90 | 275.80 |
| Container ID | | ST191 | ST155 | ST154 |
| Container mass ***A*** | g | 218.80 | 225.80 | 228.50 |
| Sample & container mass ***B*** | g | 725.10 | 769.50 | 723.30 |
| Oven dry sample & container mass ***C*** | g | 701.00 | 725.30 | 707.00 |
| Saturated Surface Dry Mass $M_{sat}$ | g | 506.30 | 543.70 | 494.80 |
| Grain Weight $M_s$ | g | 482.20 | 499.50 | 478.50 |
| Bulk Volume ***V*** | $m^3$ | 216.70 | 263.80 | 219.00 |
| Pore Volume $V_r$ | $m^3$ | 24.10 | 44.20 | 16.30 |
| Porosity ***n*** | % | 11.1 | 16.8 | 7.4 |
| Dry Density ***pd*** | $kg/m^3$ | 2230 | 1890 | 2180 |

## POROSITY/DENSITY - SATURATION & BUOYANCY
## ISRM - SUGGESTED METHODS

MATtest Limited

| | | | | | |
|---|---|---|---|---|---|
| Prepared By | GW | Date | 06/02/2020 | Project Number | 20/127 |
| Tested By | GW | Date | 07/02/2020 | | |
| Approved By | BH | Date | 07/02/2020 | | |

| | | | | |
|---|---|---|---|---|
| Borehole | | - | - | - |
| Sample | | VF16-2 | TN01 | TF09 |
| Depth | m | - | - | - |
| Sample ID | | 4 | 5 | 6 |
| Initial sample mass | g | 509.80 | 488.20 | 497.00 |
| Vacuum start time | | 09:00 | 09:00 | 09:00 |
| Vacuum end time | | 10:00 | 10:00 | 10:00 |
| Submerged sample mass $M_{sub}$ | g | 293.00 | 294.70 | 286.90 |
| Container ID | | ST192 | ST194 | ST193 |
| Container mass ***A*** | g | 230.40 | 223.20 | 222.90 |
| Sample & container mass ***B*** | g | 763.40 | 712.80 | 731.30 |
| Oven dry sample & container mass ***C*** | g | 735.20 | 709.90 | 719.20 |
| Saturated Surface Dry Mass $M_{sat}$ | g | 533.00 | 489.60 | 508.40 |
| Grain Weight $M_s$ | g | 504.80 | 486.70 | 496.30 |
| Bulk Volume ***V*** | $m^3$ | 240.00 | 194.90 | 221.50 |
| Pore Volume $V_r$ | $m^3$ | 28.20 | 2.90 | 12.10 |
| Porosity ***n*** | % | 11.8 | 1.5 | 5.5 |
| Dry Density ***pd*** | $kg/m^3$ | 2100 | 2500 | 2240 |

**POROSITY/DENSITY - SATURATION & BUOYANCY**
**ISRM - SUGGESTED METHODS**

MATtest Limited

| | | | | | |
|---|---|---|---|---|---|
| Prepared By | GW | Date | 06/02/2020 | Project Number | 20/127 |
| Tested By | GW | Date | 07/02/2020 | | |
| Approved By | BH | Date | 07/02/2020 | | |

| | | | | |
|---|---|---|---|---|
| Borehole | | - | - | - |
| Sample | | TN45 | TN31 | TN10 |
| Depth | m | - | - | - |
| Sample ID | | 4 | 5 | 6 |
| Initial sample mass | g | 150.20 | 130.10 | 171.00 |
| Vacuum start time | | 13:00 | 13:00 | 13:00 |
| Vacuum end time | | 14:00 | 14:00 | 14:00 |
| Submerged sample mass $M_{sub}$ | g | 94.30 | 77.10 | 97.20 |
| Container ID | | ST014 | ST015 | ST016 |
| Container mass ***A*** | g | 231.80 | 227.90 | 228.50 |
| Sample & container mass ***B*** | g | 387.50 | 358.20 | 403.60 |
| Oven dry sample & container mass ***C*** | g | 380.60 | 357.70 | 399.10 |
| Saturated Surface Dry Mass $M_{sat}$ | g | 155.70 | 130.30 | 175.10 |
| Grain Weight $M_s$ | g | 148.80 | 129.80 | 170.60 |
| Bulk Volume ***V*** | $m^3$ | 61.40 | 53.20 | 77.90 |
| Pore Volume $V_r$ | $m^3$ | 6.90 | 0.50 | 4.50 |
| Porosity ***n*** | % | 11.2 | 0.9 | 5.8 |
| Dry Density ***pd*** | $kg/m^3$ | 2420 | 2440 | 2190 |

## POROSITY/DENSITY - SATURATION & BUOYANCY
## ISRM - SUGGESTED METHODS

MATtest Limited

| | | | | | |
|---|---|---|---|---|---|
| Prepared By | GW | Date | 05/02/2020 | Project Number | 20/127 |
| Tested By | GW | Date | 06/02/2020 | | |
| Approved By | BH | Date | 07/02/2020 | | |

| | | | | |
|---|---|---|---|---|
| Borehole | | - | - | - |
| Sample | | TN44 | TN24 | TN25 |
| Depth | m | - | - | - |
| Sample ID | | 4 | 5 | 6 |
| Initial sample mass | g | 43.00 | 98.30 | 179.00 |
| Vacuum start time | | 11:00 | 11:00 | 11:00 |
| Vacuum end time | | 12:00 | 12:00 | 12:00 |
| Submerged sample mass $M_{sub}$ | g | 18.70 | 59.20 | 103.20 |
| Container ID | | ST168 | ST169 | ST170 |
| Container mass ***A*** | g | 228.60 | 227.30 | 230.50 |
| Sample & container mass ***B*** | g | 293.90 | 328.40 | 417.20 |
| Oven dry sample & container mass ***C*** | g | 269.10 | 324.50 | 405.60 |
| Saturated Surface Dry Mass $M_{sat}$ | g | 65.30 | 101.10 | 186.70 |
| Grain Weight $M_s$ | g | 40.50 | 97.20 | 175.10 |
| Bulk Volume ***V*** | $m^3$ | 46.60 | 41.90 | 83.50 |
| Pore Volume $V_r$ | $m^3$ | 24.80 | 3.90 | 11.60 |
| Porosity ***n*** | % | 53.2 | 9.3 | 13.9 |
| Dry Density ***pd*** | $kg/m^3$ | 870 | 2320 | 2100 |

**POROSITY/DENSITY - SATURATION & BUOYANCY**
**ISRM - SUGGESTED METHODS**

MATtest Limited

| | | | | | |
|---|---|---|---|---|---|
| Prepared By | GW | Date | 05/02/2020 | Project Number | 20/127 |
| Tested By | GW | Date | 06/02/2020 | | |
| Approved By | BH | Date | 07/02/2020 | | |

| | | | | |
|---|---|---|---|---|
| Borehole | | - | - | - |
| Sample | | TN42 | TN32 | TN46 |
| Depth | m | - | - | - |
| Sample ID | | 4 | 5 | 6 |
| Initial sample mass | g | 113.10 | 89.90 | 107.90 |
| Vacuum start time | | 09:00 | 09:00 | 09:00 |
| Vacuum end time | | 10:00 | 10:00 | 10:00 |
| Submerged sample mass $M_{sub}$ | g | 70.00 | 56.00 | 66.70 |
| Container ID | | ST162 | ST163 | ST164 |
| Container mass ***A*** | g | 229.60 | 234.50 | 231.10 |
| Sample & container mass ***B*** | g | 343.10 | 327.70 | 339.80 |
| Oven dry sample & container mass ***C*** | g | 342.10 | 323.40 | 338.30 |
| Saturated Surface Dry Mass $M_{sat}$ | g | 113.50 | 93.20 | 108.70 |
| Grain Weight $M_s$ | g | 112.50 | 88.90 | 107.20 |
| Bulk Volume ***V*** | $m^3$ | 43.50 | 37.20 | 42.00 |
| Pore Volume $V_r$ | $m^3$ | 1.00 | 4.30 | 1.50 |
| Porosity ***n*** | % | 2.3 | 11.6 | 3.6 |
| Dry Density ***pd*** | $kg/m^3$ | 2590 | 2390 | 2550 |

**POROSITY/DENSITY - SATURATION & BUOYANCY**
**ISRM - SUGGESTED METHODS**

MATtest Limited

| | | | | | |
|---|---|---|---|---|---|
| Prepared By | GW | Date | 06/02/2020 | Project Number | 20/127 |
| Tested By | GW | Date | 07/02/2020 | | |
| Approved By | BH | Date | 07/02/2020 | | |

| | | | | |
|---|---|---|---|---|
| Borehole | | - | - | - |
| Sample | | TN41 | TF03 | TF01 |
| Depth | m | - | - | - |
| Sample ID | | 1 | 2 | 3 |
| Initial sample mass | g | 216.20 | 495.90 | 519.90 |
| Vacuum start time | | 10:00 | 10:00 | 10:00 |
| Vacuum end time | | 11:00 | 11:00 | 11:00 |
| Submerged sample mass $M_{sub}$ | g | 124.80 | 284.50 | 313.70 |
| Container ID | | ST195 | ST196 | ST197 |
| Container mass ***A*** | g | 229.20 | 228.40 | 227.30 |
| Sample & container mass ***B*** | g | 462.50 | 744.80 | 748.50 |
| Oven dry sample & container mass ***C*** | g | 444.30 | 716.20 | 745.70 |
| Saturated Surface Dry Mass $M_{sat}$ | g | 233.30 | 516.40 | 521.20 |
| Grain Weight $M_s$ | g | 215.10 | 487.80 | 518.40 |
| Bulk Volume ***V*** | $m^3$ | 108.50 | 231.90 | 207.50 |
| Pore Volume $V_r$ | $m^3$ | 18.20 | 28.60 | 2.80 |
| Porosity ***n*** | % | 16.8 | 12.3 | 1.3 |
| Dry Density ***pd*** | $kg/m^3$ | 1980 | 2100 | 2500 |

**POROSITY/DENSITY - SATURATION & BUOYANCY**
**ISRM - SUGGESTED METHODS**

MATtest Limited

| | | | | | |
|---|---|---|---|---|---|
| Prepared By | GW | Date | 05/02/2020 | Project Number | 20/127 |
| Tested By | GW | Date | 06/02/2020 | | |
| Approved By | BH | Date | 07/02/2020 | | |

| | | | | |
|---|---|---|---|---|
| Borehole | | - | - | - |
| Sample | | TN33 | TN19 | TN48 |
| Depth | m | - | - | - |
| Sample ID | | 1 | 2 | 3 |
| Initial sample mass | g | 48.90 | 268.80 | 84.50 |
| Vacuum start time | | 08:00 | 08:00 | 08:00 |
| Vacuum end time | | 09:00 | 09:00 | 09:00 |
| Submerged sample mass $M_{sub}$ | g | 31.20 | 163.90 | 51.70 |
| Container ID | | ST161 | ST054 | ST055 |
| Container mass ***A*** | g | 229.40 | 229.60 | 230.20 |
| Sample & container mass ***B*** | g | 273.20 | 528.50 | 315.10 |
| Oven dry sample & container mass ***C*** | g | 272.70 | 495.60 | 313.80 |
| Saturated Surface Dry Mass $M_{sat}$ | g | 43.80 | 298.90 | 84.90 |
| Grain Weight $M_s$ | g | 43.30 | 266.00 | 83.60 |
| Bulk Volume ***V*** | $m^3$ | 12.60 | 135.00 | 33.20 |
| Pore Volume $V_r$ | $m^3$ | 0.50 | 32.90 | 1.30 |
| Porosity ***n*** | % | 4.0 | 24.4 | 3.9 |
| Dry Density ***pd*** | $kg/m^3$ | 3440 | 1970 | 2520 |

**POROSITY/DENSITY - SATURATION & BUOYANCY**
**ISRM - SUGGESTED METHODS**

MATtest Limited

| | | | | | |
|---|---|---|---|---|---|
| Prepared By | GW | Date | 06/02/2020 | Project Number | 20/127 |
| Tested By | GW | Date | 07/02/2020 | | |
| Approved By | BH | Date | 07/02/2020 | | |

| | | | | |
|---|---|---|---|---|
| Borehole | | - | - | - |
| Sample | | TN28 | TN12 | TN47 |
| Depth | m | - | - | - |
| Sample ID | | 1 | 2 | 3 |
| Initial sample mass | g | 33.80 | 223.30 | 42.10 |
| Vacuum start time | | 16:00 | 16:00 | 16:00 |
| Vacuum end time | | 17:00 | 17:00 | 17:00 |
| Submerged sample mass $M_{sub}$ | g | 20.00 | 140.30 | 24.90 |
| Container ID | | ST053 | ST052 | ST051 |
| Container mass ***A*** | g | 224.40 | 224.70 | 232.60 |
| Sample & container mass ***B*** | g | 259.30 | 449.90 | 275.00 |
| Oven dry sample & container mass ***C*** | g | 257.90 | 447.60 | 274.60 |
| Saturated Surface Dry Mass $M_{sat}$ | g | 34.90 | 225.20 | 42.40 |
| Grain Weight $M_s$ | g | 33.50 | 222.90 | 42.00 |
| Bulk Volume ***V*** | $m^3$ | 14.90 | 84.90 | 17.50 |
| Pore Volume $V_r$ | $m^3$ | 1.40 | 2.30 | 0.40 |
| Porosity ***n*** | % | 9.4 | 2.7 | 2.3 |
| Dry Density ***pd*** | $kg/m^3$ | 2250 | 2630 | 2400 |

**POROSITY/DENSITY - SATURATION & BUOYANCY**
**ISRM - SUGGESTED METHODS**

MATtest Limited

| | | | | | |
|---|---|---|---|---|---|
| Prepared By | GW | Date | 06/02/2020 | Project Number | 20/127 |
| Tested By | GW | Date | 07/02/2020 | | |
| Approved By | BH | Date | 07/02/2020 | | |

| | | | | |
|---|---|---|---|---|
| Borehole | | - | - | - |
| Sample | | TN27 | TN30 | TN38 |
| Depth | m | - | - | - |
| Sample ID | | 4 | 5 | 6 |
| Initial sample mass | g | 99.20 | 94.40 | 84.70 |
| Vacuum start time | | 15:00 | 15:00 | 15:00 |
| Vacuum end time | | 16:00 | 16:00 | 16:00 |
| Submerged sample mass $M_{sub}$ | g | 58.60 | 55.60 | 49.30 |
| Container ID | | ST059 | ST060 | ST017 |
| Container mass ***A*** | g | 226.20 | 231.00 | 226.80 |
| Sample & container mass ***B*** | g | 327.30 | 326.80 | 312.20 |
| Oven dry sample & container mass ***C*** | g | 325.20 | 325.30 | 311.30 |
| Saturated Surface Dry Mass $M_{sat}$ | g | 101.10 | 95.80 | 85.40 |
| Grain Weight $M_s$ | g | 99.00 | 94.30 | 84.50 |
| Bulk Volume ***V*** | $m^3$ | 42.50 | 40.20 | 36.10 |
| Pore Volume $V_r$ | $m^3$ | 2.10 | 1.50 | 0.90 |
| Porosity ***n*** | % | 4.9 | 3.7 | 2.5 |
| Dry Density ***pd*** | $kg/m^3$ | 2330 | 2350 | 2340 |

**POROSITY/DENSITY - SATURATION & BUOYANCY**
**ISRM - SUGGESTED METHODS**

MATtest Limited

| | | | | | |
|---|---|---|---|---|---|
| Prepared By | GW | Date | 05/02/2020 | Project Number | 20/127 |
| Tested By | GW | Date | 06/02/2020 | | |
| Approved By | BH | Date | 07/02/2020 | | |

| | | | | |
|---|---|---|---|---|
| Borehole | | - | - | - |
| Sample | | TN26 | TN04 | TN35 |
| Depth | m | - | - | - |
| Sample ID | | 1 | 2 | 3 |
| Initial sample mass | g | 49.10 | 93.90 | 49.20 |
| Vacuum start time | | 10:00 | 10:00 | 10:00 |
| Vacuum end time | | 11:00 | 11:00 | 11:00 |
| Submerged sample mass $M_{sub}$ | g | 29.00 | 56.90 | 30.00 |
| Container ID | | ST165 | ST166 | ST167 |
| Container mass ***A*** | g | 235.20 | 233.70 | 229.20 |
| Sample & container mass ***B*** | g | 286.50 | 330.80 | 278.50 |
| Oven dry sample & container mass ***C*** | g | 283.10 | 326.80 | 278.00 |
| Saturated Surface Dry Mass $M_{sat}$ | g | 51.30 | 97.10 | 49.30 |
| Grain Weight $M_s$ | g | 47.90 | 93.10 | 48.80 |
| Bulk Volume ***V*** | $m^3$ | 22.30 | 40.20 | 19.30 |
| Pore Volume $V_r$ | $m^3$ | 3.40 | 4.00 | 0.50 |
| Porosity ***n*** | % | 15.2 | 10.0 | 2.6 |
| Dry Density ***pd*** | $kg/m^3$ | 2150 | 2320 | 2530 |

**POROSITY/DENSITY - SATURATION & BUOYANCY**
**ISRM - SUGGESTED METHODS**

MATtest Limited

| | | | | | |
|---|---|---|---|---|---|
| Prepared By | GW | Date | 05/02/2020 | Project Number | 20/127 |
| Tested By | GW | Date | 06/02/2020 | | |
| Approved By | BH | Date | 07/02/2020 | | |

| | | | | |
|---|---|---|---|---|
| Borehole | | - | - | - |
| Sample | | TN18 | TN43 | VF16/3 |
| Depth | m | - | - | - |
| Sample ID | | 4 | 5 | 6 |
| Initial sample mass | g | 215.90 | 283.00 | 377.70 |
| Vacuum start time | | 13:00 | 13:00 | 13:00 |
| Vacuum end time | | 14:00 | 14:00 | 14:00 |
| Submerged sample mass $M_{sub}$ | g | 95.80 | 162.70 | 221.90 |
| Container ID | | ST184 | ST185 | ST186 |
| Container mass ***A*** | g | 227.70 | 227.30 | 228.00 |
| Sample & container mass ***B*** | g | 493.40 | 526.30 | 608.30 |
| Oven dry sample & container mass ***C*** | g | 424.40 | 505.80 | 603.80 |
| Saturated Surface Dry Mass $M_{sat}$ | g | 265.70 | 299.00 | 380.30 |
| Grain Weight $M_s$ | g | 196.70 | 278.50 | 375.80 |
| Bulk Volume ***V*** | $m^3$ | 169.90 | 136.30 | 158.40 |
| Pore Volume $V_r$ | $m^3$ | 69.00 | 20.50 | 4.50 |
| Porosity ***n*** | % | 40.6 | 15.0 | 2.8 |
| Dry Density ***pd*** | $kg/m^3$ | 1160 | 2040 | 2370 |

**POROSITY/DENSITY - SATURATION & BUOYANCY**
**ISRM - SUGGESTED METHODS**

MATtest Limited

| | | | | | |
|---|---|---|---|---|---|
| Prepared By | GW | Date | 05/02/2020 | Project Number | 20/127 |
| Tested By | GW | Date | 06/02/2020 | | |
| Approved By | BH | Date | 07/02/2020 | | |

| | | | | |
|---|---|---|---|---|
| Borehole | | - | - | - |
| Sample | | TN14 | TN29 | TF06 |
| Depth | m | - | - | - |
| Sample ID | | 1 | 2 | 3 |
| Initial sample mass | g | 206.00 | 253.00 | 504.70 |
| Vacuum start time | | 12:00 | 12:00 | 12:00 |
| Vacuum end time | | 13:00 | 13:00 | 13:00 |
| Submerged sample mass $M_{sub}$ | g | 125.40 | 156.90 | 304.50 |
| Container ID | | ST181 | ST182 | ST183 |
| Container mass ***A*** | g | 233.40 | 230.00 | 229.80 |
| Sample & container mass ***B*** | g | 439.50 | 483.30 | 737.50 |
| Oven dry sample & container mass ***C*** | g | 435.30 | 482.00 | 727.80 |
| Saturated Surface Dry Mass $M_{sat}$ | g | 206.10 | 253.30 | 507.70 |
| Grain Weight $M_s$ | g | 201.90 | 252.00 | 498.00 |
| Bulk Volume ***V*** | $m^3$ | 80.70 | 96.40 | 203.20 |
| Pore Volume $V_r$ | $m^3$ | 4.20 | 1.30 | 9.70 |
| Porosity ***n*** | % | 5.2 | 1.3 | 4.8 |
| Dry Density ***pd*** | $kg/m^3$ | 2500 | 2610 | 2450 |

**POROSITY/DENSITY - SATURATION & BUOYANCY**
**ISRM - SUGGESTED METHODS**

MATtest Limited

| | | | | | |
|---|---|---|---|---|---|
| Prepared By | GW | Date | 05/02/2020 | Project Number | 20/127 |
| Tested By | GW | Date | 06/02/2020 | | |
| Approved By | BH | Date | 07/02/2020 | | |

| | | | | |
|---|---|---|---|---|
| Borehole | | - | - | - |
| Sample | | TN08 | TN40 | TN23 |
| Depth | m | - | - | - |
| Sample ID | | 1 | 2 | 3 |
| Initial sample mass | g | 238.70 | 61.70 | 273.50 |
| Vacuum start time | | 14:00 | 14:00 | 14:00 |
| Vacuum end time | | 15:00 | 15:00 | 15:00 |
| Submerged sample mass $M_{sub}$ | g | 138.20 | 38.70 | 159.60 |
| Container ID | | ST187 | ST188 | ST189 |
| Container mass ***A*** | g | 229.80 | 233.70 | 229.50 |
| Sample & container mass ***B*** | g | 474.50 | 295.70 | 512.20 |
| Oven dry sample & container mass ***C*** | g | 464.00 | 294.90 | 501.10 |
| Saturated Surface Dry Mass $M_{sat}$ | g | 244.70 | 62.00 | 282.70 |
| Grain Weight $M_s$ | g | 234.20 | 61.20 | 271.60 |
| Bulk Volume ***V*** | $m^3$ | 106.50 | 23.30 | 123.10 |
| Pore Volume $V_r$ | $m^3$ | 10.50 | 0.80 | 11.10 |
| Porosity ***n*** | % | 9.9 | 3.4 | 9.0 |
| Dry Density ***pd*** | $kg/m^3$ | 2200 | 2630 | 2210 |

**POROSITY/DENSITY - SATURATION & BUOYANCY**
**ISRM - SUGGESTED METHODS**

MATtest Limited

| | | | | | |
|---|---|---|---|---|---|
| Prepared By | GW | Date | 05/02/2020 | Project Number | 20/127 |
| Tested By | GW | Date | 06/02/2020 | | |
| Approved By | BH | Date | 07/02/2020 | | |

| | | | | |
|---|---|---|---|---|
| Borehole | | - | - | |
| Sample | | TN06 | TN09 | |
| Depth | m | - | - | |
| Sample ID | | 4 | 5 | |
| Initial sample mass | g | 229.40 | 43.30 | |
| Vacuum start time | | 15:00 | 15:00 | |
| Vacuum end time | | 16:00 | 16:00 | |
| Submerged sample mass $M_{sub}$ | g | 136.50 | 24.30 | |
| Container ID | | ST190 | ST157 | |
| Container mass ***A*** | g | 220.10 | 229.80 | |
| Sample & container mass ***B*** | g | 460.30 | 273.00 | |
| Oven dry sample & container mass ***C*** | g | 446.70 | 272.80 | |
| Saturated Surface Dry Mass $M_{sat}$ | g | 240.20 | 43.20 | |
| Grain Weight $M_s$ | g | 226.60 | 43.00 | |
| Bulk Volume ***V*** | $m^3$ | 103.70 | 18.90 | |
| Pore Volume $V_r$ | $m^3$ | 13.60 | 0.20 | |
| Porosity ***n*** | % | 13.1 | 1.1 | |
| Dry Density ***pd*** | $kg/m^3$ | 2190 | 2280 | |

**POROSITY/DENSITY - SATURATION & BUOYANCY**
**ISRM - SUGGESTED METHODS**

MATtest Limited

| | | | | | |
|---|---|---|---|---|---|
| Prepared By | GW | Date | 06/02/2020 | Project Number | 20/127 |
| Tested By | GW | Date | 07/02/2020 | | |
| Approved By | BH | Date | 07/02/2020 | | |

| | | | | |
|---|---|---|---|---|
| Borehole | | - | - | - |
| Sample | | TN05 | TN22 | TN07 |
| Depth | m | - | - | - |
| Sample ID | | 4 | 5 | 6 |
| Initial sample mass | g | 197.40 | 119.00 | 25.10 |
| Vacuum start time | | 17:00 | 17:00 | 17:00 |
| Vacuum end time | | 18:00 | 18:00 | 18:00 |
| Submerged sample mass $M_{sub}$ | g | 115.20 | 72.00 | 13.10 |
| Container ID | | ST093 | ST056 | ST057 |
| Container mass ***A*** | g | 233.10 | 232.50 | 230.00 |
| Sample & container mass ***B*** | g | 431.30 | 351.80 | 256.30 |
| Oven dry sample & container mass ***C*** | g | 429.00 | 349.50 | 254.50 |
| Saturated Surface Dry Mass $M_{sat}$ | g | 198.20 | 119.30 | 26.30 |
| Grain Weight $M_s$ | g | 195.90 | 117.00 | 24.50 |
| Bulk Volume ***V*** | $m^3$ | 83.00 | 47.30 | 13.20 |
| Pore Volume $V_r$ | $m^3$ | 2.30 | 2.30 | 1.80 |
| Porosity ***n*** | % | 2.8 | 4.9 | 13.6 |
| Dry Density ***pd*** | $kg/m^3$ | 2360 | 2470 | 1860 |

**POROSITY/DENSITY - SATURATION & BUOYANCY**
**ISRM - SUGGESTED METHODS**

MATtest Limited

| | | | | | |
|---|---|---|---|---|---|
| Prepared By | GW | Date | 06/02/2020 | Project Number | 20/127 |
| Tested By | GW | Date | 07/02/2020 | | |
| Approved By | BH | Date | 07/02/2020 | | |

| | | | | |
|---|---|---|---|---|
| Borehole | | - | - | - |
| Sample | | TN02 | TN17 | TN03 |
| Depth | m | - | - | - |
| Sample ID | | 1 | 2 | 3 |
| Initial sample mass | g | 271.80 | 204.20 | 55.70 |
| Vacuum start time | | 14:00 | 14:00 | 14:00 |
| Vacuum end time | | 15:00 | 15:00 | 15:00 |
| Submerged sample mass $M_{sub}$ | g | 160.40 | 123.10 | 33.80 |
| Container ID | | ST018 | ST019 | ST020 |
| Container mass ***A*** | g | 223.40 | 230.70 | 228.80 |
| Sample & container mass ***B*** | g | 558.80 | 453.90 | 285.40 |
| Oven dry sample & container mass ***C*** | g | 505.60 | 433.30 | 284.40 |
| Saturated Surface Dry Mass $M_{sat}$ | g | 335.40 | 223.20 | 56.60 |
| Grain Weight $M_s$ | g | 282.20 | 202.60 | 55.60 |
| Bulk Volume ***V*** | $m^3$ | 175.00 | 100.10 | 22.80 |
| Pore Volume $V_r$ | $m^3$ | 53.20 | 20.60 | 1.00 |
| Porosity ***n*** | % | 30.4 | 20.6 | 4.4 |
| Dry Density ***pd*** | $kg/m^3$ | 1610 | 2020 | 2440 |

**POROSITY/DENSITY - SATURATION & BUOYANCY**
**ISRM - SUGGESTED METHODS**

MATtest Limited

| | | | | | |
|---|---|---|---|---|---|
| Prepared By | GW | Date | 06/02/2020 | Project Number | 20/127 |
| Tested By | GW | Date | 07/02/2020 | | |
| Approved By | BH | Date | 07/02/2020 | | |

| | | | | |
|---|---|---|---|---|
| Borehole | | - | - | - |
| Sample | | TF05 | TN15A | TN21 |
| Depth | m | - | - | - |
| Sample ID | | 1 | 2 | 3 |
| Initial sample mass | g | 515.00 | 51.00 | 76.10 |
| Vacuum start time | | 12:00 | 12:00 | 12:00 |
| Vacuum end time | | 13:00 | 13:00 | 13:00 |
| Submerged sample mass $M_{sub}$ | g | 301.40 | 28.90 | 35.20 |
| Container ID | | ST011 | ST012 | ST013 |
| Container mass ***A*** | g | 227.30 | 231.80 | 227.50 |
| Sample & container mass ***B*** | g | 764.60 | 285.60 | 334.20 |
| Oven dry sample & container mass ***C*** | g | 736.70 | 282.90 | 303.30 |
| Saturated Surface Dry Mass $M_{sat}$ | g | 537.30 | 53.80 | 106.70 |
| Grain Weight $M_s$ | g | 509.40 | 51.10 | 75.80 |
| Bulk Volume ***V*** | $m^3$ | 235.90 | 24.90 | 71.50 |
| Pore Volume $V_r$ | $m^3$ | 27.90 | 2.70 | 30.90 |
| Porosity ***n*** | % | 11.8 | 10.8 | 43.2 |
| Dry Density ***pd*** | $kg/m^3$ | 2160 | 2050 | 1060 |

**POROSITY/DENSITY - SATURATION & BUOYANCY**
**ISRM - SUGGESTED METHODS**

MATtest Limited

| | | | | | |
|---|---|---|---|---|---|
| Prepared By | GW | Date | 06/02/2020 | Project Number | 20/127 |
| Tested By | GW | Date | 07/02/2020 | | |
| Approved By | BH | Date | 07/02/2020 | | |

| | | | | |
|---|---|---|---|---|
| Borehole | | - | - | - |
| Sample | | TF04 | TF02 | VF16-5 |
| Depth | m | - | - | - |
| Sample ID | | 4 | 5 | 6 |
| Initial sample mass | g | 515.00 | 518.20 | 487.30 |
| Vacuum start time | | 11:00 | 11:00 | 11:00 |
| Vacuum end time | | 12:00 | 12:00 | 12:00 |
| Submerged sample mass $M_{sub}$ | g | 315.20 | 301.60 | 279.20 |
| Container ID | | ST198 | ST199 | ST200 |
| Container mass ***A*** | g | 224.20 | 232.80 | 237.80 |
| Sample & container mass ***B*** | g | 739.70 | 754.90 | 740.90 |
| Oven dry sample & container mass ***C*** | g | 737.70 | 747.00 | 720.50 |
| Saturated Surface Dry Mass $M_{sat}$ | g | 515.50 | 522.10 | 503.10 |
| Grain Weight $M_s$ | g | 513.50 | 514.20 | 482.70 |
| Bulk Volume ***V*** | $m^3$ | 200.30 | 220.50 | 223.90 |
| Pore Volume $V_r$ | $m^3$ | 2.00 | 7.90 | 20.40 |
| Porosity ***n*** | % | 1.0 | 3.6 | 9.1 |
| Dry Density ***pd*** | $kg/m^3$ | 2560 | 2330 | 2160 |

# **Appendix III**. Oblateness measurement dataset

| Member | Unit | Sample | 1 | | | 2 | | | 3 | | | 4 | | | 5 | | | 6 | | | 7 | | | 8 | | | 9 | | | 10 | | |
|---|---|---|---|---|---|---|---|---|---|---|---|---|---|---|---|---|---|---|---|---|---|---|---|---|---|---|---|---|---|---|---|---|
| | | | a axis | c axis | OB | a axis | c axis | OB | a axis | c axis | OB | a axis | c axis | OB | a axis | c axis | OB | a axis | c axis | OB | a axis | c axis | OB | a axis | c axis | OB | a axis | c axis | OB | a axis | c axis | OB |
| Atravesado | 1 | TN-48 | - | - | - | - | - | - | - | - | - | - | - | - | - | - | - | - | - | - | - | - | - | - | - | - | - | - | - | - | - | - |
| | | TN-47 | 1.7 | 0.3 | 0.82 | 1.2 | 0.3 | 0.75 | 1.8 | 0.4 | 0.78 | 0.8 | 0.1 | 0.88 | 1.0 | 0.3 | 0.70 | 3.0 | 0.1 | 0.97 | 0.9 | 0.1 | 0.89 | 1.0 | 0.1 | 0.90 | 2.0 | 0.1 | 0.95 | 1.6 | 0.2 | 0.88 |
| | | TN-24 | 1.6 | 0.2 | 0.88 | 0.6 | 1.0 | 0.20 | 3.0 | 0.5 | 0.83 | 0.6 | 0.6 | 0.00 | 3.0 | 2.2 | 0.27 | 1.5 | 0.9 | 0.40 | 0.4 | 0.2 | 0.50 | 0.9 | 0.4 | 0.56 | 0.4 | 0.3 | 0.25 | 2.1 | 0.9 | 0.57 |
| | 2 | TN-46 | 3.0 | 0.2 | 0.93 | 1.8 | 0.3 | 0.83 | 0.7 | 0.5 | 0.29 | 3.0 | 0.1 | 0.97 | 2.9 | 0.1 | 0.97 | 2.8 | 0.1 | 0.96 | 4.0 | 0.1 | 0.98 | 5.1 | 0.1 | 0.98 | 3.0 | 0.1 | 0.97 | 2.9 | 0.1 | 0.97 |
| | | TN-32 | 1.0 | 0.3 | 0.70 | 1.2 | 0.2 | 0.83 | 2.5 | 0.2 | 0.92 | 2.2 | 0.3 | 0.86 | 1.0 | 0.2 | 0.80 | 1.2 | 0.1 | 0.92 | 0.8 | 0.2 | 0.75 | 2.5 | 0.2 | 0.92 | 3.0 | 0.4 | 0.87 | 2.1 | 0.3 | 0.86 |
| | | TN-45 | 2.0 | 0.3 | 0.85 | 1.0 | 1.0 | 0.00 | 1.0 | 0.9 | 0.15 | 0.5 | 1.0 | -1.00 | 12.0 | 8.0 | 0.33 | 20.0 | 16.0 | 0.20 | 22.0 | 24.0 | -0.09 | 3.0 | 1.4 | 0.53 | 5.0 | 4.2 | 0.16 | 5.5 | 1.3 | 0.76 |
| | 3 | TN-33 | - | - | - | - | - | - | - | - | - | - | - | - | - | - | - | - | - | - | - | - | - | - | - | - | - | - | - | - | - | - |
| | | TN-35 | 3.0 | 0.3 | 0.90 | 0.9 | 0.1 | 0.89 | 3.1 | 0.1 | 0.97 | 3.2 | 0.3 | 0.91 | 2.1 | 0.1 | 0.95 | 1.0 | 0.1 | 0.90 | 3.2 | 0.1 | 0.97 | 4.2 | 0.1 | 0.98 | 1.0 | 0.1 | 0.90 | 3.0 | 0.1 | 0.97 |
| | 4 | TN-01 | - | - | - | - | - | - | - | - | - | - | - | - | - | - | - | - | - | - | - | - | - | - | - | - | - | - | - | - | - | - |
| | | TN-23 | - | - | - | - | - | - | - | - | - | - | - | - | - | - | - | - | - | - | - | - | - | - | - | - | - | - | - | - | - | - |
| | | TF-04 | 1.6 | 0.1 | 0.94 | 1.0 | 0.1 | 0.90 | 0.6 | 0.1 | 0.83 | 1.0 | 0.2 | 0.80 | 0.6 | 0.2 | 0.67 | 0.8 | 0.4 | 0.50 | 3.1 | 2.8 | 0.10 | 2.3 | 1.9 | 0.17 | 1.1 | 0.1 | 0.91 | 4.2 | 3.9 | 0.07 |
| | | TN-44 | 3.0 | 2.9 | 0.03 | 1.0 | 1.1 | -0.10 | 4.9 | 0.7 | 0.86 | 0.9 | 0.3 | 0.67 | 1.2 | 1.0 | 0.17 | 5.5 | 3.0 | 0.45 | 1.1 | 0.9 | 0.18 | 2.5 | 1.7 | 0.32 | 1.3 | 0.8 | 0.38 | 1.0 | 0.9 | 0.10 |
| Retamares | A | TN-40 | 1.2 | 0.2 | 0.83 | 0.8 | 0.5 | 0.38 | 2.8 | 0.3 | 0.89 | 1.0 | 0.1 | 0.90 | 1.0 | 0.1 | 0.90 | 3.3 | 0.3 | 0.91 | 2.9 | 0.3 | 0.90 | 1.1 | 0.2 | 0.82 | 8.1 | 0.3 | 0.96 | 5.5 | 0.3 | 0.95 |
| | | TN-10 | 1.0 | 0.6 | 0.40 | 1.0 | 0.5 | 0.50 | 2.0 | 1.6 | 0.20 | 0.6 | 0.3 | 0.50 | 1.0 | 0.3 | 0.70 | 1.4 | 0.6 | 0.57 | 1.0 | 0.4 | 0.60 | 1.1 | 0.6 | 0.45 | 1.1 | 0.5 | 0.55 | 3.0 | 1.0 | 0.67 |
| | | TN-02 | 2.2 | 0.6 | 0.73 | 1.0 | 0.7 | 0.30 | 1.5 | 1.1 | 0.27 | 1.7 | 1.0 | 0.41 | 1.6 | 0.7 | 0.56 | 2.2 | 0.4 | 0.82 | 1.1 | 0.3 | 0.73 | 0.8 | 0.2 | 0.75 | 1.3 | 0.3 | 0.77 | 2.1 | 0.8 | 0.62 |
| | | TN-03 | 3.2 | 0.9 | 0.72 | 3.1 | 1.2 | 0.61 | 29.0 | 0.3 | 0.99 | 8.6 | 3.3 | 0.62 | 9.1 | 3.5 | 0.62 | 0.9 | 0.1 | 0.89 | 3.1 | 1.2 | 0.61 | 8.6 | 3.9 | 0.55 | 9.4 | 5.8 | 0.38 | 3.9 | 2.1 | 0.46 |
| | B | TN-05 | 1.0 | 0.1 | 0.90 | 3.0 | 0.1 | 0.97 | 2.5 | 0.1 | 0.96 | 1.2 | 0.1 | 0.92 | 1.5 | 0.2 | 0.87 | 1.9 | 0.1 | 0.95 | 1.1 | 0.1 | 0.91 | 1.2 | 0.1 | 0.92 | 4.1 | 0.5 | 0.88 | 1.1 | 0.1 | 0.91 |
| | | TN-41 | 0.8 | 0.6 | 0.25 | 1.0 | 0.5 | 0.50 | 0.5 | 0.3 | 0.40 | 0.7 | 0.5 | 0.29 | 1.6 | 0.7 | 0.56 | 0.8 | 0.2 | 0.75 | 2.5 | 0.2 | 0.92 | 3.0 | 0.4 | 0.87 | 2.1 | 0.3 | 0.86 | 1.1 | 0.2 | 0.82 |
| | | TF-03 | 0.7 | 0.2 | 0.71 | 2.0 | 0.6 | 0.70 | 0.6 | 0.3 | 0.50 | 1.0 | 0.2 | 0.80 | 1.5 | 0.3 | 0.80 | 0.5 | 0.2 | 0.60 | 0.7 | 0.1 | 0.86 | 0.6 | 0.1 | 0.83 | 0.5 | 0.3 | 0.40 | 0.7 | 0.5 | 0.29 |
| | | VF-16/1 | 1.0 | 0.2 | 0.80 | 2.5 | 0.5 | 0.80 | 0.5 | 0.3 | 0.40 | 1.6 | 0.2 | 0.88 | 1.1 | 0.2 | 0.82 | 0.5 | 0.1 | 0.80 | 1.4 | 0.3 | 0.79 | 0.6 | 0.2 | 0.67 | 10.0 | 6.1 | 0.39 | 11.0 | 6.0 | 0.45 |
| | C | TF-02 | 0.5 | 0.1 | 0.80 | 1.7 | 0.1 | 0.94 | 2.0 | 0.2 | 0.90 | 4.5 | 0.4 | 0.91 | 3.0 | 0.3 | 0.90 | 0.9 | 0.1 | 0.89 | 3.0 | 0.1 | 0.97 | 0.7 | 0.1 | 0.86 | 6.0 | 0.3 | 0.95 | 1.0 | 0.1 | 0.90 |
| | | TN-43 | 1.6 | 0.5 | 0.69 | 1.5 | 0.6 | 0.60 | 2.2 | 0.4 | 0.82 | 1.5 | 0.4 | 0.73 | 4.6 | 0.7 | 0.85 | 5.0 | 2.0 | 0.60 | 7.0 | 4.0 | 0.43 | 12.0 | 7.0 | 0.42 | 3.1 | 0.5 | 0.84 | 5.5 | 1.0 | 0.82 |
| | | TN-06 | 15.4 | 1.6 | 0.90 | 1.6 | 0.3 | 0.81 | 1.0 | 0.4 | 0.60 | 1.1 | 0.4 | 0.64 | 1.2 | 0.4 | 0.67 | 1.1 | 0.3 | 0.73 | 0.5 | 0.3 | 0.40 | 1.0 | 0.4 | 0.60 | 5.0 | 1.0 | 0.80 | 2.5 | 0.4 | 0.84 |
| | | TN-09 | 4.0 | 2.0 | 0.50 | 0.9 | 0.4 | 0.56 | 0.7 | 0.4 | 0.43 | 1.5 | 0.4 | 0.73 | 1.0 | 0.2 | 0.80 | 0.4 | 0.1 | 0.75 | 1.2 | 0.2 | 0.83 | 0.9 | 0.1 | 0.89 | 0.4 | 0.1 | 0.75 | 1.1 | 0.1 | 0.91 |
| | D | TN-42 | - | - | - | - | - | - | - | - | - | - | - | - | - | - | - | - | - | - | - | - | - | - | - | - | - | - | - | - | - | - |
| | | TF-01 | 4.0 | 1.3 | 0.68 | 2.2 | 0.4 | 0.82 | 2.9 | 0.4 | 0.86 | 0.8 | 0.3 | 0.63 | 1.3 | 0.1 | 0.92 | 2.3 | 0.1 | 0.96 | 3.0 | 0.4 | 0.87 | 4.5 | 0.8 | 0.82 | 4.5 | 0.7 | 0.84 | 3.7 | 0.3 | 0.92 |
| | E | TN-14 | - | - | - | - | - | - | - | - | - | - | - | - | - | - | - | - | - | - | - | - | - | - | - | - | - | - | - | - | - | - |
| | | TN-22 | 1.0 | 0.1 | 0.90 | 1.9 | 0.3 | 0.84 | 0.7 | 0.3 | 0.57 | 0.6 | 0.3 | 0.50 | 0.6 | 0.2 | 0.67 | 1.7 | 0.3 | 0.82 | 1.0 | 0.2 | 0.80 | 2.0 | 0.6 | 0.70 | 3.0 | 0.1 | 0.97 | 4.2 | 0.2 | 0.95 |
| | | TN-15 | 3.3 | 0.3 | 0.91 | 1.5 | 0.3 | 0.80 | 1.9 | 0.2 | 0.89 | 1.2 | 0.1 | 0.92 | 0.9 | 0.4 | 0.56 | 0.9 | 0.4 | 0.56 | 1.0 | 0.3 | 0.70 | 1.0 | 0.3 | 0.70 | 3.3 | 0.2 | 0.94 | 3.2 | 0.2 | 0.94 |
| | | TF-09 | 1.0 | 0.3 | 0.70 | 0.5 | 0.1 | 0.80 | 0.6 | 0.4 | 0.33 | 0.6 | 0.4 | 0.33 | 0.6 | 0.3 | 0.50 | 0.9 | 0.2 | 0.78 | 0.7 | 0.1 | 0.86 | 1.1 | 0.3 | 0.73 | 0.6 | 0.2 | 0.67 | 1.1 | 0.2 | 0.82 |
| | F | TN-19 | - | - | - | - | - | - | - | - | - | - | - | - | - | - | - | - | - | - | - | - | - | - | - | - | - | - | - | - | - | - |
| | | TN-20 | 1.0 | 0.2 | 0.80 | 1.1 | 0.3 | 0.73 | 0.5 | 0.2 | 0.60 | 3.0 | 0.6 | 0.80 | 2.5 | 0.3 | 0.88 | 6.0 | 0.4 | 0.93 | 0.9 | 0.1 | 0.89 | 4.9 | 1.0 | 0.80 | 6.1 | 1.1 | 0.82 | 12.3 | 3.0 | 0.76 |
| | | TN-21 | 3.2 | 2.1 | 0.34 | 4.4 | 3.1 | 0.30 | 3.2 | 3.0 | 0.06 | 2.2 | 0.9 | 0.59 | 2.1 | 0.8 | 0.62 | 1.1 | 0.1 | 0.91 | 4.3 | 3.9 | 0.09 | 4.4 | 4.1 | 0.07 | 4.1 | 3.5 | 0.15 | 3.2 | 2.0 | 0.38 |
| | G | TN-17 | - | - | - | - | - | - | - | - | - | - | - | - | - | - | - | - | - | - | - | - | - | - | - | - | - | - | - | - | - | - |
| | | TN-18 | 1.4 | 1.0 | 0.29 | 1.0 | 0.2 | 0.80 | 0.7 | 0.3 | 0.57 | 1.0 | 0.1 | 0.90 | 1.0 | 0.2 | 0.80 | 6.1 | 0.2 | 0.97 | 3.5 | 0.1 | 0.97 | 4.2 | 0.2 | 0.95 | 1.4 | 0.1 | 0.93 | 1.1 | 1.0 | 0.09 |
| Chasna | S | VF-16/2 | - | - | - | - | - | - | - | - | - | - | - | - | - | - | - | - | - | - | - | - | - | - | - | - | - | - | - | - | - | - |
| | | TN-08 | - | - | - | - | - | - | - | - | - | - | - | - | - | - | - | - | - | - | - | - | - | - | - | - | - | - | - | - | - | - |
| | | TN-07 | 3.0 | 1.0 | 0.67 | 2.0 | 0.4 | 0.80 | 1.0 | 0.2 | 0.80 | 6.0 | 1.0 | 0.83 | 5.5 | 2.1 | 0.62 | 2.2 | 0.5 | 0.77 | 3.0 | 1.0 | 0.67 | 2.0 | 0.4 | 0.80 | 1.0 | 0.2 | 0.80 | 3.3 | 4.3 | -0.30 |
| | R | TN-38 | - | - | - | - | - | - | - | - | - | - | - | - | - | - | - | - | - | - | - | - | - | - | - | - | - | - | - | - | - | - |
| | | VF-16/3 | 3.3 | 0.4 | 0.88 | 3.4 | 0.5 | 0.85 | 1.6 | 0.4 | 0.75 | 2.0 | 0.4 | 0.80 | 1.9 | 0.1 | 0.95 | 1.0 | 0.1 | 0.90 | 1.0 | 0.1 | 0.90 | 5.1 | 0.4 | 0.92 | 2.0 | 0.3 | 0.85 | 2.0 | 0.5 | 0.75 |
| | | TF-06 | 1.5 | 0.2 | 0.87 | 0.5 | 0.2 | 0.60 | 1.0 | 0.3 | 0.70 | 0.5 | 0.1 | 0.80 | 1.0 | 0.3 | 0.70 | 1.0 | 0.2 | 0.80 | 1.0 | 0.3 | 0.70 | 1.5 | 0.4 | 0.73 | 2.0 | 0.3 | 0.85 | 2.0 | 0.5 | 0.75 |
| | 2 | TN-12 | - | - | - | - | - | - | - | - | - | - | - | - | - | - | - | - | - | - | - | - | - | - | - | - | - | - | - | - | - | - |
| Chasna ridge | | TF-05 | - | - | - | - | - | - | - | - | - | - | - | - | - | - | - | - | - | - | - | - | - | - | - | - | - | - | - | - | - | - |
| | | VF-16/4 | - | - | - | - | - | - | - | - | - | - | - | - | - | - | - | - | - | - | - | - | - | - | - | - | - | - | - | - | - | - |
| Almendros | | TN-04 | 1.0 | 0.3 | 0.70 | 2.0 | 0.2 | 0.90 | 1.1 | 1.0 | 0.09 | 1.0 | 0.4 | 0.60 | 1.0 | 0.4 | 0.60 | 1.4 | 0.2 | 0.86 | 3.0 | 0.3 | 0.90 | 3.3 | 0.3 | 0.91 | 1.7 | 0.1 | 0.94 | 0.9 | 0.1 | 0.89 |
| Arenas | SW | TN-27 | 3.3 | 0.1 | 0.97 | 4.9 | 0.3 | 0.94 | 6.9 | 0.3 | 0.96 | 7.9 | 0.1 | 0.99 | 1.1 | 0.1 | 0.91 | 1.6 | 0.1 | 0.94 | 8.9 | 1.0 | 0.89 | 22.0 | 1.0 | 0.95 | 4.1 | 0.1 | 0.98 | 4.6 | 0.3 | 0.93 |
| | | TN-31 | 10.1 | 3.0 | 0.70 | 16.0 | 0.5 | 0.97 | 7.5 | 2.5 | 0.67 | 15.0 | 4.0 | 0.73 | 6.0 | 1.0 | 0.83 | 0.7 | 0.1 | 0.86 | 0.7 | 0.1 | 0.85 | 11.0 | 3.0 | 0.73 | 3.0 | 0.6 | 0.80 | 4.1 | 0.7 | 0.83 |
| | | TN-26 | 1.6 | 0.5 | 0.69 | 1.0 | 0.6 | 0.40 | 1.5 | 0.4 | 0.73 | 2.5 | 0.5 | 0.80 | 1.1 | 0.7 | 0.36 | 2.2 | 0.5 | 0.77 | 0.7 | 0.4 | 0.43 | 0.9 | 0.1 | 0.89 | 1.8 | 0.3 | 0.83 | 6.0 | 2.7 | 0.55 |
| | | TN-25 | 4.6 | 0.2 | 0.96 | 5.5 | 0.5 | 0.91 | 14.0 | 1.0 | 0.93 | 11.0 | 0.7 | 0.94 | 3.3 | 0.3 | 0.91 | 5.1 | 0.5 | 0.90 | 5.3 | 0.6 | 0.89 | 12.2 | 1.1 | 0.91 | 20.3 | 3.3 | 0.84 | 4.4 | 0.1 | 0.98 |
| Guajara | 2 | TF-08 | 0.7 | 0.6 | 0.14 | 1.0 | 0.3 | 0.70 | 1.1 | 0.3 | 0.73 | 0.5 | 0.1 | 0.80 | 0.5 | 0.2 | 0.60 | 3.0 | 0.3 | 0.90 | 3.0 | 0.2 | 0.93 | 3.1 | 0.3 | 0.90 | 0.7 | 0.3 | 0.57 | 3.3 | 0.4 | 0.88 |

| Member | Unit | 11 | | | 12 | | | 13 | | | 14 | | | 15 | | | 16 | | | 17 | | | 18 | | | 19 | | | 20 | | | Mean OB |
|---|---|---|---|---|---|---|---|---|---|---|---|---|---|---|---|---|---|---|---|---|---|---|---|---|---|---|---|---|---|---|---|---|
| | | a axis | c axis | OB | a axis | c axis | OB | a axis | c axis | OB | a axis | c axis | OB | a axis | c axis | OB | a axis | c axis | OB | a axis | c axis | OB | a axis | c axis | OB | a axis | c axis | OB | a axis | c axis | OB | |
| Atravesado | | - | - | - | - | - | - | - | - | - | - | - | - | - | - | - | - | - | - | - | - | - | - | - | - | - | - | - | - | - | - | *lava-like |
| | 1 | 3.0 | 0.1 | 0.97 | 1.2 | 0.1 | 0.92 | 0.9 | 0.1 | 0.89 | 1.0 | 0.1 | 0.90 | 1.1 | 0.1 | 0.91 | 2.0 | 0.1 | 0.95 | 2.2 | 0.1 | 0.95 | 1.0 | 0.1 | 0.90 | 0.9 | 0.1 | 0.89 | 1.2 | 0.1 | 0.92 | 0.88 |
| | | 0.4 | 0.4 | 0.00 | 1.1 | 1.2 | -0.09 | 0.7 | 0.6 | 0.14 | 1.0 | 1.1 | -0.10 | 3.0 | 3.0 | 0.00 | 1.2 | 1.0 | 0.17 | 3.2 | 1.2 | 0.63 | 3.1 | 2.0 | 0.35 | 0.9 | 0.3 | 0.67 | 0.7 | 0.4 | 0.43 | 0.33 |
| | 2 | 3.0 | 0.1 | 0.97 | 1.8 | 0.1 | 0.94 | 4.9 | 0.1 | 0.98 | 2.9 | 0.1 | 0.97 | 2.8 | 0.1 | 0.96 | 1.0 | 0.0 | 1.00 | 3.0 | 0.1 | 0.97 | 5.0 | 0.2 | 0.96 | 4.9 | 0.1 | 0.98 | 4.0 | 0.3 | 0.93 | 0.92 |
| | | 1.1 | 0.2 | 0.82 | 0.9 | 0.2 | 0.78 | 0.6 | 0.3 | 0.50 | 0.7 | 0.3 | 0.57 | 3.0 | 1.2 | 0.60 | 0.6 | 0.4 | 0.33 | 1.0 | 0.3 | 0.70 | 1.0 | 0.4 | 0.60 | 5.0 | 3.0 | 0.40 | 1.2 | -0.3 | 1.25 | 0.75 |
| | 3 | 3.4 | 2.4 | 0.29 | 10.0 | 6.1 | 0.39 | 11.0 | 6.0 | 0.45 | 2.0 | 0.3 | 0.85 | 6.8 | 5.5 | 0.19 | 7.1 | 4.6 | 0.35 | 6.5 | 3.8 | 0.42 | 9.1 | 6.7 | 0.26 | 3.3 | 4.1 | -0.24 | 8.1 | 3.8 | 0.53 | 0.27 |
| | | - | - | - | - | - | - | - | - | - | - | - | - | - | - | - | - | - | - | - | - | - | - | - | - | - | - | - | - | - | - | *lava-like |
| | | 2.5 | 0.1 | 0.96 | 1.2 | 0.1 | 0.92 | 1.5 | 0.2 | 0.87 | 1.9 | 0.1 | 0.95 | 1.4 | 0.2 | 0.86 | 3.0 | 0.3 | 0.90 | 3.3 | 0.3 | 0.91 | 1.7 | 0.1 | 0.94 | 0.9 | 0.1 | 0.89 | 3.1 | 0.1 | 0.97 | 0.92 |
| | 4 | - | - | - | - | - | - | - | - | - | - | - | - | - | - | - | - | - | - | - | - | - | - | - | - | - | - | - | - | - | - | *lava-like |
| | | - | - | - | - | - | - | - | - | - | - | - | - | - | - | - | - | - | - | - | - | - | - | - | - | - | - | - | - | - | - | *lava-like |
| | | 2.1 | 0.2 | 0.90 | 1.6 | 0.4 | 0.75 | 3.2 | 2.2 | 0.31 | 3.2 | 2.1 | 0.34 | 4.1 | 0.1 | 0.98 | 3.2 | 0.4 | 0.88 | 1.5 | 0.2 | 0.87 | 0.6 | 0.1 | 0.83 | 0.4 | 0.1 | 0.75 | 1.3 | 0.7 | 0.46 | 0.65 |
| | | 1.0 | 1.0 | 0.00 | 7.2 | 3.3 | 0.54 | 0.4 | 0.1 | 0.75 | 3.0 | 2.1 | 0.30 | 2.6 | 1.1 | 0.58 | 0.4 | 0.3 | 0.25 | 0.9 | 0.3 | 0.67 | 2.0 | 1.1 | 0.45 | 1.0 | 0.1 | 0.90 | 2.0 | 0.4 | 0.80 | 0.42 |
| Retamares | A | 16.0 | 1.3 | 0.92 | 9.3 | 2.3 | 0.75 | 3.3 | 0.3 | 0.91 | 2.5 | 0.4 | 0.84 | 4.4 | 1.0 | 0.77 | 7.3 | 2.7 | 0.63 | 7.3 | 0.3 | 0.96 | 0.8 | 0.1 | 0.88 | 1.4 | 0.2 | 0.86 | 2.2 | 0.3 | 0.86 | 0.84 |
| | | 2.0 | 0.8 | 0.60 | 2.2 | 0.8 | 0.64 | 1.4 | 0.1 | 0.93 | 1.5 | 0.1 | 0.93 | 2.8 | 0.4 | 0.86 | 2.2 | 0.2 | 0.91 | 1.0 | 0.3 | 0.70 | 1.0 | 0.4 | 0.60 | 1.0 | 0.2 | 0.80 | 1.0 | 0.1 | 0.90 | 0.65 |
| | | 2.0 | 0.3 | 0.85 | 1.1 | 1.1 | 0.00 | 3.9 | 0.4 | 0.90 | 6.2 | 2.9 | 0.53 | 0.9 | 0.1 | 0.89 | 5.5 | 2.1 | 0.62 | 4.9 | 1.4 | 0.71 | 2.4 | 0.9 | 0.63 | 1.1 | 0.3 | 0.73 | 1.4 | 0.2 | 0.86 | 0.63 |
| | | 4.6 | 2.7 | 0.41 | 5.0 | 2.0 | 0.60 | 7.0 | 4.0 | 0.43 | 12.0 | 7.0 | 0.42 | 3.1 | 3.5 | -0.13 | 5.5 | 1.0 | 0.82 | 0.6 | 0.1 | 0.83 | 3.0 | 0.1 | 0.97 | 4.1 | 2.3 | 0.44 | 4.2 | 14.0 | -2.33 | 0.44 |
| | B | 3.0 | 0.1 | 0.97 | 6.1 | 0.2 | 0.97 | 3.5 | 0.1 | 0.97 | 4.2 | 0.2 | 0.95 | 0.9 | 0.1 | 0.89 | 1.1 | 0.1 | 0.91 | 6.4 | 0.4 | 0.94 | 0.5 | 0.1 | 0.80 | 4.3 | 0.4 | 0.91 | 3.0 | 0.1 | 0.97 | 0.92 |
| | | 0.9 | 0.2 | 0.78 | 0.6 | 0.3 | 0.50 | 2.5 | 1.7 | 0.32 | 1.3 | 0.8 | 0.38 | 1.0 | 0.9 | 0.10 | 1.0 | 1.0 | 0.00 | 7.2 | 3.3 | 0.54 | 0.6 | 0.1 | 0.83 | 3.0 | 0.1 | 0.97 | 4.2 | 3.9 | 0.07 | 0.54 |
| | | 1.6 | 0.8 | 0.50 | 0.8 | 0.2 | 0.75 | 2.5 | 0.2 | 0.92 | 2.0 | 0.3 | 0.85 | 4.0 | 2.6 | 0.35 | 0.8 | 0.6 | 0.25 | 5.2 | 5.0 | 0.04 | 2.0 | 0.4 | 0.80 | 2.1 | 0.6 | 0.71 | 0.3 | 0.3 | 0.00 | 0.58 |
| | | 2.0 | 0.3 | 0.85 | 6.8 | 5.5 | 0.19 | 2.0 | 1.3 | 0.35 | 1.7 | 1.6 | 0.06 | 1.2 | 1.0 | 0.17 | 2.0 | 1.7 | 0.15 | 3.0 | 1.8 | 0.40 | 1.0 | 0.2 | 0.80 | 2.5 | 0.5 | 0.80 | 3.0 | 3.0 | 0.00 | 0.53 |
| | C | 0.7 | 0.1 | 0.86 | 6.0 | 0.4 | 0.93 | 0.8 | 0.1 | 0.88 | 4.9 | 0.3 | 0.94 | 1.3 | 0.1 | 0.92 | 8.0 | 0.4 | 0.95 | 2.0 | 0.1 | 0.95 | 2.9 | 0.1 | 0.97 | 0.9 | 0.1 | 0.89 | 2.8 | 0.1 | 0.96 | 0.91 |
| | | 0.6 | 0.1 | 0.83 | 3.0 | 0.1 | 0.97 | 4.1 | 0.3 | 0.93 | 4.2 | 0.4 | 0.90 | 3.0 | 0.3 | 0.90 | 4.2 | 0.4 | 0.90 | 0.9 | 0.1 | 0.89 | 1.5 | 0.3 | 0.80 | 1.1 | 0.1 | 0.91 | 5.0 | 0.3 | 0.94 | 0.79 |
| | | 0.8 | 0.3 | 0.63 | 0.5 | 0.5 | 0.00 | 1.0 | 0.3 | 0.70 | 0.6 | 0.1 | 0.83 | 1.0 | 0.1 | 0.90 | 2.0 | 0.3 | 0.85 | 0.7 | 0.3 | 0.57 | 0.7 | 0.2 | 0.71 | 0.8 | 0.6 | 0.25 | 3.0 | 2.8 | 0.07 | 0.62 |
| | | 0.7 | 0.5 | 0.29 | 0.7 | 0.2 | 0.71 | 0.4 | 0.1 | 0.75 | 1.2 | 0.4 | 0.67 | 1.6 | 0.4 | 0.75 | 0.9 | 0.4 | 0.56 | 1.0 | 0.2 | 0.80 | 0.9 | 0.2 | 0.78 | 0.6 | 0.1 | 0.83 | 1.0 | 0.2 | 0.80 | 0.70 |
| | D | - | - | - | - | - | - | - | - | - | - | - | - | - | - | - | - | - | - | - | - | - | - | - | - | - | - | - | - | - | - | *lava-like |
| | | 4.0 | 1.3 | 0.68 | 2.2 | 0.4 | 0.82 | 2.9 | 0.4 | 0.86 | 0.8 | 0.3 | 0.63 | 4.0 | 0.3 | 0.93 | 4.3 | 0.3 | 0.93 | 4.0 | 1.3 | 0.68 | 2.2 | 0.4 | 0.82 | 2.9 | 0.4 | 0.86 | 0.8 | 0.3 | 0.63 | 0.81 |
| | E | - | - | - | - | - | - | - | - | - | - | - | - | - | - | - | - | - | - | - | - | - | - | - | - | - | - | - | - | - | - | *lava-like |
| | | 0.5 | 0.1 | 0.80 | 5.2 | 0.4 | 0.92 | 3.0 | 0.1 | 0.97 | 4.7 | 0.2 | 0.96 | 4.1 | 0.4 | 0.90 | 3.1 | 0.1 | 0.97 | 0.6 | 0.1 | 0.83 | 0.9 | 0.1 | 0.89 | 1.1 | 0.1 | 0.91 | 3.1 | 0.1 | 0.97 | 0.84 |
| | | 4.1 | 0.3 | 0.93 | 5.5 | 0.4 | 0.93 | 11.0 | 1.2 | 0.89 | 4.1 | 0.4 | 0.90 | 4.2 | 0.3 | 0.93 | 4.2 | 0.5 | 0.88 | 1.0 | 0.3 | 0.70 | 1.0 | 0.3 | 0.70 | 3.3 | 0.2 | 0.94 | 4.1 | 0.4 | 0.90 | 0.83 |
| | | 2.4 | 0.5 | 0.79 | 0.5 | 0.5 | 0.00 | 0.5 | 0.2 | 0.60 | 3.0 | 2.1 | 0.30 | 4.5 | 3.1 | 0.31 | 6.4 | 3.3 | 0.48 | 1.3 | 0.1 | 0.92 | 1.2 | 0.7 | 0.42 | 0.9 | 0.4 | 0.56 | 2.2 | 1.1 | 0.50 | 0.57 |
| | F | - | - | - | - | - | - | - | - | - | - | - | - | - | - | - | - | - | - | - | - | - | - | - | - | - | - | - | - | - | - | *lava-like |
| | | 1.1 | 0.3 | 0.73 | 3.3 | 1.1 | 0.67 | 6.4 | 2.4 | 0.63 | 6.3 | 2.0 | 0.68 | 5.0 | 4.1 | 0.18 | 3.0 | 2.5 | 0.17 | 3.3 | 1.1 | 0.67 | 3.2 | 2.4 | 0.25 | 1.5 | 0.3 | 0.80 | 4.5 | 4.1 | 0.09 | 0.64 |
| | | 4.4 | 3.1 | 0.30 | 3.2 | 3.0 | 0.06 | 2.2 | 0.8 | 0.64 | 2.1 | 0.8 | 0.62 | 1.1 | 0.9 | 0.18 | 17.0 | 12.0 | 0.29 | 4.5 | 2.5 | 0.44 | 4.4 | 3.4 | 0.23 | 8.1 | 6.7 | 0.17 | 3.2 | 1.9 | 0.41 | 0.34 |
| | G | - | - | - | - | - | - | - | - | - | - | - | - | - | - | - | - | - | - | - | - | - | - | - | - | - | - | - | - | - | - | *lava-like |
| | | 6.4 | 0.4 | 0.94 | 1.4 | 1.0 | 0.29 | 1.0 | 0.2 | 0.80 | 0.7 | 0.3 | 0.57 | 4.4 | 3.1 | 0.30 | 3.2 | 3.0 | 0.06 | 2.2 | 0.9 | 0.59 | 2.1 | 1.0 | 0.52 | 6.4 | 0.5 | 0.92 | 4.3 | 0.9 | 0.79 | 0.65 |
| Chasna | S | - | - | - | - | - | - | - | - | - | - | - | - | - | - | - | - | - | - | - | - | - | - | - | - | - | - | - | - | - | - | *lava-like |
| | | - | - | - | - | - | - | - | - | - | - | - | - | - | - | - | - | - | - | - | - | - | - | - | - | - | - | - | - | - | - | *lava-like |
| | | 18.0 | 7.3 | 0.59 | 7.0 | 3.0 | 0.57 | 1.1 | 0.3 | 0.73 | 1.3 | 0.2 | 0.85 | 3.3 | 0.4 | 0.88 | 2.0 | 0.4 | 0.80 | 2.1 | 0.5 | 0.76 | 10.0 | 4.5 | 0.55 | 5.5 | 1.1 | 0.80 | 5.1 | 1.0 | 0.80 | 0.69 |
| | R | - | - | - | - | - | - | - | - | - | - | - | - | - | - | - | - | - | - | - | - | - | - | - | - | - | - | - | - | - | - | *lava-like |
| | | 1.5 | 0.3 | 0.80 | 4.0 | 0.9 | 0.78 | 1.1 | 0.1 | 0.91 | 0.5 | 0.1 | 0.80 | 4.0 | 0.3 | 0.93 | 3.3 | 0.4 | 0.88 | 1.4 | 0.6 | 0.57 | 2.5 | 0.4 | 0.84 | 1.9 | 0.2 | 0.89 | 4.0 | 0.1 | 0.98 | 0.85 |
| | | 1.5 | 0.3 | 0.80 | 1.9 | 0.9 | 0.53 | 1.1 | 0.1 | 0.91 | 0.5 | 0.1 | 0.80 | 1.8 | 0.3 | 0.83 | 3.3 | 0.4 | 0.88 | 1.4 | 0.6 | 0.57 | 2.5 | 0.4 | 0.84 | 1.9 | 0.2 | 0.89 | 1.6 | 0.4 | 0.75 | 0.77 |
| | 2 | - | - | - | - | - | - | - | - | - | - | - | - | - | - | - | - | - | - | - | - | - | - | - | - | - | - | - | - | - | - | *lava-like |
| Chasna ridge | | - | - | - | - | - | - | - | - | - | - | - | - | - | - | - | - | - | - | - | - | - | - | - | - | - | - | - | - | - | - | *lava-like |
| | | - | - | - | - | - | - | - | - | - | - | - | - | - | - | - | - | - | - | - | - | - | - | - | - | - | - | - | - | - | - | *lava-like |
| Almendros | | 3.1 | 0.1 | 0.97 | 4.5 | 1.1 | 0.76 | 0.9 | 0.1 | 0.89 | 4.2 | 0.4 | 0.90 | 2.2 | 0.1 | 0.95 | 3.5 | 0.2 | 0.94 | 12.0 | 0.6 | 0.95 | 3.3 | 0.3 | 0.91 | 2.3 | 0.1 | 0.96 | 0.9 | 0.1 | 0.89 | 0.83 |
| Areñas | SW | 5.5 | 0.5 | 0.91 | 14.0 | 1.0 | 0.93 | 12.0 | 0.7 | 0.94 | 3.3 | 0.3 | 0.91 | 5.5 | 0.5 | 0.91 | 5.3 | 0.6 | 0.89 | 12.2 | 1.1 | 0.91 | 20.3 | 3.3 | 0.84 | 4.4 | 0.1 | 0.98 | 3.3 | 0.1 | 0.97 | 0.93 |
| | | 2.0 | 0.3 | 0.85 | 1.0 | 0.1 | 0.90 | 2.1 | 0.2 | 0.90 | 0.6 | 0.1 | 0.83 | 1.0 | 0.1 | 0.90 | 0.7 | 0.1 | 0.86 | 1.0 | 0.1 | 0.90 | 0.8 | 0.2 | 0.75 | 1.0 | 0.1 | 0.90 | 0.9 | 0.2 | 0.78 | 0.83 |
| | | 0.6 | 0.1 | 0.83 | 0.5 | 0.1 | 0.80 | 6.0 | 2.7 | 0.55 | 7.0 | 3.0 | 0.57 | 6.0 | 3.3 | 0.45 | 0.6 | 0.2 | 0.67 | 1.5 | 0.3 | 0.80 | 1.8 | 1.0 | 0.44 | 1.9 | 0.9 | 0.53 | 1.8 | 0.5 | 0.72 | 0.64 |
| | | 3.3 | 0.1 | 0.97 | 8.3 | 1.1 | 0.87 | 12.1 | 2.1 | 0.83 | 9.1 | 1.4 | 0.85 | 0.9 | 0.1 | 0.89 | 3.0 | 0.3 | 0.90 | 3.3 | 0.2 | 0.94 | 3.3 | 0.3 | 0.91 | 1.1 | 0.1 | 0.91 | 4.5 | 0.3 | 0.93 | 0.91 |
| Guajara | 2 | 0.7 | 0.1 | 0.86 | 1.0 | 0.3 | 0.70 | 1.1 | 0.3 | 0.73 | 0.5 | 0.1 | 0.80 | 0.5 | 0.2 | 0.60 | 3.0 | 0.3 | 0.90 | 3.0 | 0.2 | 0.93 | 3.1 | 0.3 | 0.90 | 0.7 | 0.3 | 0.57 | 3.3 | 0.4 | 0.88 | 0.75 |

# Appendix IV.

Supplementary material, including standards and calibration data from XRF and EMPA.

| Element | Line | KV | mA | Cryst | Angle (2teta) | Collimator (µm) | Detector | Time(s) |
|---|---|---|---|---|---|---|---|---|
| Si | Kα | 50 | 50 | InSb | 144.63 | 300 | Flow | 20 |
| Al | Kα | 50 | 50 | PE | 144.82 | 300 | Flow | 20 |
| Na | Kα | 50 | 50 | TlAp100 | 55.16 | 300 | Flow | 50 |
| Mg | Kα | 50 | 50 | PX1 | 22.29 | 700 | Flow | 20 |
| P | Kα | 50 | 50 | Ge | 140.98 | 300 | Flow | 20 |
| K | Kα | 50 | 50 | LIF200 | 136.71 | 300 | Flow | 20 |
| Ca | Kα | 50 | 50 | LIF200 | 113.12 | 300 | Flow | 6 |
| Ti | Kα | 50 | 50 | LIF200 | 86.14 | 300 | Flow | 14 |
| Mn | Kα | 50 | 50 | LIF200 | 62.99 | 300 | Duplex | 20 |
| Fe | Kα | 50 | 50 | LIF200 | 57.49 | 300 | Duplex | 8 |
| V | Kα | 50 | 50 | LIF200 | 123.24 | 150 | Duplex | 50 |
| Ba | Kα | 50 | 50 | LIF200 | 87.15 | 300 | Flow | 100 |
| Sc | Kα | 50 | 50 | LIF200 | 97.72 | 300 | Flow | 100 |
| Cr | Kα | 50 | 50 | LIF200 | 69.33 | 300 | Duplex | 50 |
| Ni | Kα | 50 | 50 | LIF200 | 48.62 | 300 | Duplex | 40 |
| Cu | Kα | 50 | 50 | LIF200 | 44.96 | 300 | Duplex | 40 |
| Zn | Kα | 50 | 50 | LIF200 | 41.74 | 300 | Scint. | 20 |
| Rb | Kα | 50 | 50 | LIF200 | 26.54 | 150 | Scint | 100 |
| Sr | Kα | 60 | 40 | LIF200 | 25.07 | 300 | Scint | 60 |
| Y | Kα | 60 | 40 | LIF200 | 23.73 | 300 | Scint | 100 |
| Zr | Kα | 60 | 40 | LIF200 | 31.94 | 150 | Scint | 120 |
| Nb | Kα | 60 | 40 | LIF200 | 21.23 | 150 | Scint | 500 |

Instrumental settings used for XRF analysis of samples and volcanic rock standards. Odling, N., University of Edinburgh

| Sample | $SiO_2$ | $Al_2O_3$ | $Fe_2O_3$ | MgO | CaO | $Na_2O$ | $K_2O$ | $TiO_2$ | MnO | $P_2O_5$ |
|---|---|---|---|---|---|---|---|---|---|---|
| | % | % | % | % | % | % | % | % | % | % |
| Std-BHVO-1 | 49.48 | 13.56 | 12.35 | 7.05 | 11.47 | 2.19 | 0.1515 | 2.75 | 0.166 | 0.277 |
| Govindaraju (1994) | 49.94 | 13.8 | 12.23 | 7.23 | 11.4 | 2.26 | 0.52 | 2.71 | 0.168 | 0.273 |
| | | | | | | | | | | |
| Std-Ben | 38.55 | 10.17 | 12.76 | 13.52 | 13.84 | 3.29 | 1.382 | 2.613 | 0.192 | 1.058 |
| Govindaraju (1994) | 38.2 | 10.07 | 12.84 | 13.15 | 13.87 | 3.18 | 1.39 | 2.61 | 0.2 | 1.05 |
| Std-BIR | 48.25 | 16.11 | 11.31 | 9.88 | 13.17 | 1.79 | 0.018 | 0.947 | 0.167 | 0.019 |
| | | | | | | | | | | |
| Govindaraju (1994) | 47.7 | 15.35 | 11.26 | 9.68 | 13.24 | 1.73 | 0.027 | 0.96 | 0.171 | 0.046 |
| Std-JR1 | 75.08 | 12.88 | 0.86 | 0.13 | 0.63 | 4.17 | 4.429 | 0.11 | 0.094 | 0.019 |
| | | | | | | | | | | |
| Govindaraju (1994) | 75.41 | 12.89 | 0.96 | 0.09 | 0.63 | 4.1 | 4.41 | 0.1 | 0.1 | 0.02 |
| Std-JR2 | 75.97 | 12.73 | 0.73 | -0.05 | 0.37 | 3.91 | 4.51 | 0.067 | 0.108 | 0.005 |
| | | | | | | | | | | |
| Govindaraju (1994) | 75.65 | 12.82 | 0.86 | 0.05 | 0.45 | 4.03 | 4.65 | 0.09 | 0.11 | 0.01 |
| Std-JB3 | 50.65 | 17.19 | 11.77 | 5.04 | 9.85 | 2.57 | 0.757 | 1.414 | 0.176 | 0.285 |
| | | | | | | | | | | |
| Govindaraju (1994) | 51.04 | 16.89 | 11.86 | 5.2 | 9.86 | 2.82 | 0.78 | 1.45 | 0.16 | 0.29 |

Comparison of the measured standards for XRF major elemental analysis against Govindaraju's (1994) values.

| Sample | Zn | Cu | Ni | Cr | V | Ba | Sc | La | Ce | Nd | U2 | Th | Pb | Nb | Zr1 | Y | Sr | Rb |
|---|---|---|---|---|---|---|---|---|---|---|---|---|---|---|---|---|---|---|
| | (ppm) | (ppm) | (ppm) | (ppm) | (ppm) | (ppm) | (ppm) | (ppm) | (ppm) | (ppm) | (ppm) | (ppm) | (ppm) | (ppm) | (ppm) | (ppm) | (ppm) | (ppm) |
| BCR | 125.9 | 18.3 | 12.4 | 5.4 | 406.8 | 702.6 | 31.6 | 24.2 | 54.3 | 29.2 | 1.9 | 6.0 | 14.0 | 13.6 | 195.1 | 38.2 | 331.8 | 47.5 |
| σ | 0.4 | 0.2 | 0.3 | 0.5 | 3.0 | 6.9 | 0.5 | 0.5 | 0.2 | 0.7 | 0.4 | 0.2 | 0.5 | 0.0 | 0.6 | 0.2 | 0.9 | 0.1 |
| Govindaraju (1994) | 129.5 | 19.0 | 13.0 | 16.0 | 407.0 | 681.0 | 32.6 | 24.9 | 53.7 | 28.8 | 1.8 | 6.0 | 13.6 | 14.0 | 190.0 | 38.0 | 330.0 | 47.2 |
| | | | | | | | | | | | | | | | | | | |
| BEN | 125.8 | 71.0 | 271.6 | 377.6 | 246.7 | 1059.8 | 24.1 | 88.4 | 157.7 | 70.9 | 2.2 | 10.6 | 3.4 | 116.6 | 270.0 | 29.7 | 1388.6 | 47.7 |
| σ | 1.1 | 0.3 | 1.2 | 0.8 | 1.7 | 6.9 | 0.7 | - | - | - | 0.1 | 0.1 | 0.2 | 0.4 | 0.6 | 0.1 | 2.9 | 0.2 |
| Govindaraju (1994) | 120.0 | 72.0 | 267.0 | 360.0 | 235.0 | 1025.0 | 22.0 | 82.0 | 152.0 | 67.0 | 2.4 | 10.4 | 4.0 | 105.0 | 260.0 | 30.0 | 1370.0 | 47.0 |
| | | | | | | | | | | | | | | | | | | |
| BHVO-1 | 102.8 | 131.4 | 115.9 | 288.7 | 314.0 | 121.5 | 32.2 | 11.4 | 39.0 | 25.5 | 0.1 | 0.7 | 1.7 | 19.4 | 176.1 | 27.4 | 388.1 | 9.6 |
| σ | 0.3 | 0.2 | 0.5 | 1.0 | 1.2 | 0.1 | 0.4 | 0.5 | 1.0 | 0.4 | 0.5 | 0.1 | 0.3 | 0.0 | 0.3 | 0.1 | 1.0 | 0.1 |
| Govindaraju (1994) | 105.0 | 136.0 | 121.0 | 289.0 | 317.0 | 139.0 | 31.8 | 15.8 | 39.0 | 25.2 | 0.4 | 1.1 | 2.6 | 19.0 | 179.0 | 27.6 | 403.0 | 11.0 |
| | | | | | | | | | | | | | | | | | | |
| BIR | 66.8 | 130.3 | 152.4 | 374.3 | 316.8 | 5.6 | 40.3 | n.d. | 3.4 | 2.0 | 0.1 | n.d. | 2.5 | 0.9 | 16.3 | 16.5 | 107.3 | 0.3 |
| σ | 0.8 | 3.7 | 0.8 | 6.9 | 4.8 | 1.0 | 0.8 | - | 1.3 | 0.8 | 0.2 | - | 0.2 | 0.1 | 0.2 | 0.1 | 0.3 | 0.3 |
| Govindaraju(1994) | 71.0 | 126.0 | 166.0 | 382.0 | 313.0 | 7.0 | 44.0 | 0.6 | 2.0 | 2.5 | 0.0 | 0.0 | 2.6 | 0.6 | 15.5 | 16.0 | 108.0 | 0.3 |

Comparison of the measured standards, and σ values (n=3) for XRF trace element analysis against Govindaraju's (1994) values.

| Mineral standard | Composition |
|---|---|
| Albite | O: 48.65 %, Na: 8.52 %, Mg: 0.90 %, Al: 10.12 %, Si: 31.94 %, K : 0.18 %, Ca: 0.45 %, Fe: 0.05 % |
| Periclase | O: 39.55 %, Mg: 59.58 %, Ca: 0.86 % |
| Orthoclase | O: 46.11 %, Na: 0.33 %, Al: 9.09 %, Si: 30.56 %, K : 13.03 %, Fe: 0.88 % |
| Apatite | O: 38.91 %, F: 3.40 %, P: 18.32 %, Cl: 0.35 %, Ca: 39.02 % |
| Wollastonite | O: 41.32 %, Si: 24.18 %, Ca: 34.50 % |
| Rutile | O: 39.86 %, Ti: 59.10 %, V: 0.38 %, Fe: 0.66 % |
| Hematite (synthetic) | O: 30.06 %, Fe: 69.94 % |
| Eskolaite ($Cr_2O_3$) | O: 31.58 %, Cr: 68.42 % |
| Bustamite | O: 38.39 %, Na: 0.04 %, Mg: 0.13 %, Al: 0.02 %, Si: 22.46 %, K: 0.05 %, Ca: 13.56 %, Mn: 18.83 %, Fe: 6.32 %, Zn: 0.20 % |
| Anhydrite | O: 47.01 %, S: 23.55 %, Ca: 29.44 % |
| Vanadinite | O: 13.10 %, Cl: 2.62 %, V: 10.48 %, Pb: 73.80 % |

The composition of natural and synthetic mineral standards used in EMPA on glass samples at LMU.

| Sp | Elements | Position | Bg1 | Bg2 | Slope | Gain | Dtime | Blin | Wind | Mode |
|---|---|---|---|---|---|---|---|---|---|---|
| Sp4 | Na Ka | TAP | 46354 | -600 | 600 | 1303 | 3060 | 3 | 560 | Inte |
| Sp4 | Mg Ka | TAP | 38492 | -1000 | 1000 | 1315 | 3057 | 3 | 560 | Inte |
| Sp1 | Si Ka | TAP | 27736 | -700 | 600 | 1282 | 2927 | 3 | 560 | Inte |
| Sp1 | Al Ka | TAP | 32466 | -600 | 500 | 1280 | 2978 | 3 | 560 | Inte |
| Sp5 | P Ka | LPET | 70339 | -700 | 700 | 1288 | 1005 | 3 | 560 | Inte |
| Sp2 | K Ka | PET | 42755 | -500 | 500 | 1847 | 998 | 3 | 560 | Inte |
| Sp2 | Ca Ka | PET | 38386 | -700 | 700 | 1849 | 996 | 3 | 560 | Inte |
| Sp2 | Ti Ka | PET | 31416 | -900 | 800 | 1848 | 996 | 3 | 560 | Inte |
| Sp3 | Fe Ka | LLIF | 48090 | -800 | 800 | 1857 | 478 | 3 | 560 | Inte |
| Sp3 | Cr Ka | LLIF | 56881 | -700 | 800 | 1860 | 468 | 3 | 560 | Inte |
| Sp3 | Mn Ka | LLIF | 52207 | -600 | 600 | 1855 | 468 | 3 | 560 | Inte |
| Sp5 | S Ka | LPET | 61359 | -800 | 800 | 1286 | 990 | 3 | 560 | Inte |
| Sp5 | Cl Ka | LPET | 54038 | -1100 | 600 | 1283 | 1026 | 3 | 560 | Inte |

Analysis parameters and spectrometer (sp) conditions for EMPA of glass samples at LMU.

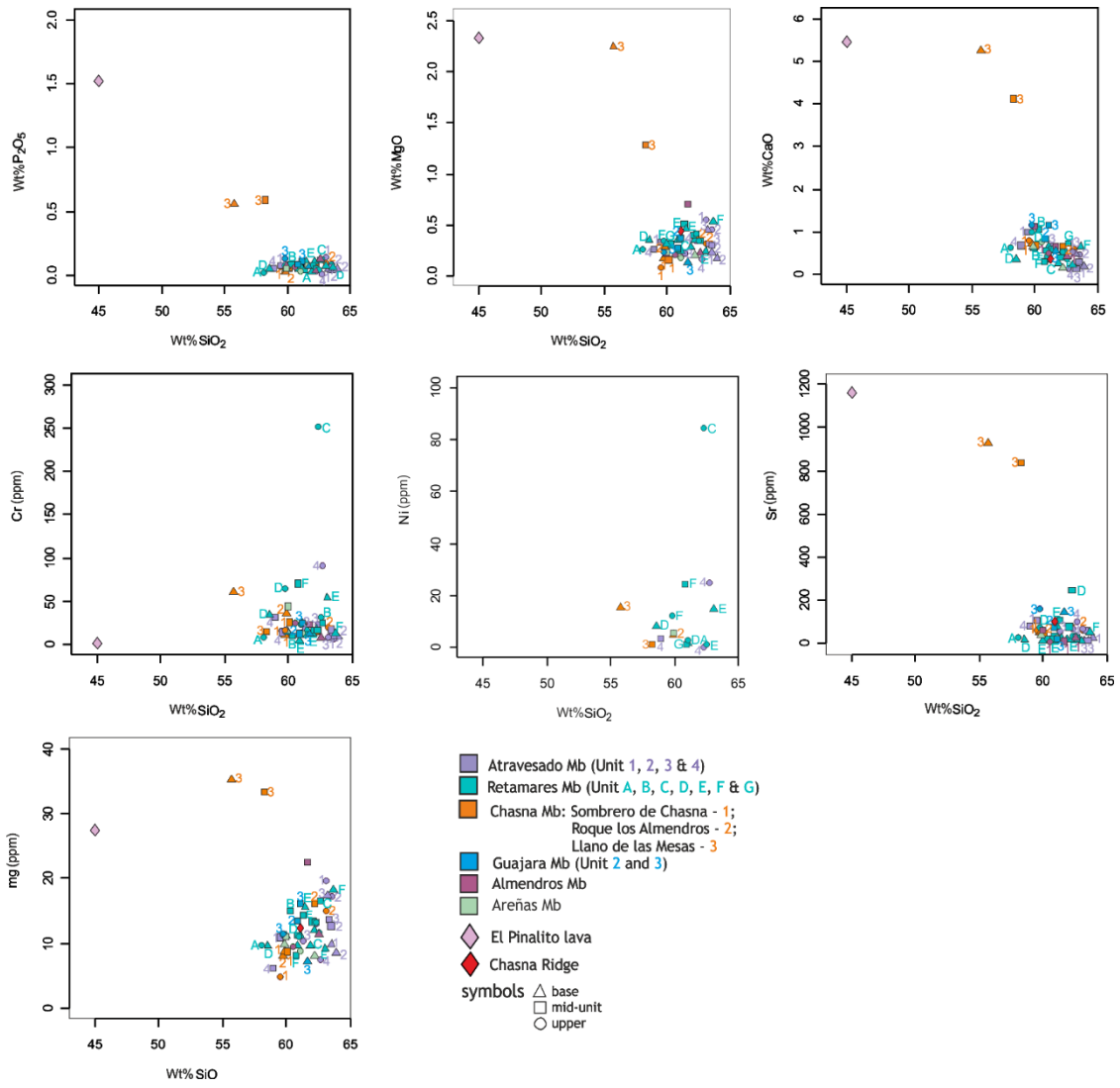


Harker plots for additional measured major and trace elements against $SiO_2$.

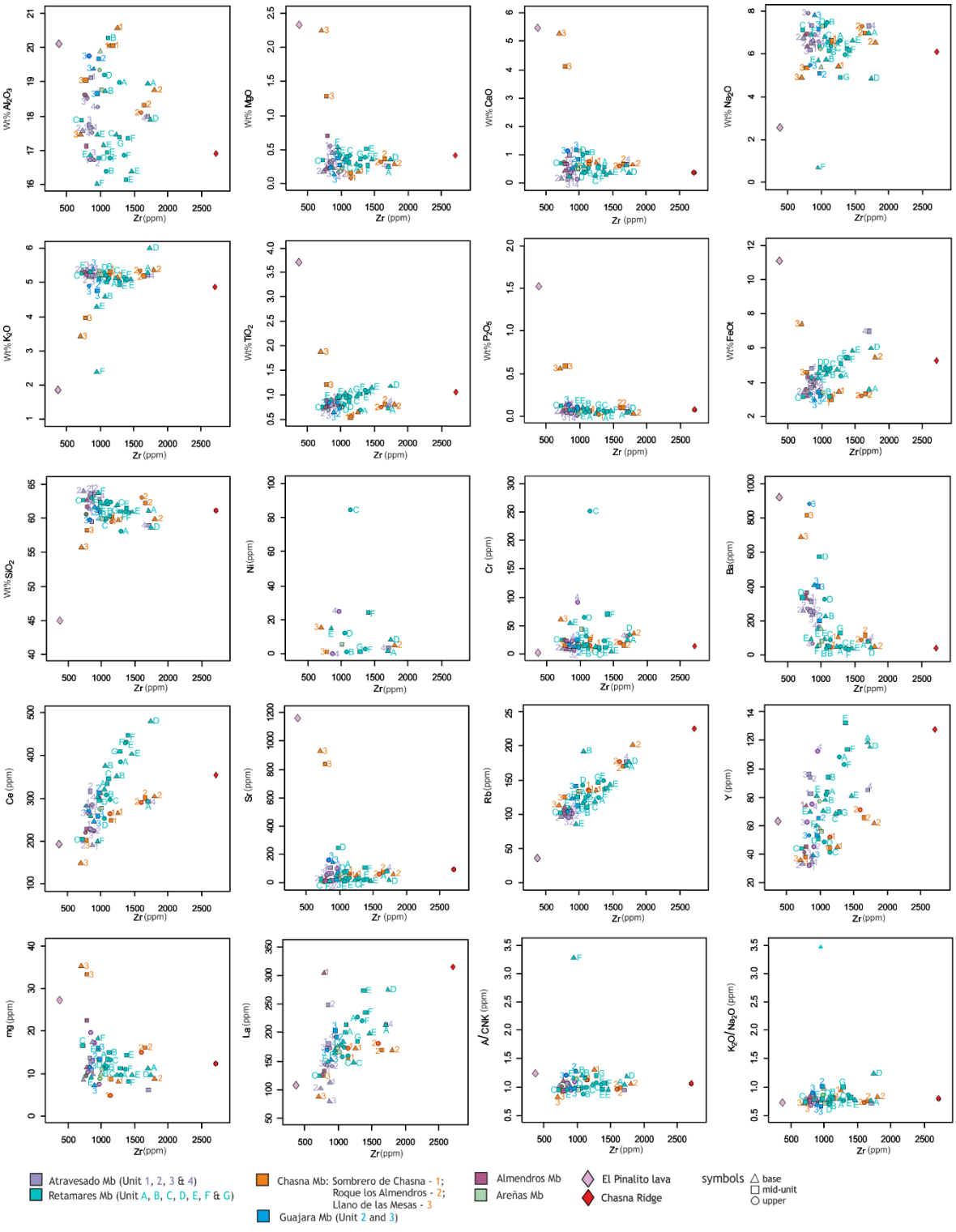


Harker plots for all measured major and trace elements against Zr.

# Appendix V

NBO/T(ratio between non-bridging oxygens and isolated tetrahedron cations) calculations for both ExRED (assumes all Fe as Fe2+) and ExOX (assumes all Fe as Fe3+) for each of the glass samples (Chapter 7).

| PP-02 (ExOX) | | | | | | | | | | | NBO/T | |
|---|---|---|---|---|---|---|---|---|---|---|---|---|
| Ar | Mr | M | O | Oxid | DRY | H2O | wt% | wt%/Mr | Molfrac | mol T | mol O | EXCESS | 1.98966 |
| 28.086 | 60.084 | 1 | 2 | SiO2 | 62.220 | | 62.63 | 1.04 | 0.71059 | 0.71 | 1.4212 | NBO/T | 0.0406 |
| 47.880 | 79.878 | 1 | 2 | TiO2 | 0.940 | | 0.95 | 0.01 | 0.00808 | 0.01 | 0.0162 | Al (I) | 1.03450 |
| 26.982 | 101.961 | 2 | 3 | Al2O3 | 16.410 | | 16.52 | 0.16 | 0.11044 | 0.22 | 0.3313 | Al (I+II | 1.15221 |
| 55.847 | 159.691 | 2 | 3 | Fe2O3 | 4.720 | | 4.75 | 0.03 | 0.02028 | 0.04 | 0.0608 | | |
| 10.811 | 69.619 | 2 | 3 | B2O3 | | | 0.00 | 0.00 | 0.00000 | 0 | 0 | | |
| 22.990 | 61.979 | 2 | 1 | Na2O | 8.760 | | 8.82 | 0.14 | 0.09699 | | 0.097 | | |
| 39.098 | 94.195 | 2 | 1 | K2O | 5.250 | | 5.28 | 0.06 | 0.03825 | | 0.0382 | | |
| 1.008 | 17.007 | 1 | 1 | OH' | | | 0.00 | 0.00 | 0.00000 | | 0 | | |
| 1.008 | 18.015 | 2 | 1 | H2O | | | 0.00 | 0.00 | 0.00000 | | 0 | | |
| 6.941 | 29.881 | 2 | 1 | Li2O | | | 0.00 | 0.00 | 0.00000 | | 0 | | |
| 85.468 | 186.935 | 2 | 1 | Rb2O | | | 0.00 | 0.00 | 0.00000 | | 0 | | |
| 132.905 | 281.809 | 2 | 1 | Cs2O | | | 0.00 | 0.00 | 0.00000 | | 0 | | |
| 24.305 | 40.304 | 1 | 1 | MgO | 0.530 | | 0.53 | 0.01 | 0.00902 | | 0.009 | | |
| 40.078 | 56.077 | 1 | 1 | CaO | 0.520 | | 0.52 | 0.01 | 0.00636 | | 0.0064 | | |
| 87.620 | 103.619 | 1 | 1 | SrO | | | 0.00 | 0.00 | 0.00000 | | 0 | | |
| 137.327 | 153.326 | 1 | 1 | BaO | | | 0.00 | 0.00 | 0.00000 | | 0 | | |
| 55.847 | 71.846 | 1 | 1 | FeO | 0.000 | | 0.00 | 0.00 | 0.00000 | | 0 | | |
| 54.938 | 70.937 | 1 | 1 | MnO | 0.000 | | 0.00 | 0.00 | 0.00000 | | 0 | | |
| | | | | Summe | 99.350 | 0.000 | 100 | 1.47 | 1 | 0.98 | 1.9801 | | |

| TN-37 (ExRED) | | | | | | | | | | | NBO/T | |
|---|---|---|---|---|---|---|---|---|---|---|---|---|
| Ar | Mr | M | O | Oxid | DRY | H2O | wt% | wt%/Mr | Molfrac | mol T | mol O | EXCESS | 5.26065 |
| 28.086 | 60.084 | 1 | 2 | SiO2 | 62.600 | | 63.09 | 1.05 | 0.70260 | 0.7 | 1.4052 | NBO/T | 0.11106 |
| 47.880 | 79.878 | 1 | 2 | TiO2 | 0.730 | | 0.74 | 0.01 | 0.00616 | 0.01 | 0.0123 | Al (I) | 1.07481 |
| 26.982 | 101.961 | 2 | 3 | Al2O3 | 18.040 | | 18.18 | 0.18 | 0.11932 | 0.24 | 0.3579 | Al (I+II | 1.44090 |
| 55.847 | 159.691 | 2 | 3 | Fe2O3 | 0.000 | | 0.00 | 0.00 | 0.00000 | 0 | 0 | | |
| 10.811 | 69.619 | 2 | 3 | B2O3 | | | 0.00 | 0.00 | 0.00000 | 0 | 0 | | |
| 22.990 | 61.979 | 2 | 1 | Na2O | 7.970 | | 8.03 | 0.13 | 0.08672 | | 0.0867 | | |
| 39.098 | 94.195 | 2 | 1 | K2O | 5.800 | | 5.85 | 0.06 | 0.04152 | | 0.0415 | | |
| 1.008 | 17.007 | 1 | 1 | OH' | | | 0.00 | 0.00 | 0.00000 | | 0 | | |
| 1.008 | 18.015 | 2 | 1 | H2O | | | 0.00 | 0.00 | 0.00000 | | 0 | | |
| 6.941 | 29.881 | 2 | 1 | Li2O | | | 0.00 | 0.00 | 0.00000 | | 0 | | |
| 85.468 | 186.935 | 2 | 1 | Rb2O | | | 0.00 | 0.00 | 0.00000 | | 0 | | |
| 132.905 | 281.809 | 2 | 1 | Cs2O | | | 0.00 | 0.00 | 0.00000 | | 0 | | |
| 24.305 | 40.304 | 1 | 1 | MgO | 0.460 | | 0.46 | 0.01 | 0.00770 | | 0.0077 | | |
| 40.078 | 56.077 | 1 | 1 | CaO | 0.760 | | 0.77 | 0.01 | 0.00914 | | 0.0091 | | |
| 87.620 | 103.619 | 1 | 1 | SrO | | | 0.00 | 0.00 | 0.00000 | | 0 | | |
| 137.327 | 153.326 | 1 | 1 | BaO | | | 0.00 | 0.00 | 0.00000 | | 0 | | |
| 55.847 | 71.846 | 1 | 1 | FeO | 2.860 | | 2.88 | 0.04 | 0.02684 | | 0.0268 | | |
| 54.938 | 70.937 | 1 | 1 | MnO | 0.000 | | 0.00 | 0.00 | 0.00000 | | 0 | | |
| | | | | Summe | 99.220 | 0.000 | 100 | 1.49 | 1 | 0.95 | 1.9474 | | |

| TN-37 (ExOX) | | | | | | | | | | | NBO/T | |
|---|---|---|---|---|---|---|---|---|---|---|---|---|
| Ar | Mr | M | O | Oxid | DRY | H2O | wt% | wt%/Mr | Molfrac | mol T | mol O | EXCESS | 1.25008 |
| 28.086 | 60.084 | 1 | 2 | SiO2 | 62.600 | | 62.89 | 1.05 | 0.71215 | 0.71 | 1.4243 | NBO/T | 0.02532 |
| 47.880 | 79.878 | 1 | 2 | TiO2 | 0.730 | | 0.73 | 0.01 | 0.00625 | 0.01 | 0.0125 | Al (I) | 0.96608 |
| 26.982 | 101.961 | 2 | 3 | Al2O3 | 18.040 | | 18.12 | 0.18 | 0.12094 | 0.24 | 0.3628 | Al (I+II | 1.09291 |
| 55.847 | 159.691 | 2 | 3 | Fe2O3 | 3.180 | | 3.19 | 0.02 | 0.01361 | 0.03 | 0.0408 | | |
| 10.811 | 69.619 | 2 | 3 | B2O3 | | | 0.00 | 0.00 | 0.00000 | 0 | 0 | | |
| 22.990 | 61.979 | 2 | 1 | Na2O | 7.970 | | 8.01 | 0.13 | 0.08790 | | 0.0879 | | |
| 39.098 | 94.195 | 2 | 1 | K2O | 5.800 | | 5.83 | 0.06 | 0.04209 | | 0.0421 | | |
| 1.008 | 17.007 | 1 | 1 | OH' | | | 0.00 | 0.00 | 0.00000 | | 0 | | |
| 1.008 | 18.015 | 2 | 1 | H2O | | | 0.00 | 0.00 | 0.00000 | | 0 | | |
| 6.941 | 29.881 | 2 | 1 | Li2O | | | 0.00 | 0.00 | 0.00000 | | 0 | | |
| 85.468 | 186.935 | 2 | 1 | Rb2O | | | 0.00 | 0.00 | 0.00000 | | 0 | | |
| 132.905 | 281.809 | 2 | 1 | Cs2O | | | 0.00 | 0.00 | 0.00000 | | 0 | | |
| 24.305 | 40.304 | 1 | 1 | MgO | 0.460 | | 0.46 | 0.01 | 0.00780 | | 0.0078 | | |
| 40.078 | 56.077 | 1 | 1 | CaO | 0.760 | | 0.76 | 0.01 | 0.00926 | | 0.0093 | | |
| 87.620 | 103.619 | 1 | 1 | SrO | | | 0.00 | 0.00 | 0.00000 | | 0 | | |
| 137.327 | 153.326 | 1 | 1 | BaO | | | 0.00 | 0.00 | 0.00000 | | 0 | | |
| 55.847 | 71.846 | 1 | 1 | FeO | 0.000 | | 0.00 | 0.00 | 0.00000 | | 0 | | |
| 54.938 | 70.937 | 1 | 1 | MnO | 0.000 | | 0.00 | 0.00 | 0.00000 | | 0 | | |
| | | | | Summe | 99.540 | 0.000 | 100 | 1.47 | 1 | 0.99 | 1.9875 | | |

| PP-02 (ExRED) | | | | | | | | | | NBO/T | | | |
|---|---|---|---|---|---|---|---|---|---|---|---|---|---|
| Ar | Mr | M | O | Oxid | DRY | H2O | wt% | wt%/Mr | Molfrac | mol T | mol O | EXCESS | 7.90758 |
| 28.086 | 60.084 | 1 | 2 | SiO2 | 62.220 | | 62.93 | 1.05 | 0.69651 | 0.7 | 1.393 | NBO/T | 0.17173 |
| 47.880 | 79.878 | 1 | 2 | TiO2 | 0.940 | | 0.95 | 0.01 | 0.00792 | 0.01 | 0.0158 | Al (I) | 1.22449 |
| 26.982 | 101.961 | 2 | 3 | Al2O3 | 16.410 | | 16.60 | 0.16 | 0.10825 | 0.22 | 0.3248 | Al (I+II | 1.73049 |
| 55.847 | 159.691 | 2 | 3 | Fe2O3 | 0.000 | | 0.00 | 0.00 | 0.00000 | 0 | 0 | | |
| 10.811 | 69.619 | 2 | 3 | B2O3 | | | 0.00 | 0.00 | 0.00000 | 0 | 0 | | |
| 22.990 | 61.979 | 2 | 1 | Na2O | 8.760 | | 8.86 | 0.14 | 0.09506 | | 0.0951 | | |
| 39.098 | 94.195 | 2 | 1 | K2O | 5.250 | | 5.31 | 0.06 | 0.03749 | | 0.0375 | | |
| 1.008 | 17.007 | 1 | 1 | OH' | | | 0.00 | 0.00 | 0.00000 | | 0 | | |
| 1.008 | 18.015 | 2 | 1 | H2O | | | 0.00 | 0.00 | 0.00000 | | 0 | | |
| 6.941 | 29.881 | 2 | 1 | Li2O | | | 0.00 | 0.00 | 0.00000 | | 0 | | |
| 85.468 | 186.935 | 2 | 1 | Rb2O | | | 0.00 | 0.00 | 0.00000 | | 0 | | |
| 132.905 | 281.809 | 2 | 1 | Cs2O | | | 0.00 | 0.00 | 0.00000 | | 0 | | |
| 24.305 | 40.304 | 1 | 1 | MgO | 0.530 | | 0.54 | 0.01 | 0.00884 | | 0.0088 | | |
| 40.078 | 56.077 | 1 | 1 | CaO | 0.520 | | 0.53 | 0.01 | 0.00624 | | 0.0062 | | |
| 87.620 | 103.619 | 1 | 1 | SrO | | | 0.00 | 0.00 | 0.00000 | | 0 | | |
| 137.327 | 153.326 | 1 | 1 | BaO | | | 0.00 | 0.00 | 0.00000 | | 0 | | |
| 55.847 | 71.846 | 1 | 1 | FeO | 4.240 | | 4.29 | 0.06 | 0.03969 | | 0.0397 | | |
| 54.938 | 70.937 | 1 | 1 | MnO | 0.000 | | 0.00 | 0.00 | 0.00000 | | 0 | | |
| | | | | Summe | 98.870 | 0.000 | 100 | 1.5 | 1 | 0.92 | 1.9209 | | |

| TN-09 (ExOX) | | | | | | | | | | NBO/T | | | |
|---|---|---|---|---|---|---|---|---|---|---|---|---|---|
| Ar | Mr | M | O | Oxid | DRY | H2O | wt% | wt%/Mr | Molfrac | mol T | mol O | EXCESS | 2.25906 |
| 28.086 | 60.084 | 1 | 2 | SiO2 | 61.870 | | 62.17 | 1.03 | 0.70649 | 0.71 | 1.413 | NBO/T | 0.04623 |
| 47.880 | 79.878 | 1 | 2 | TiO2 | 0.950 | | 0.95 | 0.01 | 0.00816 | 0.01 | 0.0163 | Al (I) | 1.06635 |
| 26.982 | 101.961 | 2 | 3 | Al2O3 | 16.300 | | 16.38 | 0.16 | 0.10968 | 0.22 | 0.329 | Al (I+II | 1.17195 |
| 55.847 | 159.691 | 2 | 3 | Fe2O3 | 5.050 | | 5.07 | 0.03 | 0.02170 | 0.04 | 0.0651 | | |
| 10.811 | 69.619 | 2 | 3 | B2O3 | | | 0.00 | 0.00 | 0.00000 | 0 | 0 | | |
| 22.990 | 61.979 | 2 | 1 | Na2O | 9.300 | | 9.34 | 0.15 | 0.10295 | | 0.1029 | | |
| 39.098 | 94.195 | 2 | 1 | K2O | 5.100 | | 5.12 | 0.05 | 0.03715 | | 0.0371 | | |
| 1.008 | 17.007 | 1 | 1 | OH' | | | 0.00 | 0.00 | 0.00000 | | 0 | | |
| 1.008 | 18.015 | 2 | 1 | H2O | | | 0.00 | 0.00 | 0.00000 | | 0 | | |
| 6.941 | 29.881 | 2 | 1 | Li2O | | | 0.00 | 0.00 | 0.00000 | | 0 | | |
| 85.468 | 186.935 | 2 | 1 | Rb2O | | | 0.00 | 0.00 | 0.00000 | | 0 | | |
| 132.905 | 281.809 | 2 | 1 | Cs2O | | | 0.00 | 0.00 | 0.00000 | | 0 | | |
| 24.305 | 40.304 | 1 | 1 | MgO | 0.470 | | 0.47 | 0.01 | 0.00800 | | 0.008 | | |
| 40.078 | 56.077 | 1 | 1 | CaO | 0.480 | | 0.48 | 0.01 | 0.00587 | | 0.0059 | | |
| 87.620 | 103.619 | 1 | 1 | SrO | | | 0.00 | 0.00 | 0.00000 | | 0 | | |
| 137.327 | 153.326 | 1 | 1 | BaO | | | 0.00 | 0.00 | 0.00000 | | 0 | | |
| 55.847 | 71.846 | 1 | 1 | FeO | 0.000 | | 0.00 | 0.00 | 0.00000 | | 0 | | |
| 54.938 | 70.937 | 1 | 1 | MnO | 0.000 | | 0.00 | 0.00 | 0.00000 | | 0 | | |
| | | | | Summe | 99.520 | 0.000 | 100 | 1.46 | 1 | 0.98 | 1.9774 | | |

| TN-09 (ExRED) | | | | | | | | | | NBO/T | | | |
|---|---|---|---|---|---|---|---|---|---|---|---|---|---|
| Ar | Mr | M | O | Oxid | DRY | H2O | wt% | wt%/Mr | Molfrac | mol T | mol O | EXCESS | 8.57844 |
| 28.086 | 60.084 | 1 | 2 | SiO2 | 61.870 | | 62.49 | 1.04 | 0.69151 | 0.69 | 1.383 | NBO/T | 0.18767 |
| 47.880 | 79.878 | 1 | 2 | TiO2 | 0.950 | | 0.96 | 0.01 | 0.00799 | 0.01 | 0.016 | Al (I) | 1.27729 |
| 26.982 | 101.961 | 2 | 3 | Al2O3 | 16.300 | | 16.46 | 0.16 | 0.10736 | 0.21 | 0.3221 | Al (I+II | 1.79905 |
| 55.847 | 159.691 | 2 | 3 | Fe2O3 | 0.000 | | 0.00 | 0.00 | 0.00000 | 0 | 0 | | |
| 10.811 | 69.619 | 2 | 3 | B2O3 | | | 0.00 | 0.00 | 0.00000 | 0 | 0 | | |
| 22.990 | 61.979 | 2 | 1 | Na2O | 9.300 | | 9.39 | 0.15 | 0.10077 | | 0.1008 | | |
| 39.098 | 94.195 | 2 | 1 | K2O | 5.100 | | 5.15 | 0.05 | 0.03636 | | 0.0364 | | |
| 1.008 | 17.007 | 1 | 1 | OH' | | | 0.00 | 0.00 | 0.00000 | | 0 | | |
| 1.008 | 18.015 | 2 | 1 | H2O | | | 0.00 | 0.00 | 0.00000 | | 0 | | |
| 6.941 | 29.881 | 2 | 1 | Li2O | | | 0.00 | 0.00 | 0.00000 | | 0 | | |
| 85.468 | 186.935 | 2 | 1 | Rb2O | | | 0.00 | 0.00 | 0.00000 | | 0 | | |
| 132.905 | 281.809 | 2 | 1 | Cs2O | | | 0.00 | 0.00 | 0.00000 | | 0 | | |
| 24.305 | 40.304 | 1 | 1 | MgO | 0.470 | | 0.47 | 0.01 | 0.00783 | | 0.0078 | | |
| 40.078 | 56.077 | 1 | 1 | CaO | 0.480 | | 0.48 | 0.01 | 0.00575 | | 0.0057 | | |
| 87.620 | 103.619 | 1 | 1 | SrO | | | 0.00 | 0.00 | 0.00000 | | 0 | | |
| 137.327 | 153.326 | 1 | 1 | BaO | | | 0.00 | 0.00 | 0.00000 | | 0 | | |
| 55.847 | 71.846 | 1 | 1 | FeO | 4.540 | | 4.59 | 0.06 | 0.04244 | | 0.0424 | | |
| 54.938 | 70.937 | 1 | 1 | MnO | 0.000 | | 0.00 | 0.00 | 0.00000 | | 0 | | |
| | | | | Summe | 99.010 | 0.000 | 100 | 1.5 | 1 | 0.91 | 1.9142 | | |

| TN-31 (ExRED) | | | | | | | | | | NBO/T | | | |
|---|---|---|---|---|---|---|---|---|---|---|---|---|---|
| Ar | Mr | M | O | Oxid | DRY | H2O | wt% | wt%Mr | Molfrac | mol T | mol O | EXCESS | 5.78852 |
| 28.086 | 60.084 | 1 | 2 | SiO2 | 60.860 | | 61.23 | 1.02 | 0.68456 | 0.68 | 1.3691 | NBO/T | 0.12288 |
| 47.880 | 79.878 | 1 | 2 | TiO2 | 0.750 | | 0.75 | 0.01 | 0.00635 | 0.01 | 0.0127 | Al (I) | 1.12540 |
| 26.982 | 101.961 | 2 | 3 | Al2O3 | 18.950 | | 19.06 | 0.19 | 0.12561 | 0.25 | 0.3768 | Al (I+II | 1.46085 |
| 55.847 | 159.691 | 2 | 3 | Fe2O3 | 0.000 | | 0.00 | 0.00 | 0.00000 | 0 | 0 | | |
| 10.811 | 69.619 | 2 | 3 | B2O3 | | | 0.00 | 0.00 | 0.00000 | 0 | 0 | | |
| 22.990 | 61.979 | 2 | 1 | Na2O | 9.450 | | 9.51 | 0.15 | 0.10304 | | 0.103 | | |
| 39.098 | 94.195 | 2 | 1 | K2O | 5.340 | | 5.37 | 0.06 | 0.03831 | | 0.0383 | | |
| 1.008 | 17.007 | 1 | 1 | OH' | | | 0.00 | 0.00 | 0.00000 | | 0 | | |
| 1.008 | 18.015 | 2 | 1 | H2O | | | 0.00 | 0.00 | 0.00000 | | 0 | | |
| 6.941 | 29.881 | 2 | 1 | Li2O | | | 0.00 | 0.00 | 0.00000 | | 0 | | |
| 85.468 | 186.935 | 2 | 1 | Rb2O | | | 0.00 | 0.00 | 0.00000 | | 0 | | |
| 132.905 | 281.809 | 2 | 1 | Cs2O | | | 0.00 | 0.00 | 0.00000 | | 0 | | |
| 24.305 | 40.304 | 1 | 1 | MgO | 0.340 | | 0.34 | 0.01 | 0.00570 | | 0.0057 | | |
| 40.078 | 56.077 | 1 | 1 | CaO | 0.580 | | 0.58 | 0.01 | 0.00699 | | 0.007 | | |
| 87.620 | 103.619 | 1 | 1 | SrO | | | 0.00 | 0.00 | 0.00000 | | 0 | | |
| 137.327 | 153.326 | 1 | 1 | BaO | | | 0.00 | 0.00 | 0.00000 | | 0 | | |
| 55.847 | 71.846 | 1 | 1 | FeO | 3.130 | | 3.15 | 0.04 | 0.02944 | | 0.0294 | | |
| 54.938 | 70.937 | 1 | 1 | MnO | 0.000 | | 0.00 | 0.00 | 0.00000 | | 0 | | |
| | | | | Summe | 99.400 | 0.000 | 100 | 1.49 | 1 | 0.94 | 1.9421 | | |

| TN-31 (ExOX) | | | | | | | | | | NBO/T | | | |
|---|---|---|---|---|---|---|---|---|---|---|---|---|---|
| Ar | Mr | M | O | Oxid | DRY | H2O | wt% | wt%Mr | Molfrac | mol T | mol O | EXCESS | 1.3876 |
| 28.086 | 60.084 | 1 | 2 | SiO2 | 60.860 | | 61.01 | 1.02 | 0.69475 | 0.69 | 1.3895 | NBO/T | 0.02814 |
| 47.880 | 79.878 | 1 | 2 | TiO2 | 0.750 | | 0.75 | 0.01 | 0.00644 | 0.01 | 0.0129 | Al (I) | 1.00699 |
| 26.982 | 101.961 | 2 | 3 | Al2O3 | 18.950 | | 19.00 | 0.19 | 0.12748 | 0.25 | 0.3824 | Al (I+II | 1.09740 |
| 55.847 | 159.691 | 2 | 3 | Fe2O3 | 3.490 | | 3.50 | 0.02 | 0.01499 | 0.03 | 0.045 | | |
| 10.811 | 69.619 | 2 | 3 | B2O3 | | | 0.00 | 0.00 | 0.00000 | 0 | 0 | | |
| 22.990 | 61.979 | 2 | 1 | Na2O | 9.450 | | 9.47 | 0.15 | 0.10458 | | 0.1046 | | |
| 39.098 | 94.195 | 2 | 1 | K2O | 5.340 | | 5.35 | 0.06 | 0.03888 | | 0.0389 | | |
| 1.008 | 17.007 | 1 | 1 | OH' | | | 0.00 | 0.00 | 0.00000 | | 0 | | |
| 1.008 | 18.015 | 2 | 1 | H2O | | | 0.00 | 0.00 | 0.00000 | | 0 | | |
| 6.941 | 29.881 | 2 | 1 | Li2O | | | 0.00 | 0.00 | 0.00000 | | 0 | | |
| 85.468 | 186.935 | 2 | 1 | Rb2O | | | 0.00 | 0.00 | 0.00000 | | 0 | | |
| 132.905 | 281.809 | 2 | 1 | Cs2O | | | 0.00 | 0.00 | 0.00000 | | 0 | | |
| 24.305 | 40.304 | 1 | 1 | MgO | 0.340 | | 0.34 | 0.01 | 0.00579 | | 0.0058 | | |
| 40.078 | 56.077 | 1 | 1 | CaO | 0.580 | | 0.58 | 0.01 | 0.00709 | | 0.0071 | | |
| 87.620 | 103.619 | 1 | 1 | SrO | | | 0.00 | 0.00 | 0.00000 | | 0 | | |
| 137.327 | 153.326 | 1 | 1 | BaO | | | 0.00 | 0.00 | 0.00000 | | 0 | | |
| 55.847 | 71.846 | 1 | 1 | FeO | 0.000 | | 0.00 | 0.00 | 0.00000 | | 0 | | |
| 54.938 | 70.937 | 1 | 1 | MnO | 0.000 | | 0.00 | 0.00 | 0.00000 | | 0 | | |
| | | | | Summe | 99.760 | 0.000 | 100 | 1.46 | 1 | 0.99 | 1.9861 | | |